UNIVERSIDADE FEDERAL DO RIO GRANDE DO SUL
INSTITUTO DE GEOCIÊNCIAS
PROGRAMA DE PÓS-GRADUAÇÃO EM GEOCIÊNCIAS

EVOLUÇÃO GEOLÓGICA (800–560 Ma) DO SETOR CENTRAL DO CINTURÃO DOM FELICIANO COM BASE NO ESTUDO PETROLÓGICO, GEOCRONOLÓGICO E DE PROVENIÊNCIA DOS COMPLEXOS PORONGOS, VÁRZEA DO CAPIVARITA E PASSO FEIO, RS

MATHEUS ARIEL BATTISTI

ORIENTADORA – Prof. Dra. Maria de Fátima Bitencourt
COORIENTADOR – Prof. Dr. Jiří Konopásek

Porto Alegre – Março, 2022

EVOLUÇÃO GEOLÓGICA (800–560 Ma) DO SETOR CENTRAL DO CINTURÃO DOM FELICIANO COM BASE NO ESTUDO PETROLÓGICO, GEOCRONOLÓGICO E DE PROVENIÊNCIA DOS COMPLEXOS PORONGOS, VÁRZEA DO CAPIVARITA E PASSO FEIO, RS

MATHEUS ARIEL BATTISTI

ORIENTADORA – Prof. Dra. Maria de Fátima Bitencourt
COORIENTADOR – Prof. Dr. Jiří Konopásek

BANCA EXAMINADORA
Profª. Dra. Brenda Chung da Rocha – Instituto de Geociências - IGC, Universidade de São Paulo (USP)
Profª. Dra. Cristine Lenz – Departamento de Geologia, Universidade Federal de Sergipe (UFS)
Prof. Dr. Sebastián Oriolo – Consejo Nacional de Investigaciones Científicas y Técnicas (CONICET) e Universidad de Buenos Aires (UBA)

Tese de doutorado apresentada como requisito parcial para a obtenção do Título de Doutor em Ciências.

Porto Alegre – Março, 2022

CIP - Catalogação na Publicação

Aos meus avós, Maria e Valdomiro

À todas as crianças,
em especial aos nossos amores:
Matteo, Lucca, Bella, Nina e Benjamin

"…Shine on, you crazy diamond!"

…

Come on, you stranger,

you legend, you martyr,

and shine!"

Pink Floyd

AGRADECIMENTOS

Eis que me sento novamente para escrever em agradecimento à muitas pessoas que tornaram esse trabalho possível; e finalizar outro ciclo marcante em minha vida.

Primeiramente agradecer aos meus orientadores, Maria de Fátima Bitencourt e Jiří Konopásek pelos valiosos ensinamentos durante esses quatro anos. Há ainda muito a aprender, mas sei que posso me espelhar em vocês. Obrigado por me acolher tão bem no seu grupo, Fátima. Jiří thank you very much for all your patience and teachings, and also for the amazing fieldtrips here in South America.

Agradeço aos membros da banca avaliadora por disponibilizar seu tempo e entusiasmo para avaliar e discutir essa tese. Dra. Brenda Chung da Rocha, Dra. Cristine Lenz e Dr. Sebastián Oriolo, muito obrigado!

Agradeço também a todos os meus coautores pelas discussões, e pelas coisas que me ensinaram durante o desenvolvimento dos artigos. Agradeço as agências de fomento CAPES e CNPq por investirem e acreditarem na nossa pesquisa, principalmente através do projeto Capes-Diku (CAPES 88881.117872/2016-01, 88887.141226/2017–00/ UTF-2018-10004). Agradeço a UFRGS e ao seu ensino público superior de extrema qualidade pela oportunidade de estudar e representar essa escola.

A minha irmã de sangue, Charline, e aos meus irmãos de coração, Junior, Maurício e Thaize, que sempre me apoiaram, obrigado. Obrigado também por aumentarem a nossa família, com a chegada dos nossos pequenos Matteo, Lucca, Bella, Nina e Benjamin (que antes de nos darmos conta serão tão grandes quanto nós). Ana, Rafa e Alexandre, meus irmãos por ''tabela'' (haha), obrigado! É muito bom compartilhar momentos com todos vocês.

Meus pais, meus heróis, meus grandes amores, nada disso seria possível sem vocês; mãe, pai, obrigado por tudo que me ensinaram! Meus avós, dedico essa tese a vocês, que mesmo sem ter tido a oportunidade estudar muito (ou mesmo de aprender a ler), sempre acreditaram em mim; sinto que esse sonho também é de vocês. Aos meus primos Rodrigo, Cawan, Ruan obrigado pelos momentos de diversão; é sempre importante sorrir em momentos tão difíceis que passamos durante dois anos de pandemia. Ao meu amigo João Augusto, por me mostrar que a vida é simples, obrigado!

Aos meus amigos Pedro, Cícero e Alejandro, que além de amigos, dividiram estadia comigo durante os tempos de doutorado. Ficar em casa na pandemia foi um

pouco mais fácil devido as nossas conversas sobre assuntos aleatórios e aos nossos churrascos sem convidados. Aos amigos que a geologia me proporcionou, que embora poucos nos vemos, sempre é um encontro especial, Thailli, Guilherme, Fernando, Ingrid, Marciéli, Gessé, Alex, Rauflin, Douglas. Obrigado também a turma de *Beverly Hills:* Renato, Christian, Gean, Pedro, Rafael e Erik... bora marcar uma janta? só decidir ''que horas mais ou menos''.

Ao maravilhoso grupo do Magmatismo Sintectônico: uma família muito unida e as vezes um pouco agitada (mas é um agitado de se amar). Dioni, Steh, Pedrinho, Gepeto, Amós, Camila T., Cris, Diegão, Duda, Felipe, Fran, Paulista, Victor, João, Pezzat, Thay, Elisa, Camila S., obrigado a todos vocês pelos almoços do RU, pelas discussões engrandecedoras de geologia e da vida, pelos cafés pós-almoço com memes e besteiras. Obrigado por todos os campos, sempre uma honra estar ao lado de vocês nessas experiências.

Aos meus amigos que conheci (e "re-conheci") na viagem mais linda de minha vida; cada paisagem, cada momento, foi tudo tão mágico! Obrigado também por embalarem madrugada a fora muitas conversas de *whatsapp* durante a pandemia. Os Andes são tão lindos, que combinam perfeitamente com o espetáculo de pessoas que vocês são! Obrigado pelos momentos únicos durante a viagem, obrigado por poder descontrair com vocês várias vezes, o que foi sem dúvida de suma importância para que hoje eu pudesse estar aqui escrevendo essa tese e esses agradecimentos. Amanda, Bibiana, Brenda, Dionatan, Fernanda, Mariane, Ricardo, Rhoana, muito obrigado! Obrigado duplo para a Amanda que revisou o texto da tese!

To the Tromsø crew: Jack Percival, Paul Heckmann and Petar Pongrac, thank you very much for the great times we spent together in Norway. That was the most amazing experience of my entire life! Hope we can meet again soon to the traditional Friday beer.

Ao elenco multimilionário do Battisti F.C., aquele abraço. Se a gente jogasse um pouco melhor, talvez nem precisaria escrever essa tese (hahaha).

Aos leitores, espero que possam desfrutar do conteúdo disposto aqui e agradeço por seu tempo. A vida é sobretudo uma questão de tempo... de meu tempo dedicado a apresentar a vocês o melhor texto que eu poderia escrever com o tempo e conhecimento que hoje possuo; e de seu tempo, em ler atenciosamente, inclusive essa frase. O conhecimento conecta, e o que eu pude aprender escrevendo essa tese, espero que também vos seja útil.

Obrigado à natureza, a única e eterna expressão de perfeição!

Perdoem-me se esqueci de alguém; mas não se
preocupem, vocês estão em minha memória,
e são, com toda certeza, muito mais que
apenas nomes em um pedaço de papel!

RESUMO

A estratigrafia original de bacias pré-colisionais é em geral bastante modificada durante as colisões devido aos diversos processos orogênicos, incluindo a intensa deformação. O Cinturão Dom Feliciano, localizado no sul do Brasil e Uruguai, é parte de um extenso sistema orogênico neoproterozoico e teve sua estruturação principal desenvolvida por deformação prolongada do final do Criogeniano ao Ediacarano. Portanto, a reconstrução de sua evolução geológica e de suas bacias sedimentares originais é bastante dificultada. Esta tese busca avaliar a história pré-colisional e colisional do setor central do Cinturão Dom Feliciano com base no estudo da relação espacial e temporal dos complexos Porongos, Várzea do Capivarita e Passo Feio. A história pré-colisional do cinturão foi investigada através do estudo geocronológico e de isótopos de oxigênio em cristais de zircão de rochas metavulcânicas intercaladas com as sequências metassedimentares dos complexos Várzea do Capivarita e Porongos. Os resultados trouxeram robustas evidências de uma conexão pré-colisional, em *ca.* 800–770 Ma, entre as rochas do antepaís e do além-país do Cinturão Dom Feliciano. A história colisional do cinturão foi investigada através do estudo de amostras metassedimentares dos complexos Porongos e Passo Feio por meio de modelamento das condições P–T, determinações geocronológicas de Lu–Hf granada-rocha total e de U–Pb *SIMS* em monazita. Os novos dados permitem estabelecer dois períodos distintos de espessamento crustal, o primeiro em *ca.* 660 Ma e o segundo em *ca.* 565 Ma e, por consequência, trazem evidências de migração para oeste da frente orogênica em um sistema orogênico transpressivo de longa duração. Os ambientes sedimentares originais e suas relações foram também investigados por meio de dados geoquímicos e isotópicos (Sr-Nd) compilados da literatura para amostras metavulcânicas intercaladas com metassedimentos dos três complexos estudados. Estes dados, em conjunto com novos dados geoquímicos, de Sr-Nd e de U-Pb em zircão obtidos para os complexos Passo Feio e Porongos, sugerem pela primeira vez um magmatismo compartilhado entre o Complexo Passo Feio e a sequência Capané do Complexo Porongos em *ca.* 600–580 Ma. Tais dados também corroboram um magmatismo compartilhado em *ca.* 810–770 Ma entre o Complexo Várzea do Capivarita e a sequência Cerro da Árvore do Complexo Porongos.

Palavras-chave: *bacias pré-colisionais; rochas metavulcânicas; espessamento crustal; sistema orogênico transpressivo; Cinturão Dom Feliciano.*

ABSTRACT

The original stratigraphy of pre-collisional basins is difficult to reconstruct due to the subsequent mountain-building processes, including extensive deformation. The Dom Feliciano Belt, situated in southern Brazil and Uruguay, is part of an extensive Neoproterozoic orogenic system which had its main structure developed by protracted deformation from the Cryogenian to the Ediacaran. Therefore, reconstructing its evolution and the stratigraphy of its original basins is arduous. The present thesis aims at evaluating the pre-collisional to collisional history of the Dom Feliciano Belt central sector, based on the spatial-temporal relationships of the Porongos, Várzea do Capivarita and Passo Feio complexes. The orogen pre-collisional history was investigated through geochronological and oxygen isotope studies in zircon from metavolcanic rocks interbedded with the metasedimentary sequences of the Várzea do Capivarita and Porongos complexes. The results provide strong evidence of a pre-collisional relationship, at *ca.* 800–770 Ma, between the Dom Feliciano Belt foreland and hinterland rocks. The collisional history of the belt was investigated through P–T petrogenetic modelling, Lu-Hf garnet-whole-rock and U–Pb SIMS monazite dating performed in metasedimentary samples from the Porongos and Passo Feio complexes. The obtained data establish two distinct periods of crustal thickening, the first at *ca.* 660 Ma and the second at *ca.* 565 Ma. Evidence points to an orogenic front migration towards the west in a long-lived transpressive orogenic system. The original sedimentary environments and the relationship of the three studied complexes were also investigated through geochemical and isotopic (Sr-Nd) data compiled from the literature for metavolcanic samples interbedded with their metasediments. The literature dataset combined with new geochemical, Sr-Nd and U-Pb data obtained for the Passo Feio and Porongos complexes leads to the novel conclusion of a shared tectonic evolution between the Passo Feio Complex and the Porongos Complex (Capané sequence) at *ca.* 600-580 Ma. Such data also corroborate the presence of a shared magmatism at *ca.* 810–770 Ma between the Várzea do Capivarita Complex and the Porongos Complex (Cerro da Árvore sequence).

Keywords: *pre-collisional basins; metavolcanic rocks; crustal thickening; transpressive orogenic system; Dom Feliciano Belt*

LISTA DE ILUSTRAÇÕES

LISTA DE TABELAS

SUMÁRIO

ESTRUTURA DA TESE

Esta tese de doutorado está estruturada em três artigos submetidos em periódicos classificados nos estratos Qualis-CAPES A1, conforme as normas estabelecidas pelo Programa de Pós-Graduação em Geociências da Universidade Federal do Rio Grande do Sul. A sua organização compreende as seguintes partes principais:

TEXTO INTEGRADOR:

Na primeira parte da tese é apresentado o texto Integrador composto pelos seguintes capítulos: introdução; objetivos da pesquisa; os materiais e métodos utilizados; o estado da arte do tema da pesquisa; resumo dos resultados; considerações finais; referências bibliográficas.

O tema abordado no estado da arte foi o arcabouço teórico necessário para a realização de estudos de ''petrocronologia''. O crescente emprego e a escassez de bibliografia em língua portuguesa embasaram a escolha deste tópico em detrimento de outros assuntos também importantes, tal como orogênese, por exemplo. O estado da arte está organizado a partir de quatro tópicos principais: i) introdução à petrocronologia; ii) conceitos termodinâmicos aplicados às rochas metamórficas; iii) petrocronologia da monazita vs granada; iv) geologia Isotópica.

ARTIGOS:

Na segunda parte da tese são apresentados os artigos científicos. Os manuscritos são idênticos aos submetidos, porém as figuras foram dispostas dentro do texto, para facilitar sua leitura. As tabelas são apresentadas ao fim de cada manuscrito.

O primeiro artigo intitulado, "*Reconstruction of a volcano-sedimentary environment shared by the Porongos and Várzea do Capivarita Complexes at 790 Ma, Dom Feliciano Belt, southern Brazil*" de Battisti, M.A.; Bitencourt, M.F.; Schmitt, R.S., Nardi, L.V.S.; Martil, M.M.D.; De Toni, G.B.; Pimentel, M.; Armstrong, R.; Konopásek, J., foi submetido ao periódico *Precambrian Research*.

O segundo artigo, intitulado "*Petrochronology of the central Dom Feliciano Belt foreland, southernmost Brazil*" de Battisti, M.A.; Konopásek, J; Bitencourt, M.F.; Sláma, J. Percival, J.J.; De Toni, G.B.; Carvalho da Silva, S.; Costa, E.O.; Trubač, J., foi submetido ao periódico *Journal of Metamorphic Geology*.

O terceiro artigo, intitulado "*Unravelling major magmatic episodes from metamorphic sequences of the Dom Feliciano Belt central sector, Brazil – a comparative study of geochronology, elemental geochemistry, and Sr-Nd data*" de Battisti, M.A.; Bitencourt, M.F.; Nardi, L.V.S.; Florisbal, L.M.; Ackerman, L.; Sláma, J.; Padilha, D. F., foi submetido ao periódico *Lithos*.

ANEXOS:

Na terceira parte da tese são apresentados anexos com os dados complementares de cada artigo. Por fim, é apresentado o resumo do artigo intitulado *''Dissolution precipitation creep as a process for the strain localisation in mafic rocks''* de Lee, A.; Stünitz, H.; Soret, M.; Battisti, M. A. publicado no *Journal of Structural Geology*, desenvolvido durante período de intercâmbio na UiT–*The Arctic University of Norway*.

1. Introdução

A arquitetura original de ambientes pré-colisionais é difícil de reconstruir devido aos processos atuantes durante as colisões (*e.g.* Cawood et al., 2009; Vanderhaeghe, 2012; Chetty, 2017), incluindo intensa deformação, e também devido ao posicionamento de magmas pós-colisionais que mascaram as antigas relações pré-colisão. Assim, bacias pré-colisionais têm sua estratigrafia original comumente bastante modificada durante a deformação (Tavani et al., 2015; Lacombe & Bellahsen, 2016). Além disso, em cinturões de dobras e cavalgamentos (*fold-and-thrust belts – e.g.* Boyer & Elliott, 1982; Sanderson, 1982) fatias de litologias alóctones podem ser transportadas por centenas de quilômetros, muitas vezes causando inversão da estratigrafia original e colocando rochas de alto grau sobre as de baixo grau metamórfico, como pode ser observado nos Himalaias, por exemplo (Harrison et al., 1999). A determinação precisa de tais eventos metamórfico-deformacionais também é essencial para a correta interpretação da evolução dos cinturões orogênicos. No entanto, uma dificuldade que surge dessa questão é que em terrenos metamórficos com evolução prolongada, a separação de eventos de deformação distintos sob um mesmo período de deformação progressiva, às vezes é de difícil reconhecimento devido à superposição de estruturas deformacionais e mineralogia metamórfica semelhantes (*e.g.* Fossen et al., 2019).

O Cinturão Dom Feliciano que se estende da margem leste do sul do Brasil até o Uruguai engloba todas as problemáticas acima discutidas, uma vez que constitui um cinturão de dobras e cavalgamentos no qual a deformação progressiva teve papel crucial na sua estruturação (*e.g.* Oriolo et al., 2016; Martil et al., 2017; De Toni et al., 2020a) e dispõe um extenso magmatismo pós-colisional (*e.g.* Bitencourt & Nardi, 1993, 2000). A complexidade da evolução do cinturão é destacada por trabalhos recentes, seja no que tange a sua configuração pré-colisional em *ca.* 800-770 Ma, interpretada tanto como arco maduro (Koester et al., 2016; Martil et al., 2017; Battisti et al., 2018) ou como rifte/bacia de retro-arco (Konopásek et al., 2018, 2020; Will et al., 2019); seja no que tange seu período contracional de prolongada duração, de *ca.* 650 Ma até <ca. 570 Ma (Philipp et al., 2016b; Oriolo et al., 2016; Battisti et al., 2018; De Toni et al., 2020a, 2021; Percival et al., 2021, 2022). No setor central do Cinturão Dom Feliciano, Rio Grande do Sul, Brasil, algumas relações não muito bem entendidas entre diferentes unidades geológicas provém dessa evolução complexa. Por exemplo, alguns autores sugeriram recentemente uma conexão entre uma porção

das rochas do antepaís (Complexo Porongos) e do além-pais (Complexo Várzea do Capivarita) do Cinturão Dom Feliciano (Martil et al., 2017; Battisti et al., 2018; De Toni et al., 2020b). Possíveis relações entre os complexos Porongos e Passo Feio também foram recentemente sugeridas (Souza, 2020; Costa et al., 2021). No entanto, o significado geológico das relações entre essas três unidades ainda carece de maiores informações, principalmente envolvendo a conexão entre os Complexos Porongos e Passo Feio.

Dessa forma, a presente tese buscou avaliar a história pré-colisional e colisional do setor central do Cinturão Dom Feliciano com base no estudo da relação espacial e temporal dos complexos Porongos, Várzea do Capivarita e Passo Feio. Apesar da dificuldade de se estudar tais situações geológicas, conforme discutido acima, algumas abordagens foram escolhidas com a finalidade de resolver as questões em aberto:

Com o intuito de investigar a história pré-colisional do Cinturão Dom Feliciano, no artigo 1 estudos geocronológicos e de isótopo de oxigênio em zircão foram analisados em rochas metavulcânicas intercaladas com as sequências metassedimentares dos complexos Várzea do Capivarita e Porongos. Os resultados sugerem novas interpretações para a história pré-colisional desse cinturão e trouxeram robustas evidências de uma conexão pré-colisional, em *ca.* 800-770 Ma, entre as rochas do antepaís (uma porção do Complexo Porongos) e do além-país (Complexo Várzea do Capivarita) do Cinturão Dom Feliciano.

Com o intuito de investigar a história colisional do Cinturão Dom Feliciano, no artigo 2 uma abordagem de petrocronologia (Fraser et al., 1997) foi utilizada. Tal abordagem combina o estudo de geocronômetros com estudo petrológico e microestrutural detalhados, cujo intuito é correlacionar com precisão os minerais datados e o evento geológico associado a esse mineral (Engi et al., 2017; Yakymchuk et al., 2017). Essa abordagem foi escolhida devido a história deformacional complexa do Cinturão Dom Feliciano, apresentada anteriormente. O estudo de amostras metassedimentares dos complexos Porongos e Passo Feio através de estimativas P–T, datações de isócrona Lu–Hf granada-rocha total e de U–Pb *SIMS* em monazita permitiu estabelecer dois períodos distintos de espessamento crustal no Cinturão Dom Feliciano, o primeiro em *ca.* 660 Ma e o segundo em *ca.* 565 Ma. Os dados trouxeram evidências de migração para oeste da frente orogênica em um sistema orogênico transpressivo de longa duração (660–560 Ma).

Com o intuito de se obter informações adicionais sobre os ambientes sedimentares originais e investigar as possíveis relações entre os complexos Porongos, Várzea do Capivarita e Passo Feio, no artigo 3, dados de geoquímica elementar e de isótopos de Sr-Nd de amostras metavulcânicas intercaladas nas sequências metassedimentares desses três complexos foram compiladas da literatura. Novos dados de geoquímica e isótopos de Sr-Nd são apresentados para sete amostras metavulcânicas dos complexos Porongos e Passo Feio. A datação de duas destas amostras metavulcânicas por U-Pb LA-ICPMS em zircão permitiu estabelecer uma idade de *ca.* 580 Ma, para o magmatismo ácido do norte do Complexo Passo Feio. A comparação dos dados sugere uma relação pré-colisional em *ca.* 800-770 Ma entre os complexos Porongos e Várzea do Capivarita, e uma relação tardi-colisional em *ca.* 600-580 Ma entre os complexos Porongos e Passo Feio, fundamentada em geoquímica elementar e isótopos de Sr-Nd.

1.1. Objetivos

Este trabalho propõe uma abordagem integrada de diversas técnicas com a finalidade de discutir a relação espacial e temporal dos complexos Porongos, Várzea do Capivarita e Passo Feio por meio do estudo de dados existentes e novos dados de geocronologia, isótopos, geoquímica e modelamento de condições metamórficas. Os objetivos específicos estão apresentados a seguir:

i) Obter dados de geocronologia (U-Pb em zircão) e isotópicos (O/Sr–Nd) para as rochas ortometamórficas intercaladas nas sequências metamórficas dos complexos Porongos, Várzea do Capivarita e Passo Feio.

ii) Compilar os dados de geocronologia, de geoquímica elementar e isotópica disponíveis para os complexos Porongos, Passo Feio e Várzea do Capivarita.

iii) Determinar por meio de modelamentos termodinâmicos as condições PT do metamorfismo das rochas metassedimentares dos complexos Porongos e Passo Feio.

iv) Determinar a(s) idade(s) de metamorfismo das rochas metassedimentares dos complexos Porongos e Passo Feio por meio de isócronas Lu–Hf em granada-rocha total e análises de U–Pb em monazita.

1.2. Materiais e métodos

O tema proposto para essa tese foi abordado através da utilização integrada de diversas técnicas. A estratégia utilizada consiste em uma revisão bibliográfica, trabalhos de campo, coleta de amostras orientadas, análises petrográfica, geoquímica de rocha total, química mineral através de microanálises em sonda eletrônica, geocronologia e geologia isotópica, e modelamentos termodinâmicos.

1.2.1. Revisão bibliográfica

O Complexo Porongos (CP), principal objeto de estudo dessa tese, apresenta diversas questões geológicas em aberto. Conforme é apresentado por esse estudo, tais questões se estendem ao Complexo Várzea do Capivarita, uma vez que a gênese destes dois complexos está associada; e também ao Complexo Passo Feio, cuja evolução metamórfica está relacionada com a evolução do CP. A revisão bibliográfica de trabalhos clássicos no CP, como Jost & Bitencourt (1980), Porcher & Fernandes (1990), Saalmann et al. (2006) e outros, permitiu resgatar indagações de aspectos ignorados pela literatura recente. Destaca-se, a hipótese de Jost e Bitencourt (1980) de que o Complexo Porongos fora formado originalmente por duas bacias sedimentares distintas. Tal hipótese se perdeu ao longo dos anos e voltou a ser levantada apenas recentemente por Höfig et al. (2018) e Battisti et al. (2018). A investigação mais aprofundada dessa questão desencadeou uma das principal problemáticas de pesquisa desta tese.

É importante salientar, no entanto, que os trabalhos mais recentes trouxeram enormes contribuições ao entendimento da geologia do complexos estudados nessa tese, principalmente devido aos novos dados geocronológicos levantados (*e.g.* Saalmann et al., 2011; Pertille et al., 2015b, 2015a, 2017; Gruber et al., 2016a). O estudo destes dados também foi de enorme importância para o levantamento e discussões das hipóteses. Assim, a revisão bibliográfica possibilitou a convergência de hipóteses mais recentes, com o resgate de algumas hipóteses mais antigas que se mostraram de extrema relevância no entendimento da geologia do Cinturão Dom Feliciano.

1.2.2. Coleta de amostras e análise petrográfica

Para o artigo 1, foram coletas amostras sistemáticas com intuito de estabelecer a idade do protólito ígneo do Complexo Várzea do Capivarita, bem como, adquirir informações sobre a idade deposicional de sua bacia original. Uma amostra do extremo leste do Complexo Porongos também foi coletada com intuito de se estabelecer a idade ígnea do protólito em uma região do complexo que carecia de dados geocronológicos.

No artigo 2, a coleta de amostras em um perfil Leste-Oeste na porção central do Cinturão Dom Feliciano permitiu investigar a evolução geológica e a trajetória PT-t dessa região a partir do estudo integrado de modelamento termodinâmico e geocronologia (Lu–Hf em granada-rocha total e U–Pb em monazita). A análise petrográfica permitiu identificar a paragênese metamórfica das rochas estudadas, além de outros aspectos, tais como feições de retrometamorfismo, porfiroblastos sin-cinemáticos, inclusões minerais etc., os quais foram de suma importância na discussão e interpretação dos resultados.

No artigo 3, a coleta das amostras foi realizada com intuito de se obter novos dados de geoquímica de rocha total e isótopos de Sr–Nd em regiões do Complexo Porongos e Complexo Passo Feio que careciam de dados. A análise petrográfica permitiu estabelecer o caráter metavulcânico/metavulcanoclástico das amostras estudadas.

1.2.3. Geoquímica de rocha total

Análises de geoquímica de rocha total foram utilizadas nos artigos 2 e 3 da presente tese. Para o artigo 2, com intuito de se realizar modelamentos termodinâmicos (ver adiante), foram obtidas análises de elementos maiores a partir de tabletes de pó de rocha em um instrumento modelo Rigaku RIX 2000 X-Ray no Laboratório de Fluorescência de raios-x da Universidade Federal do Rio Grande do Sul (UFRGS), Brasil e no AcmeLabs – Bureau Veritas Minerals, no Canadá. Para o artigo 3, elementos maiores e traços foram analisados no ActLabs – Activation Laboratories Ltd, no Canadá. Os elementos maiores foram obtidos por ICP-OES (*Inductively Coupled Plasma Optical Emission Spectrometer*), enquanto os elementos traços por ICP-MS (*Inductively Coupled Plasma-Mass Spectrometry*).

1.2.4. Geocronologia e geologia isotópica

Cinco sistemas isotópicos foram utilizados nessa tese, dos quais, dois foram empregados com intuito geocronológico: U–Pb e Lu–Hf; e três deles foram utilizados para avaliar processos mantélicos nas rochas ortometamórficas: Rb–Sr, Sm–Nd e O. Uma breve descrição dos procedimentos adotados em cada artigo são indicados abaixo. A descrição detalhada de cada método é apresentada no seu artigo correspondente.

i) No artigo 1, foram realizadas análises de U–Pb e O em zircão. Imagens de catodoluminescência foram obtidas para descrever os aspectos dos grãos selecionados e delimitar as regiões a serem analisadas. As análises de U–Pb foram realizadas nos equipamentos SHRIMP I, SHRIMP II e SHRIMP RG, enquanto as análises de oxigênio no SHRIMP SI, na *Research School of Earth Sciences* (RSES), na *Australian National University,* na Austrália*.* Os dados de U–Pb foram reduzidos de maneira similar ao descrito por (Williams, 1998, e referências ali contidas) usando o macro do Excel SQUID-1 de Ludwig (2003). Os dados de oxigênio foram normalizados pelo padrão TEMORA II com $\delta O_{18} = 8.2‰$.

ii) No artigo 2, foram realizados estudos geocronológicos de U–Pb em monazita e Lu–Hf em granada-rocha total. Imagens de elétrons retro espalhados (*backscattering*) em monazita foram obtidas com o intuito de descrever os grãos e delimitar as regiões a serem analisadas por U–Pb. Tais imagens foram obtidas no microscópico eletrônico Zeiss Merlin Scanning, na *Faculty of Health Sciences* da *UiT The Arctic University of Norway*, na Noruega. As análises de U–Pb por espectrometria de massa de íons secundários em monazita foram realizadas por sonda iônica modelo Cameca IMS 1280 no laboratório NordSIM sediado no *Swedish Museum of Natural History*, em Estocolmo, na Suécia. As análises de Lu–Hf foram realizadas no instituto de geologia da *Czech Academy of Sciences* (análises químicas) e na *Faculty of Science, Charles University* (análises de MC–ICP–MS), em Praga, na República Tcheca.

iii) No artigo 3, realizou-se análises para geocronologia U–Pb em zircão, em conjunto com dados isotópicos de Rb-Sr e Sm-Nd em rocha total. Da mesma forma que no artigo 1, imagens de catodoluminescência foram realizadas a priori para o zircão no equipamento JEOL EPMA do instituto de geologia da *Czech Academy of Sciences* em Praga, na República Tcheca. As análises de U–Pb foram realizadas por HR-LA-ICPMS no equipamento *Thermo Scientific Element 2*. Os dados isotópicos de

Rb-Sr e Sm-Nd foram analisadas através de um espectrômetro de massa por ionização térmica (*TIMS*) Thermo *Triton Plus* na mesma universidade.

1.2.5. Microanálise de Sonda Eletrônica

Análises de química mineral foram utilizadas para o modelamento termodinâmicos de rochas parametamórficas (artigo 2). Tais análises foram feitas no Laboratório de Microssonda Eletrônica do Centro de Estudos em Petrologia e geoquímica (CPGq), da UFRGS. O instrumento utilizado foi uma Microssonda Cameca SXFive com condições analíticas de 15 keV, 15 nA de corrente, e tamanho de feixe de 5 µm. O instrumento foi calibrado utilizando os seguintes padrões: diopsídio para os elementos Ca e Mg; rondonita para Mn; sanidina para Si, K e Al; Fe_2O_3 para Fe; albita para Na; rutilo para Ti; e Cr_2O_3 para Cr.

Os estudos de química mineral permitiram caracterizar os elementos maiores das fases minerais presente nas amostras, bem como calcular a fórmula estrutural destes. Além do mais, foi possível documentar a relação entre as fases minerais, e a presença de zoneamento químico em algumas dessas fases, conforme é relatado nos resultados desta tese.

1.2.6. Modelamentos termodinâmicos

Os modelamentos termodinâmicos foram elaborados para quantificar os parâmetros P e T do metamorfismo do Complexo Porongos e do Complexo Passo Feio. O método utilizado foi o de elaboração de pseudo-seções (Powell et al., 1998) utilizando a química de rocha total da amostra em questão, em conjunto com análises química pontuais dos minerais da paragênese metamórfica, através de microanálises de sonda eletrônica.

Os campos de estabilidade das assembleias minerais foram modelados utilizando o software Perplex_X 6.8.9 (Connolly, 2005, 2009), segundo a base termodinâmica publicada por Holland e Powell (1998 – atualizada em 2004). As soluções sólidas utilizadas para o modelamento termodinâmico foram: feldspato (Fuhrman & Lindsley, 1988), biotita, muscovita, clorita, estaurolita, cloritóde, cordierita e granada (White et al., 2014).

2. Estado da arte

2.1. Introdução à petrocronologia: ''subindo em ombros de gigantes''

A petrocronologia é o ramo da geologia que visa entender a história evolutiva, termal, bárica e química de uma rocha e/ou um evento geológico, através da utilização integrada de diversas ferramentas, tais como, a petrologia, o modelamento termodinâmico, a geocronologia e a química mineral (Engi et al., 2017). A petrocronologia, dessa forma, aborda não apenas a história termal de uma rocha metamórfica ou a idade de cristalização de um magma, por exemplo, mas se centra nos processos atuantes e nas taxas com que eles ocorrem nestes contextos (Engi et al., 2017). Os petrocronologistas defendem que a simples datação de um evento pode ser inútil em algumas situações geológicas, ao passo que, várias datações controladas, acompanhada de dados químicos e termodinâmicos, podem revelar diversos aspectos sobre a história evolutiva de uma rocha (Engi et al., 2017). O termo ''petrocronologia'' (Fraser et al., 1997) surge da necessidade dos petrólogos e geocronólogos em descrever essa abordagem única, que se preocupa em descrever e entender os processos ígneos e metamórficos. Em seu artigo pioneiro, por exemplo, Fraser et al. (1997) demonstraram que a quebra de fases minerais abundantes, tais como granada e anfibólio podem desencadear a formação de zircão, e desse modo, o dado geocronológico pode ser correlacionado à petrogênese e às estimativas de pressão e temperatura da rocha.

É importante salientar que a petrocronologia pode ser considerada ''ciência irmã'' da termocronologia. No entanto, segundo Engi et al. (2017), a petrocronologia normalmente se concentra nos processos que levam à formação de rochas ígneas e metamórficas – os minerais e texturas e os processos que as formaram – enquanto a termocronologia enfatiza os processos de resfriamento dos eventos ígneos, metamórficos e tectônicos (Engi et al., 2017). Uma vez que cada campo tenha suas características únicas e seus limites se sobreponham, elas são ciências complementares.

Um estudo de petrocronologia envolve, geralmente, a seguinte metodologia (Engi et al., 2017):

i) Identificar um ou mais estágios específicos da evolução metamórfica, magmática e/ou estrutural em uma determinada amostra com base em critérios texturais, como sobrecrescimentos, inclusões, etc.

ii)   Documentar as relações de fase entre os minerais com base em análises de química mineral, usualmente através de microanálise de sonda eletrônica (*EPMA – em inglês*) ou espectrometria de massa com plasma acoplado indutivamente e ablação a laser (*LA-ICP-MS - em inglês*).

iii)   Usar técnicas de termobarometria, como modelamentos termodinâmicos e/ou geotermobarômetros empíricos, para restringir as condições de pressão-temperatura (PT) do equilíbrio da assembleia mineral.

iv)   Procurar relacionar uma ou mais zonas de crescimento específicas de um geocronômetro robusto adequado para cada estágio evolutivo. Essa etapa geralmente requer obtenção auxiliar de elementos traços nos minerais estudados, usualmente através de análises por EPMA ou LA-ICP-MS, ou pode, até mesmo, ser auxiliada por estudos isotópicos (*e.g.* isótopos de oxigênio em zircão).

Desta forma, o estado da arte desta tese visa descrever e discutir aspectos cruciais na aplicação da petrocronologia em rochas metamórficas, centrada principalmente nos tópicos III e IV descritos por Engi et al. (2017). Os itens I e II de Engi et al (2017) foram abordados sucintamente nos materiais e métodos, respectivamente nos tópicos ''coleta de amostras e análise petrológica'' e ''microanálise de sonda eletrônica''.

2.2. Conceitos termodinâmicos aplicados às rochas metamórficas

Rochas metamórficas guardam evidências sobre a história geológica de uma rocha, incluindo informações sobre temperatura, pressão e, muitas vezes, deformação. Entende-se como metamorfismo o processo de mudança de mineralogia, composição química e/ou textura de uma rocha quando esta é submetida a um novo ambiente químico e/ou físico em qual sua associação mineralógica atual naquele tempo deixa de ser estável (Yardley, 1989). Por definição o metamorfismo ocorre no interior da crosta terrestre e no manto (Bucher & Grapes, 2011), e exclui os processos que levam a mudanças mineralógicos, químicas e físicas superficiais, como é o caso do intemperismo e dos processos associados a diagênese de rochas sedimentares (Yardley, 1989; Bucher & Grapes, 2011).

Durante o metamorfismo, as rochas são submetidas a dois tipos principais de mudanças: a substituição dos minerais originais por minerais metamórficos novos e

estáveis, em razão das reações químicas, e a recristalização de minerais já presentes, produzindo novas texturas, tais como a orientação de minerais lamelares ou o progressivo aumento de granulometria de alguma espécie mineral (Yardley, 1989). Ainda, um aspecto importante, e que faz parte da definição de metamorfismo, é o fato dessas mudanças ocorrerem essencialmente no estado sólido (Yardley, 1989; Bucher & Grapes, 2011). No entanto, Yardely (1989) destaca que pequenas quantidades de fluídos podem estar presentes nos poros da rocha durante o metamorfismo, os quais desempenham um papel muito importante ao facilitar as transformações metamórficas.

Ao decorrer da história evolutiva de uma rocha, a sobreposição e/ou recorrência de um ou mais eventos metamórfico-deformacionais é corriqueira e decifrar essa história evolutiva polifásica pode ser difícil. No entanto, em certas situações é possível obter informações desses diversos eventos e reconstruir uma trajetória evolutiva da rocha com base nas mudanças de pressão (P) e temperatura (T) com o passar do tempo geológico (t). Uma situação de preservação de diversos eventos pode se dar, por exemplo, através da preservação de minerais reliquiares de uma fase metamórfica pretérita inclusos nos minerais metamórficos do evento mais recente. O gráfico que representa os diversos pontos de P e T por qual uma rocha metamórfica passou durante a sua evolução ao longo do tempo (t) é conhecido como trajetória PT-t (do inglês, *PT-t paths*).

2.2.1. Trajetória PT-t

Um gráfico de pressão-temperatura-tempo (PT-t) visa reconstruir a trajetória de uma rocha metamórfica durante sua história evolutiva, através das informações pontuais de P e T que a mineralogia metamórfica da rocha fornece. Bucher & Grapes (2011) ilustram a trajetória de uma rocha em uma colisão continental (Fig. 1a), onde do tempo 1 (t_1) até o tempo 3 (t_3) o aumento da pressão é significativo, mas a temperatura permanece praticamente constante. Em t_3 a rocha atinge sua pressão máxima e um aumento de temperatura ocorre entre t_3 e t_4, mantendo a pressão constante. Entre t_4 e t_5 ocorre uma descompressão acompanhada de aumento de temperatura, com continuada descompressão, porém acompanhada de diminuição da temperatura entre t_5 e t_6. Plotando todos os pontos, de t_1 a t_6, em um gráfico (Fig. 1b) é possível observar como a rocha variou suas condições de pressão e temperatura com o passar do tempo e, dessa forma, construir a sua trajetória PT-t.
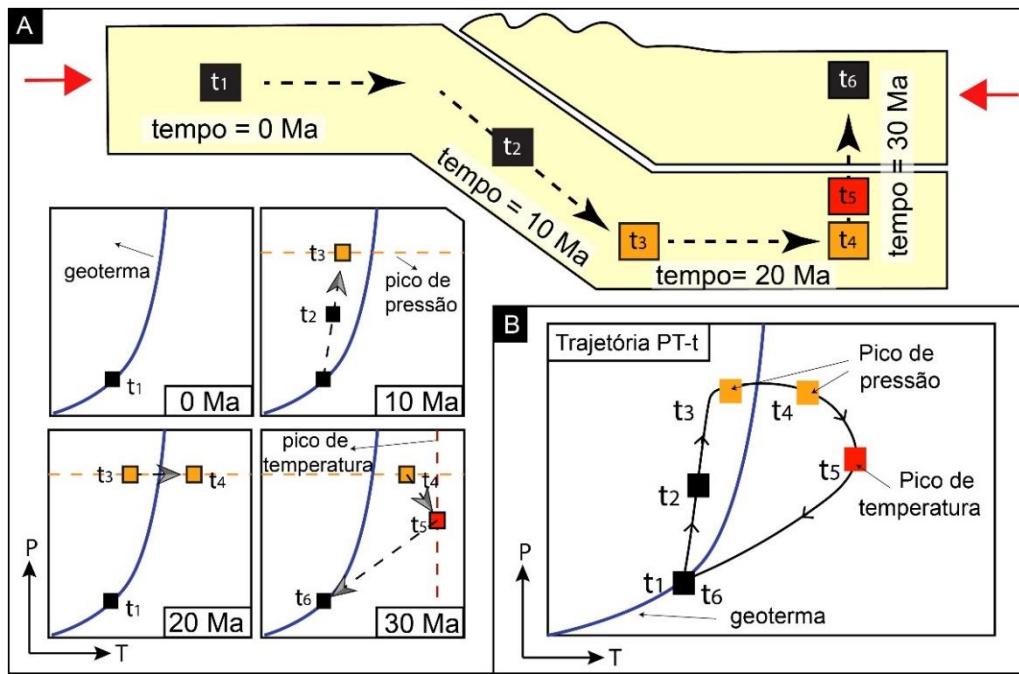
Figura 1. A) Desenho esquemático da posição de uma unidade litológica na crosta em função do tempo durante uma colisão continental e a sua representação correspondente no espaço PT. B) Trajetória PT-t da rocha do exemplo mostrado em A (Fonte: Modificado de Bucher & Grapes, 2011).

Na figura 1b, é possível observar que a trajetória PT-t apresenta um sentido horário. Segundo Bucher & Grapes (2011) trajetórias PT-t de sentido horário são características de situações de metamorfismo regional orogênico e foram documentadas em diversos cinturões orogênicos pelo mundo, tais como, Alpes ocidentais, Apalaches e Himalaias. Muito frequentemente, a trajetória horária caracteriza a seguinte sequência de eventos: i) espessamento isotérmico; ii) aquecimento isobárico; iii) descompressão isotérmica e; iv) resfriamento isobárico (England & Thompson, 1984; Bucher & Grapes, 2011). Trajetórias PT-t no sentido anti-horário, no entanto, também existem, e tem sido relatadas em terrenos de fácies granulito onde um evento de aquecimento precede o espessamento crustal (Bucher & Grapes, 2011).

Idealmente, uma rocha registraria, através de sua mineralogia e texturas, informações de toda sua história evolutiva (de t_1 a t_6). Porém, a sobreposição de eventos metamórfico-deformacionais tende a apagar os registros dos eventos mais antigos. Isso ocorre porque uma rocha, quando submetida a novas condições de P e T, tende a reorganizar sua mineralogia a fim de obter o equilíbrio termodinâmico (Spear, 1994). As decorrências do equilíbrio termodinâmico na geração e na trajetória

evolutiva de rochas metamórficas tem sido alvo crescente de estudos a partir da década de 1980 (Spear et al., 2016). Alguns conceitos fundamentais de termodinâmica e como eles podem auxiliar no estudo das rochas metamórficas serão abordados nos tópicos seguintes.

2.2.2. Regra de fase e sistemas termodinâmicos

Rochas metamórficas são tratadas como sistemas em equilíbrio termodinâmico (Yardley, 1989), os quais são formados por um conjunto de ''fases''. As fases de um sistema são formadas pela combinação de ''componentes''. Componentes são os elementos, compostos ou misturas polifásicas que compõem um sistema. No caso de um sistema simples, em que água e gelo coexistam, por exemplo, ambos serão fases desse sistema, as quais se formam a partir de um mesmo componente: H_2O. À pressão ambiente de 1×10^5 Pa, água e gelo coexistem à 0 ºC apenas (Fig. 2). Em qualquer outra temperatura sob 1×10^5 Pa, as fases não coexistirão. O mesmo vale se a pressão for alterada e a temperatura mantida em 0 ºC, as fases também não coexistirão. Para coexistirem é necessário mudar pressão e temperatura juntas, de maneira dependente e isso significa que, quando água e gelo coexistem, esse sistema apenas possui um grau de liberdade, uma vez que se pode alterar apenas uma variável independentemente, ou P ou T, pois o valor da outra variável dependerá do valor escolhido para a variável selecionada. Como mostrado por Bucher & Grapes (2011) e Yardley (1989), a quantidade de graus de liberdade (variáveis independentes) de um sistema é definida pela Regra de Fase (Eq. 1 -Gibbs, 1878):

$$F = C - P + 2$$

Equação 1

Onde, F é o número de graus independentes de liberdade do sistema, C é o número de componentes e P é o número de fases. Bucher & Grapes (2011) também destacam que, como consequência da regra de fase, o número de fases não pode exceder o número de componentes em mais de 2. No caso de um sistema água de um componente (H_2O) o número máximo de fases desse sistema será 3, representado pelo ''ponto tríplice'', onde água, gelo e vapor coexistem (Fig. 2). O ponto tríplice possui 0 graus de liberdade (C - P + 2 = 0) e por isso é chamado de ''ponto univariante'', uma vez que nem P, nem T podem ser alterados. As linhas 1, 2 e 3 da figura 2, possuem 1 grau de liberdade (C - P + 2 = 1) e são chamadas de ''curvas

univariantes''. Os campos sólido, líquido e vapor, por sua vez, possuem 2 graus de liberdade (C - P + 2 = 2), e são chamados de ''campos divariantes'', pois tanto P quanto T podem ser alterados independentemente sem que o equilíbrio do sistema seja desfeito.
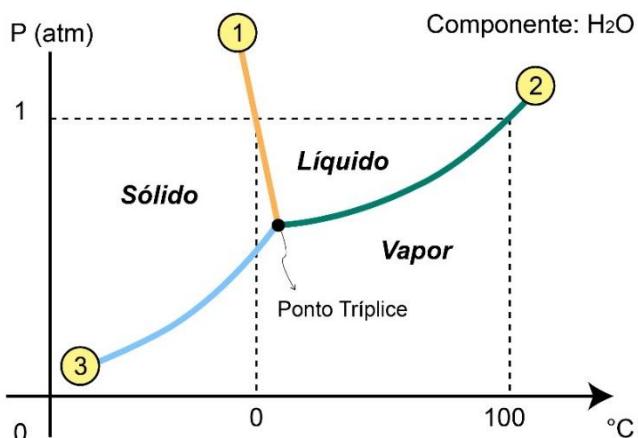
Figura 2. Diagrama de fase PT para o sistema termodinâmico onde H_2O é o único componente.

O diagrama que ilustra como se dá a disposição das fases em equilíbrio sob uma variada gama de pressões e temperatura de um sistema termodinâmico, como a exemplo da figura 2, é conhecida como ''diagrama de fase P-T'' (Bucher & Grapes, 2011). Os diagramas de fase também podem ser usados para ilustrar a variação de composição de uma fase (usualmente referida como ''X'') em função da temperatura (''diagrama de fase T-X'') ou pressão (''diagrama de fase P-X'') de um sistema. Esses últimos dois casos são muito úteis para sistemas complexos com vários componentes, grupo no qual as rochas metamórficas estão inseridas.

Rochas são sistema termodinâmicos complexos pelo fato de comumente envolverem diversos componentes. Conforme exemplificado por Yardley (1989), em uma rocha com quatro fases minerais, como mica ($(Na,K)Al_3Si_3O_{10}(OH)_2$), quartzo ($SiO_2$), cianita ($Al_2SiO_5$) e feldspato ($(Na,K)AlSi_3O_8$), cinco componentes são exigidos para que todas essas fases coexistam em equilíbrio: Na_2O, K_2O, SiO_2, Al_2O_3 e H_2O. Neste exemplo, os cálculos termodinâmicos necessários para construir um diagrama de fase P-T são muito mais complexos do que os necessários para o exemplo da água/gelo. No caso de rochas, é possível construir diagramas PT utilizando as reações metamórficas para delimitar os campos de estabilidade dos minerais. Tais diagramas recebem o nome de ''grade petrogenética'' (Bowen, 1940) (*e.g.* Fig. 3). A ideia de Bowen era que, utilizando as curvas de reação univariantes, seria possível

delimitar todas as assembleias minerais divariantes em equilíbrio concebíveis para uma determinada composição química genérica (Bucher & Grapes, 2011). Cada assembleia mineral cairia, portanto, dentro de um campo único de P-T e indicaria as condições de metamorfismo da rocha (Bucher & Grapes, 2011).
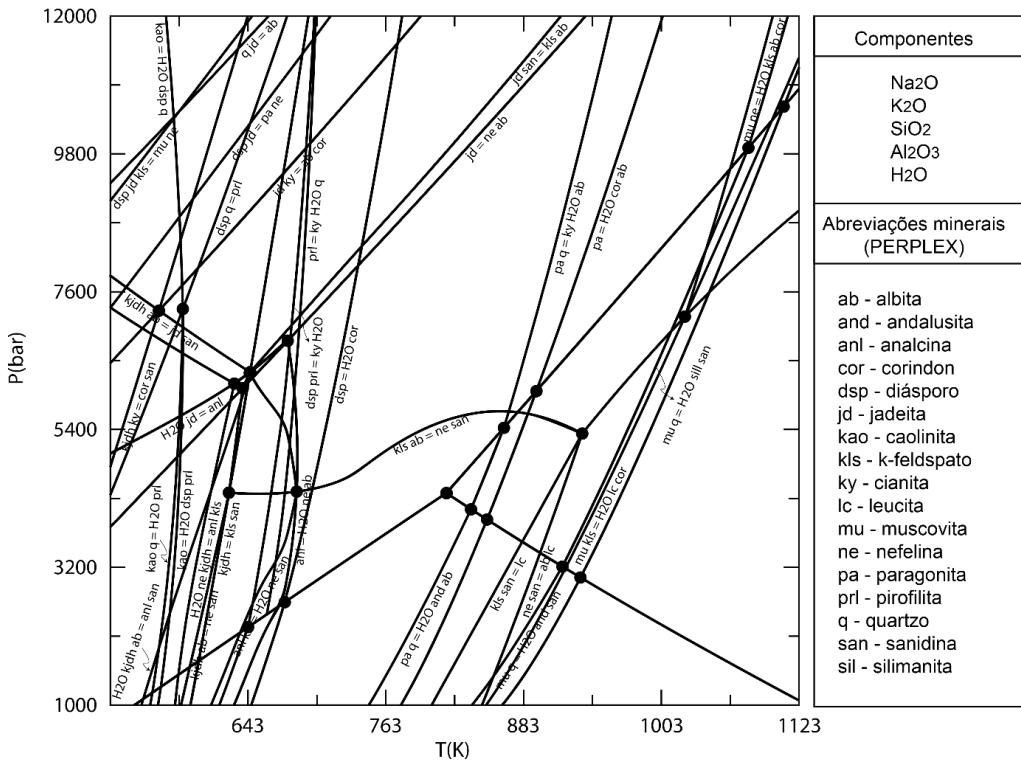
Figura 3. Grade petrogenética calculada no software PERPLEX para o exemplo de Yardley (1989), onde os componentes do sistema são Na_2O, K_2O, SiO_2, Al_2O_3 e H_2O. Os campos divariantes são delimitados pelas linhas univariantes (reações metamórficas), sendo a assembleia mineral estável a maiores temperaturas representada no lado direito da equação.

As grades petrogenéticas idealizadas por Bowen (1940) foram revolucionárias para o estudo de petrologia metamórfica e tem como base as premissas estabelecidas pelo conceito de ''estado de equilíbrio'' termodinâmico, discutidas a seguir.

2.2.3. Estado de equilíbrio, pseudo-seções e geotermobarometria

Estado de equilíbrio é, segundo Spear (1994), o primeiro conceito fundamental para o estudo de rochas metamórficas sob a luz da termodinâmica. Segundo o mesmo autor, a base para este conceito vem do estudo cinético dos processos e reações metamórficas em uma rocha durante sua trajetória de pressão-temperatura. Tais processos cinéticos, em geral, seguem a Lei de Arrhenius (Eq. 2) que prediz a ''taxa''

com que reações metamórficas ou difusões de minerais ocorrerão em uma rocha com relação a temperatura (Spear, 1994):

$$\text{Taxa} = A \exp^{\left(-\frac{\Delta H}{RT}\right)} \qquad \text{Equação 2}$$

Onde, A é uma constante pré-exponencial, ΔH é uma energia de ativação, R é a constante dos gases e T é a temperatura, em Kelvin.

Para ilustrar a importância de tal equação, Spear (1994) apresenta uma trajetória P-T (Fig. 4a) e o histórico T-t (Fig. 4b) de uma rocha em uma situação de *overtrhrusting*. O autor explica que a relação de Arrhenius (Eq. 2) prediz uma relação taxa-temperatura que pode ser projetada na curva temperatura-tempo da figura 4b e, dessa forma, representar uma curva de taxa-tempo (Fig. 4c). A figura 4c mostra que as taxas dos processos metamórficos são muito mais rápidas perto da temperatura do pico metamórfico e, portanto, as reações metamórficas e recristalização ocorrerão com muito mais intensidade perto dessa temperatura (Spear, 1994). Esse fato é de suma importância no estudo de rochas metamórficas, pois demonstra que a mineralogia e a química mineral comumente refletem as condições de pico metamórfico ao invés de qualquer outra parte da trajetória PT-t, onde as taxas dos processos são, pelo menos, dez vezes mais lentas (Spear, 1994). Dessa forma, na ausência de múltiplos eventos de aquecimento, as rochas metamórficas exibirão assembleias minerais e químicas minerais que refletem as temperaturas de pico metamórfico (Spear, 1994; Spear & Peacock, 1989). O exposto nas duas últimas sentenças explica o porquê da dificuldade de reconstruir a trajetória PT-t completa de uma rocha metamórfica.

Como demonstra a Lei de Arrenius, para que as reações químicas em uma rocha ocorram, é necessário prover calor (energia, ΔH) ao sistema e aumentar sua temperatura. Segundo Spear & Peacock (1989), o calor necessário para elevar a temperatura de uma rocha durante o metamorfismo vem de três mecanismos gerais: i) condução (fluxo de calor de rochas quentes para rochas frias); ii) advecção (por exemplo, fluídos quentes se movendo através da rocha); e iii) fontes internas de calor (por exemplo, produção de calor radioativo). As reações metamórficas, por sua vez, são o resultado dos átomos do sistema rocha se reorganizando na configuração mais estável possível sob as novas condições de T e P impostas, ou seja, buscando o estado de equilíbrio termodinâmico (Yardley, 1989).
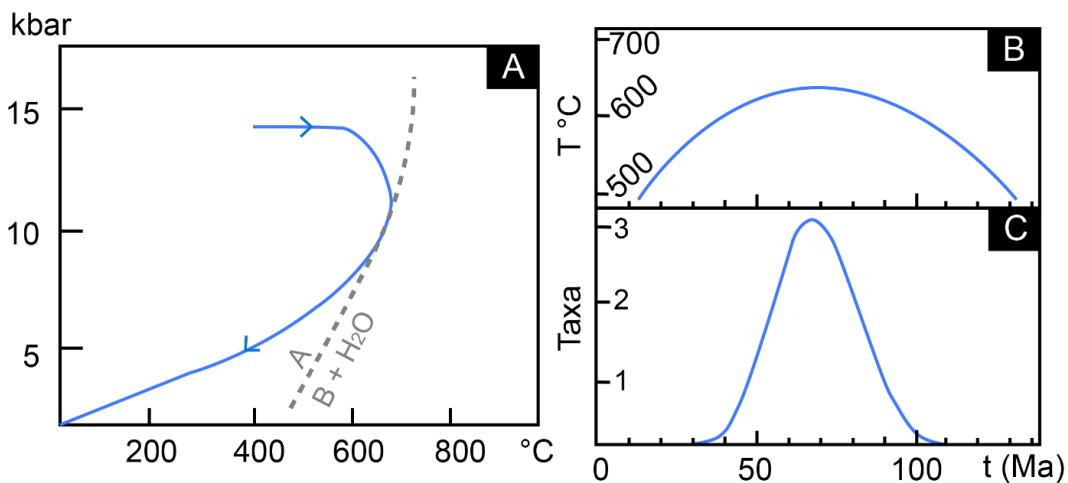
Figura 4. A) Trajetória PT-t típica de um *overthrusting*. B) Diagrama de temperatura x tempo da trajetória PT-t mostrada em A. C) Diagrama de taxa x tempo construído a partir de B. A taxa foi calculada utilizando ΔH = 250 kJ/mol (Fonte: Modificado de Spear, 1994).

Rochas são más condutoras de calor, conduzindo-o de maneira bastante lenta e, por isso, grandes volumes de rochas levam milhões de anos para sofrerem mudanças de temperatura (Yardley, 1989). Mais precisamente Bucher & Grapes (2011) estimam que para metamorfizar um pacote de 10 km de espessura de folhelho sob cerca de 400-600 ºC, com um fluxo de calor de 40 mW/m^2, comum em situações de crosta continental, seriam necessários cerca de 8 milhões de anos. Se o fluxo de calor fosse de apenas 20mW/m^2, uma camada de folhelho de 20 km de espessura com temperatura inicial de 200 ºC levaria 48 milhões de ano para atingir 600 ºC. Dessa forma, o período de tempo típico para processos metamórficos de escala regional é da ordem de 10 a 50 milhões de anos (Bucher & Grapes, 2011). Os maiores fluxos de calor são registrados ao longo das dorsais meso-oceânicas (120 mW/m^2), enquanto os mais baixos encontram-se nas regiões cratônicas (30 mW/m^2) (Bucher & Grapes, 2011).

Embora o conceito de grade petrogenética (Bowen, 1940) tenha sido revolucionário no estudo das rochas metamórficas, naquela época, os estudos termodinâmicos em minerais eram escassos, fazendo com que as primeiras grades petrogenéticas fossem simplórias e não possibilitassem estimar as condições metamórficas de uma rocha com precisão (Bucher & Grapes, 2011). Atualmente os estudos termodinâmicos desenvolvidos por muitos autores (*e.g.* Berman, 1988; Holland & Powell, 1990, 1998; Johnson; Oelkers & Helgeson, 1992), principalmente após década de 80, geraram uma base de dados muito mais robusta (Spear et al., 2016). Utilizando tais bases termodinâmicas, alguns *softwares* permitem o cálculo de

grades petrogenéticas e pseudo-seções. Segundo Bucher & Grapes (2011), os 4 principais *sofwtares* utilizados pelos petrólogos metamórficos são: *TWQ/TWEEQU* (Berman, 1991), *DOMINO/THERIAK* (de Capitani & Petrakakis, 2010), *PERPLEX* (Connolly & Kerrick, 1987; Connolly, 1990) e *THERMOCALC* (Powell & Holland, 1985, 1988).

Pseudo-seções são diagramas bastante similares as grades petrogenéticas, porém ao contrário das últimas, as primeiras levam em conta a variação composicional (X) de uma fase dentro de um campo divariante. Dessa forma as grades petrogenéticas são diagramas PT enquanto as pseudo-seções são diagramas PT-X (Bucher & Grapes, 2011; Spear, 1994). Outra vantagem das pseudo-seções é que elas são calculadas com base na análise de rocha total específica da rocha estudada, e não para uma composição química genérica, como no caso das grades petrogenéticas. Além disso, uma vez que consideram a variação da ''atividade'' dos elementos de uma ''solução sólida'' dentro de um campo de estabilidade divariante, as pseudo-seções podem ser combinadas com geotermômetros para definir com maior precisão as condições metamórficas de uma rocha.

Dois conceitos do parágrafo acima são essenciais para o estudo de pseudo-seções, são eles: solução sólida e atividade (química). Uma solução sólida é uma mistura em estado sólido de dois ou mais componentes que constituem uma fase única (IUPAC, 2014). Muitos minerais formam soluções sólidas (feldspato, granada, piroxênio, anfibólio, etc), sendo o plagioclásio o exemplo mais trivial. Este mineral possui dois membros finais (*end-members*), Anortita (An_{90-100}) e Albita (An_{0-10}) e os membros intermediários Bytownita (An_{70-90}), Labradorita (An_{50-70}), Andesina (An_{30-50}) e Oligoclasio (An_{10-30}), com quantidades variáveis de Ca, Na, Al e Si (Deer et al., 2013). Em um sistema onde todos os elementos necessários ao plagioclásio estão disponíveis, a espécie de plagioclásio que cristalizará dependerá da atividade dos cátions Ca e Na ($a_{Ca,plag}$, $a_{Na,plag}$), as quais são variáveis em resposta a composição e as condições de pressão e temperatura deste sistema (Spear, 1994). O fato de muitas soluções sólidas possuírem sua química mineral influenciadas pela pressão e/ou temperatura é a principal premissa utilizada pela geotermobarometria.

Geotermobarometria é o nome dado a técnica que utiliza da dependência da constante de equilíbrio à pressão e temperatura para inferir pressões e temperaturas metamórficas (Spear, 1994). A constante de equilíbrio é dada pela equação abaixo (Eq. 3):

$$K_{eq} = \prod_j (a_{j,k})^{vj,k}$$

Onde, K_{eq} é a constante de equilíbrio, $a_{j,k}$ é a atividade do componente j na fase k, e vj, k é o coeficiente estequiométrico do componente j na fase k. Conforme a definição de Spear (1994), essa equação é dependente da pressão e da temperatura, ou seja, para cada conjunto T e P o resultado da K_{eq} será diferente. Isso implica que a equação 3 possui infinitos resultados, devido as infinitas combinações possíveis de P e T (Bucher & Grapes, 2011). Isso significa também que a atividade de um elemento em uma mineral varia quando pressão e temperatura variam, exatamente como o exemplo do plagioclásio, acima. Apesar das infinitas respostas para a equação 3 é possível aplicar tal modelo termodinâmico pois cada solução para essa equação definirá uma linha em um diagrama PT (Spear, 1994), conhecida como *isopleth* (Fig. 5a). As *isopleths* podem ser calculados pelo mesmo *software* utilizado na elaboração da pseudo-seção. Dessa forma, as pseudo-seções preveem não só campo de estabilidade divariante de uma assembleia mineral, mas também como a composição de cada fase da assembleia mineral varia no interior daquele campo, conforme indicado pelas *isopleths*. Assim, de acordo com Spear (1994), aplicando modelos de atividade apropriados (*e.g.* Berman, 1988; Holland & Powell, 1990, 1998; etc) e aferindo com precisão e acurácia a composição dos minerais (i.e. química mineral) na rocha estudada (usualmente feito através de microanálise de sonda eletrônica) é possível estimar com precisão as condições metamórficas.

A constante de equilíbrio (Eq. 3) comumente é aplicada a diversos minerais de uma mesma assembleia simultaneamente (*e.g.* plagioclásio e piroxênio; granada, biotita e plagioclásio; etc). Tal metodologia resulta na obtenção de conjuntos de *isopleths* independentes, e logo, estimativas PT independentes para cada mineral utilizado. Segundo Spear (1994), a medida em que diferentes equilíbrios têm diferentes inclinações no espaço PT, a intersecção de dois ou mais equilíbrios (*e.g.* plg e cpx) pode ser usada para inferir um ponto PT (Fig. 5b). As inclinações variáveis ocorrem pois alguns equíbrios são controlados por processos mais dependentes da pressão, enquanto, em outros, a temperatura é mais importante. Assim, a inclinação das *isopleths* resulta em uma relação de entropia e volume ($\Delta S_r / \Delta V_r$), conhecida como equação de Clausius-Clapeyron (Bucher & Grapes, 2011).
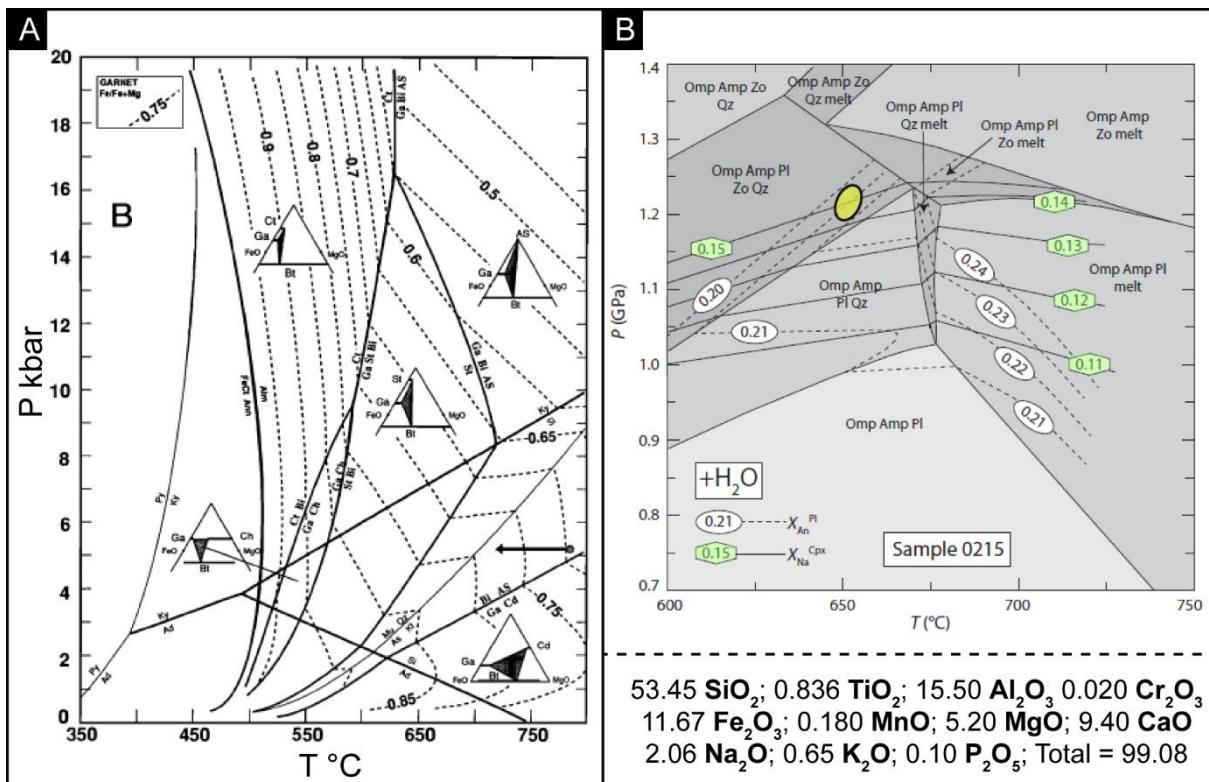
Figura 5. A) Modelo de pseudo-seção (Spear, 1994). Dentro dos campos divariantes, as *isopleths* indicam como composição XFe (Fe/Fe+Mg) da granada variam com a pressão e temperatura. Nesse exemplo as reações das curvas univariantes são mostradas. B) Exemplo real onde *isopleths* do teor de anortita em plagioclásio ($X_{an}Pl$) e teor de sódio em clinopiroxênio ($X_{na}Cpx$) foram combinadas para definir as condições de PT de uma rocha metamórfica (elipse amarela) (Modificado de Elvevold et al., 2014).

Ainda com base na equação de Clausius-Clapeyron, os geotermobarômetros podem ser divididos em dois grupos: os geotermômetros e os geobarômetros. Geotermômetros são aqueles que são mais adequados para o cálculo de temperaturas geológicas e em geral, têm pouca dependência de pressão (Spear, 1994), resultando em *isopleths* verticais no espaço PT. Os geobarômetros são aqueles que são mais adequados para o cálculo de pressões geológicas e são relativamente insensíveis à temperatura (Spear, 1994), resultando em *isopleths* horizontais no espaço PT. Vale destacar, que *isopleths* de todas as inclinações são possíveis e, por exemplo, uma isopleth com inclinação de 45 graus reflete uma dependência do processo tanto à temperatura quanto à pressão.

A classificação dos geotermobarômetros também pode ser feita com base na natureza das reações químicas que o controla. Por exemplo, a troca de Ca e Na no plagioclásio em respostas as mudanças de temperatura ocorre através de trocas catiônicas dentro da mesma fase mineral, porém, existem outros tipos de

geotermobarômetros que podem inclusive trocar cátions com outras fases do sistema em equilíbrio. De acordo com Spear (1994) e Bucher & Grapes (2011), os tipos de geotermobarômetro são (*nomes originais mantidos entre parênteses*):

- Geotermobarômetro de troca catiônica (*Exchange Geothermometer*)

Os geotermobarômetros de troca catiônica baseiam-se na troca de dois átomos similares (raio e carga) entre diferentes sítios cristalográficos de um mineral (troca intracristalina) ou entre dois minerais distintos (troca intercristalina) (Bucher & Grapes, 2011). Muitos geotermômetros são baseados em reações de troca catiônica, envolvendo principalmente a troca de Fe e Mg entre silicatos coexistentes de uma assembleia mineral (Spear, 1994; Bucher & Grapes, 2011). As reações de troca geralmente envolvem pequena mudança de volume (ΔV pequeno), devido ao raio atômico similar dos cátions trocados, com moderados ΔS (entropia) e ΔH (entalpia), de forma que as *isopleths* tenham um declive relativamente íngreme, sendo portanto, bons geotermômetros (Spear, 1994).

A constante de equilíbrio para as reações de troca pode geralmente ser simplificada como sendo a razão dos cátions de uma fase dividida pela mesma razão na segunda fase (Spear, 1994). Esta formulação é definida como coeficiente de distribuição (K_D) que, para a troca de Fe e Mg entre as fases A e B, é definido como $K_D = (Fe/Mg)_A / (Fe/Mg)_B$ (Spear, 1994). Segundo Bucher & Grapes (2011) os dois exemplos de aplicação mais comuns são:

i) Granada–Clinopiroxênio, dado pela reação piropo + hedenbergita = almandina + diopsídio, aplicado principalmente no estudo de granulitos e eclogitos;

ii) Granada-Biotita, envolvendo a reação piropo + anita = almandina + flogopita, utilizado em rochas metamórficas de fácies xisto verde, anfibolito e em alguns casos, granulito.

Além de diversos outros, tais como granada-cordierita, granada-horneblenda, granada-clorita, olivina-espinélio, ilmenita-olivina, ilmenita-piroxênio, etc (Spear, 1994; Bucher & Grapes, 2011).

- Geotermobarômetro *solvus* (*Solvus Geothermometer*)

Os geotermômetros *solvus* são embasados no fato de que alguns pares de minerais com estrutura semelhante mas com composição diferente mostram uma

solubilidade mútua que aumenta com o aumento da temperatura (Bucher & Grapes, 2011). Segundo Spear & Peacock (1989) essa terminologia é, no entanto, muitas vezes utilizada de maneira errônea, pois o termo *''solvus''* é restrito a fases isoestruturais, e muito dos geotermometros chamados de *''solvus''* não obdecem a esta regra, como por exemplo o geotermômetro *''dois-piroxênios''* (Spear & Peacock, 1989). Este último é baseado na troca de Ca e Mg entre clinopiroxênio e ortopiroxênio e por isso, deveriam ser tratados como um geotermômetro de troca catiônica (Spear & Peacock, 1989). Os pares minerais comumente usados como geotermometros *solvus* são ortopiroxênio–clinopiroxênio, feldspato alcalino-plagioclásio, calcita-dolomita e muscovita-paragonita (Bucher & Grapes, 2011).

- Equilíbrio de reações metamórficas (*Net Transfer Equilibria*)

Os geotermobarômetros desse tipo têm como base as reações químicas que ocorrem em estado sólido e ocasionam a transformação de uma fase mineral existente em outra fase mineral nova (Spear, 1994). As reações desse tipo podem ocorrer entre fases sólidas propriemente ditas (mineral A + mineral B = mineral C + mineral D) ou por reações de desvolatilização (mineral hidratado A = mineral desidratado B + H_2O) (Bucher & Grapes, 2011). Muitos desses equilíbrios geram excelentes geobarômetros pois comumente possuem mudanças de volume grandes (Spear, 1994; Bucher & Grapes, 2011). Outra vantagem é que essas reações delimitam equilíbrios multivariantes no espaço P-T-X e, como resultado, toda a assembleia termobarométrica pode coexistir em uma ampla faixa de P e T (Bucher & Grapes, 2011).

A aplicação desse tipo de equilíbrio como geobarômetro pode ser exemplificada pelo conjunto granada e plagioclásio. Tal geobarômetro envolve a troca de Ca entre o componente anortita do plagioclásio e o componente grossulária da granada (Bucher & Grapes, 2011). Uma vez que a anortita possui volume consideravelmente maior do que a grossulária, a estabilidade da grossulária é favorecida em altas pressões, ao passo que a estabilidade da anortita é favorecida em pressões menores (Bucher & Grapes, 2011). Para que o equilíbrio se mantenha, no entanto, outras fases são envolvidas nessa reação, como quartzo e aluminosilicato (Gr + 2 Als + Qz = 3 An) (Bucher & Grapes, 2011). Diversos outros geobarômetros do tipo *Net Transfer Equilibria* podem ser encontrados nos trabalhos de Bucher & Grapes (2011) e Spear (1994). Entre os principais utilizados estão Granada-Rutilo-

Aluminossilicato-Ilmenita-Quartzo - GRAIL (1 Alm + 3 Rt = 3 Ilm + 1 Als + 2 Qz), Clinopiroxênio-Plagioclásio-Quartzo (Jd + Qtz = Ab) e Esfalerita-Pirrotita-Pirita.

2.2.4. Precauções no uso de modelamentos termodinâmicos

Uma vez que são baseados em modelos, sejam computacionais ou semi-empíricos, as pseudo-seções e os geotermobarômetros podem apresentar complicações e inconsistências. Por isso, um estudo petrográfico detalhado da mineralogia, das texturas, e da relação entre as fases minerais presentes na rocha estudada sempre será o primeiro e mais importante passo a ser dado em estudos de petrocronologia. Spear & Peacock (1989) e Bucher & Grapes (2011), descrevem algumas precauções que podem ser tomadas para que um bom resultado a partir do estudo de uma pseudo-seção possa ser obtido:

i)   A assembleia mineral deve ter se formado sob condições de equilíbrio termodinâmico

A suposição básica da geotermobarometria é que a assembléia mineral considerada se formou em equilíbrio (Bucher & Grapes, 2011). Porém é impossível provar que os minerais em uma rocha já atingiram o equilíbrio (Spear & Peacock, 1989; Bucher & Grapes, 2011). O desequilíbrio, por sua vez, por ser provado e, pelo menos três testes podem ser utilizados para isso (Spear & Peacock, 1989). A lógica desses testes é que, se não houver provas de desequilíbrio, a assembléia mineral está provavelmente em equilíbrio. Os testes são:

- Verificar a existência de minerais zonados. Caso existam, é necessário elucidar qual porção do mineral zonado está em equilíbrio com os demais minerais da rocha (Fig. 6).
- Verificar a consistência do particionamento de elementos em diferentes minerais em uma mesma lâmina e em outras amostras similares.
- Determinar se a temperatura e a pressão calculadas a partir do geobarômetro e do geotermômetro são consistentes para uma pequena área (*e.g.* diferentes amostra de um mesmo afloramento).

Contudo, subdomínios em desequilíbrio ou minerais zonados preservados em escala de lâmina podem representar diferentes estados de equilíbrio pelo qual a rocha

foi submetida e auxiliar na reconstrução da trajetória PT-t (Spear, 1994; Bucher & Grapes, 2011). Usualmente granadas zonadas, como o exemplo da figura 6, fornecem condições de dois pontos distintos da trajetória PT-t. O núcleo geralmente indica as condições de um evento pretérito ou início do crescimento deste mineral, enquanto a borda se reequilibra com a assembléia metamórfica da rocha (*e.g.* biotita) e fornece dados do evento mais jovem, ou dos estágios finais de crescimento desse mineral. Granada é um dos minerais mais utilizados em petrocronologia, pois seus baixos coeficientes de difusão permitem a preservação de zonação (Spear, 1994), uma vez que minerais como biotita se reequilibram totalmente nas condições PT impostas mais rapidamente (Ehlers et al., 1994). No entanto, destaca-se que o avanço das técnicas analíticas tem revelado que zonações são muito mais comuns do que se pensava a priori e ocorrem em diversas fases minerais (Spear et al., 2016).
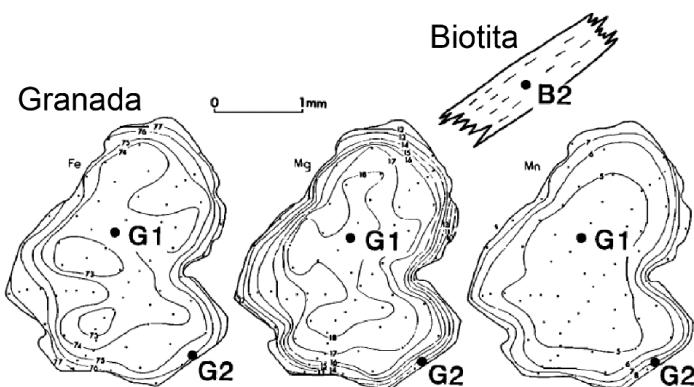
Figura 6. Exemplo teórico de porfiroblasto de granada zonado. A borda da granada (G2) encontra-se em equilíbrio com a biotita da matriz (B2), no entanto, o núcleo da granada (G1) representa um evento pretérito a G2-B2. Assim, o equilíbrio da assembleia mineral granada-biotita deve ser calculado a partir da composição (expressa pelas *isopleths*) de G2 e B2 (Fonte: Spear & Peacock, 1989).

ii)   Retrometamorfismo

Caso a assembleia mineral de equilíbrio permaneça inalterada após sua formação, os valores de PT obtidos irão refletir as condições de pico metamórfico, como discutido por Spear (1994) e Spear & Peacock (1989). Bucher & Grapes (2011) destacam, no entanto, que tais situações devem ser válidas para algumas rochas rapidamente resfriadas ou de baixa temperatura, mas não se aplicam para rochas formadas em altas temperaturas e lentamente resfriadas, como o caso de granulitos, por exemplo. Nessas últimas, o retrometamorfismo (ou metamorfismo retrogressivo)

pode ter um papel bastante atuante (Bucher & Grapes, 2011). Em alguns casos, o retometamorfismo é claramente observado em lâmina (*e.g.* cloritização de biotita e granada). O problema, de acordo com Bucher & Grapes (2011), é que em outros casos, porém, esse processo pode ser observado apenas através de microanálise cuidadosa de sonda eletrônica. Segundo exemplos da literatura essas zonações micrométricas formadas pelo retrometamorfismo podem causar alterações nos valores dos geotermobarômetros (*e.g.* Edwards & Essene, 1988).

iii)   Qualidade do modelo/base termodinâmica utilizada

Como comentando anteriormente, existem diferentes modelos/bases termodinâmicos para minerais sendo, segundo Bucher & Grapes (2011), os de Berman (1988) e Holland & Powell (1990, 1998) os mais amplamente utilizados. A principal cautela a ser tomada a respeito da escolha do modelo termodinâmico é a de não utilizar os dados termodinânicos para condições diferentes do que eles foram calibrados (Bucher & Grapes, 2011). Por exemplo, segundo os mesmos autores, a reação Grossulária + 2 Cianita + Quarzto = 3 Anortita foi experimentalmente determinada a temperaturas entre 900–1600 °C, porém, na prática, essa reação pode ocorrer até a 500 °C. Dessa forma, a aplicação desse geotermômetro para o segundo caso deve ser feita com precaução (Bucher & Grapes, 2011). Além disso, é necessário levar em conta a sensibilidade do geotermobarômetro, pois alguns sistemas são sensíveis apenas a uma faixa restrita de P e T (Bucher & Grapes, 2011). Fazem parte desse último caso muitos dos geotermômetros *solvus* que são úteis em temperaturas relativamente altas, mas menos proveitosos em temperaturas relativamente baixas (Bucher & Grapes, 2011).

iv)   Estimativa da razão Fe^{2+}/Fe^{3+} nas análises minerais

As micronálises em sonda eletrônica fornecem o teor total de ferro expresso em FeO ou Fe_2O_3, e o teor do outro estado de valência deve ser calculado assumindo o equilíbrio de cargas e os sítios cristalográficos de cada mineral (Bucher & Grapes, 2011). Para algumas espécies minerais esses cálculos são bastante complexos, devido a presença de vacâncias cristalográficas e conteúdo variável de H_2O (por exemplo, anfibólios e clorita) (Bucher & Grapes, 2011). Dessa forma, o cálculo de

Fe^{2+}/Fe^{3+} requer dados de microssonda de excelente qualidade, a fim de minimizar ao máximo as incertezas nesses valores (Bucher & Grapes, 2011).

v) Efeitos de outros componentes

A grande maioria dos geotermobarômetros é baseada em equilíbrios minerais calibrados utilizando composições minerais simples, contudo, a maioria dos minerais em rochas contêm componentes adicionais e formam soluções sólidas complexas (Bucher & Grapes, 2011). Como consequência, muitas vezes há discordância entre os petrólogos sobre o modelo termodinâmico de solução sólida mais adequado para uma determinada espécie mineral (Bucher & Grapes, 2011). Como exemplo das complexidades geradas por componentes adicionais, pode-se citar a ''difusão invertida'' de elementos (*uphill difusion*), discutida por Kohn & Penniston-Dorland (2017), entre outros autores.

As estimativas de condições metamórficas, seja por pseudo-seções ou geotermobarômetros, exige uma detalhada catacterização petrográfica, incluindo estudo de química dos minerais, e permite um bom entendimento da evolução de uma rocha metamamórfica quanto as suas condições de pressão e temperatura. A petrocronologia, no entanto, vai além, pois possibilita conectar esses estudos termodinâmicos com estudos de elementos traços, estudos isotópicos e de geocronologia desses minerais. Nesta tese foram utilizados Elementos Terras Raras para auxiliar na descrição evolutiva de granada e monazita, e as implicações da partição desses elementos entre esses dois minerais são discutidas a seguir.

2.3. *Petrocronologia da monazita (xenotima) vs granada: partição de ítrio e Elementos Terras raras*

Os elementos terras raras (ETRs) ou lantanídeos, são usualmente divididos em três grupos: i) Elementos Terras Raras leves (ETRs-L) – La, Ce, Pr e Nd; ii) Elementos Terras Leves médios (ETRs-M) – Sm, Eu, Gd e; iii) Elementos Terras Raras pesados (ETRs-P) – Tb, Dy, Ho, Er, Tm, Yb e Lu. O Y possui raio iônico dentro do intervalo dos ETRs-P e por isso é usualmente incluído neste grupo (Engi, 2017).

A monazita e a xenotima são referidas como ortofosfatos de íons grandes - (ETR)[PO4], e fazem parte do grupo dos denominados ''minerais de terras raras'', uma vez que os Elementos Terras Raras e ítrio são constituintes cruciais na formação

desses minerais (Engi, 2017). Na monazita, o íon trivalente de raio grande é coordenado com nove íons de oxigênio (ETR)O_9, formando um poliedro irregular; enquanto na xenotima, o Y (e outros ETR^{3+}) são coordenados com oito íons de oxigênio (Y)O_8 e formam um dodecaedro regular (Fig. 7 a,b - Engi, 2017). Tal diferença estrutural exerce grande influência no coeficiente de partição (K_D) dos ETRs entre esses minerais (Fig. 7c). Segundo Engi (2017), enquanto a monazita, monoclínica, favorece a entrada de ETRs-L, a xenotima, tetragonal (parte do grupo do zircão), favorece a entrada de ETRs-P. Os ETRs-L com raio iônico maior se alojam no poliedro de coordenação 9O da monazita, enquanto o Y^{3+} e os ETR-P, de raio iônico menor, se acomodam melhor no poliedro menor de 8O da xenotima (Engi, 2017). Além disso, Ce (ou La) são constituintes cruciais na monazita, os quais podem ser substituído por outros ETRs-L e Sm (Engi, 2017). Para a xenotima, o componente crucial é o Y (ou algum ETRs-P, ou ainda, Gd).
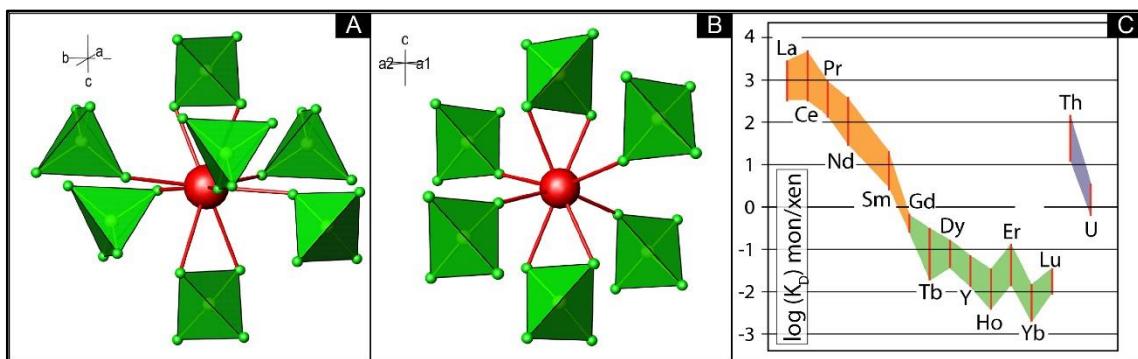
Figura 7. Arranjo cristalográfico dos sítios dos ETRs em monazita (a) e em xenotima (b). Tetraedro de fosfato (PO_4) é mostrado em verde. O íon trivalente grande (esfera vermelha) na monazita ocupa um poliedro irregular O_9 que acomoda preferencialmente ETRs de maior raio, ou seja, ETRs-L a ETRs-M e Th^{4+}. Na xenotima, o dodecaedro regular O_8 favorece entrada de Y e ETRs de raio menor e mais pesados – ETRs-P. C) Coeficiente de partição entre monazita e xenotima ($K_D = Cmon / Cxen$) para ETRs, U e Th. ETRs-L e ETRs-M em laranja; ETRs-P em verde; e actinídeos em azul. (Fonte: modificado de Engi, 2017).

Tanto a monazita quanto a xenotima são minerais que incorporam fortemente o urânio no momento da formação, mas não incorporam o chumbo (*e.g.* Williams et al., 2007). Em ambos minerais, U^{4+} pode ser substituído por Th^{4+}, sendo que a maioria das monazitas apresentam Th/U > 1, enquanto na xenotima geralmente a razão Th/U < 1 (Engi, 2017). Na xenotima, os conteúdos de Th e U são mais baixos, mas tanto a monazita quanto a xenotima são passíveis de datação. A monazita normalmente contém Th (wt%) e U (ppm) em concentrações suficientes para combinar seus

sistemas de decaimento para geocronologia; enquanto para xenotima apenas a datação U–Pb é possível (Engi, 2017). A monazita é um mineral muito mais comum e estudado que a xenotima, no entanto, segundo Engi (2017), inclusões e relações de supercrescimento são freqüentemente observadas entre esses fosfatos-ETR e podem ser de grande utilidade para relacionar idades a reações de substituição e efeitos metassomáticos.

A granada, por sua vez, é considerada um supergrupo de trinta e dois minerais (*sensu* Grew et al., 2013)*,* o qual é composto principalmente por alumonisilicatos (16 dos 32) de sistema, quase exclusivamente, cúbico (30 dos 32). A fórmula mineral da granada é escrita como $\{X_3\}[Y_2](Z_3)\varphi_{12}$; na qual X, Y, e Z se referem aos sítios dodecaédrico, octaédrico e tetraédrico, respectivamente, enquanto φ é dado por O, OH, ou F (Grew et al., 2013). O sítio cristalográfico X, pode abrigar os elementos Ca, Na, Mg, Mn^{2+}, Fe^{2+} e Y; o sítio Y pode abrigar os elementos Al, Mg, Fe^{3+}, Mn^{3+}, Si, Ti, Zr, V^{3+}, Cr^{3+} Sb^{5+}, Sn^{4+} e Te^{6+}; no sítio Z, os elementos possíveis são Si, Al, Fe^{3+}, Li, Zn, V^{5+} e As^{5+} (Grew et al., 2013).

Segundo Baxter & Scherer (2013) a granada é especialmente útil nos estudos petrocronológicos porque (i) o controle termodinâmico das condições de pressão-temperatura-composição (P-T-X) de seu crescimento é bem compreendido; (ii) a granada geralmente registra processos tectono-metamórficos progressivos, em vez de retrometamórficos; (iii) este mineral cresce em uma ampla gama de condições P–T–X, abrangendo diversos contextos tectônicos e tipos de rocha e; (iv) cristais de granada zonados preservam a química e potencialmente, idades distintas, abrangendo processos de milhões de anos. Além disso, a granada é frequentemente zoneada em elementos traços, com núcleos enriquecidos em ítrio (Y) e ETR-P (Baxter & Scherer, 2013; Kohn, 2014; Baxter et al., 2017). Esses elementos altamente compatíveis tendem a resistir ao reequilíbrio em temperaturas elevadas devido às suas baixas difusividades inter e intragranulares (Baxter et al., 2017). Assim o zoneamento de elementos traços é comumente preservado em fácies anfibolito superior e granulito, condições em quais o zoneamento de elementos maiores (como Ca, Fe, Mg e Mn) é frequentemente resetado (Kohn, 2014; Baxter et al., 2017). Segundo Baxter et al. (2017) e as referências nele contidas, a granada pode ser fortemente zoneada em ETR, bem como Y, Zr, Cr, P e As.

A monazita, no entanto, pode se cristalizar em situações de metamorfismo progressivo (Rubatto et al., 2006); ou em algum momento após o resfriamento da temperatura máxima do pico metamórfico, no caso de migmatização (*e.g.* Hagen-

Peter et al., 2016), ou até mesmo a partir da desistabilização de outros minerais no retrometamorfismo – tais como a granada e alanita, por exemplo (Bollinger & Janots, 2006; Baxter et al., 2017; Yakymchuk et al., 2017). Segundo Yakymchuk et al. (2017), a monazita e xenotima ocorrem desde condições diagenéticas até metamorfismo de fácies anfibolito, granulito e eclogito. Quanto a origem, a monazita pode ter origem detrítica, produzida por reações de estado sólido, precipitada por fluídos ou cristalizada a partir do magma anatétitco (Yakymchuk et al., 2017).

A partição de Y e ETR entre granada e monazita tem sido objeto de estudo de diversos autores (*e.g.* Pyle et al., 2001; Pyle & Spear, 2003; Rubatto et al., 2006; Hacker et al., 2019), e fornece um par robusto para estudos de petrocronologia. A granada possui um alto coeficiente de partição para Y e ETRs (Bea et al., 1994; Rubatto et al., 2006) sendo o sumidouro mineral mais importante para os ETR-P e ítrio em rochas metamórficas (Bea et al., 1994). Dessa forma, devido aos altos coeficientes de partição entre granada e matriz, um cristal de granada em crescimento incorpora Y + ETR-P no seu núcleo (*i.e.* no início de seu crescimento) (Baxter et al., 2017). A concentração desses elementos diminuem em direção às bordas do cristal de granada, gerando perfis "em forma de sino", devido ao processo de fracionamento *Rayleigh* (Kohn, 2014; Baxter et al., 2017). Em contraste, os ETR-M e ETR-L geralmente exibem um ligeiro aumento em abundância em direção às bordas do cristal de granada, ou sequer mostram zoneamento (Baxter et al., 2017). Os mesmos autores, no entanto, argumentam que os perfis de ETR na granada podem ser mais complexos, devido a uma série de fatores que podem ocorrer durante o crescimento deste mineral. Tais fatores são, por exemplo, a disponibilidade limitada de ETR na rocha durante o metamorfismo progressivo, a reabsorção de cristais de granada, a quebra de fases acessória ricas em ETR durante o crescimento da granada (*e.g.* monazita e xenotima), infiltração de fluido rico em ETR, entre outros (Baxter et al., 2017). Devido a interferência desses fatores citados, investigar outros minerais auxiliares, tal como a monazita, se faz necessário para que a história evolutiva da paragênese mineral seja compreendida de maneira integrada.

Minerais acessórios como zircão, monazita, xenotima, apatita, epidoto e alanita também são repositórios importantes para ETR-P e Y (Baxter et al., 2017). Comumente, a concentração de Y na monazita é ~1,5 ordens de magnitude maior do que na granada (Bea et al., 1994). A xenotima tem concentrações de Y que são ~2 ordens de magnitude mais altas do que na monazita (Pyle et al., 2001). No entanto, segundo Baxter & Scherer (2013), na maioria dos casos, a granada é

substancialmente mais abundante modalmente do que a monazita e a xenotima e, portanto, a quebra ou o crescimento da granada exercerá controles de primeira ordem sobre o fornecimento de Y e ETR-P da rocha. A cristalização de zircão e monazita durante o crescimento da granada (*i.e.* metamorfismo progressivo) resultará em concentrações relativamente baixas de ETR-P e Y nesses minerais acessórios, pois esses elementos são particionados para a granada principalmente, devido sua grande abundância modal (Baxter et al., 2017; Yakymchuk et al., 2017). Em contraste, a quebra de granada durante o crescimento de minerais acessórios, tal como a monazita, pode resultar em novas zonas de crescimento enriquecidas em ETR-P e Y nesses minerais acessórios (*e.g.* Foster et al., 2004; Rubatto et al., 2006). Dessa forma, zonas de alto Y e alto ETR-P em monazita podem ser vinculadas a quebra de granada e podem refletir por exemplo, o evento de soterramento ou exumação de uma trajetória P–T (Baxter et al., 2017; Yakymchuk et al., 2017). De maneira geral, os padrões de ETR e Y da monazita frequentemente refletem uma forte partição com os principais minerais coexistentes na assembleia metamórfica, notavelmente granada e feldspato (Baxter et al., 2017; Yakymchuk et al., 2017).

Os cristais de monazita podem conter importantes informações sobre eventos de retrometamorfismo em uma rocha. O crescimento retrometamórfico *subsolidus* de monazita (± xenotima) às custas de alanita ou apatita + granada, por exemplo, foi documentado em vários casos e geralmente está relacionado ao influxo de fluido (Bollinger & Janots, 2006). Ainda, de acordo com Engi (2017), os primeiros cristais de monazita a se cristalizarem em uma sequência tendem a sequestrar Th e Y, enquanto as zonas mais externas (mais jovens) são mais empobrecidas nesses elementos, embora esses padrões possam ser bastante complexos.

No caso de reabsorção da granada durante o metamorfismo, se algum elemento liberado durante esse processo não puder ser prontamente incorporado nas fases do produto (*e.g.* monazita), uma pequena quantidade de granada pode precipitar novamente, incorporando preferencialmente esse elemento (Kohn, 2014; Baxter et al., 2017). Segundo os mesmos autores, em geral, tais elementos seriam aqueles que tendem a ser fortemente particionados na granada, incluindo Mn, Y, Lu e outros ETR-P. Em alguns casos, minerais secundários podem se formar em uma superfície de reabsorção de granada impulsionada pelo influxo desses elementos particulares (Baxter et al. 2017). Xenotima, por exemplo, foi observado circundando superfícies reabsorvidas de granadas, onde o fluxo localizado de Y (da granada reabsorvida) promove o crescimento de xenotima (*e.g.*, Gatewood et al., 2015). Nesse caso, há

uma ligação textural útil entre a superfície da granada reabsorvida e a xenotima da fase acessória neocristalizada, a qual revela uma conexão temporal entre esses minerais (Gatewood et al., 2015).

Hacker et al. (2019) investigaram em detalhe a partição de ETR entre os minerais granada e monazita. Os autores observaram uma dependência no coeficiente de partição dos elementos ETR-P entre esses dois minerais, a partir do estudo de rochas metamórficas com protólitos pelíticos e quartzo-feldspáticos. Segundo Spear & Pyle (2010) no campo de estabilidade de granada + biotita + silicato de alumínio ± estaurolita (o caso das amostras de Hackler et al., 2019) o aumento da pressão e/ou a diminuição da temperatura causa o crescimento de granada e o consumo de monazita, e o teor de Y de ambos é previsto diminuir. No caso inverso, de diminuição da pressão e/ou aumento da temperatura, o teor de Y se eleva. Como resultado principal de seu trabalho, Hackler et al. (2019) demonstraram que a partição do par monazita-granada tem dependência da temperatura para ETR-P, do Dy até o Lu, e partição não sistemática para os ETR-L e ETR-M, do La ao Gd, conforme indicado na figura 8.
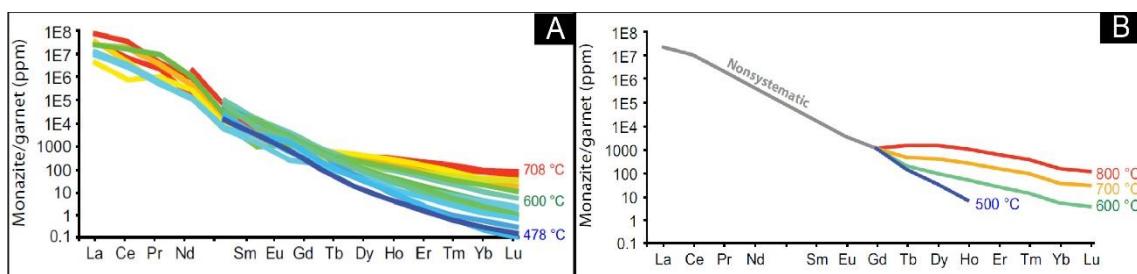
Figura 8. A) A figura acima demonstra uma clara correlação entre o particionamento dos ETR-P entre granada-monazita, como apresentado por Hacker et al. (2019 e referências ali contidas). B) Este gráfico demonstra que há também uma dependência da temperatura no particionamento de ETR-P entre monazita e granada (Fonte: modificado de Hacker et al., 2019).

Segundo Baxter et al. (2017), o referencial teórico dos estudos de petrocronologia pode ser fragmentado em dois grandes grupos: o prefixo ''petro'' envolve os assuntos abordados nos tópicos 2.2 e 2.3 desta tese. O sufixo ''cronologia'' representa o outro grupo, de crucial importância para situar os eventos metamórfico-deformacionais no tempo geológico. A geocronologia é abordada abaixo, no tópico 2.4 e seus subitens.

2.4. Geologia Isotópica: introdução

Segundo a Lei de Moseley, as propriedades físico-químicas de um elemento são uma função exclusiva de seu número atômico (número de prótons), e dessa forma, um mesmo elemento químico pode possuir variadas configurações de nêutrons em seu núcleo sem que suas propriedades físico-químicas sejam alteradas. Como o nêutron, no entanto, possui massa, o diferente número de nêutrons irá influenciar o peso atômico do elemento. As diferentes configurações de núcleo que geram um mesmo elemento químico com diferentes pesos atômicos são conhecidas como isótopos (mesmo número de prótons, diferente número de nêutrons) (Van Grieken & de Bruin, 1994).

Para que um elemento químico seja estável, a combinação de prótons e nêutrons precisa obedecer a um equilíbrio termodinâmico, sendo que, quanto menor a configuração energética do elemento, mais estável ele será (White, 2013). Caso esse equilíbrio não seja totalmente atingido um núcleo atômico se forma, mas será instável (White, 2013). Um mesmo elemento pode possuir diversos isótopos em equilíbrio (isótopos estáveis) e diversos em desequilíbrio (isótopos instáveis).

O fato de alguns isótopos serem estáveis e outros instáveis resulta com que a abundância de cada isótopo na natureza seja diferente, pois os isótopos instáveis tendem a desaparecerem, e a abundância dos isótopos estáveis dependerá da trivialidade do processo pelo qual este é formado (White, 2013). A tabela 1 ilustra a abundância isotópica natural relativa do oxigênio, rubídio, estrôncio, samário, neodímio, lutécio, háfnio, urânio, tório e chumbo, que foram os isótopos utilizados nessa tese.

Os núcleos dos isótopos instáveis com o passar do tempo, a fim de obter uma configuração mais estável, desintegram-se emitindo partículas, gerando o fenômeno conhecido como "decaimento radioativo". O decaimento radioativo pode fazer com que um isótopo instável de determinado elemento químico (chamado de isótopo radioativo ou pai) decaia para um isótopo de outro elemento (isótopo radiogênico ou filho), caso emita prótons, como por exemplo o $^{238}_{92}U$ que decai para $^{234}_{90}Th$ ($^{238}_{92}U \rightarrow$ $^{234}_{90}Th + {}^{4}_{2}\alpha$). Esse processo é a base de muitos estudos geocronológicos e será retomado no tópico 2.4.1.

Tabela 1. Abundância isotópica natural relativa dos principais isótopos dos elementos químicos utilizados nessa tese (Fonte dos dados: IAEA: Nuclear Data Section, 2019).

Isótopo*	Abundância Natural Relativa (%)	Peso Atômico (u)	Energia de Ligação (KeV)	Tipo de isótopo
$^{16}_{8}O$	99,757	15,9949	7979,206	Estável
$^{17}_{8}O$	0,038	16,9991	7750,728	Estável
$^{18}_{8}O$	0,205	17,9991	7767,097	Estável
^{85}Rb	72,17	84,9118	8697,0	Estável
^{87}Rb	27,83	86,9091	8711,0	Decai para ^{87}Sr
^{86}Sr	9,86	85,9092	8708,0	Estável
^{87}Sr	7,00	86,9088	8705,0	Estável
^{88}Sr	82,58	87,9056	8733,0	Estável
^{144}Sm	3,07	143,9120	8303,680	Estável
^{147}Sm	14,99	146,9149	8280,573	Decai para ^{143}Nd
^{148}Sm	11,24	147,9148	8279,633	Decai para ^{144}Nd
^{152}Sm	26,75	151,9197	8244,065	Estável
^{142}Nd	27,15	141,9077	8346,031	Estável
^{143}Nd	12,17	142,9098	8330,489	Estável
^{144}Nd	23,79	143,9190	8326,924	Decai para ^{140}Ce
^{146}Nd	17,18	145,9131	8304,093	Estável
$^{175}_{71}Lu$	97,401	174,9407	8069,141	Estável
$^{176}_{71}Lu$	2,599	175,9427	8059,021	Decai para $^{176}_{72}Hf$
$^{176}_{72}Hf$	5,26	175,9414	8061,360	Estável
$^{177}_{72}Hf$	18,60	176,9432	8051,836	Estável
$^{178}_{72}Hf$	27,28	177,9437	8049,444	Estável
$^{180}_{72}Hf$	35,08	179,9465	8034,932	Estável
$^{234}_{92}U$	0,0054	234,0409	7600,715	Decai para $^{230}_{90}Th$
$^{235}_{92}U$	0,7204	235,0439	7590,914	Decai para $^{231}_{90}Th$
$^{238}_{92}U$	99,2742	238,0507	7570,125	Decai para $^{234}_{90}Th$
$^{232}_{90}Th$	100	232,0380	7615,033	Decai para $^{228}_{88}Ra$
$^{204}_{82}Pb$	1,4	203,9731	7879,932	Decai para $^{200}_{80}Hg$
$^{206}_{82}Pb$	24,1	205,9744	7875,362	Estável
$^{207}_{82}Pb$	22,1	206,9758	7869,866	Estável
$^{208}_{82}Pb$	52,1	207,9766	7867,453	Estável

Os isótopos estáveis, por sua vez, possuem configuração em equilíbrio com a natureza e por isso não sofrem decaimento radioativo. No entanto, isótopos estáveis

leves de um elemento (aqueles com menores pesos atômicos) podem ser fracionados em relação aos isótopos estáveis pesados deste mesmo elemento (White, 2013). Por exemplo, a água (H_2O) possui os três isótopos estáveis de oxigênio, porém o isótopo $^{16}_{8}O$ é mais leve que o $^{17}_{8}O$ e $^{18}_{8}O$ e logo, mais fácil de ser evaporado. Isso faz com que a relação $^{16}_{8}O/^{18}_{8}O$ da atmosfera, de um rio e de uma geleira, por exemplo, sejam todas diferentes entre si (*e.g.* Rodrigues & Fauth, 2015). De maneira similar o fracionamento isotópico ocorre nos variados ambientes geológicos. Como os minerais, e por consequência as rochas, são formadas por elementos químicos, os minerais absorvem diferentes isótopos de um mesmo elemento quando cristalizados e dessa forma, guardam importantes informações sobre o ambiente geológico em que foram formados. Uma importante premissa no estudo dos isótopos estáveis é a admissão de que os isótopos de elementos pesados como Pb^{207}, Nd^{144}, Sr^{87} não são fracionados, e portanto, não são separados pelos processos geológicos (fusão parcial, metamorfismo, intemperismo, cristalização fracionada), enquanto os isótopos leves, como O^{16}, H^{1}, C^{12} são fracionados até pela ação da gravidade (*e.g.* evaporação da água) (White, 2013). O campo de aplicação dos estudos isotópicos, sejam os estáveis ou os instáveis, é bastante vasto e envolve por exemplo, estudo de gêneses de minérios, dinâmica mantélica, hidrogeologia, evolução crustal, vulcanologia, paleontologia e outros (White, 2013).

2.4.1. Isótopos instáveis: decaimento radioativo e geocronologia

A radioatividade de elementos químicos foi descoberta acidentalmente na transição entre os séculos XIX e XX pelo químico Henri Becquerel, quando este estudava os efeitos da fluorescência no mineral pechblenda e percebeu uma liberação natural de energia do átomo de urânio, capaz de ionizar gases e atravessar corpos opacos (Brennan, 2000). Subsequentemente a descoberta de Becquerel, Marie e Pierre Curie constataram que alguns isótopos de rádio e polônio liberavam muito mais energia que os de urânio e denominaram essa energia de radiação. A radioatividade pode ser definida como o processo espontâneo de emissão de radiação durante a desintegração de um núcleo atômico instável, em outras palavras, quando este núcleo passa da condição de instabilidade para a de estabilidade (Brennan, 2000). Todas as substâncias radioativas tendem a formar substâncias estáveis com o passar do tempo, e nesse processo emitem radiação (Brennan, 2000).

Posterior a descoberta da radioatividade, na mesma década, o físico Ernest Rutherford estudou a emissão de radiação atômica mais detalhadamente e demostrou que sob um campo magnético, a radiação pode ser repelida, atraída ou não sofrer interferência (Fig. 9). Com isso, o autor demonstrou que três tipos diferentes de radiação podem ser liberados: Alfa (α), Beta (β), e Gama (γ) (Brennan, 2000).

Radiação	Constituição	Carga	Massa (u)	Penetração	Exemplo
Alfa (α)	2 prótons e 2 nêutrons	+2	4	Baixa	$^{238}_{92}U \rightarrow {}^{234}_{90}Th + {}^{4}_{+2}\alpha$
Beta (β)	1 elétron	-1	0	Média	$^{17}_{7}N \rightarrow {}^{17}_{8}O + {}^{0}_{-1}\beta$
Gama (γ)	Onda eletromagnética	0	0	Alta	$^{67}_{31}Ga^* \rightarrow {}^{67}_{31}Ga + {}^{0}_{0}\gamma$

* elemento no estado excitado

Figura 9. Experimento realizado por Rutherford no qual as partículas alfa, beta e gama foram identificadas (Fonte dos dados: IAEA: Nuclear Data Section, 2019).

A maior contribuição de Ernest Rutherford, no entanto, foi sua percepção de que a desintegração dos núcleos de um isótopo instável é sempre ocasionada a uma taxa constante, porém específica para cada isótopo (Rutherford & Soddy, 1902). Dessa forma, a probabilidade de desintegração de uma quantidade de isótopos radioativos pode ser expressa em função do tempo, e assim, representar um relógio natural do universo. Essa descoberta deu início a ciência conhecida como geocronologia (Brennan, 2000). A equação básica do decaimento radioativo é expressa por:

$$\frac{dN}{dt} = -\lambda N \qquad \qquad \text{Equação 4}$$

Onde, N é o número de átomos radioativos (isótopo radioativo/pai) no tempo presente, em gramas ou mols, *t* é o tempo decorrido (idade a ser determinada), e λ é a constante de desintegração do átomo radioativo (White, 2013). Integrando a equação 4 acima, tem-se que:

$$\int_{N_0}^{N} \frac{dN}{N} = \int_{0}^{t} -\lambda \, dt \qquad \text{Equação 5}$$

Onde N_0 é o número de isótopos radioativos em t=0. Resolvendo a integral da equação 5, tem-se que:

$$\ln \frac{N}{N_0} = -\lambda t \qquad \text{Equação 6}$$

Que pode ser expressa como:

$$\frac{N}{N_0} = e^{-\lambda t} \qquad \text{Equação 7}$$

Ou, mais comumente:

$$N = N_0 \, e^{-\lambda t} \qquad \text{Equação 8}$$

A partir da equação 8, para calcular o tempo necessário para que o número de átomos radioativos diminua para a metade do número original, ou seja, quando N/N_0 = ½, a equação 8 pode ser reescrita como:

$$\ln \frac{1}{2} = -\lambda t_{1/2} \qquad \text{Equação 9}$$

Logo:

$$t_{1/2} = \frac{\ln 2}{\lambda} \qquad \text{Equação 10}$$

A equação 10 apresenta matematicamente o conceito de "meia-vida" ($t_{1/2}$), que é o tempo necessário para que metade dos núcleos radioativos de uma amostra desintegre-se, ou seja, o tempo que leva para essa amostra radioativa reduzir-se à metade (White, 2013). Uma vez que a constante de desintegração é intrínseca de cada isótopo, a ''meia-vida'' também é variável, podendo ir desde frações de segundos até bilhões de anos (Tabela 2), e isso exercerá enorme influência na abundância isotópica natural, pois, por exemplo, isótopos instáveis com meia vida de milissegundos (*e.g.* ^{19}N) tornam-se praticamente inexistentes na natureza. Destaca-se também que, visto que o decaimento radioativo é um processo que envolve apenas

o núcleo atômico, a meia-vida não varia com a pressão ou com a temperatura e nem depende da quantidade inicial de isótopos radioativos da amostra (White, 2013).

Tabela 2. Exemplos de constante de desintegração (λ) e meia-vida de alguns isótopos instáveis (Fonte dos dados: Faure (2000), White (2013) e IAEA: Nuclear Data Section, 2019).

Isótopo radioativo instável (pai)	λ	Meia-vida	Isótopo radiogênico estável (filho)
^{147}Sm	$6,54 \times 10^{-12}$ anos^{-1}	$1,06 \times 10^{11}$ anos	^{143}Nd
^{176}Lu	$1,87 \times 10^{-11}$ anos^{-1}	$3,76 \times 10^{10}$ anos	^{176}Hf
^{87}Rb	$1,42 \times 10^{-11}$ anos^{-1}	$4,8 \times 10^{10}$ anos	^{87}Sr
^{232}Th	$4,98 \times 10^{-11}$ anos^{-1}	$1,4 \times 10^{10}$ anos	^{208}Pb, ^{4}He
^{238}U	$1,551 \times 10^{-10}$ anos^{-1}	$4,47 \times 10^{9}$ anos	^{206}Pb, ^{4}He
^{235}U	$9,849 \times 10^{-10}$ anos^{-1}	$7,07 \times 10^{8}$ anos	^{207}Pb, ^{4}He
^{14}C	$1,245 \times 10^{-4}$ anos^{-1}	$5,70 \times 10^{3}$ anos	^{14}N
^{18}F	$6,3 \times 10^{-3}$ minutos^{-1}	$1,09 \times 10^{2}$ minutos	^{18}O
^{19}N	$2,55$ segundos^{-1}	$0,271$ segundos	^{18}O

A concentração do isótopo radiogênico/filho (D) de um sistema radioativo pode então ser determinada através da diferença do número de isótopos radioativos inicial (N_0) e o número de isótopos radioativos atual (N). Isso ocorre, pois em t=0 nenhum núcleo radioativo terá decaído, porém com o passar do tempo, os isótopos radioativos decairão e se transformarão em isótopos radiogênicos estáveis (D), e por consequência, a concentração de D aumentará em função do tempo às expensas de N. Assim, tem-se que:

$$D = N_0 - N \qquad \text{Equação 11}$$

Isolando N_0 na equação 8, e substituindo na equação 11 se tem que:

$$D = Ne^{\lambda t} - N \qquad \text{ou} \qquad D = N(e^{\lambda t} - 1) \qquad \text{Equação 12}$$

Onde, determinando-se N e D em laboratório, sendo λ conhecido, é possível calcular a idade (t) do sistema isotópico. No entanto, é necessário ainda considerar a provável presença do isótopo radiogênico em t=0, não pelo decaimento do isótopo

radioativo, e sim pelo simples fato de o isótopo radiogênico existir na natureza e poder ser incorporado na estrutura do mineral no momento de sua cristalização. Assim, temos a equação geral da geocronologia:

$$D = D_0 + N(e^{\lambda t}-1)$$ Equação 13

Onde D_0 é a quantidade de isótopos radiogênicos originalmente presente.

2.4.1.1. Geocronologia do sistema Lu-Hf

O sistema Lutécio-Háfnio é baseado no decaimento de ^{176}Lu para ^{176}Hf, através da emissão de radiação beta ($_{-1}^{0}\beta$), com meia vida de 3,76 x 10^{10} anos (37,6 bilhões de anos), como mostrado na tabela 2. O sistema Lu-Hf obedece a equação geral da geocronologia e dessa forma, para esse sistema, a equação 13 pode ser reescrita como:

$$^{176}\text{Hf} = \ ^{176}\text{Hf}_0 + \ ^{176}\text{Lu}(e^{\lambda t} - 1)$$ Equação 14

No entanto, devido a dificuldade de se determinar os valores absolutos de ^{176}Lu, ^{176}Hf$_0$ e ^{176}Hf por espectrometria de massa, geralmente na prática são determinadas razões isotópicas. Para isso ser possível, a amostra precisa ser ''contaminada'' com um isótopo não radiogênico de concentração conhecida, chamado de ''*spike*'', e assim os valores dos demais isótopos podem ser determinados (ver Dickin, 2005). No caso do sistema Lu-Hf o isótopo escolhido para *spike* é geralmente o ^{177}Hf e, portanto, após as razões isotópicas serem determinadas em laboratório, a idade do sistema pode ser calculada a partir da equação:

$$\frac{^{176}\text{Hf}}{^{177}\text{Hf}} = \left(\frac{^{176}\text{Hf}}{^{177}\text{Hf}}\right)_0 + \frac{^{176}\text{Lu}}{^{177}\text{Hf}}(e^{\lambda t} - 1)$$ Equação 15

A equação 15 descreve a equação de uma reta, uma vez que pode ser escrita como y = b + xm, onde a inclinação da reta é determinada por m = $e^{\lambda t}$ − 1. A variável b, ou seja (^{176}Hf/^{177}Hf)$_0$, descreve onde a reta intercepta o eixo vertical y (^{176}Hf/^{177}Hf). O eixo horizontal do gráfico é representado por x (^{176}Lu/^{177}Hf) (Fig. 10).
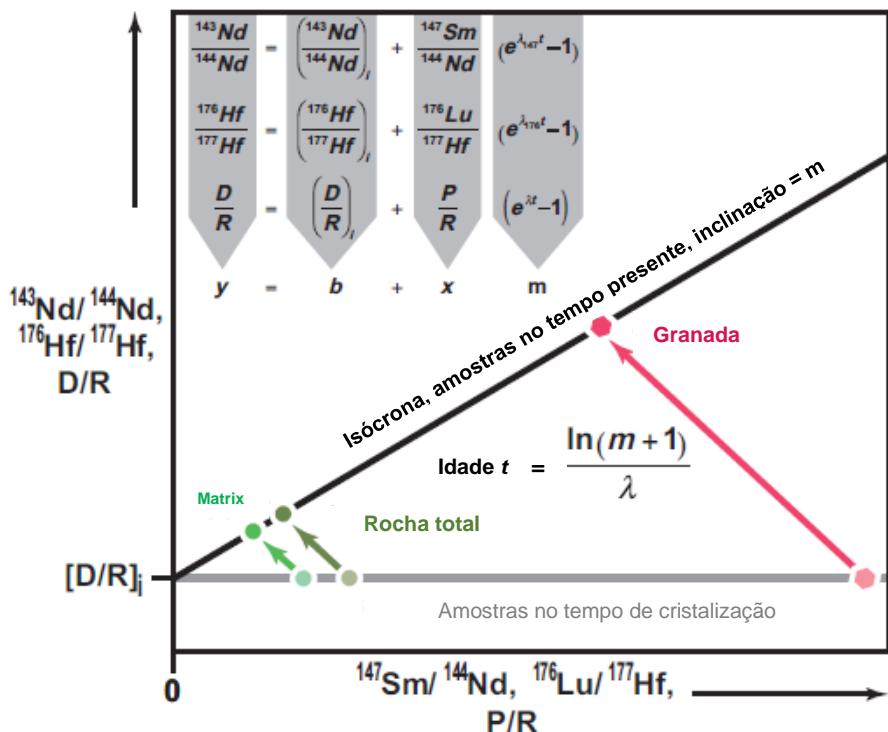
Figura 10. Datação Sm–Nd ou Lu–Hf de granada–rocha total utilizando o método da isócrona. Nos eixos são mostradas as equações de decaimento para Sm–Nd, Lu–Hf e o caso geral (P/R). As composições atuais medidas definem uma linha reta - uma "isócrona" - cuja inclinação (m) determina a idade (t) de crescimento da granada e dos demais minerais da matriz. D = isótopo radiogênico; P = isótopo radioativo; R = um isótopo de referência estável não radiogênico (Fonte: modificado de Baxter & Scherer, 2013).

Segundo Faure (2000), toda e qualquer idade de um sistema isotópico que possua a mesma razão inicial e a mesma idade (t), satisfazem a equação 15, e representam pontos sobre uma mesma reta no espaço $^{176}Hf/^{177}Hf$ *vs* $^{176}Lu/^{177}Hf$. Essa reta é dada pela inclinação m = $e^{\lambda t}$ – 1 (Fig. 10), e é denominada de ''isócrona'', uma vez que todos os pontos sobre ela apresentam a mesma idade t. A geocronologia utilizando o método de isócrona, no entanto, requer que todas as alíquotas/minerais analisados; (1) estiveram em equilíbrio isotópico, ou seja, com razão $(^{176}Hf/^{177}Hf)_0$ idêntica no tempo t_0 e; (2) mantiveram-se em sistema fechado (sem perda de isótopo radioativo e/ou radiogênico), desde então (Baxter & Scherer, 2013). A idade t da isócrona pode ser calculada isolando t na equação m = $e^{\lambda t}$ – 1:

$$t = \frac{1}{\lambda} \ln (m + 1) \qquad \qquad \text{Equação 16}$$

Uma vez que qualquer dois pontos geram uma reta, Baxter & Scherer (2013) argumentam que usualmente combinam-se pelo menos três geocronômetros distintos

equilibrados isotopicamente. O equilíbrio isotópico pode existir entre minerais cristalizados simultaneamente, ou pode se dar através da difusão, ou recristalização de minerais preexistentes durante o metamorfismo (Baxter & Scherer, 2013). No caso de estudos geocronológicos em granada, comumente, realiza-se a medição adicional das razões Lu-Hf em rocha total, e em algum outro mineral da matriz (p.e ilmenita, piroxênio, etc), conforme ilustrado na figura 10, definindo-se três pontos distintos sobre a isócrona. No entanto, em certas situações, isócronas de dois pontos são aconselháveis, uma vez que preencher uma isócrona com dados adicionais não produzirá necessariamente uma idade mais precisa (Baxter & Scherer, 2013). A ausência de equilíbrio isotópico dos minerais analisados e/ou a abertura do sistema Lu-Hf, por exemplo, farão com que os pontos se dispersem para fora da isócrona, de forma que uma única reta não consiga descrevê-los (Baxter & Scherer, 2013).

2.4.1.2. *Precisão e acurácia da isócrona Lu-Hf em granada*

A granada é referida como ''o petrocronômetro definitivo'' (Baxter & Scherer, 2013) devido aos diversos aspectos que a tornam um excelente mineral para estudos de petrocronologia (*e.g.* robustez, baixo coeficiente difusão, etc). No entanto, a precisão e a acurácia das idades de isócrona Lu-Hf obtidas neste mineral requerem considerações.

A precisão das idades de isócrona Lu-Hf, segundo Baxter et al. (2017), depende da qualidade em limitar com precisão a inclinação da isócrona, a qual depende de três fatores principais: 1) a precisão analítica das razões isotópicas de cada ponto/mineral analisado, 2) a presença de pontos que possuem razão isotópicas (radioativo/radiogênico) diferentes (*e.g.* rocha total e granada) e 3) a dispersão dos pontos de razão isotópica mais baixa e os de razão mais alta ao longo da isócrona. Cristais de granada livres de inclusões tipicamente possuem razão $^{176}Lu/^{177}Hf$ >1, sendo essa razão normalmente maior que a da rocha total e dos demais minerais presente na rocha (*e.g.* ilmenita, piroxênio, etc) (Baxter & Scherer, 2013; Baxter et al., 2017). Assim, as análises de granada comumente constituem o ponto mais afastado da origem da isócrona, enquanto os outros pontos da reta isócrona, comumente representam o ponto mais próximo da origem (Baxter et al., 2017), conforme ilustrado na figura 10.

A acurácia do método de isócrona Lu-Hf envolvendo granada depende principalmente da eliminação dos efeitos das inclusões nos cristais de granada.

Segundo Baxter & Scherer (2013), os efeitos das inclusões de monazita, apatita e zircão em granada são bem documentados e variam de acordo com i) a idade das inclusões, ii) a razão ^{176}Lu/^{177}Hf das inclusões e iii) a concentração do elemento radiogênico destas inclusões. Segundo esses autores, inclusões com concentrações muito baixas de Hf raramente afetam as idades Lu-Hf da granada. Inclusões com baixa razão ^{176}Lu/^{177}Hf (por exemplo, zircão, que possui muito Hf) de mesma idade da granada irão deslocar o ponto de "granada" na isócrona para mais próximo da origem, degradando a precisão da idade, mas não afetando a acurácia (i.e. mesma idade, maior erro - Baxter & Scherer, 2013). No entanto, inclusões com idade substancialmente diferentes da idade da granada deslocam as análises de "granada" para longe da isócrona real, levando à perda de acurácia da idade analisada (Baxter & Scherer, 2013).

As inclusões devem, portanto, ser evitadas. A cautelosa separação de granada feita por catação manual elimina o efeito das inclusões maiores, no entanto não é suficiente para eliminar as micro inclusões. Segundo Baxter et al. (2017), os métodos de maior sucesso na eliminação das micro inclusões em granada envolvem o procedimento de 'lixiviação' (leaching) ou o de 'dissolução parcial'. Ambos os processos se utilizam de vários ácidos fortes e, no primeiro caso, dissolve-se as inclusões problemáticas em solução descartada, deixando a granada pura para análise, enquanto no segundo caso, dissolve-se a granada pura na solução analisada deixando as inclusões problemáticas no resíduo sólido. O primeiro procedimento é o mais empregado para a geocronologia Sm–Nd em granada, enquanto o segundo, é mais utilizado para idades Lu-Hf em granada (Baxter et al., 2017). Ainda, é importante frisar, que, conforme discutido por Baxter et al. (2017), não há evidências que sugiram que a lixiviação/dissolução parcial afetem a concentração dos elementos Sm–Nd e Lu–Hf da granada, e deste modo, não geram influência/erro nas idades obtidas.

Duas assertivas são utilizadas com a finalidade de verificar a eficiência na remoção das inclusões (Baxter & Scherer, 2013; Baxter et al., 2017). A primeira delas é que a granada livre de inclusões produz uma razão ^{176}Lu/^{177}Hf > 1. Segundo Baxter et al. (2017), isso ocorre, pois, as inclusões contaminantes têm razões de isótopo radioativo/radiogênico muito mais baixas do que a granada hospedeira. A segunda é que a granada livre de inclusões exibe baixa concentração de Hf (<0.5, e frequentemente <0,1 ppm) (Baxter & Scherer, 2013; Baxter et al., 2017). Dessa forma, Baxter & Scherer (2013) recomendam que os efeitos da contaminação por inclusões são suficientemente reduzidos quando a granada tem razão ^{176}Lu/^{177}Hf > 1,0,

geralmente coincidindo com a concentração de Hf <1,0 ppm. Baxter et al. 2017, argumentam que esse limite é arbitrário, no entanto, serve como guia para estabelecer a confiança de uma determinada idade isócrona de granada.

2.4.1.3. *Geocronologia do sistema U-Th-Pb*

Enquanto a maioria dos sistemas isotópicos possuem apenas um isótopo radioativo que decai para um isótopo radiogênico (*e.g.* ^{176}Lu decai para ^{176}Hf), o sistema U-Th-Pb possui três sistemas de decaimento distintos: ^{238}U decai para ^{206}Pb, ^{235}U decai para ^{207}Pb e ^{232}Th decai para ^{208}Pb, com tempos de meia-vida também distintos (ver tabela 2) (Gehrels, 2014). Dessa forma, temos duas equações possíveis para o decaimento do urânio, uma para o ^{235}U e outra para o ^{238}U:

$$^{207}\text{Pb} = {}^{207}\text{Pb}_0 + {}^{235}\text{U}(e^{\lambda_{235}\,t} - 1) \hspace{2cm} \text{Equação 17}$$

e

$$^{206}\text{Pb} = {}^{206}\text{Pb}_0 + {}^{238}\text{U}(e^{\lambda_{238}\,t} - 1) \hspace{2cm} \text{Equação 18}$$

No entanto, no caso de minerais que incorporam fortemente o urânio no momento da formação, mas não incorporam o chumbo, como no zircão (ZrSiO4) e na monazita [(Ce,La,Nd,Th)PO4], as equações 17 e 18 podem ser simplificadas pela remoção dos termos ^{207}Pb$_0$ e ^{206}Pb$_0$, respectivamente, para gerar (Dickin, 2005):

$$\frac{^{207}\text{Pb}}{^{235}\text{U}} = (e^{\lambda_{235}\,t} - 1) \hspace{2cm} \text{Equação 19}$$

e

$$\frac{^{206}\text{Pb}}{^{238}\text{U}} = (e^{\lambda_{238}\,t} - 1) \hspace{2cm} \text{Equação 20}$$

Segundo Scherer et al. (2007), o zircão seja talvez o geocronômetro mais versátil disponível, justamente porque durante a sua formação incorpora urânio (U) e tório (Th) em sua estrutura cristalina, mas exclui o chumbo (Pb). Além disso o zircão é um geocronômetro ímpar devido a sua robustez, pois é um mineral que pode permanecer intacto mesmo se sua rocha hospedeira for metamorfizada, fundida ou

sofrer desgaste mecânico (Scherer et al., 2007). Ainda, as taxas de difusão dentro do zircão para muitos elementos são extremamente baixas, de modo que este mineral normalmente retém a idade e outras informações isotópicas mesmo quando expostas a temperaturas magmáticas (Lee et al., 1997; Scherer et al., 2007). O uso da monazita como geocronômetro, por sua vez, é crescente desde o início do século XXI (Williams et al., 2007). Os principais fatores para esse crescimento, segundo Williams et al. (2007), são: i) a presença da monazita em uma ampla variedade de rochas ígneas, metamórficas e sedimentares; ii) o reconhecimento de que as taxas de difusão de muitos elementos na monazita são muito lentas; iii) a expansão e aperfeiçoamento de técnicas para análise e datação de monazita; iv) uma compreensão crescente das condições sob as quais a monazita pode cristalizar e recristalizar nas rochas; e v) um crescente entendimento das relações geoquímicas e petrológicas entre a monazita e os minerais silicáticos de uma rocha.

Os três sistemas de decaimento independentes transformam a datação por U-Th-Pb um método bastante robusto, pois três geocronômetros independentes, marcados pelas razões $^{206}Pb/^{238}U$, $^{207}Pb/^{235}U$ e $^{208}Pb/^{232}Th$, idealmente resultam na mesma idade t (Gehrels, 2014). No entanto, segundo Gehrels (2014) algumas considerações devem ser feitas:

i) A concentração de Th é geralmente baixa e a razão $^{208}Pb/^{232}Th$ dificilmente é utilizada (Gehrels, 2014). Na prática, então, a idade é calculada medindo-se três razões isotópicas apenas: $^{206}Pb/^{238}U$, $^{206}Pb/^{207}Pb$ e $^{206}Pb/^{204}Pb$; e, dessa forma, dois geocronômetros independentes: $^{206}Pb/^{238}U$, $^{207}Pb/^{235}U$ (Gehrels, 2014).

ii) Como visto no item i) a razão $^{207}Pb/^{235}U$ não é medida. Isso ocorre pois tal razão pode ser calculada de forma confiável (embora, controversa) a partir das razões $^{206}Pb/^{238}U$, $^{206}Pb/^{207}Pb$ e $^{238}U/^{235}U$. Uma vez que a razão $^{238}U/^{235}U$ é constante na natureza (137,82), a razão $^{207}Pb/^{235}U$ pode então ser calculada pela fórmula abaixo (Gehrels, 2014):

$$\frac{^{207}Pb}{^{235}U} = \left(\frac{\frac{^{206}Pb}{^{238}U}}{\frac{^{206}Pb}{^{207}Pb} * 137.82} \right) \qquad \text{Equação 21}$$

iii) A razão $^{206}Pb/^{204}Pb$ é comumente medida de modo que as razões $^{206}Pb/^{238}U$ e $^{206}Pb/^{207}Pb$ possam ser corrigidas para Pb incorporado no momento da cristalização (Gehrels, 2014).

iv) Das três razões isotópicas essenciais de medição, segundo Gehrels (2014), $^{206}Pb/^{207}Pb$ e $^{206}Pb/^{204}Pb$ são relativamente mais fáceis de serem determinadas no espectrômetro de massa, devido ao baixo fracionamento dos isótopos de chumbo durante a análise. Ao contrário, a determinação da razão $^{206}Pb/^{238}U$ é mais difícil de ser feita, pois o U e o Pb se comportam diferentemente durante as análises.

Outra consideração importante nos estudos de geocronologia em zircão e monazita é a preocupação constante quanto a perda de Pb radiogênico durante a vida geológica da amostra, seja por efeito de fluídos, metamorfismo, etc. Um estudo geocronológico ideal exige que o cristal se comporte como um sistema fechado e retenha a composição original de U e Pb do momento de sua cristalização/metamorfismo. Nessa situação ideal os dois cronômetros de U-Pb, calculados de maneira independente - $^{206}Pb/^{238}U$ e $^{207}Pb/^{235}U$ – e por consequência as três razões $^{206}Pb/^{238}U$, $^{207}Pb/^{235}U$ e $^{206}Pb/^{207}Pb$ - devem resultar exatamente na mesma idade (Gehrels, 2014). Um meio conveniente de exibir os dois cronômetros U-Pb, além das três razões acima citadas, é através de um diagrama denominado de ''concórdia U-Pb'', ou simplesmente ''concórdia'' (Wetherill, 1956) (Fig. 11). Uma análise que plota em cima da curva concórdia é referida como ''concordante'' e é a situação ideal em geocronologia, pois indica que todas as três razões produziram idades semelhantes e a interpretação da idade é simples (Gehrels, 2014).

A perda de Pb durante a história evolutiva da rocha (sistema aberto), resulta em discordância entre as três razões independentemente determinadas gerando uma idade chamada de ''discordante''. Em casos de grandes discordâncias (>10%) o cálculo da idade de cristalização/metamorfismo do mineral torna-se impossibilitada, pois a imprecisão da medida cresce com o aumento da discordância. A interação da rocha com fluídos é um dos fatores mais comumente responsável pela perda de Pb. Além desses, outros processos como danos gerados por radiação, fraturamento do cristal devido à expansão diferencial da rede cristalográfica, alívio de pressão, recristalização, reações químicas e lixiviação são alguns dos outros processos que podem levar a perda de Pb radiogênico (Lee et al., 1997). Idades discordantes plotam fora da curva concórdia nos diagramas de concórdia U-Pb (Fig. 12) e, devido as três idades serem diferentes, possuem interpretação mais complexa do que as idades concordantes (Gehrels, 2014).
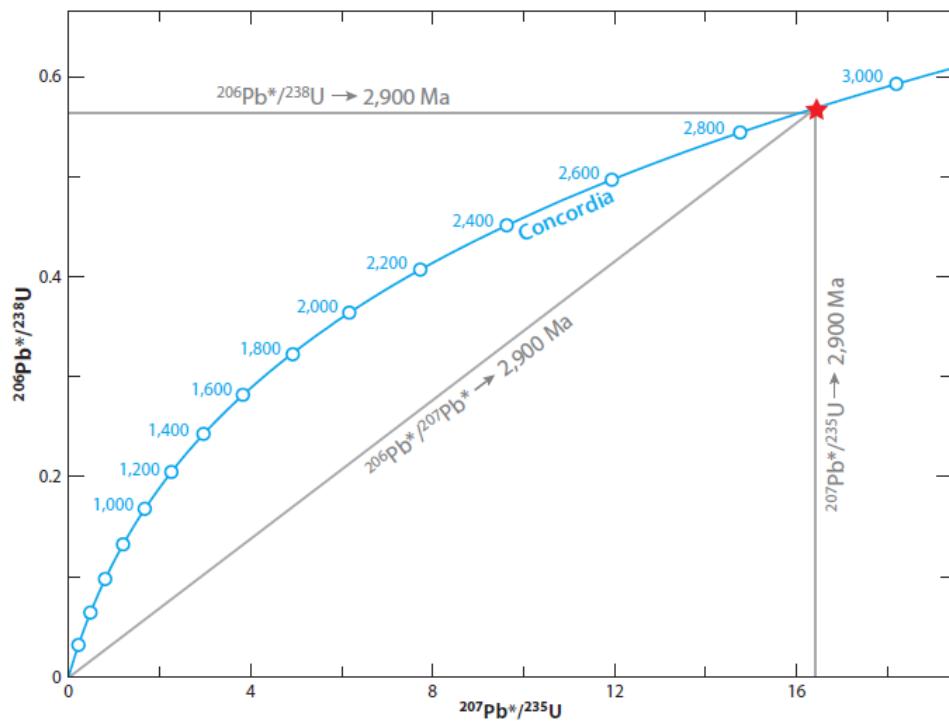
Figura 11. Exemplo de idade concordante em um diagrama Concórdia U/Pb, onde as idades indecentemente medidas por U^{235}/Pb^{207} (eixo x), U^{238}/Pb^{206} (eixo y) e Pb^{206}/Pb^{207} (diagonal) possuem o mesmo valor (2900 Ma) e, por isso, plotam sobre a curva concórdia (linha azul) (Fonte: Gehrels, 2014).

Como comentado acima, análises onde as três razões possuem mais de 10% de discordância são geralmente descartadas, no entanto, análises com discordância entre 1% e 10% são usualmente utilizadas. O impacto da perda de Pb resulta graficamente em um aumento da distância da curva concórdia, e as idades calculadas se tornam menos precisas à medida que o grau de discordância aumenta, porém este efeito é menos pronunciado para as idades Pb^{206}/Pb^{207} (detalhe da Fig. 12) (Gehrels, 2014). Por essa razão, as idades de Pb^{206}/Pb^{207} são geralmente as mais confiáveis para essas situações, embora, destaca-se que a idade verdadeira será sempre subestimadas (Gehrels, 2014). Por exemplo, na figura 12, a idade da amostra seria de 2900 Ma caso não houvesse perda de chumbo, no entanto, com a perda de chumbo as idades $^{206}Pb/^{238}U$, $^{207}Pb/^{235}U$ e $^{206}Pb/^{207}Pb$ foram, respectivamente, 2340 Ma, 2600 Ma e 2820 Ma. Ou seja, a idade obtida pela razão Pb^{206}/Pb^{207} é o valor mais próximo do valor real de 2900 Ma, embora subestimado.
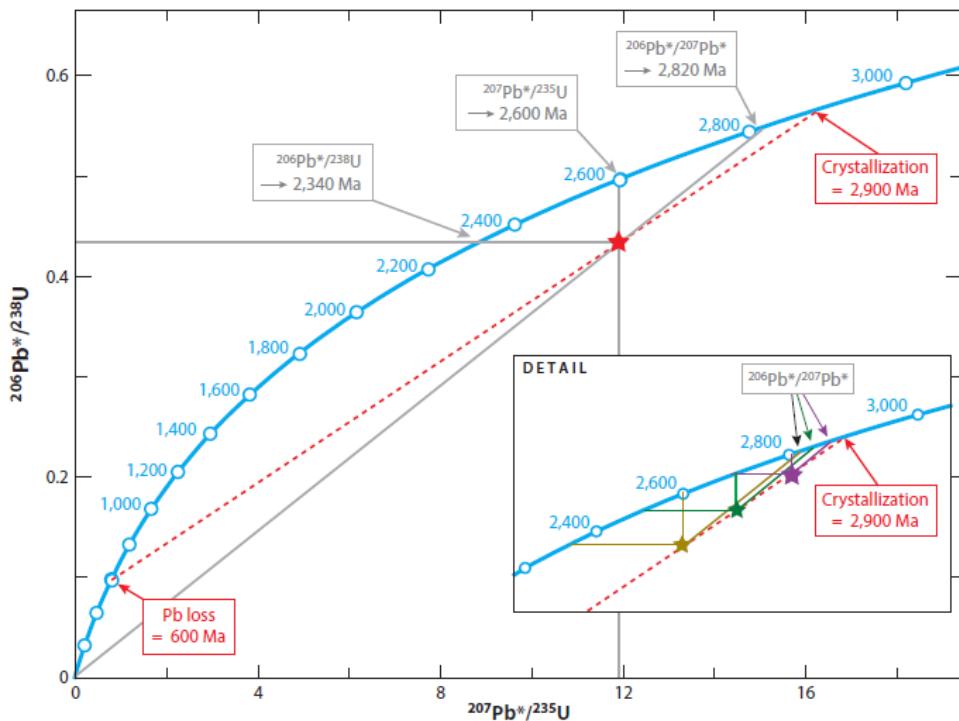
Figura 12. Exemplo de idade discordante em um diagrama Concórdia U/Pb, onde U²³⁵/Pb²⁰⁷ (eixo x), U²³⁸/Pb²⁰⁶ (eixo y) e Pb²⁰⁶/Pb²⁰⁷ (diagonal) possuem valores diferentes (2340, 2600 e 2820 Ma). Em detalhe, três amostras discordantes ilustrando que o efeito da discordância é menor sobre a idade Pb²⁰⁶/Pb²⁰⁷ (Fonte: Gehrels, 2014).

No caso de idades concordantes a escolha da razão a ser utilizada é baseada na precisão analítica que varia de tal forma que, $^{206}Pb/^{238}U$ é mais precisa para $t < 1,2$ Ga e $^{206}Pb/^{207}Pb$ é mais precisa para análises onde $t > 1,2$ Ga. A razão $^{207}Pb/^{235}U$ sempre possui maior incerteza do que as razões $^{206}Pb/^{238}U$ e $^{206}Pb/^{207}Pb$ e raramente é informada como a idade preferida. A única exceção para que a idade $^{207}Pb/^{235}U$ seja usada é no caso de zircões muito jovens, em que a idade $^{206}Pb/^{238}U$ é comprometida pelo decaimento do Th (Schärer, 1984).

2.4.2. Isótopos estáveis de oxigênio e o fracionamento isotópico

Os primeiros trabalhos que remetem ao estudo de isótopos de oxigênio em rochas são oriundos da década de 50 e 60, a exemplos dos trabalhos de Baertschi (1950) e Taylor (1968). Um dos principais aspectos positivos para o uso de isótopos estáveis de oxigênio, encontra-se no fato deste elemento estar presente na estrutura da grande maioria dos minerais, e desta forma possibilitar o emprego da técnica em variadas litologias, através do estudo de diversos minerais como, por exemplo,

quartzo, granada, olivina e, principalmente, zircão. A grande vantagem do uso do zircão, segundo Valley (2003), é que os cristais de zircão, quando não metamíticos, preservam a assinatura isotópica de oxigênio do momento da sua cristalização, mesmo quando submetidos a metamorfismo de alto grau; e, portanto, essa assinatura pode ser correlacionada com a idade U-Pb e a composição de elementos traço deste mineral. Além disso, a assinatura isotópica de oxigênio do evento metamórfico pode ser preservada nas bordas dos cristais de zircão, sem afetar a assinatura ígnea preservado no núcleo de cristais zonados (Scherer; Peck et al. (2003).

A simbologia comumente utilizada para se referir a valores de isótopos de oxigênio é $\delta^{18}O$, a qual é descrita por Garlick (1966), de forma que:

$$\delta^{18}O = \left[\frac{\frac{^{18}O}{^{16}O} \ medido \ no \ mineral \ ^*}{\frac{^{18}O}{^{16}O} \ VSMOW \ ^{**}} - 1 \right] 1000 \qquad \text{Equação 22}$$

* ou rocha total.

** do inglês *Vienna Standard Mean Ocean Water* (*VSMOW*).

SMOW é a abreviação da sigla *Standard Mean Ocean Water* que representa a razão isotópica natural medida na água oceânica. *Vienna Standard Mean Ocean Water* (VSMOW) é um padrão desenvolvido em laboratório por Craig (1961) de maneira que as razões isotópicas de oxigênio e hidrogênio fossem as mesmas das medidas naturalmente no SMOW. O padrão VSMOW possui, de fato, a mesma razão de $^{18}O/^{16}O$ do valor natural SMOW, enquanto a razão de $^2H/^1H$ é 0.2‰ menor do que no SMOV, o que, no entanto, fica dentro da margem de erro das medidas laboratoriais (International Atomic Energy Agency, 2009). A razão isotópica $^{18}O/^{16}O$ medida no padrão VSMOV é 0,00200520 ± 0,00000045 (International Atomic Energy Agency, 2009) enquanto as demais razões isotópicas são mostradas na tabela 3.

Tabela 3. Razões de abundância isotópica absoluta de isótopos de hidrogênio e oxigênio medidas no padrão VSMOW (Fonte: International Atomic Energy Agency, 2009).

	Razão Isotópica	Incerteza	Método
^{2}H/^{1}H	0,00015576	0,00000005	Espectometria de massa
^{2}H/^{1}H	0,00015575	0,00000008	Espectometria de massa
^{2}H/^{1}H	0,00015560	0,00000012	*Fourier-Transform Nuclear Magnetic Resonance*
^{18}O/^{16}O	0,00200520	0,00000045	Espectometria de massa
^{17}O/^{16}O	0,00037990	0,00000080	Espectometria de massa

A equação 22 prediz que: i) se $\frac{^{18}O}{^{16}O}$ medido no mineral $= \frac{^{18}O}{^{16}O}$ VSMOW, logo $\delta^{18}O=0$; ii) se $\frac{^{18}O}{^{16}O}$ medido no mineral $> \frac{^{18}O}{^{16}O}$ VSMOW, logo $\delta^{18}O > 0$; e iii) se $\frac{^{18}O}{^{16}O}$ medido no mineral $< \frac{^{18}O}{^{16}O}$ VSMOW, logo $\delta^{18}O < 0$. Assim, quanto mais positivo o valor de $\delta^{18}O$ for, mais enriquecido no isótopo pesado (^{18}O) o material/mineral será, e quanto menor o $\delta^{18}O$, mais empobrecido (*depleted*) em ^{18}O. O enriquecimento/empobrecimento dos isótopos estáveis pesados em relação aos isótopos estáveis leves se dá devido ao ''fracionamento isotópico''.

O fracionamento isotópico entre duas fases (mineral ou rocha) é, segundo Garlick (1966), representado pela diferença do valor de δ^{18}O registrado entre essas fases. O fracionamento de isótopos estáveis para diversos minerais foi estimado através de experimentos, medidas empíricas em amostras naturais e cálculos teóricos baseados em espectroscopia e potencial eletrostático (Valley, 2003). Desta forma, a partir de todos esses estudos combinados, pode-se estabelecer uma equação de fracionamento global que prediz o fracionamento isotópico de um elemento para um mineral em temperaturas acima de 600 ºC (Matthews et al., 1983; Valley, 2003):

$$\delta^{18}O_A - \delta^{18}O_B =$$

$$\Delta_{A-B} \approx 1000 \ln(\alpha_{A-B}) = \qquad \text{Equação 23}$$

$$A_{A-B} \, 10^6/T^2$$

Onde A_{A-B} é o coeficiente de fracionamento entre as fases ''*A*'' e ''*B*'' e T é a temperatura, expressa em Kelvin. Como cada mineral possui um valor específico para o coeficiente A_{A-B} da equação 23, é possível calcular o fracionamento de um elemento

químico entre duas fases minerais diferentes. A tabela 4 resume os valores do coeficiente A$_{A-B}$ do oxigênio para os minerais mais estudados, inclusive o zircão. A figura 13, por sua vez, demonstra os valores típicos de δ^{18}O para diferentes materiais naturais.

Tabela 4. Fracionamento de isótopos de oxigênio entre os minerais mais estudados (Fonte: Valley, 2003).

	Cc	Ab	Mu	FPh	An	Ph	Ap	Zc	Alm	Di	Gr	Gh	Ttn	Fo	Ru	Mt	Pv
Qz	0,38	0,94	1,37	1,64	1,99	2,16	2,51	2,54	2,71	2,75	3,03	3,50	3,66	3,67	4,69	6,29	6,80
Cc		0,56	0,99	1,26	1,61	1,78	2,13	2,26	2,33	2,37	2,65	3,12	3,28	3,29	4,31	5,91	6,42
Ab			0,43	0,70	1,05	1,22	1,57	1,70	1,77	1,81	2,09	2,56	2,72	2,73	3,75	5,35	5,86
Mu				0,27	0,62	0,79	1,14	1,27	1,34	1,38	1,66	2,13	2,29	2,30	3,32	4,92	5,43
FPh					0,35	0,52	0,81	1,00	1,07	1,11	1,39	1,86	2,02	2,03	3,05	4,65	5,16
An						0,17	0,52	0,65	0,72	0,76	1,04	1,51	1,67	1,68	2,70	4,30	4,81
Ph							0,35	0,48	0,55	0,59	0,87	1,34	1,50	1,51	2,53	4,13	4,64
Ap								0,13	0,20	0,24	0,52	0,99	1,15	1,16	2,18	3,78	4,29
Zc									0,07	0,11	0,39	0,86	1,02	1,03	2,05	3,65	4,16
Alm										0,04	0,32	0,79	0,95	0,96	1,98	3,58	4,09
Di											0,28	0,75	0,91	0,92	1,94	3,54	4,05
Gr												0,47	0,63	0,64	1,66	3,26	3,77
Gh													0,16	0,17	1,19	2,79	3,30
Ttn														0,01	1,03	2,63	3,14
Fo															1,02	2,62	3,13
Ru																1,60	2,11
Mt																	0,51

Abreviações: Ab = albita, Alm = almandina, An = anortita, Ap = apatita, Cc = calcita, Di = diopsídio, FPh = fluorflogopita, Fo = forsterita, Gh = gehlenita, Gr = grossulária, Um = muscovita, Mt = magnetita, Ph = flogopita, Pv = perovskita, Qz = quartzo, Ru = rutilo, Ttn = titanita, Zc = zircão.

No entanto, Valley (2003) destaca que o coeficiente A, na equação 23, assume a expressão $1000 \ln(\alpha_{A-B})$ $vs.$ $1/T^2$ como linear, o que, segundo esse autor, nem sempre é observado a baixas temperaturas, e por isso, esses coeficientes devem ser aplicados apenas em casos onde a temperatura é maior que 600 °C, como mencionado anteriormente. A aplicação da equação para temperaturas menores que 600 °C é discutida por Chacko et al. (2001). Segundo esses autores, acima de 600 °C o fracionamento isotópico de oxigênio entre os minerais anidros é aproximadamente lineares a partir da origem, quando representados em relação a 1/T^2 (a exemplo da equação 23). No entanto, abaixo de 600 °C, algumas curvas de fracionamento mineral-mineral se tornam significativamente mais complexas e extrapolações lineares dessas curvas podem resultar em cálculos errôneos de fracionamento, especialmente em temperaturas abaixo de 400 °C. Para casos de T menores que 100 °C o fracionamento entre dois minerais geralmente varia linearmente em relação 1/T^1 e não mais 1/T^2 (Chacko et al., 2001). Dessa forma, uma vez que T está no

denominador da equação, isso significa que o fracionamento isotópico é intensificado a baixas temperaturas.
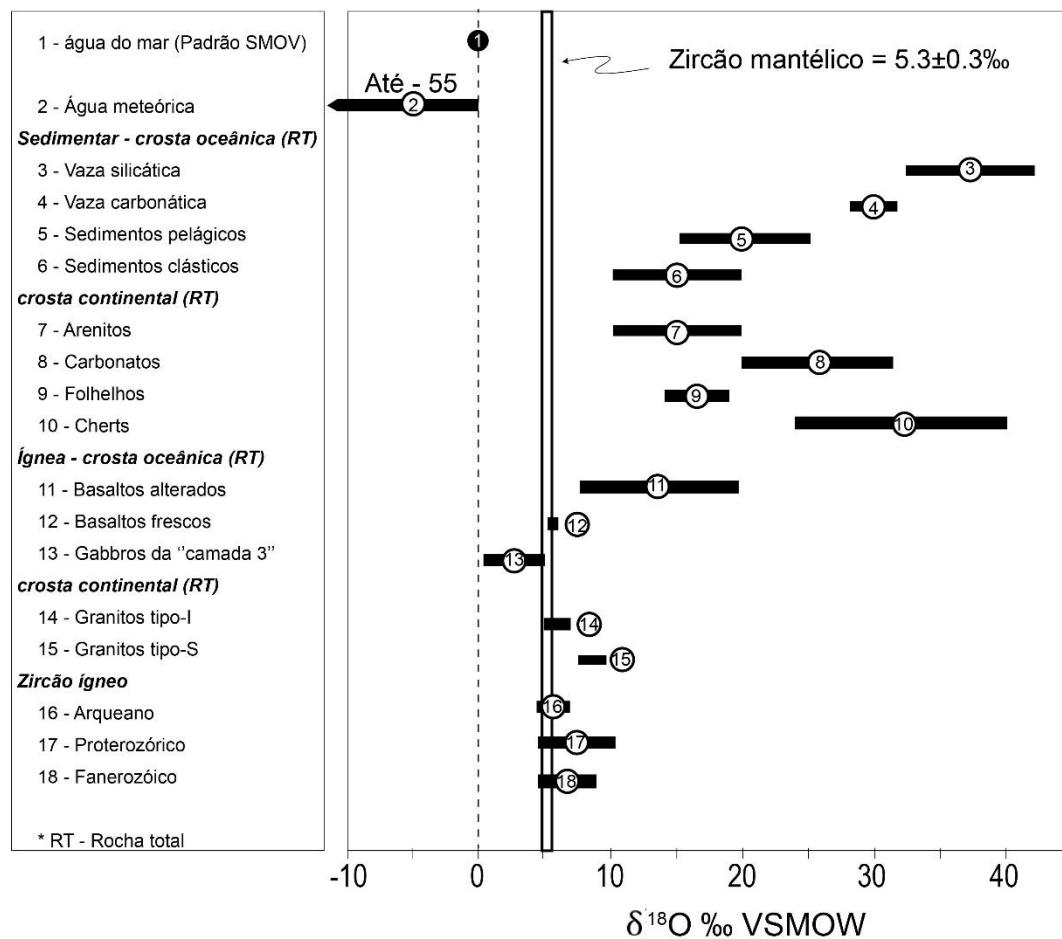
Figura 13. Valores típicos de $\delta^{18}O$ para diferentes rochas e minerais; além da água do mar (padrão VSMOW, ou seja, $\delta^{18}O=0$) e água meteórica (Fonte: Modificado de Eiler, 2001; e Valley et al., 2005).

Em se tratando do mineral zircão, a relação entre o valor de $\delta^{18}O$ deste em comparação ao $\delta^{18}O$ da rocha total em que ele se encontra, ou seja, o fracionamento entre essas duas fases ($\Delta^{18}O_{(Zrc-RT)}$), dependerá da mineralogia da rocha. Em condições de temperatura magmática este fracionamento ($\Delta^{18}O_{(Zrc-RT)}$) é uma função aproximadamente linear a porcentagem de peso de SiO2 da rocha ($wt.\% \ SiO_2$)(Valley et al., 2005). O fracionamento entre zircão e rocha total varia de $\delta^{18}O$ ~0.5‰ em rochas máficas e ~2‰ em rochas félsicas, de acordo com a relação (Valley et al., 1994):

$$\Delta^{18}O_{(Zrc-RT)} = \delta^{18}O_{(Zrc)} - \delta^{18}O_{(RT)} \approx -0.0612(wt.\% \ SiO_2) + 2.5 \qquad \text{Equação 24}$$

O motivo do fracionamento entre o $\delta^{18}O$ do zircão e o $\delta^{18}O$ da rocha total variar com o teor de sílica será abordado mais profundamente no item 2.4.4, onde é discutido sobre como os processos geológicos influenciam o $\delta^{18}O$ de rochas e minerais.

2.4.3. Taxa de difusão e temperatura de fechamento nos estudos de geocronologia

A taxa de difusão é um parâmetro crucial em estudos isotópicos, pois é ela determinará a velocidade com que um elemento químico será trocado entre o mineral e o meio em que ele se encontra. Esta propriedade é comumente modelada levando em conta todo o volume de um cristal, simulando um fluxo normal de um elemento iniciado na borda e indo em direção ao centro do grão (Valley, 2003). A taxa de difusão de cada elemento químico em um mineral específico é bastante variável, uma vez que depende das propriedades químicas e físicas de ambos. No zircão, em temperaturas de 1100°C o Pb radiogênico possui taxa de difusão quatro ordens de magnitude maior do que os elementos radioativos Th e U (Lee et al., 1997).

A difusão é também um importante mecanismo de troca de oxigênio em diversos minerais, como destacado por Cherniak & Watson (2001), Peck et al. (2003), Watson & Cherniak (1997) e outros autores. A taxa de difusão do oxigênio nos cristais de zircão é, no entanto, baixa sob altas temperaturas (Watson & Cherniak, 1997; Peck et al., 2003). Porém, vários estudos demonstram que o coeficiente de difusão de oxigênio no zircão varia com a presença ou ausência de água - com P_{H2O} ou sem P_{H2O} (Watson & Cherniak, 1997). Valley (2003) destaca que outras variáveis, incluindo recristalização, sobrecrescimentos, precipitação de material ao longo de microfraturas, além de inclusões, defeitos cristalinos e traços de fissão também podem alterar o $\delta^{18}O$ do zircão e causar heterogeneidades dentro de um mesmo cristal.

Na tentativa de melhor entender a difusão de oxigênio em diferentes minerais, Peck et al. (2003) e Valley et al. (1994) avaliaram o comportamento do oxigênio para três diferentes minerais de uma mesma rocha: quartzo, granada e zircão. Os autores demonstraram que o $\delta^{18}O$ de minerais como quartzo e granada são reequilibrados quando submetidos a um evento metamórfico de alto grau, ao passo que o zircão não sofre reequilibro e mantém seu valor magmático original. Dessa forma, nesse exemplo, a difusão de oxigênio, sob as condições acima citadas, é ativa e eficiente no quartzo e granada, porém não para zircão. Ainda, Peck et al. (2003) demonstraram a existência de uma borda formada por difusão nos cristais de zircão metamorfizados a

cerca de 675°C. O valor de $\delta^{18}O$ da borda destes cristais foram maiores que os medidos no núcleo, pois, segundo os autores, os núcleos preservam o valor de $\delta^{18}O$ do evento magmático, devido à baixa taxa de difusão do oxigênio nos cristais de zircão. Esse exemplo é uma demonstração de outra variável que controla a taxa de difusão de um cristal: o seu tamanho (Watson & Cherniak, 1997). Uma vez que a taxa de difusão é dependente do volume, cristais menores são mais comumente totalmente reequilibrados do que os de maiores dimensões. Os cristais maiores, por sua vez, podem reequilibrar apenas suas bordas e manter seus núcleos preservados.

A temperatura em que a difusão de um determinado elemento no interior do cristal cessa é conhecida como ''temperatura de fechamento''. É importante destacar que, assim como a taxa de difusão, a temperatura de fechamento é variável para diferentes elementos químicos de um mesmo mineral. No zircão, a temperatura de fechamento do Pb é superior a 900°C, enquanto para U e Th a difusão deixa de ser efetiva a 1100 °C (Lee et al., 1997). Dessa forma, Lee et al. (1997) concluem que a temperatura de fechamento do sistema U-Th-Pb se dá a 900°C no zircão, quando a difusão do chumbo deixa de ser efetiva. Alguns estudos corroboram com essa afirmativa e demonstram que o sistema U-Th-Pb se mantém fechado sob altas temperaturas em metamorfismo de alto grau (*e.g.* Maidment et al. 2013), no entanto, outros autores argumentam que esse sistema pode ser parcialmente afetado nessas condições (*e.g.* Wan et al., 2011). A temperatura de fechamento do zircão para os isótopos de oxigênio é incerta (Watson & Cherniak, 1997). Em situações onde a água não está presente, em um magma sob resfriamento lento, a temperatura de fechamento do zircão para oxigênio pode ser superior a 900°C (Watson & Cherniak, 1997), ao passo que, a adição de água no sistema, torna a difusão bem mais eficiente. Segundo estimativas dos mesmos autores, usando P_{H2O}= 70 bar, a temperatura de fechamento do zircão para a difusão de oxigênio é em torno de 500-550 °C.

2.4.4. $\delta^{18}O$ do zircão mantélico e os processos geológicos modificadores do $\delta^{18}O$ dos minerais

O valor de $\delta^{18}O$ padrão para zircões cristalizados em equilíbrio com as altas temperaturas do manto foi estabelecido por Valley et al., (1998). Os valores de δO_{18} provindos de análises de zircão em um kimberlito se situam estaticamente em 5.3±0.3‰ (1ϭ - Valley et al., 1998) (Fig. 14A). No entanto, Valley et al., (1998) e Eiler (2001), entre outros autores, destacam que o valor de $\delta^{18}O$ do manto seja

possivelmente heterogêneo e complexo, e amostras ocasionais podem apresentar variações (Fig. 14B).
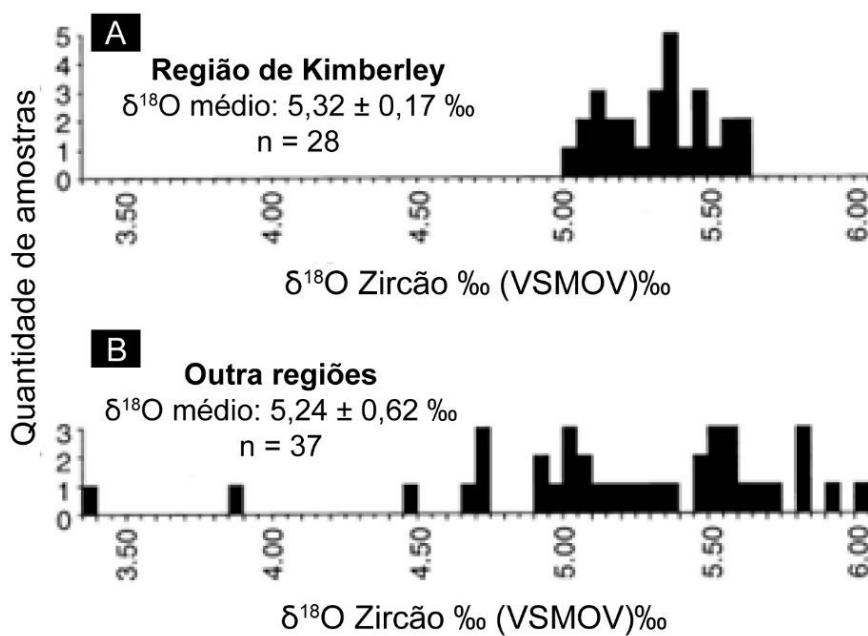
Figura 14. Valores $\delta^{18}O$ medidos em zircão de rochas máficas e ultramáficas. A) megacristais da região de Kimberley; e B) outras amostras de diferentes regiões do mundo (Fonte: modificado de Valley, 2003).

Os isótopos de oxigênio são importantes aliados na elucidação de processos atuantes durante a evolução de um magma (Eiler, 2001; Valley et al., 2005; Scherer et al., 2007), sendo que, no caso do zircão, um único grão pode registrar mais de um processo, que são comumente marcados por suas zonações ou intercrescimentos (Peck et al., 2003; Scherer et al., 2007). O registro desses processos pode auxiliar, por exemplo, para diferenciar um magma que evoluiu por cristalização fracionada, de outro que teve assimilações, ou aporte. Segundo Valley (2003), se um conjunto de magmas máficos e félsicos, em um sistema fechado, diferenciar por cristalização fracionada a partir de um magma parental, os valores de $\delta^{18}O$ dos cristais de zircão em todas as rochas dessa série serão os mesmos, mesmo que o valor de $\delta^{18}O$ de rocha total do magma félsico seja 1-2 ‰ maior do que o da rocha máfica, dada pela relação da equação 24. Isso ocorre porque todas as fases são consideradas em equilíbrio durante todo o processo e a diferenciação progride pela remoção precoce dos minerais máficos, os quais possuem menores valores de $\delta^{18}O$ em comparação com o quartzo e o feldspato, concentrados nos membros finais félsicos. Desta forma, o valor de $\delta^{18}O$ total da rocha félsica será maior pelo fato de esta possuir maior proporção de minerais enriquecidos em $\delta^{18}O$ (como quartzo e feldspato), mas o valor

de $\delta^{18}O$ de cada fase mineral individual será igual no membro máfico ou félsico da série. A figura 15 exemplifica essa questão, onde cristais de zircão com mesmo $\delta^{18}O$ são encontrados em rochas com diferentes teores de sílica de uma série magmática .
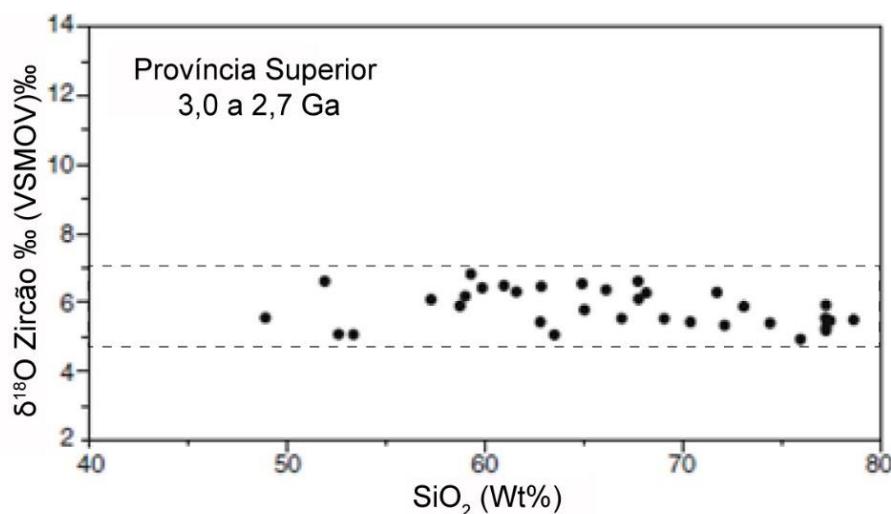
Figura 15. $\delta^{18}O$ em zircão comparados ao conteúdo de sílica de 35 amostras da Província Superior, no Canadá. Note que o teor de $\delta^{18}O$ no zircão permanece similar, mesmo o teor de sílica sendo bastante variável. A maioria das amostras são tonalitos, trondhjemitos e granodioritos (TTG) e rochas vulcânicas associadas com $\delta^{18}O$ médio de 5.5 ± 0.7 (1 SD) (Fonte: modificado de Valley et al., 2005).

Em contrapartida, a assimilação de novos materiais por um magma também pode ser registrada. Se algum material é adicionado ao magma, e este material não esteja em equilíbrio isotópico, ou seja, possua um valor de $\delta^{18}O$ diferente do magma que o está absorvendo, então o $\delta^{18}O$ do magma será alterado, assim como o $\delta^{18}O$ dos minerais subsequentes cristalizados, incluindo o zircão (Peck et al., 2001; Valley et al., 2005; Kemp et al., 2006). Os processos mais comuns que caracterizam tal tipo de situação são o aporte de outros magmas, assimilação de encaixante e fusão crustal (Peck et al., 2001; Valley et al., 2005; Kemp et al., 2006).

Processos hidrotermais também são importantes modificadores nos valores de $\delta^{18}O$ dos minerais (Peck et al., 2001; Kemp et al., 2006). Tais fluidos possuem valores de $\delta^{18}O$ muito baixos, entre 0 e -55 (Eiler, 2001; Valley et al., 2005), e dessa forma, pode reduzir drasticamente os valores de $\delta^{18}O$ dos minerais, caso haja interação entre os dois meios. Os riolitos de baixo $\delta^{18}O$ de Yellowstone (Bindeman & Valley, 2000; Valley, 2003; Valley et al., 2005), são exemplos desse fenômeno. A geração destas rochas está relacionada a câmaras magmáticas sub-vulcânicas rasas cujas paredes foram hidrotermalizadas. Essas paredes então foram assimiladas durante a geração dos riolitos por atividade magmática explosiva e influíram nos valores de $\delta^{18}O$ dos

minerais cristalizados (Bindeman & Valley, 2000; Valley, 2003; Valley et al., 2005). Desta forma, os cristais de zircão destas rochas chegam a apresentar valores de $\delta^{18}O$ menores que 5 ‰, ou seja, menores que os valores mantélicos. Ainda, em cenários de rifte, casos onde o derretimento de gelo afetaram os valores de $\delta^{18}O$ de rochas subsequentemente recristalizadas também foram reportados (Wickham & Taylor, 1985).

Com o passar do tempo geológico os processos supracitados irão exercer enorme influência sobre os valores de $\delta^{18}O$ do zircão e demais minerais, principalmente em rochas que envolvam demasiados processos crustais. Sedimentos reciclados e outros materiais supra-crustais comumente têm $\delta^{18}O$ mais alto que o do zircão mantélico (Valley et al., 2005). Tal evolução é demonstrada e discutida, por exemplo, por Peck et al. (2001), Valley (2003) e principalmente Valley et al. (2005). O resultado da atuação desses processos é que os valores de $\delta^{18}O$ para zircão são muito mais uniformes para a primeira metade da história terrestre, e muito mais variados para os tempos geológicos mais jovens (Valley et al., 2005) (Fig. 16). Tais variações nos valores de $\delta^{18}O$ do zircão ocorrem, pois a subducção, bem como os ambientes sedimentares, se tornaram mais ativos desde o Proterozóico. Os ambientes sedimentares são importantes porque favorecem a atuação de processos de baixa temperatura, os quais são muito mais eficientes no fracionamento de $\delta^{18}O$ (Matthews et al., 1998). A subducção, por sua vez, é a responsável por levar esse material fracionado, além da crosta oceânica alterada, para o manto e gerar magmas com valores de $\delta^{18}O$ maiores (Simon & Lécuyer, 2005). Dessa forma, os isótopos de oxigênio de magmas com contaminação crustal refletem uma mistura em escala geológica do manto e da crosta (Valley, 2003).

Amostras do Arqueano, revelam que os zircões magmáticos dessa idade possuem $\delta^{18}O$ variando entre 5 e 7.5‰ (Valley, 2003; Valley et al., 2005), com um valor médio de 5.82 ±0.74‰ (Valley et al., 2005) (Fig. 16). Os valores menores (5.3± 0.3‰) refletem cristais de zircão em equilíbrio com as altas temperaturas do manto (Valley et al., 2005), ao passo que, os valores levemente mais evoluídos (6.5 a 7.5‰) são interpretados como resultado da fusão de protólitos que sofreram interação com águas superficiais a baixa temperatura, gerando magmas levemente enriquecidos (Peck et al., 2001). Durante o Proterozóico, o intervalo e os valores de $\delta^{18}O$ dos cristais de zircão aumentaram gradualmente em uma mudança secular que documenta a maturação da crosta (Valley et al., 2005). Rochas mais jovens que 2.5 Ga, sejam elas Proterozóicas ou Fanerozóicas, apresentam mais comumente zircão com valores de

$\delta^{18}O$ entre 8‰ a >10‰, enquanto o $\delta^{18}O$ da rocha total, nessas ocasiões, varia de 9‰ a maiores que 12‰.
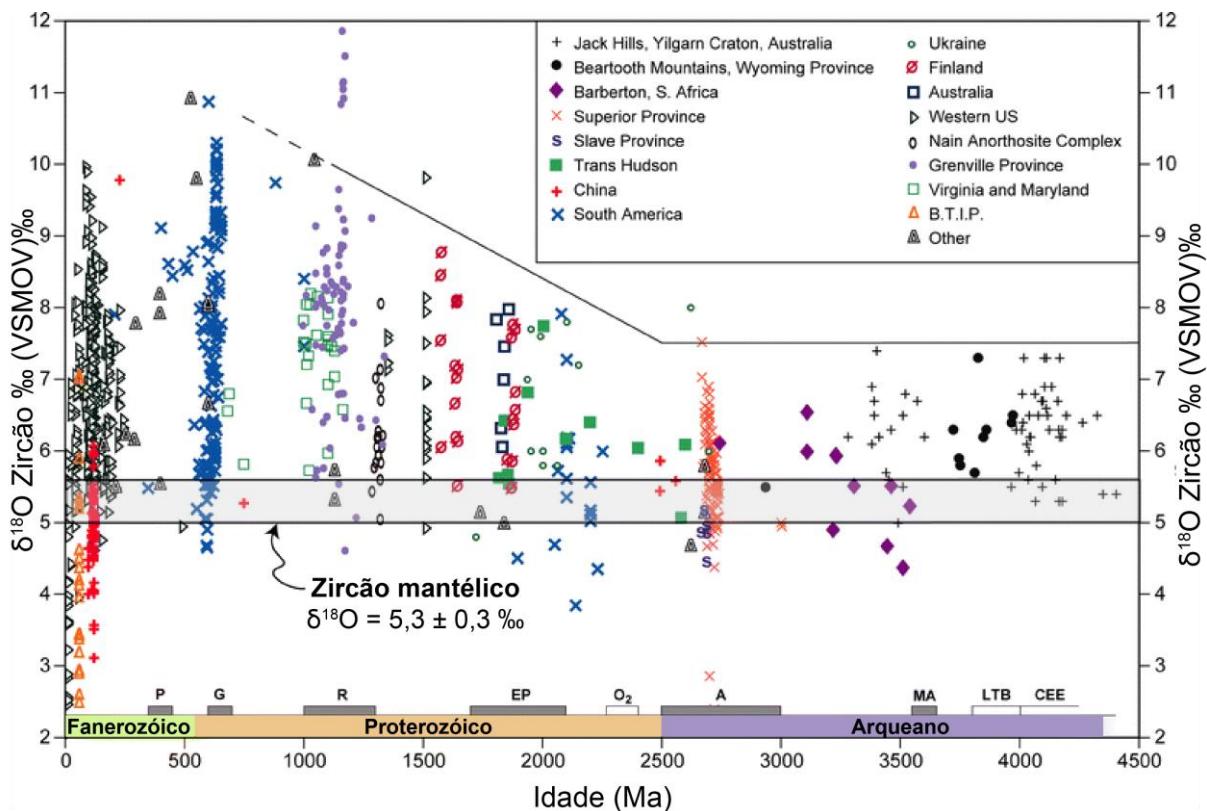
Figura 16. Compilação $\delta^{18}O$ vs idade obtidos em zircão de mais de 1200 rochas. Valores no arqueano são muito mais uniformes e próximos do manto (5,3 ± 0,3‰), enquanto, após 2,5 Ga, valores de $\delta^{18}O$ superiores a 7,5‰ são observados. Períodos de crescimento de supercontinentes são mostrados por barras na porção inferior: P - Pangea; G - Gondwana; R – Rodinia. LTB - Bombardeio Tardio, CEE - Terra primitiva fria e O_2 -aumento de oxigênio na atmosfera (Fonte: modificado de Valley et al., 2005).

2.4.5. Discordância U-Pb e a relação com $\delta^{18}O$ no zircão

A interação da rocha com fluídos é um dos fatores mais comumente responsável pela perturbação da assinatura isotópica dos minerais, incluindo elementos como chumbo e oxigênio, além de muitos outros. Sabendo desse fator determinante, Booth et al. (2005) buscaram encontrar alguma possível correlação entre o grau de discordância das idades U-Pb e os valores de $\delta^{18}O$ dos cristais de zircão. O resultado dos autores foi que, para as amostras analisadas, o zircão apresentava três texturas diferentes: A, B e C (Fig. 17).
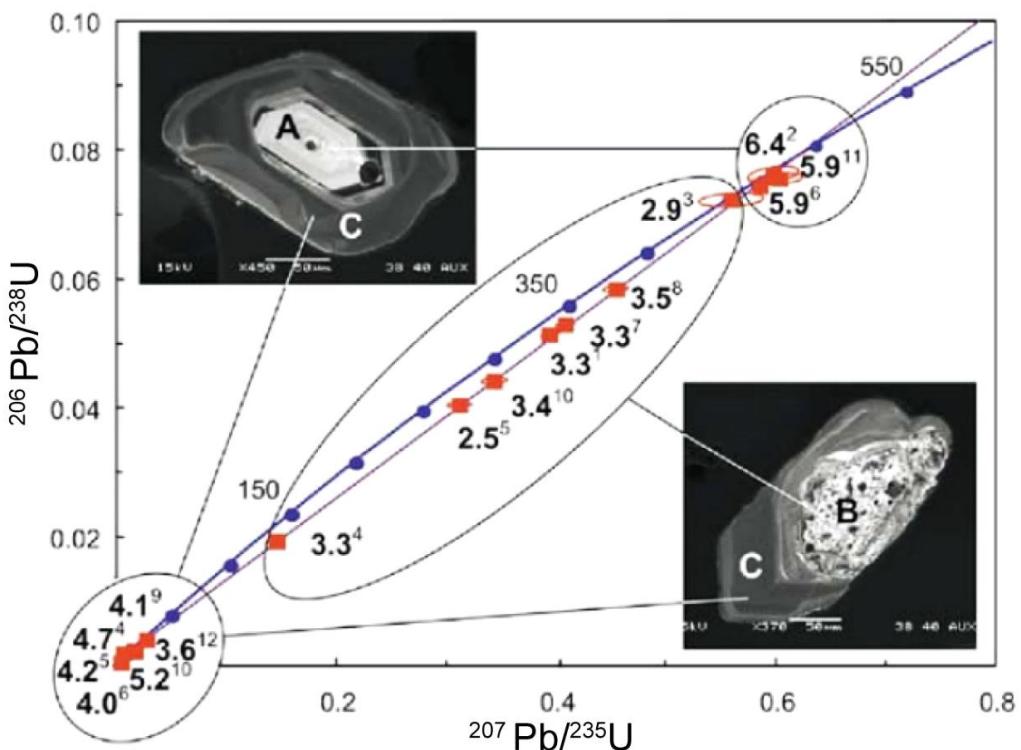
Figura 17. Diagrama concórdia U-Pb dos grãos analisados por Booth et al. (2005), em vermelho, com valores de $\delta^{18}O$ medidos, indicado em negrito. A textura representativa de cada grupo de grãos também é indicada (Fonte: Booth et al., 2005).

A textura ''A'' é caracterizada por cristais prismáticos, valores de $\delta^{18}O$ mais altos e idades concordantes, sendo a representante do magma original. A textura ''B'' apresenta cristais discordantes, com os menores valores de $\delta^{18}O$, e é resultado da recristalização por dissolução de núcleos ígneos de zircões em contato com fluídos de origem meteórica. A textura ''C'' apresenta valores de $\delta^{18}O$ intermediários entre ''A'' e ''B'', e plota no intercepto inferior da curva discórdia, interpretada como um sobrecrescimento tardio nos núcleos preexistentes de zircão.

Booth et al. (2005) concluíram que os zircões que sofreram perturbações no U-Pb original são frequentemente também empobrecidos de forma variável em $\delta^{18}O$, mas a relação entre discordância na idade U-Pb e $\delta^{18}O$ não é sistemática. A redução em $\delta^{18}O$ não depende diretamente do grau de discordância; em vez disso, é uma função da acessibilidade de um dado zircão à solução aquosa (Booth et al., 2005).

3. Resumo dos resultados

Esta tese aborda uma discussão da relação espacial e temporal de três complexos metamórficos posicionados no setor central do Cinturão Dom Feliciano, no estado do Rio Grande do Sul, Brasil. Os novos dados de geocronologia, geoquímica elementar e isotópica, e modelamento de condições metamórficas permitiram aprofundar o conhecimento sobre os complexos Porongos, Várzea do Capivarita e Passo Feio. Estes novos dados, em conjunto com os dados da literatura, possibilitaram um avanço no entendimento da evolução geológica do Cinturão Dom Feliciano. Os resultados desta tese são apresentados na forma de três artigos científico, cujas sínteses são descritas abaixo:

3.1. *O ambiente vulcanosedimentar compartilhado pelos complexos Porongos e Várzea do Capivarita em ca. 800-770 Ma.*

No primeiro artigo foi investigada a história pré-colisional do Cinturão Dom Feliciano (anterior a *ca.* 660 Ma) através do estudo de geocronologia e de isótopos de oxigênio em zircão nas rochas ortometamórficas intercaladas nas sequências metassedimentares do Complexo Várzea do Capivarita (CVC) e Complexo Porongos (CP). Duas amostras do Complexo Várzea do Capivarita e uma do Complexo Porongos foram investigadas. As idades de cristalização para o protólito ígneo (U–Pb em zircão) dos dois ortognaisses do CVC foram 786 ± 5 Ma (2σ) e 790 ± 7 Ma (2σ), respectivamente. Para o metariolito do CP a idade de cristalização obtida para o protólito ígneo foi de 787 ± 5 Ma (2σ).

O valor médio calculado para os isótopos de oxigênio (δO_{18}) nestes cristais de zircão de *ca.* 790 Ma foi de 8,41 ± 0,13‰ e 8,68 ± 0,14‰, para os ortognaisses do CVC, e 8,75 ± 0,72‰, para o metariolito do CP. Tais valores são maiores que os valores característicos de zircão mantélico (5,3 ± 0,3‰) e sugerem que provavelmente esses cristais de zircão cristalizaram em magmas mais evoluídos, seja por fusão de rochas encaixantes ou de sedimentos (*i.e.* subducção) ou por assimilação de material crustal por magmas mantélicos, como por exemplo pelo processo de assimilação–cristalização fracionada.

Uma amostra adicional de paragnaisse pelítico foi analisada com o intuito de se estabelecer a idade deposicional do Complexo Várzea do Capivarita. A população detrítica majoritária desta amostra se concentra entre 790-750 Ma. Além disso, o

espalhamento das idades detríticas está centrado em ca. 790 Ma, que corresponde à idade de cristalização dos ortognaisses. Este dado sugere uma contemporaneidade entre essas amostras, ou que o protólito sedimentar é principalmente um produto da erosão das rochas magmáticas de 790 Ma. Tais hipóteses são corroboradas pelo valor similar de δO_{18} encontrado nos cristais de zircão neoproterozóicos do paragnaisse (8.03 ± 0.33). Assim, interpretamos que esses dados sugerem uma história sin-vulcanosedimentar para o paragnaisse amostrado e, portanto, uma história sin-vulcanosedimentar para, pelo menos, parte do Complexo Várzea do Capivarita. Além disso, a correspondência dos dados geocronológicos e dos valores de δO_{18} em zircão sugerem que as rochas ortometamórficas estudadas do Complexo Várzea do Capivarita e Complexo Porongos compartilharam a mesma história ígnea. Assim, tais amostras provavelmente representem parte de um mesmo evento magmático em diferentes níveis de uma única bacia sedimentar em *ca.* 800-770 Ma.

3.2. História deformacional polifásica do Cinturão Dom Feliciano registrada nos complexos Porongos e Passo Feio.

O segundo artigo da tese teve por objetivo investigar a história colisional do Cinturão Dom Feliciano no antepaís oeste da colisão, com enfoque nos Complexos Porongos e Passo Feio, os quais careciam de dados. O Cinturão Dom Feliciano é a parte sul-americana de um extenso sistema orogênico neoproterozóico que teve sua estrutura principal desenvolvida durante o final do criogeniano e o ediacarano. Nesse artigo, modelamentos termodinâmicos (estimativas P-T), geocronologia de Lu–Hf granada–rocha total e U–Pb *SIMS* em monazita, além de elementos traços em granada e monazita foram obtidos para duas amostras metassedimentares do Complexo Porongos e uma do Complexo Passo Feio. Tais dados permitiram novas interpretações sobre a evolução tectônica do Cinturão Dom Feliciano.

O estudo na região leste do Complexo Porongos permitiu estabelecer que o evento metamórfico principal ocorreu em 662 ± 13 Ma (isócrona Lu–Hf granada–rocha total) sob condições de pico metamórfico de *ca.* 560–580 °C e 5.8–6.3 kbar. Esse episódio metamórfico-deformacional representa um evento de espessamento crustal no antepaís do Dom Feliciano em resposta ao início da tectônica transpressiva convergente do cinturão. Os cristais de monazita estudados de idade 614 ± 6 Ma (U–Pb *SIMS*) são interpretados como tendo sua gênese associada a fluídos oriundos da

atividade magmática nas proximidades, pós-exumação, e sugerem que a região leste do Complexo Porongos foi exumada em algum momento entre *ca.* 660 e 615 Ma.

O estudo de uma amostra da região oeste do Complexo Porongos permitiu estabelecer que o principal evento metamórfico-deformacional dessa região ocorreu em condições de 550–570°C e 4.5–5.5 kbar durante *ca.* 563 ± 12 Ma (isócrona Lu–Hf granada–rocha total). A exumação desta parte do antepaís é datada pela cristalização de monazita durante a quebra da granada e sugere retrometamorfismo em 541 ± 7 Ma (U–Pb *SIMS*). No Complexo Passo Feio, à oeste, a xistosidade metamórfica principal se desenvolveu durante 571 ± 13 Ma (isócrona Lu–Hf granada–rocha total) em condições de pico metamórfico de 560–580 °C e 4.7–6.4 kbar.

Os novos dados de geocronologia e modelamento termodinâmico demonstram que a região oeste do Complexo Porongos e o Complexo Passo Feio foram deformados em condições PT e gradientes geotérmicos similares em *ca.* 560-570 Ma. Esse episódio metamórfico-deformacional representa um segundo evento de espessamento crustal no antepaís do Dom Feliciano e registra uma migração para oeste da frente orogênica em um sistema orogênico transpressivo de longa duração (*ca.* 660–560 Ma).

3.3. *Caracterização dos diferentes magmatismos registrados nas sequências metamórficas dos complexos Porongos, Passo Feio e Várzea do Capivarita.*

O terceiro artigo da tese teve por objetivo investigar o magmatismo intermediário a ácido que ocorre intercalado nas sequências metassedimentares dos complexos Porongos, Passo Feio e Várzea do Capivarita, com intuito de explorar mais a fundo as relações entre esses três complexos. Assim, dados de geoquímica elementar e de isótopos de Sr-Nd foram compilados da literatura para as rochas ortomemamórficas desses complexos. Tal abordagem foi escolhida, uma vez que as assinaturas geoquímicas e isotópicas são ferramentas importantes para a investigação de fontes magmáticas e, quando aliadas a outras ferramentas (*p.e.* geologia estrutural, geocronologia), podem ser utilizadas para ajudar na reconstrução dos ambientes geológicos originais.

Além dos dados compilados da literatura, novos dados de geoquímica elementar e isotópica são apresentadas para sete rochas metavulcânicas dos complexos Porongos e Passo Feio, entre as quais, duas foram selecionadas para análises U-Pb

por LA-ICPMS em zircão. O conjunto de dados foi comparado e agrupado em padrões geoquímicos a partir da investigação dos elementos maiores e traços. O aspecto que mais realça a separação dos grupos geoquímicos são os padrões de Elementos Terras Raras (ETRs): i) O grupo 1 apresenta um enriquecimento de ETRL (leves) em relação aos ETRP (pesados) (LaN/YbN ≈ 10) e possui marcante anomalia negativa de Eu (Eu/Eu* = 0.38 a 0.86); ii) O grupo 2 não possui anomalia de Eu (Eu/Eu* = 0.94 a 1.07) e possui um enriquecimento mais pronunciado de ETRL em relação aos ETRP do que o grupo 1 (LaN/YbN = 12 a 44) e; iii) o grupo 3, que possui anomalia negativa de Eu (Eu/Eu* ≈ 0.70), porém dispõem de valores absolutos de ETRL muito maiores que os demais grupos (LaN/YbN ≈ 22). Uma amostra metavulcânica básica, referida como *Bmvc*, apresenta um quarto padrão geoquímico. Embora o padrão de ETRs se aproxime ao das amostras do grupo 2, os demais elementos traços demonstram que *Bmvc* não pertence a nenhum dos três grupos pré-estabelecidos. Os novos dados de U-Pb em zircão para duas amostras metavulcânicas ácidas da região norte do Complexo Passo Feio forneceram idades de cristalização para o protólito ígneo em ca. 580 ± 2 Ma (2σ).

Desta forma o magmatismo registrado pelas rochas ortometamórficas dos três complexos estudados pode ser agrupado em dois eventos magmáticos diacrônicos. As amostras do grupo geoquímico 1 fazem parte do primeiro evento magmático, o qual ocorreu em *ca.* 810–780 Ma no Complexo Várzea do Capivarita e na sequência Cerro da Árvore do Complexo Porongos. As rochas desse magmatismo representam uma associação magmática produzida por fontes relacionadas a subducção, e com significante contribuição de materiais crustais, como indicado pelos dados de elementos maiores e traços e pelos valores isotópicos de $^{87}Sr/^{86}Sr_{(790\ Ma)}$ > 0.715 e ℰNd$_{(790\ Ma)}$ de -5 e -11 (até -22). Tais características são plausíveis para um ambiente de arco magmático maduro, que é o ambiente sugerido para esse magmatismo toniano. Os grupos 2, 3 e *Bmvc* fazem parte do segundo evento magmático, que ocorreu em *ca.* 600–580 Ma no Complexo Passo Feio, e na sequência Capané, situada na região oeste do Complexo Porongos. As amostras do grupo 2 e 3, por sua vez, são interpretadas como tendo fonte oriunda de um manto enriquecido por subducção, porém sem contribuição elevada de materiais crustais, conforme indicado pelos valores de $^{87}Sr/^{86}Sr_{(580\ Ma)}$ = 0.7035–0.7050 e ℰNd$_{(580\ Ma)}$ > -10. Tais feições são passíveis de um ambiente de retro-arco, que é o ambiente sugerido para esse magmatismo. Para o padrão *Bmvc*, os dados sugerem uma origem mantélica sem enriquecimento por subducção e possivelmente indica fontes múltiplas para esse

magamtismo ediacarano recém-descoberto, e ainda, não completamente caracterizado.

A comparação dos dados da literatura com os novos dados apresentados, permitem uma nova interpretação quanto a evolução dos complexos Passo Feio e Porongos. Uma evolução geológica compartilhada é sugerida para o período de ca. 600–580 Ma entre os complexos Passo Feio e a sequência Capané, situada na região oeste do Complexo Porongos. Os dados também corroboram uma evolução compartilhada em *ca.* 810–770 Ma entre o Complexo Várzea do Capivarita e a sequência Cerro da Árvore do Complexo Porongos, como sugerido por outros autores.

4. Considerações Finais

A presente tese delimita alguns novos entendimentos sobre o Cinturão Dom Feliciano e como decorrência do avanço do conhecimento, abre espaço para novos questionamentos. A hipótese de correlação entre os complexos Várzea do Capivarita (CVC) e Porongos (CP) foi levantada a priori no trabalho de Martil (2016), quando esta autora demonstrou que a idade de cristalização dos ortognaisses do CVC eram semelhantes às idades das rochas metavulcânicas do CP (Saalmann et al., 2011; Pertille et al., 2017). Martil et al. (2017) e Battisti et al. (2018) exploraram mais essa relação através da comparação geoquímica de CVC e CP e, no caso de Martil et al. (2017), também de isótopos de Sr-Nd. Martil et al. (2017) compararam dados de Sr-Nd de diversas amostras do CVC com uma amostra metavulcânica ácida do CP. Além disso, Battisti et al. (2018) demonstraram uma evolução estrutural bastante semelhante entre a região leste do CP e o CVC (estudado por Martil, 2016). Os dados de ambos os autores indicaram deformação progressiva em ambos os complexos, a qual se iniciou com a movimentação de zonas de cisalhamento sub-horizontais de vergência para oeste e evoluiu para zonas de transcorrência subverticais. No entanto, as rochas do CP comparadas quimicamente com o CVC por Battisti et al. (2018) não possuíam idade de protólito conhecida. Além disso, dados de Sr-Nd de apenas uma amostra metavulcânica do CP fora comparada com o CVC por Martil et al. (2017) e, portanto, mais dados eram necessários para confirmar essa relação. No artigo 1 desta tese, demonstramos que as rochas ortometamórficas dos complexos Várzea do Capivarita e Porongos comparadas por Martil et al. (2017) e Battisti et al. (2018), respectivamente, apresentam a mesma idade de cristalização para o protólito ígneo: *ca.* 790 Ma. Além disso, a assinatura isotópica de oxigênio entre o zircão de todas

essas amostras é inteiramente similar, o que sugere a mesma fonte ígnea para tais rochas. Tal semelhança entre as rochas ortometamórficas destes complexos é corroborada ainda pelos novos dados de Sr-Nd apresentados no artigo 3. Assim a conexão entre o magmatismo de *ca.* 790 Ma no período pré-colisional do além-país (ou *hinterland*), representado pelo CVC, e do ante-país (ou *foreland*), representado pelo CP, no setor central do Cinturão Dom Feliciano é demonstrada nessa tese.

No entanto, embora a correlação entre as rochas ortoderivadas do CP e CVC possa ser feita de maneira mais direta, a correlação entre as rochas metassedimentares desses complexos exige mais cautela. Tal assertiva provém da disparidade de estudos no CP e no CVC, sendo o primeiro mais bem estudado. Apesar disso, no entanto, a julgar pelos dados disponíveis, o intervalo de proveniência para as rochas pré-colisionais de ambos complexos é bastante similar: 750 Ma – 3.0 Ga, com picos em 1.2–1.5 e 2.0–2.3 Ga no CP (Gruber et al., 2016a; Pertille et al., 2017; Höfig et al., 2018); e 730 Ma – 2.5 Ga com picos de 1.9–2.2 Ga no CVC (Gruber et al., 2016b). O artigo 1 desta tese, no entanto, apresenta um caráter vulcanosedimentar para o CVC em *ca.* 790 Ma, com proveniência característica de bacias de ante-arco ou retro-arco (Cawood et al., 2012). Tal padrão difere do padrão de sedimentação típico de rifte registrado para o Complexo Porongos e sua continuação no Dom Feliciano norte (Complexo Brusque), como discutido por Percival et al. (2021). A correlação entre os complexos Várzea do Capivarita e Porongos durante o período pré-colisional do Cinturão Dom Feliciano parece ser cada vez mais clara, no entanto, o ambiente original de sua formação ainda é ambíguo, uma vez que a geoquímica elementar aponta para um ambiente de arco maduro (Martil et al., 2017; Battisti et al., 2018, De Toni et al., 2020b, essa tese) e a sedimentação tem um caráter de rifte, em sua maioria (Konopásek et al., 2020; Percival et al., 2021). Mais estudos de proveniência no Complexo Várzea do Capivarita são necessários e talvez ajudem a responder essa questão.

Por sua vez, a relação entre os complexos Porongos e Passo Feio parece estar relacionada ao período tardi-colisional, ligeiramente anterior ao segundo (e último?) evento de espessamento crustal na porção central do Cinturão Dom Feliciano, em *ca.* 565 Ma. Magmatismo de *ca.* 600–580 Ma é registrado, tanto na porção oeste do Complexo Porongos quanto no Complexo Passo Feio (CPF). Os dados de geoquímica indicam que esse magmatismo é complexo, uma vez que três padrões distintos foram delimitados, podendo inclusive se tratar de diferentes eventos magmáticos sincrônicos, no entanto, com fontes similares, conforme indicam os novos dados de

Sr-Nd. Um estudo de maior detalhe, com maior número de amostras é necessário para uma melhor caracterização desse magmatismo. O espaço de colocação dessas rochas magmáticas (agora metamórficas) também precisa ser detalhado, uma vez que suas assinaturas isotópicas indicam pouco retrabalhamento crustal, mesmo que sua colocação se disponha temporalmente entre dois eventos contracionais de espessamento crustal (em *ca.* 660 Ma e *ca.* 565 Ma). A pouca contaminação crustal sugere um magmatismo possivelmente em um ambiente de crosta atenuada. Conforme mostrado no artigo 3 dessa tese, dados de geoquímica e Sr-Nd sugerem que as rochas metavulcânicas de *ca.* 600–580 Ma intercaladas no complexos Passo Feio e Porongos possam ter sido geradas em um ambiente de retro-arco extensional, similar ao observado para o Grupo Maricá na Bacia do Camaquã que se desenvolveu em 630–600 Ma, na vizinhança do CP e do CPF (Borba et al., 2008; Almeida et al., 2012; Paim et al., 2014). Ainda, é possível sugerir a colocação desse magmatismo em bacias transtrativas resultantes da movimentação de zonas transcorrentes, similar ao observado no Grupo Bom Jardim da Bacia do Camaquã que se depositou entre 595–580 (Janikian et al., 2008, 2012). No entanto, como acima mencionado, ainda são necessários mais estudos, principalmente de geologia estrutural, para descrever com exatidão o ambiente dos complexos Porongos em Passo Feio em 600–580 Ma.

Além do magmatismo Ediacarano, uma conexão entre a região oeste do Complexo Porongos e o Complexo Passo Feio é indicada pelo metamorfismo contemporâneo (563±12 *vs* 571±13 Ma) em condições metamórficas inteiramente similares (550–570°C/4.5–5.5 kbar *vs* 560–580°C/4.7–6.4 kbar), sob gradientes geotérmicos típicos de metamorfismo regional orogênico (25 to 35°C/km), conforme é demonstrado no artigo 2. A ocorrência desse segundo evento contracional está possivelmente associado a colisão tardia do Craton Kalahari com os crátons Río De la Plata e Congo, interpretado como responsável pela ativação de zonas transcorrentes em *ca.* 585 e *ca.* 550 Ma no Uruguai, por exemplo (Oriolo et al., 2016). É possível que a tectônica de baixo ângulo registrada no CPF e CP em *ca.* 565 Ma seja o registro de um componente compressivo ediacarano em resposta a partição da deformação dessas zonas de cisalhamento ativas no Uruguai, e que possivelmente se estenderam ao sul do Brasil. Sabe-se que a Zona de Cisalhamento de Caçapava do Sul, no limite leste do Complexo Passo Feio e oeste do Complexo Porongos, foi ativa durante a colocação do Granito Caçapava em 562 ± 8 Ma (Remus et al., 2000) e seria plausível que ela fora ativa anteriormente. No entanto, evidências para sugerir uma movimentação anterior a *ca.* 560 Ma ainda precisam ser levantadas.

Portanto, em suma, nessa tese uma conexão entre as evoluções dos complexos Porongos e Passo Feio também é sugerida. No entanto, adverte-se que para entender melhor essa relação, é necessário entender melhor o ambiente original de formação do Complexo Passo Feio e o espaço temporal no qual ele se desenvolveu. A temporalidade do complexo é pouco entendida, uma vez que existem poucos estudos de proveniência (Lopes et al., 2015; Souza, 2020; Philipp et al., 2021) e, anterior a esta tese, a idade do protólito das rochas metavulcânicas ácidas intercalados na sequência metamórfica era desconhecida. As rochas intermediárias e básicas conjuntamente intercaladas na sequência meta-vulcanossedimentar (Bitencourt, 1983) do Complexo Passo Feio também não dispõem de idades conhecidas.

5. Referências bibliográficas

Almeida, D.P.M., Chemale, F., Machado, A., 2012. **Late to Post-Orogenic Brasiliano-Pan-African Volcano-Sedimentary Basins in the Dom Feliciano Belt, Southernmost Brazil, in:** Petrology - New Perspectives and Applications. InTech.

Baertschi, P., 1950. **Isotopic composition of the oxygen in silicate rocks**. Nature v. 166, p.112–113.

Battisti, M.A., Bitencourt, M. F., De Toni, G.B., Nardi, L.V.S., Konopásek, J., 2018. **Metavolcanic rocks and orthogneisses from Porongos and Várzea do Capivarita complexes: A case for identification of tectonic interleaving at different crustal levels from structural and geochemical data in southernmost Brazil**. Journal of South American Earth Science v. 88, p.253–274.

Baxter, E.F., Caddick, M.J., Dragovic, B., 2017. **Garnet: A Rock-Forming Mineral Petrochronometer.** Reviews in Mineralogy and Geochemistry v. 83, p.469–533.

Baxter, E.F., Scherer, E.E., 2013. **Garnet Geochronology: Timekeeper of Tectonometamorphic Processes**. Elements v. 9, p.433–438.

Bea, F., Pereira, M.D., Stroh, A., 1994. **Mineral/leucosome trace-element partitioning in a peraluminous migmatite (a laser ablation-ICP-MS study)**. Chemical Geology v. 117, p.291–312.

Berman, R.G., 1988. **Internally-Consistent Thermodynamic Data for Minerals in the System Na_2O-K_2O-CaO-MgO-FeO-Fe_2O_3-Al_2O_3-SiO_2-TiO_2-H_2O-CO_2.** Journal of Petrology v. 29, p.445–522.

Berman, R.G., 1991. **Thermobarometry using multi-equilibrium calculations: a new technique, with petrological applications**. Canadian Mineralogist v. 29, p.833–855.

Bindeman, I.N., Valley, J.W., 2000. **Formation of low- δ 18O rhyolites after caldera collapse at Yellowstone , Wyoming , USA Formation of low- δ 18 O rhyolites after caldera collapse**. Geology v. 28, p.719–722.

Bitencourt, M. de F., Nardi, L.V.S., 2000. **Tectonic setting and sources of magmatism related to the southern Brazilian shear belt**. Revista Brasileira de Geociências v. 30, p.184–187.

Bitencourt, M. de F., Nardi, L.V.S., 1993. **Late- to Postcollisional Brasiliano Magmatism in Southernmost Brazil**. Anais Academia Brasileira de Ciências v. 65, p.3–16.

Bitencourt, M.F., 1983. **Metamorfitos da região de Caçapava do Sul, RS – Geologia e Relações com o Corpo Granítico**. Atas do 1º Simpósio Sul-Brasileiro Geologia p.37–48.

Bollinger, L., Janots, E., 2006. **Evidence for Mio-Pliocene retrograde monazite in the Lesser Himalaya, far western Nepal**. European Journal of Mineralogy v. 18, p.289–297.

Booth, A.L., Kolodny, Y., Chamberlain, C.P., McWilliams, M., Schmitt, A.K., Wooden, J., 2005. **Oxygen isotopic composition and U-Pb discordance in zircon**. Geochimica et Cosmochimica Acta v. 69, p.4895–4905.

Borba, A.W., Mizusaki, A.M.P., Santos, J.O.S., McNaughton, N.J., Onoe, A.T., Hartmann, L.A., 2008. **U-Pb zircon and ^{40}Ar-^{39}Ar K-feldspar dating of syn-sedimentary volcanism of the Neoproterozoic Maricá Formation: constraining the age of foreland basin inception and inversion in the Camaquã Basin of southern Brazil**. Basin Research v. 20, p.359–375.

Bowen, N.L., 1940. **Progressive Metamorphism of siliceous limestone and dolomite**. The Journal of Geology v. XLVIII, p.225–274.

Boyer, S.E., Elliott, D., 1982. **Thrust System**. The American Association of Petroleum Geologists Bulletin v. 66, p.1196–1230.

Brennan, R.P., 2000. **Gigantes da física**. Le Livros, Rio de Janeiro.

Bucher, K., Grapes, R., 2011. **Petrogenesis of metamorphic rocks**, 8th ed. Springer, Berlim.

Cawood, P.A., Hawkesworth, C.J., Dhuime, B., 2012. **Detrital zircon record and tectonic setting**. Geology v. 40, p.875–878.

Cawood, P.A., Kröner, A., Collins, W.J., Kusky, T.M., Mooney, W.D., Windley, B.F., 2009. **Accretionary orogens through Earth history**. Geological Society of London, Spec Publ v. 318, p.1–36.

Chacko, T., Cole, D., Horita, J., 2001. **Equilibrium Oxygen, Hydrogen and Carbon Isotope Fractionation Factors Applicable to Geologic Systems**. Reviews in Mineralogy and Geochemistry v. 43, p.1–81.

Cherniak, D.., Watson, E.., 2001. **Pb diffusion in zircon**. Chemical Geology v. 172, p.5–24.

Chetty, T., 2017. Orogens, Proterozoic Orogens of India.

Connolly, J.A.D., 2009. **The geodynamic equation of state: What and how**. Geochemistry, Geophysics, Geosystems v. 10.

Connolly, J.A.D., 2005. **Computation of phase equilibria by linear programming: A tool for geodynamic modeling and its application to subduction zone decarbonation**. Geological Society of London v. 236, p.524–541.

Connolly, J.A.D., 1990. **Multivariable phase diagrams: an algorithm based on generalized thermodynamics**. American Journal of Science v. 290, p.666–718.

Connolly, J.A.D., Kerrick, D.M., 1987. **An algorithm and computer program for calculating composition phase diagrams**. Calphad v. 11, p.1–55.

Costa, E.O. da, de Fátima Bitencourt, M., Tennholm, T., Konopásek, J., de Franceschi Moita, T., 2021. **P-T-D evolution of the southeast Passo Feio Complex and the meaning of the Caçapava Lineament, Dom Feliciano Belt, southernmost Brazil**. Journal of South American Earth Science p.103465.

Craig, H., 1961. **Isotopic Variations in Meteoric Waters**. Science (80) v. 133, p.1702–1703.

De Capitani, C., Petrakakis, K., 2010. **The computation of equilibrium assemblage diagrams with Theriak/Domino software**. American Mineralogist v. 95, p.1006–1016.

De Toni, G.B., Bitencourt, M.D.F., Konopásek, J., Battisti, M.A., da Costa, E.O., Savian, J.F., 2021. **Autochthonous origin of the Encruzilhada Block, Dom Feliciano Belt, southern Brazil, based on aerogeophysics, image analysis and PT-paths**. Journal of Geodynamicsv. 144.

De Toni, G.B., Bitencourt, M.F., Konopásek, J., Martini, A., Andrade, P.H.S., Florisbal, L.M., Campos, R.S., 2020a. **Transpressive strain partitioning between the Major Gercino Shear Zone and the Tijucas Fold Belt, Dom Feliciano Belt, Santa Catarina, southern Brazil**. Journal of Structural Geology p.104058.

De Toni, G.B., Bitencourt, M.F., Nardi, L.V.S., Florisbal, L.M., Almeida, B.S., Geraldes, M., 2020b. **Dom Feliciano Belt orogenic cycle tracked by its pre-collisional magmatism: the Tonian (ca. 800 Ma) Porto Belo Complex and its correlations in southern Brazil and Uruguay**. Precambrian Research p.105702.

Deer, W.A., Howie, R.A., Zussman, J., 2013. **An introduction to the rock-forming minerals, 3rd ed. Mineralogical Society of Great Britain and Ireland, London**. 3nd ed. p.510.

Dickin, A.P., 2005. **Radiogenic Isotope Geology**, 2nd ed. Cambridge University Press, New York. p.509

Edwards, R.L., Essene, E.J., 1988. **Pressure, Temperature and C-O-H Fluid Fugacities across the Amphibolite-Granulite Transition, Northwest Adirondack Mountains, New York**. Journal of Petrology v. 29, p.39–72.

Ehlers, K., Powell, R., Stuewe, K., 1994. **Cooling rate histories from garnet + biotite equilibrium**. American Mineralogist v. 79, p.737–744.

Eiler, J.M., 2001. **Oxygen Isotope Variations of Basaltic Lavas and Upper Mantle Rocks**. Reviews in Mineralogy and Geochemistry v. 43, p.319–364.

Elvevold, S., Ravna, E.J.K., Nasipuri, P., Labrousse, L., 2014. **Calculated phase equilibria for phengite-bearing eclogites from NW Spitsbergen, Svalbard Caledonides**. Geological Society of London, Spec Publ v. 390, p.385–401.

Engi, M., 2017. **Petrochronology Based on REE-Minerals: Monazite, Allanite, Xenotime, Apatite** - Reviews in Mineralogy & Geochemistry. v. 83, p.365–418.

Engi, M., Lanari, P., Kohn, M.J., 2017. **Significant Ages - An Introduction to Petrochronology**, em: Petrochronology v. 83, p.1–12.

England, P.C., Thompson, A.B., 1984. **Pressure - temperature - time paths of regional metamorphism I. heat transfer during the evolution of regions of thickened continental crust**. Journal of Petrology v. 25, p.894–928.

Faure, G., 2000. **Origin of Igneous rocks: the isotopic evidence**, 1st ed. Springer, New York.

Fossen, H., Cavalcante, G.C.G., Pinheiro, R.V.L., Archanjo, C.J., 2019. **Deformation – Progressive or multiphase?** Journal of Structural Geology v. 125, p.82–99.

Foster, G., Parrish, R.R., Horstwood, M.S.A., Chenery, S., Pyle, J., Gibson, H.D., 2004. **The generation of prograde P-T-t points and paths; a textural, compositional, and chronological study of metamorphic monazite**. Geological Society of London v. 228, p.125–142.

Fraser, G., Ellis, D., Eggins, S., 1997. **Zirconium abundance in granulite-facies minerals, with implications for zircon geochronology in high-grade rocks**. Geology v. 25, p.607–610.

Fuhrman, M.L., Lindsley, D.H., 1988. **Ternary-feldspar modeling and thermometry**. American Mineralogist v. 73, p.201–215.

Garlick, G.D., 1966. **Oxygen isotope fractionation igneous rocks** v. 1.

Gatewood, M.P., Dragovic, B., Stowell, H.H., Baxter, E.F., Hirsch, D.M., Bloom, R., 2015. **Evaluating chemical equilibrium in metamorphic rocks using major element and Sm–Nd isotopic age zoning in garnet, Townshend Dam, Vermont, USA**. Chemical Geology v. 401, p.151–168.

Gehrels, G., 2014. **Detrital Zircon U-Pb Geochronology Applied to Tectonics**. Annual Review of Earth and Planetary Sciences v. 42, p.127–149.

Gibbs, J.W., 1878. **On the Equilibrium of Heterogeneous Substances**. Tese de doutorado. Taylor, Printers, New Haven.

Grew, E.S., Locock, A.J., Mills, S.J., Galuskina, I.O., Galuskin, E. V., Hålenius, U., 2013. **Nomenclature of the garnet supergroup**. American Mineralogist v. 98, p.785–810.

Gruber, L., Porcher, C.C., Geller, H., Fernandes, L.A.D., Koester, E., 2016a. **Geochronology (U-Pb) and isotope geochemistry (Sr / Sr and Pb / Pb) applied to the Várzea do Capivarita Metamorphic Suite , Dom Feliciano Belt , Southern Brazil : Insights and paleogeographical implications to West Gondwana evolution** . Geochimica Brasiliensis v. 30, p.55–71.

Gruber, L., Porcher, C.C., Koester, E., Bertotti, A.L., Lenz, C., Fernandes, L.A.D., Remus, M.V.D., 2016b. **Isotope geochemistry and geochronology of syn-depositional volcanism in Porongos Metamorphic Complex, Santana da Boa Vista antiform, Dom Feliciano Belt, Brazil: onset of an 800 ma continental arc**. Journal of Sedimentary Environments v. 1.

Hacker, B., Kylander-Clark, A., Holder, R., 2019. **REE partitioning between monazite and garnet: Implications for petrochronology.** Journal of Metamorphic Geology v. 37, p.227–237.

Hagen-Peter, G., Cottle, J.M., Smit, M., Cooper, A.F., 2016. **Coupled garnet Lu-Hf and monazite U-Pb geochronology constrain early convergent margin dynamics in the Ross orogen, Antarctica**. Journal of Metamorphic Geology v. 34, p.293–319.

Harrison, T.M., Grove, M., Lovera, O.M., Catlos, E.J., D'Andrea, J., 1999. **The origin of Himalayan anatexis and inverted metamorphism: Models and constraints**. Journal of Asian Earth Sciences v. 17, p.755–772.

Höfig, D.F., Marques, J.C., Basei, M.A.S., Giusti, R.O., Kohlrausch, C., Frantz, J.C., 2018. **Detrital zircon geochronology (U-Pb LA-ICP-MS) of syn-orogenic basins in SW Gondwana: New insights into the Cryogenian-Ediacaran of Porongos Complex, Dom Feliciano Belt, southern Brazil**. Precambrian Research v. 306, p.189–208.

Holland, T.J.B., Powell, R., 1998. **An internally consistent thermodynamic data set for phases of petrological interest.** Journal of Metamorphic Geology v. 16, p.309–343.

Holland, T.J.B., Powell, R., 1990. **An enlarged and updated internally consistent thermodynamic dataset with uncertainties and correlations: the system K_2O-Na_2O-CaO-MgO-MnO-FeO-Fe_2O_3-Al_2O_3-TiO_2-SiO_2-C-H_2-O_2**. Journal of Metamorphic Geology v. 8, p.89–124.

IAEA: **Nuclear Data Section, 2019. Isotope Browser** [WWW Document].

International Atomic Energy Agency, 2009. **Reference Sheet for International Measurement Standards**. IAEA p.5.

IUPAC, 2014. **Gold Book** [WWW Document]. IUPAC Compendium of Chemical Terminology.

Janikian, L., De Almeida, R.P., Da Trindade, R.I.F., Fragoso-cesar, A.R.S., D'Agrella-Filho, M.S., Dantas, E.L., Tohver, E., 2008. **The continental record of Ediacaran volcano-sedimentary successions in southern Brazil and their global implications**. Terra Nova v. 20, p.259–266.

Janikian, L., de Almeida, R.P., Fragoso-Cesar, A.R.S., Martins, V.T. de S., Dantas, E.L., Tohver, E., McReath, I., D'Agrella-Filho, M.S., 2012. **Ages (U-Pb SHRIMP and LA ICPMS) and stratigraphic evolution of the Neoproterozoic volcano-sedimentary successions from the extensional Camaquã Basin, Southern Brazil**. Gondwana Research v. 21, p.466–482.

Johnson, J.W., Oelkers, E.H., Helgeson, H.C., 1992. SUPCRT92: **A software package for calculating the standard molal thermodynamic properties of minerals, gases, aqueous species, and reactions from 1 to 5000 bar and 0 to 1000°C**. Computers & Geosciences, v. 18, p.899–947.

Jost, H., Bitencourt, M.F., 1980. **Estratigrafia e tectônica de uma fração da Faixa de Dobramentos Tijucas no Rio Grande do Sul**. Acta Geologica Leopoldensia v. 11, p.27–59.

Kemp, A.I.S., Hawkesworth, C.J., Paterson, B.A., Kinny, P.D., Kemp, T., 2006. **Episodic growth of the Gondwana supercontinent from hafnium and oxygen isotopes in zircon**. Nature v. 439, p.580–583.

Koester, E., Porcher, C.C., Pimentel, M.M., Fernandes, L.A.D., Vignol-Lelarge, M.L., Oliveira, L.D., Ramos, R.C., 2016. **Further evidence of 777 Ma subduction-related continental**

arc magmatism in Eastern Dom Feliciano Belt, southern Brazil: The Chácara das Pedras Orthogneiss. Journal of South American Earth Science v. 68, p.155–166.

Kohn, M.J., 2014. **Geochemical Zoning in Metamorphic Minerals, in: Treatise on Geochemistry.** em: Treatise on Geochemistry, Elsevier, v. 4, p. 249–280.

Kohn, M.J., Penniston-Dorland, S.C., 2017. **Diffusion: Obstacles and Opportunities in Petrochronology.** Reviews in Mineralogy and Geochemistry v. 83, p.103–152.

Konopásek, J., Cavalcante, C., Fossen, H., Janoušek, V., 2020. **Adamastor – An ocean that never existed?** Earth-Science Reviews , v 205, p.2-18.

Konopásek, J., Janoušek, V., Oyhantçabal, P., Sláma, J., Ulrich, S., 2018. **Did the circum-Rodinia subduction trigger the Neoproterozoic rifting along the Congo–Kalahari Craton margin?** International Journal of Earth Sciences, v. 107, p.1859–1894.

Lacombe, O., Bellahsen, N., 2016. **Thick-skinned tectonics and basement-involved fold-thrust belts: Insights from selected Cenozoic orogens**, Geological Magazine v 153, p.763-810.

Lee, J.K.W., Williams, I.S., Ellis, D.J., 1997. **Pb, U and Th diffusion in natural zircon**. Nature v. 390, p.159–162.

Lopes, C.G., Pimentel, M.M., Philipp, R.P., Gruber, L., Armstrong, R., Junges, S., 2015. **Provenance of the Passo Feio Complex, Dom Feliciano Belt: Implications for the age of supracrustal rocks of the São Gabriel Arc, southern Brazil**. Journal of South American Earth Sciences v. 58, p.9–17.

Ludwig, K.R., 2003. **Isoplot: A Geochronological Toolkit for Microsoft Excel, version 3.00**.

Maidment, D.W., Hand, M., Williams, I.S., 2013. **High grade metamorphism of sedimentary rocks during Palaeozoic rift basin formation in central Australia**. Gondwana Research v. 24, p.865–885.

Martil, M.M.D., 2016. **O magmatismo de arco continental pré-colisional (790 ma) e a reconstituição espaço-temporal do regime transpressivo (650 ma) no Complexo Várzea Do Capivarita, Sul da Província Mantiqueira**. Tese de doutorado. Universidade Federal do Rio Grande do Sul, Porto Alegre, Brasil.

Martil, M.M.D., Bitencourt, M. de F., Nardi, L.V.S., Schmitt, R. da S., Weinberg, R., 2017. **Pre-collisional, Tonian (ca. 790 Ma) continental arc magmatism in southern Mantiqueira Province, Brazil: Geochemical and isotopic constraints from the Várzea do Capivarita Complex**. Lithos v. 274–275, p.39–52.

Matthews, A., Goldsmith, J.R., Clayton, R.N., 1983. **Oxygen isotope fractionations involving pyroxenes: The calibration of mineral-pair geothermometers**. Geochimica et Cosmochimica Acta v. 47, p.631–644.

Matthews, A., Stolper, E.M., Eiler, J.M., Epstein, S., 1998. **Oxygen isotope fractionation among melts, minerals and rocks**. Goldschmidt Conference, Toulouse p.971–972.

Oriolo, S., Oyhantçabal, P., Wemmer, K., Heidelbach, F., Pfänder, J., Basei, M.A.S., Hueck, M., Hannich, F., Sperner, B., Siegesmund, S., 2016. **Shear zone evolution and timing of deformation in the Neoproterozoic transpressional Dom Feliciano Belt, Uruguay**. Journal of Structural Geology v. 92, p.59–78.

Paim, P.S.G., Chemale Junior, F., Wildner, W., 2014. **Estágios evolutivos da Bacia Do Camaquã (RS)**. Ciência e Natura v. 36, p.183–193.

Peck, W.H., Valley, J.W., Graham, C.M., 2003. **Slow oxygen diffusion rates in igneous zircons from metamorphic rocks**. American Mineralogist v. 88, p.1003–1014.

Peck, W.H., Valley, J.W., Wilde, S.A., Graham, C.M., 2001. **Oxygen isotope ratios and rare earth elements in 3.3 to 4.4 Ga zircons: Ion microprobe evidence for high δ 18 O continental crust and oceans in the Early Archean**. Geochimica et Cosmochimica Acta v. 65, p.4215–4229.

Percival, J.J., Konopásek, J., Anczkiewicz, R., Ganerød, M., Sláma, J., Campos, R.S., Bitencourt, M.F., 2022. **Tectono-Metamorphic Evolution of the Northern Dom Feliciano Belt Foreland, Santa Catarina, Brazil: implications for models of subduction-driven orogenesis**. Tectonics v.41.

Percival, J.J., Konopásek, J., Eiesland, R., Sláma, J., de Campos, R.S., Battisti, M.A., Bitencourt, M. de F., 2021. **Pre-orogenic connection of the foreland domains of the Kaoko–Dom Feliciano–Gariep orogenic system**. Precambrian Res v. 354. p.2-20

Pertille, J., Hartmann, L.A., Philipp, R.P., 2015a. **Zircon U–Pb age constraints on the Paleoproterozoic sedimentary basement of the Ediacaran Porongos Group, Sul-Riograndense Shield, southern Brazil**. Journal of South American Earth Science v. 63, p.334–345.

Pertille, J., Hartmann, L.A., Philipp, R.P., Petry, T.S., de Carvalho Lana, C., 2015b. **Origin of the Ediacaran Porongos Group, Dom Feliciano Belt, southern Brazilian Shield, with emphasis on whole rock and detrital zircon geochemistry and U-Pb, Lu-Hf isotopes**. Journal of South American Earth Science v. 64, p.69–93.

Pertille, J., Hartmann, L.A., Santos, J.O.S., McNaughton, N.J., Armstrong, R., 2017. **Reconstructing the Cryogenian–Ediacaran evolution of the Porongos fold and thrust belt, Southern Brasiliano Orogen, based on Zircon U–Pb–Hf–O isotopes**. International Geology Review, v. 59, p.1532–1560.

Philipp, R.P., Pimentel, M.M., Basei, M.A.S., Salvi, M., De Lena, L.O.F., Vedana, L.A., Gubert, M.L., Lopes, C.G., Laux, J.H., Camozzato, E., 2021. **U–Pb detrital zircon dating applied to metavolcano-sedimentary complexes of the São Gabriel Terrane: New constraints on the evolution of the Dom Feliciano Belt**. Journal of South American Earth Science v. 110, p.1-27.

Philipp, R.P., Pimentel, M.M., Chemale Jr, F., 2016. **Tectonic evolution of the Dom Feliciano Belt in Southern Brazil: Geological relationships and U-Pb geochronology**. Brazilian Journal of Geology v. 46, p.83–104.

Porcher, C.C., Fernandes, L.A.D., 1990. **Relações embasamento-cobertura na porção ocidental do Cinturão Dom Feliciano: um esboço estrutural**. Pesquisas em Geociências v. 17, p.72–84.

Powell, R., Holland, T., Worley, B., 1998. **Calculating phase diagrams involving solid solutions via non-linear equations, with examples using THERMOCALC**. Journal of Metamorphic Geology v. 16, p.577–588.

Powell, R., Holland, T.J.B., 1985. **An internally consistent thermodynamic dataset with uncertainties and correlations: 1. Methods and a worked example**. Journal of Metamorphic Geology v. 3, p.327–342.

Powell, R., Holland, T.J.B., 1988. **An internally consistent dataset with uncertainties and correlations: 3. Applications to geobarometry, worked examples and a computer program**. Journal of Metamorphic Geology v. 6, p.173–204.

Pyle, J.M., Spear, F.S., 2003. **Yttrium zoning in garnet: Coupling of major and accessory phases during metamorphic reactions**. American Mineralogist v. 88, p.708.

Pyle, J.M., Spear, F.S., Rudnick, R.L., McDonough, W.F., 2001. **Monazite-xenotime-garnet equilibrium in metapelites and a new monazite-garnet thermometer**. Journal of Petrology v. 42, p.2083–2107.

Remus, M. V.D., Hartmann, L.A., McNaughton, N.J., Groves, D.I., Fletcher, I.R., 2000. **The link between hydrothermal epigenetic copper mineralization and the Cacapava Granite of the Brasiliano cycle in southern Brazil**. Journal of South American Earth Science v. 13, p.191–216.

Rodrigues, G.B., Fauth, G., 2015. **Isótopos estáveis de carbono e oxigênio em ostracodes do Cretáceo: metodologias, aplicações e desafios**. Terrae Didática v. 9, p.34.

Rubatto, D., Hermann, J., Buick, I.S., 2006. **Temperature and bulk composition control on the growth of monazite and zircon during low-pressure anatexis (Mount Stafford, Central Australia)**. Journal of Petrology v. 47, p.1973–1996.

Rutherford, E., Soddy, F., 1902. XLI. **The cause and nature of radioactivity – Part I**. London, Edinburgh, Dublin Philos Mag J Sci v. 4, p.370–396.

Saalmann, K., Gerdes, A., Lahaye, Y., Hartmann, L.A., Remus, M.V.D., Läufer, A., 2011. **Multiple accretion at the eastern margin of the Rio de la Plata craton: the prolonged Brasiliano orogeny in southernmost Brazil**. International Journal of Earth Sciences v. 100, p.355–378.

Saalmann, K., Remus, M.V.D., Hartmann, L.A., 2006. **Structural evolution and tectonic setting of the Porongos belt, southern Brazil**. Geological Magazine v. 143, p.59.

Sanderson, D.J., 1982. **Models of strain variation in nappes and thrust sheets: A review**. Tectonophysics v. 88, p.201–233.

Schärer, U., 1984. **The effect of initial ^{230}Th disequilibrium on young UPb ages: the Makalu case, Himalaya**. Geological Society of London v. 67, p.191–204.

Scherer, E.E., Whitehouse, M.J., Munker, C., 2007. **Zircon as a monitor of crustal growth**. Elements v. 3, p.19–24.

Simon, L., Lécuyer, C., 2005. **Continental recycling: The oxygen isotope point of view**. Geochemistry, Geophys Geosystems v. 6, p.1-10.

Souza, T.L., 2020. **Gênese dos serpentinitos e esteatitos do Complexo Passo Feio (RS-brasil): evidências mineralógicas , geoquímicas e isotópicas**. Tese de Doutorado. UFRGS, Porto Alegre - RS.

Spear, F.S., 1994. **Metamorphic phase equilibria and Pressure-temperature-time paths**, 2nd ed. Mineralogical Society of Amer, Chantilly, Estados Unidos da América.

Spear, F.S., Pattison, D.R.M., Cheney, J.T., 2016. **The metamorphosis of metamorphic petrology**, in: The Web of Geological Sciences: Advances, Impacts, and Interactions II. Geological Society of America, p. 31–73.

Spear, F.S., Peacock, S.M., 1989. **Metamorphic Pressure- Temperature-Time Paths**, 7th ed, Short Course in Geology. American Geophysical Union, Washington.

Spear, F.S., Pyle, J.M., 2010. **Theoretical modeling of monazite growth in a low-Ca metapelite**. Chemical Geology v. 273, p.111–119.

Tavani, S., Storti, F., Lacombe, O., Corradetti, A., Muñoz, J.A., Mazzoli, S., 2015. **A review of deformation pattern templates in foreland basin systems and fold-and-thrust belts: Implications for the state of stress in the frontal regions of thrust wedges**. Earth-Science Reviews v. 141, p.82–104.

Taylor, H.P., 1968. **The oxygen isotope geochemistry of igneous rocks**. Contributions to Mineralogy and Petrology v. 19, p.1–71.

Valley, J.W., 2003. **Oxygen Isotopes in Zircon**. Reviews in Mineralogy and Geochemistry v. 53, p.343–385.

Valley, J.W., Chiarenzelli, J.R., McLelland, J.M., 1994. **Oxygen isotope geochemistry of zircon**. Geological Society of London v. 126, p.187–206.

Valley, J.W., Kinny, P.D., Schulze, D.J., Spicuzza, M.J., 1998. **Zircon megacrysts from kimberlite: oxygen isotope variability among mantle melts**. Contributions to Mineralogy and Petrology v. 133, p.1–11.

Valley, J.W., Lackey, J.S., Cavosie, A.J., Clechenko, C.C., Spicuzza, M.J., Basei, M.A.S., Bindeman, I.N., Ferreira, V.P., Sial, A.N., King, E.M., Peck, W.H., Sinha, A.K., Wei, C.S., 2005**. 4.4 billion years of crustal maturation: Oxygen isotope ratios of magmatic zircon**. Contributions to Mineralogy and Petrology v. 150, p.561–580.

Van Grieken, R., de Bruin, M., 1994. **Nomenclature for radioanalytical chemistry (IUPAC Recommendations 1994)**. Pure and Applied Chemistry v. 66, p.2513–2526.

Vanderhaeghe, O., 2012. **The thermal-mechanical evolution of crustal orogenic belts at convergent plate boundaries: A reappraisal of the orogenic cycle**. Journal of Geodynamics v. 56–57, p.124–145.

Wan, Y., Liu, D., Dong, C., Liu, S., Wang, S., Yang, E., 2011. **U–Th–Pb behavior of zircons under high-grade metamorphic conditions: A case study of zircon dating of meta-diorite near Qixia, eastern Shandong**. Geoscience Frontiers v. 2, p.137–146.

Watson, E.., Cherniak, D.., 1997. **Oxygen diffusion in zircon**. Geological Society of London v. 148, p.527–544.

Wetherill, G.W., 1956. **Discordant uranium-lead ages**, I. Transactions, American Geophysical Union v. 37, p.320.

White, R.W., Powell, R., Holland, T.J.B., Johnson, T.E., Green, E.C.R., 2014. **New mineral activity-composition relations for thermodynamic calculations in metapelitic systems**. Journal of Metamorphic Geology v. 32, p.261–286.

White, W.M., 2013. **Geochemistry**, 1st ed. Wiley-Blackwell, New York.

Wickham, S.M., Taylor, H.P., 1985. **Stable isotopic evidence for large-scale seawater infiltration in a regional metamorphic terrane; the Trois Seigneurs Massif, Pyrenees, France.** Contributions to Mineralogy and Petrology v. 91, p.122–137.

Will, T.M., Gaucher, C., Ling, X.-X., Li, X.-H., Li, Q.-L., Frimmel, H.E., 2019. **Neoproterozoic magmatic and metamorphic events in the Cuchilla Dionisio Terrane, Uruguay, and possible correlations across the South Atlantic**. Precambrian Research v. 320, p.303–322.

Williams, I.S., 1998. **U-Th-Pb geochronology by ion microprobe**. Reviews in Economic Geology v. 7, p.1–35.

Williams, M.L., Jercinovic, M.J., Hetherington, C.J., 2007. **Microprobe Monazite Geochronology: Understanding Geologic Processes by Integrating Composition and Chronology**. Annual Review of Earth and Planetary Sciences v. 35, p.137–175.

Yakymchuk, C., Clark, C., White, R.W., 2017. **Phase Relations, Reaction Sequences and Petrochronology**. Reviews in Mineralogy and Geochemistry v. 83, p.13–53.

Yardley, B.W.D., 1989. **An introduction to metamorphic petrology**, 1st ed. Longman Singapore Publishers, Leeds. p. 248.

6. Apresentação dos artigos científicos

6.1. Artigo 1

O artigo intitulado ''*Reconstruction of a volcano-sedimentary environment shared by the Porongos and Várzea do Capivarita Complexes at 790 Ma, Dom Feliciano Belt, southern Brazil*'' de Battisti, M.A.; Bitencourt, M.F.; Schmitt, R.S., Nardi, L.V.S.; Martil, M.M.D.; De Toni, G.B.; Pimentel, M.; Armstrong, R.; Konopásek, J. foi submetido ao periódico *Precambrian Research* no dia 10/02/2022.

Confirming submission to Precambrian Research

De	Precambrian Research <em@editorialmanager.com>	
Remetente	<em.precam.0.79444b.64c6268e@editorialmanager.com>	
Para	Matheus Ariel Battisti <matheus.battisti@ufrgs.br>	
Responder p...	Precambrian Research <support@elsevier.com>	
Data	2022-02-10 11:09	

```
*This is an automated message.*

Reconstitution of a volcano-sedimentary environment shared by the Porongos and Várzea do Capivarita Complexes at 790 Ma, Dom
Feliciano Belt, southern Brazil

Dear Mr. Battisti,

We have received the above referenced manuscript you submitted to Precambrian Research.

To track the status of your manuscript, please log in as an author at https://www.editorialmanager.com/precam/, and navigate to the
"Submissions Being Processed" folder.

Thank you for submitting your work to this journal.

Kind regards,
Precambrian Research

More information and support

You will find information relevant for you as an author on Elsevier's Author Hub: https://www.elsevier.com/authors

FAQ: How can I reset a forgotten password?
    https://service.elsevier.com/app/answers/detail/a_id/28452/supporthub/publishing/kw/editorial+manager/

For further assistance, please visit our customer service site: https://service.elsevier.com/app/home/supporthub/publishing/. Here
you can search for solutions on a range of topics, find answers to frequently asked questions, and learn more about Editorial
Manager via interactive tutorials. You can also talk 24/7 to our customer support team by phone and 24/7 by live chat and email.

#AU_PRECAM#

To ensure this email reaches the intended recipient, please do not delete the above code


In compliance with data protection regulations, you may request that we remove your personal registration details at any time.  (Use
the following URL:


        https://www.editorialmanager.com/precam/login.asp?a=r). Please contact the publication office if you have any
questions.
```

Reconstruction of a volcano-sedimentary environment shared by the Porongos and Várzea do Capivarita Complexes at 790 Ma, Dom Feliciano Belt, southern Brazil

Matheus Ariel **Battisti**[a], Maria de Fátima **Bitencourt**[a], Renata da Silva **Schmitt**[b], Lauro Valentim Stoll **Nardi**[a], Mariana Maturano Dias **Martil**[a], Giuseppe Betino **De Toni**[c], Márcio **Pimentel**[a], Richard **Armstrong**[d], Jiri **Konopásek**[e, f]

a- Programa de Pós-graduação em Geociências, Instituto de Geologia, Universidade Federal do Rio Grande do Sul, Porto Alegre, Brazil

b- Departamento de Geologia – IGEO, Universidade Federal do Rio de Janeiro, Rio de Janeiro, Brazil

c- Curso de Geologia, Escola Politécnica, Universidade do Vale do Rio dos Sinos (UNISINOS)

d- Research School of Earth Science, Australian National University, ANU, Canberra, Australia

e- Department of Geosciences, UiT–The Arctic University of Norway, Tromsø, Norway

f- Czech Geological Survey, Prague, Czech Republic

Corresponding author: Matheus Ariel Battisti, matheus.ariel.battisti@gmail.com

Address: Av. Bento Gonçalves, 9500 – Porto Alegre, Rio Grande do Sul state, Brasil. IGEO – Universidade Federal do Rio Grande do Sul, Campus do Vale – Zip Code: 91501-970.

ABSTRACT

This work investigates the pre-collisional (before ca. 650 Ma) history of the Dom Feliciano Belt in southernmost Brazil through geochronological and zircon oxygen isotope study. U–Pb SHRIMP dating of two orthogneiss samples from the Várzea do Capivarita Complex, and one metarhyolite sample from the Porongos Complex yielded crystallization ages of 786 ± 5 Ma, 790 ± 7 Ma and 787 ± 5 Ma, respectively. The mean oxygen isotopic values calculated for the ca. 790 Ma zircon cores from the orthogneisses yielded 8.41 ± 0.13‰ and 8.68 ± 0.14‰, and 8.75 ± 0.72‰ for the metarhyolite. Such values suggest that zircon crystallized in the more evolved magmas, either from melting of host rocks and sediments or assimilation of crustal material by mantle-derived magmas, as for example by assimilation-fractional crystallization process. Detrital zircon population was analysed in one additional paragneiss sample from the Várzea do Capivarita Complex, and most of the values cluster at 790–750 Ma. The spread of the data is centered at ca. 790 Ma, which is the crystallization age of the interleaved orthogneisses. In our interpretation, such dataset suggests a syn-volcanic origin of the paragneiss protolith, and therefore a volcano–sedimentary origin of the Várzea do Capivarita Complex. The correspondence of geochronological data and zircon oxygen isotope values for the studied meta-igneous samples suggests that the Várzea do Capivarita and Porongos complexes shared the same igneous history, and the samples probably represent a magmatic event at different levels of a single basin at ca. 800-770 Ma.

1   **1. INTRODUCTION**

2

3   The original architecture of pre-collisional scenarios is difficult to reconstruct due
4   to the subsequent mountain-building processes (e.g. Cawood et al., 2009;
5   Vanderhaeghe, 2012; Chetty, 2017), including extensive deformation and
6   emplacement of post-orogenic magmatic rocks that mask the former pre-orogenic
7   relations. Thus, pre-orogenic basins commonly have their original stratigraphy
8   completely modified during deformation (Tavani et al., 2015; Lacombe & Bellahsen,
9   2016), disturbed also by contemporaneous high-grade metamorphism and partial
10 melting (Collins, 2002), and thrusting of the basement (Lacombe & Bellahsen, 2016).
11 Furthermore, in fold-and-thrust belts, as the case of the Dom Feliciano Belt in South
12 America, horizontal thrust sheets and shear-zones make the pre-orogenic
13 reconstitution even more difficult, as allochthonous sheets can be carried over
14 thousands of kilometres, often causing an inversion of the original stratigraphy and
15 higher-grade rocks are placed on top of lower grade ones, as can be observed in the
16 Himalayas, for instance (Harrison et al., 1999). Nevertheless, some approaches can
17 be chosen to address these problems despite the difficulty.

18 This paper provides an attempt to reconstruct the pre-orogenic scenario of the
19 Central Dom Feliciano Belt, in southeast South America, based on geochronological
20 and oxygen zircon isotope studies in metavolcanic rocks interleaved with
21 metasedimentary sequences. We present new U-Pb and O isotope data on zircons of
22 para- and ortho-derived rocks from two Tonian metavolcano-sedimentary
23 complexes: Várzea do Capivarita and Porongos. The results are compared with
24 geochronological and oxygen zircon isotopic data reported for these complexes in the
25 literature, in addition to data for the Cerro Olivo Complex (Uruguay), and provide new
26 insights on the tectonic evolution of a belt that runs along the actual southeastern South
27 America and southwestern Africa coasts. Our data provide evidence for a connection
28 between the early Neoproterozoic pre-tectonic processes (at 800-770 Ma) in the
29 hinterland and foreland of the Dom Feliciano Belt in southernmost Brazil.

30

31 **2. GEOLOGICAL SETTING**

32

33 ***2.1 Dom Feliciano–Kaoko–Gariep Orogenic System***

34

35   The study area is located in the Dom Feliciano Belt (DFB, Fig. 1). The DFB is the

36 South American counterpart of a NS-trending Neoproterozoic orogenic system that

37 also involves the African Kaoko and Gariep belts. The overall architecture of this

38 orogenic system has developed during the tectonic events that happened between ca.

39 800 Ma and 550 Ma (Frimmel & Frank, 1998; Oriolo et al., 2017). The ca. 800 Ma

40 Neoproterozoic units, which consist of igneous complexes of this age, are interpreted

41 by some authors as related to a continental arc (Koester et al., 2016; Martil et al., 2017;

42 De Toni et al., 2020b) or as generated in a back-arc/rift setting (Konopásek et al., 2018;

43 Will et al., 2019). The system evolved into a contraction tectonic regime generating a

44 ca. 650-620 Ma transpressive regime in the Dom Feliciano Belt (e.g. Gross et al., 2006,

45 2009; Oyhantçabal et al., 2009; Lenz et al., 2011; Martil, 2016; Peel et al., 2018; Will

46 et al., 2019; De Toni et al., 2020a; Percival et al., 2021, 2022). The contraction

47 continued until at least 580–550 Ma, as recorded by ongoing crustal thickening and

48 associated metamorphism in the orogenic system of African and South American sides

49 (Frimmel and Frank, 1998; Goscombe and Gray, 2008; Höfig et al., 2018; Percival et

50 al., 2022). Such convergent period is related to the final amalgamation of the

51 Gondwana supercontinent (e.g. Rapela et al., 2011; Ramos et al., 2017; Oriolo et al.,

52 2017; Schmitt et al., 2018).

53   In southernmost Brazil, the DFB is usually divided into Western, Central and

54 Eastern domains (Fragoso-Cesar et al., 1986; Fernandes et al., 1992; Basei et al.,

55 2000 - Fig. 1). The Western Domain comprises the Pre-Neoproterozoic basement (2.5

56 to 2.0 Ga - Hartmann et al., 2000) intruded by arc-related rocks of Tonian–Cryogenian

57 ages (the São Gabriel Arc; 750–680 Ma - Nardi and Bitencourt, 2007; Philipp et al.,

58 2016b).

59   The Central Domain is represented by low- to medium-grade volcano-

60 sedimentary rocks (Porongos Complex; Jost and Bitencourt, 1980 - Fig. 1) of Tonian

61 to Ediacaran age (e.g. Saalmann et al., 2011; Pertille et al., 2017; Höfig et al., 2018)

62 with locally exposed Paleoproterozoic basement (Encantadas Complex; 2.26–2.0 Ga

63 – (Hartmann et al., 2003; Philipp et al., 2008). Both the Central and Western Domains

64 are partially covered by late-orogenic, Ediacaran to Ordovician volcano-sedimentary

65 rocks (Paim et al., 2014). Considering the portion of the orogenic belt closer to the

66 undeformed continental interiors as forelands, and the internal part of the orogen closer

67 to the high-grade core as hinterland (*sensu* Van Der Pluijm and Marshak, 2003), the

68 Western and Central domains of DFB are interpreted as belonging to the foreland.

69   The Eastern Domain represents the hinterland and features mainly granitic rocks.
70   These batholiths are interpreted as a post-collisional granitic belt (Bitencourt and Nardi
71   1993; Bitencourt and Nardi 2000; Philipp and Machado, 2002), whose emplacement
72   was controlled by a lithospheric-scale discontinuity called Southern Brazilian Shear
73   Belt (SBSB) active between ca. 650 and 580 Ma (Bitencourt & Nardi, 2000; Nardi &
74   Bitencourt, 2007). In Brazil, the Neoproterozoic granitic rocks contain roof pedants of
75   at least three distinct ages: Paleoproterozoic (2.2 and 2.0 Ga – Leite et al., 2000;
76   Gregory et al., 2015), Mesoproterozoic (ca. 1.5 Ga – Chemale et al., 2011) and Tonian
77   (ca. 800-770 Ma - Martil et al., 2011, 2017). The latter are the high-grade metamorphic
78   rocks known as Várzea do Capivarita Complex (VCC) (Fig. 1), which are, according to
79   many authors (e.g. Oyhantçabal et al., 2009; Martil et al., 2017; Konopásek et al.,
80   2018), related with the high-grade rocks of the Cerro Olivo Complex (Masquelin et al.,
81   2011) in the Uruguayan part of the DFB hinterland (Fig. 1).
82
83   **2.2. Tonian metavolcano-sedimentary sequences from DFB**
84
85   ***2.2.1. Várzea do Capivarita Complex - Neoproterozoic high-grade***
86   ***metamorphic rocks in southernmost Brazil***
87
88   The Várzea do Capivarita Complex (VCC - Martil et al., 2011, 2017) comprises
89   part of the basement intruded by Late Neoproterozoic granites in the southernmost
90   Brazil (Fig.1). It is interpreted as a W-verging nappe body thrust onto the Central
91   Domain (Martil et al., 2017; Battisti et al., 2018; De Toni et al., 2021). These well-
92   preserved roof pendants (Martil et al., 2017 - Fig. 2) comprise tectonically interleaved
93   granulite facies orthogneisses and paragneisses (Martil et al., 2011, 2017). According
94   to these authors, the orthogneisses are mostly tonalitic and related to a Tonian mature
95   magmatic arc (790–780 Ma - U–Pb zircon). Paragneisses comprise metapelites and
96   calc-silicate rocks (Martil et al., 2011). The VCC was intruded by syntectonic to post-
97   tectonic plutons from ca. 629 Ma to 578 Ma (e.g. Philipp and Machado, 2002; De Toni
98   et al., 2016; Lyra et al., 2018; Padilha et al., 2019).
99
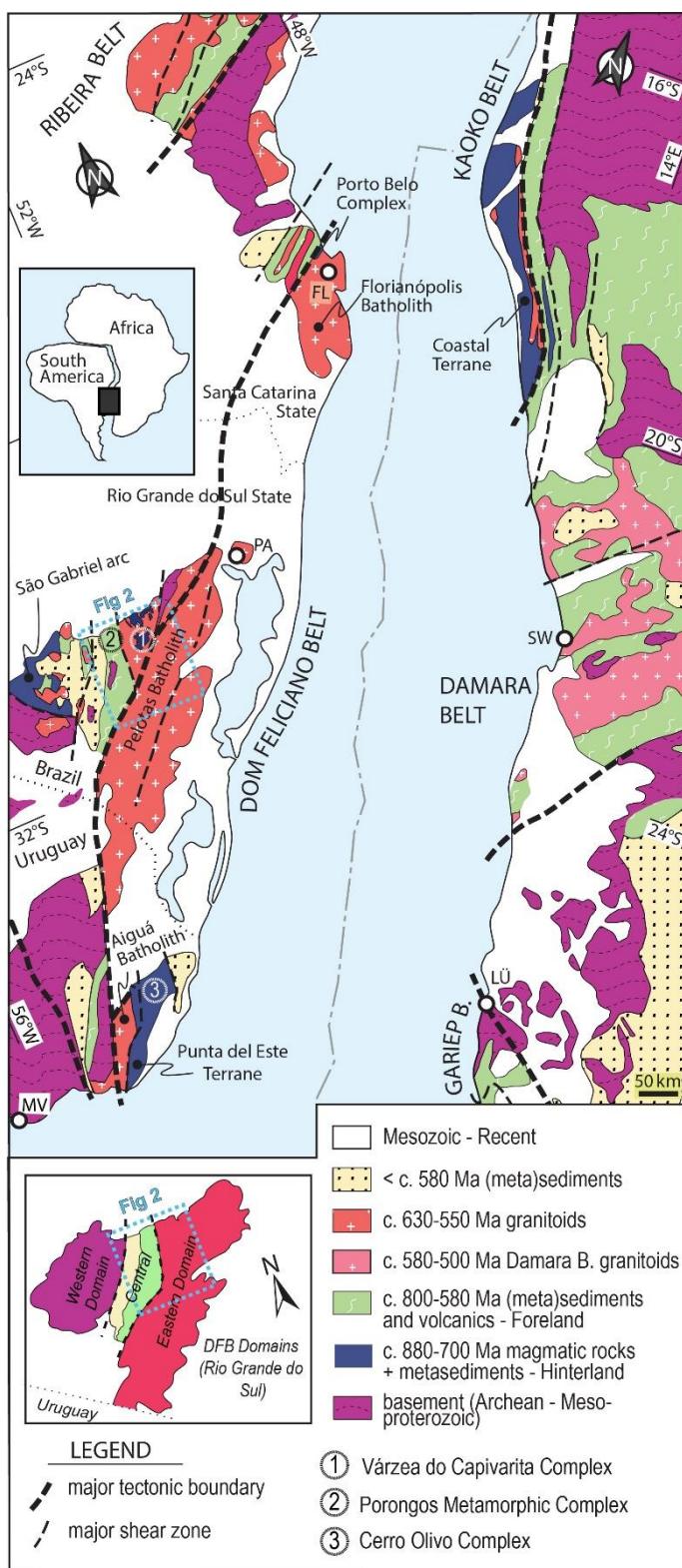
Figure 1. A) Overview geological map and main tectonic domains of the Dom Feliciano–Kaoko–Gariep orogenic system (modified after Bitencourt and Nardi, 2000 and Konopásek et al., 2018). Relative Position of Africa and South America is shown at 140 Ma - after Heine et al., 2013. Dom Feliciano Belt domains in the Rio Grande do Sul state are shown in the inset. Location of figure 2 is indicated. Cities: FL – Florianópolis, PA – Porto Alegre, MV – Montevideo.
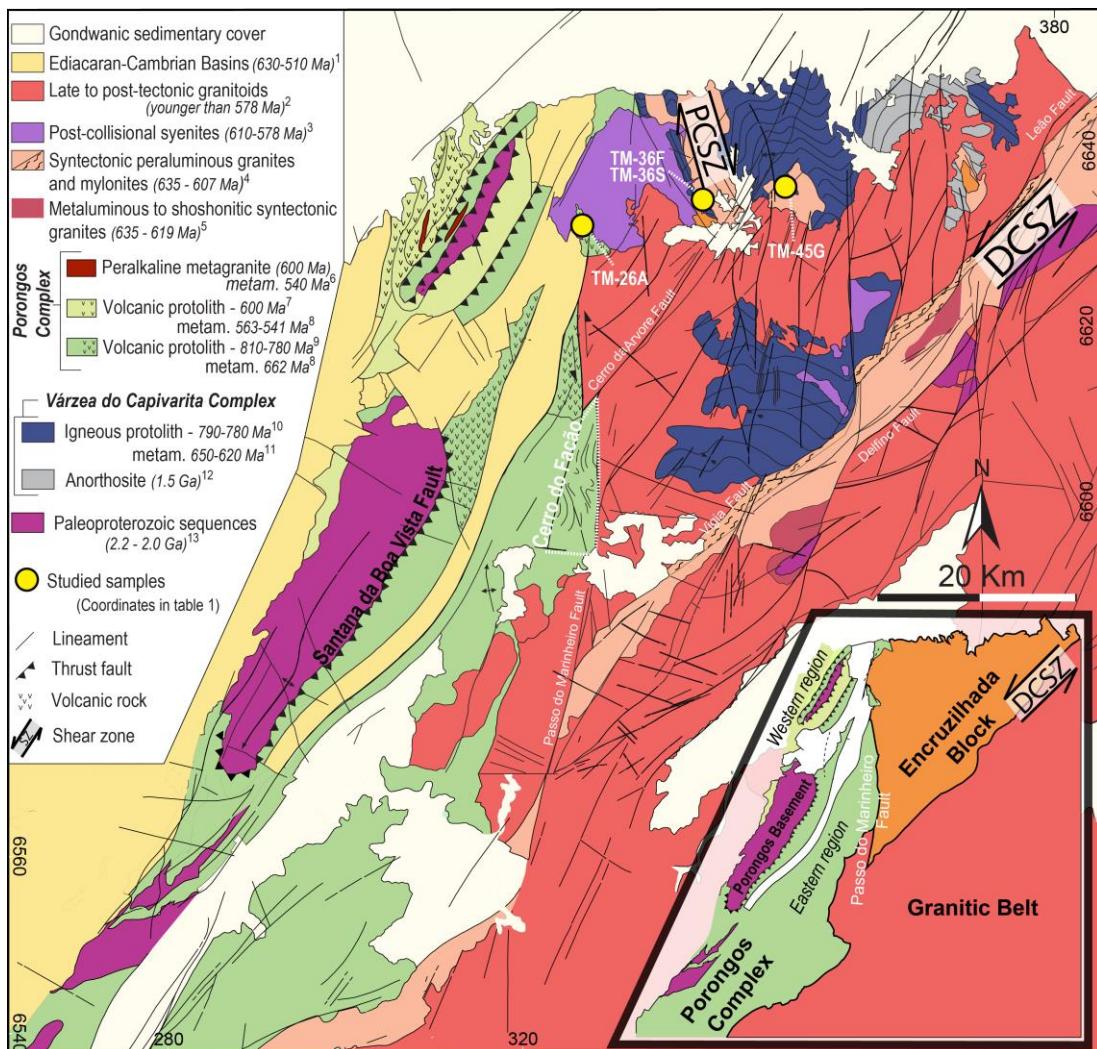
Figure 2. Geological map of the study area with sampled sites indicated. DCZS – Dorsal do Canguçu Shear Zone; PCSZ – Passo das Canas Shear Zone. Tectonic compartments shown in the inset (after De Toni et al., 2021). Porongos Complex is divided into eastern and western regions (inset) separated by the Santana da Boa Vista fault. Such names do not represent any stratigraphic proposal and should be used only as geographical references. They are used in this paper to guide the reader through our discussion. – References: 1- (Paim et al., 2014); 2-(Padilha et al., 2019); 3-(Rivera, 2016; Padilha et al., 2019); 4-(Bitencourt et al., 2015; Knijnik, 2018; Vieira et al., 2020); 5-(Knijnik, 2018; Vieira et al., 2020); 6-(Philipp et al., 2016b); 7-(Höfig et al., 2018); 8-(Battisti, 2022); 9-(Saalmann et al., 2011; Pertille et al., 2017); 10-(Martil et al., 2017); 11-(Gross et al., 2006; Chemale et al., 2011; Philipp et al., 2016a; Martil et al., 2017); 12-(Chemale et al., 2011); 13-(Leite et al., 2000; Hartmann et al., 2003; Saalmann et al., 2011; Gregory et al., 2015).

Two main deformation phases are described in the VCC and are related to one single tectono-metamorphic event under granulite facies conditions (Gross et al., 2006; Martil, 2016). VCC gneisses were tectonically interleaved along a sub horizontal banding, with top-to-the-west shear sense (Martil et al., 2011; Martil, 2016). Dextral

125 strike-slip to slightly oblique vertical NNE-SSW shear zones superpose the thrusting in
126 a progressive deformation (Martil, 2016). The granulite-facies conditions achieved ca.
127 750–800ºC and 3–5 kbar in the VCC metapelites (Gross et al., 2006; Costa et al.,
128 2020; De Toni et al., 2021) at 650–640 Ma (Martil, 2016).

129   Provenance zircon U-Pb SHRIMP studies of the VCC metasedimentary rocks
130 performed by Gruber et al. (2016a) indicated ages of 2.3 – 2.0 Ga, 1.5 Ga, 1.3 Ga, 930
131 and 730 Ma for the main source areas, and the maximum deposition age was
132 estimated at 728 ± 11 Ma. According to the same authors, associated marbles were
133 deposited in an interval of ca. 717–750 Ma ($^{87}Sr/^{86}Sr$ initial ratio in whole-rock
134 analyses).

135

136 ***2.2.2. Cerro Olivo Complex Complex - Neoproterozoic high-grade***
137 ***metamorphic rocks in Uruguay***

138

139   Roughly going southwards along strike, in the Uruguayan part of DFB, crops out
140 the Cerro Olivo Complex (COC - Fig. 1). It is a metamorphic-plutonic complex with E–
141 W to NW–SE tectonic foliation crosscut by NE-SW strike–slip shear zones (Masquelin
142 et al., 2011). Protolith ages of the COC orthogneisses are reported to be ca. 800-760
143 Ma (Hartmann et al., 2002; Oyhantçabal et al., 2009; Lenz et al., 2011; Basei et al.,
144 2011; Masquelin et al., 2011; Will et al., 2019). Peak metamorphic conditions have
145 been determined at 830–950 ºC and 7–10 kbar (Gross et al., 2009), dated at ca. 650
146 Ma (Gross et al., 2009; Oyhantçabal et al., 2009; Lenz et al., 2011; Basei et al., 2011;
147 Peel et al., 2018; Will et al., 2019) and this metamorphic event is interpreted as related
148 to the assembly of the Gondwana supercontinent.

149

150   2.2.3. *Porongos Complex – Neoproterozoic low- to medium-grade metamorphic*
151 *unit in Southernmost Brazil*

152

153   The Porongos Complex (PC; Jost and Bitencourt, 1980) is interpreted as part of
154 the Dom Feliciano Belt western foreland and comprises Neoproterozoic supracrustal
155 rocks metamorphosed at lower greenschist to middle amphibolite facies (Fig. 1 and 2).
156 The PC comprises metasedimentary and metavolcanic rocks, some ultramafic lenses
157 and, less often, deformed granitoids (Jost & Bitencourt, 1980; Marques et al., 2003;
158 Zvirtes et al., 2017). The PC metamorphic grade increases from west to east, and
159 staurolite-bearing metapelites at the PC easternmost border (Fig. 2) record the highest

160   metamorphic grade of the complex (Jost & Bitencourt, 1980; Lenz, 2006). The PT

161   conditions were estimated at 560–580°C and 5.8–6.3 kbar by De Toni et al. (2021) and

162   the metamorphism was dated at 658 ± 26 Ma (Lenz, 2006; Rb–Sr in muscovite and

163   whole-rock).

164   Provenance studies in the PC have shown two distinct sources for the

165   metamorphosed clastic sediments (Gruber et al., 2011; Pertille et al., 2015a, 2015b,

166   2017; Höfig et al., 2018). Based on this diference, Höfig et al. (2018) suggested that

167   the precursor of the Porongos Complex could have been two distinct and diachronous

168   basins. The older PC metasedimentary rocks (mostly at its eastern part – Fig. 2)

169   represent mostly clastic infill of a pre-orogenic basin with dominant Paleoproterozoic

170   (2.0–2.3 Ga), subordinate Mesoproterozoic (1.2–1.5 Ga) and rare ca. 750-800 Ma

171   detrital sources (provenance interval: 750 Ma to 3.0 Ga - Gruber et al., 2016b; Pertille

172   et al., 2017; Höfig et al., 2018). The younger PC basin presents metasedimentary rocks

173   related to the syn-orogenic (from ca 650 Ma) evolution, as discussed by Höfig et al.

174   (2018) and Battisti et al. (2018). In the western part of the PC (Fig. 2), the syn-orogenic

175   metasedimentary rocks are interleaved with the rocks of the older basin. Their detrital

176   zircon populations show mainly Paleoproterozoic (2.0–2.3 Ga) and Neoproterozoic (ca

177   600 and ca 800 Ma) sources (provenance interval: 570 Ma to 3.2 Ga - Pertille et al.,

178   2015b, 2017; Gruber et al., 2016b; Höfig et al., 2018). Associated intermediate to acid

179   metavolcanic rocks also yielded contrasting ages in different regions of the complex.

180   The PC eastern region contains metavolcanic rocks with protolith ages of ca 800–770

181   Ma (Saalmann et al., 2011; Pertille et al., 2017), whereas magmatic ages of 600 and

182   601 Ma were obtained for metavolcano-sedimentary rocks of the PC western region

183   (LA–MC–ICP–MS, U–Pb zircon - Höfig et al., 2018). Such dataset shows that the

184   igneous activity and late sedimentation in the western PC is younger than the

185   metamorphic peak recorded in its eastern portion (658 ± 26 Ma - Lenz, 2006). The so-

186   called Eastern and Western Porongos Complex regions are distinguished based on

187   their position relative to the main W-verging thrust fault, the Santana da Boa Vista

188   Thrust Fault, as originally defined by Jost and Bitencourt (1981 – fig. 2).

189

190   **3. PETROGRAPHY**

191

192   Four representative samples were selected considering previous detailed field

193   studies (location in Fig. 2). Three samples represent the lithological variations of the

194   Várzea do Capivarita Complex. They include orthogneisses of tonalitic (TM-36F), or

195 granitic composition(TM-45G) and an aluminous paragneiss (TM-36S), all
196 metamorphosed under granulite facies conditions. The tonalitic orthogneiss and the
197 aluminous paragneiss are interleaved along a flat-lying foliation related to the main
198 deformation phase D_1 (Martil, 2016). The granitic orthogneiss sample has a subvertical
199 fabric S_2 in high-strain zones that overprint the flat foliation. A sample of metavolcanic
200 rock (TM-26A) with geochemical features and structural evolution similar to the VCC
201 samples (Martil, 2016; Martil et al., 2017; Battisti et al., 2018), was collected in the
202 eastern portion of the Porongos Complex, at the contact of Central and Eastern
203 domains (Fig. 1 and 2). Outcrop features of the investigated samples are shown in
204 figure 3.

205 　　　Sample TM-36F is a poorly-banded, fine- to medium-grained hornblende-biotite
206 tonalitic orthogneiss with granolepidoblastic seriate–interlobate texture (Fig. 4a, b).
207 Rounded plagioclase megacrysts and rare K-feldspar are ca. 1 mm-large but can reach
208 up to 3 mm. They are set in a fine-grained (0.3 mm) matrix containing plagioclase, K-
209 feldspar, quartz and biotite (Fig. 4b). Biotite is subhedral and does not form well-
210 developed bands. Remnant orthopyroxene is locally preserved in pseudomorphic
211 clusters in which hornblende crystals up to 0.5 mm long with nematoblastic to
212 decussate texture and biotite crystals have grown at the expense of the former
213 orthopyroxene. Secondary chlorite, opaque minerals and zircon are also present.

214 　　　Sample TM-36S is an irregularly banded, dark-grey coloured, sillimanite-bearing
215 garnet-cordierite-biotite paragneiss from the same outcrop as the previous sample
216 (Fig. 3). Mafic-rich bands are up to several cm thick and alternate with felsic
217 bands/lenses of millimetre thicknesses (Fig. 4c). Biotite is the main mafic mineral,
218 displaying continuous bands with 0.3 and 0.5 mm-size subhedral crystals. Felsic bands
219 are composed of 0.5 to 1 mm large quartz, less plagioclase and rare K-feldspar, all of
220 which exhibit granoblastic interlobate to granoblastic polygonal texture (Fig. 4d).
221 Garnet and cordierite are present in both mafic- and felsic-rich layers. Garnet is
222 subhedral (0.5 to 1 mm), poikiloblastic and includes numerous quartz crystals.
223 Cordierite is commonly transformed into pinnite. Rare dark-green chromium-rich spinel
224 is preserved as inclusions in cordierite. The rock contains rare tiny sillimanite crystals
225 (0.1 mm), apatite and zircon. The interpretation of sample TM-36S as a paragneiss is
226 based on the following criteria: i) At the same outcrop, TM-36S is interleaved with
227 calcsilicate layers, while in TM-36F tonalitic orthogneiss bands, calcsilicate layers are
228 absent; and ii) The amount of quartz is larger than the feldspar content in TM-36S,
229 which is not expected for a granitic origin.

230

231
232
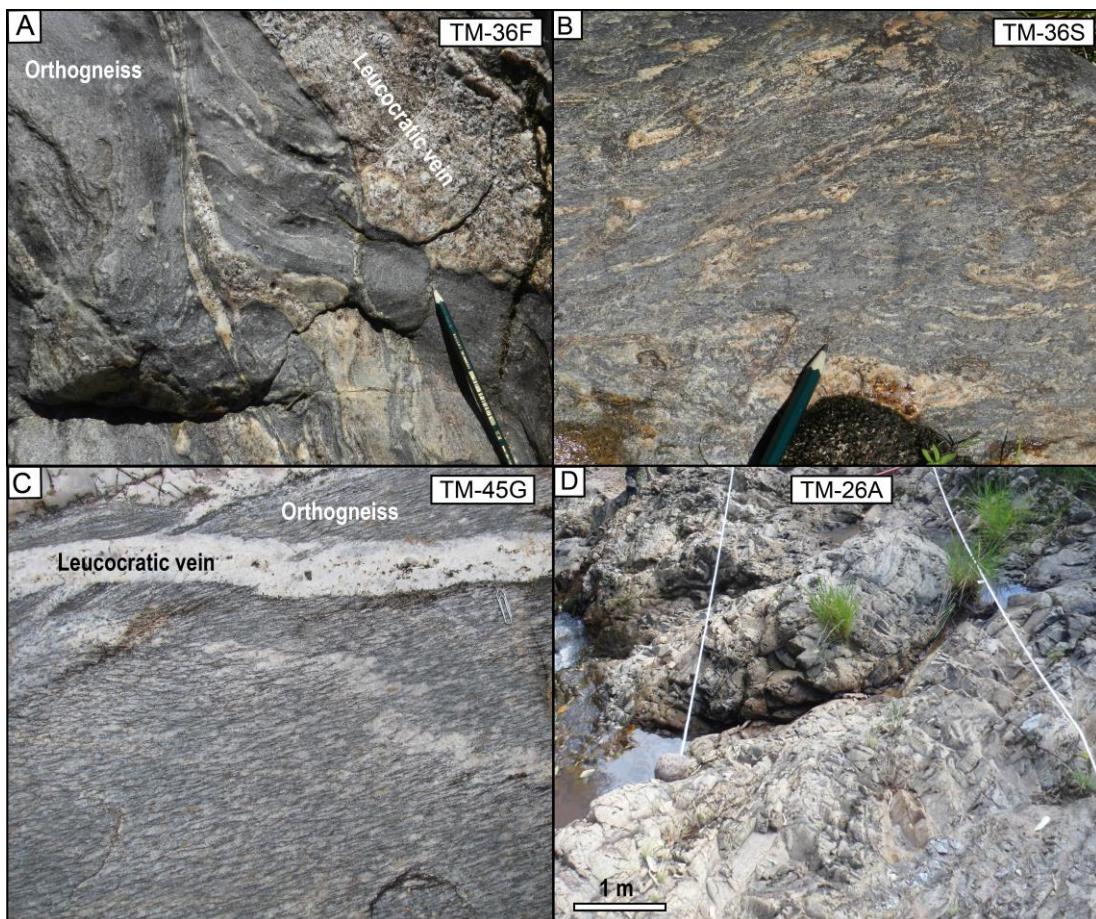
Figure 3. A) Fine-grained TM-36F orthogneiss. B) Outcrop of the sampled paragneiss TM-36S with local veins resulting from partial melting. C) TM-45G granitic orthogneiss. D) Outcrop view of the metarhyolite TM-26 A.

236

Sample TM-45G is a granolepidoblastic, well-foliated garnet-biotite granitic orthogneiss (Fig. 4e, f) of medium-grained equigranular texture. Plagioclase, K-feldspar and quartz exhibit high-temperature recrystallisation features. Biotite crystals are 1 to 2 mm long and occur in mm-thick, mica-rich layers. Garnet is an accessory mineral with 0.2 to 0.5 mm. Zircon crystals are 0.05–0.1 mm long and exhibit zonation visible in the transmitted light.

243
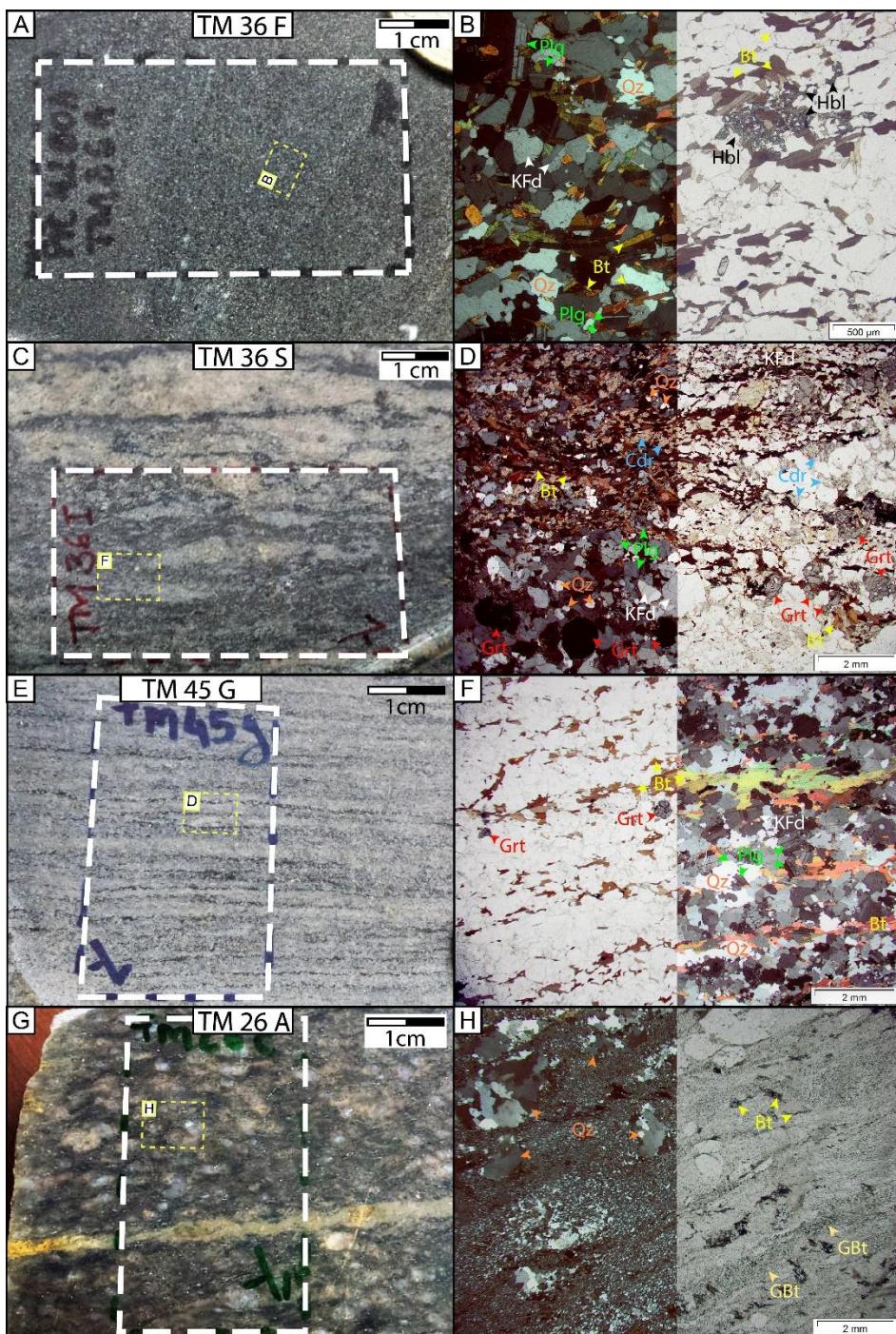
Figure 4. The four studied samples (location in fig. 2): three are from Várzea do Capivarita Complex: A) and B) TM-36F - tonalitic orthogneiss; C) and D) TM-36S - paragneiss; and E) and F) TM-45G - granitic orthogneisses. One sample is from the Porongos Complex eastern region: G) and H) TM-26A - blastoporphyritic metarhyolite. Thin-section locations and pictures of detailed areas are indicated. Note at the right column that photomicrographs were taken in both plane-polarized (PPL) and cross-polarised light (XPL) to highlight textural aspects of the rock. Mineral abbreviations: Qz – quartz, Plg – Plagioclase, KFd – K-feldspar, Bt – biotite, GBt– green biotite, Hbl – hornblende, Grt – garnet, Cdr – cordierite.

254   TM-26A is a PC blastoporphyritic metarhyolite with ca. 3 mm-long aggregates of
255   blue quartz (Fig. 4g, h) set in a very fine-grained (0.01 mm) granolepidoblastic matrix
256   composed of quartz, feldspar and greenish biotite (Fig. 4h). Millimetre-sized quartz
257   aggregates are often stretched, and quartz crystals are either partially or completely
258   recrystallized to granoblastic texture with interlobate contacts. Larger brown biotite
259   crystals (0.2 mm) display poorly-developed, mm-thick layers. Accessory minerals are
260   opaque minerals (mainly ilmenite), apatite and zircon.

261

262   **4. ANALYTICAL TECHNIQUES**

263

264   The samples were crushed and the zircons were separated using standard
265   magnetic and heavy liquid density separation techniques. The clean zircon separates
266   were mounted in epoxy at the Research School of Earth Sciences (RSES), in
267   Australian National University, together with the RSES reference zircon AS3 and SL13.
268   Zircon grains were handpicked under a binocular microscope or, in the case of the
269   detrital zircons, scattered onto double-sided tape prior to mounting in epoxy to ensure
270   a random selection of grains.

271   Photomicrographs of all zircons were taken in transmitted and reflected light and
272   these, together with SEM cathodoluminescence (CL) images, were used to decipher
273   the internal structures of the sectioned grains and to select specific areas within the
274   zircons for spot analysis. U–Pb analysis was carried out using SHRIMP I, SHRIMP II
275   and SHRIMP RG at the RSES. The data were reduced in a manner similar to that
276   described by (Williams, 1998, and references therein), using the SQUID-1 Excel Macro
277   of Ludwig (2003). For the zircon calibration the Pb/U ratios were normalized relative to
278   a value of 0.1859 for the $^{206*}Pb/^{238}U$ ratio of AS3 reference zircons, equivalent to an
279   age of 1099 Ma (Paces & Miller, 1993). U and Th concentrations were determined
280   relative to the SL13 standard. Uncertainties given for single analyses (ratios and ages)
281   are at the 1σ level, but uncertainties in any calculated weighted mean, concordia age
282   (Paces & Miller, 1993) or intercept age are reported as 95% confidence limits (unless
283   indicated otherwise) and include the uncertainties in the standard calibrations where
284   appropriate. Concordia plots, regressions and age calculations were carried out using
285   Isoplot/Ex and SQUID-1 (Ludwig, 2003). Zircon oxygen isotopic data were analyzed
286   by SHRIMP SI and, when possible, spots were made directly below to the polished
287   locations of ages measurements. All δO_{18} data were normalized to a TEMORA II value

288   of 8.2‰. Complete data of analyzed zircons from each sample are presented as
289   supplementary data.
290
291   **5. U-Pb RESULTS IN ZIRCON**
292
293   ***5.1. Orthogneisses (TM-36F and TM-45G)***
294
295   Samples TM-36F and TM-45G were analysed to determine the crystallisation age
296   of the VCC tonalitic and granitic composition protolith, respectively. In TM-36F, the
297   zircon population is rather homogeneous, and the grains are euhedral to subhedral
298   with shapes ranging from square and almost equidimensional to more elongate
299   prismatic forms (Fig. 5a). CL imaging reveals that internal structures are dominated by
300   sectors with oscillatory zoning of variable intensity. Crystal sizes are ca. 100–250 µm.
301   Some crystals show a core with no zoning, which grades into the oscillatory-zoned
302   rims, the latter showing the most concordant analyses (Fig. 6a). Nineteen spot
303   analyses in the oscillatory zoned domains yielded an upper intercept age of 786 ± 18
304   Ma (2σ) (Fig. 6b). Discarding the three youngest domains, a concordia age of 786 ± 5
305   Ma was calculated (95% confidence), which is considered the best estimate for the
306   crystallization age of the igneous protolith (Fig. 6c). Th/U ratios determined for the
307   concordant spots range between 0.28 and 0.68. One crystal (#14.1) without oscillatory
308   zoning and Th/U ratio of 0.84 gave a Mesoproterozoic concordant age of 1119 ± 40
309   Ma (Fig. 4c, 5a), interpreted here as an inherited grain.
310   Zircon population from sample TM-45G is rather homogeneous and shows
311   euhedral to subhedral, mainly elongate prismatic crystals smaller than 200 µm. Their
312   CL images show typical igneous oscillatory zoning (Fig. 5b). Some crystals present an
313   inner part with no zoning and a light grey area at the rims. Most zircon crystals have a
314   very thin, CL-bright rim, which probably indicates a metamorphic overgrowth; however,
315   the rims are too thin for analysis. Twenty-two SHRIMP analyses were performed in ten
316   different zircon grains, and eleven analyses, with Th/U ratios between 0.16 and 0.54
317   yielded a mean $^{207}Pb/^{206}Pb$ age of 790 ± 7 Ma (MSWD = 0.69; probability of
318   concordance = 0.73), which is interpreted as the age of the orthogneiss protolith (Fig
319   7). Two spots yielded concordant dates at ca. 1.8 and 2.0 Ga, and these are interpreted
320   as inherited grains. Other older grains were dated, but with discordant ages (Fig. 7a).
321
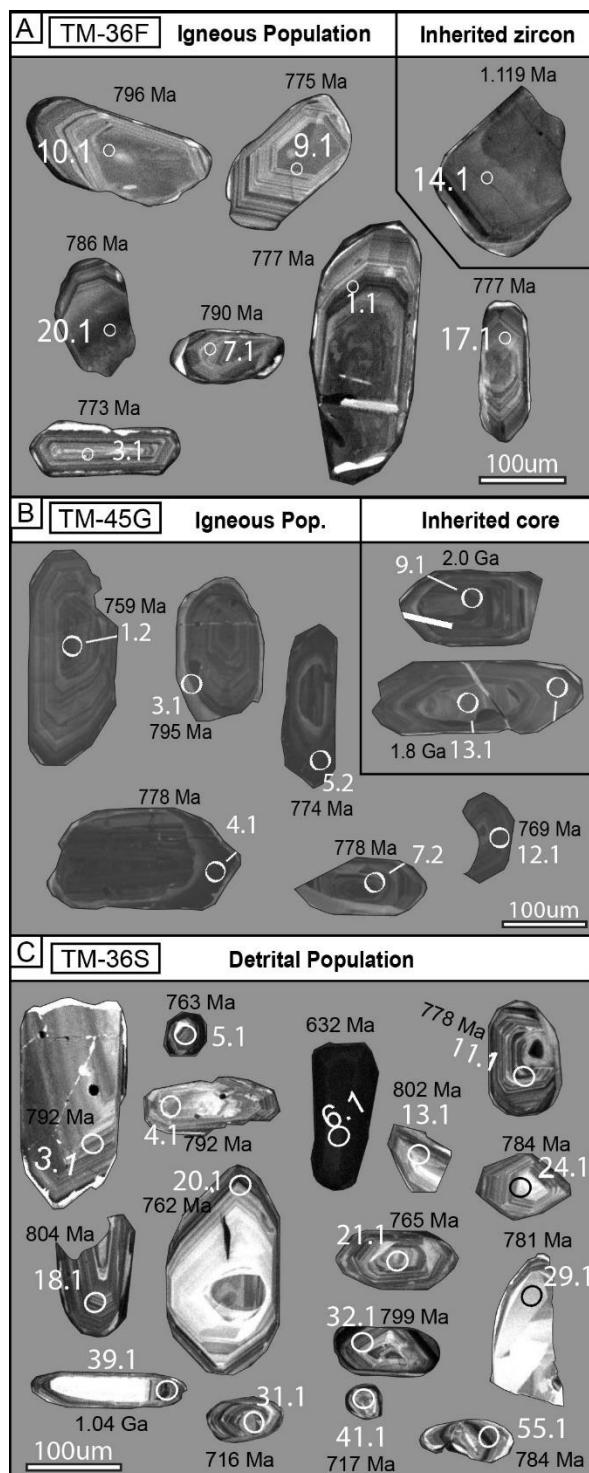
Figure 5. A) Cathodoluminescence images from some zircon crystals of sample TM-36F. Note the bright, thin metamorphic rim on crystals #3.1, #7.1, #17.1, and dark thin metamorphic rims on crystals #9.1 and #10.1. One crystal (#14.1) without oscillatory zoning gave a Mesoproterozoic concordant age (Fig. 6A). B) Examples of CL images of zircon crystals from sample TM-45G. Inherited cores are found in spots #9.1 and #13.1. c) Cathodoluminescence images from some detrital zircons of sample TM-36S. Note the youngest analysed zircons (#31.1 and #41.1) at the bottom of the figure. Ages are given as ^{206}Pb/^{238}U – complete information is available as supplementary data.
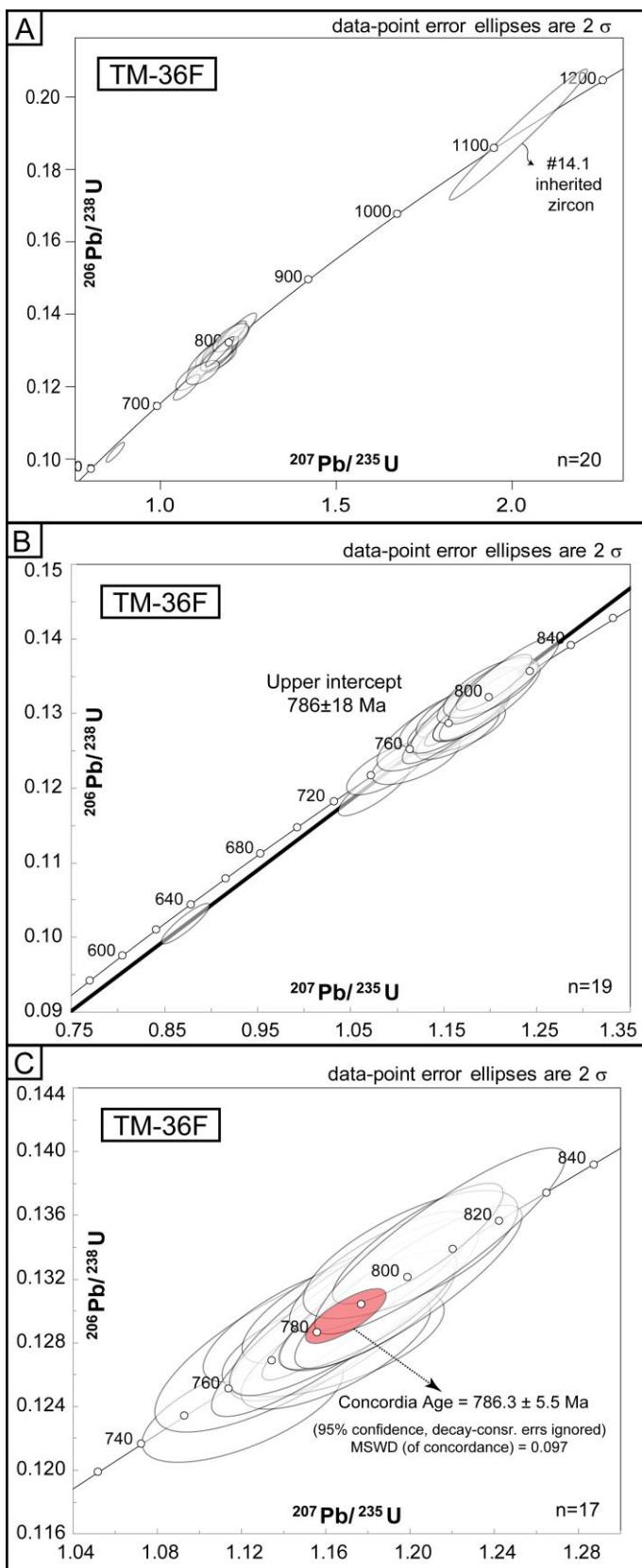
Figure 6. A) Concordia U-Pb diagram with all zircons analysed from sample TM-36F, a tonalitic orthogneiss. B) U-Pb upper intercept age for TM-36F Neoproterozoic zircons. C) U-Pb concordant age is interpreted as the best age for the crystallisation of the protolith.
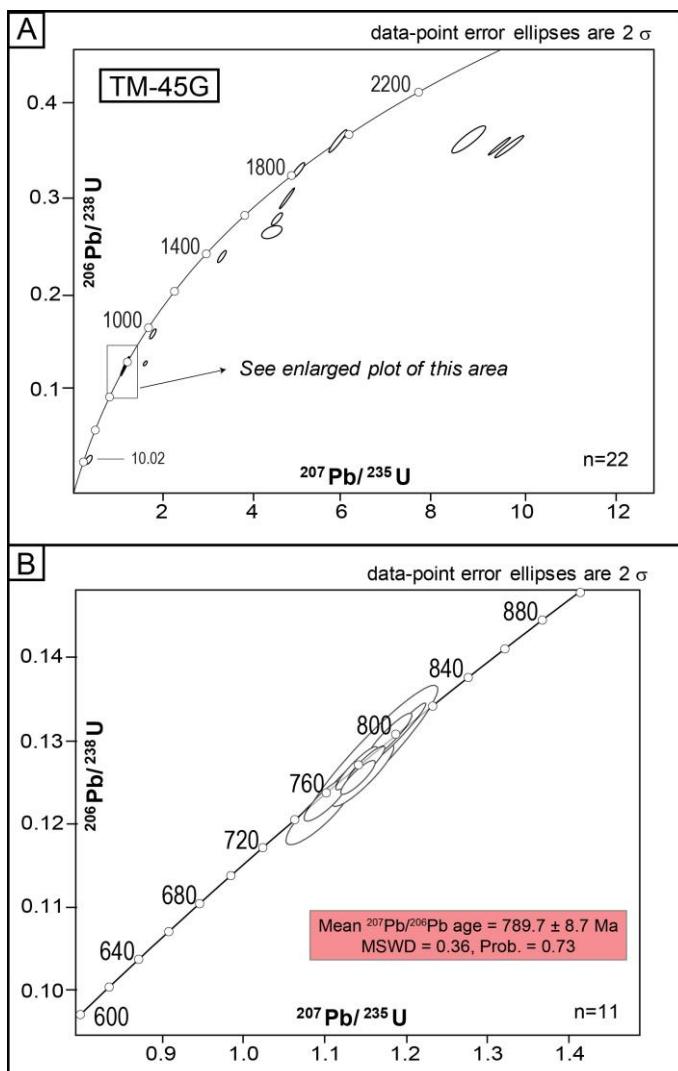
Figure 7. A) Concordia U-Pb diagram with all zircons analysed from sample TM-45G, a granitic orthogneiss. B) Concordant Neoproterozoic zircons used to calculate the mean $^{206}Pb/^{207}Pb$, interpreted as the crystallisation age of the ortho-derived protolith.

5.2. Paragneiss (TM-36S)

To constrain the maximum age of sedimentation for the VCC, 65 zircon grains were analysed from the paragneiss sample TM-36S. The CL images show typical igneous oscillatory zoning, and the crystal sizes are between 50 and 200 μm. Most crystals are prismatic, euhedral to sub-euhedral (Fig. 5c) with no sign of abrasion, and their sharp pyramidal tips are preserved. Thin CL-bright overgrowths are rare and too thin to be analysed.

The data is shown in two separate concordia diagrams and one relative probability plot (Fig. 8). Considering only the concordant (>95%) analyses, detrital zircon grains from sample TM-36S provided two populations: a minor one at ca. 1.1

353   Ga, and a more significant at ca. 790 Ma (Fig.8). Some discordant grains suggest older

354   sources (Fig. 8a).

355   The 790-750 Ma age interval indicates a major source for the deposition of these

356   para-derived protoliths (Fig. 8b). The analysed grains show Th/U ratios between 0.18

357   and 0.70, although spot #23.1 has a Th/U ratio of 0.08. The data spread is centred at

358   ca. 790 Ma, which corresponds also to the crystallization age of the tonalitic

359   orthogneiss TM-36F, as shown by curves of relative probability (Fig. 8c). This would

360   suggest that they are coeval or that the sedimentary protolith of sample TM-36S is

361   mostly a product of erosion of the 790 Ma tonalite/dacite. The predominantly euhedral

362   detrital zircons with well-preserved prismatic tips indicate a short sedimentary transport

363   (near to source). The two youngest detrital zircons constrain the maximum age of

364   sedimentation at 716 Ma (spots 31.1 and 41.1 - at the bottom of Fig 5c).

365   One crystal reveals a much younger age of 632± 9 Ma (spot 6.1 – Fig. 5c, 8b). It

366   is interpreted as related to the metamorphic granulite facies event because it is

367   morphologically distinct from the others with a homogenous black domain and has

368   Th/U ratio of 0.01.

369
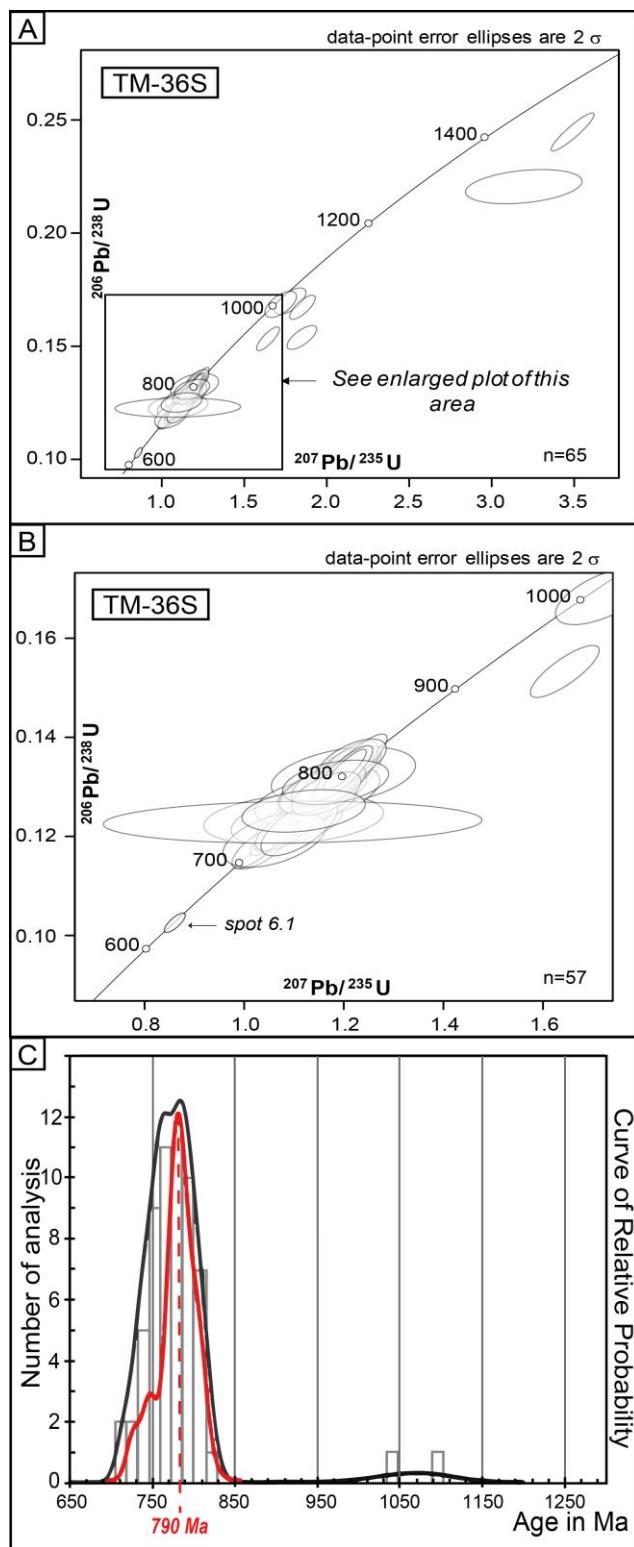
Figure 8. A) Concordia U-Pb diagram with all zircons analysed from sample TM-36S, a paragneiss. B) Zoom in Fig. 8A, showing the Neoproterozoic population of detrital zircons. C) Histogram with the detrital zircon population of sample TM-36S (in black). Note the curve of relative probability for TM-36S compared to the relative probability curve of the igneous zircons from the orthogneiss sample TM-36F (in red). The calculated crystallisation age of the orthogneiss is shown in the dashed red line.

5.3. Metarhyolite (TM-26A)

Sample TM-26A shows zircons 100 to 300 μm long with elongate prismatic habits and well-preserved to sub-rounded bipyramidal tips (Fig. 9a). Some zircon grains display darker cores, sometimes with well-defined oscillatory zoning. The U-Pb ages reveal that the rounded cores are inherited zircon grains, and the oscillatory-zoned overgrowths or rims represent magmatic zircon.

Twenty-three SHRIMP analyses were performed in fifteen different zircon grains, and the resulting data were plotted in conventional Wetherill U–Pb concordia diagram (Fig. 9b, c). In this dataset, 17 spots represent the most concordant analyses, whereas the data with discordance higher than 5% were excluded. Fifteen analyses of grains, with Th/U ratios between 0.26 and 0.67, define a concordia age of 787 ± 5 Ma (2σ), which is interpreted as the best estimate for crystallization of the volcanic protolith (Fig. 9c).

Although most of the analyses on xenocrystic cores yielded highly discordant data, two spots (#11.2 and #14.2 - Th/U ratios of 0.65 and 0.44 – Fig. 9a) yielded nearly concordant data suggesting ages of *ca.* 2.0 Ga. Both also have oscillatory overgrowths of ca. 760 Ma, suggesting that the protolith age of crystallization is Tonian, and the Paleoproterozoic core might indicate a source partially melted during the Tonian magmatic event.

The other two spots with discordance <10% yielded $^{206}Pb/^{238}U$ dates represent inheritance (Fig. 9b). Spot #2.1 gave a date around 2.0 Ga; however, the Th/U ratio is relatively low (0.03) compared to the inherited concordant cores of similar age. Spot #8.1 indicates a core of approximately 2.5 Ga and a Th/U ratio of 0.62.
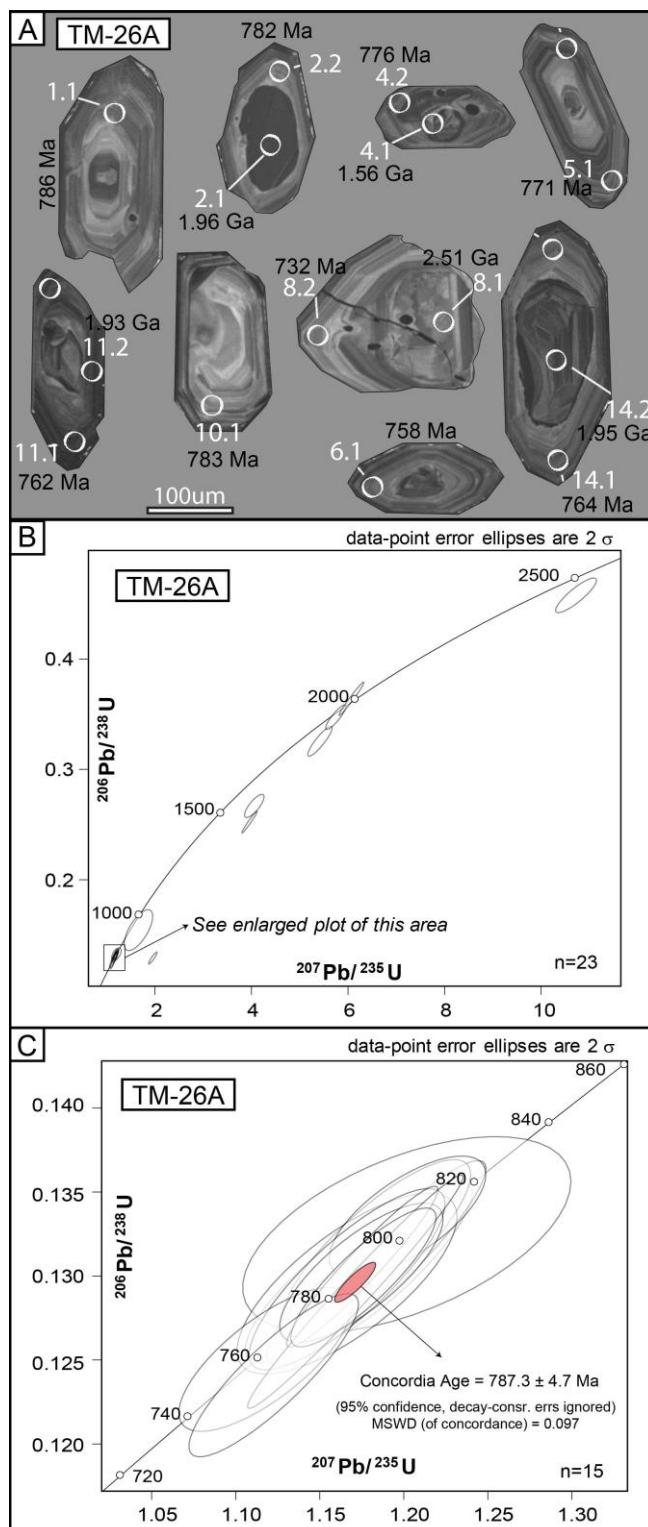
Figure 9. A) Cathodoluminescence images from some zircon crystals of sample TM-26A, a blastoporphyritic metarhyolite from PMC (ages are given ages as ^{206}Pb/^{238}U – complete information is available as supplementary data). Note the inherited core on crystals #2.1, #4.1 and #14.2. B) Concordia U-Pb diagram with all zircons analysed from sample TM-26A. C) Neoproterozoic zircons enlarged plot, where the concordia age is interpreted as the crystallisation age of this rock.

412   **6. OXYGEN ISOTOPES RESULTS**

413

414   Oxygen isotope studies in zircon crystals are important allies to elucidate

415   processes during magma evolution (Eiler, 2001; Valley et al., 2005; Scherer et al.,

416   2007). A single zircon grain may even register more than one process, which is

417   commonly marked by its zones or intergrows (Scherer et al., 2007). Therefore,

418   whenever possible, the U–Pb ratios and the δO_{18} values were determined in the same

419   spot to correlate the δO_{18} values with the U/Pb age of the analysed grain. The four

420   studied samples show similar δO_{18} values, most commonly ranging from 7.9‰ to 9.7‰

421   (Fig. 10a). δO_{18} values lower than 7 were registered in all samples, but values lower

422   than "mantle values" (δO_{18} mantle = 5.3±0.3‰ – Valley et al., 1998) were only

423   measured in sample TM-36S (VCC para-derived gneiss). Only one analytical spot in

424   the PC sample (TM-26A) yielded a δO_{18} value typical for the mantle zircon crystal. The

425   highest δO_{18} value found in the VCC samples is 9.4‰, registered in the ortho-derived

426   gneiss TM-36F (Fig. 10b), whilst the highest value in the PC sample TM-26A is 10.2‰

427   (Fig. 10c).

428   Most of the spots were performed on Neoproterozoic igneous zircons, either on

429   their cores or rims (Fig. 11). Crystal cores (Fig. 11a) and crystal rims (Fig. 11b)

430   generally show similar δO_{18} values, although they present some differences. For

431   example, in the PC sample TM-26A, δO_{18} values measured in some zircon rims are

432   slightly higher than values from zircon cores of the same sample. Conversely, in the

433   para-derived VCC gneiss TM-36S, the calculated mean δO_{18} values are much smaller

434   in crystal rims (6.45±1.48‰) than in crystal cores (8.03±33‰). Nevertheless, the large

435   statistical error and standard deviation indicate that these data require caution since

436   only two spots were analysed in zircon rims of sample TM-36S (Fig. 11b). Mean δO_{18}

437   values with their error, standard deviation and number of analysed spots (n) for each

438   sample are shown in figure 11, where 11a only presents the data from igneous zircons

439   cores; 11b presents the data from igneous zircons rims and in 11c is showed all

440   statistical data together (zircons core + zircons rims). Examples of analysed zircon in

441   each sample are also shown as cathodoluminescence images, where each spot's U-

442   Pb age and δO18 value are indicated (Fig. 11). All analysed spots are available as

443   supplementary data.
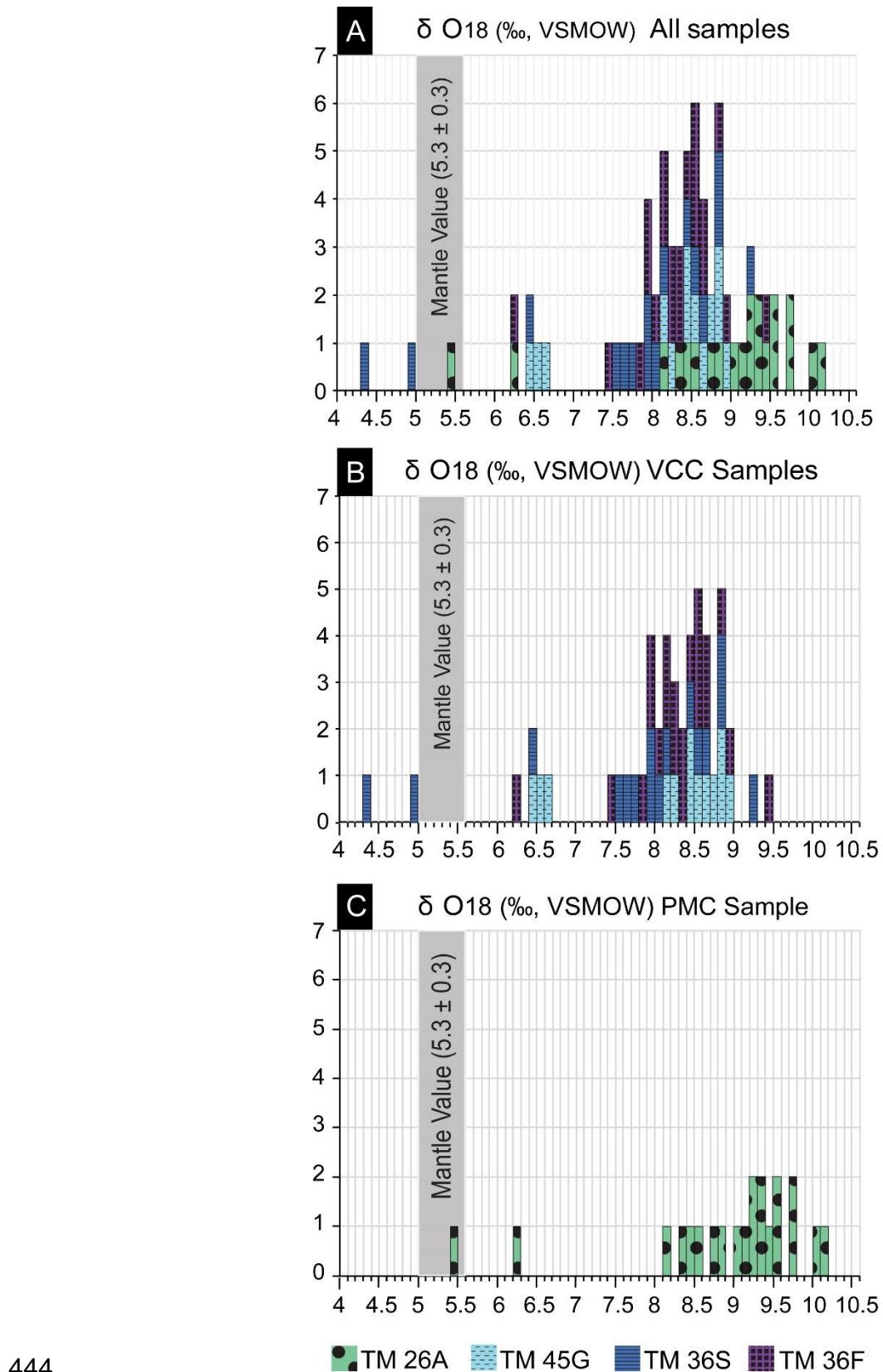
Figure 10. Zircon oxygen isotopic values measured in the four studied samples. A) δO18 zircon values from all samples; B) δO18 zircon values from Várzea do Capivarita Complex samples; C) δO18 zircon values from Porongos Complex sample.
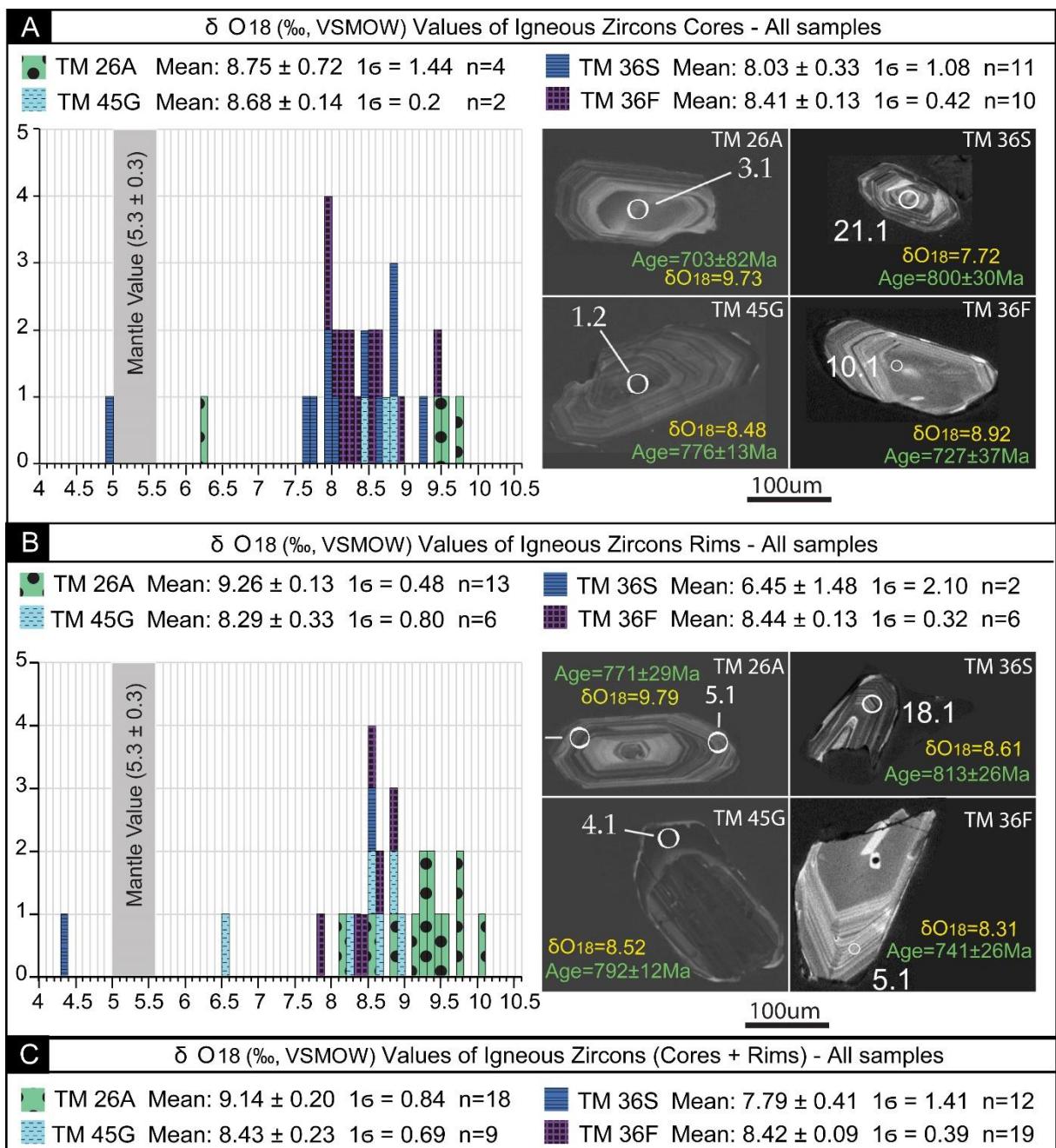
Figure 11 - δO18 values from Neoproterozoic zircons. A) Data from spots analysed in zircon cores, B) Data from spots analysed in zircon rims. C) General δO18 zircon values, considering all measured data (core spots + rim spots).

As described above, inherited zircons cores were registered in all studied samples. In order to compare them with Neoproterozoic igneous zircons, δO_{18} values were also measured in some of these inherited zircon cores. The results are indicated in figure 12, with their statistical data and some examples of analysed spots. As expected, many of the smallest δO_{18} values found in the studied samples are related to inherited zircons (Fig. 12). However, two points do not follow the expectations: 1)

461 the smallest δO_{18} value in sample TM-36S is related to Neoproterozoic igneous zircon
462 and not to inherited population; 2) despite the smallest δO_{18} value of the sample TM-
463 26A be from an inherited zircon, one spot performed in inherited zircons gave δO_{18}
464 value (10.2‰) higher than those found to the igneous zircons (δO_{18}<10.1‰).
465
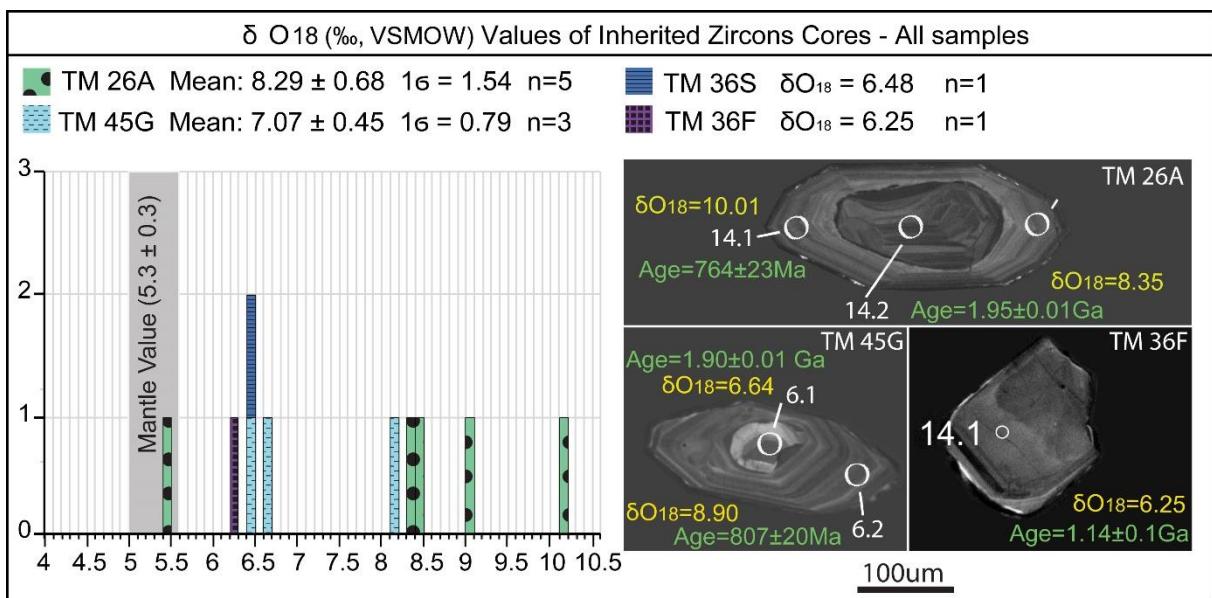
466
467
468 Figure 12 - δO_{18} values measured in inherited zircons cores.
469

470 The correlation of δO_{18} values with the U-Pb ages of analyzed zircon crystals,
471 considering only the U-Pb ages with less than 5% of discordance, show no statistical
472 correlation between those values (Fig. 13). Inherited zircons (older than 1000 Ma, in
473 figure 13) have δO_{18} values from 6.3‰ to 10.2‰. The studied Neoproterozoic igneous
474 zircons of 800-750 Ma have commonly δO_{18} values higher than 7.5‰ to slightly higher
475 than 10‰, although also values around 6.5‰ and smaller than 5‰ are reported. Note
476 in figure 13, the magmatic zircon evolution curve through the geological time (Valley
477 et al., 2005) in which the highest expected magmatic δO_{18} values to a given age are
478 delimited by the curve, according to Valley et al. (2005). In other words, magmatic
479 zircons should plot under the curve. However, as shown in figure 13, two inherited
480 zircons from PC sample TM-26A (#2.1 and #11.2) have plotted above such a curve
481 and will be discussed later.
482
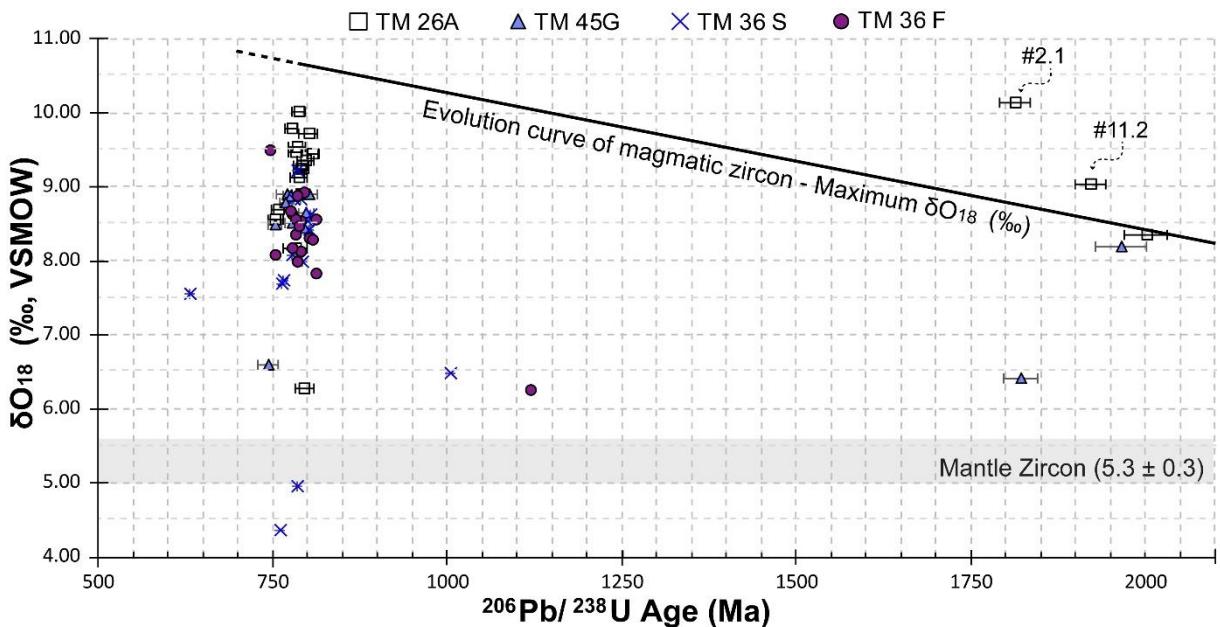
Figure 13 – δO_{18} zircon value plotted against the magmatic age of the grains (spots #2.1 and #11.2 are indicated – see text for further information). The magmatic zircon evolution curve through geological time (Valley et al., 2005) suggest the highest expected magmatic δO_{18} values to a given age. Horizontal bars indicate $^{206}Pb/^{238}U$ ages errors (±).

7. DISCUSSION

7.1. *Timing of pre-collisional igneous events in the hinterland and foreland of the Dom Feliciano Belt*

The new geochronological data obtained for the Várzea do Capivarita Complex orthogneisses demonstrate the Tonian age of their protolith, with Meso- to Paleoproterozoic inheritance ages, and reveals that such rocks are related to a magmatic event at ca. 790 Ma, in the DFB hinterland. The tonalitic orthogneiss (TM-36F) yielded a concordant U-Pb SHRIMP age of 786 ± 5 Ma (2σ) with one ca. 1.1 Ga inherited zircon. Likewise, the granitic orthogneiss (TM-45G) yielded the same (within error) mean Pb^{207}/Pb^{206} SHRIMP age of 790 ± 7 Ma with ca. 1.8 and 2.0 Ga inherited zircon xenocrysts. This magmatic event has the same age interval reported for the protoliths of granulitic orthogneisses in the Cerro Olivo Complex (COC) within the Uruguayan part of the DFB, further south along strike belt (Fig.1). The U–Pb SHRIMP ages for COC are:(Will et al., 2019), 802–767 Ma (Lenz et al., 2011), 782 ± 7 Ma (Masquelin et al., 2011), 761 ± 7 (Basei et al., 2011), 776 ± 12 Ma (Oyhantçabal et al., 2009) and 762 ± 8 (Hartmann et al., 2002). In the Brazilian part of the DFB, high-grade

507 igneous rocks with ca. 800-770 Ma protolith ages were discussed by Koester et al.
508 (2016), Martil et al. (2017) and De Toni et al. (2020b).

509   The Porongos Complex metarhyolite yielded a concordant U–Pb SHRIMP
510 crystallization age of 787 ± 2 Ma (2σ) with inheritance at ca. 2.0 Ga. Such age and the
511 Th/U ratios obtained in these igneous zircon grains are similar to those of the VCC
512 (Table 1). Our data represent the first dating of the metavolcanics lying at the PC
513 easternmost border (Fig. 2). The geochemical similarities of all samples studied in this
514 paper were pointed out by Martil et al. (2017) and Battisti et al. (2018). The obtained
515 age for the PC metarhyolite falls in the time interval of 800-770 Ma for pre-collisional
516 magmatic events in the PC established by previous studies (Soliani Jr, 1986;
517 Saalmann et al., 2011; Pertille et al., 2017). Thus, our data is also coherent and confirm
518 that the ca. 790 Ma magmatism was also important in the DFB foreland. In our view,
519 this magmatism in the PC is mainly found eastwards of the Santana da Boa Vista thrust
520 fault (see further discussion). Furthermore, our geochronological data in meta-igneous
521 rocks demonstrate that a magmatic activity had occurred in both hinterland and
522 foreland of the DFB at ca. 790 Ma.

523

524   INSERT TABLE 1

525

526 ***7.2. Syn-volcanic sedimentation in the Várzea do Capivarita Complex***

527

528   Provenance studies in the paragneiss sample (TM-36S) demonstrated the main
529 detrital population between 790 and 750 Ma. Such detrital population is coeval with the
530 magmatic event that generated the protoliths of the orthogneisses TM-36F and TM-
531 45G from the same complex (Fig. 8C). The time interval of 790-750 Ma is also coeval
532 with the igneous protolith ages reported in the literature for the Cerro Olivo Complex in
533 Uruguay, as shown in item 7.1 (Hartmann et al., 2002; Oyhantçabal et al., 2009; Lenz
534 et al., 2011; Basei et al., 2011; Masquelin et al., 2011; Will et al., 2019). The
535 coincidence of ages in the VCC ortho and paragneisses can be interpreted in two
536 alternative ways. The protolith of the paragneiss sample originated as volcanoclastic
537 debris, as in a mature arc setting, for instance, or was deposited in a tectonically very
538 active environment, with rapid exhumation, erosion and deposition in a rift setting, for
539 instance. Both alternatives suggest short transport of the detritus that would explain
540 the preservation of the pyramidal tips of the detrital zircons (Fig. 5). The first hypothesis

541 is suggested based on the geochemical signature of the VCC orthogneisses, which is
542 compatible with that found in a mature arc setting (Martil et al., 2017).

543   The entirely similar morphology and age of the igneous and detrital zircon crystals
544 from the studied VCC samples strongly suggest that some parts of this unit might
545 represent metamorphosed syn- sedimentary volcanic or volcano-sedimentary
546 deposits. This data also implies that the interleaving of orthogneiss and paragneiss in
547 the VCC, in part, represents its original S_0, which might have also been interleaved
548 tectonically later, during the transpressive deformation. The high metamorphic grade
549 (granulite facies) and intense deformation that affected these rocks obliterated any
550 additional depositional features of the protoliths that would permit a better
551 interpretation of their mutual relationships. One single spot (#6.1) in a zircon grain from
552 the paragneiss sample TM-36S yielded an age of 632± 9 Ma, which is interpreted as
553 related to such metamorphic granulite facies event, based on its distinct morphology
554 and low Th/U ratio (0.01). This interpretation is in agreement with the well-known time
555 interval for the main collision in the DFB at ca. 650–620 Ma (Gross et al., 2006, 2009;
556 Oyhantçabal et al., 2009; Chemale et al., 2011; Lenz et al., 2011; Basei et al., 2011;
557 Philipp et al., 2016a; Peel et al., 2018; Will et al., 2019; Percival et al., 2022).

558   According to Gruber et al. (2016a), the maximum depositional age for the VCC
559 clastic sedimentary rocks is 728 ± 11 Ma (U–Pb SHRIMP), and an interval of ca. 717–
560 750 Ma ($^{87}Sr/^{86}Sr$ whole rock) is proposed for the marble sequence deposition.
561 Considering the error, our data (716 ± 10 Ma) corroborate the maximum VCC
562 depositional age interpretation.

563

564   **7.3. *Interpretation and correlation of the zircon oxygen isotopic data***

565

566   The reliability of geochronological data from high-grade rocks, such as in the VCC
567 and COC, is discussed in the literature, as in the Harts Range Group, Australia, for
568 example (Maidment et al., 2013). Such preservation is common in zircon due to the
569 extremely low diffusion rates of Pb, Th and U in the crystal lattice, even at high
570 temperature and pressure (Lee et al., 1997; Cherniak & Watson, 2001, 2003; Scherer
571 et al., 2007). The diffusion rate of oxygen in zircon under high-temperature conditions
572 is also low (Peck et al., 2003), with effective closure temperatures at around 700°C
573 (Watson & Cherniak, 1997), and suggests that δO_{18} values are reliable even in high-
574 grade metamorphic rocks (e.g. Valley et al., 1994). However, in extreme cases,

575   radiation damage, metamictization and micro fracturing could facilitate the late
576   exchange of oxygen (Valley, 2003).

577   As established by Valley et al. (1998) and discussed by Bindeman (2008), among
578   many other authors, zircon in equilibrium with mantle-derived melts has an average
579   δO_{18} value of 5.3 ± 0.3‰. Higher δO_{18} values reflect the presence of ^{18}O-enriched
580   components, as, for instance, the melting or assimilation of crustal material or
581   hydrothermally altered oceanic crust (Peck et al., 2001; Valley et al., 2005; Kemp et
582   al., 2006). Such δO_{18} enrichment process results in an expected "evolutionary curve of
583   magmatic zircons" over the geological time (Fig. 13) (Valley et al., 2005). As predicted
584   by this curve, δO_{18} values higher than 7.5‰ are not recorded in igneous zircons older
585   than 2.5 Ga, but they are common in zircon crystallized in the Proterozoic times. Lastly,
586   zircon crystals could also present δO_{18} values lower than 5‰. Such values commonly
587   represent shallow sub-volcanic magma chambers where low δO_{18} values resulted from
588   melting of hydrothermally altered wall rock (Bindeman & Valley, 2000; Valley, 2003;
589   Valley et al., 2005) or, less often, from the contribution of glacial ice melting in rifting
590   scenarios (Wickham & Taylor, 1985), since meteoric water has negative (to strongly
591   negative) δO_{18} values.

592   Our data demonstrate that δO_{18} values from VCC and PC samples are quite
593   similar, where the most common δO_{18} values range between 7.9‰ and 9.7‰. δO_{18}
594   lower than 7.5‰ were registered in all studied samples, in which four of these spots
595   are related to the Neoproterozoic zircon population. Two of these spots are from the
596   paragneiss TM-36S (#24.1 and #20.1 - all analysed spots are available as
597   supplementary data). They could represent the source of detrital zircons from
598   neighbouring lithologies and thus, may not provide reliable information for further
599   interpretations about the VCC syn-volcanic-sedimentary scenario. Nevertheless, the
600   two other spots with δO_{18} values of 6.5‰ and 6.2‰ were registered in the
601   orthogneisses TM-45G and TM-26A, respectively (Fig. 11). Such values could be
602   easily explained by a lower-δO_{18} mantle-derived input (Valley, 2003). Moreover, some
603   hydrothermal water could also be responsible for reducing the δO_{18} values of such
604   Neoproterozoic grains (Bindeman & Valley, 2000). However, the crystals do not show
605   any cracks to permit such interaction. Irrespective of the meaning of those lower δO_{18}
606   zircons, only a few of them record such effect, which suggests that it was not a
607   significant event.

608   The highest value of δO_{18} found in the VCC samples is 9.4‰, in a zircon core of
609   TM-36F (VCC orthogneiss). On the other hand, the highest δO_{18} values of the PC

610   sample are mostly related to the igneous zircon rims. Surprisingly, the highest value

611   for the PC sample was found in the core of an inherited zircon (1.96 Ga): $\delta O_{18} = 10.2‰$

612   (Fig. 11) (spot #2.1-supplementary data). Spot #2.1 is 9% discordant, it has a relatively

613   low Th/U ratio (0.03), and in figure 13 plots above the "evolutionary curve of magmatic

614   zircons". Such indications mean that this zircon is non-magmatic or, most probably, a

615   magmatic zircon affected by a younger hydrothermal or metamorphic event. As

616   suggested by the low Th/U ratio, the latter option is more probable. Spot #11.2 also

617   plots above the expected curve (Fig. 13). However, it is 2% discordant and has a Th/U

618   ratio equal to 0.65, which suggest an igneous origin for this grain.

619   As shown in figures 10, 11 and 12, only one inherited zircon crystal has

620   crystallized in equilibrium with mantle $\delta O18$ values. The vast majority of analysed

621   zircon grains have higher $\delta O18$ values following the expected evolution magmatic

622   zircon curve of Valley et al. (2005). The main calculated δO_{18} for Neoproterozoic

623   igneous zircons in all studied samples, summarized in table 1, also show higher δO_{18}

624   values than the mantle value. Such data suggest that most zircons crystallized in more

625   evolved magmas, either as a response to melting of host rocks and sediments (buried

626   and/or subducted) or as a response to the assimilation of crustal material by mantle-

627   derived magmas, as by assimilation-fractional crystallization (AFC) processes (Peck

628   et al., 2001; Valley, 2003; Kemp et al., 2006). If a subduction event is considered in an

629   arc setting (see section 7.5 for such discussion), recycling of hydrothermally altered

630   oceanic crust may also be responsible for raising the zircon δO_{18} values (Valley et al.,

631   2005). Accordingly, Martil et al. (2017) present $^{87}Sr/^{86}Sr_{(i)}$ values for the VCC, from

632   0.71628 to 0.72509, $\varepsilon Nd_{(790)}$ values from −7.19 to −10.06, and Meso to

633   Paleoproterozoic Nd-TDM and inheritance ages, which these authors interpreted as "a

634   more evolved magmatic source with strong evidence of crustal assimilation/

635   contamination". Further discussions regarding the magmatic processes using the δO_{18}

636   data would require additional sampling of a larger SiO_2 range (magmatic series) to

637   correlate the fractionation of zircon δO_{18} in comparison to the δO_{18} of the whole rock.

638   The values determined in most zircon grains from the studied VCC and PC rocks

639   are in the range of Proterozoic igneous zircons, as discussed by Valley et al. (2005)

640   amongst other authors. The similarity of the zircon oxygen isotopic values for the

641   studied samples suggests a similar magmatic source for generating protoliths of the

642   VCC and PC orthometamorphic rocks. The available δO_{18} data from the literature,

643   acquired in other ortho-derived rocks from DFB with ca. 800-770 Ma protolith age

644   reinforces this statement, as demonstrated in Figure 14, where our present data are

645 compared with three other acid metavolcanics from the PC (Pertille et al., 2017) and
646 three granulitic orthogneisses from the Cerro Olivo Complex, in Uruguay (Will et al.,
647 2019).

648
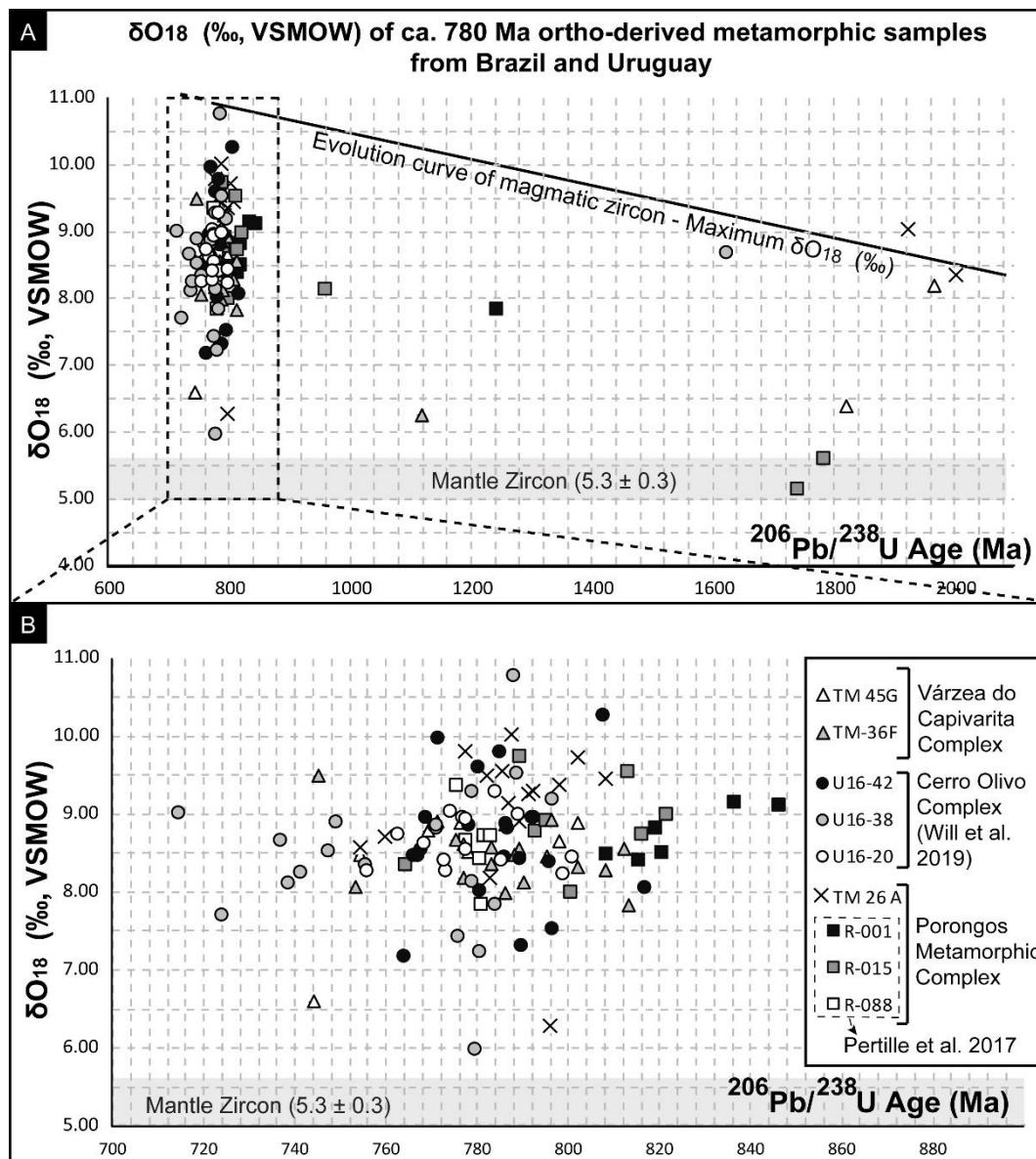
649
650

651 Figure 14. Comparison of δO_{18} zircon values among ca. 770-800 Ma ortho-derived
652 metamorphic rocks from Brazil (Várzea do Capavarita Complex, Porongos Complex) and
653 Uruguay (Cerro Olivo Complex).

654

655 **7.4. *Shared pre-collisional evolution of Dom Feliciano Belt hinterland and***
656 ***foreland units***

657

658 The coeval protolith ages obtained for the Várzea do Capivarita Complex (TM-
659 36F, TM-45G) and the Porongos Complex (TM-26A) samples pointed out age

660 similarities of part of the protoliths in both units (table 2 and 3). Such temporal
661 connection, together with geochemical and structural results of Martil et al. (2017) and
662 Battisti et al. (2018), lead us to strengthen our interpretation that both complexes
663 represent different parts of a single basin at some point in their geological history.
664 According to our geochronological data from meta-igneous rocks, this connection was
665 very likely at 790–780 Ma.

666   Nevertheless, it should be noted that the PC western region contains younger
667 metavolcanic rocks (e. g. Höfig et al., 2018) and also younger sources of detrital
668 material than its eastern region, as showed by Pertille et al. (2015a, 2017), Gruber et
669 al. (2016b) and Höfig et al. (2018). These data reflect distinct evolutionary histories for
670 the western and eastern regions of the PC, as discussed by Battisti (2022). For these
671 reasons, the data discussed here indicate a direct correlation only between the VCC
672 and the PC eastern region but not with the PC as a whole. The geochronological
673 differences between the western and eastern PC rocks are summarized in tables 2
674 and 3 and figure 15. Aiming to compare DFB units, tables 2 and 3 also show the data
675 from granulitic rocks of the Cerro Olivo Complex in Uruguay.

676   As seen in Figure 13, the δO_{18} values in zircon also demonstrate a direct
677 correlation between ortho metamorphic samples from the VCC and PC eastern region.
678 Moreover, zircon δO_{18} also point out a correlation between the ca. 800-770 Ma
679 magmatic event in Brazil and Uruguay, as already suggested in other
680 geochronological, isotopic and structural studies (e.g. Basei et al., 2000; Martil et al.,
681 2017; Konopásek et al., 2018; De Toni et al., 2020b).

682

683   INSERT TABLE 2

684

685   INSERT TABLE 3

686

687
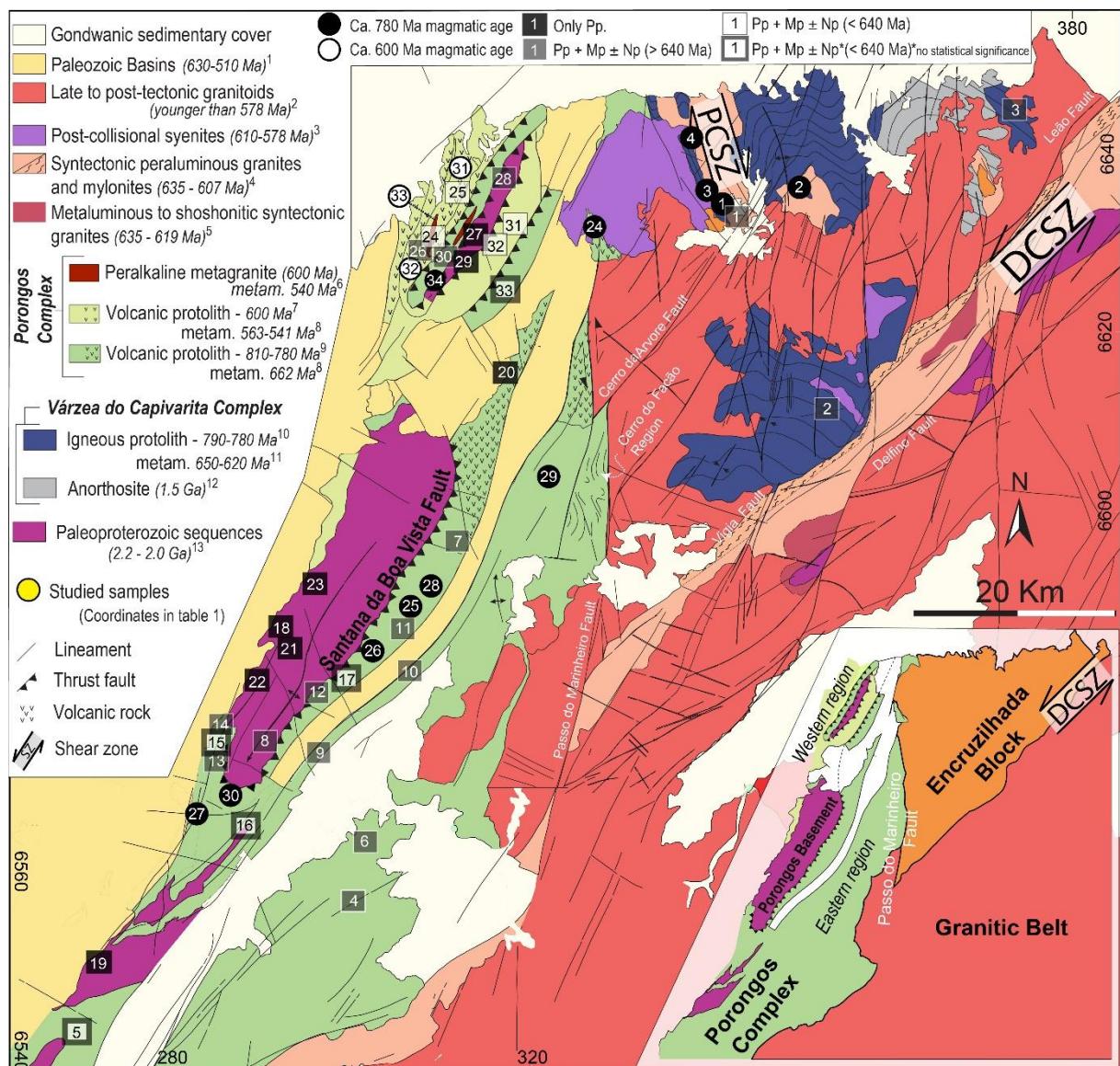
Figure 15. Geological map of the study area illustrating the sample sites from Tables 2 and 3. Please note the similar magmatic and provenance ages between VCC and eastern PC and the difference between the magmatic and provenance ages between the PC eastern and western regions - separated by the Santana da Boa Vista thrust fault (inset sketch). Eastern PC has mainly provenance sources older than the main metamorphic-deformational event (at ca. 650 Ma), and the western PC has provenance sources both older and younger than this time. Circles are magmatic ages, while squares represent provenance source ages. Abbreviations: Pp – Paleoproterozoic, Mp – Mesoproterozoic, Np – Neoproterozoic. References are the same as in figure 2.

While the correlations among various meta-igneous rocks of early Neoproterozoic age are straightforward, the correlation of metasedimentary rocks from the PC and VCC requires more caution. That is because the detrital provenance in the PC rocks is much better studied than in the VCC ones. However, keeping this in mind,

704 some considerations can be made. Both complexes present a similar detrital interval
705 for pre-collisional metasedimentary rocks: 750 Ma – 3.0 Ga for PC (Gruber et al.,
706 2016b; Pertille et al., 2017; Höfig et al., 2018), and 730 Ma – 2.5 Ga for VCC (Gruber
707 et al., 2016a). Regarding the main age peaks, the PC rocks show two main peaks (1.2–
708 1.5 and 2.0–2.3 Ga), while the VCC samples show only one well-marked peak at 1.9–
709 2.2 Ga (Gruber et al., 2016a). Moreover, the well pronounced ca 790 Ma age peak
710 found in the paragneiss TM-36S has not yet been registered in the VCC
711 metasedimentary rocks, although individual data showing such detrital age were
712 reported by Gruber et al. (2016a) also in other parts of the VCC.

713   On the other hand, it is important to point out that the latter two differences may
714 be explained by a shortage of data from the VCC. Thus, we interpret that the absence
715 of age peaks at ca. 1.2-1.5 Ga in the VCC will probably be solved when sufficient
716 detrital studies are available. Therefore, despite the caution considered in interpreting
717 the relationship between the para-metamorphic rocks of VCC and PC, they also
718 suggest a shared depositional origin by VCC and PC, indicated by our data in the ortho-
719 metamorphic rocks of both complexes.

720

721 **7.5.** *The geological setting of ca. 800-770 Ma magmatic event*

722

723   The geological setting in which the ca. 800-770 Ma metaigneous rocks of the
724 DFB was generated is debatable. Two main interpretations are found in the literature,
725 and for this reason, a continental arc (Koester et al., 2016; Martil et al., 2017; De Toni
726 et al., 2020b) or a back-arc/rift setting (Konopásek et al., 2018, 2020; Will et al., 2019)
727 are assumed as possible environments. Geochemical and isotopic features favour the
728 first hypothesis (Martil et al., 2017; De Toni et al., 2020b), and the structural data are
729 not discriminant. However, this discussion is not the focus of the present work, and
730 apart from the zircon oxygen isotope data, our data does not bring further arguments
731 to this discussion. Moreover, our zircon data demonstrate that the generation of 800-
732 770 protoliths has involved contamination/assimilation of crustal material, which is very
733 likely in both scenarios. Finally, it is important to highlight that our proposed VCC-PC
734 syn-volcano-sedimentary environment is not exclusive of either a continental arc or a
735 back-arc/rift. For that reason, our model is supported in both scenarios, as shown in
736 figure 16.

HYPOTHESIS 1 - The ca. 800–770 Ma magmatism was generated in a rift / back-arc scenario [1]

HYPOTHESIS 2 - The ca. 800–770 Ma magmatism was generated in a volcanic arc [2]

Ca 800–770 Ma

■ Syn-sedimentary magmatism ■ Sedimentary and volcano-sedimentary rocks (future Porongos Complex)

Ca 800–770 Ma

■ Sedimentary and volcano-sedimentary rocks (future Várzea do Capivarita Complex)

W erosion E erosion
volcanic debris
basement mantle

intra-arc basin volcanic debris
W E
basement
subducting plate melting
Subducting Oceanic plate

Between 760–660 Ma the crustal stretching has continued

Ca 760–660 Ma

rewokerd volcanoclastic sediments
W erosion erosion E
inative volcanos inative volcanos
Subducting oceanic plate mantle basement

■ 800–770 Ma magmatic rocks

■ Sedimentary and volcano-sedimentary rocks (future Porongos Complex)

■ Sedimentary and volcano-sedimentary rocks (future Várzea do Capivarita Complex)

Flat subduction evolves to steep subduction generating a strechting back-arc basin

Ca 650–620 Ma (Collision)

W South America E
Erosion ② ①
basement mantle

■ Syn-orogenic sedimentary basin (younger Porongos Complex basin)
■ Syn-tectnonic magmatism and partial melting
■ Ca 800–770 metaigneous rocks of Várzea do Capivarita and Porongos (greenschist to granulite facies)
■ Greenschist to amphibolite facies meta(volcano)-sedimentary rocks
■ Granulite facies meta(volcano)-sedimentary rocks

① Várzea do Capivarita Complex (in Brazil) ② Porongos Metamorphic Complex (in Brazil)

Figure 16. Models proposed in the literature for the study region: Hypothesis 1 is an idealised drawing after the discussion of Konopásek et al. (2020), in which a rift/back-arc scenario was responsible for generating 800-770 Ma VCC, PC and COC ortho-protoliths. Hypothesis 2 is a redrawing of De Toni et al. (2020b), in which the authors proposed arc magmatism as the best scenario for the emplacement of 800-770 Ma VCC, PC and COC ortho-protoliths. The syn-volcano-sedimentary environment proposed in this paper is achievable in both situations, irrespective of the chosen model.

747   Thus, our geochronological and isotopic data suggest that at least part of the
748   VCC represents former sedimentary rocks that originated through erosion of coeval
749   igneous rocks. Furthermore, the similar age and isotopic record of zircon in the VCC
750   and PC meta-igneous samples raises the hypothesis that the Várzea do Capivarita
751   Complex and part of the Porongos Complex represent different portions of a former
752   single volcano-sedimentary basin (Fig. 16). This basin was inverted at ca. 650 Ma by
753   progressive dextral/top-to-W transpressive deformation resulting in exhumation and
754   thrusting of its deeper and hotter part (VCC) over its margins (PC) (Fig. 16). However,
755   the contact between VCC and PC is now obliterated by younger magmatic activity.
756   After the basin inversion, such contact was probably represented by thrust faults, as
757   discussed in Battisti et al. (2018). The age of ca. 650–620 Ma for this inversion event
758   is supported by several authors in Brazil (in VCC: Gross et al., 2006; Chemale et al.,
759   2011; Martil, 2016; Philipp et al., 2016; in PC: Lenz, 2006, Battisti, 2022 and in Uruguay
760   Gross et al., 2009; Oyhantçabal et al., 2009; Lenz et al., 2011; Basei et al., 2011; Peel
761   et al., 2018; Will et al., 2019). The relationship between the high-grade Uruguayan
762   rocks and VCC–PC basin is more obscure. However, our isotopic comparison and
763   many other isotopic and geochronological data from the literature show that the
764   generation of all these rocks is probably the result of the same tectono-magmatic
765   evolution.

766

767   **8. CONCLUSIONS**

768

769   New geochronological data indicate that the Várzea do Capivarita Complex
770   (VCC) in southernmost Brazil has, at least in part, a syn-volcanic–sedimentary origin
771   at ca. 790 Ma. The geochronological dataset also constrains a maximum depositional
772   age of 716 ± 10 Ma for the VCC original basin. The geochronological and zircon oxygen
773   isotopic similarities shown for the VCC and Porongos Complex (PC) samples imply
774   igneous protoliths of the Várzea do Capivarita Complex. They also imply that part of
775   the Porongos Complex (mostly its eastern region) has represented different parts of a
776   single basin at ca. 800-770 Ma. As demonstrated by δO_{18} zircon data, the ca. 800-770
777   Ma protoliths of the VCC and PC metaigneous rocks have crystallized in more evolved
778   magmas, either from the melting of host rocks and sediments or assimilation of crustal
779   material by mantle-derived magmas, as by assimilation-fractional crystallization (AFC)
780   process. Only a negligible number of zircon grains crystallized in equilibrium with
781   mantle-derived melts free of crustal contamination/assimilation. A connection between

782 the ca. 800-770 Ma protoliths of the Cerro Olivo Complex in southernmost Dom
783 Feliciano Belt and the high-grade rocks and metasediments of the VCC–PC basin is
784 supported by geochronological and zircon isotopic oxygen data presented in this study.
785

795

9. REFERENCES

797

798   Arena, K.R., Hartmann, L.A., Lana, C., 2018. U–Pb–Hf isotopes and trace elements of
799 metasomatic zircon delimit the evolution of neoproterozoic Capané ophiolite in the southern Brasiliano
800 Orogen. Int Geol Rev 60, 911–928. https://doi.org/10.1080/00206814.2017.1355269

801   Basei, M., Siga, O., Masquelin, H., Harara, O., Reis Neto, J., Preciozzi, F., 2000. The Dom
802 Feliciano belt (Brazil-Uruguay)and its foreland (Rio de la Plata Craton): framework, tectonic evolution
803 and correlations with similar terranes of southwestern Africa.

804   Basei, M.A.S., Peel, E., Sánchez Bettucci, L., Preciozzi, F., Nutman, A.P., 2011. The basement
805 of the Punta del Este Terrane (Uruguay): an African Mesoproterozoic fragment at the eastern border of
806 the South American Río de La Plata craton. Int J Earth Sci 100, 289–304.
807 https://doi.org/10.1007/s00531-010-0623-1

808   Battisti, M.A., 2022. Evolução geológica do Cinturão Dom Feliciano (800-560 Ma) a partir do
809 estudo das rochas metamórficas da sua região central. PhD Thesis. Universidade Federal do Rio
810 Grande do Sul, Porto Alegre - RS.

811   Battisti, M.A., Bitencourt, M. de F., De Toni, G.B., Nardi, L.V.S., Konopásek, J., 2018.
812 Metavolcanic rocks and orthogneisses from Porongos and Várzea do Capivarita complexes: A case for
813 identification of tectonic interleaving at different crustal levels from structural and geochemical data in
814 southernmost Brazil. J South Am Earth Sci 88, 253–274. https://doi.org/10.1016/j.jsames.2018.08.009

815   Bindeman, I., 2008. Oxygen Isotopes in Mantle and Crustal Magmas as Revealed by Single
816 Crystal Analysis. Rev Mineral Geochemistry 69, 445–478. https://doi.org/10.2138/rmg.2008.69.12

817   Bindeman, I.N., Valley, J.W., 2000. Formation of low- δ 18O rhyolites after caldera collapse at
818 Yellowstone , Wyoming , USA Formation of low- δ 18 O rhyolites after caldera collapse. Geology 28,
819 719–722. https://doi.org/10.1130/0091-7613(2000)28

820   Bitencourt, M. de F., Nardi, L.V.S., 1993. Late- to Postcollisional Brasiliano Magmatism in
821   Southernmost Brazil. An Acad Bras Cienc 65, 3–16.

822   Bitencourt, M. de F., Nardi, L.V.S., 2000. Tectonic setting and sources of magmatism related to
823   the southern Brazilian shear belt. Rev Bras Geociencias 30, 184–187.

824   Bitencourt, M.F., Nardi, L.V.S., Florisbal, L.M., Heaman, L.M., 2015. Geology, geochronology and
825   petrogenesis of a Neoproterozoic, syntectonic sillimanite- muscovite-biotite granite from southernmost
826   Brazil. B Abstr 8th Hutt Sympo- sium Granites Relat Rocks 179.

827   Cawood, P.A., Kröner, A., Collins, W.J., Kusky, T.M., Mooney, W.D., Windley, B.F., 2009.
828   Accretionary orogens through Earth history. Geol Soc London, Spec Publ 318, 1–36.
829   https://doi.org/10.1144/SP318.1

830   Chemale, F., 2000. Evolução Geológica do Escudo Sul-rio- grandense, in: Holz, M., De Ros, L.F.
831   (Eds.), Geologia Do Rio Grande Do Sul. Universidade Federal do Rio Grande do Sul, Porto Alegre,
832   Brasil, pp. 13–52.

833   Chemale, F., Philipp, R.P., Dussin, I.A., Formoso, M.L.L., Kawashita, K., Berttotti, A.L., 2011. Lu–
834   Hf and U–Pb age determination of Capivarita Anorthosite in the Dom Feliciano Belt, Brazil. Precambrian
835   Res 186, 117–126. https://doi.org/10.1016/j.precamres.2011.01.005

836   Cherniak, D.., Watson, E.., 2001. Pb diffusion in zircon. Chem Geol 172, 5–24.
837   https://doi.org/10.1016/S0009-2541(00)00233-3

838   Cherniak, D.J., Watson, E.B., 2003. Diffusion in Zircon history - A brief review of bulk-release and
839   early lower-resolution diffusion measurements. Rev Mineral Geochemistry 53, 113–143.
840   https://doi.org/10.2113/0530089

841   Chetty, T., 2017. Orogens, Proterozoic Orogens of India. https://doi.org/10.1016/b978-0-12-
842   804441-4.00001-8

843   Collins, W.J., 2002. Hot orogens, tectonic switching, and creation of continental crust. Geology
844   30, 535. https://doi.org/10.1130/0091-7613(2002)030<0535:HOTSAC>2.0.CO;2

845   Costa, E.O. da, Gomes, E.M., Bitencourt, M. de F., De Toni, G.B., Nardi, L.V.S., 2020.
846   Reassessing the PT conditions of Neoproterozoic collisional metamorphism and partial melting in
847   southernmost Brazil. J South Am Earth Sci 100, 102584. https://doi.org/10.1016/j.jsames.2020.102584

848   De Toni, G.B., Bitencourt, M.D.F., Konopásek, J., Battisti, M.A., da Costa, E.O., Savian, J.F.,
849   2021. Autochthonous origin of the Encruzilhada Block, Dom Feliciano Belt, southern Brazil, based on
850   aerogeophysics, image analysis and PT-paths. J Geodyn 144.
851   https://doi.org/10.1016/j.jog.2021.101825

852   De Toni, G.B., Bitencourt, M.F., Konopásek, J., Martini, A., Andrade, P.H.S., Florisbal, L.M.,
853   Campos, R.S., 2020a. Transpressive strain partitioning between the Major Gercino Shear Zone and the
854   Tijucas Fold Belt, Dom Feliciano Belt, Santa Catarina, southern Brazil. J Struct Geol 104058.
855   https://doi.org/10.1016/j.jsg.2020.104058

856   De Toni, G.B., Bitencourt, M.F., Nardi, L.V.S., 2016. Strain partitioning into dry and wet zones
857   and the formation of Ca-rich myrmekite in syntectonic syenites: A case for melt-assisted dissolution-
858   replacement creep under granulite facies conditions. J Struct Geol 91, 88–101.
859   https://doi.org/10.1016/j.jsg.2016.08.002

860   De Toni, G.B., Bitencourt, M.F., Nardi, L.V.S., Florisbal, L.M., Almeida, B.S., Geraldes, M., 2020b.
861   Dom Feliciano Belt orogenic cycle tracked by its pre-collisional magmatism: the Tonian (ca. 800 Ma)

862 Porto Belo Complex and its correlations in southern Brazil and Uruguay. Precambrian Res 105702.
863 https://doi.org/10.1016/j.precamres.2020.105702

864 Eiler, J.M., 2001. Oxygen Isotope Variations of Basaltic Lavas and Upper Mantle Rocks. Rev
865 Mineral Geochemistry 43, 319–364. https://doi.org/10.2138/gsrmg.43.1.319

866 Fernandes, L.A.D., Tommazi, A., Porcher, C.C., 1992. Deformation patterns in the southern
867 Brazilian branch of the Dom Feliciano Belt: A reppraisal. J South Am Earth Sci 5, 77–96.

868 Fragoso-Cesar, A.R.S., Figueiredo, M.C.H., Soliani Jr, E., Faccini, U.F., 1986. O Batólito Pelotas
869 (Proterozóico Superior/Eopaleozóico) no escudo do Rio Grande do Sul. XXXIV Congr Bras Geol 1321–
870 1342.

871 Frimmel, H., Frank, W., 1998. Neoproterozoic tectono-thermal evolution of the Gariep Belt and its
872 basement, Namibia and South Africa. Precambrian Res 90, 1–28. https://doi.org/10.1016/S0301-
873 9268(98)00029-1

874 Goscombe, B.D., Gray, D.R., 2008. Structure and strain variation at mid-crustal levels in a
875 transpressional orogen: A review of Kaoko Belt structure and the character of West Gondwana
876 amalgamation and dispersal. Gondwana Res 13, 45–85. https://doi.org/10.1016/j.gr.2007.07.002

877 Gregory, T.R., Bitencourt, M. de F., Nardi, L.V.S., Florisbal, L.M., Chemale, F., 2015.
878 Geochronological data from TTG-type rock associations of the Arroio dos Ratos Complex and
879 implications for crustal evolution of southernmost Brazil in Paleoproterozoic times. J South Am Earth
880 Sci 57, 49–60. https://doi.org/10.1016/j.jsames.2014.11.009

881 Gross, A.O.M.., Porcher, C.C., Fernandes, L.A.D., Koester, E., 2006. Neoproterozoic low-
882 pressure/high-temperature collisional metamorphic evolution in the Varzea do Capivarita Metamorphic
883 Suite, SE Brazil: Thermobarometric and Sm/Nd evidence. Precambrian Res 147, 41–64.
884 https://doi.org/10.1016/j.precamres.2006.02.001

885 Gross, A.O.M.S., Droop, G.T.R., Porcher, C.C., Fernandes, L.A.D., 2009. Petrology and
886 thermobarometry of mafic granulites and migmatites from the Chafalote Metamorphic Suite: New
887 insights into the Neoproterozoic P–T evolution of the Uruguayan—Sul-Rio-Grandense shield.
888 Precambrian Res 170, 157–174. https://doi.org/10.1016/j.precamres.2009.01.011

889 Gruber, L., Lenz, C., Porcher, C.C., Fernandes, L.A.D., 2011. Geocronologia e geoquímica
890 isotópica no estudo das áreas fonte dos metassedimentos do complexo metamórfico Porongos,
891 cinturão Dom Feliciano, RS. Congr Bras Geoquímica (13 2011 out 9-14 Gramado, RS); Simpósio
892 Geoquímica dos Países do Mercosul (3 2011 out 9-14 Gramado, RS) [Anais] [Porto Alegre]
893 UFRGS/IGEO, 2011 1 CD-ROM 1159–1162.

894 Gruber, L., Porcher, C.C., Geller, H., Fernandes, L.A.D., Koester, E., 2016a. Geochronology (U-
895 Pb) and isotope geochemistry (Sr / Sr and Pb / Pb) applied to the Várzea do Capivarita Metamorphic
896 Suite , Dom Feliciano Belt , Southern Brazil : Insights and paleogeographical implications to. Geochim
897 Bras 30, 55–71. https://doi.org/10.21715/GB2358-2812.2016301055

898 Gruber, L., Porcher, C.C., Koester, E., Bertotti, A.L., Lenz, C., Fernandes, L.A.D., Remus, M.V.D.,
899 2016b. Isotope geochemistry and geochronology of syn-depositional volcanism in Porongos
900 Metamorphic Complex, Santana da Boa Vista antiform, Dom Feliciano Belt, Brazil: onset of an 800 ma
901 continental arc. J Sediment Environ 1. https://doi.org/10.12957/jse.2016.22722

902   Harrison, T.M., Grove, M., Lovera, O.M., Catlos, E.J., D'Andrea, J., 1999. The origin of Himalayan
903 anatexis and inverted metamorphism: Models and constraints. J Asian Earth Sci 17, 755–772.
904 https://doi.org/10.1016/S1367-9120(99)00018-8

905   Hartmann, L.A., Leite, J.A.D., Da Silva, L.C., Remus, M.V.D., McNaughton, N.J., Groves, D.I.,
906 Fletcher, I.R., Santos, J.O.S., Vasconcellos, M.A.Z., 2000. Advances in SHRIMP geochronology and
907 their impact on understanding the tectonic and metallogenic evolution of southern Brazil. Aust J Earth
908 Sci 47, 829–844. https://doi.org/10.1046/j.1440-0952.2000.00815.x

909   Hartmann, L.A., Philipp, R.P., Liu, D., Wan, Y., Wang, Y., Santos, J.O.S., Vasconcellos, M.A.Z.,
910 2004. Paleoproterozoic Magmatic Provenance of Detrital Zircons, Porongos Complex Quartzites,
911 Southern Brazilian Shield. Int Geol Rev 46, 127–157. https://doi.org/10.2747/0020-6814.46.2.127

912   Hartmann, L.A., Santos, J.O.S., Bossi, J., Campal, N., Schipilov, A., McNaughton, N.J., 2002.
913 Zircon and titanite U–Pb SHRIMP geochronology of Neoproterozoic felsic magmatism on the eastern
914 border of the Rio de la Plata Craton, Uruguay. J South Am Earth Sci 15, 229–236.
915 https://doi.org/10.1016/S0895-9811(02)00030-5

916   Hartmann, L.A., Santos, J.O.S., Leite, J.A.D., Porcher, C.C., Mcnaughton, N.J., 2003.
917 Metamorphic evolution and U-Pb zircon SHRIMP geochronology of the Belizário ultramafic amphibolite,
918 Encantadas Complex, southernmost Brazil. An Acad Bras Cienc 75, 393–403.
919 https://doi.org/10.1590/S0001-37652003000300010

920   Heine, C., Zoethout, J., Müller, R.D., 2013. Kinematics of the South Atlantic rift. Solid Earth 4,
921 215–253. https://doi.org/10.5194/se-4-215-2013

922   Höfig, D.F., Marques, J.C., Basei, M.A.S., Giusti, R.O., Kohlrausch, C., Frantz, J.C., 2018. Detrital
923 zircon geochronology (U-Pb LA-ICP-MS) of syn-orogenic basins in SW Gondwana: New insights into
924 the Cryogenian-Ediacaran of Porongos Complex, Dom Feliciano Belt, southern Brazil. Precambrian Res
925 306, 189–208. https://doi.org/10.1016/j.precamres.2017.12.031

926   Jost, H., Bitencourt, M.F., 1980. Estratigrafia e tectônica de uma fração da Faixa de Dobramentos
927 Tijucas no Rio Grande do Sul. Acta Geol Leop 11, 27–59.

928   Kemp, A.I.S., Hawkesworth, C.J., Paterson, B.A., Kinny, P.D., Kemp, T., 2006. Episodic growth
929 of the Gondwana supercontinent from hafnium and oxygen isotopes in zircon. Nature 439, 580–583.
930 https://doi.org/10.1038/nature04505

931   Knijnik, D.B., 2018. Geocronologia U-Pb e geoquímica isotópica Sr-Nd dos granitoides
932 sintectônicos às zonas de cisalhamento transcorrentes Quitéria Serra do Erval e Dorsal de Canguçu,
933 Rio Grande do Sul, Brasil. Universidade Federal do Rio Grande do Sul, Porto Alegre - RS.

934   Koester, E., Porcher, C.C., Pimentel, M.M., Fernandes, L.A.D., Vignol-Lelarge, M.L., Oliveira,
935 L.D., Ramos, R.C., 2016. Further evidence of 777 Ma subduction-related continental arc magmatism in
936 Eastern Dom Feliciano Belt, southern Brazil: The Chácara das Pedras Orthogneiss. J South Am Earth
937 Sci 68, 155–166. https://doi.org/10.1016/j.jsames.2015.12.006

938   Konopásek, J., Cavalcante, C., Fossen, H., Janoušek, V., 2020. Adamastor – An ocean that never
939 existed? Earth-Science Rev 103201. https://doi.org/10.1016/j.earscirev.2020.103201

940   Konopásek, J., Janoušek, V., Oyhantçabal, P., Sláma, J., Ulrich, S., 2018. Did the circum-Rodinia
941 subduction trigger the Neoproterozoic rifting along the Congo–Kalahari Craton margin? Int J Earth Sci
942 107, 1859–1894. https://doi.org/10.1007/s00531-017-1576-4

943 Lacombe, O., Bellahsen, N., 2016. Thick-skinned tectonics and basement-involved fold-thrust
944 belts: Insights from selected Cenozoic orogens, Geological Magazine.
945 https://doi.org/10.1017/S0016756816000078

946 Lee, J.K.W., Williams, I.S., Ellis, D.J., 1997. Pb, U and Th diffusion in natural zircon. Nature 390,
947 159–162. https://doi.org/10.1038/36554

948 Leite, J.A.D., Hartmann, L.A., Fernandes, L.A.D., McNaughton, N.J., Soliani, Jr., Ê., Koester, E.,
949 Santos, J.O.S., Vasconcellos, M.A.Z., 2000. Zircon U–Pb SHRIMP dating of gneissic basement of the
950 Dom Feliciano Belt, southernmost Brazil. J South Am Earth Sci 13, 739–750.
951 https://doi.org/10.1016/S0895-9811(00)00058-4

952 Lenz, C., 2006. Evolução metamórfica dos metapelitos da Antiforme Serra dos Pedrosas:
953 condições e idades do metamorfismo 111.

954 Lenz, C., Fernandes, L.A.D., McNaughton, N.J., Porcher, C.C., Masquelin, H., 2011. U–Pb
955 SHRIMP ages for the Cerro Bori Orthogneisses, Dom Feliciano Belt in Uruguay: Evidences of a ~800Ma
956 magmatic and ~650Ma metamorphic event. Precambrian Res 185, 149–163.
957 https://doi.org/10.1016/j.precamres.2011.01.007

958 Ludwig, K.R., 2003. Isoplot: A Geochronological Toolkit for Microsoft Excel, version 3.00.

959 Lyra, D.S., Savian, J.F., Bitencourt, M. de F., Trindade, R.I.F., Tomé, C.R., 2018. AMS fabrics
960 and emplacement model of Butiá Granite, an Ediacaran syntectonic peraluminous granite from
961 southernmost Brazil. J South Am Earth Sci 87, 25–41. https://doi.org/10.1016/j.jsames.2017.12.006

962 Maidment, D.W., Hand, M., Williams, I.S., 2013. High grade metamorphism of sedimentary rocks
963 during Palaeozoic rift basin formation in central Australia. Gondwana Res 24, 865–885.
964 https://doi.org/10.1016/j.gr.2012.12.020

965 Marques, J.C., Roisenberg, A., Jost, H., Frantz, J.C., Teixeira, R.S., 2003. Geologia e geoquímica
966 das rochas metaultramáficas da antiforme Capané, suíte metamórfica Porongos, RS. Rev Bras
967 Geociências 33, 83–94.

968 Martil, M.M.D., 2016. O magmatismo de arco continental pré-colisional (790 ma) e a
969 reconstituição espaço-temporal do regime transpressivo (650 ma) no Complexo Várzea Do Capivarita,
970 Sul da Província Mantiqueira. Universidade Federal do Rio Grande do Sul, Porto Alegre, Brasil.

971 Martil, M.M.D., Bitencourt, M. de F., Nardi, L.V.S., 2011. Caracterização estrutural e petrológica
972 do magmatismo pré-colisional do Escudo Sul-rio-grandense: Os ortognaisses do Complexo
973 Metamórfico Várzea do Capivarita. Pesqui em Geociencias 38, 181–201.

974 Martil, M.M.D., Bitencourt, M. de F., Nardi, L.V.S., Schmitt, R. da S., Weinberg, R., 2017. Pre-
975 collisional, Tonian (ca. 790 Ma) continental arc magmatism in southern Mantiqueira Province, Brazil:
976 Geochemical and isotopic constraints from the Várzea do Capivarita Complex. Lithos 274–275, 39–52.
977 https://doi.org/10.1016/j.lithos.2016.11.011

978 Masquelin, H., D'Avila Fernandes, L.A., Lenz, C., Porcher, C.C., McNaughton, N.J., 2011. The
979 Cerro Olivo Complex: a pre-collisional Neoproterozoic magmatic arc in Eastern Uruguay. Int Geol Rev
980 54, 1161–1183. https://doi.org/10.1080/00206814.2011.626597

981 Nardi, L.V.S., Bitencourt, M. de F., 2007. Magmatismo Granítico e Evolução Crustal no Sul do
982 Brasil. 50 anos Geol - Inst Geociências da Univ Fed do Rio Gd do Sul 1, 125–141.

983   Oriolo, S., Oyhantçabal, P., Wemmer, K., Siegesmund, S., 2017. Contemporaneous assembly of
984   Western Gondwana and final Rodinia break-up: Implications for the supercontinent cycle. Geosci Front
985   8, 1431–1445. https://doi.org/10.1016/j.gsf.2017.01.009

986   Oyhantçabal, P., Siegesmund, S., Wemmer, K., Presnyakov, S., Layer, P., 2009.
987   Geochronological constraints on the evolution of the southern Dom Feliciano Belt (Uruguay). J Geol Soc
988   London 166, 1075–1084. https://doi.org/10.1144/0016-76492008-122

989   Paces, J.B., Miller, J.D., 1993. Precise U-Pb ages of Duluth Complex and related mafic intrusions,
990   northeastern Minnesota: Geochronological insights to physical, petrogenetic, paleomagnetic, and
991   tectonomagmatic processes associated with the 1.1 Ga Midcontinent Rift System. J Geophys Res Solid
992   Earth 98, 13997–14013. https://doi.org/10.1029/93JB01159

993   Padilha, D.F., Bitencourt, M. de F., Nardi, L.V.S., Florisbal, L.M., Reis, C., Geraldes, M., Almeida,
994   B.S., 2019. Sources and settings of Ediacaran post-collisional syenite-monzonite-diorite shoshonitic
995   magmatism from southernmost Brazil. Lithos. https://doi.org/10.1016/j.lithos.2019.06.004

996   Paim, P.S.G., Chemale Junior, F., Wildner, W., 2014. ESTÁGIOS EVOLUTIVOS DA BACIA DO
997   CAMAQUÃ (RS). Ciência e Nat 36, 183–193. https://doi.org/10.5902/2179460X13748

998   Peck, W.H., Valley, J.W., Graham, C.M., 2003. Slow oxygen diffusion rates in igneous zircons
999   from metamorphic rocks. Am Mineral 88, 1003–1014. https://doi.org/10.2138/am-2003-0708

1000   Peck, W.H., Valley, J.W., Wilde, S.A., Graham, C.M., 2001. Oxygen isotope ratios and rare earth
1001   elements in 3.3 to 4.4 Ga zircons: Ion microprobe evidence for high δ 18 O continental crust and oceans
1002   in the Early Archean. Geochim Cosmochim Acta 65, 4215–4229. https://doi.org/10.1016/S0016-
1003   7037(01)00711-6

1004   Peel, E., Sánchez, L., Angelo, M., Basei, S., 2018. Journal of South American Earth Sciences
1005   Geology and geochronology of Paso del Dragón Complex (northeastern Uruguay): Implications on the
1006   evolution of the Dom Feliciano Belt (Western Gondwana). J South Am Earth Sci 85, 250–262.
1007   https://doi.org/10.1016/j.jsames.2018.05.009

1008   Percival, J.J., Konopásek, J., Anczkiewicz, R., Ganerød, M., Sláma, J., Campos, R.S., Bitencourt,
1009   M.F., 2022. Tectono-Metamorphic Evolution of the Northern Dom Feliciano Belt Foreland, Santa
1010   Catarina, Brazil: implications for models of subduction-driven orogenesis. Tectonics.
1011   https://doi.org/10.1029/2021TC007014

1012   Percival, J.J., Konopásek, J., Eiesland, R., Sláma, J., de Campos, R.S., Battisti, M.A., Bitencourt,
1013   M. de F., 2021. Pre-orogenic connection of the foreland domains of the Kaoko–Dom Feliciano–Gariep
1014   orogenic system. Precambrian Res 354. https://doi.org/10.1016/j.precamres.2020.106060

1015   Pertille, J., Hartmann, L.A., Philipp, R.P., 2015a. Zircon U–Pb age constraints on the
1016   Paleoproterozoic sedimentary basement of the Ediacaran Porongos Group, Sul-Riograndense Shield,
1017   southern Brazil. J South Am Earth Sci 63, 334–345. https://doi.org/10.1016/j.jsames.2015.08.005

1018   Pertille, J., Hartmann, L.A., Philipp, R.P., Petry, T.S., de Carvalho Lana, C., 2015b. Origin of the
1019   Ediacaran Porongos Group, Dom Feliciano Belt, southern Brazilian Shield, with emphasis on whole rock
1020   and detrital zircon geochemistry and U-Pb, Lu-Hf isotopes. J South Am Earth Sci 64, 69–93.
1021   https://doi.org/10.1016/j.jsames.2015.09.001

1022   Pertille, J., Hartmann, L.A., Santos, J.O.S., McNaughton, N.J., Armstrong, R., 2017.
1023   Reconstructing the Cryogenian–Ediacaran evolution of the Porongos fold and thrust belt, Southern

Brasiliano Orogen, based on Zircon U–Pb–Hf–O isotopes. Int Geol Rev 59, 1532–1560. https://doi.org/10.1080/00206814.2017.1285257

Philipp, R., Machado, R., 2002. O magmatismo granítico Neoproterozóico do Batólito Pelotas no sul do Brasil: novos dados e revisão da geocronologia regional. Rev Bras Geociencias 32, 277–290.

Philipp, R.P., Bom, F.M., Pimentel, M.M., Junges, S.L., Zvirtes, G., 2016a. SHRIMP U-Pb age and high temperature conditions of the collisional metamorphism in the Várzea do Capivarita Complex: Implications for the origin of Pelotas Batholith, Dom Feliciano Belt, southern Brazil. J South Am Earth Sci 66, 196–207. https://doi.org/10.1016/j.jsames.2015.11.008

Philipp, R.P., Lusa, M., Nardi, L.V.S., 2008. Petrology of dioritic, tonalitic and trondhjemitic gneisses from Encantadas Complex, Santana da Boa Vista, southernmost Brazil: paleoproterozoic continental-arc magmatism. An Acad Bras Cienc 80, 735–748. https://doi.org/10.1590/S0001-37652008000400013

Philipp, R.P., Pimentel, M.M., Chemale Jr, F., 2016b. Tectonic evolution of the Dom Feliciano Belt in Southern Brazil: Geological relationships and U-Pb geochronology. Brazilian J Geol 46, 83–104. https://doi.org/10.1590/2317-4889201620150016

Ramos, V.A., Cingolani, C., Junior, F.C., Naipauer, M., Rapalini, A., 2017. The Malvinas (Falkland) Islands revisited: The tectonic evolution of southern Gondwana based on U-Pb and Lu-Hf detrital zircon isotopes in the Paleozoic cover. J South Am Earth Sci 76, 320–345. https://doi.org/10.1016/j.jsames.2016.12.013

Rapela, C.W., Fanning, C.M., Casquet, C., Pankhurst, R.J., Spalletti, L., Poiré, D., Baldo, E.G., 2011. The Rio de la Plata craton and the adjoining Pan-African/brasiliano terranes: Their origins and incorporation into south-west Gondwana. Gondwana Res 20, 673–690. https://doi.org/10.1016/j.gr.2011.05.001

Rivera, C.B., 2016. Construção do maciço sienítico Piquiri (609 a 683 Ma) por colocação sucessiva de pulsos de magma ultrapotássico e shoshonítico sob extensão no Escudo sul-rio-grandense. Universidade Federal do Rio Grande do Sul, Porto Alegre, Brasil.

Saalmann, K., Gerdes, A., Lahaye, Y., Hartmann, L.A., Remus, M.V.D., Läufer, A., 2011. Multiple accretion at the eastern margin of the Rio de la Plata craton: the prolonged Brasiliano orogeny in southernmost Brazil. Int J Earth Sci 100, 355–378. https://doi.org/10.1007/s00531-010-0564-8

Scherer, E.E., Whitehouse, M.J., Munker, C., 2007. Zircon as a Monitor of Crustal Growth. Elements 3, 19–24. https://doi.org/10.2113/gselements.3.1.19

Schmitt, R. da S., Fragoso, R. de A., Collins, A.S., 2018. Suturing Gondwana in the Cambrian: The Orogenic Events of the Final Amalgamation, in: Siegesmund, S., Basei, M.A.S., Oyhantçabal, P., Oriolo, S. (Ed.), Geology of Southwest Gondwana. Springer International Publishing, pp. 411–432. https://doi.org/10.1007/978-3-319-68920-3_15

Soliani Jr, E., 1986. Os Dados Geocronológicos do Escudo Sul-Rio-Grandense e Suas Implicações de Ordem Geotectônica 417.

Tavani, S., Storti, F., Lacombe, O., Corradetti, A., Muñoz, J.A., Mazzoli, S., 2015. A review of deformation pattern templates in foreland basin systems and fold-and-thrust belts: Implications for the state of stress in the frontal regions of thrust wedges. Earth-Science Rev 141, 82–104. https://doi.org/10.1016/j.earscirev.2014.11.013

1065   Valley, J.W., 2003. Oxygen Isotopes in Zircon. Rev Mineral Geochemistry 53, 343–385.

1066   https://doi.org/10.2113/0530343

1067   Valley, J.W., Chiarenzelli, J.R., McLelland, J.M., 1994. Oxygen isotope geochemistry of zircon.

1068   Earth Planet Sci Lett 126, 187–206. https://doi.org/10.1016/0012-821X(94)90106-6

1069   Valley, J.W., Kinny, P.D., Schulze, D.J., Spicuzza, M.J., 1998. Zircon megacrysts from kimberlite:

1070   oxygen isotope variability among mantle melts. Contrib to Mineral Petrol 133, 1–11.

1071   https://doi.org/10.1007/s004100050432

1072   Valley, J.W., Lackey, J.S., Cavosie, A.J., Clechenko, C.C., Spicuzza, M.J., Basei, M.A.S.,

1073   Bindeman, I.N., Ferreira, V.P., Sial, A.N., King, E.M., Peck, W.H., Sinha, A.K., Wei, C.S., 2005. 4.4

1074   billion years of crustal maturation: Oxygen isotope ratios of magmatic zircon. Contrib to Mineral Petrol

1075   150, 561–580. https://doi.org/10.1007/s00410-005-0025-8

1076   Van Der Pluijm, B.A., Marshak, S., 2003. Earth Structure: An Introduction to Structural Geology

1077   and Tectonics, 2nd ed. W. W. Norton & Compan.

1078   Vanderhaeghe, O., 2012. The thermal-mechanical evolution of crustal orogenic belts at

1079   convergent plate boundaries: A reappraisal of the orogenic cycle. J Geodyn 56–57, 124–145.

1080   https://doi.org/10.1016/j.jog.2011.10.004

1081   Vieira, D.T., Koester, E., Ramos, R.C., Porcher, C.C., D'Ávila Fernandes, L.A., 2020. SHRIMP

1082   U-Pb zircon ages for the synkinematic magmatism in the Dorsal de Canguçu Transcurrent Shear Zone,

1083   Dom Feliciano Belt (Brazil): Tectonic implications. J South Am Earth Sci 100, 102603.

1084   https://doi.org/10.1016/j.jsames.2020.102603

1085   Watson, E.., Cherniak, D.., 1997. Oxygen diffusion in zircon. Earth Planet Sci Lett 148, 527–544.

1086   https://doi.org/10.1016/S0012-821X(97)00057-5

1087   Wickham, S.M., Taylor, H.P., 1985. Stable isotopic evidence for large-scale seawater infiltration

1088   in a regional metamorphic terrane; the Trois Seigneurs Massif, Pyrenees, France. Contrib to Mineral

1089   Petrol 91, 122–137. https://doi.org/10.1007/BF00377760

1090   Will, T.M., Gaucher, C., Ling, X.-X., Li, X.-H., Li, Q.-L., Frimmel, H.E., 2019. Neoproterozoic

1091   magmatic and metamorphic events in the Cuchilla Dionisio Terrane, Uruguay, and possible correlations

1092   across the South Atlantic. Precambrian Res 320, 303–322.

1093   https://doi.org/10.1016/j.precamres.2018.11.004

1094   Williams, I.S., 1998. U-Th-Pb geochronology by ion microprobe. Rev Econ Geol 7, 1–35.

1095   Zvirtes, G., Philipp, R.P., Camozzato, E., Guadagnin, F., 2017. Análise estrutural do Metagranito

1096   Capané, Complexo Porongos, Cachoeira do Sul, RS. Pesqui em Geociências 44, 05.

1097   https://doi.org/10.22456/1807-9806.78250

1098

1099

TABLES

Table 1. Comparison of the zircon data among studied samples: their ages, Th/U ratios and isotopic oxygen data (consider only the spots less than 5% discordant).

Coordinate (Zone 22J) Córrego Alegre	Sample	Neoprot. Zircon	Protolith Age (Ma - 2σ)	Th/U Ratio	Mean δO_{18} (‰ VSMOV)				Inhereted Zircon	Age (Ga)	Th-U Ratio
					Neoprot. zircon cores		Neoprot. zircon rims				
					n		n				
341622 m W 6632227 m S	TM-36F	21	786 ± 5	0.28 to 0.68	10	8.41 ± 0.13	6	8.44 ± 0.13	1	Ca. 1.1	0.84
348665 m W 6634440 m S	TM-45G	11	790 ± 7	0.16 to 0.47	2	8.68 ± 0.14	6	8.29 ± 0.33	2	Ca. 1.8 and 2.0 Ga	0.48 to 1.07
326982 m W 6632336 m S	TM-26A	15	787 ± 5	0.26 to 0.67	4	8.75 ± 0.72	13	9.26 ± 0.13	2	Ca. 2.0	0.44 to 0.65
-	-	Neoprot. Population	Provenance Peak (Ma)	-	-	-	-	-	Mesoprot. Zircons	-	-
341622 m W 341622 m S	TM-36S	45	750-790	0.18 to 0.70	11	8.03 ± 0.33	2	6.45 ± 1.48	2	Ca. 1.0 and 1.1	0.42 to 0.44

Table 2. Ortho-metamorphic protoliths ages of VCC, PMC and COC.

Complex	Symbology	Sample	Lithology	SHRIMP	LA-ICP-MS	TIMS	Age (Ma)	Inherited Zircon Age(Ga)	Reference
				U-Pb Zircon (number analyses)					
VCC		**TM-36F**	**Tonalitic orthogneiss**	**21**			**785 ± 9**	**Ca. 1.1**	**This paper**
	1	TM 36 B	Mafic Gneiss	12			782 ± 9.7		(Martil, 2016)
	1	TM 36 B	Mafic Gneiss		9		790 ± 34		
	1	TM 36 L	Mafic Gneiss	13			788 ± 5.3		
	2	**TM-45G**	**Granitic orthogneiss**	**11**			**789 ± 7**	**Ca. 1.8 and Ca 2.0**	**This paper**
	3	TM 01 E	Tonalitic orthogneiss		22		791 ± 30	1.6, 1.8 and 3.1	(Martil, 2016)
	4	TM 96 A	Granitic Vein	6			770 ± 9.9	Ca 1.8	
Cerro Olivo Complex		U16-20	Orthogneiss	13 spot SIMS			777 ± 6.1		(Will et al., 2019)
		U16-38	Orthogneiss	12 spot SIMS			782 ± 5.1		
		U16-42	Orthogneiss	21 spot SIMS			783 ± 4.2		
		AC-133-B	Mafic granulite	25			794±8	Ca. 1.2	(Lenz et al., 2011)
		AC296-M	Mafic granulite	18			796±8	Ca. 1.4 and Ca 0.8	
		AC-373-B	Mafic granulite	29			795±8	Ca 0.8	
		PCH-0869	Mafic granulite	36			788±6		
		CH-33-A	Mafic granulite	12			767±9		
		CH-43-D	Mafic granulite	16			772–765?	1.3 and 1.0	
		UY-2-A	Mafic Gneiss	18			771±6	Ca 1.1 to Ca 0.8	
		AC-137-B	Felsic gneiss	20			793±4	Ca 2.1 and Ca 1.2	
		AC-338-A	Felsic gneiss	12			802±12	Ca 1.1	
		CH-174	Felsic gneiss	15			786±9	Ca 1.5 and Ca 0.9	
		COR-42	Felsic mylonite	27			797±8		
		AC-370-A	Felsic migmatite	40			780±5		
		AC-104	Cerro Bori metatonalite	29			779 ± 6	1.3 to 1.0	(Masquelin et al., 2011)
		UCUR-03	Deformed migmatite	15			761 ± 7	Ca 1.1	(Basei et al., 2011)
		UY-10-05	Grt leucocratic gneiss	5			776 ± 12		(Oyhantçabal et al., 2009)
		Sample 1	Migmatite Rocha Syenogranite	10			762 ± 8	Ca. 2.0 and Ca 1.9	(Hartmann et al., 2002)
Eastern	24	**TM-26A**	**Metarhyolite**	**15**			**788 ± 5**	**Ca. 2.0**	**This paper**
	25	R-088	Metarhyolite	9			773 ± 3	Ca 2.1	(Pertille et al., 2017)

	26	R-015	Metarhyodacite	11	801 ± 4	Ca 1.7	
	27	R-001	Metarhyodacite	14	809 ± 4.1	Ca 2.1 and Ca 1.7	
	28	BR-145	Metarhyolite	29	789 ± 7		(Saalmann et al., 2011)
		ESJ-HH7-1D	Metandesite	Rb-Sr Ishocrons	789 ± 39		
	29	ESJ-HH7-1E	Metandesite	Rb-Sr Ishocrons	949 ± 45		(Soliani Jr, 1986)
		ESJ-HH7-2C	Metandesite	Rb-Sr Ishocrons	1542 ± 83		
	30		Metaandesite	x	773 ± 8		(Chemale, 2000)
Western - PMC	31	CA-16	Metavolcano-sedimentary rock	24	615 ± 3.4		(Höfig et al., 2018)
	32	CA-11	Metavolcano-sedimentary rock	15	600 ± 7		
	33		Deformed alkaline gneiss	x	603 ± 6		(Zvirtes et al., 2017)
			Deformed alkaline gneiss	x	543 ± 5		(Chemale, 2000)
	34	CP3	Rodingite blackwall (Capané ophiolite)	131	793±1 to 715±2		(Arena et al., 2018)

Table 3. Provenances sources ages of VCC, PMC and COC

Complex	Simbology	Sample	Lithology	U-Pb Zircon (number analyses) SHRIMP	LA-ICP-MS	Provenance interval (Ma)	Provenance Peak (Ma)	Provenance Younger than 640 Ma (N of grains)	Reference
VCC	1	**TM-36S**	**paragnaisse**	**45**		**716 - 1091**	**750-790**	**No**	**This paper**
	2	SMVC80	Metapelitic Gneisse	32				No	
	3	SMVCA	Metapelitic Gneisse		20	728 - 2497	2107.9 ± 2.4	No	(Gruber et al., 2016a)
		SMVCB	Metapelitic Gneisse		64			No	
	2	13-Mar VC12-03 PO 21	Marble	Whole-rock 87Sr/86S		715 - 750		Not aplicable	
	3	VC 13-1							
COC		UA-37	Quartzite		122	650* - 2800	1450, 1750 and 2000	No	(Konopásek et al., 2018)
		UB-18	Quartzite		112	1100 - 3100	1750 and 2005	No	
Eastern Porongos Metamorphic Complex	4	P-122	quartzite	36		994 ± 5 - 2,705±17	1306	No	(Pertille et al., 2017)
	5	T-148	plg-qtz-chl-ms schist	28		605±5 - 2,937 ± 8	2171	Yes (2)**	
	6	PJP-06	ms schist		61	1008±12 - 2863±24	1187	No	(Pertille et al., 2015a)
	7	POR-18	Metarenite		9	765±19 - 796±19		No	(Gruber et al., 2016b)
	8	RIP-08	qtz mylonite		19	1,750±18 - 2,910±24	2045	No	
	9	POR-04A	chl-ms schist		39	1,010±17 - 2,520±51	2254	No	
	10	POR-12A	qtz-ms schist		22	1,149±26 - 2,652±32	1217	No	
	11	POR-13A	chl-ms schist		11	1,113±42 - 2,195±31	1488	No	
	12	POR-06A	chl-ms schist		2	1,262±31 - 2,093±61		No	
	13	RIP-06	chl-ms schist		15	1,041±46 - 2,220±28		No	(Gruber et al., 2011a)
	14	RIP-03	chl-ms schist		11	1,164±21 - 2,414±31	2175	No	
	15	RIP-05	chl-ms schist		11	1,153±20 - 2,169±15		Yes (1)**	
	16	RIP-11	qtz mylonite		48	1,619±39 - 2,906±42	2039	Yes (1)**	
	17	BRAF34	sericitic phyllite	23		620 - 2,200		Yes (1)**	Basei et al. (2008)
Basement Cover	18	Sample 3	Godinho quartzite		98	1766±40 - 3384±24	2082	No	(Pertille et al., 2015a)
	18	3 - Godinho	quartzite	31		1,990±15 - 2,488±12	2079±14	No	Hartmann et al. (2004)
	19	6 - Jaíba	quartzite	43		1,998±15 - 2,454±12	2070	No	
	20	5 - Figueiras	quartzite	7		2,004±13 - 2,486±20	2100	No	
	21	1 - Alto Bonito	quartzite	21		2,030±21 - 2,459±22	2096	No	

	22	2 - Aberto dos Cerros	quartzite	34		2,015±15 - 3,092±19	2082	No	
	23	4 - Coxilha do Raio	quartzite	31		1,950±78 - 2,449±28	2056±14	No	
		Sample 4	Coxilha do Raio quartzite		96	1980±34 - 2506±38	2074	No	(Pertille et al., 2015a)
Western Porongos Metamorphic Complex	***	CA-11	metavolcano-sedimentary rock		20	584±9 – 2252±34	600	Yes (>10)	(Höfig et al., 2018)
	***	CA-16	metavolcano-sedimentary rock		76	599±5 – 2273±25	615	Yes (>10)	
	24	198	qtz-ms schist	30		579±20 - 2267±14	585 and 2266	Yes (4)	(Pertille et al., 2015b)
		300	alb-chl schist	66		553±6 - 2249±15	619	Yes (>10)	
	25	C-275	metagreywake	33		569±8 - 2,231±16	606	Yes (>10)	(Pertille et al., 2017)
		C-025	metapelite	29		550±10 - 2,811±12	585	Yes (>10)	
	26	C-175	qtz-ms schist	34		751±18 - 2,917±10	2196	No	
	27	CA-02A	phyllonite		56	1890 - 3260	2130	No	
	28	CA-17	qtz mylonite		83	1300 - 2800	2290	No	
	29	CA-21B	qtz-ms ultramyloite		59	2040 - 2860	2170	No	(Höfig et al., 2018)
	30	CA-22	str-grt schist		81	820 – 2250	2120	No	
	31	CA-19	qtz-ms schist		95	572±7 - 1971±27	610 and 770	Yes (>10)	
	32	C-041	gr-bt-ms schist	42		576±8 - 3,156±7	2186	Yes (5)	(Pertille et al., 2017)
	33	C-040	quartzite	36		618±15 - 2,481±30	2.105	Yes (1)**	

*Interpreted as recrystallization of the detrital grains during high-grade metamorphism.

** In spite of the fact that some grains are younger than 640 Ma, such data do not have any statistical meaning. Ca. 640 Ma was set as an age limit for the Neoproterozoic detrital zircon population, as this is the timing of the main metamorphic–deformational phase recorded in the hinterland of DFB (VCC and COC). The best metamorphic age for PMC is a Rb–Sr isochron in muscovite and whole-rock - 658 ± 26 Ma (Lenz, 2006).

*** The location of these samples is provided in table 2.

6.2. Artigo 2

O artigo intitulado '*Petrochronology of the central Dom Feliciano Belt foreland, southernmost Brazil"* de Battisti, M.A.; Konopásek, J; Bitencourt, M.F.; Slama, J. Percival, J.J.; De Toni, G.B.; Carvalho da Silva, S.; Costa, E.O.; Trubač, J. foi submetido ao periódico *Journal of Metamorphic Geology* no dia 22/02/2022.

Manuscript submitted to Journal of Metamorphic Geology
2 mensagens

Journal of Metamorphic Geology <no-reply@atyponrex.com>   22 de fevereiro de 2022 às 09:25
Para: Matheus Battisti <matheus.ariel.battisti@gmail.com>

Dear Matheus Battisti,

Your manuscript entitled "Petrochronology of the central Dom Feliciano Belt foreland, southernmost Brazil" has been successfully submitted online and is being delivered to the Editorial Office of *Journal of Metamorphic Geology* for consideration.

You will receive a follow-up email with further instructions from our electronic editorial office platform, ScholarOne Manuscripts, typically within one business day. That message will confirm that the Editorial Office has received your submission and will provide your Manuscript ID.

Thank you for submitting your manuscript to *Journal of Metamorphic Geology*

Sincerely,
The Editorial Staff at Journal of Metamorphic Geology

By submitting a manuscript to or reviewing for this publication, your name, email address, and affiliation, and other contact details the publication might require, will be used for the regular operations of the publication, including, when necessary, sharing with the publisher (Wiley) and partners for production and publication. The publication and the publisher recognize the importance of protecting the personal information collected from users in the operation of these services and have practices in place to ensure that steps are taken to maintain the security, integrity, and privacy of the personal data collected and processed. You can learn more by reading our data protection policy. In case you don't want to be contacted by this publication again, please send an email to JMGoffice@wiley.com.

Petrochronology of the central Dom Feliciano Belt foreland, southernmost Brazil

Matheus Ariel Battisti[1], Jiří Konopásek[2,3], Maria de Fátima Bitencourt[1], Jiří Sláma[4], Jack James Percival[2], Giuseppe Betino De Toni[1], Stephanie Carvalho da Silva[1], Elisa Oliveira da Costa[1], Jakub Trubač[5]

1- Programa de Pós-graduação em Geociências, Instituto de Geociências, Universidade Federal do Rio Grande do Sul, Porto Alegre, Brazil

2- Department of Geosciences, UiT–The Arctic University of Norway, Tromsø, Norway

3- Czech Geological Survey, Prague, Czech Republic

4- Institute of Geology of the Czech Academy of Sciences, Prague, Czech Republic

5- Faculty of Science, Charles University in Prague, Czech Republic

Corresponding author: Matheus Ariel Battisti, matheus.ariel.battisti@gmail.com

Address: Av. Bento Gonçalves, 9500 – Porto Alegre, Rio Grande do Sul state, Brasil. IGEO – Universidade Federal do Rio Grande do Sul, Campus do Vale – Zip Code: 91501-970.

Abstract:

The Dom Feliciano Belt is the South American part of an extensive Neoproterozoic orogenic system that developed during late Cryogenian–early Cambrian close to the margin of southwest Gondwana. P–T estimates, Lu–Hf garnet–whole-rock ages, U–Pb monazite SIMS ages and Y–REE garnet and monazite data from samples of the Porongos and Passo Feio complexes provide information about the tectonic evolution of the central Dom Feliciano Belt foreland. Metasedimentary rocks of the eastern Porongos Complex display a main metamorphic event at 662 ± 13 Ma (Lu–Hf isochron garnet–whole-rock age) and metamorphic peak conditions of ca. 560–580 °C, 5.8–6.3 kbar. This episode represents an early orogenic thickening event in the foreland as a response to the beginning of transpressive convergent evolution of the belt. The monazite age of 614 ± 6 Ma (U–Pb SIMS) is interpreted as associated with post-exhumation magmatic activity in the foreland and suggests that the eastern Porongos Complex was exhumed sometime between ca. 660 and 615 Ma. The main metamorphic and deformational event in the western region of Porongos Complex took place at ca. 550–570°C and 4.5–5.5 kbar at 563 ± 12 Ma (garnet–WR Lu–Hf isochron age). The exhumation of this part of the foreland is dated by using monazite crystalizing during garnet breakdown and suggests retrograde metamorphism at 541 ± 7 Ma (U–Pb SIMS). The main metamorphic fabric in the Passo Feio Complex further to the west developed at 571 ± 13 Ma (garnet–WR Lu–Hf isochron age) at metamorphic conditions of 560–580 °C and 4.7–6.4 kbar. The western part of the Porongos Complex and the Passo Feio Complex were deformed at similar PT conditions and apparent geothermal gradients at ca. 570–565 Ma. These regions record a second crustal thickening event in the Dom Feliciano Belt foreland and the orogenic front migration towards the west in a long-lived transpressive orogenic system.

1   **1.   INTRODUCTION**

2

3   Determination of the timing of metamorphic events is critical for the correct

4   interpretation of the evolution of orogenic belts. In metamorphic terranes with

5   protracted evolution, separation of distinct deformation events from a progressive, but

6   single period of deformation is sometimes difficult due to the similar fabric

7   superposition and comparable changes in the metamorphic mineralogy. The

8   petrochronological approach (Fraser et al., 1997) combines the application of various

9   geochronometers with detailed petrological and microstructural observations in order

10   to accurately link the appearance of various mineral phases used for geochronology

11   with metamorphic–deformation events in a specific rock (Engi et al., 2017; Yakymchuk

12   et al., 2017). Due to different physical and chemical properties of each mineral and to

13   the specific closure temperature of their isotopic systems, various minerals such as

14   zircon (e.g. Rubatto et al., 2006), monazite (e.g. Rocha et al., 2017), garnet (Baxter et

15   al., 2017), titanite (Kohn, 2017), allanite, xenotime or apatite (Engi, 2017) can be

16   applied in petrochronological studies. Moreover, due to specific physical properties of

17   the datable minerals, it has become common to investigate more than one mineral

18   (and isotopic system) in the same rock in order to interpret the evolution of separate

19   geological units of metamorphic terranes in time (Hermann & Rubatto, 2003; Rubatto

20   et al., 2006; Stevens et al., 2015; Hagen-Peter et al., 2016; Regis et al., 2016; Rocha

21   et al., 2017; Schaltegger & Davies, 2017; Walczak et al., 2017; Konopásek et al., 2019;

22   Soret et al., 2019; Percival et al., 2022).

23   The Dom Feliciano Belt in SE South America (Fig. 1) is a case of a long-lived

24   Neoproterozoic belt built by protracted deformation. The complexity of its evolution is

25   highlighted by recent papers, which have suggested that the contractional period

26   lasted from ca. 660–650 Ma up to < ca. 570 Ma (e.g. Philipp et al., 2016; Oriolo et al.,

27   2016; Battisti et al., 2018; De Toni et al., 2020a, 2021; Percival et al., 2021, 2022;

28   Hueck et al., 2022). The main purpose of this paper is to determine the timing of critical

29   deformation events that shaped the present-day structure of the central Dom Feliciano

30   Belt. For this reason, two metamorphic complexes (Porongos and Passo Feio) of the

31   central Dom Feliciano Belt foreland were studied and compared. P–T estimates, Lu–

32   Hf garnet–whole-rock isochron ages and U–Pb SIMS monazite ages from

33   metasedimentary samples provided metamorphic and geochronological data, which

34   point at two separate and well-constrained periods of crustal thickening, followed by

35   periods of intense magmatic activity. The data provide evidence for progressive

36 migration of foreland deformation towards the west, away from the centre of the

37 orogenic system, and explain the recently discussed involvement of syn-orogenic

38 sediments and magmatic rocks in the deformation of the orogenic foreland (Battisti et

39 al., 2018 and submitted; Höfig et al., 2018).

40

41 **2.   GEOLOGICAL SETTING**

42

43 **2.1   Dom Feliciano–Kaoko–Gariep orogenic system**

44

45   The study area is located in the central Dom Feliciano Belt (Fig. 1 – DFB), which

46 is the South American part of a N-S trending Neoproterozoic orogenic system involving

47 also the Kaoko and Gariep belts along the Atlantic coast of southern Africa. The Dom

48 Felicano Belt is the result of the Brasiliano/Pan-African cycle which started at ca. 840–

49 800 Ma by igneous activity and associated sedimentation interpreted by some authors

50 as related to a continental arc (Koester et al., 2016; Martil et al., 2017; Battisti et al.,

51 2018; De Toni et al., 2020a) or as generated in a back-arc/rift setting (Konopásek et

52 al., 2018; Will et al., 2019). The system evolved into a contractional tectonic regime,

53 which started at ca. 660–650 Ma (e.g. Gross et al., 2006, 2009; Oyhantçabal et al.,

54 2009; Lenz et al., 2011; Martil, 2016; Peel et al., 2018; Will et al., 2019; De Toni et al.,

55 2020a; Konopásek et al., 2020; Percival et al., 2021, 2022). The contraction continued

56 until at least 580–550 Ma, as recorded by ongoing thickening and associated

57 metamorphism of both forelands of the orogenic system (Frimmel & Frank, 1998;

58 Goscombe & Gray, 2008; Höfig et al., 2018; Percival et al., 2022). Such convergent

59 period is related to the formation of the Gondwana supercontinent (e.g. Rapela et al.,

60 2011; Ramos et al., 2017; Oriolo et al., 2017).

61   Central DFB outcrops in southernmost Brazil (Rio Grande do Sul state) and is

62 usually divided into Western, Central and Eastern domains (Fragoso-Cesar et al.,

63 1986; Fernandes et al., 1992; Basei et al., 2000) (Fig. 1). The Western domain consists

64 of Paleoproterozoic rocks (2.5–2.0 Ga - Hartmann et al., 2000) of the foreland

65 basement, ophiolites reminiscent of an oceanic crust (920–890 Ma - Arena et al., 2016)

66 and juvenile arc-related rocks of the São Gabriel Block (750–690 Ma - Lena et al.,

67 2014) with associated metasedimentary complexes (as for example, the Passo Feio

68 Complex - Bitencourt, 1983).
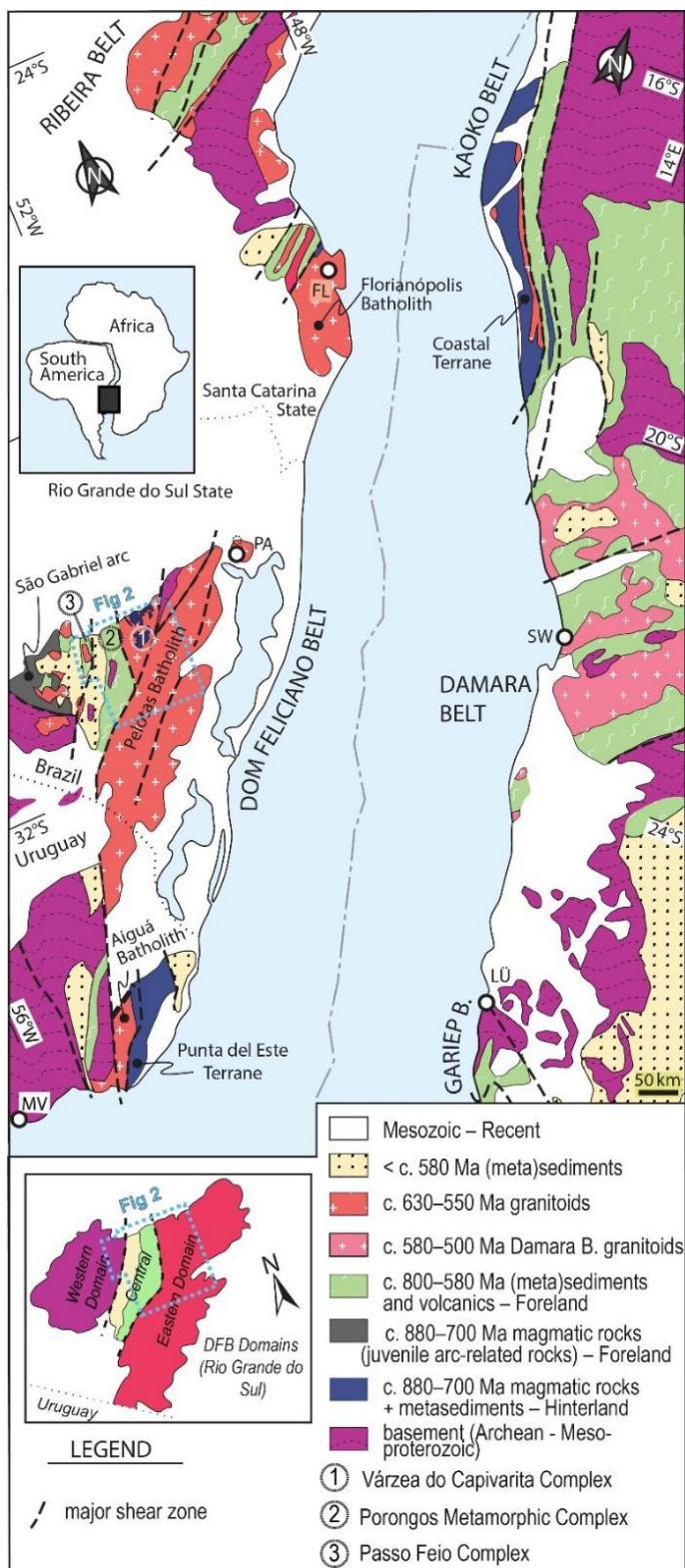
Figure 1. A) Overview geological map and main tectonic domains of the Dom Feliciano–Kaoko–Gariep orogenic system (modified after Konopásek et al., 2018 and Bitencourt and Nardi, 2000). Relative position of Africa and South America is shown at 140 Ma - after Heine et al., 2013. Dom Feliciano Belt domains in the Rio Grande do Sul state are shown in the inset. Location of figure 2 is indicated. FL – Florianópolis, PA – Porto Alegre, MV – Montevideo.

76   The Central Domain is represented mainly by the Porongos Complex (PC)
77 composed of low- to medium-grade volcano-sedimentary rocks (Jost & Bitencourt,
78 1980; Saalmann et al., 2005; Pertille et al., 2017) of Tonian to Ediacaran age (e.g.
79 Saalmann et al., 2011; Pertille et al., 2017; Höfig et al., 2018; Battisti et al., submitted)
80 with locally exposed Paleoproterozoic basement (Encantadas Complex; 2.26–2.0 Ga
81 – Hartmann et al., 2003; Philipp et al., 2008). The foreland (Western and Central
82 domain) is extensively covered by late-orogenic, Ediacaran to Ordovician volcano-
83 sedimentary deposits (Oliveira et al., 2014; Paim et al., 2014).

84   The Eastern Domain represents the hinterland and in the Rio Grande do Sul state
85 it features mainly granitic rocks (also called Pelotas Batholith - Fragoso-Cesar et al.,
86 1986). The batholith is interpreted as part of a post-collisional granitic belt (Bitencourt
87 and Nardi 1993; Bitencourt and Nardi 2000; Philipp and Machado, 2002), whose
88 emplacement was controlled by a large-scale discontinuity (Southern Brazilian Shear
89 Belt - SBSB) active between ca. 650 and 580 Ma (Bitencourt & Nardi, 2000; Nardi &
90 Bitencourt, 2007). In Brazil, the Neoproterozoic granitic rocks contain roof pedants and
91 xenoliths of at least three distinct ages: Paleoproterozoic (2.2 and 2.0 Ga – Leite et al.,
92 2000; Gregory et al., 2015), Mesoproterozoic (ca 1.5 Ga – Chemale et al., 2011) and
93 Tonian (ca. 770–800 Ma - Koester et al., 2016; Martil et al., 2017, 2011). The most
94 extensive occurrence of the ca. 770–800 Ma rocks is the high-grade Várzea do
95 Capivarita Complex (VCC) (Fig. 1).

96

97 **2.2   Porongos Complex**

98

99   The Porongos Complex is a part of the Dom Feliciano Belt foreland and
100 comprises Neoproterozoic supracrustal rocks metamorphosed at lower greenschist to
101 middle amphibolite facies (Jost & Bitencourt, 1980; Saalmann et al., 2006; Pertille et
102 al., 2017; Höfig et al., 2018; De Toni et al., 2021). The complex comprises
103 metasedimentary and metavolcanic rocks, some ultramafic lenses, and less often,
104 deformed granitic rocks (Jost & Bitencourt, 1980; Marques et al., 2003; Zvirtes et al.,
105 2017). Some authors interpret these ultramafic lenses as ophiolite remnants (Arena et
106 al., 2018; Werle et al., 2020). The PC metamorphic grade increases from west to
107 east.The Cerro do Facão staurolite-bearing metapelites at the easternmost border
108 (Fig. 2) record the highest metamorphic grade of the complex (Jost & Bitencourt, 1980;
109 Lenz, 2006). The peak PT conditions of these rocks were estimated at 560–580°C and

110 5.8–6.3 kbar (De Toni et al., 2021) and the only available metamorphic age is an
111 unpublished age of 658 ± 26 Ma (Lenz, 2006; Rb–Sr in muscovite and whole-rock).

112   Provenance studies in the PC have shown two distinct sources of the
113 metamorphosed clastic sediments (Gruber et al., 2011b, 2016b; Pertille et al., 2015b,
114 2015a, 2017; Höfig et al., 2018). Based on this data, Höfig et al. (2018) suggested that
115 the precursor of the Porongos Complex could have been at least two distinct and
116 diachronous basins. The older PC metasedimentary rocks (located mainly in the
117 eastern part – Fig. 2) represent mostly clastic infill of a pre-orogenic basin(s). The
118 younger PC basin is related to the syn-orogenic (< ca. 650 Ma) evolution, as discussed
119 by Höfig et al. (2018) and Battisti et al. (2018 and submitted). In the western part of the
120 PC (Fig. 2), the syn-orogenic sedimentary rocks are interleaved with the rocks of the
121 pre-orogenic PC basin(s) (Höfig et al., 2018). Ages of associated intermediate to acid
122 metavolcanic rocks also yielded contrasting ages in different regions of the complex.
123 Eastern regions of the PC contain metavolcanic rocks with protolith ages of ca. 770–
124 800 Ma (Saalmann et al., 2011; Pertille et al., 2017; Battisti et al., submitted), whereas
125 studies of meta-volcanosedimentary rocks in the western portion of the complex (Höfig
126 et al., 2018) reported magmatic ages of ca. 600 and 601 Ma (LA–MC–ICP–MS, U–Pb
127 zircon). Such a dataset shows that the igneous activity and late sedimentation in the
128 northwestern PC are younger than the metamorphic peak recorded in the eastern
129 portion of the PC (658 ± 26 Ma - Lenz, 2006). According to the data compiled by
130 Battisti et al. (submitted – after authors quoted above), these two diachronous basins
131 are separated by the main W-verging thrust fault in the Porongos Complex called
132 Santana da Boa Vista thrust fault (Jost & Bitencourt, 1980). The metamorphosed pre-
133 orogenic sediments appear mostly east of the fault, whereas the rocks of the syn-
134 orogenic basin appear exclusively west of the fault.

135   Recent papers suggested that a part of the pre-orogenic basin of the PC and a
136 part of the Várzea do Capivarita Complex may have shared a similar sedimentary
137 depositional environment in their pre-collisional setting (Martil et al., 2017; Battisti et
138 al., 2018 and submitted). Battisti et al. (submitted) argued that both complexes share
139 igneous rocks with the same ca. 780 Ma protolith age and identical REE geochemistry,
140 similar isotopic Nd–Sr and oxygen signatures, similar structural evolution, and
141 convergent P–T–t evolution. These similarities led Battisti et al. (2018) and De Toni et
142 al. (2021) to conclude that the higher grade, deeper VCC hinterland rocks were thrust
143 over the lower grade, shallower PC foreland during a ca. 650 Ma collisional event.
144
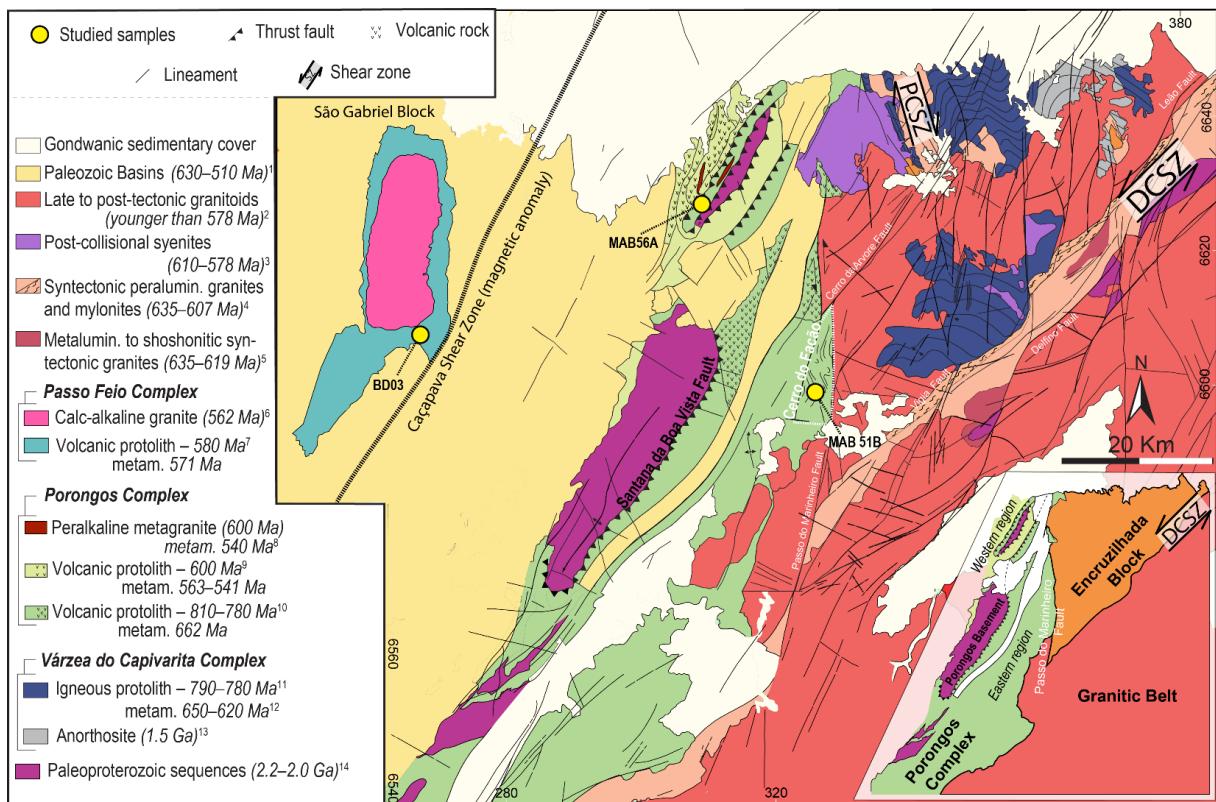
Figure 2. Geological map of the studied area with the sampled sites indicated. DCZS – Dorsal do Canguçu Shear Zone; PCSZ – Passo das Canas Shear Zone. Tectonic division shown in inset (*sensu* De Toni et al. (2021). References: 1 – Paim et al. (2014); 2 – Padilha et al. (2019); 3 – Rivera (2016), Padilha et al. (2019); 4 – Bitencourt et al. (2015), Knijnik (2018), Vieira et al. (2020); 5 – Knijnik (2018), Vieira et al. (2020); 6 – Remus et al. (2000); 7 – Battisti et al. (n.d.); 8 – Philipp et al. (2016b); 9 – Höfig et al. (2018); 10 – Saalmann et al. (2011), Pertille et al.(2017); 11 – Martil et al. (2017); 12 – Gross et al. (2006), Chemale et al. (2011), Philipp et al. (2016a), Martil et al. (2017); 13 – Chemale et al. (2011); 14 – Leite et al. (2000), Hartmann et al. (2003), Saalmann et al. (2011), Gregory et al. (2015).

2.3   São Gabriel Block

The São Gabriel Block the largest occurrence of juvenile magmatic rocks in the DFB (e.g. Arena et al., 2017, 2016; Lena et al., 2014; Saalmann et al., 2007, 2005). Although many authors do not consider the São Gabriel Block as part of the Dom Feliciano Belt and interpret it as a tectonic unit resulting from an independent orogeny (e.g. Chemale, 2000; Philipp et al., 2016b; Arena et al., 2017). there seems to be a consensus that its long-lived history also influenced the evolution of the DFB (Philipp et al., 2016; Konopásek et al., 2018; De Toni et al., 2020a).

166   According to Arena et al. (2016), some igneous rocks of the block may represent
167   part of an oceanic domain (ophiolites - 920–890 Ma), accreted to a juvenile arc (ca.
168   880 Ma Passinho event of Leite et al., 1998) that evolved towards a continental
169   magmatic arc (770–690 Ma - Lena et al., 2014). The oceanic closure is interpreted to
170   have happened between 690–650 Ma (Lena et al., 2014) or 650–600 (Arena et al.,
171   2017), whereas late granitic magmatism took place at ca. 585 Ma (Arena et al., 2017).
172   The São Gabriel Block structural framework features NE-striking planar fabrics,
173   predominantly dipping NW at low to medium angle, reworked by oblique, SE-verging
174   plus dextral transpression (Saalmann et al., 2005).

175   Metaigneous, arc-related rocks of the São Gabriel Block are surrounded by
176   metamorphic supracrustal complexes. The intrinsic characteristics of such complexes
177   (Pontas do Salso, Cambaí, Bossoroca, Imbicuí and Passo Feio - Philipp et al., 2021
178   and references therein) are beyond the scope of this work. The exception is the Passo
179   Feio Complex, introduced in detail.

180

181   **2.3.1   Passo Feio Complex**

182

183   The Passo Feio Complex is traditionally considered as the eastern-most unit of
184   the São Gabriel Block (Fig. 1, 2), separated from the easterly Porongos Complex by a
185   geophysical anomaly (Costa, 1997). However, the meaning of such anomaly is unclear
186   because its area is covered by post-orogenic sediments (Fig. 2). This has led some
187   authors to interpret the anomaly as a manifestation of a suture (Fernandes et al., 1995;
188   Costa, 1997); whereas others ((Costa et al., 2021), interpret it as a regional dextral
189   shear zone. As no further arguments are provided to confirm this magnetic anomaly
190   as a suture, the relation between the Passo Feio Complex and the rocks to the east
191   (Central and Eastern domains) remains uncertain, as does the eastern limit of the São
192   Gabriel Block.

193   The PFC comprises phyllites, metapelitic schists, amphibole-bearing rocks such
194   as amphibolites, metagabbros and amphibole schists, acid to intermediate
195   metavolcanoclastic rocks, and subordinate magnesian schists and marble lenses
196   (Bitencourt, 1983; Bitencourt & Hartmann, 1984a, 1984b; Costa et al., 2021). The PFC
197   outcrops as an antiformal structure with subhorizontal axis plunging either NNE or
198   SSW (Costa et al., 2021) with the 562 ± 8 Ma (SHRIMP U–Pb zircon - Remus et al.,
199   2000) calc-alkaline Caçapava Granite in its core. The PFC is surrounded by Ediacaran

200 to Ordovician volcano-sedimentary sequences of the Camaquã Basin (Oliveira et al.,
201 2014; Paim et al., 2014 - Fig. 2a), and in the northeast by the Parana Basin.

202   Three deformation events related to two metamorphic events were described in
203 the PFC (Bitencourt, 1983; Costa et al., 2021). The first two events are progressive
204 and coeval with the growth of garnet up to the peak metamorphic conditions (M_1). M_1
205 was estimated by Costa et al. (2021) at 560–570 °C and 5–5.5 kbar for a garnet–
206 staurolite schist and 500–510 °C and 5–6.4 kbar for a garnet phyllite. D_3 deformation
207 event and M_2 metamorphic event are closely related to the emplacement of the
208 Caçapava Granite (Bitencourt, 1983). According to Costa et al. (2021), the
209 crystallization of andalusite marks the effect of contact metamorphism caused by the
210 Caçapava Granite during M_2–D_3. S_3 has developed by folding of S_2 and locally displays
211 shear zones that drag S_2 with dextral shear sense. Regions where S_3 developed show
212 mainly recrystallization of biotite and relic minerals of M_1, which indicates that M_2
213 reached intermediate greenschist facies (biotite zone) with pressures no higher than
214 ca. 4 kbar, as indicated by the crystallization of andalusite (Costa et al., 2021).

215   Geochronological data for the PFC first metamorphic event are rather limited and
216 obscure. A single SHRIMP spot in a zircon rim of 685 ± 12 Ma (Remus et al., 2000)
217 was associated with M_1 (which is probably a mixed age – see discussion). On the other
218 hand, the age of M_2 is better constrained as this metamorphism was interpreted
219 contemporaneous to the emplacement of the Caçapava Granite at ca. 562 Ma (see
220 above).

221

222 **3.   RESULTS**

223

224 **3.1   Sample description and estimates of metamorphic conditions**

225

226   To quantify the metamorphic evolution of the Porongos and Passo Feio
227 complexes, the conditions of equilibration of mineral assemblages in three samples
228 (MAB51B, MAB56A and BD03) were modelled by calculating P–T pseudosections
229 based on the whole-rock chemical composition and H_2O component in excess. Due to
230 the absence of minerals with elevated content of Fe^{3+}, all Fe in the samples was
231 considered as FeO. The stability of the mineral assemblages was modelled using
232 Perple_X 6.8.9 software (Connolly, 2005, 2009) and thermodynamic properties of
233 mineral endmembers published by Holland and Powell (1998 – updated in 2004). The
234 mixing properties of the minerals were taken from Fuhrman and Lindsley (1988) for

235 feldspar and White et al. (2014) for biotite, white mica, chlorite, staurolite, chloritoid,
236 cordierite and garnet.

237   Whole-rock compositions were obtained from rock powder tablets using a Rigaku
238 RIX 2000 X-Ray Fluorescence analyser at the X-ray Fluorescence Laboratory of the
239 Universidade Federal do Rio Grande do Sul (UFRGS), Brazil and at AcmeLabs -
240 Bureau Veritas Minerals in Canada. Mineral compositions were determined at the
241 Microprobe Laboratory, CPGq, UFRGS, using the Cameca SXFive microprobe at
242 analytical conditions of 15 keV, 15 nA current, and beam size of 5 µm. The instrument
243 was calibrated using diopside (Ca, Mg), rhodonite (Mn), sanidine (Si, K, Al), Fe_2O_3
244 (Fe), albite (Na), rutile (Ti) and Cr_2O_3 (Cr) as standards. Mineral abbreviations used
245 through this paper are after Whitney and Evans (2010).

246

3.1.1   MAB51B – Eastern region of the Porongos Complex

248

249   Sample MAB51B (30.73782° S, 52.81326° W – all coordinates in WGS84) is a
250 garnet-plagioclase-biotite-muscovite schist (Fig. 3a, b) collected in the eastern part of
251 the Porongos complex, in the hanging wall of the Santana da Boa Vista thrust fault.
252 The schistosity is marked by lepidoblastic muscovite (ca. 65 vol.%) and biotite (ca. 15
253 vol.%). Both types of mica form crystals up to 0.5 mm long and commonly display
254 isoclinal micro folds and undulose extinction. Muscovite contains 3.06–3.20 atoms per
255 formula unit (a.p.f.u.) of Si and 0.02 a.p.f.u. of Ti. Biotite shows X_{Mg} = (Mg/(Mg + Fe^{2+})
256 of 0.47–0.49, 0.09 a.p.f.u. of Ti and 1.27–1.33 of Al^{IV} (Table 1 and supplementary data).
257 Plagioclase (ca. 8 vol.%), quartz (ca. 2 vol.%), and accessory K-feldspar (<<1 vol.%)
258 appear in lenses with fine-grained (0.06–0.2 mm) inequigranular texture. Garnet (ca. 5
259 vol.%) forms 3-4 mm large isometric grains, usually with well-developed crystal faces
260 and internal cracks. The grains show very weak chemical zoning with slight increase
261 in pyrope (Prp) and almandine (Alm) components from core to rim, compensated by a
262 decrease in grossular (Grs) and spessartine (Sps) components. General garnet core-
263 to-rim composition (mol.%) is Alm_{53-58}, Prp_{6-7}, Grs_{10-8}, Sps_{31-27}. The X_{Mg} value of 0.10–
264 0.11 is almost constant across the entire crystal. Chlorite (ca. 3 vol.%) has X_{Mg} of 0.50–
265 0.53 and forms isolated, ca. 1 mm long individual clusters interpreted as late
266 overgrowths on muscovite-biotite crystals. Rare tiny staurolite crystals (<0.05 mm, <<1
267 vol.%) were found by SEM. A sample nearby (see fig. 7b in De Toni et al., 2021)
268 suggests the presence of staurolite completely replaced by muscovite (Fig. 3c). The
269 main opaque phase is ilmenite (ca. 1 vol.%).

270   P–T pseudosection calculated for sample MAB51B (Fig. 4, bulk composition in
271   mass proportions: SiO_2 – 42.05; Al_2O_3 – 30.37; TiO_2 – 1.41; FeO – 6.53; MnO – 0.29;
272   MgO – 2.92; CaO – 0.20; Na_2O – 0.59; K_2O – 8.69) indicates that the assemblage Chl
273   + Grt + Ms + Bt + Pl + Qz + Ilm is stable approximately at 470–560°C, and in a pressure
274   range below 5.0 kbar. The isopleths calculated for endmember proportions in the
275   garnet core revealed pre-peak conditions of 515–535°C and 3.4–4.4 kbar. Isopleths
276   for garnet rim endmembers suggest equilibration with the matrix at 530–550°C and
277   3.6–4.5 kbar. Although biotite is locally replaced by chlorite in the sample MAB51B, its
278   observed X_{Mg} values agree with those for estimated metamorphic conditions of the
279   matrix assemblage. The incipient crystallization of staurolite (only observed in SEM
280   images) suggests the peak metamorphic conditions close to the staurolite-in reaction,
281   which is modelled at ca. 10 to 15°C higher than the peak metamorphic conditions
282   estimated by isopleths at 3.6 and 4.5 kbar, respectively. For this reason, the best
283   estimate for the metamorphic peak of this sample is 530–565°C and 3.6–4.5 kbar.
284   Comparison of the observed vs. modelled mineral compositional parameters from all
285   studied samples is shown in table 2.
286
287   **INSERT TABLE 1**
288
289   **INSERT TABLE 2**
290
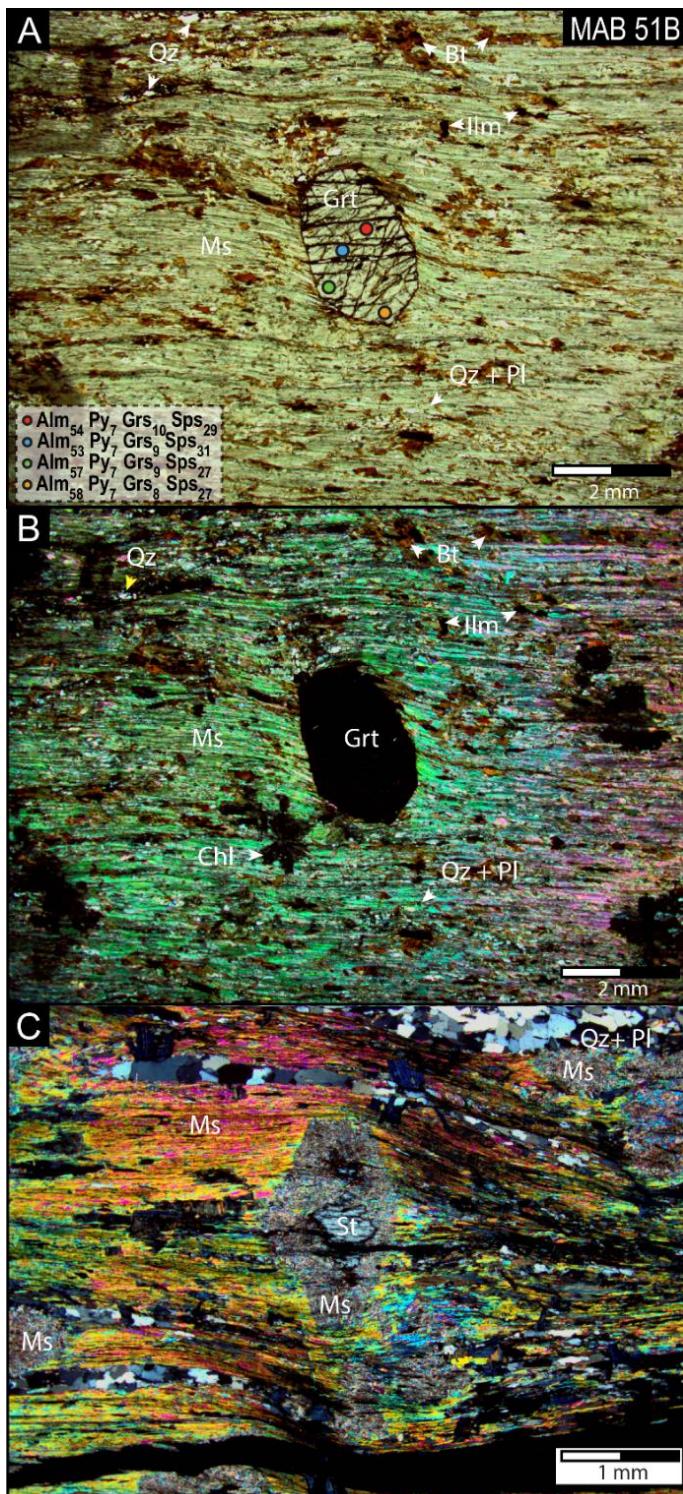
Figure 3. A–B) MAB51B garnet–plagioclase–biotite–muscovite schist. Representative garnet chemistry is indicated by colored dots. Notice post-tectonic chlorite clusters in B); C) Fluid-induced replacement of staurolite by muscovite halos in a nearby sample (30.74621º S, 52.81647 º W – De Toni et al., 2021).
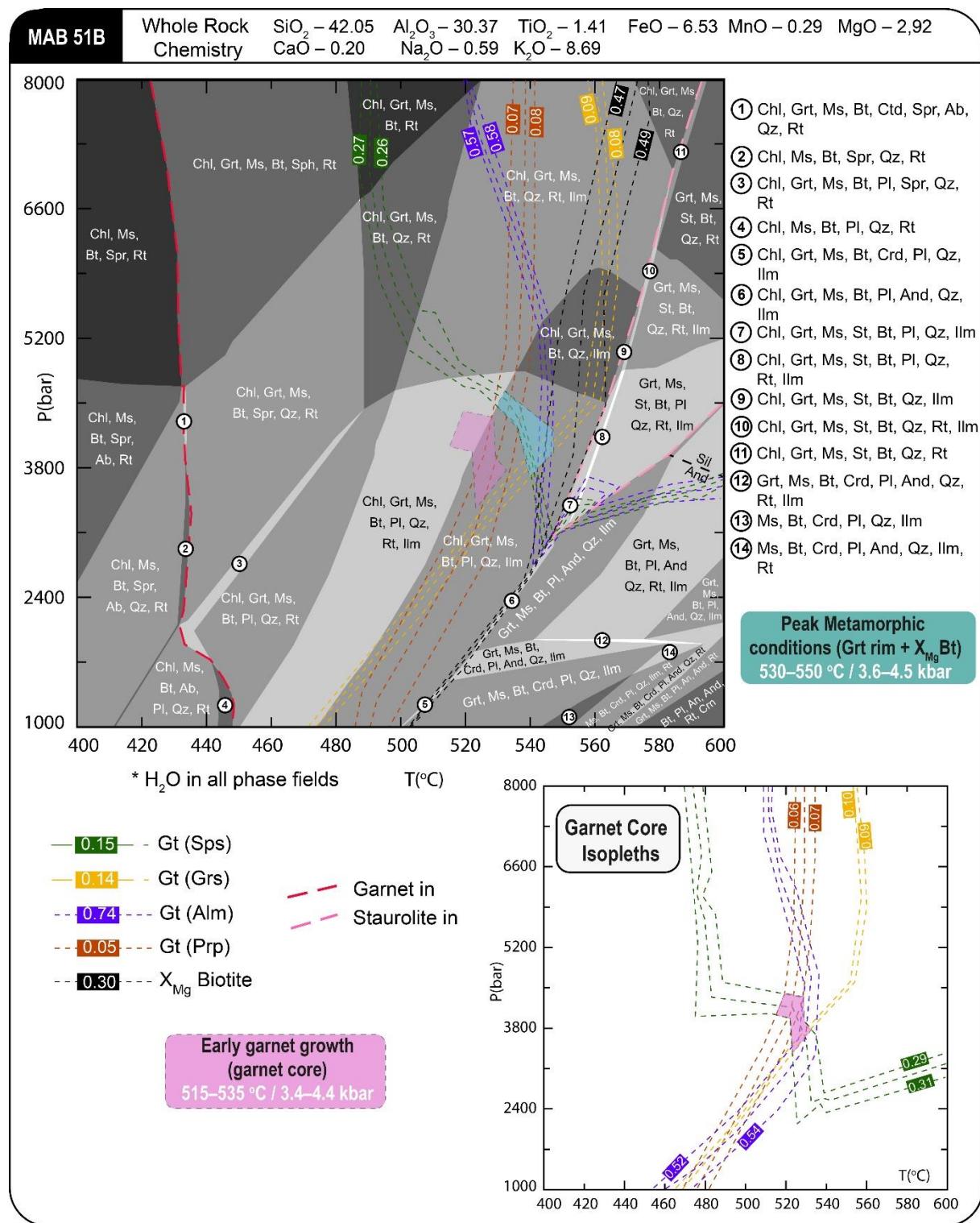
Figure 4. P–T pseudosection calculated for the sample MAB51B with the stability field of the peak metamorphic assemblage highlighted in green. Isopleths for the composition of garnet rim + biotite cross in the polygon highlighted in blue. The pink polygon shows the of the area where isopleths of the garnet core cross (see details in bottom-right P–T diagram).

307 **3.1.2 MAB56A – Northwestern region of the Porongos Complex**

308

309   Sample MAB56A (30.4767° S; 52.9818° W) is a garnet-bearing plagioclase–
310 biotite–quartz–muscovite schist (Fig. 5) from the northwestern part of the Porongos
311 Complex, where the pre-orogenic metasedimentary rocks were tectonically interleaved
312 with the syn-orogenic flysch sediments (Höfig et al., 2018; Battisti et al., submitted).
313 The sample was collected in the structural footwall of the Santana da Boa Vista thrust
314 fault. The schistosity is marked by an alternation of muscovite-rich and quartz-
315 plagioclase-rich layers, both intensely microfolded. The lepidoblastic texture and shape
316 preferred orientation of muscovite (ca. 40 vol.%) with crystal sizes up to 2 mm mark
317 the main schistosity. Muscovite contains 2.98–3.08 a.p.f.u. of Si and 0.02–0.04 a.p.f.u.
318 of Ti. Quartz and plagioclase are fine-grained (up to 0.4 mm) and display lenses with
319 intergranular interlobate texture. Together, Qz and Pl make ca. 45% of the rock
320 volume. Plagioclase is albite (An_{0-2}) with <1 mol.% of K-feldspar component. Biotite
321 (ca. 10 vol.%) crystals are up to 0.5 mm long with lepidoblastic texture in mica-rich
322 layers. Biotite shows X_{Mg} between 0.31 and 0.35, 0.09–0.16 a.p.f.u. of Ti and 1.32–
323 1.45 of Al^{IV}.

324   Garnet (ca. 3 vol.%) forms mostly equant, up to 5 mm large porphyroblasts,
325 usually cracked and partly consumed along the edges. They rarely show sigmoidal
326 quartz and ilmenite inclusion trails that mark the porphyroblast rotation relative to the
327 external matrix foliation during growth (Fig. 5c). In the fractures, chlorite commonly
328 grows due to garnet dissolution (Fig. 5 and 12). We interpret the garnet as a relic
329 mineral phase in the sample, otherwise subject to severe retrogression. Garnet grains
330 show strong chemical zoning with increasing pyrope and almandine components from
331 core to rim compensated by a decrease in grossular and spessartine components.
332 General garnet core-to-rim composition (mol.%) is Alm_{67-82}, Py_{5-10}, Grs_{12-6}, Sps_{16-2}.
333 The X_{Mg} value increases from 0.07 to 0.11 from core to rim (Table 1, 2).

334   Chlorite (ca. 2 vol.%) crystals are up to 0.3 mm long, and they occur as both
335 dispersed in the rock matrix and in cracks and pressure shadow tails of garnet
336 porphyroblasts. Chlorite X_{Mg} varies from 0.37 to 0.43. Chlorite is interpreted to have
337 formed after the metamorphic peak by a retrogressive reaction that consumed garnet
338 and some biotite in the matrix. Accessory minerals are tourmaline, apatite, monazite,
339 and zircon.

340
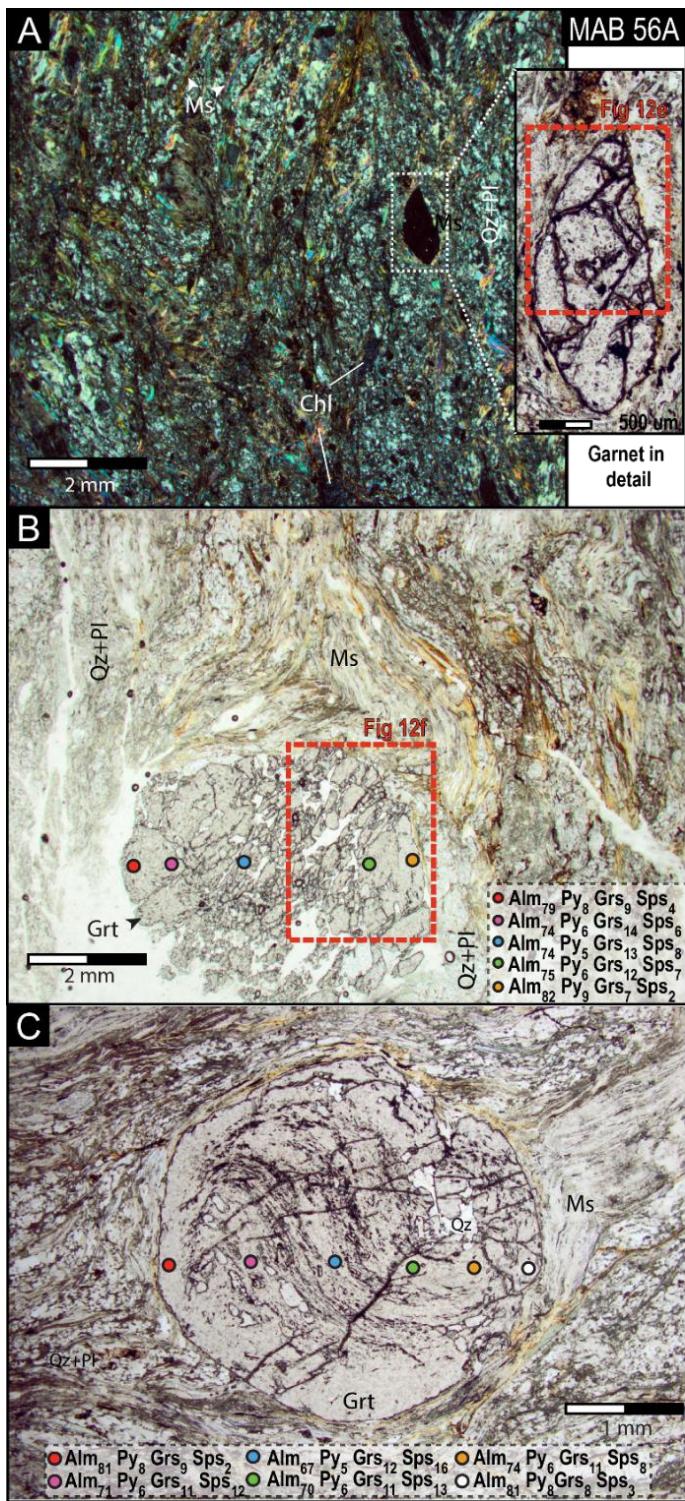
Figure 5. MAB56A garnet-bearing plagioclase–biotite–quartz–muscovite schist. A) general view of the rock microstructure with detail of a relic of strongly dissolved garnet crystal. B, C) Representative mineral chemistry of garnet indicated by colored dots. Location of SEM images presented in Figs 12e and f are indicated.

P–T pseudosection calculated for sample MAB56A (Fig. 6, bulk composition in mass proportions: SiO_2 – 62.15; Al_2O_3 – 18.34; TiO_2 – 1.11; FeO – 8.14; MnO – 0.14;

350 MgO – 1.96; CaO – 0.89; Na_2O – 0.45; K_2O – 3.23) indicates that the matrix
351 assemblage Chl + Grt + Ms + Bt + Qz + Pl + Ilm is stable approximately at 490–560°C,
352 and in the pressure range of 1.5 to 5.3 kbar. However, garnet grains represent relics
353 of larger porphyroblasts consumed by retrograde reactions. Such observation
354 suggests that rims of the least re-equilibrated porphyroblasts that survived the
355 retrogression may represent higher metamorphic conditions than the matrix
356 assemblage itself. Isopleths for such garnet rim compositions overlap in an interval of
357 550–570°C at 4.5–5.5 kbar, reaching even the staurolite stability field (field 24 – figure
358 6). Thus, staurolite might have been present at the metamorphic peak and then all
359 consumed during retrogression. The isopleths calculated for the garnet core
360 composition revealed conditions of 520–540°C and 3.9–5.3 kbar for the early garnet
361 growth.

362   Based on petrological evidence, chlorite in the sample MAB56A grew during the
363 retrograde breakdown of garnet. Therefore, five chlorite analyses were performed by
364 EPMA to apply chlorite geothermometers and retrieve information about retrograde
365 metamorphic temperature (Fig. 7). For the geothermometers of Cathelineau (1988),
366 Cathelineau and Nieva (1985) and De Caritat et al. (1993) we assumed $Fe_{total}=FeO$,
367 and the temperatures were calculated using the software of Yavuz et al. (2015). When
368 applying the geothermometer of Vidal et al. (2001), two estimates were made, one
369 assuming $Fe_{total}=FeO$, and the other considering the presence of Fe^{3+} based on the
370 calculations described in Vidal et al. (2001). The obtained results vary from ca. 250 to
371 ca. 500°C. Using the mean calculated temperatures with 1σ standard deviation for all
372 values calculated by the six different methods as indicated in figure 7, the most
373 probable temperature of chlorite formation is considered between ca. 310–440°C.

374
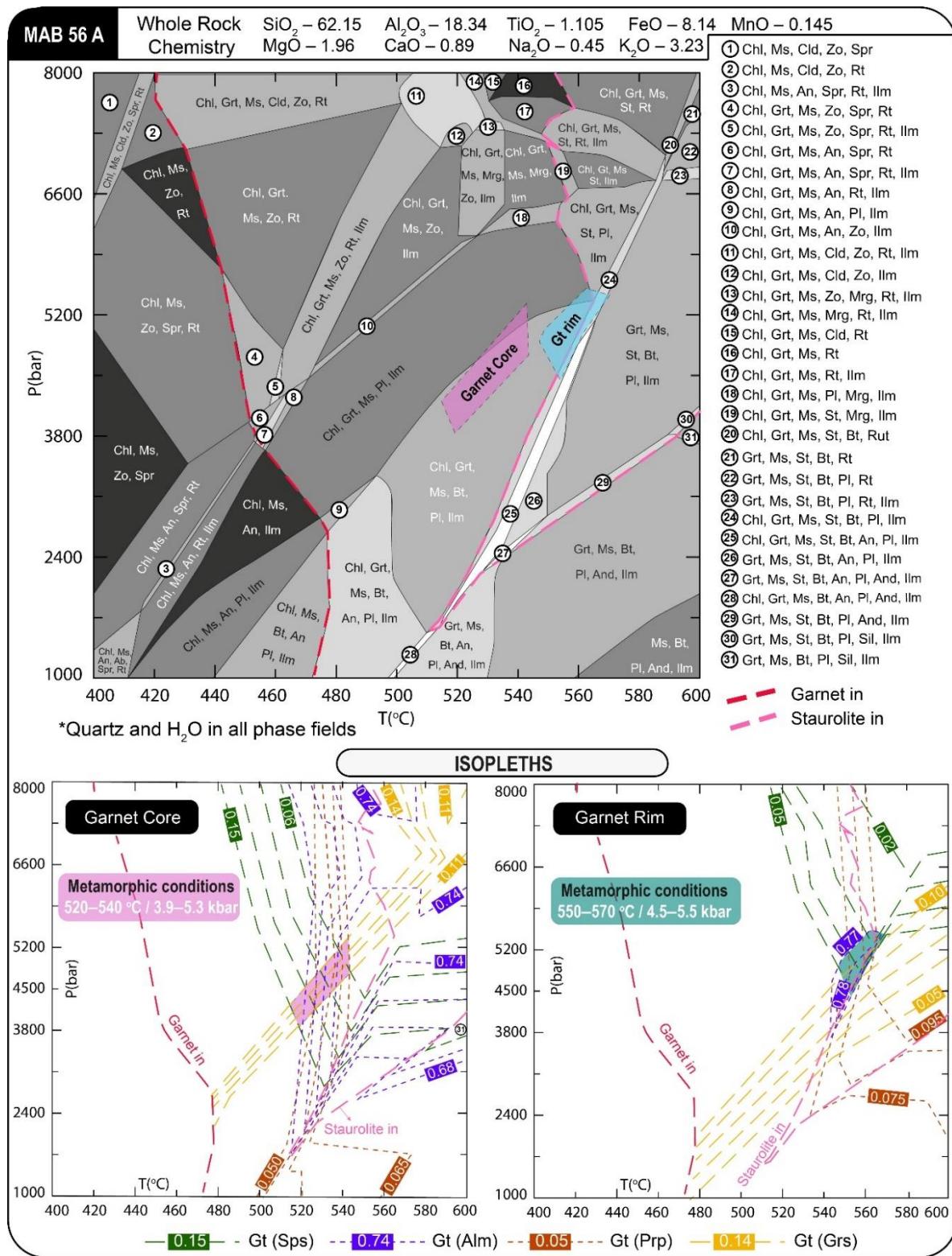
Figure 6. P–T pseudosection calculated for the sample MAB56A. Metamorphic conditions for the early garnet growth (pink polygon) and for the garnet rim stability (blue polygon) were estimated only from the observed garnet chemistry, because the mineral assemblage of the matrix is interpreted as not reflecting the peak metamorphic conditions (see text for explanation). Isopleths for garnet rim and core compositions are presented in P–T diagrams at the bottom of the figure.
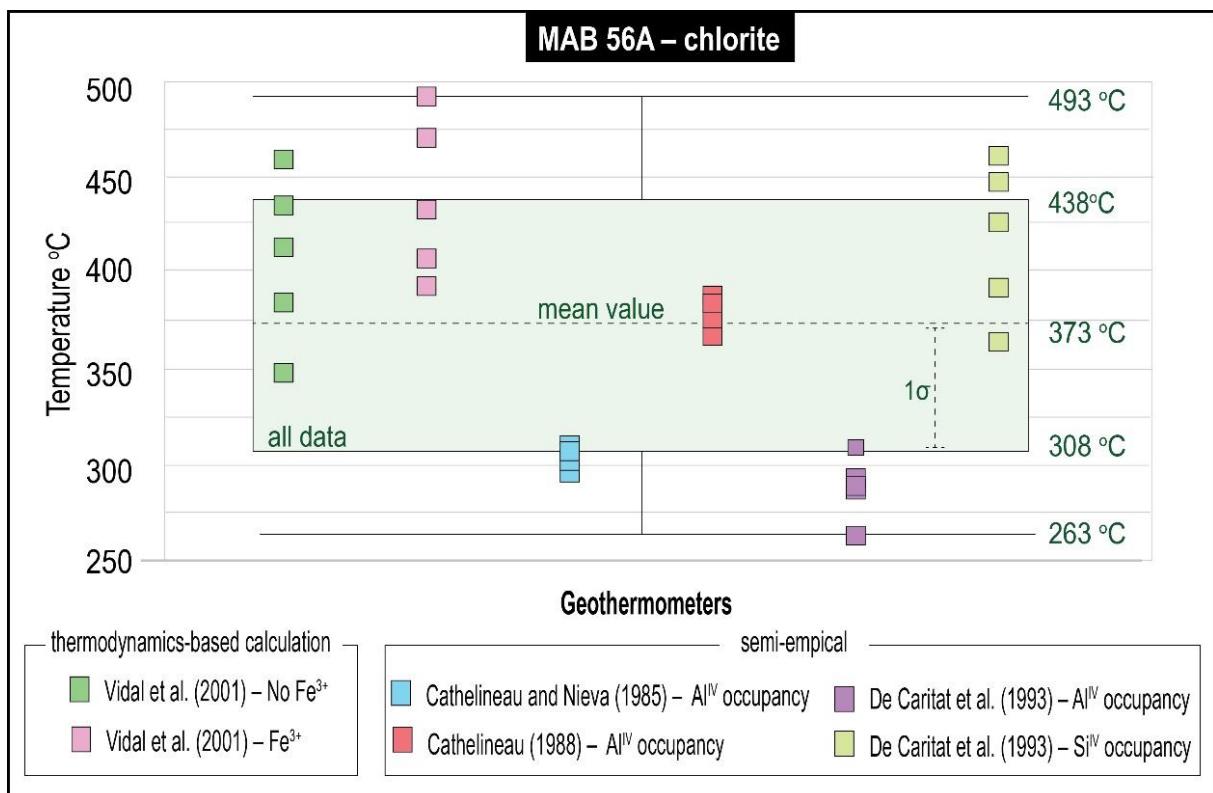
Figure 7. Estimated temperature of retrograde chlorite growth in sample MAB56A based on some commonly applied geothermometers. Considering all individual calculations from all geothermometers, the best estimated temperature for chlorite growth appears between 438–308 °C (mean ± 1σ). Temperature estimates by each geothermometer are the following: 439±39 °C not considering Fe^{3+} and 408±38 °C considering Fe^{3+} (Vidal et al., 2001); 418±38 °C using Si^{IV} occupancy and 295±9 °C using Al^{iv} occupancy (De Caritat et al., 1993); 379±7 °C (Cathelineau, 1988); 304±5 °C (Cathelineau & Nieva, 1985).

3.1.3. BD03 - Passo Feio Complex

Sample BD03 (30.64389° S; 53.45345° W) is a muscovite–garnet–staurolite–biotite–plagioclase–quartz schist (Fig. 8) collected in the southern part of the Passo Feio Complex (Fig. 2). The schistosity is marked by alternating mica-rich and quartz-rich layers (Fig. 8a). Mica-rich layers are discontinuous, up to 1 mm thick and composed of lepidoblastic biotite (ca. 25 vol.%) and muscovite (ca. 5 vol.%) up to 1.5 mm in length, and locally chlorite (ca. 1 vol.%). Muscovite contains 3.02–3.04 a.p.f.u. of Si and 0.02 a.p.f.u. of Ti, whereas biotite shows X_{Mg} between 0.44–0.51, 0.04–0.09 a.p.f.u. of Ti and 1.26–1.32 of Al^{IV}. Chlorite has X_{Mg} of 0.51–0.53. Quartz-rich layers also contain some fine-grained (0.05 to 1 mm) plagioclase with inequigranular seriate texture (both adding up to ca. 45 vol.%). Plagioclase is andesine (An_{32-34}) with <1

406   mol.% of K-feldspar component. The opaque phase is ilmenite and represents ca. 2
407   vol.%.

408   The external foliation wraps around the garnet and staurolite porphyroblasts and
409   their pre- to syn-tectonic origin is suggested by the rotation of their internal foliation
410   highlighted by opaque minerals and quartz inclusions (Fig 8b). Staurolite
411   porphyroblasts (ca. 15 vol.%; X_{Mg} = 0.16–0.20) are up to 3.5 mm large and appear
412   mostly in the mica-rich layers. Garnet (ca. 8 vol.%) forms 0.8–1.5 mm large equant
413   grains, usually with internal cracks (Fig. 8c). Such grains usually contain quartz, and
414   opaque mineral inclusions and pressure shadows made up of biotite, muscovite, and
415   quartz. Garnet grains show a strong chemical zoning with increasing almandine
416   component from core to rim compensated by a decrease of spessartine component.
417   On the other hand, grossular and pyrope display a very weak chemical zoning. General
418   garnet core-to-rim composition (mol.%) is Alm_{65-75}, Prp_{7-11}, Grs_{8-6}, Sps_{20-8}. The X_{Mg} =
419   0.10–0.13 is almost constant from core to rim. Accessory phases are represented
420   mainly by ilmenite, tourmaline and zircon.

421   P–T pseudosection calculated for sample BD03 (bulk composition in mass
422   proportions: SiO_2 – 64.13; Al_2O_3 – 15.61; TiO_2 – 0.96; FeO – 7.95; MnO – 0.12; MgO
423   – 3.13; CaO – 1.53; Na_2O – 1.81; K_2O – 2.60) is presented in figure 9. The estimate of
424   peak metamorphic conditions has been made using garnet fractionation routine
425   available in the Perple_X software. The reason for the subtraction of garnet interior
426   from the bulk is that the garnet shows strong chemical zonation from core to rim, which
427   together with its high modal proportion (ca. 8 vol.%) may influence the effective
428   composition available during peak metamorphic conditions (Lanari & Engi, 2017).
429   Garnet core conditions were established at 525–545°C and 4.1 – 4.5 kbar (Fig. 9a)
430   without applying the fractionation routine (Table 2). Several fractionation paths with
431   different slopes in the PT space were tested (always crossing the garnet core
432   conditions) to find out PT conditions at which the modelled final garnet composition
433   successfully reproduced the observed composition of the garnet rim in the sample.
434   Four fractionation paths met such condition and all of them led to similar results (Fig.
435   9b), which indicate that the assemblage Chl + Grt + Ms + St + Bt + Pl + Qz + Ilm was
436   stable at ca. 560–600°C and above 4.7 kbar (Fig. 9). Isopleths for garnet rim
437   endmembers, in addition to X_{Mg} in staurolite and biotite, and X_{An} in plagioclase, suggest
438   equilibration conditions at 560–580°C and 4.7–6.5 kbar.
439
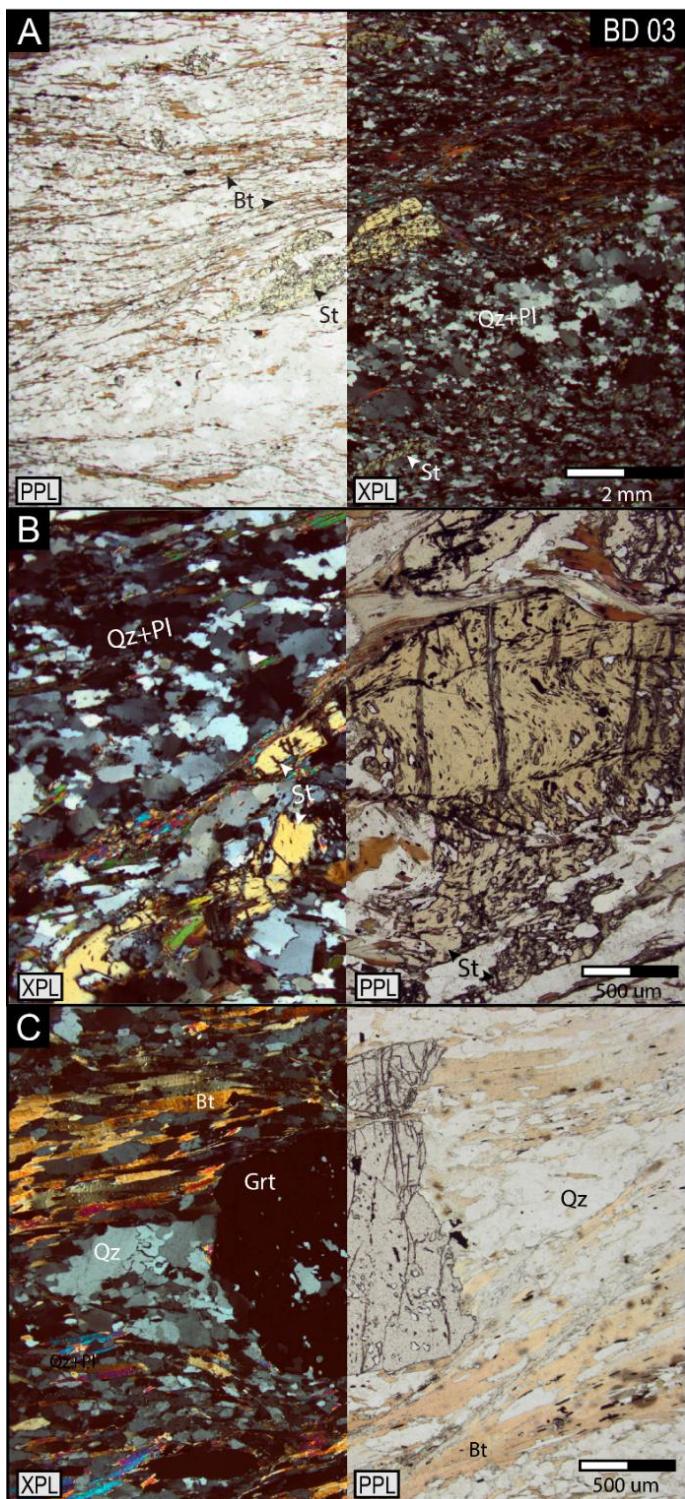
Figure 8. BD03 muscovite–garnet–staurolite–biotite–plagioclase–quartz schist. A) General view of the rock microstructure; B) Syn-kinematic staurolite porphyroblast; C) Detail of a garnet porphyroblast. Photomicrographs were taken in both plane-polarized (PPL) and cross-polarized light (XPL) to highlight textural aspects of the rock.
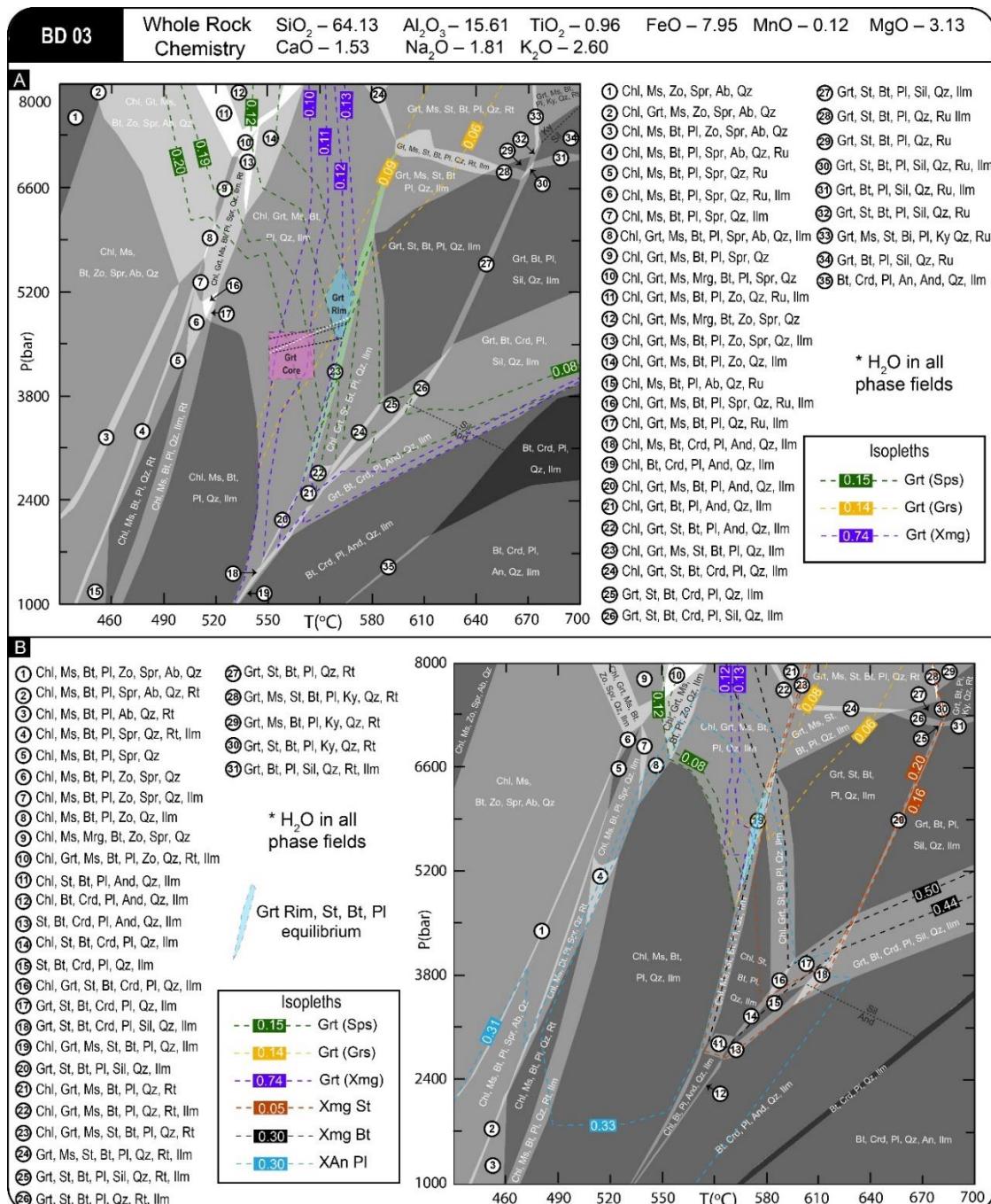
Figure 9. Calculated P–T pseudosections for the sample BD03. A) Phase diagram calculated for the bulk chemistry of the sample. Various paths tested during utilization of the fractionation routine are indicated by dashed sub-horizontal black lines connecting the colored fields delimiting estimated P–T conditions for garnet core and rim compositions. b) Phase diagram calculated for the bulk rock chemistry modified by gradual removal of corresponding garnet volume and composition along the selected fractionation path (white dashed line). Although the P–T conditions of stabilization of the matrix mineral assemblage are similar in both diagrams, the P–T diagram for fractionated bulk rock composition shows better match of the mineral composition with the peak metamorphic assemblage field (field 23 in A, and field 19 in B).

458 **3.2   Lu–Hf garnet geochronology and trace elements chemistry**

459

460   Lu–Hf garnet–whole-rock isochron ages were obtained for three samples to
461   provide a temporal framework for the studied metamorphic evolution of the central
462   Dom Feliciano Belt foreland (Table 3, figure 10). In addition, Y–REE and additional
463   trace elements (Hf, U, Ti, Nd – see supplementary file) were analysed along transects
464   across garnet to determine the potential influence of inclusions on bulk mineral
465   separate isotopic systematics, and the influence of zonation on age interpretation. The
466   results of trace element analysis are summarized in figures 11, 12 and 13, and
467   complete data are available in supplementary files. Complete analytical methods for
468   the Lu–Hf isotopic dating are described in appendix 1. Standards reproducibility and
469   constants used for the Lu–Hf isochron calculations are given in the footnote to Table
470   3.

471

472 **INSERT TABLE 3**

473

474 **3.2.1 MAB51B – Eastern region of the Porongos Complex**

475

476   Lu–Hf isotopic analysis of sample MAB51B yielded a garnet–whole-rock isochron
477   age of 662 ± 13 Ma, based on six garnet aliquots and two representative whole-rock
478   powder aliquots (Fig. 10a).

479   Rim-to-rim profiles of two garnet crystals in this sample were analysed for Y–REE
480   and trace element contents. The Y–REE data present an almost homogeneous pattern
481   for all analysed spots (Fig. 11a). The data demonstrate a well-known (e.g. Hacker et
482   al., 2019; Rubatto et al., 2006) enrichment of Heavy Rare Earth Elements (HREE –
483   10^2 to 10^3 ppm) over Light Rare Earth Elements (LREE – 10^{-3} to 10^1 ppm). Although
484   garnet cores are somewhat enriched in LREE compared to garnet rims, and HREE
485   concentrations increase slightly towards the rims, this variation is negligible. The data
486   in figure 11 also indicate a negligible europium anomaly Eu/Eu* [(Eu$_{norm}$)/(Sm$_{norm}$ x
487   Gd$_{norm}$)$^{0.5}$] ranging from 0.26 to 0.60, for garnet 1 and 0.24 to 0.60, for garnet 2 (see
488   details in supplementary file).

489   The Lu profile is rather flat, with only a slightly higher concentration in the garnet
490   core and an anomalous enrichment in the right-hand outermost rim (Fig 12a). Hf shows
491   peaks that coincide with peaks in U suggesting the presence of zircon inclusions.
492   Presence of ilmenite inclusions is also indicated by peaks of Ti (Fig. 12a). Considering

493 the clean part of garnet (without mixed analyses from mineral inclusions), Lu shows a
494 mean value of 30 ppm and Hf 1 ppm. All isotopic and trace element data are available
495 as supplementary material.

496
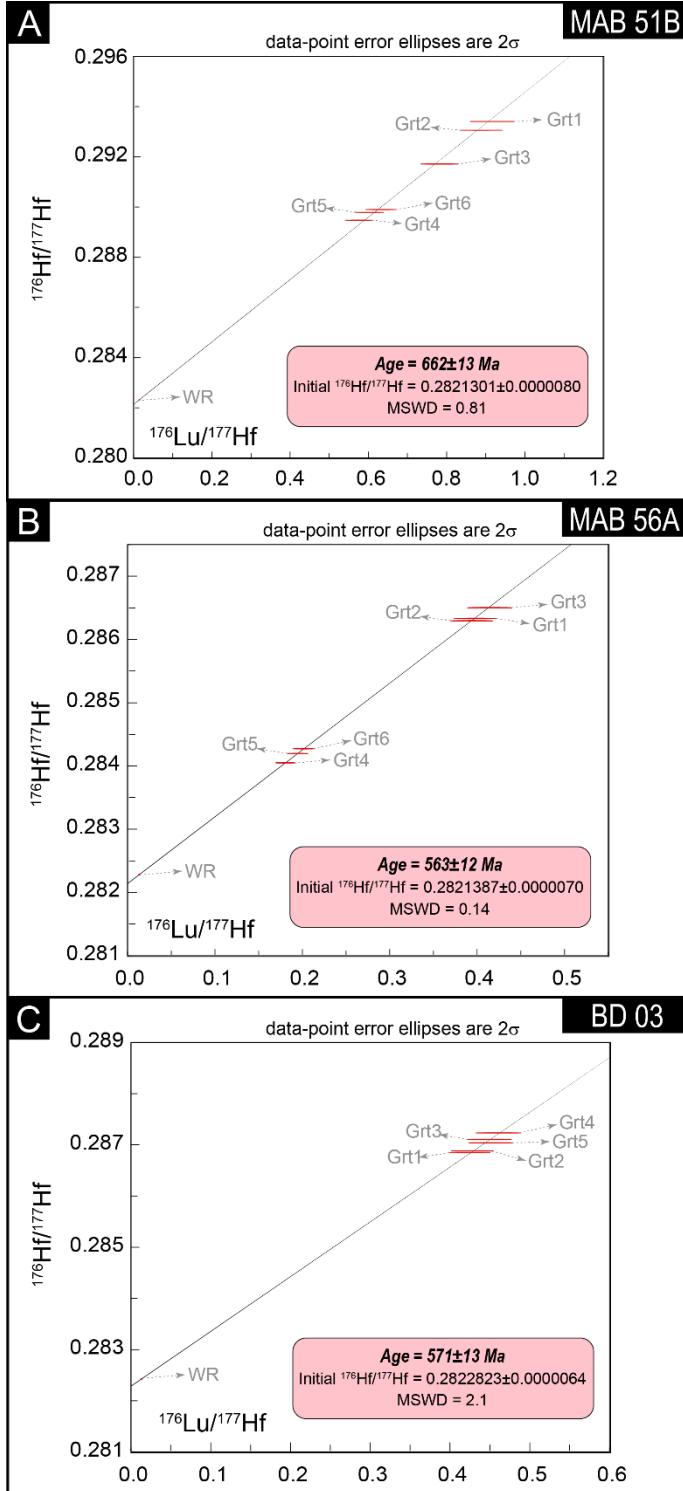
497
498
499 Figure 10. Results of the garnet–whole-rock Lu–Hf dating. Porongos Complex – sample
500 MAB51B (A) and sample MAB56A (B) and Passo Feio Complex – sample BD03 (C).
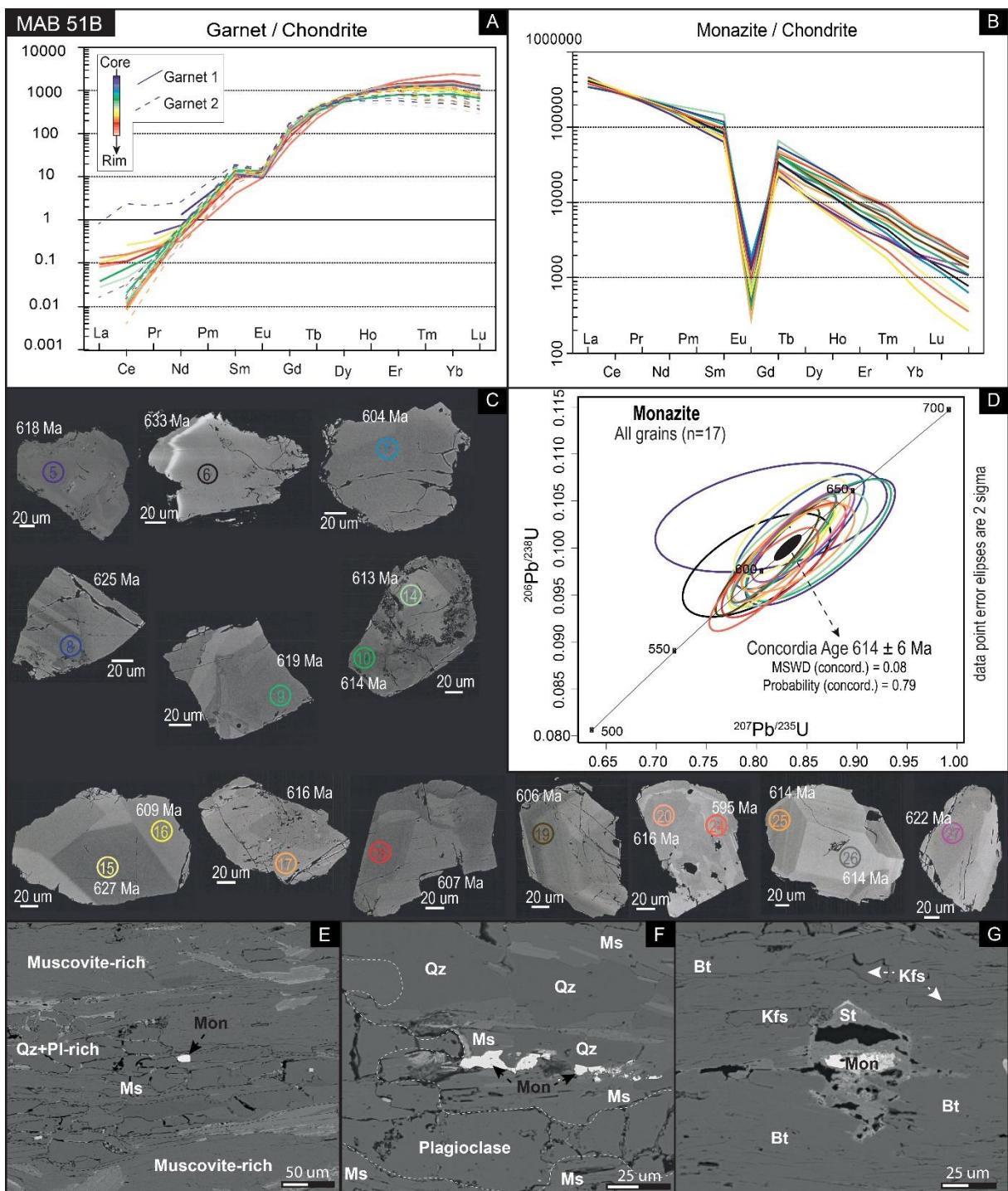
Figure 11. REE data for garnet (A) and monazite (B) in sample MAB51B, normalized to chondrite (Boyton, 1984). In (A), color coding of the REE curves indicates the distance of each analytical spot from the garnet center. (C) BSE images showing textures of analysed monazite grains and their respective U^{238}/Pb^{206} dates. (D) U–Pb SIMS concordia age of monazite calculated from all analysed grains. In (B) and (D), color-coded REE curves and ellipses distinguish each SIMS spot in monazite grains shown in (C). Textural relationship of monazite with other mineral phases in the thin section are illustrated in BSE images in (E), (F) and (G). Additional trace element data and garnet laser spots are presented as supplementary material.
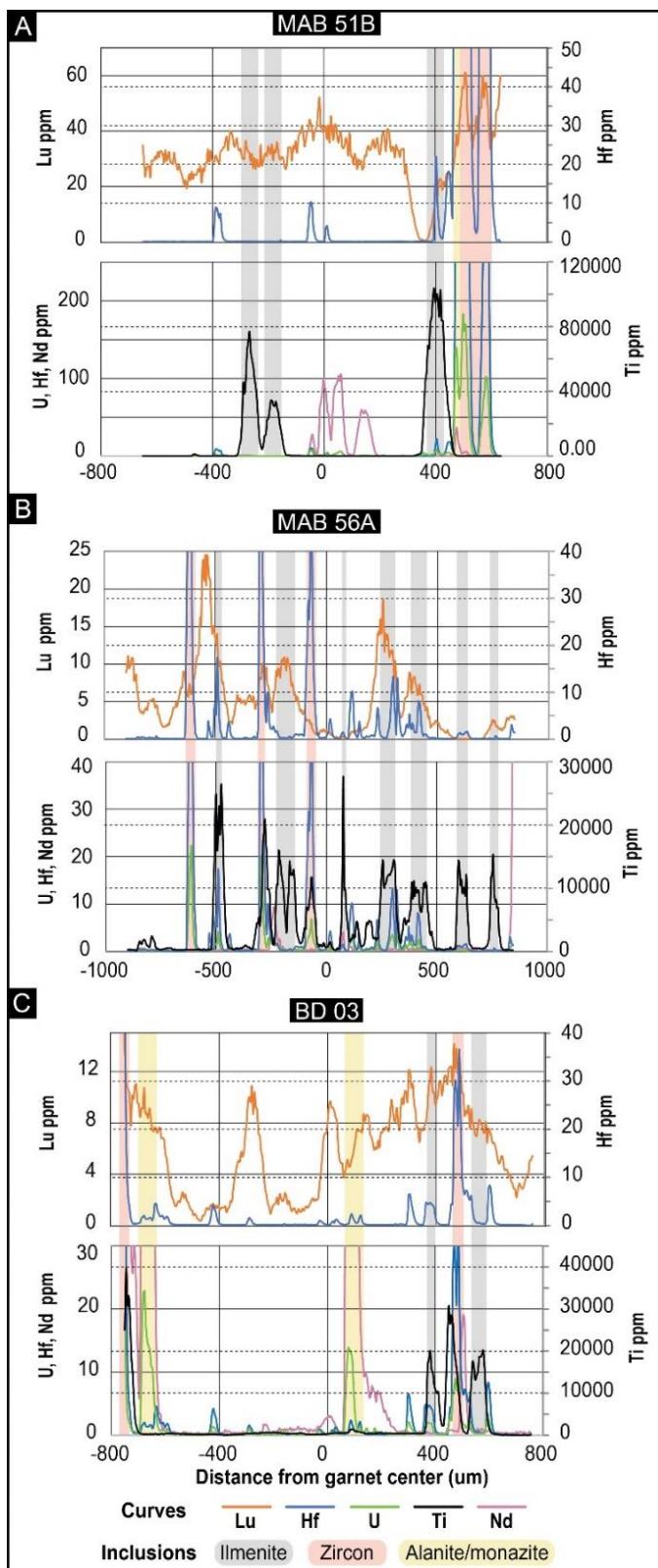
Figure 12. Lu–Hf–U–Ti–Nd curves from garnet of MAB51B (a – grt1) and MAB56A (b – grt3) – Porongos Complex; and garnet of BD03 (c – grt5) – Passo Feio Complex. The colored bars indicate presence of inclusions.

3.2.2 MAB56A – Northwestern region of the Porongos Complex

Lu–Hf isotopic analysis of six garnet aliquots and two representative whole-rock powder aliquots yielded a garnet–whole-rock isochron age of 563 ± 12 Ma for sample MAB56A (Fig. 10b).

Two crystals (garnet 3 and 4) were selected for Y–REE data acquisition in thin section by LA–ICP–MS. The REE patterns show mild enrichment in LREE of the rim over the core, whereas the core is strongly enriched in HREE. Eu/Eu* values for garnet 3 range from 0.69 to 1.56, and from 0.59 to 0.78 for garnet 4 (Fig 13a).

Garnet 3 presents complex zoning of Lu with several peaks in different crystal growth zones (Fig. 12b). Several Hf+U peaks suggests presence of zircon inclusions, whereas inclusions of ilmenite are evident from numerous peaks in Ti. In the clean garnet Lu shows a mean value of 5 ppm and Hf 2 ppm.

3.2.3 BD03 – Passo Feio Complex

For sample BD03, Lu–Hf isotopic analysis of five garnet aliquots and two representative whole-rock powder aliquots yielded a garnet–whole-rock isochron age of 571 ± 13 Ma (Fig. 10c).

The analysed garnet in sample BD03 (garnet 5) displays a general enrichment in Lu towards the right-hand side of the crystal (Fig. 12c). The appearance of Hf+U, Ti and U+Nd peaks suggests the presence of zircon, ilmenite and monazite/allanite inclusions, respectively. Lu shows a mean value of 6 ppm and Hf 1 ppm in the regions not affected by inclusions.
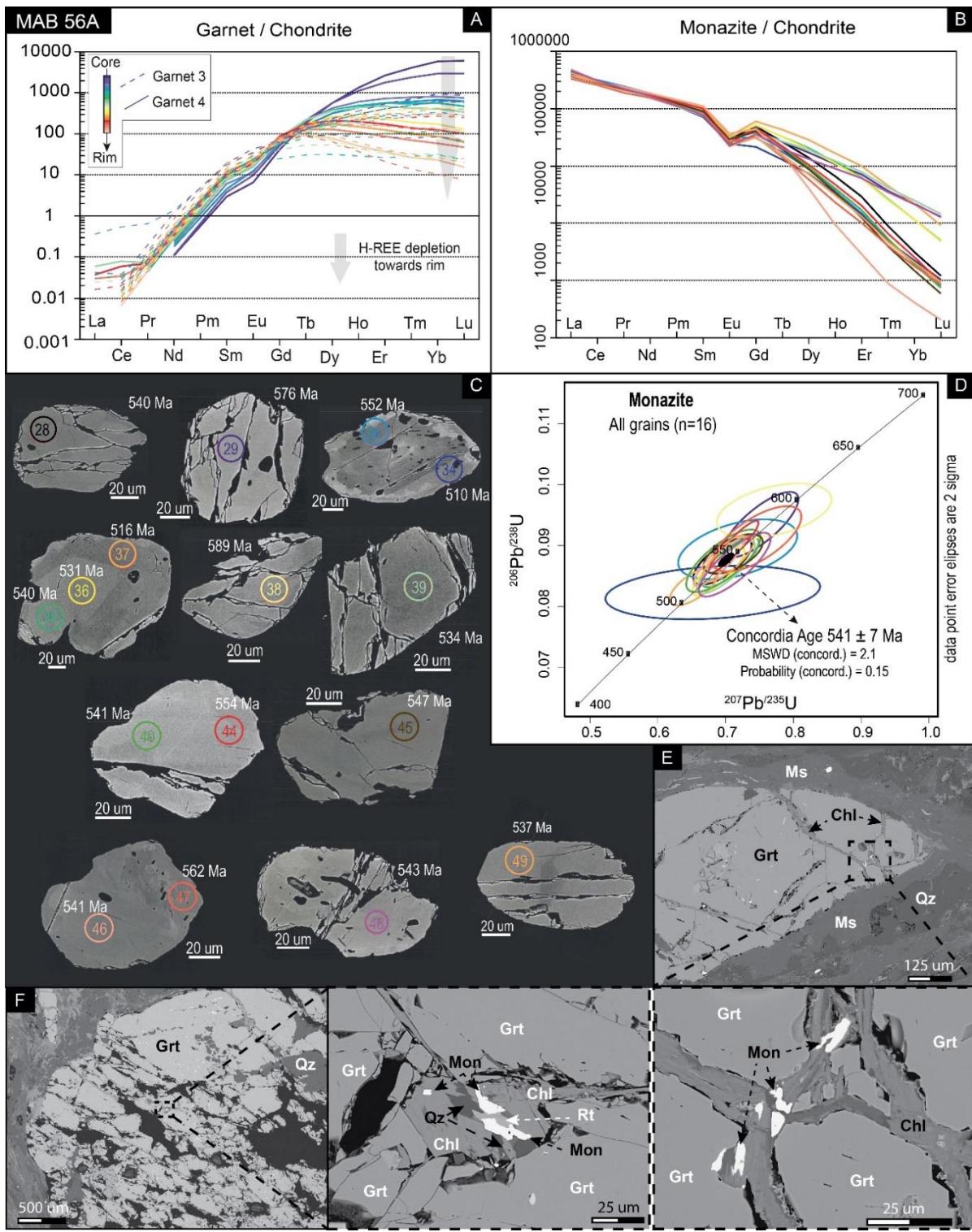
Figure 13. REE data for garnet (A) and monazite (B) in sample MAB56A), normalized to chondrite (Boyton, 1984). In (A), color coding of the REE curves indicates the distance of each analytical spot from the garnet center. (C) BSE images showing textures of analysed monazite grains and their respective U^{238}/Pb^{206} dates. (D) U–Pb SIMS concordia age of monazite calculated from all analysed spots. In (B) and (D), color-coded REE curves and ellipses distinguish each SIMS spot in monazite grains shown in (C). Textural relationship of monazite with other mineral phases in the thin section are illustrated in BSE images in (E) and (F). Additional trace element data and garnet laser spots are presented as supplementary material.

3.3   U–Pb SIMS monazite geochronology and trace elements chemistry

Monazite crystals were separated from samples MAB51B and MAB56A, whilst no monazite was found in sample BD03. The monazite age was determined by U–Pb isotopic dating using the Secondary Ion Mass Spectrometry (SIMS) at the NORDSIM facility hosted by the Swedish Natural History Museum in Stockholm. Y–REE data for monazite were acquired by LA–ICP–MS in individual monazite grains (in mount – near spots previously analysed for U–Pb age dating) to compare their chemistry with that of garnet. These data were completed by concentration maps for selected trace elements to understand their spatial distribution in the analysed grains. Details of both separation and analytical methods are provided in appendix 1.

3.3.1 MAB51B – Eastern region of the Porongos Complex

Monazite extracted from sample MAB51B forms irregular grains up to 200 μm large, which display various zoning patterns (Fig. 11). Most grains show well-preserved sector or oscillatory zoning; however, zoning in some grains is more complex. SEM imaging of monazite crystals in the thin section revealed eithersingle crystals in the matrix (Fig. 11e, f), or grains apparently crystallized during the replacement of some other mineral (Fig. 11g).

Seventeen SIMS isotopic analyses were performed in thirteen different monazite grains and the resulting data are plotted in a conventional Wetherill U–Pb concordia diagram. Considering all data, the 17 spots yielded a pooled concordia age of 614 ± 6 Ma (2σ), which we consider as the age of crystallization of monazite in the sample (Fig. 11d).

REE data normalized to chondrite (Boyton, 1984) show enrichment of LREE over HREE (Fig. 11b). A pronounced Eu/Eu* anomaly ranges from 0.007 to 0.040. Th/U ratios of the grains range between 13.3 to 46.2, with one outlier of 70.8.

3.3.2 MAB56A – Northwestern region of the Porongos Complex

Monazite separated from sample MAB56A is up to 200 μm large (Fig 13). The crystals are usually rounded and cracked and display weak zoning. Concentric zoning is observed in some crystals and two crystals preserve a central part rich in inclusions with a darker color. In the thin section, monazite is found in garnet cracks together with

587 chlorite (Fig 13e, f), which suggests that monazite growth is closely related to the
588 destabilization of garnet during retrogression.

589   Sixteen SIMS isotopic analyses were performed in eleven monazite grains of
590 the sample. The data were plotted in the Wetherill U–Pb concordia diagram (Fig 13d)
591 and yielded a pooled concordia age of 541 ± 7 Ma (2σ).

592   REE data of monazite normalized to chondrite (Boyton, 1984) show enrichment
593 of LREE over HREE (Fig. 13a). Although the LREE concentration is rather
594 homogeneous in all analysed grains, they show a strong variation in HREE content. A
595 small Eu/Eu* anomaly ranges from 0.36 to 0.63). Th/U ratios range between 3.3 and
596 26.0.

597

598 **4.   Discussion**

599

600 **4.1.   Garnet and monazite petrochronology**

601

602 **4.1.1. MAB51B – Metamorphic peak in the eastern Porongos Complex (ca. 660**
603   **Ma)**

604

605   In sample MAB51B, garnet displays a homogenous REE pattern for both rim and
606 core suggesting equilibrium with stable minerals in the matrix during its growth (Lanari
607 and Engi, 2017). Furthermore, the weak Eu anomaly recorded by the garnet (Eu/Eu*
608 0.24 to 0.60) likely suggests its growth in equilibrium with the matrix plagioclase. The
609 Lu–Hf isochron age suggests that the metamorphic event responsible for the growth
610 of garnet took place at 662 ± 13 Ma.

611   Trace element data suggest mild enrichment of Lu in garnet core (Fig. 12a). In
612 metamorphic rocks, Lu usually shows partitioning into garnet core relative to rims due
613 to Rayleigh fractionation. Consequently, the Lu–Hf bulk garnet age is biased towards
614 an early garnet growth (e.g. Baxter and Scherer, 2013). In our case, the weak Lu
615 enrichment in the centre of the profile either means that this element is more
616 homogeneously distributed than in typical prograde garnet, or that the analysed section
617 did not reach the very core of the crystal. Thus, the above-reported garnet age should
618 be considered as an average age for garnet growth in the sample MAB51B. The mean
619 Hf content acquired by LA–ICP–MS analysis of clean garnet (1 ppm) presents
620 discrepancy when compared to the value found from garnet isotope dilution (4 ppm –
621 Table 3). This disparity is likely attributed to contamination from Hf-rich accessory

622   mineral inclusions in garnet. The presence of micro-inclusions of zircon and ilmenite in

623   garnet is confirmed by spikes in U+Hf and Ti respectively in figure 12. Despite efforts

624   to reduce the presence of such inclusions in garnet (after Anczkiewicz et al., 2004)

625   some Hf-rich inclusions may have dissolved together with the garnet. Although, a huge

626   Hf contamination, as the case of zircon inclusions, would swipe off the isochron, which

627   seems not the case, as all analyses stay aligned. Thus, it is most likely the Hf

628   contamination was generated by some other 'low-Hf' mineral than zircon, as for

629   example ilmenite, which would not pose any problems to the age estimates. This age

630   estimate overlaps within error with an unpublished Rb–Sr white mica/whole-rock age

631   of 658 ± 26 Ma from the same region (Lenz, 2006).

632   The peak conditions of the metamorphic event responsible for garnet growth

633   estimated by thermodynamic modeling were calculated at ca. 530–565°C and 3.6–4.5

634   kbar (Fig. 4). This estimate is ca. 15°C lower than the maximum temperature

635   suggested by De Toni et al. (2021). Pressure estimates by De Toni et al. (2021) and

636   Lenz (2006) range from 5.4 to 6.3 kbar, which is ca. 1–2 kbar more than found in

637   MAB51B (Table 4). However, both authors worked with staurolite-rich samples from

638   an outcrop ca. 100 m away from the location of MAB51B, and it is likely that those

639   rocks reached somewhat higher metamorphic grade.

640

641   **4.1.2. MAB51B – Exhumation of the eastern Porongos Complex (ca. 615 Ma)**

642

643   Monazite in sample MAB51B displays a generally homogenous REE pattern, with

644   only a small spread in the HREE content for individual grains. Such variation in HREE

645   can be either interpreted as local heterogeneities in rock chemistry or as a time-related

646   HREE zoning. The first possibility seems to be more likely, as the individual U–Pb

647   dates form a homogeneous cluster in the concordia diagram (Fig. 11d). Thus, we

648   interpret that all the analysed monazite grains represent the same event of monazite

649   growth and the observed HREE variation may reflect a variable availability of HREE in

650   the rock.

651   Monazite grains in this sample present an extremely pronounced Eu anomaly

652   (Eu/Eu* = 0.040 to 0.007). Usually, such highly negative Eu anomaly is interpreted to

653   represent monazite growth in equilibrium with plagioclase during melt crystallisation

654   (Rubatto et al., 2006; Johnson et al., 2015; Hagen-Peter et al., 2016). This is also a

655   common situation in high-grade, migmatitic metamorphic rocks (e.g. Rubatto et al.,

656   2013; Johnson et al., 2015; Hagen-Peter et al., 2016), but clearly not the case for our

657 lower-amphibolite facies schist. Moreover, the Eu anomaly in monazite is much
658 stronger than that found in the garnet of the same sample (Fig. 11a, b), suggesting that
659 the monazite did not grow during the garnet-forming metamorphic event (e.g. Rubatto
660 et al., 2006).

661   Calculated distribution coefficients of REE between monazite and garnet (Fig.
662 14a, b) may be used as another proxy for interpreting the mutual stability of these two
663 minerals during their growth. Kd curves were calculated for the REE content of each
664 analytical spot in monazite divided by REE content of one representative spot for each
665 garnet region (core, mantle and rim; for values see supplementary data file). The Kd
666 values for garnet 1 (Fig 14a) and garnet 2 (Fig 14b) of sample MAB51B show similar
667 results for all three garnet regions. Although, the LREE distribution coefficients are in
668 the range expected for equilibrium growth by previous studies (Hermann & Rubatto,
669 2003; Rubatto et al., 2006; Warren et al., 2019), the MREE and HREE present lower
670 (to much lower – e.g. Eu) distribution coefficients than expected for monazite which
671 would crystallize in equilibrium with garnet. Such results may be seen as another
672 indication that garnet and monazite in sample MAB51B did not crystallize in
673 equilibrium.

674   All the data presented and discussed above point to a monazite-forming event
675 postdating the metamorphic peak reached by the schists of the eastern Porongos
676 Complex. A significant activity of fluids altering the peak metamorphic assemblage is
677 widespread in the region of sample MAB51B, as documented by muscovite halos
678 replacing staurolite crystals and growth of andalusite crystals up to 10 cm in size in
679 staurolite schists of the region (Lenz, 2006; De Toni et al., 2021), or by the high density
680 of quartz veins close to the nearby Passo do Marinheiro Fault. Thus, we interpret the
681 large Eu anomaly found in the dated monazite from this sample as reflecting growth of
682 the crystals triggered by Eu-depleted fluids. The best candidates for releasing such
683 fluids are the nearby magmatic rocks. The Encruzilhada Granite is the closest, however
684 it assimilates ca. 580 Ma syenitic rocks (Padilha et al., 2019), and thus, it is too young
685 to be the fluid source. On the other hand, the ca. 609 Ma pulse of the multiphase Piquiri
686 Syenite Massif (Rivera, 2016; Sbaraini et al., 2020), which has also caused local
687 contact metamorphism in PC rocks (Battisti et al., 2018), is the most likely candidate
688 for the fluid source. K-feldspar may show a stronger positive anomaly than plagioclase
689 (Bea et al., 1994), and feldspar-rich magmatic rocks tend to concentrate Eu in the
690 primary feldspar (Larsen, 2002; Gahlan et al., 2016), which in turn may lead to the
691 release of strongly Eu-depleted fluid during their crystallization. Therefore, we interpret

692 the ca. 615 Ma monazite crystals as dating the time of release of fluids from
693 crystallizing syenitic rocks in the close vicinity. Furthermore, we associate the monazite
694 growth with other features,e.g., the post-kinematic growth of andalusite or replacement
695 of staurolite by muscovite coronas (De Toni et al., 2021). Together with the Lu-Hf
696 garnet age, these features suggest that the eastern Porongos Complex was exhumed
697 between ca. 660–615 Ma.

698
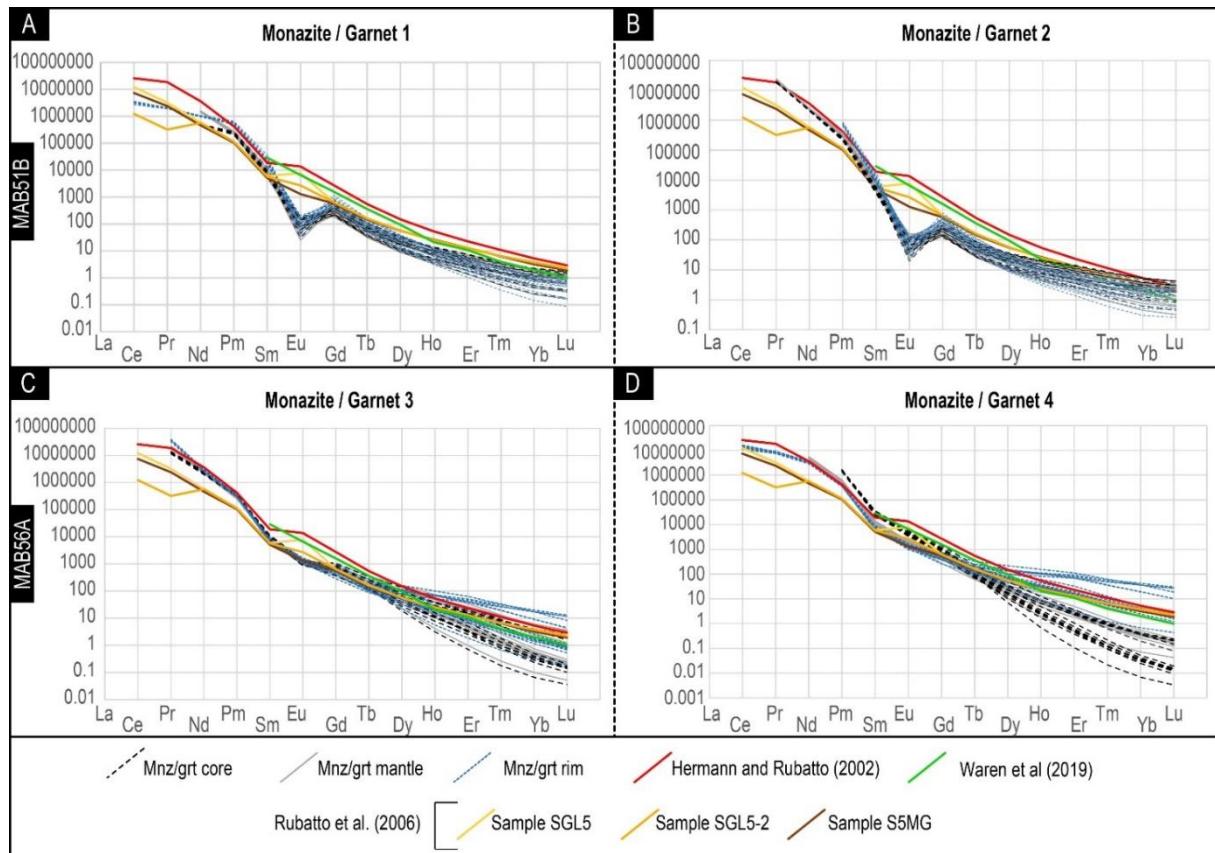
699
700
701 Figure 14. Calculated distribution coefficients of REE between: A) monazite and garnet 1 and
702 B) monazite and garnet 2 in sample MAB51B, and C) monazite and garnet 3 and D) monazite
703 and garnet 4 in sample MAB 56A. Dashed black lines: Mnz/Grt core, gray lines: Mnz/Grt
704 mantle, dashed blue lines: Mnz/Grt rim.

705

706 **4.1.3. MAB56A – Metamorphic peak in the northwestern Porongos Complex (ca.**
707 **560 Ma)**

708

709 In sample MAB56A, relict garnet grains present a systematic variation of HREE
710 content, where the HREE are strongly enriched in garnet cores and the concentrations
711 decreases towards the rims. Despite five spots with a slightly positive Eu anomaly
712 (Eu/Eu* = 1.01 to 1.57), the generally mild negative Eu anomaly (Eu/Eu* = 0.59 to

713 0.98) in this sample is interpreted as a response to the presence of plagioclase in the
714 metamorphic assemblage. Garnet from this sample shows Lu enrichment in several
715 growth zones of the crystal (Fig. 12b), whereas another analysed crystal (Fig. S4)
716 shows a bell-shaped profile suggesting Lu partitioning into the core. For this reason,
717 we interpret the Lu–Hf garnet-WR age of 563 ± 12 Ma as representing an average age
718 of the garnet growth in sample MAB56A. Hf mean content acquired in LA–ICP–MS
719 analyses (2 ppm) slightly differ from the value found after garnet isotope dilution (2.5
720 ppm) and may suggest that some ilmenite micro-inclusions were dissolved together
721 with garnet. However, ilmenite is considered part of the stable mineral assemblage,
722 together with garnet. As such, its presence as inclusions in the garnet crystals should
723 not influence the resulting age estimate.

724   The peak PT conditions reached during garnet growth were estimated at ca. 550–
725 570°C and 4.5–5.5 kbar (Fig. 6). We emphasize, however, that preserved garnet grains
726 are often only relict crystals, which we interpret as the result of strong retrogression.
727 Thus, as our PT estimates are based primarily on garnet compositions, this suggests
728 potentially higher peak metamorphic conditions than is indicated by the matrix
729 assemblage. Thus, staurolite crystals might have been present during the
730 metamorphic peak, as suggested by the thermodynamic model (Fig. 6), and it were
731 subsequently consumed during retrogression, while some garnet crystals remained
732 preserved. Therefore, we interpret the Lu–Hf garnet age (563 ± 12 Ma) and the PT
733 conditions estimated from the garnet composition as reflecting the metamorphic peak
734 in this region of the PC prior to the retrograde re-equilibration of sample MAB56A.

735

736 **4.1.4. MAB56A - Retrogression in the northwestern Porongos Complex (ca. 540**
737   **Ma)**

738

739   Monazite in sample MAB56A appears in garnet cracks together with chlorite, and
740 its growth thus appears to be closely related to garnet chloritization (Fig. 13e, f) and
741 overall retrograde overprint of the (unknown) peak mineral assemblage. Monazite
742 grains display a strong variation in HREE content. Colour-coded REE curves and
743 corresponding dates in the U–Pb concordia diagram (Fig 13c, d) show that the variation
744 in HREE content is not reflected in the U–Pb date of the analysed grains, as they all
745 overlap and form a homogeneous cluster in the concordia diagram. Such results
746 suggest that all dated grains represent the same monazite-growing event. The Th/U
747 ratios of the analysed crystals are similar and thus support this interpretation. In this

748   sample, garnet cores are systematically richer in HREE than their rims (Fig. 13a). We

749   thus interpret the variation of monazite HREE content as related to the position of the

750   monazite grain during its growth with respect to the garnet i.e., monazites that grew

751   due to breakdown of the garnet core are richer in HREE, whilst those related to the

752   breakdown of garnet rims have lower HREE.

753   An alternative interpretation by Hagen-Peter et al. (2016) suggests a time-related

754   coupling of garnet breakdown and monazite growth. In such a case, the older monazite

755   grains would be HREE depleted, as they would have grown from garnet rims, whereas

756   the younger monazites related to the dissolution of garnet cores would be richer in

757   HREE. Although this interpretation cannot be fully discarded, the resolution of our

758   dating is not high enough to determine a relationship between age and HREE content.

759   Another alternative proposed by Hacker et al. (2019) suggests that temperature

760   elevation caused by a heating event could raise the partitioning coefficient of HREE

761   into monazite, allowing new grains to support a larger amount of HREE in their

762   structure. The spatially and temporally nearest intrusion is the Capané metagranite,

763   which according to Zvirtes et al. (2017) crystallized at 603 ± 6 Ma (U–Pb zircon age)

764   and has a metamorphic age of 539 ± 9 Ma (U–Pb age from zircon rims and titanite

765   age). Such data indicate that the intrusion is too old to provide heat at ca. 540 Ma. On

766   the other hand, the metamorphic age of the Capané metagranite is in accord with the

767   monazite age of the metasedimentary sample MAB56A.

768   The Eu anomalies in MAB56A monazite and garnet are similar (Eu/Eu*$_{mon}$ =

769   0.36 to 0.63; Eu/Eu*$_{grt}$ = 0.59 to 1.56). Also, distribution coefficients between monazite

770   and garnet for some REEs (La–Tb; Fig 14c, d) follow the expected equilibrium values

771   from previous studies (Hermann & Rubatto, 2003; Rubatto et al., 2006), although

772   petrographic observations attest to disequilibrium between these minerals (Fig. 14f).

773   On the other hand, Kd curves for the HREE suggest equilibrium only in a few cases

774   and most of the HREE Kd curves for monazite/garnet core and garnet mantle deviate

775   from expected equilibrium values (Fig. 14c, d). The HREE Kd values for

776   monazite/garnet rim show a large spread (up to three orders of magnitude) for each

777   element, where some of the values match the expected equilibrium values, some are

778   higher, and some are lower (Fig. 14c, d). This reflects the strongly variable HREE

779   content of the monazite itself (Fig. 13b), and as mentioned above, we interpret this

780   feature as a result of the variable availability of HREEs during monazite growth, which

781   will largely depend on the distance of the growing monazite from the dissolving garnet,

782   as well as on the particular part of the garnet (core, mantle, rim) releasing the HREEs.

783   Thus, we interpret the monazite U–Pb SIMS concordia age of 541 ± 7 Ma (2σ)

784 as the time of retrograde overprint of sample MAB56A.

785

786 **4.1.5. BD03 – Prograde metamorphism in the Passo Feio Complex (ca. 570 Ma)**

787

788   The garnet Lu–Hf dating of sample BD03 yielded an age of 571 ± 13 Ma. In

789 agreement with previous works (Bitencourt, 1983; Costa et al., 2021), we interpret the

790 garnet in this sample as syn-kinematic to the main progressive deformational-

791 metamorphic event in the complex, which is represented by the main schistosity.

792 Therefore, the ca. 570 Ma age is interpreted as the mean age of the prograde

793 metamorphism of the Passo Feio Complex. Also, as Lu is not concentrated within one

794 growth zone of the garnet (Fig. 12c), the result of the Lu–Hf garnet–WR dating is

795 considered an average age of the garnet growth in sample BD03. The mean Hf content

796 acquired by LA-ICP-MS (1 ppm) presents a discrepancy when compared to the value

797 found from garnet isotope dilution (4 ppm). However, as in sample MAB51B, all the

798 garnet aliquots stay aligned in the isochron, and thus, the same interpretation is applied

799 to BD03 sample, as well, which indicates the age is likely trustful.

800   Thermodynamic modelling of sample BD03 places the peak metamorphic

801 conditions of this event at 560–580 °C and 4.7–6.4 kbar, with initial garnet growth at

802 525–545 °C and 4.1–4.5 kbar. The data agree with estimates of Costa et al. (2021) for

803 a nearby sample of a garnet-staurolite schist, whereas their additional estimate for a

804 staurolite-free garnet phyllite places the metamorphic peak to 500–510 °C and 5–6.4

805 kbar (Table 4).

806   Published geochronological data for the main metamorphic event in the PFC are

807 rather limited. A single SHRIMP spot in a zircon rim yielded a date of 685 ± 12 Ma

808 (Remus et al., 2000) was associated with the metamorphic peak and thus contrasts

809 with the 571 ± 13 Ma Lu–Hf garnet age. However, the available image (Fig. 5i in Remus

810 et al., 2000) suggests that the microprobe beam size was larger than the zircon rim

811 width, which points to a possible mixed analysis with the Tonian (843 Ma) zircon core.

812 A metamorphic event at ca. 685 Ma cannot be discarded, however if it took place, it

813 must have been erased by the ca. 570 Ma metamorphic event, as the sample used in

814 this paper was collected from the highest metamorphic zone of the complex.

815   A second, low-pressure metamorphic event (M_2) overprinted the peak mineral

816 assemblage in the PFC (Bitencourt, 1983; Costa et al., 2021) and it was interpreted as

817 being related to the emplacement of the Caçapava Granite at 562 ± 8 Ma (SHRIMP

818 U–Pb zircon – Remus et al., 2000). The dextral transcurrent fabric generated in such

819 second event cross-cuts the main metamorphic foliation (Costa et al., 2021). Thus,

820 despite the overlap of the ages within their respective errors (M_1 at 571 ± 13 Ma, and

821 M_2 at 562 ± 8 Ma), metamorphic and structural field relations attest that M_1 have

822 preceded the M_2 event, or they are even progressive phases.

823

824 **INSERT TABLE 4**

825

826 **4.2. Geological significance of the data and an evolutionary scenario of the**

827 **Porongos and Passo Feio complexes**

828

829 The geochronological and metamorphic data presented in this work can be

830 summarized in a P–T–t diagram showing evolution and mutual relationship of the

831 Porongos and Passo Feio complexes (Fig. 15). The data show progressive thickening

832 of the central Dom Feliciano foreland that took place in at least two distinct time

833 periods.

834 The early phase of orogenic evolution in the foreland is recorded by the prograde

835 metamorphism of micaschists in the eastern region of the Porongos Complex.

836 Estimates of metamorphic conditions for the sample MAB51B, and data of De Toni et

837 al. (2021) and Lenz (2006) suggest a clockwise path for this region (see lines 1 and 2

838 in fig. 15). Garnet started to grow at ca. 515–535°C and 3.4–4.4 (MAB51B) and the

839 metamorphic peak was reached at conditions of 560–580ºC and 5.8–6.3 kbar

840 (MAB52A – De Toni et al, 2021). Such data demonstrate early thickening of the

841 foreland crust with apparent geothermal gradient of 25 to 35ºC/km at ca. 660 Ma, as

842 demonstrated by the Lu–Hf garnet–WR age.

843 The post-exhumation evolution of the eastern Porongos Complex is registered by

844 the destabilization of the peak metamorphic assemblage and growth of andalusite

845 crystals in some of the micaschist samples (De Toni et al., 2021; Lenz, 2006). Lenz

846 (2006) estimated the conditions of this event at 550–560°C and 2.7 kbar. As discussed

847 above, we associate these fluid-triggered mineralogical changes with the growth of

848 monazite in sample MAB51B dated at ca. 615 Ma. All these data suggest that the

849 eastern PC was exhumed between ca. 660 and 615 Ma, before the onset of extensive

850 magmatic activity in the region.

851 The second phase of thickening of the foreland is recorded in the northwestern

852 region of the Porongos Complex (lines 3 and 4 in fig. 15) and in the Passo Feio

853   complexes (lines 5, 6 and 7 in fig. 15). The evolution of sample MAB56A from the
854   northwestern Porongos Complex shows the onset of garnet growth at 520–540°C and
855   3.9–5.3 kbar and the metamorphic peak at ca. 550–570°C, and 4.5–5.5 kbar. Together
856   with Lu–Hf garnet–WR dating, such data indicate a burial event at ca. 565 Ma. The
857   exhumation of the northwest region of the PC was associated with severe chloritization
858   of the garnet-bearing peak mineral assemblage. It took place at around 540 Ma, as
859   suggested by monazite growth at the expense of the ca. 565 Ma garnet. Chlorite
860   geothermometers (Cathelineau & Nieva, 1985; Cathelineau, 1988; De Caritat et al.,
861   1993; Vidal et al., 2001) suggest temperatures of 310–440°C during the retrograde
862   overprint, yet the pressure could not be established.

863   Burial of the Passo Feio Complex took place at ca. 570 Ma, as determined by
864   Lu–Hf dating of garnet growth during the main regional metamorphism of the complex.
865   Sample BD03 registers the metamorphic peak of this event at ca. 560–580°C, and 4.7–
866   6.4 kbar. The exhumation of the complex occurred before ca. 560 Ma, which is the age
867   of the Caçapava granite intrusion triggering contact metamorphism at depths shallower
868   than 14 km, as indicated by the crystallization of andalusite (Costa et al., 2021). The
869   exact exhumation path is unclear (line 7 in fig. 15), and either corresponds to a near
870   isothermal decompression path or to exhumation and cooling path followed by re-
871   heating (Costa et al., 2021), both due to the heat input caused by the Caçapava granite
872   intrusion. PT modelling also indicates that andalusite is only stable at temperatures
873   similar to those of the metamorphic peak but at lower pressures (Fig. 9).
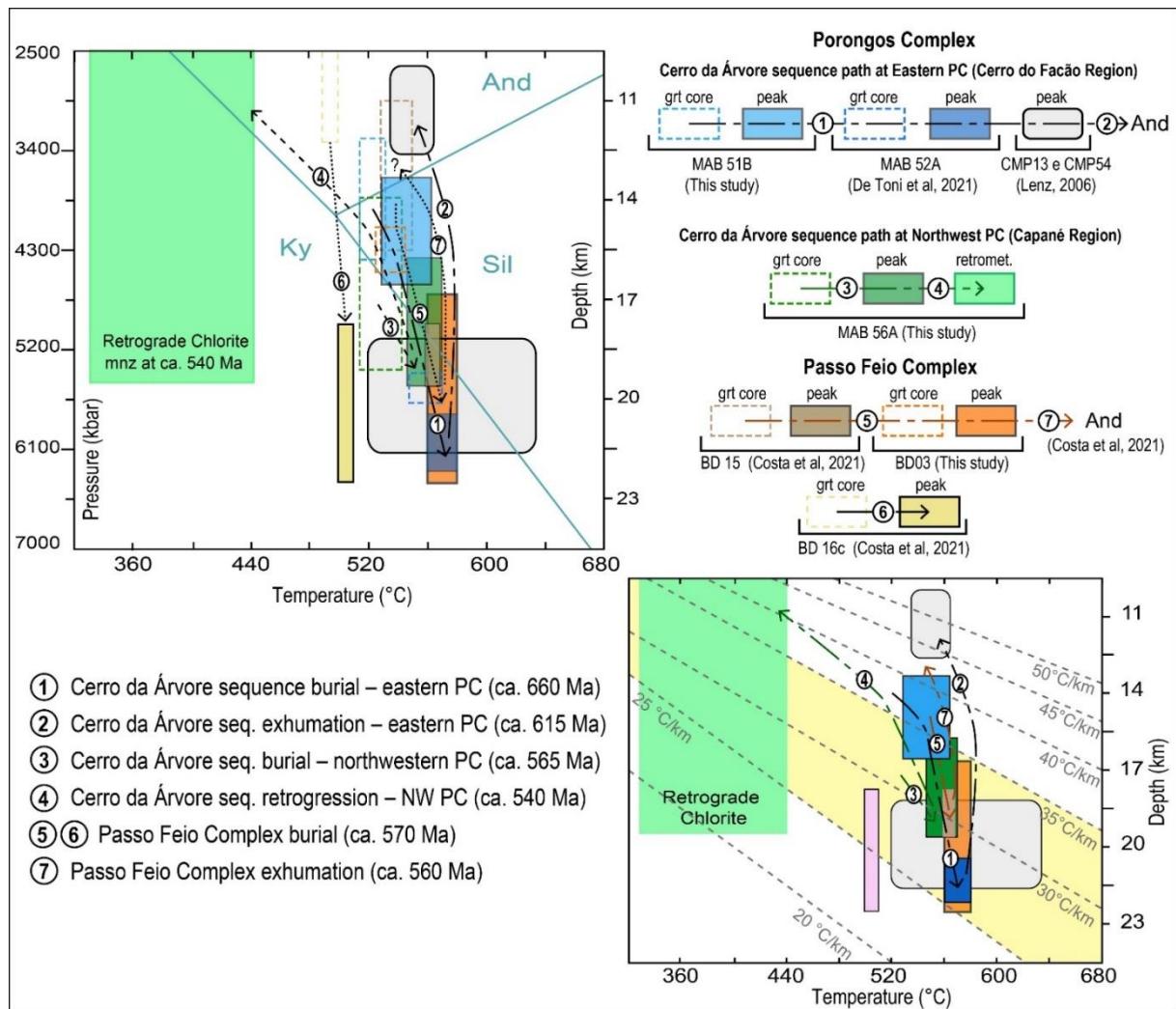
Figure 15. P–T–t evolution of the Porongos and Passo Feio complexes, based on the data of this paper and literature. Depth calculated using average crustal density of 2.8 g/cm^3.

4.3.   Tectonostratigraphic subdivision of the Porongos Complex

Our geochronological and metamorphic data indicate a diachronous metamorphic evolution of the eastern and northwestern regions of the Porongos Complex. Such results explain the difference between these two regions, mainly noticed in the zircon provenance patterns of metasedimentary rocks (Gruber et al., 2011b, 2016b; Pertille et al., 2015b, 2015a, 2017; Höfig et al., 2018) and protolith ages of metaigneous rocks (Saalmann et al., 2011; Pertille et al., 2017; Höfig et al., 2018; Battisti et al., submitted).

For many authors (e.g. Saalmann et al., 2006; Höfig et al., 2018; Battisti et al., 2018; De Toni et al., 2021), the main metamorphic–deformational event in the PC is related to the well-known collision in the DFB at ca. 650 Ma (Chemale et al., 2011;

891 Martil, 2016), which generated W-verging thrusting of hinterland nappes on top of the

892 foreland (Battisti et al., 2018; De Toni et al., 2021). Our Lu–Hf garnet–WR dating

893 confirms the timing of the main fabric development and metamorphic peak in the

894 eastern region of PC during this ca. 660–650 Ma event. Such data demonstrate that

895 the igneous activity, and the late sedimentation in the northwestern PC are younger

896 than the metamorphic peak recorded in the eastern portion of the PC (Table 5).

897 Battisti et. al. (2018) suggested a second metamorphic–deformational event in

898 the PC, but its absolute timing was unknown. Our Lu–Hf garnet–WR isochron and U–

899 Pb SIMS monazite ages from sample MAB56A indicate that the second event took

900 place from ca. 560–540 Ma and is exclusively recorded west of the Santana da Boa

901 Vista thrust fault. These data indicate that the two basins proposed by Höfig et al.

902 (2018) have had different geological evolution in space and time. The Santana da Boa

903 Vista fault, the main W-verging thrust fault of the Porongos Complex (Jost & Bitencourt,

904 1980), represents the best possible limit between these two diachronous basins,

905 referred to as the Cerro da Árvore and Capané sequences in Table 5. To the east of

906 the Santana da Boa Vista fault (eastern Porongos region), the detrital zircon age

907 patterns in metasedimentary rocks suggest pre-collisional deposition of the Cerro da

908 Árvore sequence. On the other hand, to the west of the fault (western Porongos region)

909 the rocks of the pre-orogenic PC basin are interleaved with metamorphosed syn-

910 orogenic sedimentary rocks of the Capané sequence, as first suggested by Höfig et al.

911 (2018).

912

913 **INSERT TABLE 5**

914

915 **4.4. Evolutionary model**

916

917 The Cerro da Árvore sequence of the Porongos Complex, and metasedimentary

918 rocks of the Várzea do Capivarita Complex have been deposited from before ca. 810

919 Ma, as indicated by the age of the associated volcanic rocks (Saalmann et al., 2011;

920 Pertille et al., 2017; Battisti et al., submitted), until < ca. 660–650 Ma, when the early

921 orogenic deformation and metamorphism took place (Fig. 16a). The ca. 660–620 Ma

922 collisional event affected the easternmost part of the Cerro da Árvore sequence, which

923 was thrust under the developing hinterland represented by the W-verging nappes of

924 the Várzea do Capivarita Complex (Martil et al., 2017; Battisti et al., 2018; De Toni et

925 al., 2021), but had minor effect on the westernmost part of this sequence (Fig. 16b).

926   Sometime between ca. 660 Ma and ca. 615 Ma, the eastern PC was exhumed. The

927   exhumation preceded an extensive magmatic activity in the region, during which at

928   least some intrusions likely exploited the existing nappe boundaries.

929   In the western region, the basin with the pre-orogenic infill of the Cerro da Árvore

930   sequence was probably only mildly affected by the early (660–615 Ma) orogenic

931   phase. On the other hand, after a certain time the basin started receiving syn-orogenic

932   (flysch) sediments of the present-day Capané sequence, now interleaved with the

933   Cerro da Árvore sequence rocks. The flysch sedimentation occurred from ca. 660 Ma

934   to < ca. 570–560 Ma (Fig 16b). At ca. 570–560 Ma, the second episode of crustal

935   thickening occurred. It thrust the eastern region of PC on top of its western region,

936   which caused metamorphism and deformation of both the Capané and Cerro da Árvore

937   (at the bottom) sequences (Fig 16c). The MAB56A locality represents the region where

938   the Cerro da Árvore and Capané sequences are interleaved. The destabilization of

939   garnet and appearance of monazite in equilibrium with retrograde chlorite at ca. 540

940   Ma likely indicates the exhumation-related decrease of metamorphic temperatures

941   from ca. 560 Ma to ca. 540 Ma.

942   We speculate that the Passo Feio Complex further to the west of the Porongos

943   Complex represents an originally independent basin, which seems to register only the

944   younger metamorphic and deformation event at ca. 570 Ma (Fig. 16b,c). Our new data

945   suggest that the crustal thickening and overall tectonic activity in the central Dom

946   Feliciano Belt foreland at this time was much more extensive than so far published.

947   Such data indicate that the Passo Feio and western Porongos complexes record an

948   orogenic front migration towards the west as a part of a long-lived transpressive

949   deformation in the Dom Feliciano Belt, which has started at ca. 660–650 Ma (see also

950   De Toni et al., 2021 or Percival et al., 2022).
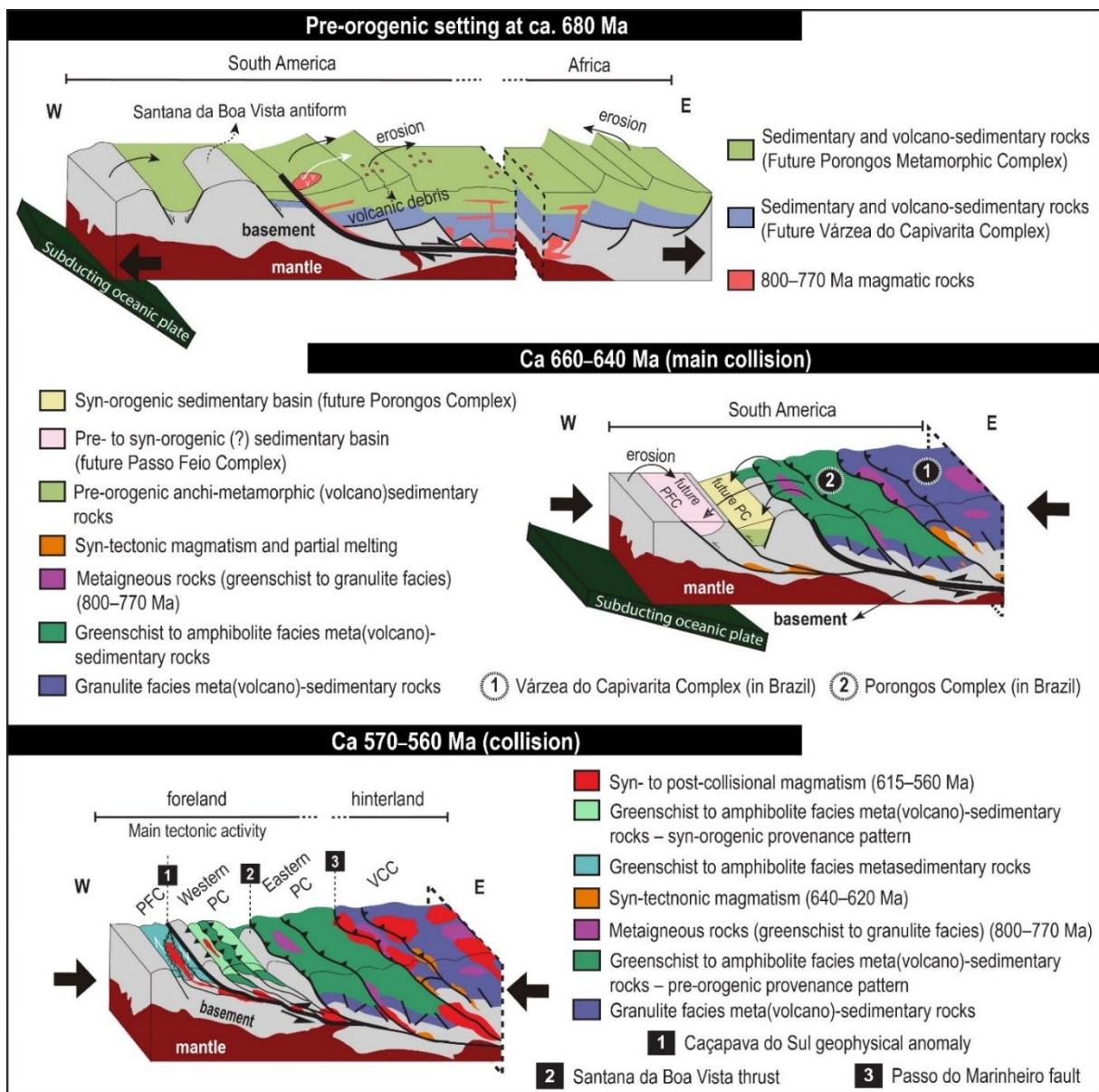
Figure 16 – Model of pre-orogenic setting and orogenic evolution of the Central Dom Feliciano Belt foreland (Porongos and Passo Feio complexes) and hinterland (Várzea do Capivarita Complex).

5.   Conclusions

Petrochronological study utilizing petrological modelling combined with Lu–Hf garnet–WR ages, U–Pb monazite SIMS ages and Y–REE data in garnet and monazite was performed in metasedimentary rocks of the central Dom Feliciano Belt foreland. The results allow us to draw the following conclusions:

1)   Metasedimentary rocks of the eastern Porongos Complex display a main metamorphic event at 662 ± 13 Ma (Lu–Hf isochron garnet–whole-rock age). Such

965 event took place at ca. 515–535°C and 3.4–4.4 kbar and reached metamorphic peak
966 at ca. 560–580 °C, 5.8-6.3 kbar. This episode represents an early orogenic thickening
967 event in the foreland as a response to the beginning of transpressive convergent
968 evolution of the Dom Feliciano Belt.

969   2)   The monazite age of 614 ± 6 Ma (U–Pb SIMS) suggests that the eastern
970 Porongos Complex was exhumed sometime between ca. 660 and 615 Ma. The growth
971 of monazite, andalusite and secondary white mica was likely triggered by a release of
972 fluids during crystallization of neighboring syenitic rocks of simiar age.

973   3)   Syn-orogenic sediments (Capané sequence) were deposited in the
974 western part of the Porongos Complex at unspecified time between ca. 660 to ca. 560
975 Ma. The main metamorphic and deformational event in this region took place at
976 conditions of ca. 550–570°C and 4.5–5.5 kbar at 563 ± 12 Ma (garnet–WR Lu–Hf
977 isochron age).

978   4)   The exhumation of the western PC is dated by the appearance of
979 monazite crystalizing during garnet breakdown, suggesting retrograde metamorphism
980 at 541 ± 7 Ma (U–Pb SIMS).

981   5)   The main metamorphic fabric in the Passo Feio Complex was developed
982 at 571 ± 13 Ma (garnet–WR Lu–Hf isochron age) at metamorphic conditions of 560–
983 580°C and 4.7–6.4 kbar.

984   6)   The Western part of the Porongos Complex and the Passo Feio Complex
985 were deformed at ca. 570–565 Ma at similar PT conditions and geothermal gradients.
986 These regions record a second crustal thickening event in the Dom Feliciano Belt and
987 the orogenic front migration towards the west in a long-lived transpressive orogenic
988 system.

989

990 6.   ACKNOWLEDGEMENTS

991

1000 and Heejin Jeon for their support while using the Nordsim ion probe in Stockholm (this
1001 is Nordsim publication # XXX).

1002

1003 **Supplementary files content description:**

1004

1005 **File 1: Supplementary figures**
1006 **File 2: Mineral chemistry data**
1007 **File 3: Garnet and monazite trace elements data**
1008 **File 4: Monazite U-Pb results**
1009 **File 5: Monazite/garnet trace elements partitioning**

1010

1011 **7.   REFERENCES**

1012

1013 Aleinikoff, J.N., Schenck, W.S., Plank, M.O., Srogi, L.A., Fanning, C.M., Kamo, S.L., Bosbyshell,
1014 H., 2006. Deciphering igneous and metamorphic events in high-grade rocks of the Wilmington complex,
1015 Delaware: Morphology, cathodoluminescence and backscattered electron zoning, and SHRIMP U-Pb
1016 geochronology of zircon and monazite. Bull Geol Soc Am 118, 39–64. https://doi.org/10.1130/B25659.1
1017 Anczkiewicz, R., Platt, J.P., Thirlwall, M.F., Wakabayashi, J., 2004. Franciscan subduction off to
1018 a slow start: Evidence from high-precision Lu-Hf garnet ages on high grade-blocks. Earth Planet Sci Lett
1019 225, 147–161. https://doi.org/10.1016/j.epsl.2004.06.003
1020 Arena, K.R., Hartmann, L.A., Lana, C., 2016. Evolution of Neoproterozoic ophiolites from the
1021 southern Brasiliano Orogen revealed by zircon U-Pb-Hf isotopes and geochemistry. Precambrian Res
1022 285, 299–314. https://doi.org/10.1016/j.precamres.2016.09.014
1023 Arena, K.R., Hartmann, L.A., Lana, C., 2018. U–Pb–Hf isotopes and trace elements of
1024 metasomatic zircon delimit the evolution of neoproterozoic Capané ophiolite in the southern Brasiliano
1025 Orogen. Int Geol Rev 60, 911–928. https://doi.org/10.1080/00206814.2017.1355269
1026 Arena, K.R., Hartmann, L.A., Lana, C., 2017. Tonian emplacement of ophiolites in the southern
1027 Brasiliano Orogen delimited by U-Pb-Hf isotopes of zircon from metasomatites. Gondwana Res 49,
1028 296–332. https://doi.org/10.1016/j.gr.2017.05.018
1029 Basei, M., Siga, O., Masquelin, H., Harara, O., Reis Neto, J., Preciozzi, F., 2000. The Dom
1030 Feliciano belt (Brazil-Uruguay)and its foreland (Rio de la Plata Craton): framework, tectonic evolution
1031 and correlations with similar terranes of southwestern Africa.
1032 Battisti, M.A., Bitencourt, M. de F., De Toni, G.B., Nardi, L.V.S., Konopásek, J., 2018.
1033 Metavolcanic rocks and orthogneisses from Porongos and Várzea do Capivarita complexes: A case for
1034 identification of tectonic interleaving at different crustal levels from structural and geochemical data in
1035 southernmost Brazil. J South Am Earth Sci 88, 253–274. https://doi.org/10.1016/j.jsames.2018.08.009
1036 Battisti, M.A., Bitencourt, M.F., Schimit, R., Nardi, L.V.S., Martil, M.M.D., De Toni, G.B.,
1037 Armstrong, R., Konopásek, J., submitted. Reconstitution of a volcano-sedimentary environment shared

1038 by the Porongos and Várzea do Capivarita Complexes at 790 Ma, Dom Feliciano Belt, southern Brazil.
1039 Precambrian Res.

1040 Baxter, E.F., Caddick, M.J., Dragovic, B., 2017. Garnet: A Rock-Forming Mineral
1041 Petrochronometer. Rev Mineral Geochemistry 83, 469–533. https://doi.org/10.2138/rmg.2017.83.15

1042 Baxter, E.F., Scherer, E.E., 2013. Garnet Geochronology: Timekeeper of Tectonometamorphic
1043 Processes. Elements 9, 433–438. https://doi.org/10.2113/gselements.9.6.433

1044 Bea, F., Pereira, M.D., Stroh, A., 1994. Mineral/leucosome trace-element partitioning in a
1045 peraluminous migmatite (a laser ablation-ICP-MS study). Chem Geol 117, 291–312.
1046 https://doi.org/10.1016/0009-2541(94)90133-3

1047 Bitencourt, M. de F., Nardi, L.V.S., 1993. Late- to Postcollisional Brasiliano Magmatism in
1048 Southernmost Brazil. An Acad Bras Cienc 65, 3–16.

1049 Bitencourt, M. de F., Nardi, L.V.S., 2000. Tectonic setting and sources of magmatism related to
1050 the southern Brazilian shear belt. Rev Bras Geociencias 30, 184–187.

1051 Bitencourt, M.F., 1983. Metamorfitos da região de Caçapava do Sul, RS – Geologia e Relações
1052 com o Corpo Granítico. Atas do 1o Simpósio Sul-Brasileiro Geol 37–48.

1053 Bitencourt, M.F., Hartmann, L.A., 1984a. Geoquímica das Rochas anfibolíticas da região de
1054 Caçapava do Sul - RS - Parte 1: caracterização geológica e petrográfica, elementos maiores e menores.
1055 An DO XXXIII Congr Bras Geol 4266–4277.

1056 Bitencourt, M.F., Hartmann, L.A., 1984b. Reconhecimento geoquimico dos xistos magnesianos
1057 da região do Passo Feio, Cacapava do Sul - RS. Congr Bras Geol (33 1984 Rio Janeiro, Rj) Anais Rio
1058 Janeiro SBG, 1984.

1059 Bitencourt, M.F., Nardi, L.V.S., Florisbal, L.M., Heaman, L.M., 2015. Geology, geochronology and
1060 petrogenesis of a Neoproterozoic, syntectonic sillimanite- muscovite-biotite granite from southernmost
1061 Brazil. B Abstr 8th Hutt Sympo- sium Granites Relat Rocks 179.

1062 Boyton, W. V., 1984. Geochemistry of Rare Earth Elements: Meteorite studies, in: Henderson, P.
1063 (Ed.), Rare Earth Element Geochemistry. Elsevier, New York, p. 63.

1064 Cathelineau, M., 1988. Cation site occupancy in chlorites and illites as a function of temperature.
1065 Clay Miner 23, 471–485. https://doi.org/10.1180/claymin.1988.023.4.13

1066 Cathelineau, M., Nieva, D., 1985. A chlorite solid solution geothermometer the Los Azufres
1067 (Mexico) geothermal system. Contrib to Mineral Petrol 91, 235–244. https://doi.org/0.1007/BF00413350

1068 Chemale, F., 2000. Evolução Geológica do Escudo Sul-rio- grandense, in: Holz, M., De Ros, L.F.
1069 (Eds.), Geologia Do Rio Grande Do Sul. Universidade Federal do Rio Grande do Sul, Porto Alegre,
1070 Brasil, pp. 13–52.

1071 Chemale, F., Philipp, R.P., Dussin, I.A., Formoso, M.L.L., Kawashita, K., Berttotti, A.L., 2011. Lu–
1072 Hf and U–Pb age determination of Capivarita Anorthosite in the Dom Feliciano Belt, Brazil. Precambrian
1073 Res 186, 117–126. https://doi.org/10.1016/j.precamres.2011.01.005

1074 Chu, N.-C., Taylor, R.N., Chavagnac, V., Nesbitt, R.W., Boella, R.M., Milton, J.A., German, C.R.,
1075 Bayon, G., Burton, K., 2002. Hf isotope ratio analysis using multi-collector inductively coupled plasma
1076 mass spectrometry: an evaluation of isobaric interference corrections. J Anal At Spectrom 17, 1567–
1077 1574. https://doi.org/10.1039/b206707b

1078 Connolly, J.A.D., 2009. The geodynamic equation of state: What and how. Geochemistry,
1079 Geophys Geosystems 10. https://doi.org/10.1029/2009GC002540

Connolly, J.A.D., 2005. Computation of phase equilibria by linear programming: A tool for geodynamic modeling and its application to subduction zone decarbonation. Earth Planet Sci Lett 236, 524–541. https://doi.org/10.1016/j.epsl.2005.04.033

Costa, A.F.U., 1997. Teste e modelagem geofísica da estruturação das associações litotectônicas pré-cambrianas no Escudo Sul-Rio-Grandense. PhD Thesis. Universidade Federal do Rio Grande do Sul, Porto Alegre, Brazil.

Costa, E.O. da, de Fátima Bitencourt, M., Tennholm, T., Konopásek, J., de Franceschi Moita, T., 2021. P-T-D evolution of the southeast Passo Feio Complex and the meaning of the Caçapava Lineament, Dom Feliciano Belt, southernmost Brazil. J South Am Earth Sci 103465. https://doi.org/10.1016/j.jsames.2021.103465

De Caritat, P., Hutcheon, I., Walshe, J.L., 1993. Chlorite geothermometry: a review 41, 219–239.

De Toni, G.B., Bitencourt, M.D.F., Konopásek, J., Battisti, M.A., da Costa, E.O., Savian, J.F., 2021. Autochthonous origin of the Encruzilhada Block, Dom Feliciano Belt, southern Brazil, based on aerogeophysics, image analysis and PT-paths. J Geodyn 144. https://doi.org/10.1016/j.jog.2021.101825

De Toni, G.B., Bitencourt, M.F., Konopásek, J., Martini, A., Andrade, P.H.S., Florisbal, L.M., Campos, R.S., 2020a. Transpressive strain partitioning between the Major Gercino Shear Zone and the Tijucas Fold Belt, Dom Feliciano Belt, Santa Catarina, southern Brazil. J Struct Geol 104058. https://doi.org/10.1016/j.jsg.2020.104058

De Toni, G.B., Bitencourt, M.F., Nardi, L.V.S., Florisbal, L.M., Almeida, B.S., Geraldes, M., 2020b. Dom Feliciano Belt orogenic cycle tracked by its pre-collisional magmatism: the Tonian (ca. 800 Ma) Porto Belo Complex and its correlations in southern Brazil and Uruguay. Precambrian Res 105702. https://doi.org/10.1016/j.precamres.2020.105702

Engi, M., 2017. Petrochronology Based on REE-Minerals: Monazite, Allanite, Xenotime, Apatite BT - Reviews in Mineralogy & Geochemistry. Rev Mineral Geochemistry 83, 365–418.

Engi, M., Lanari, P., Kohn, M.J., 2017. Significant Ages - An Introduction to Petrochronology. Petrochronology 83, 1–12. https://doi.org/10.1515/9783110561890-002

Fernandes, L.A.D., Menegat, R., Costa, A.F.U., Koester, E., Porcher, C.C., Tommasi, A., Kraemer, G., Ramgrab, G.E., Camozzato, E., 1995. Evolução Tectônica Do Cinturão Dom Feliciano No Escudo Sul-Rio-Grandense: Parte Ii - Uma Contribuição a Partir Das Assinaturas Geofísicas. Rev Bras Geociências 25, 375–384. https://doi.org/10.25249/0375-7536.1995375384

Fernandes, L.A.D., Tommazi, A., Porcher, C.C., 1992. Deformation patterns in the southern Brazilian branch of the Dom Feliciano Belt: A reppraisal. J South Am Earth Sci 5, 77–96.

Fragoso-Cesar, A.R.S., Figueiredo, M.C.H., Soliani Jr, E., Faccini, U.F., 1986. O Batólito Pelotas (Proterozóico Superior/Eopaleozóico) no escudo do Rio Grande do Sul. XXXIV Congr Bras Geol 1321–1342.

Fraser, G., Ellis, D., Eggins, S., 1997. Zirconium abundance in granulite-facies minerals, with implications for zircon geochronology in high-grade rocks. Geology 25, 607–610. https://doi.org/10.1130/0091-7613(1997)025<0607:ZAIGFM>2.3.CO;2

Frimmel, H., Frank, W., 1998. Neoproterozoic tectono-thermal evolution of the Gariep Belt and its basement, Namibia and South Africa. Precambrian Res 90, 1–28. https://doi.org/10.1016/S0301-9268(98)00029-1

Fuhrman, M.L., Lindsley, D.H., 1988. Ternary-feldspar modeling and thermometry. Am Mineral 73, 201–215.

Gahlan, H., Azer, M., Asimow, P., Al-Kahtany, K., 2016. Late Ediacaran post-collisional A-type syenites with shoshonitic affinities, northern Arabian-Nubian Shield: a possible mantle-derived A-type magma. Arab J Geosci 9. https://doi.org/10.1007/s12517-016-2629-x

Gasser, D., Jeřábek, P., Faber, C., Stünitz, H., Menegon, L., Corfu, F., Erambert, M., Whitehouse, M.J., 2015. Behaviour of geochronometers and timing of metamorphic reactions during deformation at lower crustal conditions: phase equilibrium modelling and U-Pb dating of zircon, monazite, rutile and titanite from the Kalak Nappe Complex, northern Norway. J Metamorph Geol 33, 513–534. https://doi.org/10.1111/jmg.12131

Goscombe, B.D., Gray, D.R., 2008. Structure and strain variation at mid-crustal levels in a transpressional orogen: A review of Kaoko Belt structure and the character of West Gondwana amalgamation and dispersal. Gondwana Res 13, 45–85. https://doi.org/10.1016/j.gr.2007.07.002

Gregory, T.R., Bitencourt, M. de F., Nardi, L.V.S., Florisbal, L.M., Chemale, F., 2015. Geochronological data from TTG-type rock associations of the Arroio dos Ratos Complex and implications for crustal evolution of southernmost Brazil in Paleoproterozoic times. J South Am Earth Sci 57, 49–60. https://doi.org/10.1016/j.jsames.2014.11.009

Gross, A.O.M.., Porcher, C.C., Fernandes, L.A.D., Koester, E., 2006. Neoproterozoic low-pressure/high-temperature collisional metamorphic evolution in the Varzea do Capivarita Metamorphic Suite, SE Brazil: Thermobarometric and Sm/Nd evidence. Precambrian Res 147, 41–64. https://doi.org/10.1016/j.precamres.2006.02.001

Gross, A.O.M.S., Droop, G.T.R., Porcher, C.C., Fernandes, L.A.D., 2009. Petrology and thermobarometry of mafic granulites and migmatites from the Chafalote Metamorphic Suite: New insights into the Neoproterozoic P–T evolution of the Uruguayan—Sul-Rio-Grandense shield. Precambrian Res 170, 157–174. https://doi.org/10.1016/j.precamres.2009.01.011

Gruber, L., Porcher, C.C., Koester, E., Bertotti, A.L., Lenz, C., Fernandes, L.A.D., Remus, M.V.D., 2016. Isotope geochemistry and geochronology of syn-depositional volcanism in Porongos Metamorphic Complex, Santana da Boa Vista antiform, Dom Feliciano Belt, Brazil: onset of an 800 ma continental arc. J Sediment Environ 1. https://doi.org/10.12957/jse.2016.22722

Gruber, L., Porcher, C.C., Lenz, C., Fernandes, L.A.D. ávila, 2011. Proveniência de metassedimentos das sequências arroio Areião, Cerro Cambará e quartzo milonitos no Complexo Metamórfico Porongos, Santana da Boa Vista, RS. Pesqui em Geociencias 38, 205–223.

Hacker, B., Kylander-Clark, A., Holder, R., 2019. REE partitioning between monazite and garnet: Implications for petrochronology. J Metamorph Geol 37, 227–237. https://doi.org/10.1111/jmg.12458

Hagen-Peter, G., Cottle, J.M., Smit, M., Cooper, A.F., 2016. Coupled garnet Lu-Hf and monazite U-Pb geochronology constrain early convergent margin dynamics in the Ross orogen, Antarctica. J Metamorph Geol 34, 293–319. https://doi.org/10.1111/jmg.12182

Hartmann, L.A., Leite, J.A.D., Da Silva, L.C., Remus, M.V.D., McNaughton, N.J., Groves, D.I., Fletcher, I.R., Santos, J.O.S., Vasconcellos, M.A.Z., 2000. Advances in SHRIMP geochronology and their impact on understanding the tectonic and metallogenic evolution of southern Brazil. Aust J Earth Sci 47, 829–844. https://doi.org/10.1046/j.1440-0952.2000.00815.x

Hartmann, L.A., Santos, J.O.S., Leite, J.A.D., Porcher, C.C., Mcnaughton, N.J., 2003. Metamorphic evolution and U-Pb zircon SHRIMP geochronology of the Belizário ultramafic amphibolite, Encantadas Complex, southernmost Brazil. An Acad Bras Cienc 75, 393–403. https://doi.org/10.1590/S0001-37652003000300010

Hermann, J., Rubatto, D., 2003. Relating zircon and monazite domains to garnet growth zones: Age and duration of granulite facies metamorphism in the Val Malenco lower crust. J Metamorph Geol 21, 833–852. https://doi.org/10.1046/j.1525-1314.2003.00484.x

Höfig, D.F., Marques, J.C., Basei, M.A.S., Giusti, R.O., Kohlrausch, C., Frantz, J.C., 2018. Detrital zircon geochronology (U-Pb LA-ICP-MS) of syn-orogenic basins in SW Gondwana: New insights into the Cryogenian-Ediacaran of Porongos Complex, Dom Feliciano Belt, southern Brazil. Precambrian Res 306, 189–208. https://doi.org/10.1016/j.precamres.2017.12.031

Holland, T.J.B., Powell, R., 1998. An internally consistent thermodynamic data set for phases of petrological interest. J Metamorph Geol 16, 309–343. https://doi.org/https://doi.org/10.1111/j.1525-1314.1998.00140.x

Hueck, M., Oriolo, S., Basei, M.A.S., Oyhantçabal, P., Heller, B.M., Wemmer, K., Siegesmund, S., 2022. Archean to early Neoproterozoic crustal growth of the southern South American Platform and its wide-reaching "African" origins. Precambrian Res 369. https://doi.org/10.1016/j.precamres.2021.106532

Johnson, T.E., Clark, C., Taylor, R.J.M., Santosh, M., Collins, A.S., 2015. Prograde and retrograde growth of monazite in migmatites: An example from the Nagercoil Block, southern India. Geosci Front 6, 373–387. https://doi.org/10.1016/j.gsf.2014.12.003

Jost, H., Bitencourt, M.F., 1980. Estratigrafia e tectônica de uma fração da Faixa de Dobramentos Tijucas no Rio Grande do Sul. Acta Geol Leop 11, 27–59.

Jweda, J., Bolge, L., Class, C., Goldstein, S.L., 2016. High Precision Sr-Nd-Hf-Pb Isotopic Compositions of USGS Reference Material BCR-2. Geostand Geoanalytical Res 40, 101–115. https://doi.org/10.1111/j.1751-908X.2015.00342.x

Kirkland, C.L., Whitehouse, M.J., Slagstad, T., 2009. Fluid-assisted zircon and monazite growth within a shear zone: A case study from Finnmark, Arctic Norway. Contrib to Mineral Petrol 158, 637–657. https://doi.org/10.1007/s00410-009-0401-x

Knijnik, D.B., 2018. Geocronologia U-Pb e geoquímica isotópica Sr-Nd dos granitoides sintectônicos às zonas de cisalhamento transcorrentes Quitéria Serra do Erval e Dorsal de Canguçu, Rio Grande do Sul, Brasil. PhD Thesis. Universidade Federal do Rio Grande do Sul, Porto Alegre - RS.

Koester, E., Porcher, C.C., Pimentel, M.M., Fernandes, L.A.D., Vignol-Lelarge, M.L., Oliveira, L.D., Ramos, R.C., 2016. Further evidence of 777 Ma subduction-related continental arc magmatism in Eastern Dom Feliciano Belt, southern Brazil: The Chácara das Pedras Orthogneiss. J South Am Earth Sci 68, 155–166. https://doi.org/10.1016/j.jsames.2015.12.006

Kohn, M.J., 2017. Titanite Petrochronology. Rev Mineral Geochemistry 83, 419–441. https://doi.org/10.2138/rmg.2017.83.13

Konopásek, J., Anczkiewicz, R., Ábek, P.J., Corfu, F., Žáčková, E., 2019. Chronology of the saxothuringian subduction in the west sudetes (Bohemian massif, Czech Republic and Poland). J Geol Soc London 176, 492–504. https://doi.org/10.1144/jgs2018-173

1204   Konopásek, J., Cavalcante, C., Fossen, H., Janoušek, V., 2020. Adamastor – An ocean that never
1205 existed? Earth-Science Rev 103201. https://doi.org/10.1016/j.earscirev.2020.103201

1206   Konopásek, J., Janoušek, V., Oyhantçabal, P., Sláma, J., Ulrich, S., 2018. Did the circum-Rodinia
1207 subduction trigger the Neoproterozoic rifting along the Congo–Kalahari Craton margin? Int J Earth Sci
1208 107, 1859–1894. https://doi.org/10.1007/s00531-017-1576-4

1209   Lanari, P., Engi, M., 2017. Local Bulk Composition Effects on Metamorphic Mineral Assemblages.
1210 Rev Mineral Geochemistry 83, 55–102.

1211   Larsen, R.B., 2002. The distribution of rare-earth elements in K-feldspar as an indicator of
1212 petrogenetic processes in granitic pegmatites: Examples from two pegmatite fields in southern Norway.
1213 Can Mineral 40, 137–151. https://doi.org/10.2113/gscanmin.40.1.137

1214   Lee, D., 1999. Hafnium Isotope Stratigraphy of Ferromanganese Crusts. Science (80-) 285,
1215 1052–1054. https://doi.org/10.1126/science.285.5430.1052

1216   Leite, J.A.D., Hartman, L.O.A., McNaughton, N.J., Chemale, F., 1998. SHRIMP U/Pb zircon
1217 geochronology of neoproterozoic juvenile and crustal-reworked terranes in southernmost brazil. Int Geol
1218 Rev 40, 688–705. https://doi.org/10.1080/00206819809465232

1219   Leite, J.A.D., Hartmann, L.A., Fernandes, L.A.D., McNaughton, N.J., Soliani, Jr., Ê., Koester, E.,
1220 Santos, J.O.S., Vasconcellos, M.A.Z., 2000. Zircon U–Pb SHRIMP dating of gneissic basement of the
1221 Dom Feliciano Belt, southernmost Brazil. J South Am Earth Sci 13, 739–750.
1222 https://doi.org/10.1016/S0895-9811(00)00058-4

1223   Lena, L.O., Pimentel, M.M., Philipp, R.P., Armstrong, R., Sato, K., 2014. The evolution of the
1224 Neoproterozoic São Gabriel juvenile terrane, southern Brazil based on high spatial resolution U-Pb ages
1225 and δ18O data from detrital zircons. Precambrian Res 247, 126–138.
1226 https://doi.org/10.1016/j.precamres.2014.03.010

1227   Lenz, C., 2006. Evolução metamórfica dos metapelitos da Antiforme Serra dos Pedrosas:
1228 condições e idades do metamorfismo 111. Master's Thesis. Universidade Federal do Rio Grande do
1229 Sul, Porto Alegre, Brazil.

1230   Lenz, C., Fernandes, L.A.D., McNaughton, N.J., Porcher, C.C., Masquelin, H., 2011. U–Pb
1231 SHRIMP ages for the Cerro Bori Orthogneisses, Dom Feliciano Belt in Uruguay: Evidences of a ~800Ma
1232 magmatic and ~650Ma metamorphic event. Precambrian Res 185, 149–163.
1233 https://doi.org/10.1016/j.precamres.2011.01.007

1234   Marques, J.C., Roisenberg, A., Jost, H., Frantz, J.C., Teixeira, R.S., 2003. Geologia e geoquímica
1235 das rochas metaultramáficas da antiforme Capané, suíte metamórfica Porongos, RS. Rev Bras
1236 Geociências 33, 83–94.

1237   Martil, M.M.D., 2016. O magmatismo de arco continental pré-colisional (790 ma) e a
1238 reconstituição espaço-temporal do regime transpressivo (650 ma) no Complexo Várzea Do Capivarita,
1239 Sul da Província Mantiqueira. PhD Thesis. Universidade Federal do Rio Grande do Sul, Porto Alegre,
1240 Brasil.

1241   Martil, M.M.D., Bitencourt, M. de F., Nardi, L.V.S., 2011. Caracterização estrutural e petrológica
1242 do magmatismo pré-colisional do Escudo Sul-rio-grandense: Os ortognaisses do Complexo
1243 Metamórfico Várzea do Capivarita. Pesqui em Geociencias 38, 181–201.

1244   Martil, M.M.D., Bitencourt, M. de F., Nardi, L.V.S., Schmitt, R. da S., Weinberg, R., 2017. Pre-
1245 collisional, Tonian (ca. 790 Ma) continental arc magmatism in southern Mantiqueira Province, Brazil:

Geochemical and isotopic constraints from the Várzea do Capivarita Complex. Lithos 274–275, 39–52. https://doi.org/10.1016/j.lithos.2016.11.011

Nardi, L.V.S., Bitencourt, M. de F., 2007. Magmatismo Granítico e Evolução Crustal no Sul do Brasil. 50 anos Geol - Inst Geociências da Univ Fed do Rio Gd do Sul 1, 125–141.

Oliveira, C.H.E., Chemale, F., Jelinek, A.R., Bicca, M.M., Philipp, R.P., 2014. U-Pb and Lu-Hf isotopes applied to the evolution of the late to post-orogenic transtensional basins of the dom feliciano belt, Brazil. Precambrian Res 246, 240–255. https://doi.org/10.1016/j.precamres.2014.03.008

Oriolo, S., Oyhantçabal, P., Wemmer, K., Heidelbach, F., Pfänder, J., Basei, M.A.S., Hueck, M., Hannich, F., Sperner, B., Siegesmund, S., 2016. Shear zone evolution and timing of deformation in the Neoproterozoic transpressional Dom Feliciano Belt, Uruguay. J Struct Geol 92, 59–78. https://doi.org/10.1016/j.jsg.2016.09.010

Oriolo, S., Oyhantçabal, P., Wemmer, K., Siegesmund, S., 2017. Contemporaneous assembly of Western Gondwana and final Rodinia break-up: Implications for the supercontinent cycle. Geosci Front 8, 1431–1445. https://doi.org/10.1016/j.gsf.2017.01.009

Oyhantçabal, P., Siegesmund, S., Wemmer, K., Presnyakov, S., Layer, P., 2009. Geochronological constraints on the evolution of the southern Dom Feliciano Belt (Uruguay). J Geol Soc London 166, 1075–1084. https://doi.org/10.1144/0016-76492008-122

Padilha, D.F., Bitencourt, M. de F., Nardi, L.V.S., Florisbal, L.M., Reis, C., Geraldes, M., Almeida, B.S., 2019. Sources and settings of Ediacaran post-collisional syenite-monzonite-diorite shoshonitic magmatism from southernmost Brazil. Lithos. https://doi.org/10.1016/j.lithos.2019.06.004

Paim, P.S.G., Chemale Junior, F., Wildner, W., 2014. ESTÁGIOS EVOLUTIVOS DA BACIA DO CAMAQUÃ (RS). Ciência e Nat 36, 183–193. https://doi.org/10.5902/2179460X13748

Patchett, P.J., Tatsumoto, M., 1980. Hafnium isotope variations in oceanic basalts. Geophys Res Lett.

Peel, E., Sánchez, L., Angelo, M., Basei, S., 2018. Journal of South American Earth Sciences Geology and geochronology of Paso del Dragón Complex (northeastern Uruguay): Implications on the evolution of the Dom Feliciano Belt (Western Gondwana). J South Am Earth Sci 85, 250–262. https://doi.org/10.1016/j.jsames.2018.05.009

Percival, J.J., Konopásek, J., Anczkiewicz, R., Ganerød, M., Sláma, J., Campos, R.S., Bitencourt, M.F., 2022. Tectono-Metamorphic Evolution of the Northern Dom Feliciano Belt Foreland, Santa Catarina, Brazil: implications for models of subduction-driven orogenesis. Tectonics. https://doi.org/10.1029/2021TC007014

Percival, J.J., Konopásek, J., Eiesland, R., Sláma, J., de Campos, R.S., Battisti, M.A., Bitencourt, M. de F., 2021. Pre-orogenic connection of the foreland domains of the Kaoko–Dom Feliciano–Gariep orogenic system. Precambrian Res 354. https://doi.org/10.1016/j.precamres.2020.106060

Pertille, J., Hartmann, L.A., Philipp, R.P., 2015a. Zircon U–Pb age constraints on the Paleoproterozoic sedimentary basement of the Ediacaran Porongos Group, Sul-Riograndense Shield, southern Brazil. J South Am Earth Sci 63, 334–345. https://doi.org/10.1016/j.jsames.2015.08.005

Pertille, J., Hartmann, L.A., Philipp, R.P., Petry, T.S., de Carvalho Lana, C., 2015b. Origin of the Ediacaran Porongos Group, Dom Feliciano Belt, southern Brazilian Shield, with emphasis on whole rock and detrital zircon geochemistry and U-Pb, Lu-Hf isotopes. J South Am Earth Sci 64, 69–93. https://doi.org/10.1016/j.jsames.2015.09.001

1288   Pertille, J., Hartmann, L.A., Santos, J.O.S., McNaughton, N.J., Armstrong, R., 2017.
1289 Reconstructing the Cryogenian–Ediacaran evolution of the Porongos fold and thrust belt, Southern
1290 Brasiliano Orogen, based on Zircon U–Pb–Hf–O isotopes. Int Geol Rev 59, 1532–1560.
1291 https://doi.org/10.1080/00206814.2017.1285257

1292   Philipp, R., Machado, R., 2002. O magmatismo granítico Neoproterozóico do Batólito Pelotas no
1293 sul do Brasil: novos dados e revisão da geocronologia regional. Rev Bras Geociencias 32, 277–290.

1294   Philipp, R.P., Bom, F.M., Pimentel, M.M., Junges, S.L., Zvirtes, G., 2016a. SHRIMP U-Pb age
1295 and high temperature conditions of the collisional metamorphism in the Várzea do Capivarita Complex:
1296 Implications for the origin of Pelotas Batholith, Dom Feliciano Belt, southern Brazil. J South Am Earth
1297 Sci 66, 196–207. https://doi.org/10.1016/j.jsames.2015.11.008

1298   Philipp, R.P., Lusa, M., Nardi, L.V.S., 2008. Petrology of dioritic, tonalitic and trondhjemitic
1299 gneisses from Encantadas Complex, Santana da Boa Vista, southernmost Brazil: paleoproterozoic
1300 continental-arc magmatism. An Acad Bras Cienc 80, 735–748. https://doi.org/10.1590/S0001-
1301 37652008000400013

1302   Philipp, R.P., Pimentel, M.M., Basei, M.A.S., Salvi, M., De Lena, L.O.F., Vedana, L.A., Gubert,
1303 M.L., Lopes, C.G., Laux, J.H., Camozzato, E., 2021. U–Pb detrital zircon dating applied to metavolcano-
1304 sedimentary complexes of the São Gabriel Terrane: New constraints on the evolution of the Dom
1305 Feliciano Belt. J South Am Earth Sci 110, 103409. https://doi.org/10.1016/j.jsames.2021.103409

1306   Philipp, R.P., Pimentel, M.M., Chemale Jr, F., 2016b. Tectonic evolution of the Dom Feliciano
1307 Belt in Southern Brazil: Geological relationships and U-Pb geochronology. Brazilian J Geol 46, 83–104.
1308 https://doi.org/10.1590/2317-4889201620150016

1309   Ramos, V.A., Cingolani, C., Junior, F.C., Naipauer, M., Rapalini, A., 2017. The Malvinas
1310 (Falkland) Islands revisited: The tectonic evolution of southern Gondwana based on U-Pb and Lu-Hf
1311 detrital zircon isotopes in the Paleozoic cover. J South Am Earth Sci 76, 320–345.
1312 https://doi.org/10.1016/j.jsames.2016.12.013

1313   Rapela, C.W., Fanning, C.M., Casquet, C., Pankhurst, R.J., Spalletti, L., Poiré, D., Baldo, E.G.,
1314 2011. The Rio de la Plata craton and the adjoining Pan-African/brasiliano terranes: Their origins and
1315 incorporation into south-west Gondwana. Gondwana Res 20, 673–690.
1316 https://doi.org/10.1016/j.gr.2011.05.001

1317   Regis, D., Warren, C.J., Mottram, C.M., Roberts, N.M.W., 2016. Using monazite and zircon
1318 petrochronology to constrain the P–T–t evolution of the middle crust in the Bhutan Himalaya. J
1319 Metamorph Geol 34, 617–639. https://doi.org/10.1111/jmg.12196

1320   Remus, M. V.D., Hartmann, L.A., McNaughton, N.J., Groves, D.I., Fletcher, I.R., 2000. The link
1321 between hydrothermal epigenetic copper mineralization and the Cacapava Granite of the Brasiliano
1322 cycle in southern Brazil. J South Am Earth Sci 13, 191–216. https://doi.org/10.1016/S0895-
1323 9811(00)00017-1

1324   Rivera, C.B., 2016. Construção do maciço sienítico Piquiri (609 a 683 Ma) por colocação
1325 sucessiva de pulsos de magma ultrapotássico e shoshonítico sob extensão no Escudo sul-rio-
1326 grandense. PhD Thesis. Universidade Federal do Rio Grande do Sul, Porto Alegre, Brasil.

1327   Rocha, B.C., Moraes, R., Möller, A., Cioffi, C.R., Jercinovic, M.J., 2017. Timing of anatexis and
1328 melt crystallization in the Socorro–Guaxupé Nappe, SE Brazil: Insights from trace element composition

1329 of zircon, monazite and garnet coupled to U–Pb geochronology. Lithos 277, 337–355.
1330 https://doi.org/10.1016/j.lithos.2016.05.020

1331 Rubatto, D., Chakraborty, S., Dasgupta, S., 2013. Timescales of crustal melting in the Higher
1332 Himalayan Crystallines (Sikkim, Eastern Himalaya) inferred from trace element-constrained monazite
1333 and zircon chronology. Contrib to Mineral Petrol 165, 349–372. https://doi.org/10.1007/s00410-012-
1334 0812-y

1335 Rubatto, D., Hermann, J., Buick, I.S., 2006. Temperature and bulk composition control on the
1336 growth of monazite and zircon during low-pressure anatexis (Mount Stafford, Central Australia). J Petrol
1337 47, 1973–1996. https://doi.org/10.1093/petrology/egl033

1338 Saalmann, K., Gerdes, A., Lahaye, Y., Hartmann, L.A., Remus, M.V.D., Läufer, A., 2011. Multiple
1339 accretion at the eastern margin of the Rio de la Plata craton: the prolonged Brasiliano orogeny in
1340 southernmost Brazil. Int J Earth Sci 100, 355–378. https://doi.org/10.1007/s00531-010-0564-8

1341 Saalmann, K., Hartmann, L.A., Remus, & M., 2005. Tectonic Evolution of Two Contrasting Schist
1342 Belts in Southernmost Brazil: A Plate Tectonic Model for the Brasiliano Orogeny. Int Geol Rev 4712,
1343 1234–1259. https://doi.org/10.2747/0020-6814.47.12.1234

1344 Saalmann, K., Hartmann, L.A., Remus, M. V.D., 2007. The assembly of West Gondwana—The
1345 view from the Rio de la Plata craton, in: Special Paper 423: The Evolution of the Rheic Ocean: From
1346 Avalonian-Cadomian Active Margin to Alleghenian-Variscan Collision. Geological Society of America,
1347 pp. 1–26. https://doi.org/10.1130/2007.2423(01)

1348 Saalmann, K., Remus, M.V.D., Hartmann, L.A., 2006. Structural evolution and tectonic setting of
1349 the Porongos belt, southern Brazil. Geol Mag 143, 59. https://doi.org/10.1017/S0016756805001433

1350 Sbaraini, S., B. Raposo, M.I., Bitencourt, M. de F., Rocha Tomé, C., 2020. Magnetic fabrics of
1351 the neoproterozoic piquiri syenite massif (Southernmost Brazil): Implications for 3D geometry and
1352 emplacement. J Geodyn 134, 101691. https://doi.org/10.1016/j.jog.2019.101691

1353 Schaltegger, U., Davies, J.H.F.L., 2017. Petrochronology of Zircon and Baddeleyite in Igneous
1354 Rocks: Reconstructing Magmatic Processes at High Temporal Resolution. Rev Mineral Geochemistry
1355 83, 297–328. https://doi.org/10.2138/rmg.2017.83.10

1356 Soret, M., Larson, K.P., Cottle, J.M., Smit, M., Johnson, A., Shrestha, S., Ali, A., Faisal, S., 2019.
1357 Mesozoic to Cenozoic tectono-metamorphic history of the South Pamir–Hindu Kush (Chitral, NW
1358 Pakistan): Insights from phase equilibria modelling, and garnet–monazite petrochronology. J
1359 Metamorph Geol 37, 633–666. https://doi.org/10.1111/jmg.12479

1360 Stevens, L.M., Baldwin, J.A., Cottle, J.M., Kylander-Clark, A.R.C., 2015. Phase equilibria
1361 modelling and LASS monazite petrochronology: P-T-t constraints on the evolution of the Priest River
1362 core complex, northern Idaho. J Metamorph Geol 33, 385–411. https://doi.org/10.1111/jmg.12125

1363 Thirlwall, M.F., Anczkiewicz, R., 2004. Multidynamic isotope ratio analysis using MC–ICP–MS
1364 and the causes of secular drift in Hf, Nd and Pb isotope ratios. Int J Mass Spectrom 235, 59–81.
1365 https://doi.org/10.1016/j.ijms.2004.04.002

1366 Vidal, O., Parra, T., Trotet, F., 2001. A thermodynamic model for FE-MG aluminous chlorite using
1367 data from phase equilibrium experiments and natural pelitic assemblages in the 100 to 600 C, 1 to 25
1368 kb range. Am J Sci 301, 557–592. https://doi.org/10.2475/ajs.301.6.557

1369 Vieira, D.T., Koester, E., Ramos, R.C., Porcher, C.C., D'Ávila Fernandes, L.A., 2020. SHRIMP
1370 U-Pb zircon ages for the synkinematic magmatism in the Dorsal de Canguçu Transcurrent Shear Zone,

Dom Feliciano Belt (Brazil): Tectonic implications. J South Am Earth Sci 100, 102603. https://doi.org/10.1016/j.jsames.2020.102603

Walczak, K., Anczkiewicz, R., Szczepański, J., Rubatto, D., Košler, J., 2017. Combined garnet and zircon geochronology of the ultra-high temperature metamorphism: Constraints on the rise of the Orlica-Śnieżnik Dome, NE Bohemian Massif, SW Poland. Lithos 292–293, 388–400. https://doi.org/10.1016/j.lithos.2017.09.013

Warren, C.J., Greenwood, L. V., Argles, T.W., Roberts, N.M.W., Parrish, R.R., Harris, N.B.W., 2019. Garnet-monazite rare earth element relationships in sub-solidus Metapelites: A case study from Bhutan. Geol Soc Spec Publ 478, 145–166. https://doi.org/10.1144/SP478.1

Werle, M., Hartmann, L.A., Queiroga, G.N., Lana, C., Pertille, J., Michelin, C.R.L., Remus, M.V.D., Roberts, M.P., Castro, M.P., Leandro, C.G., Savian, J.F., 2020. Oceanic crust and mantle evidence for the evolution of Tonian-Cryogenian ophiolites, southern Brasiliano Orogen. Precambrian Res 351, 105979. https://doi.org/10.1016/j.precamres.2020.105979

White, R.W., Powell, R., Holland, T.J.B., Johnson, T.E., Green, E.C.R., 2014. New mineral activity-composition relations for thermodynamic calculations in metapelitic systems. J Metamorph Geol 32, 261–286. https://doi.org/10.1111/jmg.12071

Will, T.M., Gaucher, C., Ling, X.-X., Li, X.-H., Li, Q.-L., Frimmel, H.E., 2019. Neoproterozoic magmatic and metamorphic events in the Cuchilla Dionisio Terrane, Uruguay, and possible correlations across the South Atlantic. Precambrian Res 320, 303–322. https://doi.org/10.1016/j.precamres.2018.11.004

Yakymchuk, C., Clark, C., White, R.W., 2017. Phase Relations, Reaction Sequences and Petrochronology. Rev Mineral Geochemistry 83, 13–53. https://doi.org/10.2138/rmg.2017.83.2

Yavuz, F., Kumral, M., Karakaya, N., Karakaya, M.Ç., Yıldırım, D.K., 2015. A Windows program for chlorite calculation and classification. Comput Geosci 81, 101–113. https://doi.org/10.1016/j.cageo.2015.04.011

Zvirtes, G., Philipp, R.P., Camozzato, E., Guadagnin, F., 2017. Análise estrutural do Metagranito Capané, Complexo Porongos, Cachoeira do Sul, RS. Pesqui em Geociências 44, 05. https://doi.org/10.22456/1807-9806.78250

1399   Appendix

1400

1401   1.   Lu–Hf isotope analysis

1402

1403   The Lu–Hf analyses were carried out at the Geological Institute of the Czech
1404   Academy of Sciences (chemistry) and Faculty of Science, Charles University (MC–
1405   ICP–MS). Garnet concentrate and whole-rock powder were weighted and mixed with
1406   the ^{176}Lu–^{180}Hf tracer solution. The samples were digested in closed 30ml Savillex
1407   teflon vials using combined acid attack (HF–HNO3–HCl). First, 0.5 ml HNO_3 + 2 ml HF
1408   (concentrated acids) was added to each sample and left to stand cold in closed vial for
1409   3 hours. Subsequently the bombs were opened and warmed on the hotplate to 90 ºC
1410   to evaporate Si and all acids. During this step the major minerals are attacked by the
1411   acids, most of the Si evaporates with the excess HF and the acids used in the following
1412   step thus have the opportunity to attack any resistant minerals without being depleted
1413   by reaction with major silicate phases. After complete evaporation, the mixture of 1.5
1414   ml HNO3 + 4.5 ml HF was added to the samples, left on a hotplate for two days at 160
1415   ºC, and then evaporated to dryness. After that, the samples were treated three times
1416   with 2 ml of concentrated HNO3 and evaporated to dryness. Next, 1 ml of 6 M HCl was
1417   added and immediately dried down. Finally, 8 ml of 6 M HCl was added and left on a
1418   hotplate at 160 ºC in a sealed beaker for 24 hours. The sample was then evaporated
1419   to dryness and 2 ml of 1 M HCl was added for subsequent column chemistry.

1420   The ion exchange column chemistry follows closely that of Anczkiewicz et al.
1421   (2004), which is a down-scale modification of the original setup of Patchett and
1422   Tatsumoto (1980). The separation of Hf (+ Ti) and Lu (+ Yb and LREE) fractions is first
1423   carried out on a standard cation exchange column using AG50W–X8 resin (200–400
1424   mesh size) and 1 M HCl–0.06 M HF (HFSE elution) and 2.5 M HCl (REE elution). The
1425   final purification of Hf from other HFSE and potentially interfering Lu and Yb takes
1426   place on a second column with Eichrom LN resin (50–100 μm) using technique based
1427   on Lee (1999) employing the mixture of 2 M HCl–0.1 M. The same column is then used
1428   for purification of Lu from other REEs and reduction of Yb in the Lu cut using 4M HCl.

1429   All measurements of Lu and Hf fractions were carried out using a THERMO
1430   Neptune multi-collector (MC) ICP–MS in the labs of the Faculty of Science, Charles
1431   University in Prague. Hafnium isotopic compositions were analysed in a static mode
1432   using Faraday cups with the following configuration: L4 – ^{172}Yb, L3 – ^{174}Yb, L2 – ^{175}Lu,
1433   L1 – ^{176}Hf, C – ^{177}Hf, H1 – ^{178}Hf, H2 – ^{179}Hf, H3 – ^{180}Hf, H4 – ^{182}W. Samples were

1434　aspirated to the instrument in 0.5 M HNO_3–0.25 M HF mixture using CETAC Aridus II

1435　desolvating nebulizer. The data acquisition procedure consisted of 40 integration

1436　cycles acquired over a period of ca. 6 min, followed by ca 5 min of washout with a

1437　mixture of 1.2 M HNO_3–0.5 M HF composition. The raw data were processed off-line

1438　using on-purpose-built calculation EXCEL spreadsheet. Repeated measurements of

1439　50 ppb JMC–475 standard over the period of analyses yield $^{176}Hf/^{177}Hf$ =0.282158 ± 7

1440　(2SE, n=7), which is in agreement within the error with the reference data (Chu et al.,

1441　2002). The spike stripping routine employing the ratio of $^{179}Hf/^{177}Hf$ iteratively

1442　deconvoluting to the natural value of 0.7325 (Patchett & Tatsumoto, 1980) and

1443　exponential mass-bias correction were used to obtain Hf isotopic composition and Hf

1444　concentration of the spiked samples.

1445　　　　For Lu isotopic analyses, Faraday cup configuration was as follows: L3 – ^{171}Yb,

1446　L2 – ^{172}Yb, L1 – ^{173}Yb, C – ^{174}Yb, H1 – ^{175}Lu, H2 – ^{176}Lu, H3 – ^{177}Hf. The sample

1447　aspiration was identical to the Hf measurements with the difference that HF-free acids

1448　were used for sample introduction (0.5 M HNO_3) and washout (1.5 M HNO_3). The data

1449　acquisition procedure consisted of 40 integration cycles acquired over a period of ca.

1450　3 minutes, followed by 4 min of washout. The raw data were processed off-line using

1451　on-purpose-built calculation EXCEL spreadsheet. Repeated measurements of natural

1452　Lu and Yb standard solutions were carried out to check the accuracy of the isotopic

1453　ratios measurements. The mass-bias correction (exponential law) of the spiked

1454　$^{176}Lu/^{175}Lu$ ratio was done using the natural Yb present in the sample (reduced in the

1455　3rd step of column chromatography to be ca. 1/10 of the amount of Lu to be suitable

1456　for mass bias correction while not causing excessive interference on ^{176}Lu mass) and

1457　the true ratio of $^{174}Yb/^{172}Yb$ = 1.45198 (Thirlwall & Anczkiewicz, 2004). The value of

1458　$^{176}Lu/^{175}Lu$ was then used to calculate the concentration of Lu in the samples. The

1459　accuracy of the method was checked by measurement of spiked aliquot of BCR–2

1460　reference material, which gave $^{176}Hf/^{177}Hf$ = 0.282859 ± 11, Hf = 5.00 ppm and Lu =

1461　0.514 ppm, which are in good agreement with published values of 0.282866 ± 11

1462　(Jweda et al., 2016), 4.8 ± 0.2 and 0.51 ± 0.02 (U.S. Geological Survey Certificate of

1463　Analysis, online source) respectively.

1464   2.   U–Pb monazite dating methodology

1465

1466   The samples were processed through a rock crusher and a hammer mill.
1467   Monazite and garnet were separated using a Wilfley table, a Frantz™ isodynamic
1468   magnetic separator and heavy liquids in the laboratories of the Department of
1469   Geosciences at the UiT The Arctic University of Norway in Tromsø. Subsequently,
1470   monazite grains were handpicked under a binocular microscope and selected grains
1471   were mounted in one-inch epoxy disks. In order to identify internal microstructures and
1472   possible compositional zoning, backscattered electron (BSE) images of monazite
1473   grains were made by Zeiss Merlin Scanning Electron Microscope (SEM) housed at the
1474   Faculty of Health Sciences of the same university.

1475   Monazite U–Th–Pb analyses by SIMS were performed on a Cameca IMS 1280
1476   ion probe at NordSIM at the Swedish Museum of Natural History in Stockholm.
1477   Operating parameters with regard to primary beam and mass resolution were similar
1478   to those used for zircon, broadly following the protocols described in (Gasser et al.,
1479   2015). The principal difference from zircon is that the monazite analyses employed
1480   both a smaller entrance slit (30 μm instead of 75 μm) to limit the secondary beam
1481   intensity, as well as a smaller energy slit (30 eV instead of 45 eV) together with a -30
1482   eV energy offset (applied via sample high voltage) on all the Pb, ThO_x and UO_x (where
1483   x = 0, 1 or 2) peaks of interest in order to minimize matrix differences in potentially
1484   chemically diverse monazite, and eliminate a small $ThNdO_2^{2+}$ interference on [204]Pb
1485   identified in earlier monazite studies (e.g. Kirkland et al., 2009). Secondary beam
1486   centring and optimization steps were performed as for zircon, but using the $CePO_2^+$
1487   matrix peak at nominal mass 203. U–Pb ratios were calibrated against a 425 Ma
1488   reference monazite from a metapelite of the Wilmington Complex, Delaware (sample
1489   44069, Aleinikoff et al., 2006), using a two-dimensional power law calibration
1490   approach, i.e. $(Pb/U)_{true} = f.(Pb/U)_{meas}, UO2/U_{meas})$ based on measurement of these
1491   ratios in the reference monazite.

492 Table 1. Representative microprobe analyses of minerals (The analyses were recalculated based on the following nr. of oxygen atoms:
493 Pl = 8O; Bt, Ms = 11O; Grt = 12O; Chl = 14O; St=24O). All analyses are available as supplementary data.

494

Sample	MAB51B					MAB56A						BD03						
Wt%	Bt	Ms	Chl	Grt Core	Grt Rim	Bt	Ms	Pl	Chl	Grt core	Grt rim	Bt	Ms	Chl	Plg	St	Grt core	Grt rim
SiO_2	35.61	45.77	26.08	36.73	37.06	33.75	45.11	68.04	24.71	37.29	37.02	35.60	45.75	24.74	59.95	27.65	36.62	36.84
TiO_2	1.64	0.34	0.11	0.12	0.02	1.90	0.30	0.05	0.07	0.13	0.07	1.19	0.45	0.13	0.03	0.67	0.04	0.03
Al_2O_3	19.24	35.87	23.96	20.94	20.99	20.49	36.90	20.32	21.66	20.87	21.39	19.91	37.13	23.29	24.63	53.66	20.76	20.84
FeO	18.73	0.98	24.16	23.50	25.51	22.90	1.03	0.19	31.60	29.50	35.13	18.03	0.73	23.48	0.08	13.37	29.01	33.56
MnO	0.25	0	0.50	13.39	11.74	0.07	0.02	-	0.20	6.86	1.11	0.10	0.04	0.17	0.00	0.19	8.78	3.41
MgO	9.70	0.63	13.97	1.67	1.79	6.82	0.35	0	10.10	1.29	1.98	10.01	0.56	15.02	0.00	1.73	1.92	2.72
CaO	0	0	0.01	3.17	2.80	0	0	0.10	0.03	4.00	2.82	0.00	0.01	0.02	6.95	0.04	2.66	2.20
Na_2O	0.10	0.94	-	-	-	0.16	1.24	11.97	0.02	-	-	0.16	1.23	0.00	7.95	0.03	0.05	0.00
K_2O	9.05	9.75	0.01	-	-	8.41	9.21	0.01	-	-	-	9.06	9.41	0.03	0.10	0.00	0.00	0.00
Cr_2O_3	-	-	0.01	-	-	0.10	0.07	-	0.08	0.08	0.01	0.09	0.18	0.03	0.00	0.06	0.02	0.01
ZnO	-	-	-	-	-	-	-	-	-	-	-	0.00	0.00	0.00	0.00	0.15	0.00	0.00
Total	94.33	94.29	88.93	99.62	99.94	94.58	94.26	100.68	88.55	100.03	99.52	94.12	94.84	86.92	99.68	97.55	99.87	99.60
Si	2.72	3.06	2.63	2.99	3.00	2.62	3.02	2.96	2.67	3.00	2.99	2.71	3.02	2.62	2.67	3.93	2.97	2.98
Al^{IV}	1.28	0.94	1.36	0.01	0	1.38	0.98	1.04	1.33	0	0.01	1.29	0.98	1.38	1.32	0.07	0.03	0.02
Al^{VI}	0.46	1.89	1.39	1.99	2.00	0.50	1.92	0	1.50	1.99	2.04	0.50	1.91	1.51	0	8.92	1.95	1.97
Cr	-	-	0	-	-	0.01	0	-	0.01	0.01	0	0.01	0.01	0	0	0.01	0	0
Fe^{3+}	0	0	-	0	0	0	0	-	-	0	0	0	0	-	0	0	0.08	0.04
Ti	0.01	0.02	0.01	0.01	0.01	0.11	0.02	0.001	0.01	0.01	0.01	0.07	0.02	0.01	0	0.07	0	0
Fe^{2+}	1.20	0.05	2.07	1.60	1.73	1.49	0.06	0.01	2.85	1.99	2.38	1.15	0.04	2.08	0	1.59	1.89	2.23
Mn	0.02	0	0.04	0.92	0.81	0.01	0	-	0.02	0.47	0.08	0.01	0.00	0.02	0	0.02	0.60	0.23
Mg	1.11	0.06	2.14	0.20	0.18	0.79	0.04	0	1.63	0.16	0.24	1.14	0.05	2.37	0	0.37	0.23	0.33
Ca	0	0	0.01	0.28	0.24	0	0	0.01	0.003	0.35	0.25	0	0.00	0	0.33	0.01	0.23	0.19
Na	0.01	0.12	0.00	-	-	0.02	0.16	0.99	0.01	-	-	0.02	0.16	0	0.69	0.01	0.01	0
K	0.88	0.83	0.00	-	-	0.83	0.79	0.001	-	-	-	0.88	0.79	0	0.01	0.00	0	0
Zn	-	-	-	-	-	-	-	-	-	-	-	0	0	0	0	0.02	0	0
X_{Mg}	0.48	0.53	0.51	0.11	0.11	0.35	0.39	-	0.36	0.07	0.09	0.50	0.58	0.53	-	0.19	0.11	0.13
X_{An}	-	-	-	-	-	-	-	0.99	-	-	-	-	-	-	0.32	-	-	-
X_{Grs}	-	-	-	0.09	0.08	-	-	-	-	0.12	0.08	-	-	-	-	-	0.07	0.06
X_{Alm}	-	-	-	0.53	0.57	-	-	-	-	0.67	0.81	-	-	-	-	-	0.67	0.75
X_{Py}	-	-	-	0.06	0.07	-	-	-	-	0.05	0.08	-	-	-	-	-	0.07	0.11
X_{Sps}	-	-	-	0.31	0.27	-	-	-	-	0.16	0.03	-	-	-	-	-	0.19	0.08

495

Table 2. Summary of estimated PT conditions and comparision of observed vs. modelled mineral compositional parameters.

	PT estimates					Mineral Compositions								
	T °C		P (kbar)			X_{Alm}	X_{Spss}	X_{Prp}	X_{Grs}	Grt X_{Mg}	Bt X_{Mg}	Chl X_{Mg}	X_{An}	St X_{Mg}
Sample	min max	*mean*	min max	*mean*										
MAB51B core	515 535	**525**	3.4 4.4	**3.9**	Obs.*	0.53	0.31	0.07	0.10	0.11	-	-	-	-
					Mod. ♠	0.51	0.31	0.07	0.11	0.12	-	-	-	-
					% diff.	-2	0	0	+1	+1	-	-	-	-
MAB51B rim	530 550	**540**	3.6 4.5	**4.1**	Obs.*	0.58	0.27	0.07	0.08	0.11	0.48	0.52	-	-
					Mod.	0.56	0.26	0.08	0.10	0.13	0.46	0.57	-	-
					% diff.	-2	-1	+1	+2	+2	-2	+5	-	-
MAB56A core	520 540	**530**	3.9 5.3	**4.6**	Obs.*	0.74	0.09	0.06	0.11	0.08	-	-	-	-
					Mod.♠	0.72	0.10	0.05	0.12	0.07	-	-	-	-
					% diff.	-2	+1	-1	+1	-1	-	-	-	-
MAB56A rim	550 570	**560**	4.5 5.5	**5.0**	Obs.*	0.79	0.04	0.08	0.09	0.09	0.34	0.37	1.00	-
					Mod.	0.78	0.04	0.09	0.09	0.10	0.35	0.44	0.89	-
					% diff.	-1	0	+1	0	+1	+1	+7	-11	-
BD03 core	525 545	**535**	4.1 4.5	**4.3**	Obs.*	0.65	0.20	0.07	0.08	0.10	-	-	-	-
					Mod.♠	0.65	0.20	0.08	0.07	0.11	-	-	-	-
					% diff.	0	0	+1	-1	+1	-	-	-	-
BD03 rim	560 580	**570**	4.7 6.5	**5.6**	Obs.*	0.73	0.10	0.10	0.07	0.12	0.49	0.52	0.32	0.18
					Mod.♠	0.77	0.05	0.10	0.08	0.12	0.41	0.50	0.50	0.18
					% diff.	+4	-5	0	+1	0	-8	-2	+18	0

* Median values shown for observed mineral compositions ♠ Modelled mineral compositions calculated using mean PT estimates

Table 3. Summary of the Lu–Hf dating results.

Sample	Fraction	Weight (mg)	Lu (ppm)	Hf (ppm)	$^{176}Lu/^{177}Hf$	Error	$^{176}Hf/^{177}Hf$	Error	Age (Ma)
MAB51B	Grt1	60.80	24.11	3.65	0.9167	0.0458387	0.2934	0.0000031	
	Grt2	59.77	24.42	3.81	0.8879	0.0443961	0.2930	0.0000024	
	Grt3	60.23	23.61	4.19	0.7820	0.0391048	0.2917	0.0000039	
	Grt4+inc	60.83	26.93	6.49	0.5758	0.0287879	0.2895	0.0000028	662±13
	Grt5+inc	62.97	25.09	5.77	0.6026	0.0301315	0.2898	0.0000025	
	Grt6+inc	190.89	25.91	5.68	0.6323	0.0316155	0.2899	0.0000025	
	WR	31.75	0.73	6.77	0.0148	0.0007436	0.2823	0.0000027	
	WR	31.26	0.72	6.62	0.0151	0.0007551	0.2823	0.0000042	
MAB56A	Grt1	61.05	7.88	2.74	0.3981	0.0199052	0.2863	0.0000031	
	Grt2	60.18	7.60	2.68	0.3938	0.0196920	0.2863	0.0000048	
	Grt3	91.16	8.06	2.70	0.4144	0.0207188	0.2865	0.0000049	
	Grt4+inc	64.30	6.45	4.96	0.1805	0.0090225	0.2840	0.0000036	563±12
	Grt5+inc	208.00	7.13	5.08	0.1946	0.0097286	0.2842	0.0000025	
	Grt6+inc	192.72	7.26	5.00	0.2015	0.0100729	0.2842	0.0000043	
	WR	29.92	0.54	5.42	0.0137	0.0006862	0.2823	0.0000059	
	WR	31.47	0.53	5.37	0.0137	0.0006851	0.2823	0.0000035	
BD03	Grt1	100.80	12.15	3.97	0.4246	0.0212277	0.2868	0.0000017	
	Grt2	100.56	11.63	3.77	0.4280	0.0213986	0.2869	0.0000031	
	Grt3	123.17	12.54	3.87	0.4495	0.0224754	0.2871	0.0000035	
	Grt4	121.95	12.15	3.66	0.4606	0.0230301	0.2872	0.0000029	571±13
	Grt5	190.70	12.34	3.79	0.4510	0.0225523	0.2870	0.0000031	
	WR	30.13	0.42	4.31	0.0135	0.0006776	0.2824	0.0000028	
	WR	30.12	0.40	4.20	0.0131	0.0006550	0.2824	0.0000034	

All errors are 2 SE (standard errors) and relate to the last significant digits. Constants used for data reduction: $^{179}Hf/^{177}Hf=0.7325$ (Patchett & Tatsumoto, 1980) and the exponential law were used for mass bias correction of interfering Yb and Lu isotopes and isotopes of Hf; ^{176}Lu decay constant = 1.867×10^{-11} (Söderlund, 2004).

Table 4. Comparison of the P–T estimates from the Porongos and Passo Feio complexes presented in this paper with the data available in the literature.

Complex		Sample	Early garnet growth	Metamorphic peak	Garnet + whole rock age (Ma)	Monazite age (Ma)	Reference
Porongos	Eastern region	*MAB 51B*	*515–535 °C at 3.4–4.4 kbar*	*530–565°C at 3.6–4.5 kbar*	*662±13*	*614±6*	*This paper*
		MAB 52A	555–565 °C at 5.4–5.7 kbar	560–580 °C at 5.8–6.3 kbar	-	-	De Toni et al. (2021)
		CMP13		584 ± 50 °C at 5–6 kbar	658±26 (Rb–Sr, Ms–WR)	-	Lenz (2006)
		CMP54					
	Northwestern region	*MAB 56A*	*520–540 °C at 3.9–5.3 kbar*	*Ca. 550–570 °C at 4.5–5.5 kbar*	*563±12*	-	*This paper*
				370–480°C (retrogression)	-	*541±7*	
Passo Feio		*BD 03*	*525–545 °C at 4.1–4.5 kbar*	*560–580 °C at 4.7–6.4 kbar*	*571±13*	-	*This paper*
		BD 16C	490–500 °C at 2.5–3.3 kbar	500–510 °C at 5–6.4 kbar	-	-	Costa et al. (2021)
		BD 15	530–550 °C at 3.0–4.3 kbar	560–570 °C at 5–5.5 kbar	-	-	

Table 5. Summary of geochronological and geological data for rocks of the Porongos Complex presented in an inferred stratigraphic order.

	Detrital provenance interval	Main Provenance peaks	Depositional age	Associated Igneous rocks (protolith ages)	Main tectonic events	Metamorphic grade	Tectonic setting
Capané sequence	550 Ma – 3.2 Ga[6,9,13]	ca. 600 Ma, 770 Ma and 2.0-2.2 Ga[6,9,13]	650 – 540 Ma	600 Ma[10,13]	Metamorphic peak at ca. 560 Ma Retrogression and exhumation ca. 540 Ma	Anchi- to medium-grade (up to amphibolite facies)[1,6,9,13]	Syn-collisional to post-collisional[12,13]
Cerro da Árvore sequence	750 Ma – 3.4 Ga[3,4,7,8,9]	1.2–1.4, 2.0–2.2 Ga[3,4,7,8,9]	min. 810 Ma – max. 660 Ma	810 – 780 Ma[5,9,18]	Metamorphic peak at ca. 660 Ma Exhumation at ca. 615 Ma (in the east) Exhumation at ca. 540 Ma (in the west)	Low- to medium grade (up to lower-amphibolite facies)[1,5,8,12,17]	Pre-collisional (Mature arc-setting[12,16] or back-arc/rift[14])
Capané ultramafic rocks (interpreted as ophiolite fragments[2,11,15])				Older than 794 Ma[11]	794 – 715 Ma metassomatism[11] Obducted from 715 – 650 Ma[11]	Lower greenschist facies[15]	Pre-collisional – oceanic[11,15]
Encantadas Complex (Porongos basement)				2.2 Ga[5,19]	Regional metamorphism at ca. 2.0 Ga[20]	Medium grade (up to upper-amphibolite facies)[1,21]	Mature arc-setting[21]

References: 1 – Jost and Bitencourt (1980); 2 – Marques et al. (2003); 3 – Basei et al. (2008) 4 – Gruber et al. (2011); 5 – Saalmann et al. (2011) 6 – Pertille et al. (2015a); 7 – Pertille et al. (2015b); 8 – Gruber et al., (2016); 9 – Pertille et al. (2017); 10 – Zvirtes et al. (2017); 11 – Arena et al. (2018); 12 – Battisti et al. (2018); 13 – Höfig et al. (2018); 14 – Konopásek et al. (2020); 15 – Werle et al. (2020); 16 – De Toni et al. (2020); 17 – De Toni et al. (2021); 18 – Battisti et al. (submitted). 19 – Hartmann et al. (2003); 20 – Hartmann et al. (2000); 21 – Philipp et al. (2008)

6.3. Artigo 3

O artigo intilulado "*Unravelling major magmatic episodes from metamorphic sequences of the Dom Feliciano Belt central sector, Brazil – a comparative study of geochronology, elemental geochemistry, and Sr-Nd data*" de Battisti, M.A.; Bitencourt, M.F.; Nardi, L.V.S.; Florisbal, L.M.; Sláma, J.; Ackerman, L.; Padilha, D. F. foi submetido ao periódico *Lithos*, no dia 07/03/2022.

Acknowledgement of receipt of your submitted article

3 mensagens

em@editorialmanager.com <em@editorialmanager.com>   7 de março de 2022 às 22:48
Responder a: support@elsevier.com
Para: Matheus Ariel Battisti <matheus.ariel.battisti@gmail.com>

Re:Unravelling major magmatic episodes from metamorphic sequences of the Dom Feliciano Belt central sector, Brazil – a comparative study of geochronology, elemental geochemistry, and Sr-Nd data
  by Matheus Ariel Battisti; Maria de Fátima Bitencourt; Lauro Valentim Stoll Nardi; Luana Moreira Florisbal; Lukáš Ackerman; Jiří Sláma; Dionatan Ferri Padilha
  Regular Article

Dear Mr. Battisti,

Your submission entitled "Unravelling major magmatic episodes from metamorphic sequences of the Dom Feliciano Belt central sector, Brazil – a comparative study of geochronology, elemental geochemistry, and Sr-Nd data" (Regular Article) has been received by Lithos.

Please note that submission of an article is understood to imply that the article is original and is not being considered for publication elsewhere, Submission also implies that all authors have approved the paper for release and are in agreement with its content,

You will be able to check on the progress of your paper by logging on to https://www.editorialmanager.com/lithos/ as Author.

Your manuscript will be given a reference number in due course.

Thank you for submitting your work to this journal.

Kind regards,

Journal management
LITHOS

#AU_LITHOS#

To ensure this email reaches the intended recipient, please do not delete the above code

In compliance with data protection regulations, you may request that we remove your personal registration details at any time, (Use the following URL: https://www.editorialmanager.com/lithos/login.asp?a=r), Please contact the publication office if you have any questions,

Unravelling major magmatic episodes from metamorphic sequences of the Dom Feliciano Belt central sector, Brazil – a comparative study of geochronology, elemental geochemistry, and Sr-Nd data

Matheus Ariel Battisti[1*], Maria de Fátima Bitencourt[1], Lauro Valentim Stoll Nardi[1], Luana Moreira Florisbal[2], Lukáš Ackerman[3], Jiří Sláma[3], Dionatan Ferri Padilha[1]

1- Programa de Pós-graduação em Geociências, Instituto de Geociências, Universidade Federal do Rio Grande do Sul, Porto Alegre, Brazil

2- Programa de Pós-graduação em Geociências, Instituto de Geociências, Universidade Federal de Santa Catarina, Florianópolis, Brazil

3- Institute of Geology of the Czech Academy of Sciences, Prague, Czech Republic

* Corresponding author: Matheus Ariel Battisti, matheus.ariel.battisti@gmail.com

Address: Av. Bento Gonçalves, 9500 – Porto Alegre, Rio Grande do Sul state, Brasil. PPGGEO – UFRGS, Campus do Vale – Zip Code: 91501-970.

ABSTRACT

The geochemical and isotopic signatures of magmatic events preserved in deformed metasedimentary sequences may inform about the basin's geological setting and reconstruct its original stratigraphy. This paper discusses geochemical and Sr-Nd isotopic data available in the literature for the metavolcanic rocks interleaved with highly-deformed metasedimentary rocks in three metamorphic complexes from the Dom Feliciano Belt, central sector, southernmost Brazil: the high-grade Várzea do Capivarita, and the lower greenschist to amphibolite facies Porongos and Passo Feio complexes. We also provide new elemental and isotopic geochemical data for seven metavolcanic samples collected from the Passo Feio and Porongos complexes along with U–Pb LA-ICPMS zircon determinations for selected metavolcanic rocks. The dataset was initially sorted into three groups based on REE patterns: i) Group 1 - LREE enrichment over HREE (LaN/YbN ≈ 10) with negative Eu anomalies (Eu/Eu* = 0.38 to 0.86); ii) Group 2 - enhanced LREE enrichment (LaN/YbN = 12 to 44) and no Eu anomaly (Eu/Eu* = 0.94 to 1.07), and iii) Group 3 - negative Eu anomaly (Eu/Eu* ≈ 0.70), but higher LREEs absolute values (LaN/YbN ≈ 22). A basic metavolcaniclastic sample, referred to as *Bmvc*, displays a fourth pattern, as trace element data show that it does not belong to any of the three established groups. New U-Pb LA-ICPMS zircon analyses of two acidic metavolcanic rocks from the Passo Feio Complex yielded crystallisation age of the protolith at 580 ± 2 Ma (2σ). Magmatism in the three studied complexes can be grouped into two diachronous magmatic events. Group 1 samples account for a first magmatic event at 810–780 Ma in the Várzea do Capivarita and Porongos (Cerro da Árvore sequence) complexes. They represent a magmatic association produced from subduction-related sources, with significant contribution of crustal materials, according to geochemical arguments expressed as $^{87}Sr/^{86}Sr_{(790\ Ma)}$ > 0.715 and $\varepsilon Nd_{(790\ Ma)}$ from -5 and -11 (up to -22). Groups 2 and 3 and Bmvc account for the second magmatic event at ca. 600 to 580 Ma as recorded in the Passo Feio and western Porongos (Capané sequence) complexes. Groups 2 and 3 rocks are interpreted to have been sourced from a subduction-related enriched mantle, but without major crustal contamination, as in a back-arc geological setting, as expressed by $^{87}Sr/^{86}Sr_{(580\ Ma)}$ = 0.7035–0.7050 and $\varepsilon Nd_{(580\ Ma)}$ > -10. For Bmvc, the data suggest a mantle-derived origin without a significant contribution of subduction-related sources, possibly indicating multiple sources for this newly-described and not yet fully reconstructed Ediacaran magmatism. Our comparative study leads to the novel

conclusion of a shared tectonic evolution between the Passo Feio Complex and the eastern Porongos Complex (Capané sequence) at ca. 600–580 Ma. Our data also corroborate a shared tectonic evolution between the western Porongos Complex (Cerro da Árvore sequence) and the Várzea do Capivarita Complex at ca. 810–770 Ma, as reported by previous authors.

1   *1. INTRODUCTION*

2

3   Magmatic events in sedimentary sequences, represented either as sills, dykes or

4   volcaniclastic successions, can provide elucidative information about the timing during

5   the deposition (e.g. Vidal and Alric, 1994; Tull et al., 2014). Moreover, elemental and

6   isotopic signatures of such magmatic members can provide first-order information

7   about the geological setting of the studied basin (DePaolo and Wasserburg, 1979;

8   Pearce et al., 1984). When deformed within the metasedimentary package, meta-

9   igneous rocks may also help construct the minimum timing of

10   deformation/metamorphism of the sequence (e.g. Martil et al., 2017; Percival et al.,

11   2021). Therefore, interbedded metavolcanic and metasedimentary successions

12   present in strongly deformed belts can be used to reconstruct the original stratigraphic

13   record that was commonly modified due to deformation and metamorphism (e.g. Vidal

14   and Alric, 1994; Tull et al., 2014; Martil et al., 2017; Percival et al., 2021).

15   In southeastern South America, the Dom Feliciano Belt is a long-lived

16   Neoproterozoic belt with counterparts in the Kaoko and Gariep belts on the African

17   side. Its original stratigraphic relations are strongly overprinted by later deformation.

18   Reconstructing the original stratigraphy of its deformed basins is difficult, as it is for

19   most of the ancient belts in the world. Consequently, the DFB medium to high-grade

20   metamorphic units discussed in this paper have been treated as unrelated for several

21   decades.

22   However, the recognition of volcanic rocks common to some highly contrasting

23   final products as granulites and greenschists or similar rock types in different structural

24   settings led Martil et al. (2017) to admit that such sequences might have been part of

25   a single basin. Structural studies carried out by Battisti et al. (2018) explored this

26   possibility further and first attempted to reconstruct the paleoenvironment by using also

27   the geochronological data reported by several authors (e.g. Saalmann et al., 2011;

28   Martil, 2016; Martil et al., 2017; Pertille et al., 2017) by which it became clear that both

29   volcanic protoliths were ca. 790 Ma old and closely related in composition. The

30   synchronicity of the magmatism and sedimentation between these high- and low-grade

31   metamorphic complexes was explored by several authors (e.g. Battisti et al., 2018; De

32   Toni et al., 2020b) for structural correlation. An elemental and isotope geochemistry

33   approach of these high- and low-grade sequences (Martil et al., 2017) hints further at

34   their correlation but does not present enough data to be statistically representative.

35   On the other hand, provenance studies of greenschist-facies supracrustal rocks
36   carried out by Pertille et al. (2015, 2017) and Höfig et al. (2018) reported the presence
37   of much younger zircons in parts of this supracrustal sequence, which put previous
38   results in check and would call for structural data to explain. The scarcity of integrative
39   approaches has thus hindered further correlations of these metamorphic sequences
40   that would consider aspects such as structural geology, elemental and isotope
41   geochemistry, petrology and geochronology.

42   This paper discusses geochemical and Sr-Nd isotopic data available in the
43   literature for the metavolcanic interleaved with metasedimentary rocks of three
44   metamorphic complexes from the Dom Feliciano Belt: the high-grade Várzea do
45   Capivarita Complex (i), and the lower greenschist to amphibolite facies Porongos (ii)
46   and Passo Feio (iii) complexes. We also present new major/trace element and Sr-Nd
47   isotope data for seven metavolcanic samples collected from the Passo Feio and
48   Porongos complexes along with U–Pb LA-ICPMS zircon determinations for selected
49   metavolcanic rocks. The integration of pre-existing and newly-obtained data allows us
50   to go further into the discussion of possible correlations among these metamorphic
51   sequences and their implications for the reconstruction of pre-orogenic environments
52   and the evolution of the DFB central sector.

53
54   *2.   GEOLOGICAL SETTING*
55
56   *2.1   Dom Feliciano-Kaoko-Gariep orogenic system*
57

58   The study area is located in the central sector of the Dom Feliciano Belt (DFB –
59   Fig. 1), which is the South American part of an N–S trending Neoproterozoic orogenic
60   system that also involves the Kaoko and Gariep belts along the Atlantic coast of
61   southern Africa. The main tectonic fabric of the whole orogenic system was developed
62   during the amalgamation of the Gondwana supercontinent (e.g. Rapela et al., 2011;
63   Ramos et al., 2017; Oriolo et al., 2017).

64   The Dom Felicano Belt (DFB) was formed during the Brasiliano/Pan-African
65   Orogenic Cycle, which started at ca. 840–770 Ma by igneous activity and associated
66   sedimentation interpreted by some authors as related to a continental arc (Koester et
67   al., 2016; Martil et al., 2017; Battisti et al., 2018; De Toni et al., 2020b) or as generated
68   in a back-arc/rift setting (Konopásek et al., 2018; Will et al., 2019). The main
69   contractional tectonic regime started at ca. 660–650 Ma (e.g. Gross et al., 2006, 2009;

70   Oyhantçabal et al., 2009; Lenz et al., 2011; Martil, 2016; Peel et al., 2018; Will et al.,
71   2019; De Toni et al., 2020a; Percival et al., 2021, 2022). However, the contraction
72   continued until at least 580–550 Ma, as recorded by ongoing crustal thickening and
73   associated metamorphism on both sides of the orogenic system (Frimmel and Frank,
74   1998; Goscombe and Gray, 2008; Höfig et al., 2018; Percival et al., 2022).

75   The DFB central sector outcrops in southernmost Brazil (Rio Grande do Sul state)
76   and is usually divided into Western, Central and Eastern domains (Fragoso-Cesar et
77   al., 1986; Fernandes et al., 1992; Basei et al., 2000) (Fig. 1). The Western and Central
78   domains represent the orogenic foreland, which is now extensively covered by late-
79   orogenic volcano-sedimentary deposits (Oliveira et al., 2014; Paim et al., 2014). The
80   Western Domain consists of Paleoproterozoic rocks (~2.5 to 2.0 Ga - Hartmann et al.,
81   2000), ophiolite remnants (~920-890 Ma - Arena et al., 2016) and juvenile, arc-related
82   rocks of the São Gabriel Block (~750-690 Ma - Lena et al., 2014) with associated
83   metasedimentary complexes. The Central Domain is represented mainly by the
84   Porongos Complex (PC), composed of volcano-sedimentary rocks (Jost and
85   Bitencourt, 1980; Saalmann et al., 2006; Pertille et al., 2017) of Tonian to Ediacaran
86   age (Saalmann et al., 2011; Pertille et al., 2017; Höfig et al., 2018) with locally exposed
87   Paleoproterozoic basement (~2.26-2.0 Ga - Hartmann et al., 2003; Philipp et al., 2008).

88   The Eastern Domain represents the hinterland of the Dom Feliciano Belt, and it
89   features mostly post-collisional granitic rocks (Bitencourt and Nardi, 1993, 2000;
90   Philipp and Machado, 2002). In southernmost Brazil, such Neoproterozoic (~650 and
91   580 Ma) granitic rocks contain roof pendants and crustal xenoliths with at least three
92   distinct ages: (i) Paleoproterozoic (2.2 and 2.0 Ga – Leite et al., 2000; Gregory et al.,
93   2015), (ii) Mesoproterozoic (ca 1.5 Ga – Chemale et al., 2011) and (iii) Tonian (ca. 770
94   - 800 Ma - Koester et al., 2016; Martil et al., 2017, 2011). The most extensive
95   occurrence of the ca. 770 - 800 Ma rocks is the high-grade Várzea do Capivarita
96   Complex (VCC) (Fig. 1, 2).

97
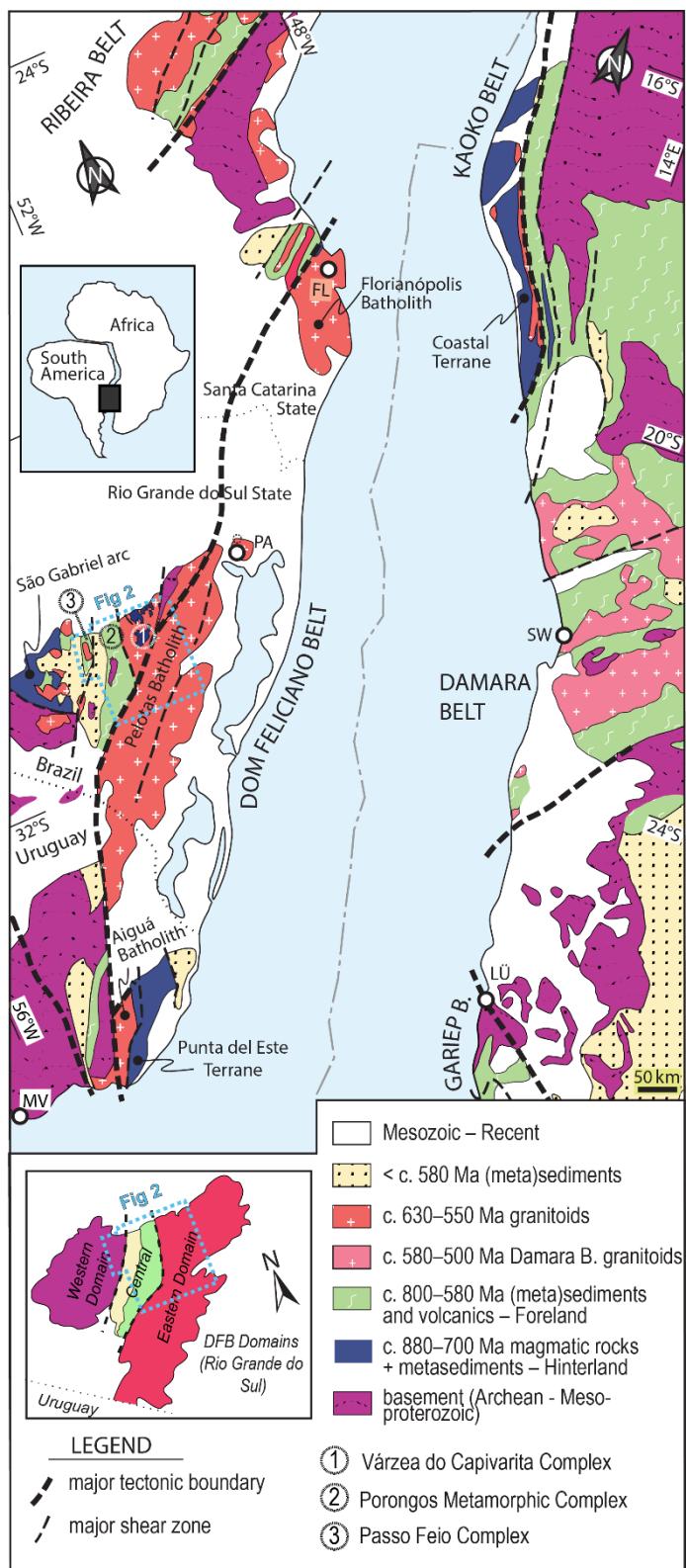
Figure 1. A) Overview geological map and main tectonic domains of the Dom Feliciano–Kaoko–Gariep orogenic system (modified after Bitencourt and Nardi, 2000 and Konopásek et al., 2018). Relative Position of Africa and South America is shown at 140 Ma - after Heine et al., 2013. Dom Feliciano Belt domains in the Rio Grande do Sul state are shown in the inset. Location of figure 2 is indicated. Cities: FL – Florianópolis, PA – Porto Alegre, MV – Montevideo.

105   ## 2.2   *Várzea do Capivarita Complex*

106

107   The Várzea do Capivarita Complex (VCC - Martil et al., 2011, 2017) is situated in
108   the DFB hinterland. It comprises part of the basement intruded by Late Neoproterozoic
109   granites in southernmost Brazil (Fig. 1). It is interpreted as a W-verging nappe thrust
110   onto the Central Domain (Battisti et al., 2018; De Toni et al., 2021). These well-
111   preserved roof pendants (Martil et al., 2017 - Fig. 2) comprise tectonically interleaved
112   granulite facies orthogneisses and paragneisses (Martil et al., 2011, 2017). According
113   to these authors, the orthogneisses are mostly tonalitic and related to a Tonian mature
114   magmatic arc (~790-780 Ma – U–Pb zircon). Paragneisses comprise metapelites and
115   calc-silicate rocks (Martil et al., 2011).

116   Two main deformation phases are described in the VCC and are related to one
117   single tectono-metamorphic event under granulite facies conditions (Gross et al., 2006;
118   Martil, 2016). The VCC gneisses were tectonically interleaved along a sub-horizontal
119   banding, with top-to-the-west shear sense (Martil et al., 2011; Martil, 2016). Dextral
120   strike-slip to slightly oblique vertical NNE-SSW shear zones progressively overprint the
121   thrusting structures, which are locally preserved (Martil, 2016). The granulite-facies
122   conditions achieved ca. 750 - 800 ºC and 3-5 kbar in the VCC metapelites (Gross et
123   al., 2006; Costa et al., 2020; De Toni et al., 2021) at 650 – 640 Ma (Martil, 2016).

124

125   ## 2.3   *Porongos Complex*

126

127   The Porongos Complex (PC) is part of the Dom Feliciano Belt foreland and
128   comprises Neoproterozoic supracrustal rocks metamorphosed at lower greenschist to
129   middle amphibolite facies (Jost and Bitencourt, 1980; Saalmann et al., 2006; Pertille
130   et al., 2017; Höfig et al., 2018; De Toni et al., 2021). The PC comprises
131   metasedimentary and metavolcanic rocks, some ultramafic lenses, and less often,
132   deformed granitoids (Jost and Bitencourt, 1980; Marques et al., 2003; Zvirtes et al.,
133   2017). Some authors interpret the ultramafic lenses as ophiolite remnants (e.g. Arena
134   et al., 2018; Werle et al., 2020).

135   The PC is divided into two tectonic-stratigraphic sequences – Cerro da Árvore
136   and Capané, of different geological evolution (Battisti, 2022). Apart from their
137   contrasting metamorphic evolution, the Cerro da Árvore and Capané sequences also
138   display variable ages of their associated intermediate to acidic metavolcanic rocks
139   (Saalmann et al., 2011; Zvirtes et al., 2017; Pertille et al., 2017; Höfig et al., 2018).

140 Cerro da Árvore is the oldest sequence, and its pre-collisional sedimentation is
141 associated with ca. 810-780 Ma metavolcanic rocks, while the Capané sequence was
142 deposited in a syn- to late-collisional scenario and is interleaved with ca. 600 Ma
143 metavolcanic rocks (Battisti, 2022).

144
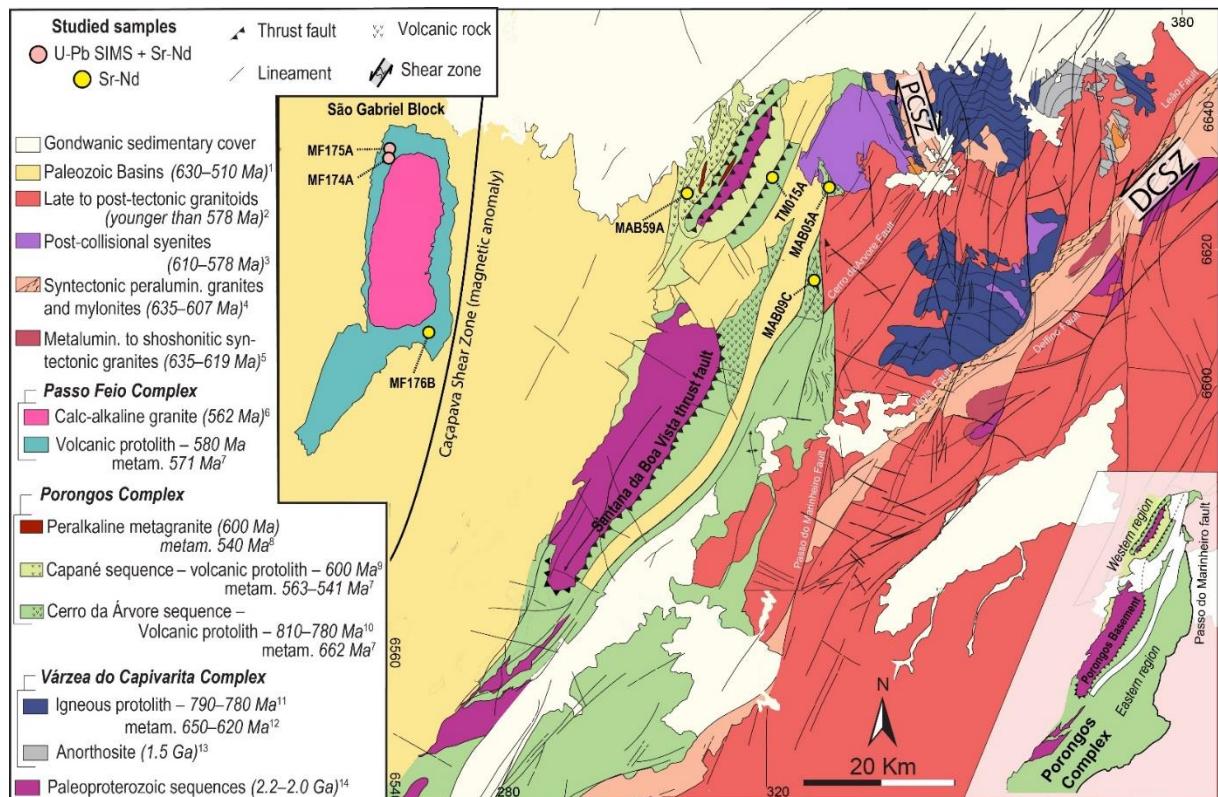
145
146

147 Figure 2. Geological map of the studied area with the sampled sites indicated. DCZS – Dorsal
148 do Canguçu Shear Zone; PCSZ – Passo das Canas Shear Zone. Regions of Porongos
149 Complex are shown inset. − References: 1- (Paim et al., 2014); 2-(Padilha et al., 2019); 3-(Rivera,
150 2016; Padilha et al., 2019); 4-(Bitencourt et al., 2015; Knijnik, 2018; Vieira et al., 2020); 5-(Knijnik, 2018;
151 Vieira et al., 2020); 6-(Remus et al., 2000); 7-Battisti et al submitted b; 8-(Philipp et al., 2016b); 9-(Höfig
152 et al., 2018); 10-(Saalmann et al., 2011; Pertille et al., 2017); 11-(Martil et al., 2017); 12-(Gross et al.,
153 2006; Chemale et al., 2011; Philipp et al., 2016a; Martil et al., 2017); 13-(Chemale et al., 2011); 14-
154 (Leite et al., 2000; Hartmann et al., 2003; Saalmann et al., 2011; Gregory et al., 2015).

155

156   The Porongos Complex is divided into Eastern and Western regions separated
157 by the main W-verging structure called Santana da Boa Vista thrust fault (Jost and
158 Bitencourt, 1980 - Fig. 2). Rocks of the Cerro da Árvore sequence are widespread over
159 the Eastern and Western Porongos regions, whilst the Capané sequence rocks are
160 only present in the Western region. The peak PT conditions of the PC Eastern region
161 were estimated at 560–580 °C, and 5.8–6.3 kbar (Lenz, 2006; De Toni et al., 2021)

162　and the metamorphic age was established at 662 ± 13 Ma (Lu-Hf garnet–whole-rock –
163　Battisti, 2022). In contrast, the metamorphic peak in the Western region occurred at
164　550 - 570°C and 4.5 - 5.5 kbar at 563 ± 12 Ma (Lu-Hf garnet-whole-rock – Battisti,
165　2022). Such metamorphic ages are associated with two different periods of crustal
166　thickening in the Dom Feliciano Belt.
167
168　***2.4　Passo Feio Complex***
169
170　　The Passo Feio Complex is part of the so-called São Gabriel Block, sited in the
171　Western Domain, that contains the largest volume of juvenile magmatic rocks in the
172　DFB (e.g. Saalmann et al., 2005, 2007; Lena et al., 2014; Arena et al., 2016, 2017).
173　According to Arena et al. (2016), some igneous rocks of this block may have been part
174　of an oceanic domain (ophiolites at 920–890 Ma), accreted to a juvenile arc (ca. 880
175　Ma Passinho event of Leite et al., 1998) that evolved towards a continental magmatic
176　arc (770–690 Ma; Lena et al., 2014). The ocean closure was interpreted to have
177　occurred at 690–650 Ma (Lena et al., 2014) or 650–600 Ma (Arena et al., 2017),
178　whereas late granitic magmatism took place at ca. 585 Ma (Arena et al., 2017). Arc-
179　related metaigneous rocks of the São Gabriel Block are surrounded by supracrustal
180　metamorphic rocks.
181　　The Passo Feio Complex is traditionally considered to be located at the eastern
182　border of the São Gabriel Block (Fig. 1, 2), separated from the easterly Porongos
183　Complex by a geophysical anomaly (Costa, 1997). However, the meaning of such
184　anomaly is unclear because it is covered by post-orogenic sediments of the Camaquã
185　Basin (Fig. 2). Furthermore, some authors interpreted this anomaly as a suture
186　(Fernandes et al., 1995; Costa, 1997), whereas others (e.g. Costa et al., 2021) interpret
187　it to represent a dextral transcurrent shear zone. As no further arguments confirm this
188　magnetic anomaly as a suture, the relation between the Passo Feio Complex (in the
189　Western Domain) and the units to the east (Central and Eastern domains) remains
190　uncertain.
191　　The PFC (Fig. 2) comprises phyllites, metapelitic schists, amphibole-bearing
192　rocks such as amphibolites, metagabbros and amphibole schists, acidic to
193　intermediate metavolcaniclastic rocks, magnesian schists and marble lenses
194　(Bitencourt, 1983; Bitencourt and Hartmann, 1984a, 1984b; Costa et al., 2021). The
195　age of the associated meta-igneous rocks is unknown. The PFC is part of an antiformal
196　structure of sub-horizontal axis plunging either NNE or SSW (Bitencourt, 1983) with

197   the 562 ± 8 Ma (SHRIMP U–Pb zircon - Remus et al., 2000) calc-alkaline Caçapava

198   Granite in its centre.

199   Three deformation events related to two metamorphic events were described in

200   the PFC (Bitencourt, 1983; Costa et al., 2021). The first two deformation events (D_1-

201   D_2) are progressive (Costa et al., 2021) and related to a ca. 570 Ma crustal thickening

202   episode, which is part of a long-lived transpressive deformation in the Dom Feliciano

203   Belt, starting at ca. 660–650 Ma (Battisti, 2022). The peak metamorphic conditions

204   (M_1) were estimated at 560–580 ºC and 5–6.4 kbar (Costa et al., 2021; Battisti, 2022).

205   On the other hand, the M_2 metamorphic event is closely related to the emplacement of

206   the Caçapava Granite at ca. 562 Ma. According to Costa et al. (2021), the

207   crystallisation of andalusite marks the effect of contact metamorphism caused by the

208   Caçapava Granite during M_2–D_3.

209

210   ***2.5. Available geochemical and Sr-Nd isotopic data for the studied meta-***

211   ***igneous rocks***

212

213   Geochemical studies of the Várzea do Capivarita Complex meta-igneous rocks

214   were performed by Martil et al. (2011, 2017). According to these authors, the ca. 790

215   Ma orthogneisses of the complex are metaluminous to peraluminous, calc-alkaline

216   rocks. Their composition and trace-element patterns are compatible with continental

217   arc-magmatism, with crustal contamination of parental magmas indicated by high

218   contents of Rb, Cs and Na_2O. This interpretation is corroborated by the isotopic studies

219   of Martil et al. (2017), which reveal $^{87}Sr/^{86}Sr_{(i)}$ ratios varying from 0.7163 to 0.7251 and

220    $\varepsilon Nd_{(790)}$ values from −7.2 to −10.1 for these rocks. According to the same authors, the

221   atypical, high $^{87}Sr/^{86}Sr$ values and their variable inherited zircon ages of 3.1, 2.0, 1.8,

222   1.6, 1.1, and 1.0 Ga (Martil, 2016) confirm the re-working of older crust and are

223   consistent with their mature-arc signature.

224   Elemental geochemical studies of the Porongos Complex metavolcanics were

225   performed in its western (Marques et al., 1998, 2003; Gollmann et al., 2008) and

226   eastern (Saalmann et al., 2006; Battisti et al., 2018) regions. On the other hand, Sr-Nd

227   Isotopic studies are far more limited and comprise only a few samples with Sr isotopic

228   data included (Saalmann et al., 2006; Martil et al., 2017). Nevertheless, the Porongos

229   Complex intermediate to acidic metavolcanic rocks (ca. 810–780 Ma) are assumed to

230   have formed in a continental magmatic arc (Gollmann et al., 2008; Battisti et al., 2018).

231   Among the samples from Western PC, three distinct groups of felsic rocks and
232   one group of mafic rocks were defined by Gollmann et al. (2008). However, the
233   presence of diachronous magmatic events (ca. 810-780 and 600 Ma) in the Porongos
234   Complex western region was not recognised at that time. Therefore, the meaning of
235   these different geochemical patterns remains unknown, as rocks associated with both
236   magmatic events might have been indistinctly compared. Moreover, no data has been
237   collected for the ca. 600 Ma Porongos magmatism.

238   Recent papers have suggested that part of the Porongos and Várzea do
239   Capivarita complexes may have shared similar sedimentary and volcanic history at
240   810–780 Ma (Martil et al., 2017; Battisti et al., 2018; De Toni et al., 2020b, 2021),
241   based on identical protolith ages, REE geochemistry and similar isotopic oxygen
242   signatures of meta-igneous rocks, structural evolution, and convergent PT-t evolution.
243   In addition, the overlapping Nd–Sr signatures of the VCC and one metavolcanic
244   sample of the PC Cerro da Árvore sequence was discussed by Martil et al. (2017).

245   Geochemical studies of the Passo Feio Complex meta-igneous rocks are rare
246   and focused only on the metabasic rocks so far (Bitencourt, 1983; Bicalho et al., 2019).
247   According to Bicalho et al. (2019), these basic rocks would have formed during a rifting
248   stage followed by an island arc situated in a restricted ocean environment. However,
249   the protolith ages of both basic and acidic Passo Feio metavolcanic rocks remain
250   unknown. Moreover, virtually no geochemical data has been published so far on the
251   intermediate to acidic metavolcanic rocks interleaved with the metasediments.

252

253   **3.   MATERIALS AND METHODS**

254

255   **3.1.   Data from the literature**

256

257   We have compiled published data for elemental and isotopic geochemical data
258   from metavolcanic rocks interleaved with the metasedimentary sequences from the
259   Passo Feio, Porongos, and Várzea do Capivarita complexes. The expressive majority
260   of data from Porongos and Várzea do Capivarita complexes display SiO_2 > 55 wt.%,
261   and such value was used as the lower threshold for the Passo Feio Complex samples.
262   Therefore, only intermediate to acidic metavolcanic rocks were considered in this
263   study. Samples with SiO_2 higher than 55 wt.% that lacked complete trace element data
264   were discarded, as those of Saalmann et al. (2006). However, two samples from their
265   paper were kept based on two criteria: i) such samples represent the most studied

266 region of the Porongos Complex (Santana da Boa Vista region); ii) although
267 incomplete, Ce, Eu, Tb, Yb and Lu data are available for these samples.

268   Regarding isotope data, as different papers used different laboratories for Sr-Nd
269 analysis, we have double-checked all the isotopic calculations based on the
270 information available in the papers. The recalculated values for each sample are found
271 in Tables 1 and 2 (original values are provided in supplementary files). Samples with
272 similar recalculated values were maintained, but we have discarded samples with
273 strong discrepancies in the recalculated values. Such discarded samples are K-04C
274 (Table 1) and BR-152/1 (Table 2). Gollmann et al. (2008) reported only Nd isotopic
275 values, and therefore their data do not appear in diagrams considering $^{87}Sr/^{86}Sr$ at one
276 of the axes.

277

278   **INSERT TABLE 1**

279

280   **INSERT TABLE 2**

281

282   *3.2.   Whole-rock geochemical analyses*

283

284   Elemental geochemistry data were obtained from four metavolcanic samples
285 from the Passo Feio Complex and one from the Porongos Complex. They were
286 analysed through inductively coupled plasma - optical emission spectrometry (ICP-
287 OES) and inductively coupled plasma mass spectrometer (ICP-MS) for major and trace
288 elements, respectively, at ActLab (Canada).

289

290   *3.3.   Sm-Nd and Rb-Sr isotope determination*

291

292   Four of the abovementioned samples, in addition to two metavolcanic samples
293 from Battisti et al. (2018) and one from Martil et al. (2017), were selected for Sm-Nd
294 and Rb-Sr analyses. Thus, Sm-Nd and Rb-Sr isotope compositions were determined
295 in seven metavolcanic samples from the Passo Feio and Porongos complexes. Two
296 analyses were carried out at the Laboratory of Isotopic Geology of Universidade
297 Federal do Rio Grande do Sul (LGI-UFRGS). The other five analyses were carried out
298 at the Institute of Geology of the Czech Academy of Sciences (IG CAS). Detailed
299 analytical procedures are given available in Appendix 1.

300

301   ***3.4.   U-Pb LA-ICPMS geochronology***

302

303   Two samples from the Passo Feio Complex northern region were processed

304   through a rock crusher and a hammer mill for the studied metavolcanic rocks. Zircon

305   was separated using a Frantz™ isodynamic magnetic separator and heavy liquids at

306   the Geosciences Institute of Universidade Federal do Rio Grande do Sul (UFRGS)

307   laboratories. Subsequently, zircon grains were handpicked under a binocular

308   microscope, and selected grains were mounted in one-inch epoxy disks and polished.

309   In order to identify internal microstructures and possible compositional zoning,

310   cathodoluminescence (CL) images of grains were made by JEOL EPMA housed at the

311   Charles University in Prague. The zircon U–Pb LA-ICPMS isotopic dating was

312   performed at the Institute of Geology of the Czech Academy of Sciences in Prague

313   (see the detailed analytical conditions provided in supplementary material).

314

315   ***4.   RESULTS***

316

317   ***4.1.   Petrography of Porongos and Passo Feio metavolcanic rocks***

318

319   Seven metavolcanic samples were studied at systematic locations to gather a

320   representative set of Porongos and Passo Feio rock types and fill the current gap of

321   Rb-Sr and Sm-Nd isotopic data (Fig. 2). In addition, two samples from this set were

322   selected for U–Pb geochronology (Fig. 3). The group comprises two samples from the

323   Passo Feio Complex northern region and one from its southern region, two samples

324   from the Eastern Porongos Complex region and two from the Western PC. The

325   petrography of metavolcanic rocks is briefly summarised below.

326

327   ***i) Northern Passo Feio Complex region:*** Sample MF-174A is a grey

328   metavolcanic rock from a rhyolitic layer in the metasedimentary package (Fig. 3a), with

329   a poorly-developed foliation marked by feldspar porphyroclasts set in a fine-grained,

330   granoblastic matrix and biotite-rich layers, with small amounts of white mica (Fig. 4a).

331   Feldspar forms porphyroclasts up to 1.5 mm-long, mainly potassic in composition, with

332   few plagioclase crystals. The feldspar often preserves igneous zoning at the centre,

333   with recrystallised margins. Opaque minerals and zircon are accessories.

334   Sample MF-175A is a grey hypabyssal rhyolitic to dacitic rock from a boudinaged

335   sill. It shows a weakly-deformed fabric (Fig. 3b) that displays a massif texture

336 composed of relic feldspar and quartz crystals set in a fine-grained granoblastic matrix
337 containing green biotite (Fig. 4b). K-feldspar and quartz form up to 1.5 mm-long relic
338 crystals. The matrix comprises granoblastic quartz and feldspar (Fig. 4b). Accessory
339 minerals are chlorite, titanite, opaque minerals and zircon.

340
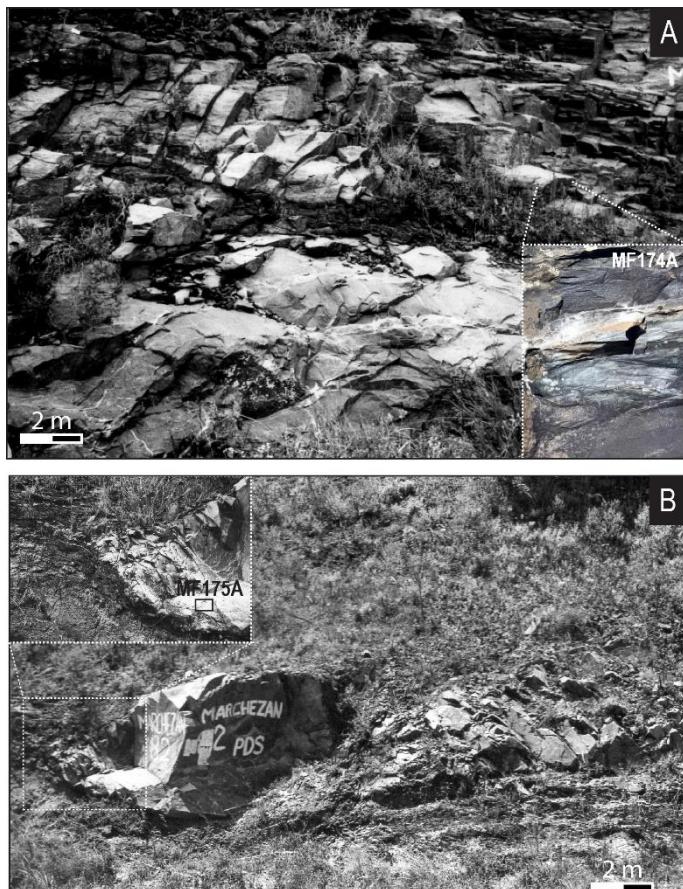
341
342

343 Figure 3. Outcrop features and location of samples from low-grade northern Passo Feio
344 Complex dated with U-Pb LA-ICPMS in zircon: a) rhyolitic metavolcanic layer, and (b)
345 metamorphosed and boudinaged sill of hypabyssal rhyolite.

346

347   *ii) Southern Passo Feio Complex region:* Sample MF-176B is a well-foliated
348 granonematoblastic, grey metavolcaniclastic rock of andesitic/trachytic composition,
349 with alternating irregular quartz-feldspathic and amphibole-rich seams (Fig. 4c). Up to
350 1 mm-sized porphyroclasts of feldspar, commonly with deformed twins, and rarely
351 quartz are preserved mainly in the fine-grained, quartz-feldspathic matrix. Opaque
352 minerals and titanite are accessory phases.
353   *iii) Western Porongos Complex region:* sample MAB59A is a dark-green, low-
354 grade meta volcaniclastic rock with a poorly-developed foliation. It is an albite-chlorite
355 schist in which a fine-grained, opaque-chlorite-rich matrix surrounds albite-rich pockets

356 containing larger, angular crystals of albite with wavy extinction (Fig. 4d). Within the
357 albite-rich pockets, some chlorite, opaque phases and rare apatite are also found. SEM
358 studies confirm the absence of quartz from these rocks.

359   TM015A is a light-grey, foliated, rhyolitic metavolcaniclastic rock with narrow,
360 alternating mica-rich lepidoblastic and quartz-rich, fine-grained levels and feldspar
361 fragments up to 0.5 mm-long (Fig. 4e). Feldspar and quartz are often recrystallised in
362 a fine-grained granoblastic matrix.

363
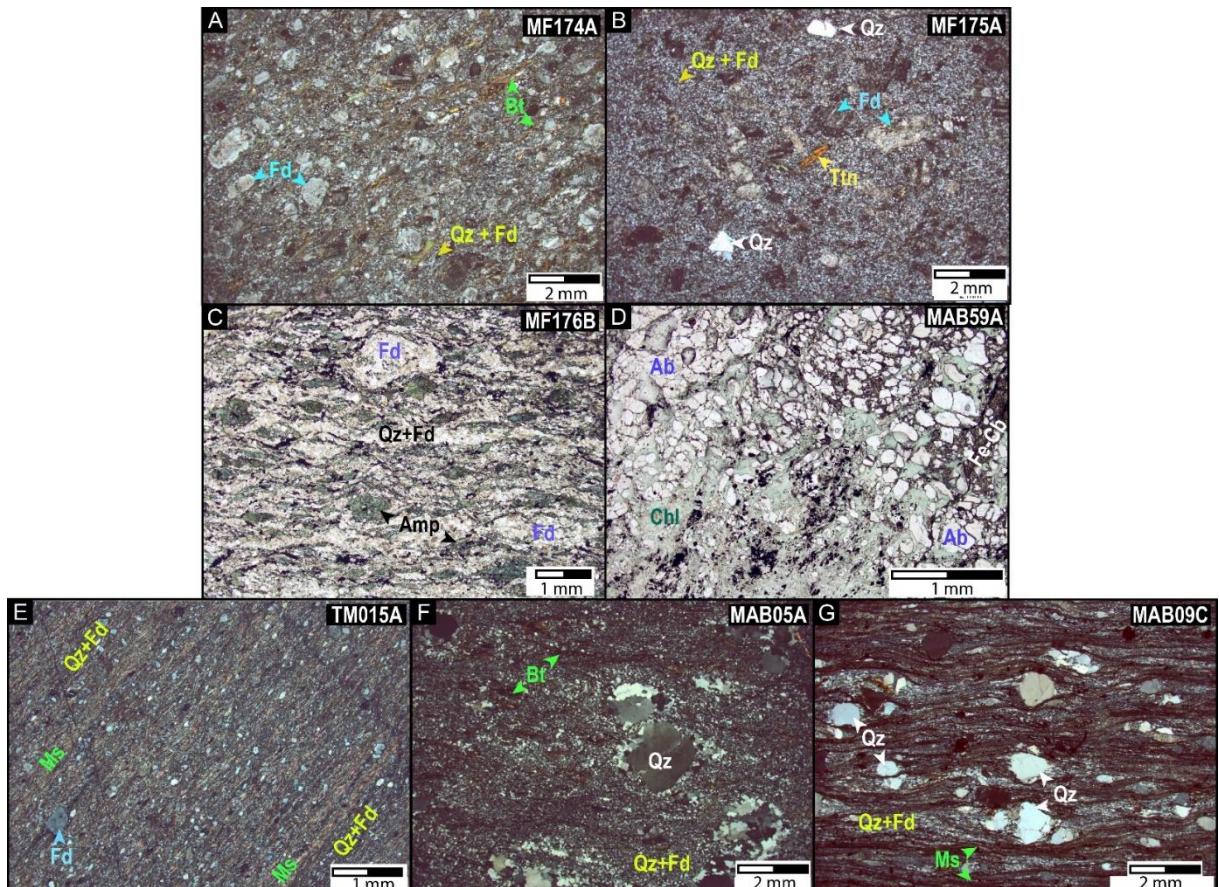
364
365

366 Figure 4. Petrographic aspects of the studied metavolcanic samples. Northern Passo Feio
367 Complex (a) rhyolitic metavolcanic rock, (b) metamorphosed hypabyssal rhyolite; (c) Southern
368 Passo Feio Complex metavolcaniclastic rock. Western Porongos Complex: (d) basic
369 metavolcanoclastic rock and (e) rhyolitic metavolcanic rock (e). Eastern Porongos Complex
370 rhyolitic metavolcanic rock (f) and (g). Mineral abbreviations (after Whitney and Evans, 2010):
371 Qz – quartz, Fd –feldspar, Bt – biotite, Amp – amphibole, Ab – albite, Chl – Chlorite, Fe-Cb –
372 Iron-carbonate, Ms – Muscovite.

373

374   *iv) Eastern Porongos Complex region:* Sample MAB05A is a well-foliated, grey
375 blastoporphyritic metavolcanic rock containing up to 2 mm-long crystals of blue quartz

376   and rare feldspar in a fine-grained (0.05 mm), granolepidoblastic matrix (Fig. 4f). The

377   matrix comprises quartz, feldspar and biotite, the latter mostly in mm-thick, irregular

378   layers (Fig. 4f).

379   MAB09C is a grey metavolcanic rock with well-developed mylonitic foliation

380   marked by 1 mm-long blue quartz porphyroclasts (rare feldspar) in a fine-grained

381   granolepidoblastic matrix composed of white mica, quartz and feldspar (Fig. 4g). The

382   porphyroclast-rich levels alternate with white mica-rich layers, occasionally containing

383   also biotite and chlorite. Tiny amphibole crystals are found in the matrix and rarely in

384   the phyllosilicate-rich layers.

385

386   **4.2.   Whole-rock chemistry and geochemical signatures of intermediate**

387   **to acidic metavolcanic rocks**

388

389   The measured whole-rock data for the metavolcanic rocks of this paper are

390   shown in Table 3. For the Passo Feio samples, SiO_2 ranges from 55.03 to 72.54 wt.%,

391   whereas for the Porongos Complex, SiO_2 are mainly from 67.00 to 71.74 wt.%. Such

392   values are in the range of the data selected from the literature for comparison (SiO_2 >

393   55 wt.%). The exception is sample MAB59A from western PC, which contains 52.4

394   wt.% silica, and the reason for maintaining it is its younger crystallisation age (600 Ma

395   – see discussion).

396

397   *INSERT TABLE 3*

398

399   The new data collected within the framework of this study is supplemented by the

400   compiled data given as supplementary material. Altogether, the full dataset is

401   composed of four samples from the Passo Feio Complex (this paper), twenty-seven

402   samples from the Porongos Complex, whereby twelve from its eastern region

403   (Saalmann et al., 2006; Martil et al., 2017; Battisti et al., 2018), and fifteen from the

404   western region (Gollmann et al., 2008; Martil et al., 2017), and twenty-four from the

405   Várzea do Capivarita Complex (Martil et al., 2017).

406   The whole set was analysed and grouped based on geochemical patterns, where

407   the REEs provide the best patterns chosen for grouping distinct samples. Each pattern

408   is placed in a *Group*, together with other distinctive geochemical characteristics, as

409   presented next. The REEs patterns normalised to Chondrite (Boyton, 1984) display

410   three contrasting distributions (Fig. 5a): i) *Group 1* characterised by LREE enrichment

411 over HREE (La$_N$/Yb$_N$ = ~10) with largely negative Eu anomalies (Eu/Eu* values mostly

412 from 0.38 to 0.86); ii) *Group 2* with enhanced LREE enrichment (La$_N$/Yb$_N$ = 12 to 44)

413 compared to *Group 1* and no Eu anomaly (Eu/Eu* = 0.94 to 1.07), and iii) *Group 3* with

414 negative Eu anomaly (Eu/Eu* of ca. 0.70), but higher LREEs absolute values than

415 those found in groups 1 and 2 (La$_N$/Yb$_N$ = ~22). Colour-labelled curves (Fig. 5) are

416 used to evaluate the role of SiO$_2$ content in groups 1 and 2 and demonstrate that SiO$_2$

417 variation is not responsible for the observed REE variability (Fig. 5a).

418   *Group 1* includes all samples from the eastern Porongos Complex region (Fig.

419 5b), eleven samples from the western Porongos Complex region (Fig. 5c), and all the

420 Várzea do Capivarita Complex samples (Fig. 5d). In comparison, *Group 2* comprises

421 five samples: two from the Passo Feio Complex northern region and three from the

422 Porongos Complex western region (Fig. 5a). The two samples from the PFC southern

423 region do not belong either to *group 1* or *2*, and they were labelled as *Group 3* (Fig.

424 5a). Moreover, the basic metavolcaniclastic sample MAB59A from western PC will be

425 treated individually as a fourth pattern, referred to as *Bmvc*, as despite roughly

426 following *Group 2*, further trace element data show that it does not belong to any of the

427 three established groups.

428   In *Group 1*, SiO$_2$ ranges from 56.49 to 75.53 wt%. (Fig. 6); total alkali contents

429 (Na$_2$O + K$_2$O) are 3.58–8.23 wt%, K$_2$O/Na$_2$O ratios range from 0.39 to 2.83 (with two

430 outliers of 18.1 and 23.7) and CaO/(Na$_2$O + K$_2$O) ratios lie between 0.06 and 1.23 (with

431 two outliers of 0.01 and 0.02). On the other hand, characterisation and assumptions

432 concerning *groups 2* and *3* need to be made with caution, considering the small

433 number of samples. Nevertheless, *Group 2* samples show a narrower SiO$_2$ range than

434 *Group 1*, from 63.07 to 72.54 wt% (Fig. 7). The total alkali contents (Na$_2$O + K$_2$O) are

435 5.76–8.14 wt%, K$_2$O/Na$_2$O ratios vary from 0.21 to 0.63, and CaO/(Na$_2$O + K$_2$O) ratios

436 lie between 0.06 and 0.37. The two *Group 3* samples comprise the least evolved set

437 of samples, with SiO$_2$ at 55.03 and 55.12 wt% (Fig. 7), with total alkali contents (Na$_2$O

438 + K$_2$O) at 7.45 and 7.34 wt%, K$_2$O/Na$_2$O ratios are from 0.20 to 0.21, and CaO/(Na$_2$O

439 + K$_2$O) ratios range between 0.74 and 0.75. *Bmvc* has SiO$_2$ = 52.40 wt.% (Fig. 7); total

440 alkali contents of 3.56 wt.%; K$_2$O/Na$_2$O ratio of 0.06 and CaO/(Na$_2$O + K$_2$O) ratio of

441 0.46.
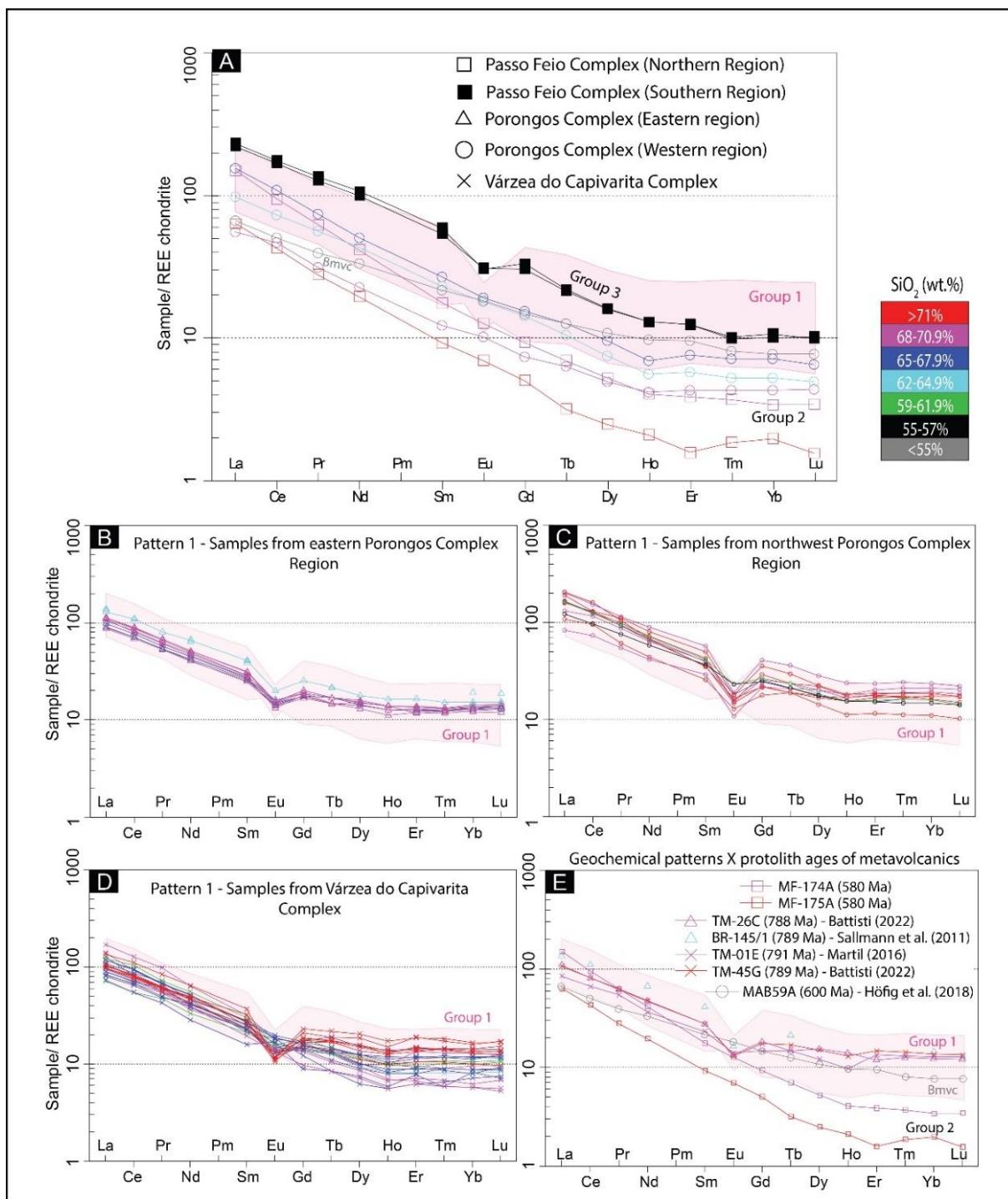
Figure 5. Rare Earth Element fractionation patterns normalised by chondrite (Boyton, 1984). A) Comparison of REE data of groups 1 (pink box), 2, 3 and Bmvc. *Group 1* consists of samples from (b) eastern, and (c) western regions of the Porongos Complex and from (d) Várzea do Capivarita Complex. E) REE patterns for metavolcanic samples with available crystallisation ages are highlighted. Colour-coded curves indicate SiO_2 content in all plots.
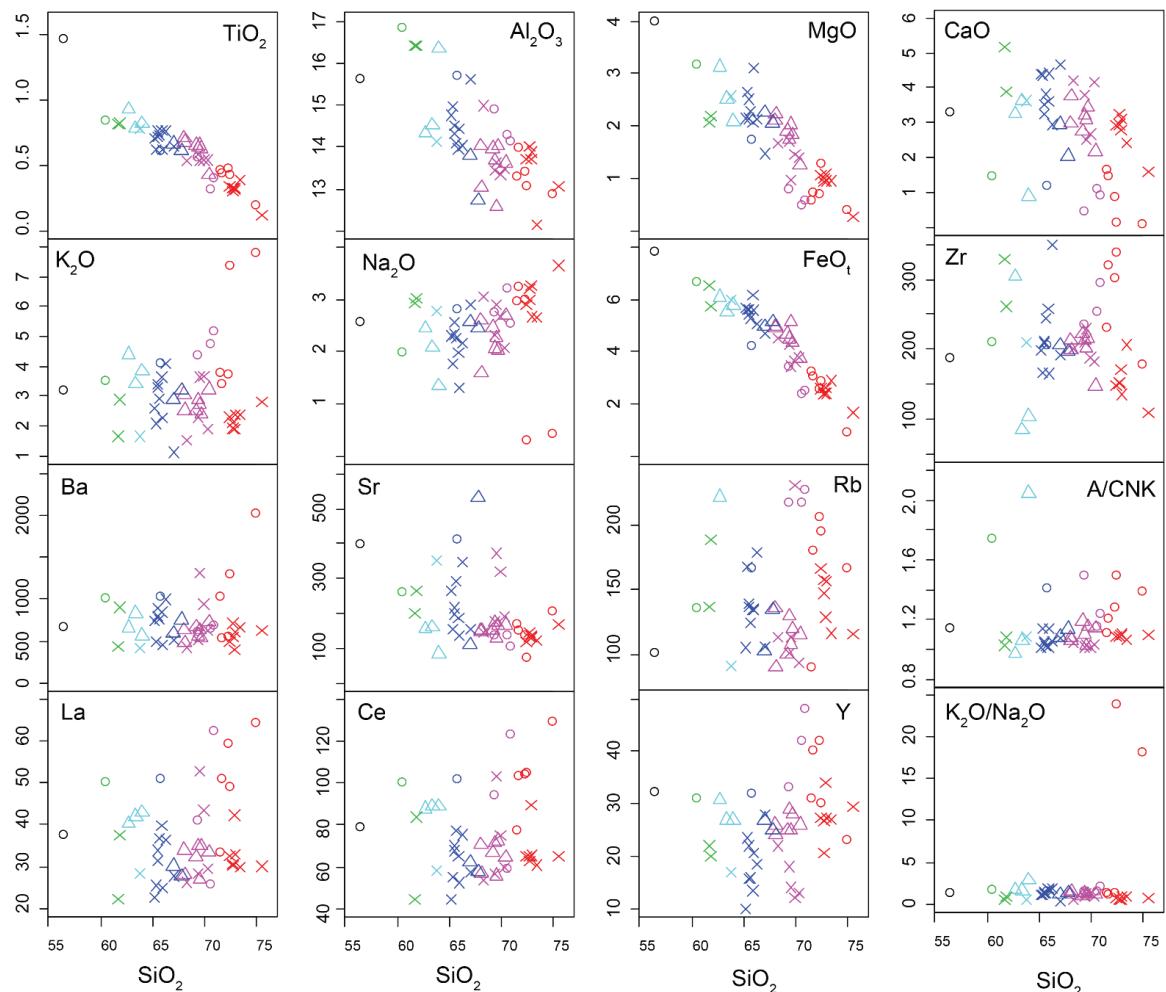
Figure 6. Major and some trace element variation diagrams using SiO_2 as differentiation index for *Group 1* metavolcanic rocks. Major elements in wt% and trace elements in ppm. Colour-code indicates SiO_2 content as in figure 5.

In the Harker diagrams for *Group 1* (Fig. 6), TiO_2, Al_2O_3, MgO, CaO and FeO_t decrease when SiO_2 content increases, whilst K_2O and Na_2O do not show any correlation. Regarding trace elements, Rb, La, Ce and Y show a slight increase in the more differentiated samples; Ba and Sr have moderate to low contents and do not correlate with differentiation. Zirconium shows moderate contents, increasing in the Western Porongos more differentiated samples. The K_2O/Na_2O values range between ~1 and 2 and do not vary with differentiation; two high-SiO_2 samples show high ratios. Harker diagrams for *Group 2* samples (Fig. 7) indicate a decrease of TiO_2, Al_2O_3, MgO, CaO, K_2O and FeO_t when SiO_2 content increases, whilst an opposite trend is noticed for Na_2O. Despite the low number of samples, a negative correlation between Zr, Rb and Y versus SiO_2 can be pointed out. Other trace elements do not show clear trends in the Harker diagrams. The two *Group 3* samples and the *Bmvc* were plotted together

467 with those of *Group 2* in Harker diagrams (Fig. 7) for further comparison of the data.

468 Their very contrasting Ca, Sr, and Zr contents, not justified by magmatic differentiation,

469 together with their different REE patterns and the lack of correlation in most trace-

470 element diagrams, indicate that *groups 2* and *3* samples do not belong to the same

471 magmatic series. Therefore, using the same criteria, it is possible to state that *Bmvc*

472 does not belong to any of the above groups.

473
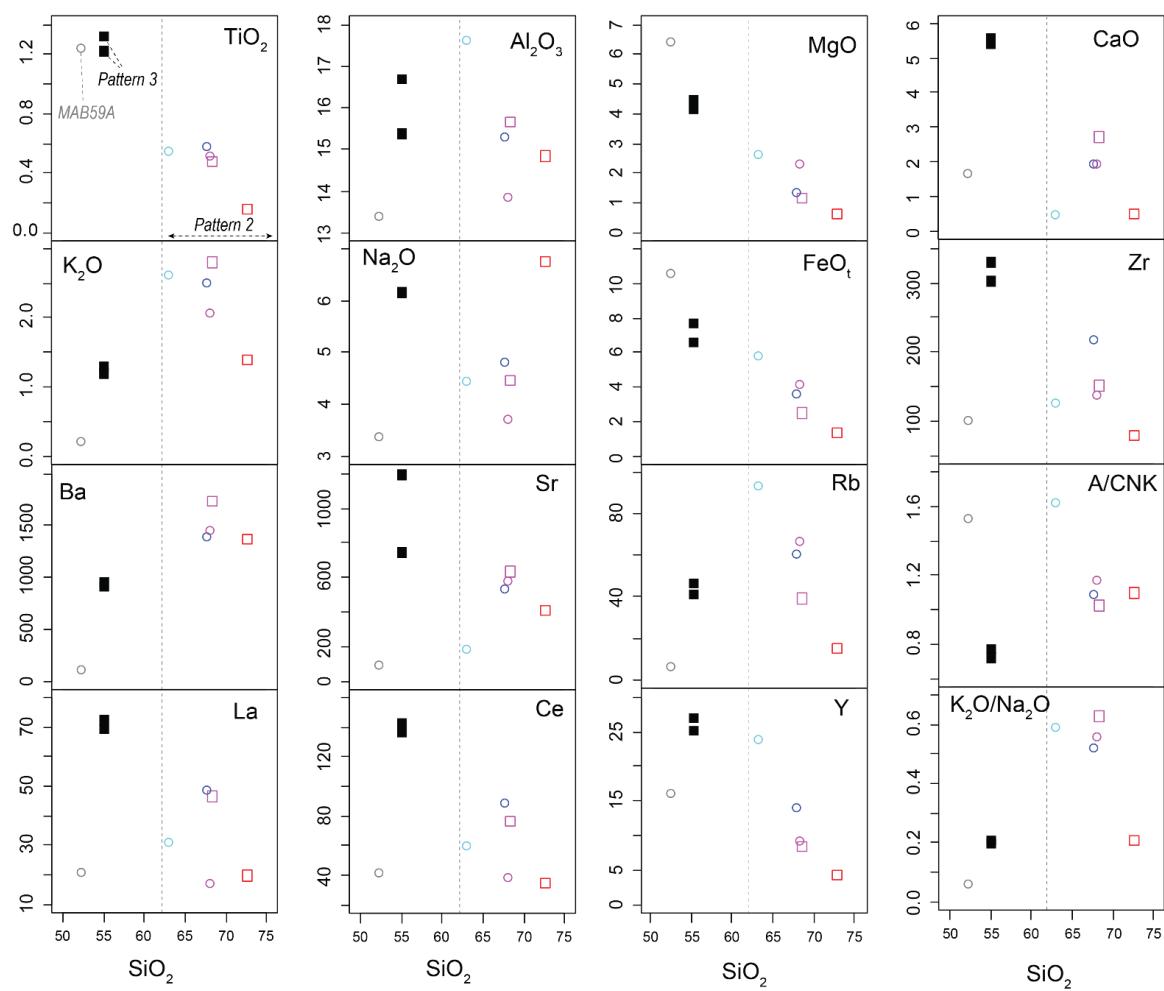
474
475

476 Figure 7. Major and some trace-element variation diagrams using SiO_2 as differentiation index

477 for *Group 2* metavolcanic rocks (coloured forms), 3 (black squares) and Bmvc (grey circle).

478 Data for these three different groups were plotted together to compare the data (see

479 discussion). Major elements in wt% and trace elements in ppm. Colour-code indicates SiO_2

480 content as in figure 5.

481

482 Samples from g*roups 1* and *2* are mostly dacites and rhyolites in the diagram of

483 Le Bas et al. (1986) (Fig. 8a, b). According to the same diagram, *Group 3* samples are

484 classified as trachy-andesites, and *Bmvc* as basaltic andesite. Because mobilisation

of elements such as LILE and Na during metamorphism can happen, we have employed some classification diagrams based on the ratios of relatively immobile elements, for instance, Zr/TiO_2 versus Nb/Y and SiO_2 versus Zr/TiO_2 (Winchester and Floyd, 1977). As shown in Fig. 8a, the resulting plots for *Group 1* samples corroborate the TAS results (Le Bas et al.,1986) since most samples (36 from 47) are classified as dacite to rhyodacite, suggesting that metamorphism did not significantly change their alkali contents. The same was observed for *Group 3* samples (Fig 8b). All *Group 2* samples show different classification in Winchester and Floyd (1977) compared to the TAS diagram (Fig 8b). Such data may indicate a significant change in alkali contents during the metamorphism of *Group 2* samples. *Bmvc* also displays a different classification, as it plots into the field of alkali-basalt (Fig 8b).
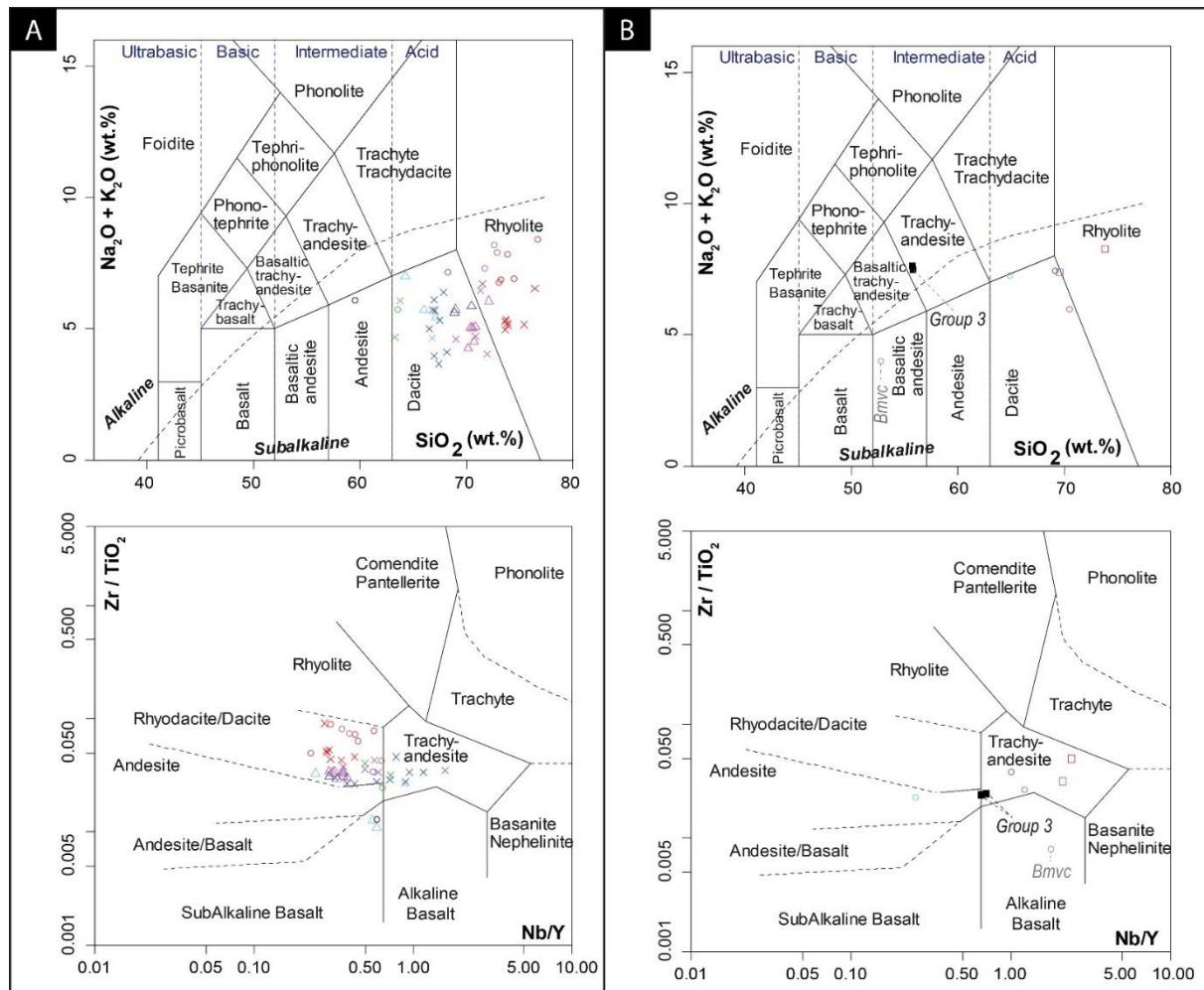
Figure 8. Discrimination diagrams for the studied metavolcanic rocks. At the top TAS diagram of Le Bas et al. (1986) for Group 1 rocks (a), groups 2, 3 and Bmvc (b). At the bottom, Winchester and Floyd's (1977) diagrams based on the ratios of relatively immobile elements for Group 1 (a) and groups 2, 3 and Bmvc (b).

4.3.   Zircon U-Pb geochronology

U-Pb LA-ICPMS geochronological data were obtained in two acidic metavolcanic samples of *Group* 2 from the northern Passo Feio Complex to constrain their protolith ages for the first time. Furthermore, as these rocks make up deformed lenses surrounded by metapelitic rocks, they may also help constrain the timing of the main deformation of the complex (Fig. 3a, b).

In sample MF174A, the zircon population is rather homogeneous. The grains are euhedral to subhedral with shapes ranging from stubby, almost equidimensional prisms to often more elongated prismatic forms (Fig. 9a) with sizes of ca. 50–200 μm. Cathodoluminiscence (CL) imaging reveals that well-developed oscillatory zoning dominates internal structures. Few grains show complex zoning patterns in the core (spot #107 and #116 – all spots are given in Supplementary data). However, the ages obtained are similar to those from the oscillatory zoning (Fig. 9c). Forty-four analyses were performed in forty-four different zircon grains, and in this dataset, thirty-four spots represent the most concordant analyses (discordance < 5% - Fig. 9c). A cluster of twenty-seven spots produces a mean age of 577 ± 1 Ma (2σ) (Fig. 9e) and presents Th/U ratios ranging from 0.49 to 2.06 (Supplementary data). Discarding the outlier values of such mean age (blue rectangles in Fig. 9e), twenty-two spots define a concordia age of 580 ± 1 Ma (2σ), which is very similar to the mean age of the cluster (Fig 9c). Thus, the concordia age is interpreted as the best estimate for the crystallisation of the metavolcanic protolith. Four spots with younger ages (#74, #91, #94, #98) and three with older ages (#92, #96, #120) have discordance lower than 5%, and they occupy the ages of ca. 540 Ma (green ellipses) and ca. 600 Ma (pink ellipses), respectively. Despite their similarity in Th/U ratios (0.57 to 2.07), the younger zircon grains show an internal striped zonation that strongly indicates perturbation of U–Pb systematics. Thus, we interpret these four younger ages as a consequence of Pb loss. We also observe some discordance for the three older grains, all obtained in central parts of euhedral grains, representing older grains with Pb loss or other U–Pb system disturbance.
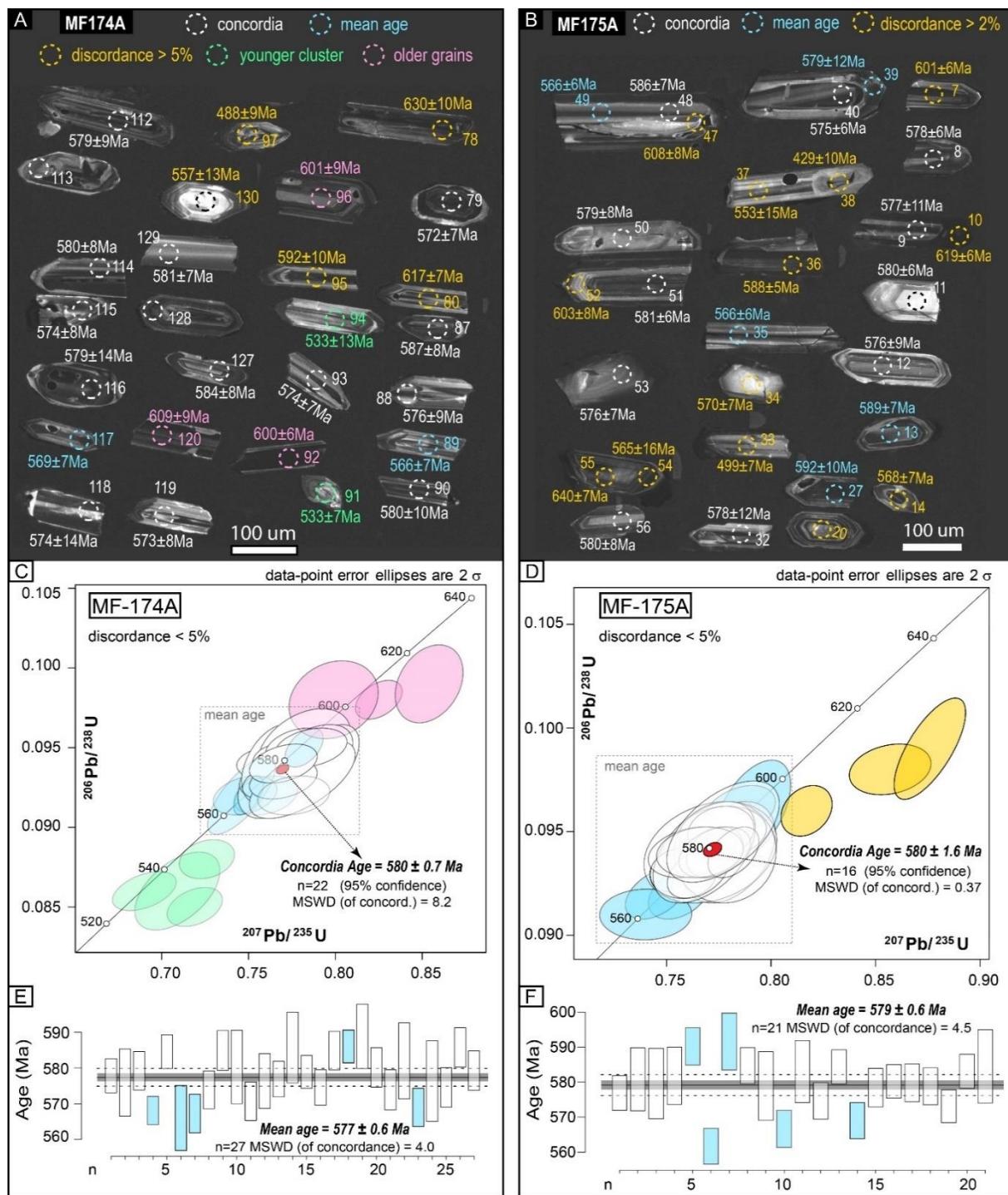
Figure 9. Cathodoluminescence images of representative zircon grains from sample MF-174A (a) and MF-175A (b) (ages are given as ^{206}Pb/^{238}U – complete information is available in Supplementary data). Concordia U–Pb diagram with less than 5% discordance zircon crystals for MF-174A (c) and MF-175A (d). Colour-coded spots distinguish each LA-ICPMS spot in zircon grains shown in (a) and (b), respectively. The concordia age is interpreted as the crystallisation age of both samples. The ^{207}Pb/^{206}Pb mean age for the main cluster centred at ca. 580 Ma in MF-174A (e) and MF-175A (f), the spots in blue were discarded for the calculation of concordia age in (c) and (d), respectively.

544   Zircon from sample MF175A has similar characteristics as in sample MF174A.
545   The zircon population is also rather homogeneous, and the grains are euhedral to
546   subhedral with elongate prismatic shapes and crystal sizes at ca 100–300 µm (Fig. 9b)
547   with well-developed oscillatory zoning observed in CL. However, acquired ages do not
548   vary through the oscillatory zoning regions (Fig. 9d). Forty-two analyses were
549   performed in thirty-three different zircon grains, and the most concordant analyses
550   (discordance < 5%) were displayed in a Wetherill U–Pb diagram (all spots are available
551   in Supplementary material). Such dataset comprises twenty-four spots, in which
552   twenty-one define a cluster with a mean age of 579 ± 1 Ma (2σ) and Th/U ratios from
553   0.29 to 1.55 (Fig. 9d, f). Discarding the outlier values of such mean age (blue
554   rectangles in Fig. 9f), sixteen spots define a concordia age of 580 ± 2 Ma (2σ), which
555   is very similar to the cluster mean age, and it is interpreted as the best estimate for
556   crystallisation of the metavolcanic protolith (Fig. 9d).

557

558   ***4.4.   Sr and Nd isotopic compositions***

559

560   The Sr-Nd isotopic data obtained for the studied metavolcanic rocks from Passo
561   Feio and Porongos complexes are given in Table 4. In the Passo Feio Complex, the
562   acidic to intermediate metavolcanic rocks show slight differences in Sr-Nd values when
563   comparing the northern (NPFC, 580 Ma) and southern (SPFC, 580 Ma) regions. The
564   ca. 580 Ma crystallisation age of the NPFC metavolcanic protolith was described
565   above. The acidic metavolcanic rocks from NPFC (580 Ma) have restricted and low
566    $^{87}Sr/^{86}Sr_t$ values of 0.7041 – 0.7035 and εNd_t *ca.* -10, with Mesoproterozoic TDMs
567   (1555 – 1579). On the other hand, the intermediate metavolcanic rock from SPFC,
568   whose age is still unknown but also estimated in 580 Ma for calculation purposes
569   (which is the only known age for the metavolcanic rocks in the complex), have slightly
570   higher $^{87}Sr/^{86}Sr_t$ values of 0.7064 and less negative εNd_t of -2.1, with Mesoproterozoic
571   TDM as well (1235 Ma).
572   The Porongos Complex Sr-Nd values are more homogeneous when considering
573   the Eastern (EPC, 790 Ma) and Western (WPC, 790 or 600 Ma) regions. The acidic
574   metavolcanic rocks from the EPC have high $^{87}Sr/^{86}Sr_t$ values of 0.7248 to 0.7305 and
575   εNd_t *ca.* -10, with Paleoproterozoic TDMs (2019 – 2080 Ma). In contrast, the WPC
576   samples comprise one acidic metavolcanic rock with 790 Ma that has $^{87}Sr/^{86}Sr_t$ values
577   of 0.7083, εNd_t -6.2 and Paleoproterozoic TDM of 1822 Ma; and one basic
578   metavolcaniclastic rock with 600 Ma (Höfig et al., 2018) with contrasting $^{87}Sr/^{86}Sr_t$

579 values of 0.7065, ℰNd$_t$ +1.2, and Neoproterozoic (Tonian) TDM of 1079 Ma. The

580 contrasting Sr-Nd isotopic values of the basic metavolcaniclastic (*Bmvc*) sample are

581 consistent with mantle-derived source rocks and also consistent with its

582 metavolcaniclastic origin, low SiO$_2$ content and the data from Höfig et al. (2018), which

583 present a nearly unimodal provenance peak of 600 Ma. Therefore, considering the

584 entire dataset permits us to interpret this sample as part of the WPC basic magmatism.

585 The new data were compared with data available in the literature for the PC and

586 VCC since there are no other data for PFC. The complete dataset will be integrated in

587 the Discussion section. A summary of the U–Pb dating and Sr-Nd isotopic results

588 obtained in this paper with sampling coordinates is shown in table 5.

589

590 ***INSERT TABLE 4***

591

592 ***INSERT TABLE 5***

593

594 ***5.   DISCUSSION***

595

596 ***5.1   Significance and implications of elemental and isotopic***

597 ***geochemical data for the studied complexes***

598

599 In the set of forty-seven *Group 1* samples, igneous crystallisation ages are known

600 for two Várzea do Capivarita Complex samples and two Porongos Complex eastern

601 region samples. They vary between ~810 and 780 Ma (Saalmann et al., 2011; Martil

602 et al., 2017; Battisti, 2022). As shown in Fig. 5e, these four specimens are probably

603 related to the same magmatic event, as indicated by their similar geochemistry, in

604 addition to the similar crystallisation ages and geological field relations. The

605 geochronological data from this study point out that the Passo Feio Complex *Group 2*

606 samples have a crystallisation age of 580 Ma. Three other *Group 2* samples are from

607 the western PC region, and their crystallisation ages are unknown. Such lack of data

608 in the western PC region also indicates that assumptions concerning *Group 2* samples

609 must be made with caution. The two *Group 3* samples are also of unknown age, whilst

610 the individual *Bmvc* has an igneous age of 600 ± 7 Ma Ma (Höfig et al., 2018 – Fig.

611 5e).

612 Based on this assumption, Sr-Nd data from *Group 1* rocks were recalculated to

613 initial isotopic ratios based on a crystallisation age of 790 Ma (Fig. 10). Aiming at a

614 consistent comparison, the original Sr-Nd data from Gollmann et al. (2008) and
615 Saalmann et al. (2006) were recalculated to 790 Ma (Table 1 and 2). On the other
616 hand, for *Group 2* rocks, Sr-Nd data were calculated using a crystallisation age of 580
617 Ma. Due to the geographical proximity (see Fig. 2) with this group, samples from *Group*
618 *3* were also calculated for 580 Ma, as no other crystallisation age is known for the
619 metavolcanic rocks of the region. For the individual basic metavolcanoclastic rock
620 (*Bmvc)*, the value used for isotope calculations was 600 Ma based on the age obtained
621 by Höfig et al. (2018).

622

623
624
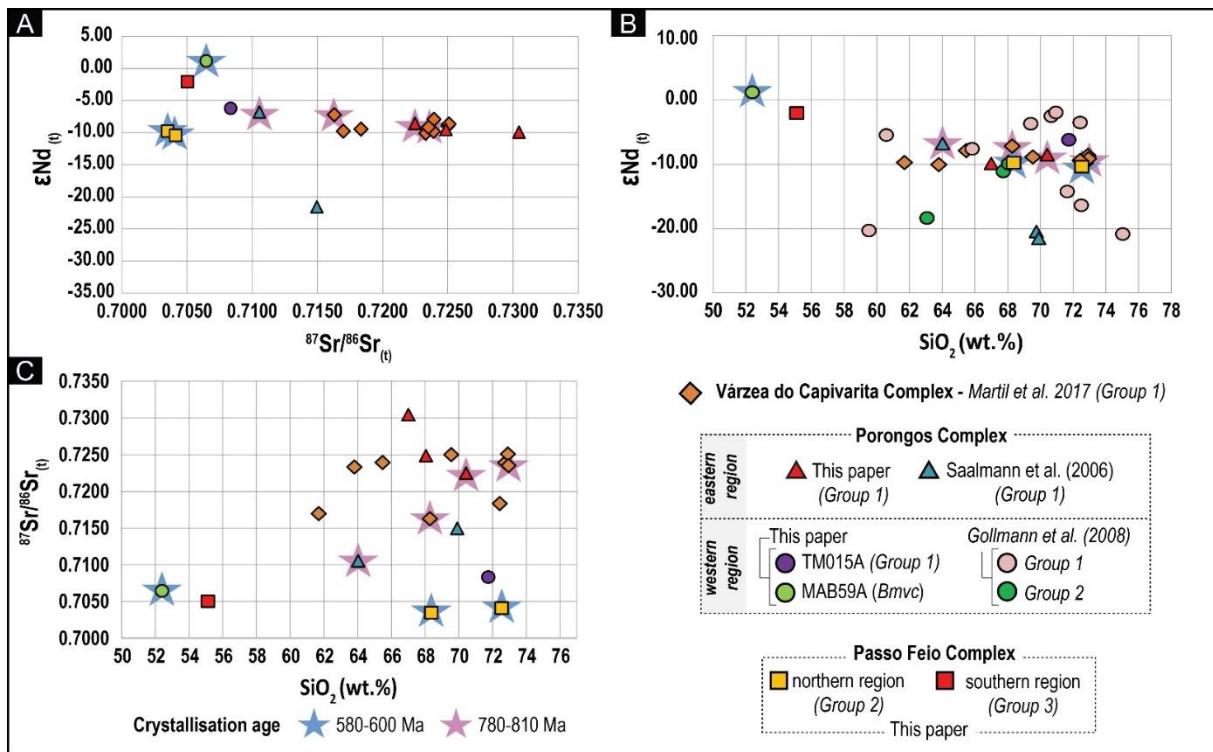
625 Figure 10. Whole-rock Rb–Sr and Sm-Nd isotope data for the Passo Feio, Porongos and
626 Várzea do Capivarita complexes meta-igneous rocks: (a) ENd_t relative to $^{87}Sr/^{86}Sr_i$; (b) ENd_t
627 relative to SiO_2; (c) $^{87}Sr/^{86}Sr_i$ relative to SiO_2; and (d) ENd_t relative to TDM.

628

629 In *Group 1* rocks, $^{87}Sr/^{86}Sr_{(790\ Ma)}$ values exhibit a wide range for the PC samples
630 (0.7083–0.7305) and a narrower range for VCC (0.7163 and 0.7251). The $ENd_{(790\ Ma)}$
631 values are mainly between -5 and -11 for both PC and VCC. However, $ENd_{(790}$ Ma)
632 values as high as -2 and as low as -22 are found only in the PC samples. Such
633 $^{87}Sr/^{86}Sr_{(790\ Ma)}$ values higher than 0.715 and $ENd_{(790\ Ma)}$ mainly from -5, and -11 (up to
634 -22) indicate an important contribution of crustal materials due to crustal melting or
635 assimilation of host rocks for the VCC and PC region ca. 790 Ma metavolcanic rocks.

636 However, two *Group 1* samples have slightly lower $^{87}Sr/^{86}Sr_{(790\ Ma)}$ - BR-143/1 and TM-
637 015, with 0.7106 and 0.7083, respectively. Such low values may indicate that crustal
638 contamination may have had some spatially-controlled variation in the PC or that the
639 ca. 790 Ma magmatism had different amounts of mantle contribution in different
640 regions, as BR-143/1 and TM-015 come from the eastern and western Porongos
641 regions, respectively.

642 The integration of geochronological, geochemical and Sr-Nd isotopic data allows
643 us to consider that *Group 1* samples belong to the same magmatic event, i.e., they are
644 probably coeval and produced by melting of the same sources at 810-780 Ma. The
645 relatively high Al_2O_3 contents of intermediate to acidic *Group 1* rocks, their subalkaline
646 character, trends illustrated in the FMA diagram, and the K_2O contents (Fig. 11a)
647 indicate that they are part of a medium- to high-K calc-alkaline series. Furthermore,
648 the REE patterns and trace elements are coherent with the hypothesis of *Group 1*
649 rocks representing magmatic associations produced from subduction-related sources,
650 probably along active continental margins (e.g. Martil et al., 2017), as suggested by
651 relatively high K_2O and Sr contents and by trace elements in Fig. 12a. Therefore, such
652 observations are coherent with the Sr-Nd data, which suggest an important
653 contribution of crustal materials for *Group 1* rocks. Lastly, when compared to OIB
654 (Oceanic Island Basalts), *Group 1* spidergrams (Fig. 13) show enrichment in LILE and
655 LREE relative to HFSE (Na, Ta, Hf, Zr) and HREE. In addition, Nb-Ti-Ta-P negative
656 anomalies are present in all samples from this group, which is a well-known signature
657 inherited from subduction-related sources (e.g. Briqueu et al., 1984; Pearce, 1995).

658 In *Group 2*, PFC samples exhibit $^{87}Sr/^{86}Sr_{(580\ Ma)}$ values of 0.7035 and 0.7041,
659 and $\varepsilon Nd_{(580\ Ma)}$ values of -10, whilst PC samples show variable $\varepsilon Nd_{(580\ Ma)}$ values of -
660 13, -14 and -21 (no Sr data). The only analysed *Group* 3 specimen displays $^{87}Sr/^{86}Sr_{(580}$
661 $_{Ma)}$ of 0.7050 and $\varepsilon Nd_{(580\ Ma)}$ = -2. The *Bmvc* presents $^{87}Sr/^{86}Sr_{(600\ Ma)}$ equal to 0.7065
662 and $\varepsilon Nd_{(600\ Ma)}$ = +1. Such values indicate that at least part of these rocks are related
663 to mantle-derived sources, with absent or low crustal assimilation, except for the ones
664 with strongly negative $\varepsilon Nd_{(580\ Ma)}$ values for which $^{87}Sr/^{86}Sr_{(580\ Ma)}$ data are not available
665 for further evaluation.

666 We emphasise that rocks of *Group*s 2 and 3 are represented by few samples,
667 which do not permit us to fully explore the nature of magmas, sources, and geotectonic
668 settings. Nevertheless, their moderate to high Al_2O_3 contents, subalkaline character,
669 and trends observed in the FMA diagram (Fig. 11b), together with their K_2O contents,
670 suggest their close relationship to acidic rocks of medium-K calc-alkaline series, or

671   magmatism with a strong crustal contribution. In addition to high Sr contents, such
672   aspects point out a subduction-related source for *groups 2* and *3* rocks. However, Sr-
673   Nd isotopic data suggest that at least part of *groups* 2 and 3 rocks are related to mantle-
674   derived sources. Additional trace element diagrams based on Nb, Ta and Y suggest a
675   rather volcanic arc environment for *Group 2* rocks (Fig. 11b). On the other hand, *Bmvc*
676   has low Al_2O_3 content and high MgO and FeO_t contents, characteristic of the tholeiite
677   series, as indicated by the FMA diagram.

678

679
680
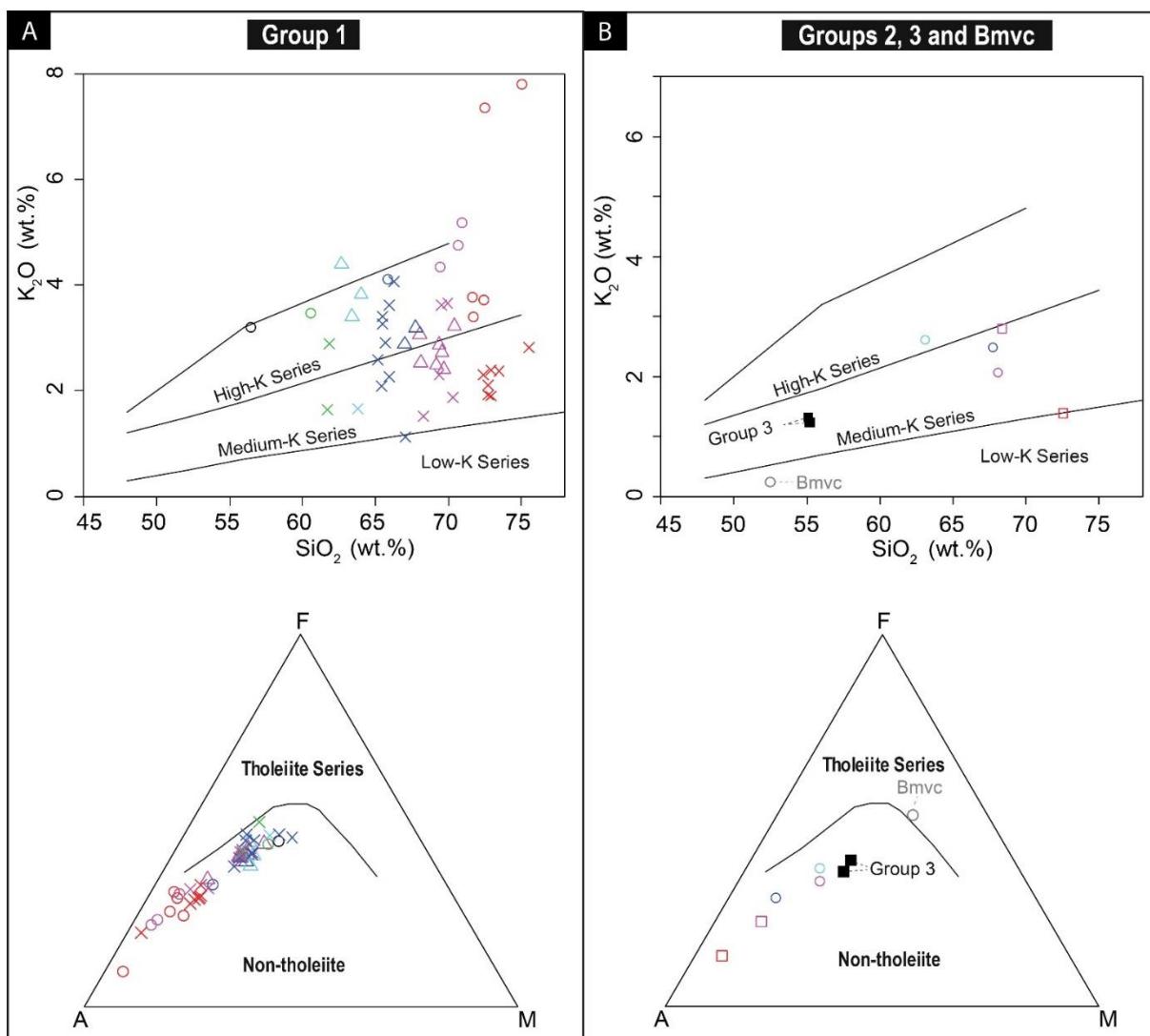
681   Figure 11. SiO_2 x K_2O diagram (modified from Peccerillo and Taylor, 1976), at the top; for
682   Group 1 (a), and groups 2, 3 and Bmvc (b). At the bottom, AFM diagram (modified after Irvine
683   and Baragar, 1971) for Group 1 (a) and groups 2, 3 and Bmvc (b).

684
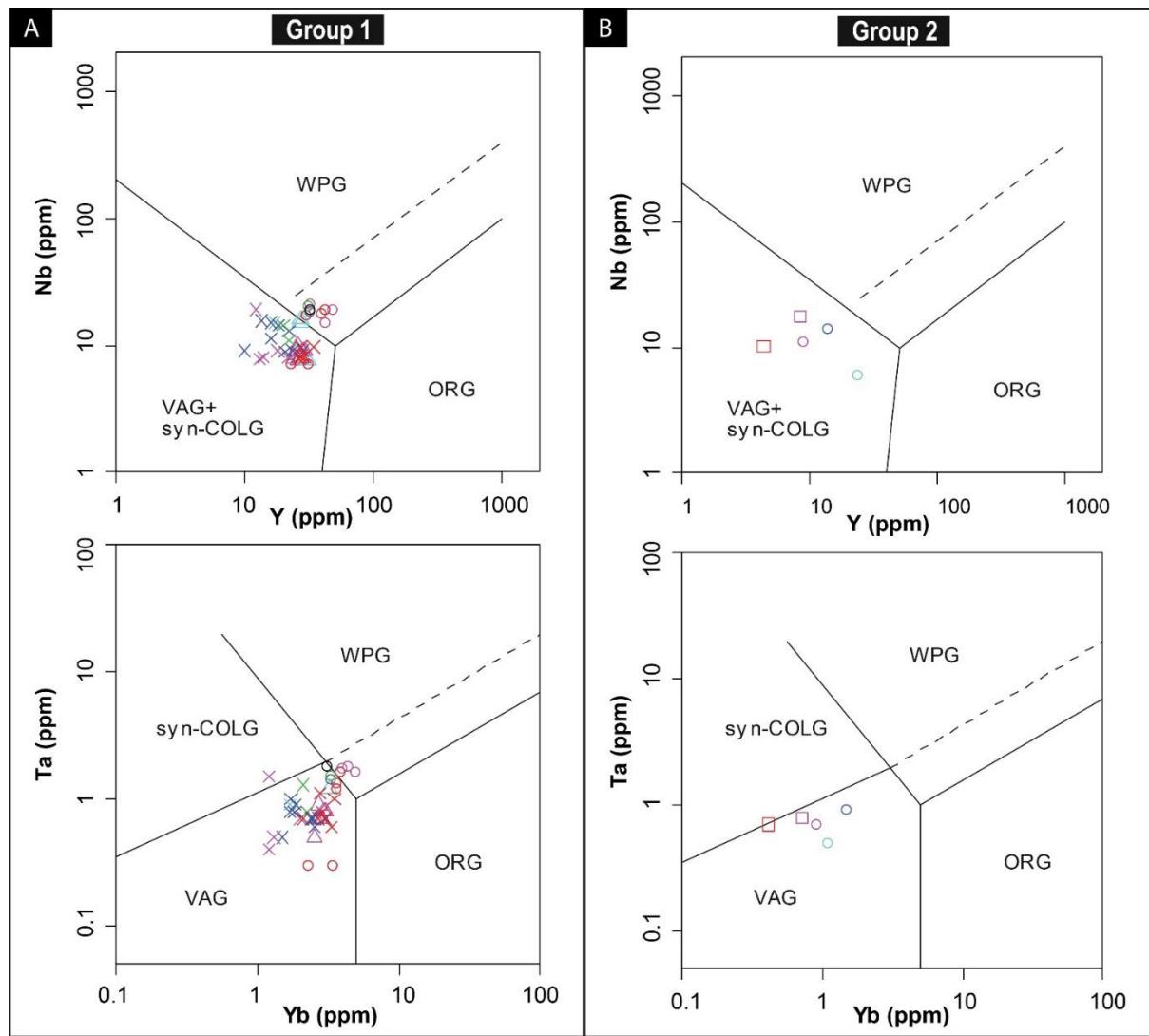
Figure 12. Tectonic setting discriminant diagram for granitoids from Pearce et al. (1984) applied to *Group 1* (a) and *Group 2,* (b) acidic metavolcanic rocks. Diagrams containing Rb were excluded due to the high mobility of this element.

When compared to OIB*, groups* 2 and 3 present more discrete LILE and LREE enrichment over HREE and HFSE, although both group patterns display Nb-Ta negative anomalies, which suggest a subduction-related magmatic source. It is important to point out that Ti and P anomalies are expected for intermediate to acidic-rocks (as in *groups* 1, 2 and 3) due to magmatic differentiation and irrespective of the magmatism geological setting. *Bmvc*, when compared to OIB, does not display Nb, Ta, P and Ti negative anomalies. Together with the probable tholeiitic affinity of this sample, such characteristics suggest it is not a product of sources affected by subduction-related metasomatism. However, it is important to point out that *Bmvc*

700 LREE content is higher than expected for tholeiitic rocks, which indicates that
701 contamination or assimilation processes cannot be ruled out.

702
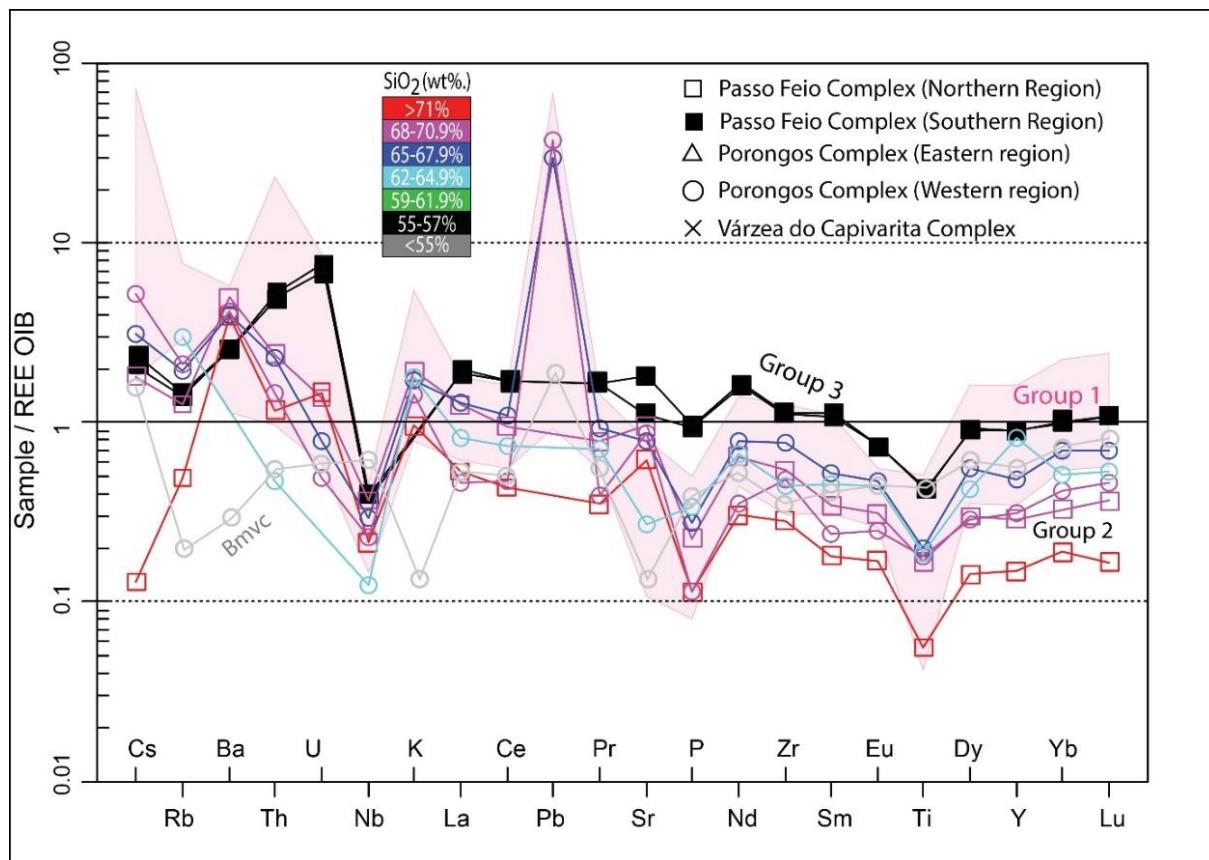
703

704

705 Figure 13. Spidergrams normalised by Oceanic Island Basalts (OIB – Sun and McDonough,
706 1989) for groups 1, 2, 3 and *Bmvc*.

707

708 When considering the correlations of $^{87}Sr/^{86}Sr_t$ values, $\mathcal{E}Nd_t$ values and SiO_2
709 contents, as shown in figure 10, we can see that *groups* 2 and 3 (580 Ma) and some
710 least differentiated samples from *Group* 1 (790 Ma) show lower $^{87}Sr/^{86}Sr_t$ values (<
711 0.7100) and variable $\mathcal{E}Nd_t$ (+2 to -10) which suggest mantle contribution with variable
712 amounts of crustal contamination. On the other hand, most of *Group* 1 samples (790
713 Ma) show the highest $^{87}Sr/^{86}Sr_t$ values (> 0.7100) and negative $\mathcal{E}Nd_t$ (-10) besides the
714 strong positive correlation between $^{87}Sr/^{86}Sr_t$ values and SiO_2 contents, suggesting
715 strong crustal contamination potentially correlated to assimilation and crustal
716 contamination processes (AFC).

717

718

5.2 Timing and geotectonic setting of the magmatic events in the Passo Feio, Porongos, and Várzea do Capivarita complexes

Combined major and trace element data and Sr-Nd isotopes with U–Pb geochronology can be used to constrain the temporal evolution of the magmatic events in metavolcanic rocks from ancient basins. According to previous studies and new geochronological data, the intermediate to acidic meta-igneous rocks discussed in this paper may be grouped into two diachronous episodes of magmatism, one at ca. 810–780 Ma and the other at ca. 600–580 Ma (Fig. 6e). The ca. 810–780 Ma magmatic event is documented in the PC (Saalmann et al., 2011; Pertille et al., 2017; Battisti, 2022) and VCC (Martil et al., 2017; Battisti, 2022). Samples belonging to this magmatic event fit into *Group 1* samples derivated from subduction-related sources with strong crustal contribution, probably associated with AFC processes, as evidenced by Sr-Nd isotopic and geochemical data. If mantle contribution would be considered at this time, it should be minor, and the geochemical and isotopic signatures of such mantle source contribution are diluted. Such characteristics are very common along active continental margins, as in Andean-type mature arcs. Thus, this is the environment suggested for the generation of the ca.780-810 Ma Porongos and Várzea do Capivarita orthometamorphic rocks. Our interpretation corroborates previous studies dealing with major/trace elements (Martil et al., 2017; De Toni et al., 2020b) as well as Sr-Nd systematics (Martil et al., 2017) and oxygen isotopic composition of zircon (Battisti, 2022). However, the nature of this magmatism is still a matter of debate, as other authors interpret it as back-arc/rift magmatism (Konopásek et al., 2018; Will et al., 2019).

The 600–580 Ma magmatism is documented in the western Porongos region (Zvirtes et al., 2017; Höfig et al., 2018) and in the Passo Feio Complex (this paper). Sample MAB59A (*Bmvc*) represents this younger magmatism in the Porongos Complex. Moreover, *Group 2* Porongos metavolcanic rocks display a strong geochemical similarity with the ca. 580 Ma PFC metavolcanic rocks, which suggests they are also part of this Ediacaran magmatism. Thus, considering the small number of samples, our restricted data suggests coeval magmatism within ca. 600–580 Ma between northern PFC and western PC.

The unknown crystallisation age, in addition to a different geochemical pattern, makes it difficult to estimate the timing of *Group 3* magmatism from southern PFC. However, in the absence of further geochronological data from this complex, it is

754   strongly possible that *Group 3* magmatism also sits around ca. 600–580 Ma, as the
755   northern PFC magmatism. Dating based on Lu-Hf isochron in garnet from the southern
756   PFC metapelites interleaved with the studied metavolcanic rocks places the event
757   which deformed the whole package at 571 ± 13 Ma (Battisti, 2022). Thus, *Group 3*
758   magmatism ought to have happened before ca. 570 Ma, very likely at ca. 600-580 Ma.
759   At 600–580 Ma, no magmatism is registered in the Várzea do Capivarita
760   Complex, or eastern region of Porongos Complex, although rocks of such age are
761   reported in the western Porongos region and Passo Feio, as discussed above. *Groups*
762   *2* and *3* rocks and *Bmvc* possibly belong to coeval magmatism, but they have specific
763   characteristics. Elemental geochemistry suggests subduction-related sources for
764   *groups* 2 and 3, but not clearly for the *Bmvc*. However, differently from *Group 1* rocks,
765   elemental geochemistry and Sr-Nd isotopic data suggest less evolved sources for
766   *groups 2* and *3* magmatism, i.e., mantle-derived sources. Such data might indicate that
767   a subduction-related enriched mantle generated *groups* 2 and 3 rocks with minor
768   crustal contribution. A back-arc scenario at ca. 600–580 Ma would be a possible
769   environment to generate rocks with such characteristics. The *Bmvc*, however, has
770   different geochemical aspects relative to *groups* 2 and 3. In this sample, both elemental
771   and Sr-Nd isotopic data suggest a mantle-derived origin without significant contribution
772   of subduction-related sources, crustal melting, and contamination, even though LILEs
773   are somewhat higher than expected for tholeiitic rocks. Such differences in *Bmvc* may
774   also have been caused by heterogeneities in the mantle source of the Ediacaran
775   magmatism.
776
777   ***5.3   Geological relations between Passo Feio, Porongos and Várzea do***
778   ***Capivarita complexes***
779
780   The Várzea do Capivarita Complex is traditionally interpreted as the granulitic
781   basement of the Dom Feliciano Belt intruded by Neoproterozoic granites (Gross et al.,
782   2006; Martil et al., 2011), although the real age of the complex was unknown. Recent
783   studies (Martil, 2016) revealed that the crystallisation age of meta-igneous rocks
784   tectonically interleaved with the metasedimentary VCC sequence is ca. 790 Ma. Such
785   age is the same as the traditionally known Porongos Complex metavolcanic rocks
786   (Saalmann et al., 2011; Pertille et al., 2017) and is also found in other regions of the
787   Dom Feliciano Belt (Koester et al., 2016; De Toni et al., 2020b). Thus, after the paper
788   of Martil (2016), the synchronicity of the magmatism and sedimentation between these

789 high- and low-grade metamorphic complexes was explored by several authors (e.g.
790 Battisti et al., 2018; De Toni et al., 2020b), which concluded that they had shared
791 volcano-sedimentary sources at ca. 790 Ma. Such interpretation is corroborated by the
792 geochemical similarities found among the studied *Group 1* rocks.

793　　　However, the geological history of the Porongos Complex is indeed complex. For
794 example, Höfig et al. (2018) demonstrated that besides the ca. 810–780 Ma
795 magmatism, a magmatic event of ca. 600 Ma was also registered in Porongos, which
796 is related to a completely different geological evolution (Battisti, 2022). Based on this,
797 Battisti (2022) proposed that the Porongos Complex would have to be treated as two
798 individual sequences called Cerro da Árvore and Capané.

799　　　The Cerro da Árvore sequence (CAs) is the oldest Porongos sequence and
800 comprises metasedimentary rocks interleaved with ca. 810–780 Ma meta-igneous
801 rocks. This sequence is the part of the Porongos Complex that can directly correlate
802 with the Várzea do Capivarita Complex. Both CAs and VCC sediments were deposited
803 before ca. 810 Ma, as indicated by the crystallisation age of the associated
804 metavolcanic rocks in both complexes (Saalmann et al., 2011; Pertille et al., 2017),
805 until < ca. 660–650 Ma, when the collisional setting took place, as registered by
806 metamorphic ages found in both complexes (Chemale et al., 2011; Martil, 2016,
807 Battisti, 2022). Most of the PC metavolcanic rocks discussed in this paper fall into
808 geochemical *Group 1*, indicating that the 810-780 Ma magmatism is the most
809 expressive and widespread in the Porongos Complex (both eastern and western
810 regions).

811　　　The Capané sequence is the younger one and comprises metasedimentary rocks
812 deposited in the western region of the Porongos Complex at an unspecified time
813 between ca. 660 to ca. 560 Ma (Pertille et al., 2015, 2017; Höfig et al., 2018), with
814 contemporaneous ca. 600 Ma meta-igneous rocks (Zvirtes et al., 2017; Höfig et al.,
815 2018). PC *Group 2* and *Bmvc* rocks are part of the igneous event of this sequence,
816 exclusively found in the western Porongos Complex region. However, their
817 geochemical differences indicate that the Capané sequence magmatism (600-580 Ma)
818 was probably complex and demands further studies.

819　　　Moreover, based on geochemical and Sr-Nd isotopic data, the ca. 600 Ma
820 magmatism (to possibly 580 Ma) in the Capané sequence can be related to the
821 magmatism in the northern PFC, as rocks of both complexes bear *Group 2* features.
822 Also, the comparison can be extended to the southern PFC magmatism in a less
823 straightforward interpretation. Such data point to the PC and PFC as sharing margins

824 at 600–580 Ma, which corroborates the interpretation that the PC Capané sequence
825 and the PFC were deformed together at ca. 570–565 Ma (Battisti, 2022). According to
826 the same authors, such ca. 570-565 Ma deformation records a front migration towards
827 the west of a long-lived transpressive deformation, which started at ca. 660-650 Ma,
828 as registered in the Porongos Cerro da Árvore sequence and Várzea do Capivarita
829 Complex. Thus, it is possible to state that the geological evolution of Passo Feio,
830 Porongos, and Várzea do Capivarita complexes are at some point all connected.

831

832 *5.4   Is the generation of a back-arc setting at ca. 600-580 Ma a space*
833 *problem?*

834

835   The ca. 600–580 Ma magmatic rocks of Porongos and Passo Feio complexes
836 were emplaced between two events of crustal thickening in the central Dom Feliciano
837 Belt foreland (660 and 565 Ma – Battisti, 2022 – Fig. 14). However, such metavolcanic
838 rocks do not show significant crustal contribution, suggesting that they were emplaced
839 in a geological scenario of attenuated crust. Moreover, it is important to point out that
840 an extensive 630–580 Ma post-collisional batholith is situated only some kilometres
841 east of the studied area, which indicates magmatism was going on all over the Dom
842 Feliciano Belt at that time (Fig 14).

843   Studies carried out in undeformed sedimentary basins neighbouring the Passo
844 Feio and Porongos complexes demonstrated back-arc stratigraphy for 630–600 Ma
845 units (Borba et al., 2008; Almeida et al., 2012; Paim et al., 2014) and transtentional
846 position for the 595–580 Ma units (Janikian et al., 2008, 2012; Paim et al., 2014) in
847 such basins. The stratigraphic record of these basins demonstrates that local spaces
848 have been created in the Dom Feliciano Belt foreland from 630–580 Ma, and a similar
849 situation might have happened in the western Porongos Complex region and Passo
850 Feio Complex. For some reason still unexplained, the rocks of such sedimentary
851 basins remained undeformed during the ca. 565 Ma crustal thickening event that
852 deformed and metamorphosed the Passo Feio Complex and the western region of
853 Porongos Complex.

854   Thus, the emplacement of the Ediacaran magmatism of Passo Feio and western
855 Porongos region in a back-arc scenario does not pose a structural problem.
856 Alternatively, a transtensive basin is suggested as a possible scenario, as drawn in
857 figure 14. Both scenarios would be in accordance with the reported geochemical and

858 isotopic signatures and would fit geometrically with the contemporaneous undeformed
859 volcano-sedimentary basins of the Dom Felicano Belt foreland.
860
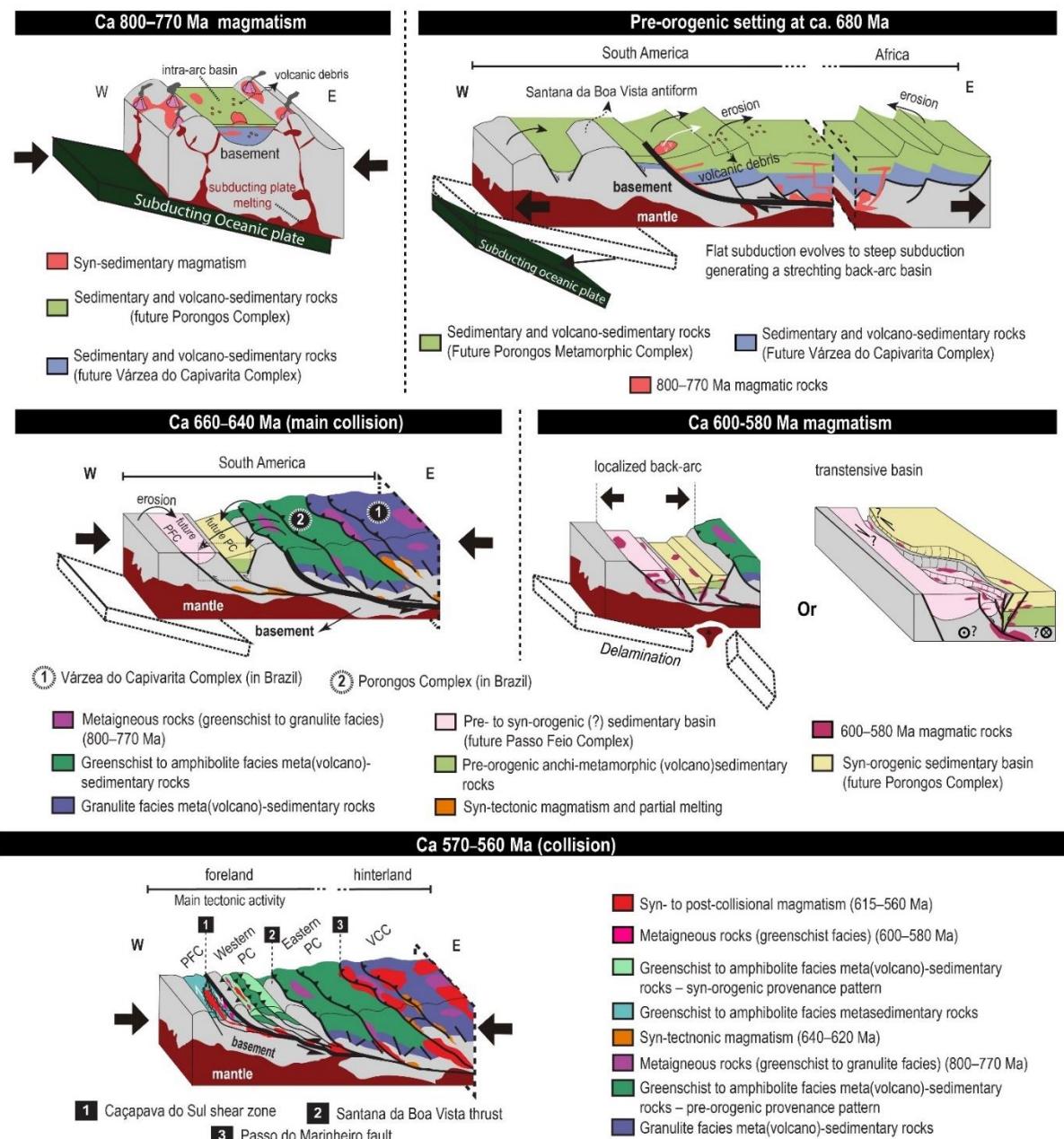
861
862
863 Figure 14. Evolutionary model of Porongos, Várzea do Capivarita and Passo Feio complexes
864 (modified after Battisti, 2022). Possible scenarios for the magmatic events in the Dom Feliciano
865 Belt central sector are drawn at the top left (ca. 800–770 Ma) and the middle right (600-580
866 Ma).
867
868
869

870   **6. Conclusions**

871

872   New Sr-Nd isotopic data from metavolcanic rocks interleaved with

873   metasedimentary sequences of the Passo Feio and Porongos complexes, combined

874   with U-Pb zircon ages of acidic metavolcanic rocks from the Passo Feio Complex, were

875   performed. In addition, the new data were compared with meta-igneous data available

876   in the literature for the Passo Feio, Porongos, and Várzea do Capivarita complexes.

877   The results allow us to draw the following conclusions.

878   i) U-Pb LA-ICPMS zircon analyses in two acidic metavolcanic rocks from the

879   northern region of Passo Feio Complex yielded crystallisation age of the protolith at

880   580 ± 2 Ma (2σ).

881   ii) Magmatism in the Passo Feio, Porongos, and Várzea do Capivarita complexes

882   can be grouped into two diachronous magmatic events and three geochemical groups

883   plus one distinct sample.

884   The first magmatic event has happened at 810–780 Ma, in the Várzea do

885   Capivarita and Porongos complexes (both eastern and western regions). It is

886   represented by the rocks grouped in geochemical *Group* 1. The rocks of this pattern

887   represent magmatic associations produced from subduction-related sources, with

888   significant contribution of crustal materials, due to the crustal recycling and/or

889   assimilation of host rocks and crustal melts, based on geochemical arguments and

890   $^{87}Sr/^{86}Sr_{(790\ Ma)}$ values higher than 0.715 and $\varepsilon Nd_{(790\ Ma)}$ mainly from -5 and -11 (up to

891   -22). The proposed geological scenario is an active continental margin, as in Andean-

892   type mature arcs. In the Porongos Complex, such rocks are part of the Cerro da Árvore

893   sequence.

894   The second period of magmatism extends from ca. 600 to 580 Ma and is

895   registered in the Passo Feio Complex and the western Porongos Complex. The

896   geochemical *groups* 2 and 3 plus a basic metavolcanoclastic sample (*Bmvc*) are part

897   of this magmatism. According to the $^{87}Sr/^{86}Sr_{(580\ Ma)}$ values of 0.7035–0.7050 and εNd

898   $_{(580\ Ma)}$ values higher than -10, and elemental geochemistry, metavolcanic rocks of

899   *groups* 2 and 3 were generated from a subduction-related enriched mantle, but without

900   major crustal contamination, as in a back-arc setting. However, for *Bmvc*, both

901   elemental and isotope ($^{87}Sr/^{86}Sr_{(600\ Ma)}$) = 0.7065; $\varepsilon Nd_{(600\ Ma)}$ = +1) geochemistry

902   suggest a mantle-derived origin without significant contribution of subduction-related

903   sources, crustal melting and contamination. Such differences may indicate the

complexity of this Ediacaran magmatism (600-580 Ma) and demand further studies. In the Porongos Complex, this magmatism is related to the Capané sequence.

iii) Our data comparison indicates a shared tectonic evolution between the Passo Feio Complex and the western Porongos Complex (Capané sequence) at *ca.* 600–580 Ma, and also a shared tectonic evolution between the eastern Porongos Complex (Cerro da Árvore sequence) and Várzea do Capivatira Complex at *ca.* 810–770 Ma.

7. . Acknowledgements

8. REFERENCES

Almeida, D.P.M., Chemale, F., Machado, A., 2012. Late to Post-Orogenic Brasiliano-Pan-African Volcano-Sedimentary Basins in the Dom Feliciano Belt, Southernmost Brazil, in: Petrology - New Perspectives and Applications. InTech. https://doi.org/10.5772/25189

Arena, K.R., Hartmann, L.A., Lana, C., 2016. Evolution of Neoproterozoic ophiolites from the southern Brasiliano Orogen revealed by zircon U-Pb-Hf isotopes and geochemistry. Precambrian Res 285, 299–314. https://doi.org/10.1016/j.precamres.2016.09.014

Arena, K.R., Hartmann, L.A., Lana, C., 2018. U–Pb–Hf isotopes and trace elements of metasomatic zircon delimit the evolution of neoproterozoic Capané ophiolite in the southern Brasiliano Orogen. Int Geol Rev 60, 911–928. https://doi.org/10.1080/00206814.2017.1355269

Arena, K.R., Hartmann, L.A., Lana, C., 2017. Tonian emplacement of ophiolites in the southern Brasiliano Orogen delimited by U-Pb-Hf isotopes of zircon from metasomatites. Gondwana Res 49, 296–332. https://doi.org/10.1016/j.gr.2017.05.018

Basei, M., Siga, O., Masquelin, H., Harara, O., Reis Neto, J., Preciozzi, F., 2000. The Dom Feliciano belt (Brazil-Uruguay)and its foreland (Rio de la Plata Craton): framework, tectonic evolution and correlations with similar terranes of southwestern Africa.

Battisti, M.A., 2022. Evolução geológica (800-560 Ma) do setor central Do Cinturão Dom Feliciano com base no estudo petrológico, geocronológico e de proveniência dos complexos Porongos, Várzea

941 Do Capivarita e Passo Feio, RS, Ph Thesis. Universidade Federal do Rio Grande do Sul, Porto
942 Alegre - RS.

943 Battisti, M.A., Bitencourt, M. de F., De Toni, G.B., Nardi, L.V.S., Konopásek, J., 2018. Metavolcanic
944 rocks and orthogneisses from Porongos and Várzea do Capivarita complexes: A case for
945 identification of tectonic interleaving at different crustal levels from structural and geochemical
946 data in southernmost Brazil. J South Am Earth Sci 88, 253–274.
947 https://doi.org/10.1016/j.jsames.2018.08.009

948 Bicalho, V., Remus, M.V.D., Rizzardo, R., Dani, N., 2019. Geochemistry, metamorphic evolution and
949 tectonic significance of metabasites from Caçapava do Sul, southern Brazil. Brazilian J Geol 49,
950 1–16. https://doi.org/10.1590/2317-4889201920180039

951 Bitencourt, M.F., Nardi, L.V.S., 1993. Late- to Postcollisional Brasiliano Magmatism in Southernmost
952 Brazil. An Acad Bras Cienc 65, 3–16.

953 Bitencourt, M.F., Nardi, L.V.S., 2000. Tectonic setting and sources of magmatism related to the southern
954 Brazilian shear belt. Rev Bras Geociencias 30, 184–187.

955 Bitencourt, M.F., 1983. Metamorfitos da região de Caçapava do Sul, RS – Geologia e Relações com o
956 Corpo Granítico. Atas do 1o Simpósio Sul-Brasileiro Geol 37–48.

957 Bitencourt, M.F., Hartmann, L.A., 1984a. Geoquímica das Rochas anfibolíticas da região de Caçapava
958 do Sul - RS - Parte 1: caracterização geológica e petrográfica, elementos maiores e menores. An
959 DO XXXIII Congr Bras Geol 4266–4277.

960 Bitencourt, M.F., Hartmann, L.A., 1984b. Reconhecimento geoquimico dos xistos magnesianos da
961 região do Passo Feio, Cacapava do Sul - RS. Congr Bras Geol (33 1984 Rio Janeiro, Rj) Anais
962 Rio Janeiro SBG, 1984.

963 Bitencourt, M.F., Nardi, L.V.S., Florisbal, L.M., Heaman, L.M., 2015. Geology, geochronology and
964 petrogenesis of a Neoproterozoic, syntectonic sillimanite- muscovite-biotite granite from
965 southernmost Brazil. B Abstr 8th Hutt Sympo-sium Granites Relat Rocks 179.

966 Borba, A.W., Mizusaki, A.M.P., Santos, J.O.S., McNaughton, N.J., Onoe, A.T., Hartmann, L.A., 2008.
967 U-Pb zircon and 40Ar-39Ar K-feldspar dating of syn-sedimentary volcanism of the Neoproterozoic
968 Maricá Formation: constraining the age of foreland basin inception and inversion in the Camaquã
969 Basin of southern Brazil. Basin Res 20, 359–375. https://doi.org/10.1111/j.1365-
970 2117.2007.00349.x

971 Boyton, W. V., 1984. Geochemistry of Rare Earth Elements: Meteorite studies, in: Henderson, P. (Ed.),
972 Rare Earth Element Geochemistry. Elsevier, New York, p. 63.

973 Briqueu, L., Bougault, H., Joron, J.L., 1984. Quantification of Nb, Ta, Ti and V anomalies in magmas
974 associated with subduction zones: Petrogenetic implications. Earth Planet Sci Lett 68, 297–308.
975 https://doi.org/10.1016/0012-821X(84)90161-4

976 Chemale, F., Philipp, R.P., Dussin, I.A., Formoso, M.L.L., Kawashita, K., Berttotti, A.L., 2011. Lu–Hf and
977 U–Pb age determination of Capivarita Anorthosite in the Dom Feliciano Belt, Brazil. Precambrian
978 Res 186, 117–126. https://doi.org/10.1016/j.precamres.2011.01.005

979 Costa, A.F.U., 1997. Teste e modelagem geofísica da estruturação das associações litotectônicas pré-
980 cambrianas no Escudo Sul-Rio-Grandense. PhD Thesis. Universidade Federal do Rio Grande do
981 Sul. Porto Alegre, Brazil.

Costa, E.O. da, de Fátima Bitencourt, M., Tennholm, T., Konopásek, J., de Franceschi Moita, T., 2021. P-T-D evolution of the southeast Passo Feio Complex and the meaning of the Caçapava Lineament, Dom Feliciano Belt, southernmost Brazil. J South Am Earth Sci 103465. https://doi.org/10.1016/j.jsames.2021.103465

Costa, E.O., Gomes, E.M., Bitencourt, M. de F., De Toni, G.B., Nardi, L.V.S., 2020. Reassessing the PT conditions of Neoproterozoic collisional metamorphism and partial melting in southernmost Brazil. J South Am Earth Sci 100, 102584. https://doi.org/10.1016/j.jsames.2020.102584

De Toni, G.B., Bitencourt, M.F., Konopásek, J., Battisti, M.A., Costa, E.O., Savian, J.F., 2021. Autochthonous origin of the Encruzilhada Block, Dom Feliciano Belt, southern Brazil, based on aerogeophysics, image analysis and PT-paths. J Geodyn 144. https://doi.org/10.1016/j.jog.2021.101825

De Toni, G.B., Bitencourt, M.F., Konopásek, J., Martini, A., Andrade, P.H.S., Florisbal, L.M., Campos, R.S., 2020a. Transpressive strain partitioning between the Major Gercino Shear Zone and the Tijucas Fold Belt, Dom Feliciano Belt, Santa Catarina, southern Brazil. J Struct Geol 104058. https://doi.org/10.1016/j.jsg.2020.104058

De Toni, G.B., Bitencourt, M.F., Nardi, L.V.S., Florisbal, L.M., Almeida, B.S., Geraldes, M., 2020b. Dom Feliciano Belt orogenic cycle tracked by its pre-collisional magmatism: the Tonian (ca. 800 Ma) Porto Belo Complex and its correlations in southern Brazil and Uruguay. Precambrian Res 105702. https://doi.org/10.1016/j.precamres.2020.105702

DePaolo, D.J., Wasserburg, G.J., 1979. Petrogenetic mixing models and Nd-Sr isotopic patterns. Geochim Cosmochim Acta 43, 615–627. https://doi.org/10.1016/0016-7037(79)90169-8

Fernandes, L.A.D., Menegat, R., Costa, A.F.U., Koester, E., Porcher, C.C., Tommasi, A., Kraemer, G., Ramgrab, G.E., Camozzato, E., 1995. Evolução Tectônica Do Cinturão Dom Feliciano No Escudo Sul-Rio-Grandense: Parte Ii - Uma Contribuição a Partir Das Assinaturas Geofísicas. Rev Bras Geociências 25, 375–384. https://doi.org/10.25249/0375-7536.1995375384

Fernandes, L.A.D., Tommazi, A., Porcher, C.C., 1992. Deformation patterns in the southern Brazilian branch of the Dom Feliciano Belt: A reppraisal. J South Am Earth Sci 5, 77–96.

Fragoso-Cesar, A.R.S., Figueiredo, M.C.H., Soliani Jr, E., Faccini, U.F., 1986. O Batólito Pelotas (Proterozóico Superior/Eopaleozóico) no escudo do Rio Grande do Sul. XXXIV Congr Bras Geol 1321–1342.

Frimmel, H., Frank, W., 1998. Neoproterozoic tectono-thermal evolution of the Gariep Belt and its basement, Namibia and South Africa. Precambrian Res 90, 1–28. https://doi.org/10.1016/S0301-9268(98)00029-1

Gollmann, K., Marques, J., Frantz, C., Farid, &, Junior, C., 2008. Geoquímica e Isotópos de Nd de Rochas Metavulcânicas da Antiforme Capané, Complexo Metamórfico Porongos, RS. Rev Pesqui em Geociências 35, 83–95.

Goscombe, B.D., Gray, D.R., 2008. Structure and strain variation at mid-crustal levels in a transpressional orogen: A review of Kaoko Belt structure and the character of West Gondwana amalgamation and dispersal. Gondwana Res 13, 45–85. https://doi.org/10.1016/j.gr.2007.07.002

Gregory, T.R., Bitencourt, M. de F., Nardi, L.V.S., Florisbal, L.M., Chemale, F., 2015. Geochronological data from TTG-type rock associations of the Arroio dos Ratos Complex and implications for

1023   crustal evolution of southernmost Brazil in Paleoproterozoic times. J South Am Earth Sci 57, 49–
1024   60. https://doi.org/10.1016/j.jsames.2014.11.009

1025   Gross, A.O.M., Porcher, C.C., Fernandes, L.A.D., Koester, E., 2006. Neoproterozoic low-pressure/high-
1026   temperature collisional metamorphic evolution in the Varzea do Capivarita Metamorphic Suite,
1027   SE Brazil: Thermobarometric and Sm/Nd evidence. Precambrian Res 147, 41–64.
1028   https://doi.org/10.1016/j.precamres.2006.02.001

1029   Gross, A.O.M.S., Droop, G.T.R., Porcher, C.C., Fernandes, L.A.D., 2009. Petrology and
1030   thermobarometry of mafic granulites and migmatites from the Chafalote Metamorphic Suite: New
1031   insights into the Neoproterozoic P–T evolution of the Uruguayan—Sul-Rio-Grandense shield.
1032   Precambrian Res 170, 157–174. https://doi.org/10.1016/j.precamres.2009.01.011

1033   Hartmann, L.A., Leite, J.A.D., Da Silva, L.C., Remus, M.V.D., McNaughton, N.J., Groves, D.I., Fletcher,
1034   I.R., Santos, J.O.S., Vasconcellos, M.A.Z., 2000. Advances in SHRIMP geochronology and their
1035   impact on understanding the tectonic and metallogenic evolution of southern Brazil. Aust J Earth
1036   Sci 47, 829–844. https://doi.org/10.1046/j.1440-0952.2000.00815.x

1037   Hartmann, L.A., Santos, J.O.S., Leite, J.A.D., Porcher, C.C., Mcnaughton, N.J., 2003. Metamorphic
1038   evolution and U-Pb zircon SHRIMP geochronology of the Belizário ultramafic amphibolite,
1039   Encantadas Complex, southernmost Brazil. An Acad Bras Cienc 75, 393–403.
1040   https://doi.org/10.1590/S0001-37652003000300010

1041   Heine, C., Zoethout, J., Müller, R.D., 2013. Kinematics of the South Atlantic rift. Solid Earth 4, 215–253.
1042   https://doi.org/10.5194/se-4-215-2013

1043   Höfig, D.F., Marques, J.C., Basei, M.A.S., Giusti, R.O., Kohlrausch, C., Frantz, J.C., 2018. Detrital zircon
1044   geochronology (U-Pb LA-ICP-MS) of syn-orogenic basins in SW Gondwana: New insights into
1045   the Cryogenian-Ediacaran of Porongos Complex, Dom Feliciano Belt, southern Brazil.
1046   Precambrian Res 306, 189–208. https://doi.org/10.1016/j.precamres.2017.12.031

1047   Irvine, T.N., Baragar, W.R.A., 1971. A Guide to the Chemical Classification of the Common Volcanic
1048   Rocks. Can J Earth Sci 8, 523–548. https://doi.org/10.1139/e71-055

1049   Janikian, L., De Almeida, R.P., Da Trindade, R.I.F., Fragoso-cesar, A.R.S., D'Agrella-Filho, M.S.,
1050   Dantas, E.L., Tohver, E., 2008. The continental record of Ediacaran volcano-sedimentary
1051   successions in southern Brazil and their global implications. Terra Nov 20, 259–266.
1052   https://doi.org/10.1111/j.1365-3121.2008.00814.x

1053   Janikian, L., de Almeida, R.P., Fragoso-Cesar, A.R.S., Martins, V.T. de S., Dantas, E.L., Tohver, E.,
1054   McReath, I., D'Agrella-Filho, M.S., 2012. Ages (U-Pb SHRIMP and LA ICPMS) and stratigraphic
1055   evolution of the Neoproterozoic volcano-sedimentary successions from the extensional Camaquã
1056   Basin, Southern Brazil. Gondwana Res 21, 466–482. https://doi.org/10.1016/j.gr.2011.04.010

1057   Jost, H., Bitencourt, M.F., 1980. Estratigrafia e tectônica de uma fração da Faixa de Dobramentos
1058   Tijucas no Rio Grande do Sul. Acta Geol Leop 11, 27–59.

1059   Knijnik, D.B., 2018. Geocronologia U-Pb e geoquímica isotópica Sr-Nd dos granitoides sintectônicos às
1060   zonas de cisalhamento transcorrentes Quitéria Serra do Erval e Dorsal de Canguçu, Rio Grande
1061   do Sul, Brasil. Universidade Federal do Rio Grande do Sul, Porto Alegre - RS.

1062   Koester, E., Porcher, C.C., Pimentel, M.M., Fernandes, L.A.D., Vignol-Lelarge, M.L., Oliveira, L.D.,
1063   Ramos, R.C., 2016. Further evidence of 777 Ma subduction-related continental arc magmatism

1064   in Eastern Dom Feliciano Belt, southern Brazil: The Chácara das Pedras Orthogneiss. J South
1065   Am Earth Sci 68, 155–166. https://doi.org/10.1016/j.jsames.2015.12.006

1066 Konopásek, J., Janoušek, V., Oyhantçabal, P., Sláma, J., Ulrich, S., 2018. Did the circum-Rodinia
1067   subduction trigger the Neoproterozoic rifting along the Congo–Kalahari Craton margin? Int J Earth
1068   Sci 107, 1859–1894. https://doi.org/10.1007/s00531-017-1576-4

1069 Le Bas, M.J., Le Maitre, R.W., Streckeisen, A., Zanettin, B., 1986. A chemical classification of volcanic
1070   rocks based on the total alkali silica diagram. J Petrol 27, 745–750.
1071   https://doi.org/10.1093/petrology/27.3.745

1072 Leite, J.A.D., Hartman, L.O.A., McNaughton, N.J., Chemale, F., 1998. SHRIMP U/Pb zircon
1073   geochronology of neoproterozoic juvenile and crustal-reworked terranes in southernmost brazil.
1074   Int Geol Rev 40, 688–705. https://doi.org/10.1080/00206819809465232

1075 Leite, J.A.D., Hartmann, L.A., Fernandes, L.A.D., McNaughton, N.J., Soliani, Jr., Ê., Koester, E., Santos,
1076   J.O.S., Vasconcellos, M.A.Z., 2000. Zircon U–Pb SHRIMP dating of gneissic basement of the
1077   Dom Feliciano Belt, southernmost Brazil. J South Am Earth Sci 13, 739–750.
1078   https://doi.org/10.1016/S0895-9811(00)00058-4

1079 Lena, L.O., Pimentel, M.M., Philipp, R.P., Armstrong, R., Sato, K., 2014. The evolution of the
1080   Neoproterozoic São Gabriel juvenile terrane, southern Brazil based on high spatial resolution U-
1081   Pb ages and δ18O data from detrital zircons. Precambrian Res 247, 126–138.
1082   https://doi.org/10.1016/j.precamres.2014.03.010

1083 Lenz, C., 2006. Evolução metamórfica dos metapelitos da Antiforme Serra dos Pedrosas: condições e
1084   idades do metamorfismo. Master´s thesis. Universidade Federal do Rio Grande do Sul, Brazil, p.
1085   111.

1086 Lenz, C., Fernandes, L.A.D., McNaughton, N.J., Porcher, C.C., Masquelin, H., 2011. U–Pb SHRIMP
1087   ages for the Cerro Bori Orthogneisses, Dom Feliciano Belt in Uruguay: Evidences of a ~800Ma
1088   magmatic and ~650Ma metamorphic event. Precambrian Res 185, 149–163.
1089   https://doi.org/10.1016/j.precamres.2011. 01.007

1090 Marques, J.C., Jost, H., Roisenberg, A., Frantz, J.C., 1998. Eventos ígneos da Suíte Metamórfica
1091   Porongos na área da Antiforme Capané, Cachoeira do Sul, RS. Rev Bras Geociências 28, 419–
1092   430. https://doi.org/10.25249/0375-7536.1998419430

1093 Marques, J.C., Roisenberg, A., Jost, H., Frantz, J.C., Teixeira, R.S., 2003. Geologia e geoquímica das
1094   rochas metaultramáficas da antiforme Capané, suíte metamórfica Porongos, RS. Rev Bras
1095   Geociências 33, 83–94.

1096 Martil, M.M.D., 2016. O magmatismo de arco continental pré-colisional (790 ma) e a reconstituição
1097   espaço-temporal do regime transpressivo (650 ma) no Complexo Várzea Do Capivarita, Sul da
1098   Província Mantiqueira. Universidade Federal do Rio Grande do Sul, Porto Alegre, Brasil. In:
1099   https://lume.ufrgs.br/handle/10183/149194

1100 Martil, M.M.D., Bitencourt, M. de F., Nardi, L.V.S., 2011. Caracterização estrutural e petrológica do
1101   magmatismo pré-colisional do Escudo Sul-rio-grandense: Os ortognaisses do Complexo
1102   Metamórfico Várzea do Capivarita. Pesqui em Geociencias 38, 181–201.

1103 Martil, M.M.D., Bitencourt, M. de F., Nardi, L.V.S., Schmitt, R. da S., Weinberg, R., 2017. Pre-collisional,
1104   Tonian (ca. 790 Ma) continental arc magmatism in southern Mantiqueira Province, Brazil:

1105   Geochemical and isotopic constraints from the Várzea do Capivarita Complex. Lithos 274–275,
1106   39–52. https://doi.org/10.1016/j.lithos.2016.11.011

1107 Oliveira, C.H.E., Chemale, F., Jelinek, A.R., Bicca, M.M., Philipp, R.P., 2014. U-Pb and Lu-Hf isotopes
1108   applied to the evolution of the late to post-orogenic transtensional basins of the dom feliciano belt,
1109   Brazil. Precambrian Res 246, 240–255. https://doi.org/10.1016/j.precamres.2014.03.008

1110 Oriolo, S., Oyhantçabal, P., Wemmer, K., Siegesmund, S., 2017. Contemporaneous assembly of
1111   Western Gondwana and final Rodinia break-up: Implications for the supercontinent cycle. Geosci
1112   Front 8, 1431–1445. https://doi.org/10.1016/j.gsf.2017.01.009

1113 Oyhantçabal, P., Siegesmund, S., Wemmer, K., Presnyakov, S., Layer, P., 2009. Geochronological
1114   constraints on the evolution of the southern Dom Feliciano Belt (Uruguay). J Geol Soc London
1115   166, 1075–1084. https://doi.org/10.1144/0016-76492008-122

1116 Padilha, D.F., Bitencourt, M. de F., Nardi, L.V.S., Florisbal, L.M., Reis, C., Geraldes, M., Almeida, B.S.,
1117   2019. Sources and settings of Ediacaran post-collisional syenite-monzonite-diorite shoshonitic
1118   magmatism from southernmost Brazil. Lithos. https://doi.org/10.1016/j.lithos.2019.06.004

1119 Paim, P.S.G., Chemale Junior, F., Wildner, W., 2014. Estágios Evolutivos Da Bacia Do Camaquã (RS).
1120   Ciência e Nat 36, 183–193. https://doi.org/10.5902/2179460X13748

1121 Pearce, J.A., 1995. Tectonic Implications of Volcanic Arc Magmas. Annu Rev Earth Planet Sci 23, 251–
1122   285. https://doi.org/0084-6597/95/0515-0251

1123 Pearce, J.A., Harris, N.B.W., Tindle, A.G., 1984. Trace Element Discrimination Diagrams for the
1124   Tectonic Interpretation of Granitic Rocks. J Petrol 25, 956–983.
1125   https://doi.org/10.1093/petrology/25.4.956

1126 Peccerillo, A., Taylor, S.R., 1976. Geochemistry of eocene calc-alkaline volcanic rocks from the
1127   Kastamonu area, Northern Turkey. Contrib to Mineral Petrol 58, 63–81.
1128   https://doi.org/10.1007/BF00384745

1129 Peel, E., Sánchez, L., Angelo, M., Basei, S., 2018. Journal of South American Earth Sciences Geology
1130   and geochronology of Paso del Dragón Complex (northeastern Uruguay): Implications on the
1131   evolution of the Dom Feliciano Belt (Western Gondwana). J South Am Earth Sci 85, 250–262.
1132   https://doi.org/10.1016/j.jsames.2018.05.009

1133 Percival, J.J., Konopásek, J., Anczkiewicz, R., Ganerød, M., Sláma, J., Campos, R.S., Bitencourt, M.
1134   de F., 2022. Tectono-Metamorphic Evolution of the Northern Dom Feliciano Belt Foreland, Santa
1135   Catarina, Brazil: Implications for Models of Subduction-Driven Orogenesis. Tectonics 41.
1136   https://doi.org/10.1029/2021TC007014

1137 Percival, J.J., Konopásek, J., Eiesland, R., Sláma, J., de Campos, R.S., Battisti, M.A., Bitencourt, M. de
1138   F., 2021. Pre-orogenic connection of the foreland domains of the Kaoko–Dom Feliciano–Gariep
1139   orogenic system. Precambrian Res 354, 106060.
1140   https://doi.org/10.1016/j.precamres.2020.106060

1141 Pertille, J., Hartmann, L.A., Philipp, R.P., Petry, T.S., de Carvalho Lana, C., 2015. Origin of the
1142   Ediacaran Porongos Group, Dom Feliciano Belt, southern Brazilian Shield, with emphasis on
1143   whole rock and detrital zircon geochemistry and U-Pb, Lu-Hf isotopes. J South Am Earth Sci 64,
1144   69–93. https://doi.org/10.1016/j.jsames.2015.09.001

1145 Pertille, J., Hartmann, L.A., Santos, J.O.S., McNaughton, N.J., Armstrong, R., 2017. Reconstructing the
1146   Cryogenian–Ediacaran evolution of the Porongos fold and thrust belt, Southern Brasiliano

Orogen, based on Zircon U–Pb–Hf–O isotopes. Int Geol Rev 59, 1532–1560. https://doi.org/10.1080/00206814.2017.1285257

Philipp, R., Machado, R., 2002. O magmatismo granítico Neoproterozóico do Batólito Pelotas no sul do Brasil: novos dados e revisão da geocronologia regional. Rev Bras Geociencias 32, 277–290.

Philipp, R.P., Lusa, M., Nardi, L.V.S., 2008. Petrology of dioritic, tonalitic and trondhjemitic gneisses from Encantadas Complex, Santana da Boa Vista, southernmost Brazil: paleoproterozoic continental-arc magmatism. An Acad Bras Cienc 80, 735–748. https://doi.org/10.1590/S0001-37652008000400013

Philipp, R.P., Bom, F.M., Pimentel, M.M., Junges, S.L., Zvirtes, G., 2016a. SHRIMP U-Pb age and high temperature conditions of the collisional metamorphism in the Várzea do Capivarita Complex: Implications for the origin of Pelotas Batholith, Dom Feliciano Belt, southern Brazil. J South Am Earth Sci 66, 196–207. https://doi.org/10.1016/j.jsames.2015.11.008

Philipp, R.P., Pimentel, M.M., Chemale Jr, F., 2016b. Tectonic evolution of the Dom Feliciano Belt in Southern Brazil: Geological relationships and U-Pb geochronology. Brazilian J Geol 46, 83–104. https://doi.org/10.1590/2317-4889201620150016

Pin, C., Gannoun, A., Dupont, A., 2014. Rapid, simultaneous separation of Sr, Pb, and Nd by extraction chromatography prior to isotope ratios determination by TIMS and MC-ICP-MS. J Anal At Spectrom 29, 1858–1870. https://doi.org/10.1039/C4JA00169A

Ramos, V.A., Cingolani, C., Junior, F.C., Naipauer, M., Rapalini, A., 2017. The Malvinas (Falkland) Islands revisited: The tectonic evolution of southern Gondwana based on U-Pb and Lu-Hf detrital zircon isotopes in the Paleozoic cover. J South Am Earth Sci 76, 320–345. https://doi.org/10.1016/j.jsames.2016.12.013

Rapela, C.W., Fanning, C.M., Casquet, C., Pankhurst, R.J., Spalletti, L., Poiré, D., Baldo, E.G., 2011. The Rio de la Plata craton and the adjoining Pan-African/brasiliano terranes: Their origins and incorporation into south-west Gondwana. Gondwana Res 20, 673–690. https://doi.org/10.1016/j.gr.2011.05.001

Remus, M. V.D., Hartmann, L.A., McNaughton, N.J., Groves, D.I., Fletcher, I.R., 2000. The link between hydrothermal epigenetic copper mineralization and the Cacapava Granite of the Brasiliano cycle in southern Brazil. J South Am Earth Sci 13, 191–216. https://doi.org/10.1016/S0895-9811(00)00017-1

Rivera, C.B., 2016. Construção do maciço sienítico Piquiri (609 a 683 Ma) por colocação sucessiva de pulsos de magma ultrapotássico e shoshonítico sob extensão no Escudo sul-rio-grandense. PhD Thesis. Universidade Federal do Rio Grande do Sul, Porto Alegre, Brasil.

Saalmann, K., Gerdes, A., Lahaye, Y., Hartmann, L.A., Remus, M.V.D., Läufer, A., 2011. Multiple accretion at the eastern margin of the Rio de la Plata craton: the prolonged Brasiliano orogeny in southernmost Brazil. Int J Earth Sci 100, 355–378. https://doi.org/10.1007/s00531-010-0564-8

Saalmann, K., Hartmann, L.A., Remus, & M., 2005. Tectonic Evolution of Two Contrasting Schist Belts in Southernmost Brazil: A Plate Tectonic Model for the Brasiliano Orogeny. Int Geol Rev 4712, 1234–1259. https://doi.org/10.2747/0020-6814.47.12.1234

Saalmann, K., Hartmann, L.A., Remus, M. V.D., 2007. The assembly of West Gondwana—The view from the Rio de la Plata craton, in: Special Paper 423: The Evolution of the Rheic Ocean: From

Avalonian-Cadomian Active Margin to Alleghenian-Variscan Collision. Geological Society of America, pp. 1–26. https://doi.org/10.1130/2007.2423(01)

Saalmann, K., Remus, M.V.D., Hartmann, L.A., 2006. Structural evolution and tectonic setting of the Porongos belt, southern Brazil. Geol Mag 143, 59. https://doi.org/10.1017/S0016756805001433

Tull, J., Holm-Denoma, C.S., Barineau, C.I., 2014. Early to middle Ordovician back-arc basin in the southern Appalachian Blue Ridge: Characteristics, extent, and tectonic significance. Bull Geol Soc Am 126, 990–1015. https://doi.org/10.1130/B30967.1

Vidal, M., Alric, G., 1994. The palaeoproterozoic (Birimian) of Haute-Comoé in the West African craton, Ivory Coast: a transtensional back-arc basin. Precambrian Res 65, 207–229. https://doi.org/10.1016/0301-9268(94)90106-6

Vieira, D.T., Koester, E., Ramos, R.C., Porcher, C.C., D'Ávila Fernandes, L.A., 2020. SHRIMP U-Pb zircon ages for the synkinematic magmatism in the Dorsal de Canguçu Transcurrent Shear Zone, Dom Feliciano Belt (Brazil): Tectonic implications. J South Am Earth Sci 100, 102603. https://doi.org/10.1016/j.jsames.2020.102603

Werle, M., Hartmann, L.A., Queiroga, G.N., Lana, C., Pertille, J., Michelin, C.R.L., Remus, M.V.D., Roberts, M.P., Castro, M.P., Leandro, C.G., Savian, J.F., 2020. Oceanic crust and mantle evidence for the evolution of Tonian-Cryogenian ophiolites, southern Brasiliano Orogen. Precambrian Res 351, 105979. https://doi.org/10.1016/j.precamres.2020.105979

Will, T.M., Gaucher, C., Ling, X.-X., Li, X.-H., Li, Q.-L., Frimmel, H.E., 2019. Neoproterozoic magmatic and metamorphic events in the Cuchilla Dionisio Terrane, Uruguay, and possible correlations across the South Atlantic. Precambrian Res 320, 303–322. https://doi.org/10.1016/j.precamres.2018.11.004

Whitney, D.L., Evans, B.W., 2010. Abbreviations for names of rock-forming minerals. Am Mineral 95, 185–187. https://doi.org/10.2138/am.2010.3371

Winchester, J.A., Floyd, P.A., 1977. Geochemical discrimination of different magma series and their differentiation products using immobile elements. Chem Geol 20, 325–343. https://doi.org/10.1016/0009-2541(77)90057-2

Zvirtes, G., Philipp, R.P., Camozzato, E., Guadagnin, F., 2017. Análise estrutural do Metagranito Capané, Complexo Porongos, Cachoeira do Sul, RS. Pesqui em Geociências 44, 05. https://doi.org/10.22456/1807-9806.78250

1218 **Appendix**

1219

1220 **1 -** *Sm-Nd and Rb-Sr isotope analyses*

1221

1222   Sm-Nd and Rb-Sr isotope compositions analyses were carried out at the

1223 Institute of Geology of the Czech Academy of Sciences (IG CAS). Two additional

1224 analyses were investigated at the Laboratório de Geologia Isotópica, of the

1225 Universidade Federal do Rio Grande do Sul (LGI-UFRGS).

1226   At the Institute of Geology of the Czech Academy of Sciences (IG CAS),

1227 about 100 mg of sample was dissolved on a hot plate for ~72 hours at 140 °C in

1228 a mixture of 23 M HF and 7 M HNO_3 in the presence of an appropriate amount of

1229 mixed ^{150}Nd–^{149}Sm spike. Afterwards, the solution was dried down, re-dissolved

1230 several times using concentrated HCl and HNO_3, and finally dissolved in 2 ml of

1231 1 M HNO_3. Strontium, Sm, and Nd were extracted from the matrix using an ion-

1232 exchange chromatography procedure outlined in Pin et al. (2014). This includes

1233 Sr isolation by Sr.resin (Triskem, France) and Sm-Nd extraction by a combination

1234 of TRU and LN resins (both from Triskem, France). The isotopic analyses of Sr,

1235 Sm, and Nd were performed using the Thermo Triton Plus thermal ionisation

1236 mass spectrometer (TIMS, Thermo) housed at the IG CAS operated at static

1237 mode and using a Re single filament and Ta-activator for Sr and a double Re and

1238 Ta–Re filament assembly for Nd and Sm, respectively. Mass fractionation

1239 correction was performed using a $^{88}Sr/^{86}Sr = 8.3752$, $^{146}Nd/^{144}Nd = 0.7219$ and

1240 $^{147}Sm/^{152}Sm = 0.56081$. The Sm and Nd concentrations were calculated by the

1241 isotope dilution method. The external reproducibility of Sr and Nd isotopic

1242 analyses was demonstrated by the long-term measurements of the NIST SRM

1243 987 yielding $^{87}Sr/^{86}Sr$ ratio of 0.710239 ± 0.000009 (2s, n = 4) and JNdi-1 with a

1244 determined $^{143}Nd/^{144}Nd$ value of 0.512104 ± 0.000007 (2s, n = 4).

1245   At the Laboratório de Geologia Isotópica (LGI-UFRGS), the samples were

1246 washed in 2.5 N HCl and then spiked with $^{149}Sm/^{150}Nd$ tracers and completely

1247 dissolved in HF, HNO_3 and HCl. Anionic LN-B50-A resin (100–150 μm) was used

1248 to separate Sm and Nd. Each element was collected, and afterwards, the

1249 samples were dried and loaded with 0.25 N H_3PO_4 on a single Ta (for Sm) and

1250 on a triple Ta-Re-Ta (for Nd) filament. The samples were run in a VG Sector 54

1251 multi-collector thermal ionisation mass spectrometer in static mode. Sr ratios

1252 were normalised to $^{86}Sr/^{88}Sr = 0.1194$. Standard values of $^{86}Sr/^{86}Sr$ ($SrCO_3$ NBS-

1253   987 standard) are 0.71026 ± 0.000010. Nd ratios were normalised to ^{146}Nd/^{144}Nd

1254   = 0.7219. Standard values of ^{143}Nd/^{144}Nd (Nd_2O_3 LaJolla Nd standard) are

1255   0.511856 ± 0.000010.

Table 1. Sm-Nd data for Porongos and Várzea do Capivarita complexes available in the literature (no data for the Passo Feio Complex).

Sample	Location	Sm (ppm)	Nd (ppm)	$^{147}Sm/^{144}Nd$	$^{143}Nd/^{144}Nd$	Error	$\varepsilon Nd_{(0)}$	Age	$\varepsilon Nd_{(t)}$	TDM (Ma)
TM-026C	EPC	7	42	0.101	0.511706	0.000009%	-18.2	790	-8.5	1809
BR-143/1	EPC	7	34	0.112	0.511889	15 ppm	-14.6	790	-6.8	1856
BR-152/1	EPC	4	26	0.105	0.511114	14 ppm	-29.7	790	-20.5	2730
BR-152/2	EPC	3	22	0.091	0.510985	14 ppm	-32.2	790	-21.6	2565
PM-01-1	WPC	7	41	0.096	0.511035		-31.0	790	-20.9	2601
PM-06	WPC	5	26	0.110	0.511444		-23.0	790	-14.2	2330
PM-19	WPC	5	30	0.097	0.511538	Initial $^{143}Nd/^{144}Nd$	-23.8	580	-16.4	2122
PM-28	WPC	2	14	0.106	0.511643	in Gollmann et	-21.9	580	-15.2	1955
PM-31B	WPC	7	39	0.107	0.511322	al. (2008) were	-25.4	790	-16.4	2459
PM-33	WPC	6	25	0.138	0.512185	recalculated	-8.5	790	-2.5	1679
PM-34	WPC	11	54	0.124	0.512145	based on the	-9.3	790	-2.0	1493
PM-36A	WPC	8	41	0.112	0.511791	available	-16.2	790	-7.6	1838
PM-37	WPC	8	43	0.115	0.511922	$^{143}Nd/^{144}Nd$	-13.7	790	-5.5	1711
PM-38	WPC	8	38	0.122	0.512044	ratios at t=770	-11.3	790	-3.7	1624
K-04C	WPC	7	35	0.118	0.512226	Ma (error were	**-7.7**	790	**0.2**	1281
K-05A	WPC	5	26	0.104	0.511204	not considered)	-30.5	580	-23.7	2764
K-10-1	WPC	10	48	0.117	0.512033		-11.5	790	-3.5	1573
TM 01 E	VCC	4	23	0.115	0.511851	0.000007%	-15.4	790	-7.2	1855
TM 29B	VCC	7	43	0.103	0.511697	0.000009%	-18.4	790	-8.9	1849
TM 35 A	VCC	5	23	0.132	0.511899	0.000006%	-14.4	790	-7.9	2139
TM 35 B	VCC	5	28	0.114	0.511697	0.000007%	-18.4	790	-10.1	2069
TM 36 G	VCC	5	22	0.131	0.511799	0.000010%	-16.4	790	-9.8	2304
TM 45 B	VCC	5	27	0.105	0.511660	0.000013%	-19.1	790	-9.8	1934
TM 45 C	VCC	7	35	0.112	0.511760	0.000009%	-17.1	790	-8.6	1932
TM 45 G	VCC	6	29	0.123	0.511787	0.000015%	-16.6	790	-9.1	2105
TM 45 H	VCC	6	33	0.111	0.511709	0.000012%	-18.1	790	-9.4	1972

EPC – Eastern region of Porongos Complex; WPC – Western region of Porongos Complex; VCC – Várzea do Capivarita Complex
Samples labelled as TM are from Martil et al. (2017); PM and K are from Gollmann et al. (2008); BR are from Saalmann et al. (2006).
Data highlighted in *italic blue* are values recalculated that match with the available published data. Recalculated data that do not match are highlighted in **bold red**.
Errors reported as in the original papers. Neodymium crustal residence ages (TDM) were calculated following the depleted mantle model of DePaolo (1981).
$\varepsilon Nd(t)$ values were recalculated using U-Pb zircon ages as reference. Original papers data are available as supplementary.

Table 2. Rb-Sr data for Porongos and Várzea do Capivarita complexes available in the literature (no data for the Passo Feio Complex).

Sample	Location	Rb (ppm)	Sr (ppm)	Rb/Sr	$^{87}Rb/^{86}Sr$	Error (SD abs)	87Sr/86Sr (present)	Error (SD abs)	Age (Ma)	$^{87}Sr/^{86}Sr_{(t)}$
TM-026C	EPC	116	167	0.692	0.69190	-	0.7452	0.000010	790	*0.7225*
BR-143/1	EPC	175	127	1.380	4.03714	0.002873	0.7558	0.000096	790	*0.7106*
BR-152/1	EPC	184	106	1.730	1.62931	0.162930	0.7425	0.000224	790	**0.6860**
BR152/2	EPC	61	237	0.260	0.72699	0.072699	0.7234	0.000800	790	*0.7150*
TM 01 E	VCC	111	136	0.812	0.81160	-	0.7429	0.000016	790	*0.7163*
TM 29 B	VCC	98	346	0.283	0.28315	-	0.7343	0.000009	790	*0.7250*
TM 35 A	VCC	148	204	0.727	0.28315	-	0.7478	0.000010	790	*0.7239*
TM 35 B	VCC	82	334	0.247	0.24709	-	0.7314	0.000013	790	*0.7233*
TM 36 G	VCC	131	187	0.703	0.70284	-	0.7400	0.000014	790	*0.7170*
TM 45 B	VCC	134	134	0.999	0.99983	-	0.7567	0.000011	790	*0.7239*
TM 45 C	VCC	120	116	1.029	1.02893	-	0.7589	0.000016	790	*0.7251*
TM 45 G	VCC	159	143	1.109	1.10948	-	0.7599	0.000007	790	*0.7235*
TM 45 H	VCC	166	108	1.538	1.53801	-	0.7687	0.000012	790	*0.7183*

EPC – Eastern region of Porongos Complex; VCC – Várzea do Capivarita Complex

Samples labelled as TM are from Martil et al. (2017); PM and K are from Gollmann et al. (2008); BR are from Saalmann et al. (2006). – Errors reported as in the original papers

**Data highlighted in *italic blue* are values recalculated that match with the available published data. Recalculated data that do not match are highlighted in bold red.
Original papers data are available as supplementary.**

Table 3 – Results of the whole rock analyses of the studied samples

Complex	Passo Feio Complex				Porongos Complex			
	Northern region		Southern region		Eastern region		Western region	
Sample name	MF-174A	MF-175A	MF-176A	MF-176B	MAB 05 A	MAB 09 C	TM-015A	MAB59A
SiO2	68.36	72.54	55.03	55.12	68.05	67.00	71.74	52.40
TiO2	0.48	0.16	1.22	1.32	0.707	0.667	0.44	1.23
Al2O3	15.66	14.84	16.69	15.38	14.03	13.8	13.99	13.36
Fe2O3T	2.78	1.54	7.33	8.51	5.48	5.49	3.36	11.73
MnO	0.04	0.02	0.09	0.11	0.098	0.107	0.07	0.28
MgO	1.17	0.63	4.14	4.47	2.1	2.26	0.73	6.41
CaO	2.71	0.50	5.58	5.42	2.99	2.96	1.44	1.66
Na2O	4.46	6.75	6.16	6.14	2.59	2.57	3.23	3.37
K2O	2.80	1.39	1.29	1.20	3.07	2.88	3.4	0.19
P2O5	0.14	0.07	0.57	0.58	0.09	0.09	0.1	0.24
LOI	1.1	1.3	1.4	1.3	1.02	2.02	1.3	0.24
Total	99.85	99.92	99.64	99.68	100.2	99.86	99.76	98.31
Sc	4	2	16	17	16	18	7	29
Be					3	2	6	1
V	33	21	155	164	89	92	39	222
Ba	1735	1370	950	911	625	591	528	102
Sr	633.8	407.5	1194.4	743.4	149	109	150.7	91
Y	8.4	4.3	25.2	26.9	26	27	40.3	19
Zr	151.3	79.4	302.3	329.7	213	206	319.2	99
La	46.5	19.7	69.2	72.2	34	30.2	50.7	20.6
Ce	76.3	34.7	136.7	143.0	70.4	62.2	103.2	40.8
Pr	7.59	3.40	15.61	16.58	8	7.02	11.98	4.83
Nd	24.9	11.7	59.9	64.1	29.7	26.6	43.1	20.1
Sm	3.43	1.80	10.55	11.54	5.6	5.2	8.3	4.2
Eu	0.93	0.51	2.28	2.23	1.1	1.1	1.13	1.35
Gd	2.42	1.30	7.89	8.64	4.9	4.5	7.55	3.8
Tb	0.33	0.15	1.01	1.04	0.8	0.7	1.11	0.6
Dy	1.68	0.80	5.16	5.20	4.8	4.5	7.11	3.5
Ho	0.29	0.15	0.93	0.93	1	0.9	1.25	0.7
Er	0.81	0.33	2.60	2.62	2.8	2.7	3.69	2
Tm	0.12	0.06	0.32	0.33	0.42	0.4	0.54	0.26
Yb	0.71	0.41	2.11	2.24	2.7	2.8	3.65	1.6
Lu	0.11	0.05	0.33	0.32	0.44	0.42	0.56	0.25
Hf	3.9	2.2	7.7	8.3	5.5	5.2	9.1	2.6
Ta	0.8	0.7	0.9	1.0	0.9	0.7	1.3	1.6
W	-	-	-	-	< 1	2	-	<1
Pb	-	-	-	-	16	14	8.2	6
Th	9.6	4.7	19.5	21.3	12.3	9.5	23.6	2.2
U	1.4	1.5	7.0	7.5	3.1	2.4	5	0.6
Co	6.8	5.1	28.1	28.4	12	12	5.8	49
Ni	<20	<20	35	49	20	< 20	56.2	220
Cu	<20	<20	35	49	20	10	10.6	<10
Zn	1.7	4.9	29.6	10.6	70	70	56	90
Ga	13.7	11.7	19.6	17.6	16	16	18.9	14
Rb	39.1	15.2	46.3	41.1	136	103	179.5	6
Nb	17.7	10.3	16.5	18.5	10	8	17.3	29
Cs	0.7	<0.1	0.9	0.8	4.5	1.9	13.8	0.6
Cr					50	40	40	560
Reference	This paper				Battisti et al. (2018)		Martil et al. (2017)	This paper

Table 4. New Rb-Sr and Sm-Nd data of the samples studied in this paper.

Sample	Location	Rb (ppm)	Sr (ppm)	$^{87}Rb/^{86}Sr$	$^{87}Sr/^{86}Sr$ (present)	Error	Age (Ma)	$^{87}Sr/^{86}Sr_{(t)}$	Sm (ppm)	Nd (ppm)	$^{147}Sm/^{144}Nd$	$^{143}Nd/^{144}Nd$	Error	eNd$_{(i)}$	eNd$_{(t)}$	TDM (Ma)
MF174A	NPFC	39	634	0.178	0.7050	0.001%	580	0.7035	2	13	0.086	0.511716	8 ppm	-17.9	-9.8	1579
MF175A	NPFC	15	408	0.106	0.7050	0.001%	580	0.7041	4	27	0.077	0.511653	15 ppm	-19.2	-10.4	1555
MF176B	SPFC	41	743	0.160	0.7064	6×10^{-6}	580	0.7050	12	65	0.110	0.512205	4.1×10^{-6}	-8.5	-2.1	1235
MAB05A	EPC	136	149	2.654	0.7548	7×10^{-6}	790	0.7248	6	30	0.114	0.511723	5.8×10^{-6}	-17.9	-9.5	2019
MAB09C	EPC	103	109	2.749	0.7615	7×10^{-6}	790	0.7305	5	28	0.116	0.511713	5.5×10^{-6}	-18.1	-9.9	2080
TM015A	WPC	179	151	3.461	0.7474	7×10^{-6}	790	0.7083	9	44	0.120	0.511925	6.4×10^{-6}	-13.9	-6.2	1822
MAB59A	WPC	6	91	0.191	0.7081	5×10^{-6}	600	0.7065	4	19	0.125	0.512417	5.7×10^{-6}	-4.3	1.2	1079

NPF – Northern region of Passo Feio Complex; SPF – Southern region of Passo Feio Complex; EPC – Eastern region of Porongos Complex; WPC – Western region of Porongos Complex
Errors reported as in the original laboratories report. Neodymium crustal residence ages (TDM) were calculated following the depleted mantle model of De Paolo (1981). 87Sr/86Sr$_{(t)}$ and
ℰNd$_{(t)}$ values were recalculated using U-Pb zircon ages as reference.

Table 5. Summary of the results obtained in this study (coordinates in UTM – fuse 22J – datum Córrego Alegre, 1984)

Complex	*Region*	Sample	Coordinates	U-Pb crystallization age (Ma)	Whole Rock geochemistry	Isotopes Sm-Nd	Isotopes Rb-Sr
Passo Feio	*Northern*	MF174A	260068; 6632226	580 ± 1	x	x	x
		MF175A	260017; 6633605	580 ± 2	x	x	x
	Southern	MF176A	266358; 6607278	-	x	--	--
		MF176B		-	x	x	x
Porongos	*Eastern*	MAB05A	328255; 6631286	-	Battisti et al (2018)	x	x
		MAB09C	324433; 6614439	-	Battisti et al (2018)	x	x
	Western	TM015A	317896; 6630029	-	Martil et al (2017)	x	x
		MAB59A	306859; 6627775	-	x	x	x

Anexos

Artigo 1
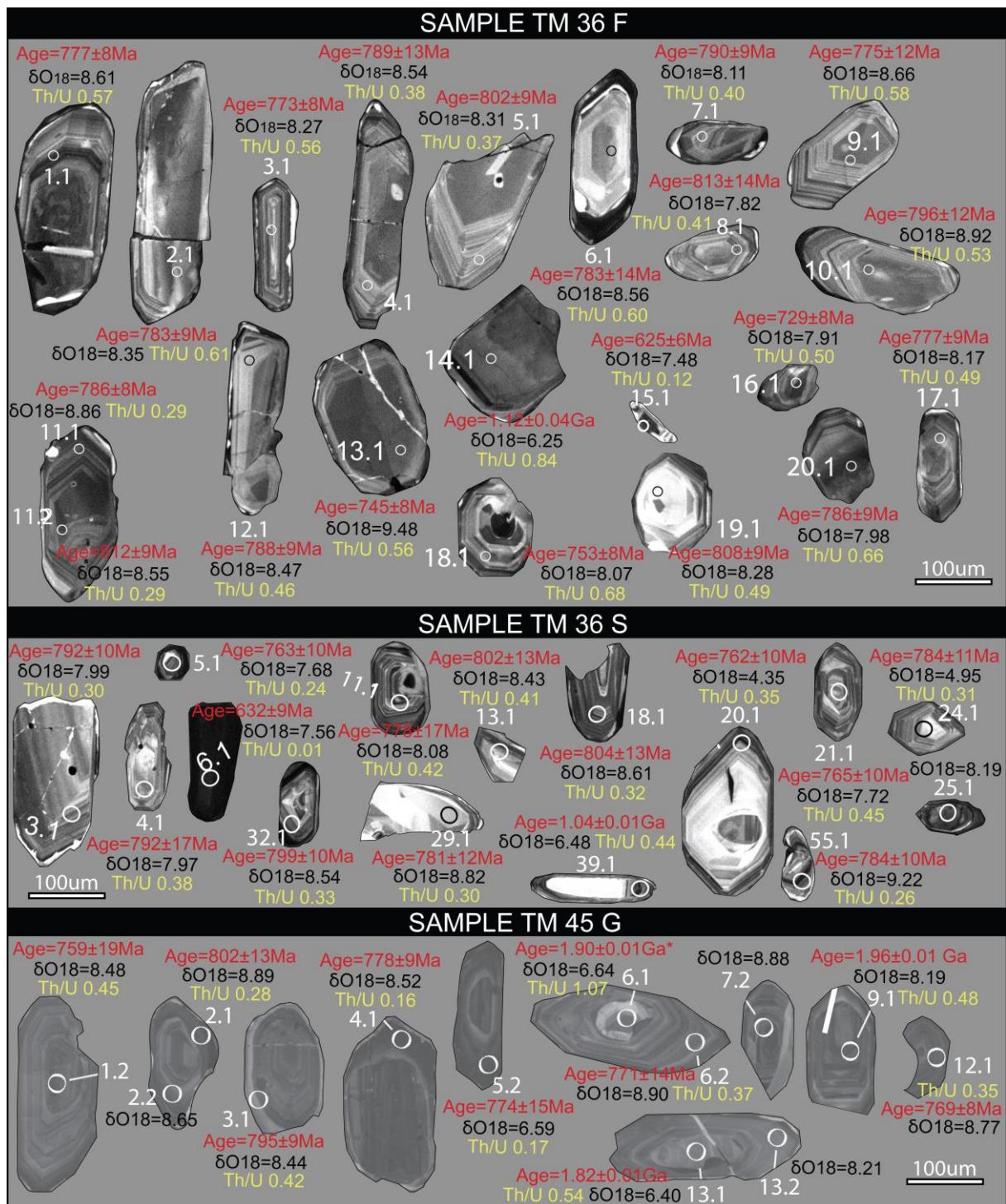
Figura S1. Imagem de catodoluminescência dos cristais de zircão das amostras TM36F, TM36S e TM45G com idade ^{238}U–^{206}Pb, δO_{18} e razões Th/U indicadas.
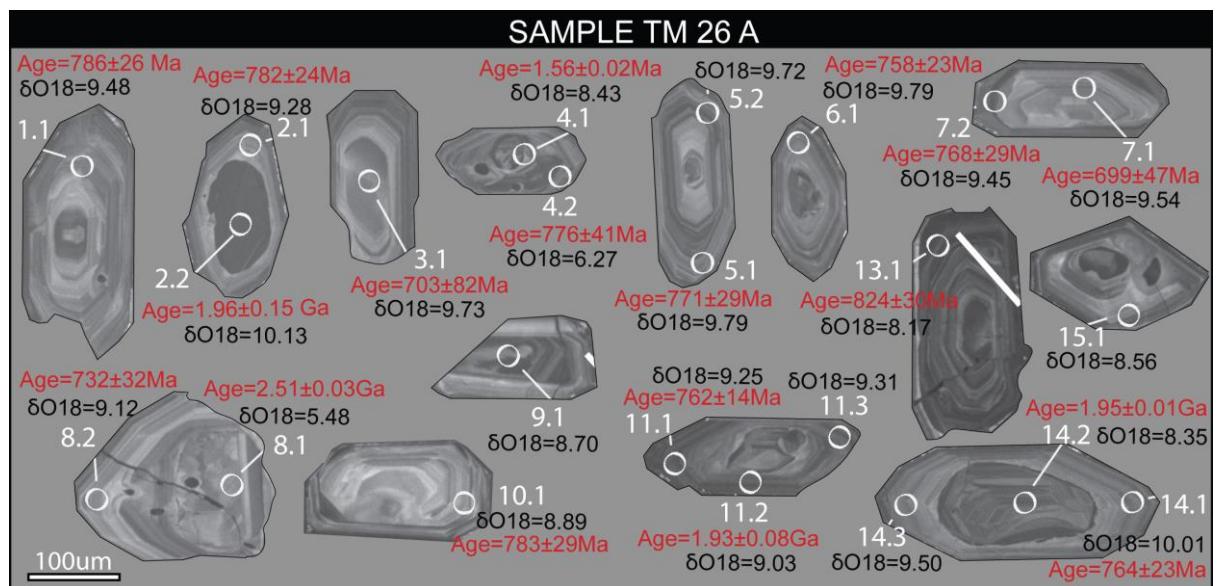
Figura S2. Imagem de catodoluminescência dos cristais de zircão da amostra TM26A com idade $^{238}U–^{206}Pb$ e δO_{18} indicados.

Tabela S1: Resumo dos dados SHRIMP U-Pb em zircão da amostra TM-36F

Grain.Spot	% $^{206}Pb_c$	ppm U	ppm Th	$^{232}Th/^{238}U$	±%	(1) ppm $^{206}Pb^*$	(1) $^{206}Pb/^{238}U$ Age		(1) $^{207}Pb/^{206}Pb$ Age		% Dis-cor-dant	(1) $^{207}Pb^*/^{206}Pb^*$	±%	(1) $^{207}Pb^*/^{235}U$	±%	(1) $^{206}Pb^*/^{238}U$	±%	err corr
1.1	0.72	431	238	0.571	0.23	47	777	±8	803	±31	+3	0.0659	1.48	1.164	1.8	0.1281	1.1	0.59
2.1	0.08	175	104	0.613	0.30	19	783	±9	752	±22	-4	0.0643	1.03	1.145	1.5	0.1292	1.2	0.75
3.1	0.20	199	109	0.569	0.29	22	773	±8	816	±23	+6	0.0663	1.08	1.165	1.6	0.1274	1.1	0.73
4.1	0.07	138	51	0.384	0.36	15	789	±13	785	±23	-1	0.0653	1.11	1.173	2.1	0.1302	1.7	0.84
5.1	0.02	155	56	0.372	0.65	18	802	±9	772	±20	-4	0.0649	0.93	1.186	1.5	0.1325	1.2	0.78
6.1	0.04	164	95	0.601	1.16	18	783	±14	788	±21	+1	0.0654	0.98	1.166	2.1	0.1292	1.9	0.88
7.1	0.11	178	68	0.396	0.33	20	790	±9	766	±22	-3	0.0648	1.03	1.164	1.5	0.1304	1.2	0.75
8.1	0.05	181	71	0.409	1.50	21	813	±14	791	±19	-3	0.0655	0.91	1.214	2.0	0.1344	1.8	0.89
9.1	0.47	186	104	0.581	0.57	20	775	±12	769	±31	-1	0.0648	1.45	1.141	2.2	0.1277	1.7	0.76
10.1	0.06	183	95	0.534	0.34	21	796	±12	811	±19	+2	0.0661	0.92	1.199	1.8	0.1315	1.6	0.87
11.1	0.03	389	108	0.287	0.28	43	786	±8	805	±19	+2	0.0660	0.92	1.180	1.4	0.1297	1.1	0.77
11.2	--	226	62	0.285	2.71	26	812	±9	776	±16	-5	0.0650	0.75	1.204	1.4	0.1342	1.2	0.84
12.1	--	157	70	0.461	0.33	18	788	±9	801	±18	+2	0.0658	0.88	1.180	1.5	0.1300	1.2	0.80
13.1	0.20	182	99	0.559	0.53	19	745	±8	755	±24	+1	0.0644	1.14	1.088	1.6	0.1226	1.2	0.71
14.1	0.05	185	152	0.845	2.73	30	1119	±40	1127	±15	+1	0.0772	0.77	2.020	3.9	0.1896	3.9	0.98
15.1	--	541	64	0.122	1.60	47	625	±6	678	±11	+8	0.0621	0.54	0.872	1.2	0.1019	1.1	0.90
16.1	--	186	90	0.498	0.30	19	729	±8	777	±17	+7	0.0651	0.82	1.075	1.4	0.1198	1.2	0.82
17.1	0.09	149	71	0.488	1.52	16	777	±9	796	±22	+3	0.0657	1.06	1.159	1.6	0.1281	1.2	0.74
18.1	0.04	293	192	0.678	0.25	31	753	±8	793	±28	+5	0.0656	1.33	1.120	1.7	0.1239	1.1	0.64
19.1	0.06	102	48	0.482	0.38	12	808	±9	781	±26	-4	0.0652	1.23	1.200	1.7	0.1335	1.2	0.71
20.1	--	375	240	0.660	0.24	42	786	±9	788	±12	+0	0.0654	0.57	1.169	1.4	0.1297	1.3	0.91

Errors are 1-sigma; Pb_c and Pb^* indicate the common and radiogenic portions, respectively.

Error in Standard calibration was 0.23% (not included in above errors but required when comparing data from different mounts).

(1) Common Pb corrected using measured ^{204}Pb.

Tabela S2: Resumo dos dados SHRIMP U-Pb em zircão da amostra TM-36S.

Grain.Spot	% $^{206}Pb_c$	ppm U	ppm Th	$^{232}Th/^{238}U$	±%	(1) ppm $^{206}Pb^*$	(1) $^{206}Pb/^{238}U$ Age		(1) $^{207}Pb/^{206}Pb$ Age		% Dis-cor-dant	(1) $^{207}Pb^*/^{206}Pb^*$	±%	(1) $^{207}Pb^*/^{235}U$	±%	(1) $^{206}Pb^*/^{238}U$	±%	err corr
1.1	0.07	229	83	0.37	0.37	25	774	±10	762	±28	-2	0.0646	1.3	1.14	1.9	0.128	1.4	0.72
2.1	0.05	190	78	0.42	0.38	21	788	±13	782	±29	-1	0.0652	1.4	1.17	2.2	0.130	1.7	0.78
3.1	0.03	290	83	0.30	0.37	33	792	±10	799	±26	+1	0.0658	1.2	1.19	1.8	0.131	1.4	0.75
4.1	--	208	76	0.38	0.40	23	792	±17	807	±41	+2	0.0660	2.0	1.19	3.0	0.131	2.2	0.75
5.1	0.02	438	100	0.24	0.34	47	763	±10	780	±23	+2	0.0652	1.1	1.13	1.7	0.126	1.4	0.78
6.1	0.00	893	8	0.01	1.10	79	632	±9	636	±15	+1	0.0609	0.7	0.87	1.6	0.103	1.4	0.89
7.1	0.03	378	65	0.18	1.08	39	737	±9	756	±22	+3	0.0645	1.0	1.08	1.7	0.121	1.3	0.79
8.1	0.07	409	177	0.45	0.28	44	761	±10	823	±22	+8	0.0665	1.1	1.15	1.7	0.125	1.3	0.79
9.1	0.03	80	22	0.29	0.77	8	751	±12	762	±136	+2	0.0646	6.5	1.10	6.7	0.123	1.7	0.26
10.1	0.03	327	182	0.57	0.28	36	775	±10	810	±23	+5	0.0661	1.1	1.16	1.8	0.128	1.4	0.79
11.1	0.03	348	142	0.42	0.31	38	778	±17	796	±22	+2	0.0657	1.1	1.16	2.5	0.128	2.3	0.90
12.1	0.22	213	87	0.42	0.72	31	1012	±13	1091	±35	+8	0.0759	1.7	1.78	2.2	0.170	1.4	0.64
13.1	--	257	101	0.41	0.37	29	802	±13	798	±33	-1	0.0657	1.6	1.20	2.3	0.133	1.7	0.74
14.1	--	384	162	0.44	0.29	43	785	±10	813	±24	+4	0.0662	1.1	1.18	1.8	0.130	1.4	0.77
15.1	0.21	102	41	0.41	1.07	11	748	±11	741	±82	-1	0.0640	3.9	1.09	4.2	0.123	1.6	0.38
16.1	0.10	385	166	0.45	0.35	41	750	±10	756	±30	+1	0.0644	1.4	1.10	2.0	0.123	1.4	0.70
17.1	0.04	63	19	0.31	0.84	7	801	±13	799	±97	-0	0.0658	4.6	1.20	4.9	0.132	1.8	0.36
18.1	0.08	385	121	0.32	0.34	44	804	±13	813	±26	+1	0.0662	1.3	1.21	2.1	0.133	1.7	0.81
19.1	0.07	294	86	0.30	0.94	32	762	±10	761	±33	-0	0.0646	1.6	1.12	2.1	0.125	1.4	0.66
20.1	0.09	218	74	0.35	0.43	23	762	±10	789	±43	+4	0.0655	2.0	1.13	2.5	0.125	1.4	0.57
21.1	--	272	119	0.45	0.35	29	765	±10	800	±30	+5	0.0658	1.4	1.14	2.0	0.126	1.4	0.70
22.1	0.14	637	325	0.53	0.21	66	738	±9	777	±21	+5	0.0651	1.0	1.09	1.7	0.121	1.3	0.80
23.1	0.05	957	70	0.08	0.40	103	758	±11	808	±14	+6	0.0660	0.7	1.14	1.7	0.125	1.5	0.92
24.1	0.18	202	61	0.31	0.55	22	784	±11	798	±47	+2	0.0657	2.2	1.17	2.7	0.129	1.4	0.54
25.1	0.03	428	76	0.18	0.40	81	1285	±16	1716	±79	+28	0.1051	4.3	3.20	4.5	0.221	1.4	0.30
26.1	0.46	494	291	0.61	1.28	53	754	±11	745	±31	-1	0.0641	1.5	1.10	2.1	0.124	1.6	0.73
27.1	0.16	237	97	0.42	0.38	25	747	±10	746	±38	-0	0.0641	1.8	1.09	2.3	0.123	1.5	0.63
28.1	0.03	327	63	0.20	0.45	37	791	±16	811	±25	+3	0.0662	1.2	1.19	2.4	0.131	2.1	0.87
29.1	0.28	117	34	0.30	0.64	13	781	±12	800	±66	+2	0.0658	3.2	1.17	3.6	0.129	1.7	0.47
30.1	--	284	135	0.49	0.34	31	761	±10	771	±25	+1	0.0649	1.2	1.12	1.8	0.125	1.4	0.76
31.1	--	236	45	0.20	1.67	24	716	±10	732	±33	+2	0.0637	1.6	1.03	2.1	0.117	1.4	0.67
32.1	0.07	333	107	0.33	0.36	38	799	±10	814	±29	+2	0.0662	1.4	1.20	1.9	0.132	1.4	0.71
33.1	0.07	416	164	0.41	0.30	46	785	±12	775	±27	-1	0.0650	1.3	1.16	2.1	0.130	1.6	0.79

34.1	0.03	506	120	0.24	0.33	52	730	±9	734	±21	+1	0.0638	1.0	1.05	1.7	0.120	1.3	0.80
35.1	0.10	422	152	0.37	0.73	44	737	±10	745	±27	+1	0.0641	1.3	1.07	1.9	0.121	1.4	0.74
36.1	0.16	426	290	0.70	1.19	47	782	±12	780	±29	-0	0.0652	1.4	1.16	2.1	0.129	1.7	0.77
37.1	0.25	128	46	0.38	0.56	14	770	±11	749	±73	-3	0.0642	3.4	1.12	3.8	0.127	1.5	0.41
38.1	0.07	742	155	0.22	1.39	80	759	±10	742	±22	-2	0.0640	1.0	1.10	1.7	0.125	1.3	0.79
39.1	0.15	351	150	0.44	0.69	51	1004	±13	1043	±37	+4	0.0741	1.8	1.72	2.3	0.169	1.4	0.60
40.1	0.36	261	87	0.34	0.41	29	782	±10	758	±50	-3	0.0645	2.4	1.15	2.8	0.129	1.4	0.51
41.1	0.04	290	55	0.20	0.89	29	717	±9	713	±29	-1	0.0631	1.3	1.02	1.9	0.118	1.4	0.72
42.1	0.01	298	70	0.24	0.54	31	738	±10	763	±37	+4	0.0647	1.7	1.08	2.2	0.121	1.4	0.62
43.1	--	195	97	0.52	0.41	22	800	±11	783	±40	-2	0.0653	1.9	1.19	2.4	0.132	1.5	0.61
44.1	--	179	56	0.33	0.61	21	807	±11	785	±39	-3	0.0653	1.8	1.20	2.4	0.133	1.5	0.62
46.1	0.11	737	225	0.32	0.24	80	767	±10	778	±19	+2	0.0651	0.9	1.13	1.6	0.126	1.3	0.83
47.1	0.01	397	156	0.41	0.30	52	919	±12	1143	±19	+21	0.0778	1.0	1.65	1.7	0.153	1.4	0.82
48.1	--	371	90	0.25	0.82	43	814	±11	779	±29	-5	0.0652	1.4	1.21	2.0	0.135	1.4	0.71
50.1	0.07	279	82	0.30	0.41	31	790	±10	781	±36	-1	0.0652	1.7	1.17	2.2	0.130	1.4	0.63
51.1	--	347	101	0.30	0.37	38	773	±10	795	±22	+3	0.0656	1.0	1.15	1.7	0.127	1.4	0.80
52.1	0.09	634	242	0.39	0.24	68	754	±10	831	±18	+10	0.0668	0.9	1.14	1.6	0.124	1.3	0.84
54.1	0.04	483	134	0.29	0.32	56	815	±14	805	±24	-1	0.0659	1.1	1.23	2.1	0.135	1.8	0.84
55.1	0.03	876	224	0.26	0.24	97	784	±10	793	±19	+1	0.0656	0.9	1.17	1.6	0.129	1.3	0.83
56.1	0.13	232	101	0.45	0.39	27	816	±11	784	±40	-4	0.0653	1.9	1.22	2.4	0.135	1.4	0.60
57.1	0.93	189	45	0.24	0.55	19	727	±13	759	±74	+4	0.0645	3.5	1.06	4.0	0.119	1.9	0.48
58.1	--	224	80	0.37	0.42	23	741	±14	812	±43	+9	0.0662	2.1	1.11	2.8	0.122	1.9	0.68
59.1	0.21	247	85	0.35	0.75	27	782	±10	754	±47	-4	0.0644	2.2	1.14	2.6	0.129	1.4	0.54
60.1	0.58	429	67	0.16	0.43	57	923	±12	1364	±27	+35	0.0872	1.4	1.85	1.9	0.154	1.4	0.70
61.1	0.11	228	58	0.26	0.50	26	791	±11	773	±45	-2	0.0650	2.2	1.17	2.6	0.130	1.4	0.55
62.1	0.09	474	118	0.26	0.34	54	804	±13	791	±23	-2	0.0655	1.1	1.20	2.0	0.133	1.7	0.85
63.1	0.01	794	265	0.34	0.23	91	807	±10	786	±14	-3	0.0654	0.7	1.20	1.5	0.133	1.3	0.89
64.1	0.15	200	62	0.32	0.46	22	780	±11	796	±41	+2	0.0657	2.0	1.16	2.4	0.129	1.4	0.59
65.1	3.88	334	85	0.26	0.39	35	747	±10	767	±297	+3	0.0648	14.1	1.10	14.2	0.123	1.4	0.10
66.1	0.01	364	69	0.20	0.42	76	1411	±17	1688	±10	+18	0.1035	0.6	3.49	1.5	0.245	1.4	0.92
67.1	0.01	240	73	0.31	0.43	27	793	±11	792	±71	-0	0.0656	3.4	1.18	3.6	0.131	1.4	0.39
68.1	1.07	222	62	0.29	0.46	24	760	±10	771	±91	+2	0.0649	4.3	1.12	4.6	0.125	1.4	0.31
69.1	0.36	425	125	0.30	0.32	61	997	±12	1208	±21	+19	0.0804	1.1	1.85	1.7	0.167	1.3	0.78

Errors are 1-sigma; Pb$_c$ and Pb indicate the common and radiogenic portions, respectively.*

Error in Standard calibration was 0.28% (not included in above errors but required when comparing data from different mounts).

(1) Common Pb corrected using measured ^{204}Pb.

Tabela S3: Resumo dos dados SHRIMP U-Pb em zircão da amostra TM-45G.

Grain Spot	% 206 PBc	Ppm U	Ppm Th	232Th /238U	± %	(1) ppm 206Pb*	(1) 206Pb/238U Age		(1) 207Pb/206Pb Age		% disc	(1) 207Pb*/206Pb*	± [%]	(1) 207Pb*/35U	± [%]	206Pb*/238U	± [%]	err Corr
1.1	0.09	316	124	0.41	0.25	34	754	±10	772	±18	3	0.06493	0.84	1.11	1.6	0.124	1.4	0.86
1.2	0.07	503	219	0.45	4.42	54	759	±19	776	±13	2	0.06506	0.62	1.121	2.8	0.125	2.7	0.97
2.1	--	736	197	0.28	0.45	84	802	±13	800	±10	0	0.06579	0.46	1.202	1.8	0.1325	1.7	0.97
3.1	0.33	368	151	0.42	1.19	41	795	±9	1410	±27	46	0.08927	1.39	1.615	1.9	0.1312	1.2	0.66
4.1	0.01	2575	389	0.16	1.62	284	778	±9	792	±12	2	0.06556	0.57	1.16	1.3	0.1283	1.2	0.9
4.2	0	1109	786	0.73	2.96	341	1974	±43	2648	±21	29	0.17943	1.28	8.865	2.8	0.3583	2.5	0.89
5.1	0	1180	114	0.1	2.94	356	1939	±36	2842	±9	37	0.20197	0.53	9.772	2.2	0.3509	2.1	0.97
5.2	0.15	4307	692	0.17	0.7	453	744	±15	783	±26	5	0.06528	1.24	1.101	2.4	0.1224	2.1	0.86
6.1	0.05	239	247	1.07	0.25	61	1684	±34	1904	±9	13	0.11653	0.48	4.796	2.3	0.2985	2.3	0.98
6.2	--	333	120	0.37	0.29	36	771	±14	807	±20	5	0.06601	0.93	1.156	2.2	0.127	2	0.9
7.1	0.22	413	111	0.28	0.41	46	785	±32	784	±32	0	0.06531	1.52	1.167	4.6	0.1296	4.4	0.94
8.1	0.58	124	106	0.88	0.72	29	1578	±21	1945	±18	21	0.11922	1.01	4.559	1.8	0.2773	1.5	0.83
4.3	0.06	876	615	0.73	0.32	264	1940	±28	2804	±5	36	0.19725	0.32	9.552	1.7	0.3512	1.7	0.98
2.2	0.01	447	173	0.4	0.23	51	798	±11	787	±13	-2	0.0654	0.61	1.189	1.5	0.1319	1.4	0.92
9.1	0.06	412	193	0.48	2.09	126	1965	±36	1966	±14	0	0.12063	0.76	5.929	2.3	0.3565	2.1	0.94
7.2	0.04	476	215	0.47	0.43	52	776	±10	778	±13	0	0.06511	0.6	1.148	1.5	0.1279	1.4	0.92
10.1	0.02	383	156	0.42	1.67	79	1384	±21	1638	±19	17	0.10075	1.02	3.326	2	0.2394	1.7	0.85
10.2	14.46	382	108	0.29	2.53	11	210	±18	1066	±232	82	0.07492	12	0.342	14.5	0.0331	8.8	0.6
11.1	0.24	454	151	0.34	0.72	63	962	±18	1203	±30	22	0.08024	1.52	1.781	2.5	0.161	2	0.8
12.1	0.02	468	160	0.35	0.41	51	769	±8	800	±13	4	0.06579	0.6	1.15	1.2	0.1268	1.1	0.88
13.1	0.03	209	110	0.54	0.27	59	1822	±25	1829	±16	0	0.11182	0.86	5.036	1.8	0.3266	1.6	0.88
14.1	0.01	216	63	0.3	0.53	49	1512	±22	1985	±53	27	0.12197	2.96	4.446	3.4	0.2644	1.6	0.48

Errors are 1-sigma; Pb$_c$ and Pb* indicate the common and radiogenic portions, respectively.

Error in Standard calibration was 0.28% (not included in above errors but required when comparing data from different mounts).

(1) Common Pb corrected using measured ^{204}Pb.

Tabela S4: Resumo dos dados SHRIMP U-Pb em zircão da amostra TM-26A.

Grain.Spot	% $^{206}Pb_c$	ppm U	ppm Th	^{232}Th /^{238}U	±%	(1) ppm $^{206}Pb^*$	(1) ^{206}Pb /^{238}U Age		(1) ^{207}Pb /^{206}Pb Age		% Dis-cor-dant	(1) $^{207}Pb^*$ /$^{206}Pb^*$	±%	(1) $^{207}Pb^*$ /^{235}U	±%	(1) $^{206}Pb^*$ /^{238}U	±%	err corr
1.1	0.06	188	66	0.36	0.81	21	782	±9	767	±20	-2	0.06477	0.95	1.152	1.6	0.1290	1.3	0.81
1.2	0.04	292	141	0.50	4.25	39	925	±42	1147	±107	+21	0.07799	5.37	1.659	7.3	0.1543	4.9	0.67
2.1	0.01	646	20	0.03	0.50	181	1816	±27	1968	±15	+9	0.12083	0.83	5.422	1.9	0.3254	1.7	0.90
2.2	--	260	98	0.39	0.60	29	792	±11	808	±17	+2	0.06606	0.83	1.191	1.7	0.1308	1.5	0.87
3.1	0.49	185	121	0.67	1.75	21	802	±14	801	±59	-0	0.06583	2.79	1.202	3.3	0.1325	1.8	0.54
4.1	0.03	428	248	0.60	0.22	103	1598	±24	1800	±13	+13	0.11005	0.72	4.268	1.8	0.2813	1.7	0.92
4.2	0.04	300	134	0.46	1.64	34	796	±13	805	±16	+1	0.06596	0.75	1.195	1.9	0.1314	1.7	0.92
5.1	0.00	318	124	0.40	0.54	36	798	±12	780	±23	-2	0.06518	1.09	1.184	2.0	0.1318	1.6	0.83
6.1	0.00	243	92	0.39	0.30	27	777	±8	791	±17	+2	0.06552	0.79	1.157	1.4	0.1281	1.1	0.82
6.2	0.04	403	144	0.37	0.58	87	1450	±20	1863	±6	+25	0.11394	0.35	3.962	1.6	0.2522	1.6	0.98
7.1	0.05	162	97	0.62	0.88	18	785	±13	785	±32	-0	0.06532	1.54	1.167	2.3	0.1295	1.7	0.75
7.2	0.00	289	88	0.31	1.03	33	808	±8	785	±24	-3	0.06532	1.14	1.203	1.6	0.1335	1.1	0.69
8.1	0.04	186	111	0.62	0.53	73	2430	±28	2558	±13	+6	0.17001	0.78	10.730	1.6	0.4577	1.4	0.87
8.2	0.08	155	62	0.41	0.59	17	787	±13	780	±24	-1	0.06519	1.13	1.167	2.0	0.1298	1.7	0.83
9.1	0.13	463	177	0.40	0.89	50	759	±10	770	±27	+1	0.06486	1.26	1.118	1.9	0.1250	1.4	0.74
10.1	--	133	59	0.46	0.35	15	789	±10	790	±23	+0	0.06547	1.08	1.175	1.7	0.1302	1.3	0.78
11.1	--	651	162	0.26	0.23	73	791	±11	785	±10	-1	0.06532	0.45	1.176	1.5	0.1306	1.5	0.96
11.2	0.02	282	178	0.65	5.88	84	1922	±21	1957	±12	+2	0.12007	0.68	5.751	1.5	0.3474	1.3	0.89
12.1	0.01	681	78	0.12	1.43	156	1525	±22	1806	±23	+17	0.11038	1.25	4.062	2.1	0.2669	1.6	0.80
13.1	0.00	875	264	0.31	1.59	97	783	±16	801	±9	+2	0.06584	0.41	1.172	2.2	0.1291	2.2	0.98
14.1	0.01	277	129	0.48	0.26	31	787	±10	796	±15	+1	0.06568	0.73	1.177	1.5	0.1299	1.3	0.87
14.2	--	308	130	0.44	0.26	96	2001	±30	1972	±6	-2	0.12105	0.33	6.076	1.7	0.3640	1.7	0.98
15.1	0.02	204	81	0.41	0.67	22	754	±11	795	±19	+5	0.06564	0.91	1.123	1.8	0.1241	1.6	0.87

Errors are 1-sigma; Pb$_c$ and Pb* indicate the common and radiogenic portions, respectively.

Error in Standard calibration was 0.18% (not included in above errors but required when comparing data from different mounts).

(1) Common Pb corrected using measured ^{204}Pb.

Artigo 2

Tabela S1: Resumo dos dados SIMS U-Pb em monazita das amostras MAB51B e MAB56A.

MAB51B

	ISOTOPIC RATIOS							ELEMENT CONCENTRATIONS			CALCULATED AGES Ma						
$^{207}Pb/^{235}U$	± 1 σ (%)	$^{206}Pb/^{238}U$	± 1 σ (%)	Rho	$^{207}Pb/^{206}Pb$	± 1 σ	$^{206}Pb/^{204}Pb$	U (ppm)	Th (ppm)	Pb (ppm)	$^{207}Pb/^{235}U$	± 1 σ	$^{206}Pb/^{238}U$	± 1 sigma	$^{207}Pb/^{206}Pb$	± 1 σ	Disc %
# 1	0.8143	5.7809	0.1033	2.2993	0.40	0.0636	2.6433	2259	1975	71213	2498	605	27	633	14	499	117	28.2
# 2	0.8635	3.5314	0.1006	2.7351	0.77	0.0622	2.2338	20175	944	40435	1329	632	17	618	16	682	48	-9.8
# 3	0.8000	3.7682	0.0982	2.2940	0.61	0.0591	2.9894	>1e6	767	22239	650	597	17	604	13	571	65	6.1
# 4	0.8423	3.1521	0.1017	2.4649	0.78	0.0600	1.9646	27643	1235	57045	1866	620	15	625	15	605	43	3.4
# 5	0.8616	3.4417	0.1008	2.6325	0.76	0.0637	1.8220	8196	3427	72498	3019	631	16	619	16	673	47	-8.4
# 6	0.8269	2.6071	0.0999	2.3296	0.89	0.0600	1.1705	>1e6	3008	53750	1993	612	12	614	14	605	25	1.6
- 7	0.8403	3.4209	0.0998	2.4860	0.73	0.0611	2.3500	>1e6	1285	32690	1026	619	16	613	15	641	51	-4.6
# 8	0.8338	2.7596	0.1022	2.0928	0.76	0.0592	1.7988	>1e6	1229	54556	1662	616	13	627	13	573	39	9.9
# 9	0.8252	2.6105	0.0991	2.2956	0.88	0.0604	1.2431	>1e6	3455	60559	2307	611	12	609	13	617	27	-1.4
# 10	0.8298	2.2127	0.1002	1.9562	0.88	0.0600	1.0340	176782	4201	65276	2559	614	10	616	12	605	22	1.9
# 11	0.8270	3.0625	0.0987	2.5253	0.82	0.0608	1.7325	12977	1641	54608	1929	612	14	607	15	631	37	-4.0
# 12	0.8107	2.6139	0.0985	2.3627	0.90	0.0597	1.1181	>1e6	3608	85786	3160	603	12	606	14	592	24	2.4
# 13	0.8347	2.8671	0.1003	2.4594	0.86	0.0604	1.4737	46273	2080	60809	2045	616	13	616	14	617	32	-0.2
# 14	0.8070	2.7485	0.0966	2.3280	0.85	0.0606	1.4610	18768	1980	68679	2364	601	13	595	13	624	32	-4.9
# 15	0.8411	2.7524	0.0999	1.9261	0.70	0.0610	1.9662	>1e6	1242	87883	2909	620	13	614	11	641	42	-4.3
# 16	0.8270	2.5821	0.1000	2.3761	0.92	0.0606	0.9443	24259	4376	63321	2330	612	12	614	14	604	22	1.8
# 17	0.8464	2.4730	0.1014	2.0194	0.82	0.0606	1.4275	>1e6	3248	43267	1769	623	12	623	12	623	31	-0.1

MAB56A

# 1	0.6954	2.5321	0.0874	1.7722	0.70	0.0577	1.8085	7069	2964	36468	1167	536	11	540	9	519	40	4.4
# 2	0.7518	3.0156	0.0934	2.3565	0.78	0.0584	1.8817	>1e6	1481	3281	224	569	13	576	13	543	41	6.2
# 3	0.7178	5.0160	0.0894	2.2442	0.45	0.0582	4.4860	1058	1700	44262	1256	549	22	552	12	539	98	2.6
# 4	0.6811	9.4931	0.0823	2.1775	0.23	0.0600	9.2400	660	1268	32457	1235	527	40	510	11	604	201	-16.2
# 5	0.7067	2.4356	0.0873	1.9225	0.79	0.0587	1.4954	16769	3000	32051	1119	543	10	540	10	556	33	-3.1
# 6	0.6895	2.2700	0.0858	1.8907	0.83	0.0583	1.2562	18846	3573	19557	816	533	9	531	10	540	27	-1.8
# 7	0.6533	2.2383	0.0833	1.5253	0.68	0.0569	1.6382	5175	3527	40790	1383	511	9	516	8	486	36	6.4
# 8	0.7716	4.4836	0.0957	1.9032	0.42	0.0585	4.0596	11436	1012	3230	186	581	20	589	11	547	89	8.1
# 9	0.7008	2.5001	0.0864	2.0203	0.81	0.0588	1.4728	10177	3192	42889	1468	539	11	534	10	560	32	-4.7
# 10	0.6967	3.2113	0.0875	2.3950	0.75	0.0577	2.1392	6210	2298	35409	1144	537	13	541	12	520	47	4.2
# 11	0.7118	2.1032	0.0898	1.9426	0.92	0.0575	0.8062	20829	8651	30688	1611	546	9	554	10	510	18	9.1
# 12	0.7112	2.5082	0.0886	1.4919	0.59	0.0582	2.0163	6640	2551	37427	1249	545	11	547	8	537	44	2.0
# 13	0.6910	2.2442	0.0875	1.9505	0.87	0.0573	1.1099	146584	4656	31620	1238	533	9	541	10	502	24	8.1
# 14	0.7467	3.5579	0.0911	2.4077	0.68	0.0594	2.6195	26984	1179	3852	201	566	16	562	13	584	57	-3.9
# 15	0.7038	2.2144	0.0878	1.7466	0.79	0.0581	1.3612	14348	3272	34419	1190	541	9	542	9	535	30	1.5
# 16	0.7135	3.0304	0.0869	2.4651	0.81	0.0596	1.7627	29283	2859	35104	1220	547	13	537	13	587	38	-8.9

Tabela S2: Dados de química mineral da amostra MAB51B a partir de microanálises de sonda eletrônica.

Sample	MAB51B																			
Wt%	Grt Core	Grt Rim	Grt Core	Grt Rim	Grt Core	Grt Core	Grt Rim	Bt	Bt	Bt	Bt	Bt	Bt	Ms	Ms	Ms	Ms	Chl	Chl	Ilm
	1 / 1 .	2 / 1 .	3 / 1 .	11 / 1 .	12 / 1 .	13 / 1 .	14 / 1 .	5 / 1 .	6 / 1 .	7 / 1 .	8 / 1 .	16 / 1 .	19 / 1 .	9 / 1 .	10 / 1 .	15 / 1 .	20 / 1 .	17 / 1 .	18 / 1 .	4 / 1 .
SiO2	37.24	37.06	37.24	37.44	37.44	36.73	37.47	35.40	34.48	35.79	35.16	35.40	35.61	45.77	47.96	47.71	47.13	25.21	26.08	0.01
TiO2	0.08	0.00	0.09	0.02	0.04	0.12	0.02	1.62	1.49	1.65	1.55	1.50	1.64	0.34	0.33	0.32	0.44	0.12	0.11	52.99
Al2O3	20.98	20.99	20.97	21.28	21.16	20.94	20.99	19.16	18.89	19.03	19.32	19.14	19.24	35.87	32.63	33.76	34.63	22.32	23.96	0.01
FeO	23.41	25.51	24.17	26.02	24.22	23.50	25.86	19.10	19.69	19.05	18.84	19.60	18.73	0.98	1.58	1.24	1.02	24.10	24.16	42.25
MnO	13.75	11.74	12.87	12.02	12.93	13.39	11.80	0.21	0.26	0.18	0.23	0.22	0.25	0.00	0.00	0.00	0.05	0.43	0.50	4.75
MgO	1.53	1.79	1.68	1.77	1.71	1.67	1.76	9.91	10.70	9.93	9.74	9.97	9.70	0.63	1.67	1.30	0.90	15.53	13.97	0.03
CaO	3.47	2.80	3.50	3.02	3.40	3.17	2.89	0.00	0.01	0.00	0.00	0.00	0.00	0.00	0.00	0.00	0.00	0.00	0.01	0.02
Na2O	-	-	-	-	-	-	-	0.07	0.02	0.05	0.07	0.03	0.10	0.94	0.63	0.54	0.52	0.01	-	-
K2O	-	-	-	-	-	-	-	8.99	7.67	8.95	9.06	8.76	9.05	9.75	9.96	9.74	9.36	0.00	0.01	-
Cr2O3	-	-	-	-	-	-	-	-	-	-	-	-	-	-	-	-	-	0.04	0.01	0.02
ZnO	-	-	-	-	-	-	-	-	-	-	-	-	-	-	-	-	-	0.07	0.11	-
Total	100.46	99.89	100.52	101.57	100.90	99.53	100.80	94.46	93.21	94.63	93.97	94.61	94.33	94.29	94.76	94.61	94.04	87.86	88.93	100.07
Si	3.00	3.00	3.00	2.99	3.00	2.99	3.01	2.71	2.67	2.73	2.70	2.71	2.72	3.06	3.20	3.17	3.14	2.64	2.67	0.00
AlIV			0.00	0.01		0.01		1.29	1.33	1.27	1.30	1.29	1.28	0.94	0.80	0.83	0.86	1.36	1.33	0.00
AlVI	1.99	2.00	1.99	1.99	2.00	1.99	1.99	0.43	0.39	0.44	0.45	0.43	0.46	1.89	1.77	1.82	1.87	1.39	1.42	0.00
Cr	-	-	-	-	-	-	-	-	-	-	-	-	-	-	-	-	-	0.01	0.00	0.00
Fe3+	0.00	0.00	0.01	0.01	0.00	0.00	0.01	0.00	0.00	0.00	0.00	0.00	0.00	0.00	0.00	0.00	0.00	-	-	-
Ti	0.00	0.00	0.01	0.00	0.00	0.01	0.00	0.09	0.09	0.09	0.09	0.09	0.09	0.02	0.02	0.02	0.02	0.01	0.01	1.00
Fe2+	1.58	1.73	1.62	1.73	1.62	1.60	1.72	1.22	1.27	1.21	1.21	1.25	1.20	0.05	0.09	0.07	0.06	2.11	2.09	0.89
Mn	0.94	0.80	0.88	0.81	0.88	0.92	0.80	0.01	0.02	0.01	0.01	0.01	0.02	0.00	0.00	0.00	0.00	0.04	0.05	0.10
Mg	0.18	0.22	0.20	0.21	0.20	0.20	0.21	1.13	1.23	1.13	1.12	1.14	1.11	0.06	0.17	0.13	0.09	2.42	2.33	0.00
Ca	0.30	0.24	0.30	0.26	0.29	0.28	0.25	0.00	0.00	0.00	0.00	0.00	0.00	0.00	0.00	0.00	0.00	0.00	0.01	0.00
Na	-	-	-	-	-	-	-	0.01	0.00	0.01	0.01	0.00	0.01	0.12	0.08	0.07	0.07	0.00	0.00	-
K	-	-	-	-	-	-	-	0.88	0.76	0.87	0.89	0.85	0.88	0.83	0.85	0.83	0.80	0.00	0.00	-
Zn	-	-	-	-	-	-	-	-	-	-	-	-	-	-	-	-	-	-	-	-
Total	8.00	8.00	8.00	8.01	8.00	8.00	8.00	8.00	8.00	8.00	8.00	8.00	8.00	7.00	7.00	7.00	7.00	10.00	10.00	2.00
XMg	0.10	0.11	0.11	0.11	0.11	0.11	0.11	0.48	0.49	0.48	0.48	0.48	0.48	0.53	0.65	0.65	0.61	0.53	0.51	0.00
XAn	-	-						-	-	-	-	-	-	-	-	-	-	-	-	-
XGrs	0.10	0.08	0.10	0.09	0.10	0.09	0.08	-	-	-	-	-	-	-	-	-	-	-	-	-
XAlm	0.53	0.58	0.54	0.57	0.54	0.53	0.58	-	-	-	-	-	-	-	-	-	-	-	-	-
XPy	0.06	0.07	0.07	0.07	0.07	0.07	0.07	-	-	-	-	-	-	-	-	-	-	-	-	-
XSps	0.31	0.27	0.29	0.27	0.29	0.31	0.27	-	-	-	-	-	-	-	-	-	-	-	-	-

Tabela S3: Dados de química mineral da amostra MAB56A a partir de microanálises de sonda eletrônica.

Sample	MAB56A																			
Wt%	Grt Rim	Grt Rim	Grt Core	Grt Core	Grt Core	Grt Core	Grt Core	Grt Rim	Grt Rim	Grt Rim	Grt	Grt	Grt	Grt	Grt	Grt	Grt Rim	Grt Rim	Grt Core	Grt Core
	1 / 1 .	2 / 1 .	3 / 1 .	4 / 1 .	5 / 1 .	6 / 1 .	7 / 1 .	8 / 1 .	9 / 1 .	10 / 1 .	11 / 1 .	21 / 1 .	22 / 1 .	32 / 1 .	33 / 1 .	34 / 1 .	40 / 1 .	41 / 1 .	42 / 1 .	43 / 1 .
SiO2	37.02	36.85	37.46	37.29	37.45	37.15	37.73	37.36	37.62	37.05	37.34	36.64	36.60	37.68	37.14	37.31	37.45	37.48	37.42	37.48
TiO2	0.07	0.05	0.08	0.13	0.12	0.12	0.06	0.05	0.07	0.09	0.05	0.01	0.04	0.05	0.00	0.00	0.02	0.13	0.07	0.08
Al2O3	21.39	21.06	21.03	20.87	20.93	21.04	21.04	21.08	21.24	21.32	21.11	21.48	21.39	21.19	21.40	20.99	20.91	20.99	20.97	21.01
FeO	35.13	31.96	31.09	29.50	29.65	30.95	35.84	34.69	34.50	34.03	35.07	35.30	36.04	34.15	34.78	35.01	34.41	32.39	32.58	32.86
MnO	1.11	3.52	5.60	6.86	7.10	5.27	0.71	1.65	1.82	2.12	1.44	1.09	1.05	1.98	2.24	2.67	1.63	2.76	3.47	2.91
MgO	1.98	1.51	1.38	1.29	1.27	1.39	2.14	1.85	1.79	1.86	2.08	2.31	2.28	2.25	2.21	2.15	1.84	1.42	1.36	1.51
CaO	2.82	3.81	3.86	4.00	4.07	3.86	2.81	3.10	3.25	3.29	2.82	2.43	1.98	3.11	2.25	1.63	3.05	4.70	4.22	4.33
Na2O	-	-	-	-	-	-	-	-	-	-	-	-	-	-	-	-	-	-	-	-
K2O	-	-	-	-	-	-	-	-	-	-	-	-	-	-	-	-	-	-	-	-
Cr2O3	0.01	0.10	0.13	0.08	0.00	0.00	0.04	0.08	0.05	0.05	0.05	0.02	0.06	0.02	0.03	0.00	0.08	0.03	0.04	0.00
ZnO	-	-	-	-	-	-	-	-	-	-	-	-	-	-	-	-	-	-	-	-
Total	99.52	98.84	100.63	100.03	100.60	99.78	100.36	99.86	100.3	99.81	99.97	99.28	99.43	100.4	100.0	99.77	99.39	99.89	100.1	100.2
Si	3.00	3.00	3.01	3.01	3.01	3.01	3.03	3.02	3.02	2.99	3.01	2.98	2.97	3.02	2.99	3.02	3.03	3.02	3.02	3.02
AlIV	0.00									0.01		0.02	0.03		0.01					
AlVI	2.04	2.02	1.99	1.99	1.98	2.01	1.99	2.01	2.01	2.02	2.01	2.03	2.02	2.00	2.03	2.00	2.00	1.99	1.99	1.99
Cr	0.00	0.01	0.01	0.01	0.00	0.00	0.00	0.01	0.00	0.00	0.00	0.00	0.00	0.00	0.00	0.00	0.01	0.00	0.00	0.00
Fe3+	-	-	-	-	-	-	-	-	-	-	-	-	-	-	-	-	-	-	-	-
Ti	0.00	0.00	0.00	0.01	0.01	0.01	0.00	0.00	0.00	0.01	0.00	0.00	0.00	0.00	0.00	0.00	0.00	0.01	0.00	0.00
Fe2+	2.38	2.18	2.09	1.99	1.99	2.10	2.40	2.34	2.32	2.30	2.36	2.40	2.45	2.29	2.34	2.37	2.33	2.18	2.20	2.21
Mn	0.08	0.24	0.38	0.47	0.48	0.36	0.05	0.11	0.12	0.15	0.10	0.07	0.07	0.13	0.15	0.18	0.11	0.19	0.24	0.20
Mg	0.24	0.18	0.17	0.16	0.15	0.17	0.26	0.22	0.21	0.22	0.25	0.28	0.28	0.27	0.27	0.26	0.22	0.17	0.16	0.18
Ca	0.24	0.33	0.33	0.35	0.35	0.33	0.24	0.27	0.28	0.28	0.24	0.21	0.17	0.27	0.19	0.14	0.26	0.41	0.36	0.37
Na	-	-	-	-	-	-	-	-	-	-	-	-	-	-	-	-	-	-	-	-
K	-	-	-	-	-	-	-	-	-	-	-	-	-	-	-	-	-	-	-	-
Zn	-	-	-	-	-	-	-	-	-	-	-	-	-	-	-	-	-	-	-	-
Total	8.00	8.00	8.00	8.00	8.00	8.00	8.00	8.00	8.00	8.00	8.00	8.00	8.00	8.00	8.00	8.00	8.00	8.00	8.00	8.00
XMg	0.09	0.08	0.07	0.07	0.07	0.07	0.10	0.09	0.08	0.09	0.10	0.10	0.10	0.11	0.10	0.10	0.09	0.07	0.07	0.08
XAn	-	-	-	-	-	-	-	-	-	-	-	-	-	-	-	-	-	-	-	-
XGrs	0.08	0.11	0.11	0.12	0.12	0.11	0.08	0.09	0.10	0.10	0.08	0.07	0.06	0.09	0.07	0.05	0.09	0.14	0.12	0.13
XAlm	0.81	0.74	0.70	0.67	0.67	0.71	0.82	0.80	0.79	0.78	0.80	0.81	0.82	0.77	0.79	0.80	0.80	0.74	0.74	0.75
XPy	0.08	0.06	0.06	0.05	0.05	0.06	0.09	0.08	0.07	0.08	0.08	0.09	0.09	0.09	0.09	0.09	0.08	0.06	0.06	0.06
XSps	0.03	0.08	0.13	0.16	0.16	0.12	0.02	0.04	0.04	0.05	0.03	0.03	0.02	0.05	0.05	0.06	0.04	0.06	0.08	0.07

Tabela S3: continuação...

Sample	MAB56A																			
Wt%	Grt Rim	Grt Rim	Grt	Grt	Ms	Ms	Ms	Ms	Ms	Ms	Ms	Ms	Ms	Ms	Ms	Ms	Ms	Ms	Ms	Ms
	44 / 1 .	45 / 1 .	56 / 1 .	57 / 1 .	12 / 1 .	13 / 1 .	14 / 1 .	15 / 1 .	16 / 1 .	17 / 1 .	18 / 1 .	28 / 1 .	46 / 1 .	48 / 1 .	49 / 1 .	50 / 1 .	52 / 1 .	53 / 1 .	58 / 1 .	59 / 1 .
SiO2	37.56	37.38	37.16	37.17	45.65	45.11	45.77	45.50	45.38	45.96	45.03	45.27	45.82	45.83	44.99	46.25	45.76	45.03	45.50	45.46
TiO2	0.04	0.04	0.10	0.08	0.62	0.30	0.37	0.55	0.47	0.87	0.41	0.67	0.37	0.47	2.84	0.51	0.42	0.54	0.54	0.46
Al2O3	21.03	21.19	21.01	21.43	36.59	36.90	36.76	36.87	36.15	35.44	36.94	36.60	36.86	36.38	35.00	35.83	36.77	35.57	37.06	37.46
FeO	35.60	35.67	34.57	36.02	0.98	1.03	0.96	1.05	0.90	1.15	1.06	1.03	0.97	0.93	0.90	1.10	1.08	1.75	1.12	0.90
MnO	0.68	0.72	2.45	0.93	0.01	0.02	0.01	0.00	0.00	0.00	0.00	0.03	0.01	0.02	0.00	0.00	0.02	0.00	0.00	0.00
MgO	2.33	2.43	1.86	1.98	0.36	0.37	0.37	0.39	0.41	0.57	0.35	0.41	0.34	0.36	0.34	0.42	0.34	0.58	0.41	0.29
CaO	2.30	2.25	2.74	2.46	0.00	0.00	0.00	0.00	0.00	0.00	0.00	0.00	0.00	0.00	0.00	0.00	0.00	0.00	0.00	0.00
Na2O	-	-	-	-	1.25	1.24	1.23	1.09	1.14	0.68	1.27	1.26	1.26	1.14	1.01	1.13	1.20	0.79	1.20	1.27
K2O	-	-	-	-	8.98	9.21	9.14	9.04	9.25	9.64	9.06	8.97	9.08	9.24	8.62	9.14	8.84	9.09	9.22	9.13
Cr2O3	0.05	0.03	0.06	0.03	0.00	0.07	0.00	0.00	0.02	0.04	0.04	0.00	0.03	0.07	0.09	0.00	0.03	0.11	0.02	0.01
ZnO	-	-	-	-	-	-	-	-	-	-	-	-	-	-	-	-	-	-	-	-
Total	99.60	99.71	99.95	100.11	94.44	94.26	94.60	94.49	93.72	94.36	94.15	94.24	94.74	94.42	93.80	94.38	94.45	93.46	95.06	94.97
Si	3.03	3.01	3.01	3.00	3.04	3.02	3.04	3.03	3.05	3.07	3.01	3.02	3.04	3.05	3.02	3.08	3.04	3.04	3.02	3.01
AlIV				0.00	0.96	0.98	0.96	0.97	0.95	0.93	0.99	0.98	0.96	0.95	0.98	0.92	0.96	0.96	0.98	0.99
AlVI	2.00	2.01	2.00	2.03	1.91	1.92	1.92	1.92	1.91	1.86	1.92	1.90	1.92	1.91	1.79	1.90	1.92	1.88	1.91	1.93
Cr	0.00	0.00	0.00	0.00	-	-	-	-	-	-	-	-	-	-	-	-	-	-	-	-
Fe3+	-	-	-	-	-	-	-	-	-	-	-	-	-	-	-	-	-	-	-	-
Ti	0.00	0.00	0.01	0.00	0.03	0.02	0.02	0.03	0.02	0.04	0.02	0.03	0.02	0.02	0.14	0.03	0.02	0.03	0.03	0.02
Fe2+	2.40	2.41	2.34	2.43	0.05	0.06	0.05	0.06	0.05	0.06	0.06	0.06	0.05	0.05	0.05	0.06	0.06	0.10	0.06	0.05
Mn	0.05	0.05	0.17	0.06	0.00	0.00	0.00	0.00	0.00	0.00	0.00	0.00	0.00	0.00	0.00	0.00	0.00	0.00	0.00	0.00
Mg	0.28	0.29	0.22	0.24	0.04	0.04	0.04	0.04	0.04	0.06	0.03	0.04	0.03	0.04	0.03	0.04	0.03	0.06	0.04	0.03
Ca	0.20	0.19	0.24	0.21	0.00	0.00	0.00	0.00	0.00	0.00	0.00	0.00	0.00	0.00	0.00	0.00	0.00	0.00	0.00	0.00
Na	-	-	-	-	0.16	0.16	0.16	0.14	0.15	0.09	0.16	0.16	0.16	0.15	0.13	0.15	0.15	0.10	0.15	0.16
K	-	-	-	-	0.76	0.79	0.78	0.77	0.79	0.82	0.77	0.76	0.77	0.79	0.74	0.78	0.75	0.78	0.78	0.77
Zn	-	-	-	-	-	-	-	-	-	-	-	-	-	-	-	-	-	-	-	-
Total	8.00	8.00	8.00	8.00	7.00	7.00	7.00	7.00	7.00	7.00	7.00	7.00	7.00	7.00	7.00	7.00	7.00	7.00	7.00	7.00
XMg	0.10	0.11	0.09	0.09	0.40	0.39	0.41	0.40	0.45	0.47	0.37	0.42	0.38	0.41	0.40	0.40	0.36	0.37	0.39	0.36
XAn	-	-	-	-	-	-	-	-	-	-	-	-	-	-	-	-	-	-	-	-
XGrs	0.07	0.07	0.08	0.07	-	-	-	-	-	-	-	-	-	-	-	-	-	-	-	-
XAlm	0.82	0.82	0.79	0.83	-	-	-	-	-	-	-	-	-	-	-	-	-	-	-	-
XPy	0.10	0.10	0.08	0.08	-	-	-	-	-	-	-	-	-	-	-	-	-	-	-	-
XSps	0.02	0.02	0.06	0.02	-	-	-	-	-	-	-	-	-	-	-	-	-	-	-	-

Tabela S3: continuação...

Sample										MAB56A										
Wt%	Bt	Bt	Bt	Bt	Bt	Pl	Pl	Pl	Pl	Pl	Pl	Pl	Pl	Pl	Chl	Chl	Chl	Chl	Chl	Chl
	24 / 1 .	31 / 1 .	35 / 1 .	36 / 1 .	77 / 1 .	26 / 1 .	27 / 1 .	62 / 1 .	63 / 1 .	64 / 1 .	65 / 1 .	66 / 1 .	71 / 1 .	72 / 1 .	37 / 1 .	38 / 1 .	39 / 1 .	55 / 1 .	61 / 1 .	74 / 1 .
SiO2	33.28	33.86	32.18	33.75	32.63	66.89	69.59	69.34	69.15	68.98	68.04	68.81	69.01	67.66	24.48	23.72	24.23	24.10	24.71	24.36
TiO2	1.55	2.20	2.64	1.90	1.62	0.00	0.05	0.02	0.00	0.00	0.05	0.01	0.00	0.00	0.13	0.07	0.07	0.07	0.07	0.23
Al2O3	20.49	20.63	19.89	20.49	20.30	19.86	19.22	19.94	20.54	19.79	20.32	20.10	20.12	20.18	21.98	22.33	21.86	21.87	21.66	22.81
FeO	23.89	22.92	25.01	22.90	24.61	0.03	0.07	0.17	0.11	0.21	0.19	0.20	0.08	0.09	30.20	29.81	29.32	31.41	31.60	30.09
MnO	0.08	0.08	0.11	0.07	0.08	-	-	-	-	-	-	-	-	-	0.17	0.12	0.12	0.22	0.20	0.14
MgO	6.67	6.56	6.37	6.82	7.03	0.01	0.01	0.00	0.00	0.00	0.00	0.00	0.01	0.02	10.90	10.35	9.51	10.19	10.10	10.37
CaO	0.00	0.00	0.01	0.00	0.00	0.02	0.00	0.01	0.01	0.00	0.10	0.05	0.09	0.33	0.01	0.00	0.07	0.00	0.03	0.02
Na2O	0.12	0.14	0.10	0.16	0.11	11.78	11.45	11.90	12.06	12.00	11.97	11.72	11.79	11.56	0.00	0.01	0.01	0.00	0.02	0.06
K2O	7.92	8.14	7.17	8.41	6.75	0.02	0.00	0.00	0.00	0.01	0.01	0.01	0.05	0.02	0.00	0.03	0.06	0.00	0.00	0.11
Cr2O3	0.02	0.00	0.03	0.10	0.08	-	-	-	-	-	-	-	-	-	0.08	0.07	0.09	0.00	0.08	0.01
ZnO	-	-	-	-	-	-	-	-	-	-	-	-	-	-	0.06	0.10	0.08	0.05	0.09	0.16
Total	94.05	94.53	93.50	94.58	93.21	98.62	100.40	101.39	101.87	100.99	100.68	100.90	101.14	99.87	88.03	86.60	85.43	87.98	88.55	88.37
Si	2.61	2.63	2.55	2.62	2.58	2.97	3.02	2.99	2.97	2.99	2.96	2.98	2.98	2.96	2.64	2.60	2.69	2.62	2.67	2.61
AlIV	1.39	1.37	1.45	1.38	1.42	1.04	0.98	1.01	1.04	1.01	1.04	1.03	1.02	1.04	1.36	1.40	1.31	1.38	1.33	1.39
AlVI	0.50	0.51	0.41	0.50	0.47	-	-	-	-	-	-	-	-	-	1.43	1.49	1.54	1.43	1.42	1.49
Cr	-	-	-	-	-	-	-	-	-	-	-	-	-	-	0.01	0.01	0.01	0.00	0.01	0.00
Fe3+	-	-	-	-	-	-	-	-	-	-	-	-	-	-						
Ti	0.09	0.13	0.16	0.11	0.10	0.00	0.00	0.00	0.00	0.00	0.00	0.00	0.00	0.00	0.01	0.01	0.01	0.01	0.01	0.02
Fe2+	1.57	1.49	1.66	1.49	1.63	0.00	0.00	0.01	0.00	0.01	0.01	0.01	0.00	0.00	2.72	2.73	2.72	2.86	2.85	2.70
Mn	0.01	0.01	0.01	0.00	0.01	-	-	-	-	-	-	-	-	-	0.02	0.01	0.01	0.02	0.02	0.01
Mg	0.78	0.76	0.75	0.79	0.83	0.00	0.00	0.00	0.00	0.00	0.00	0.00	0.00	0.00	1.75	1.69	1.57	1.65	1.62	1.66
Ca	0.00	0.00	0.00	0.00	0.00	0.00	0.00	0.00	0.00	0.00	0.00	0.00	0.00	0.02	0.00	0.00	0.01	0.00	0.00	0.00
Na	0.02	0.02	0.02	0.02	0.02	1.01	0.96	0.99	1.00	1.01	1.01	0.98	0.99	0.98	0.00	0.00	0.00	0.00	0.01	0.02
K	0.79	0.81	0.73	0.83	0.68	0.00	0.00	0.00	0.00	0.00	0.00	0.00	0.00	0.00	0.00	0.00	0.00	0.00	0.00	0.01
Zn	-	-	-	-	-	-	-	-	-	-	-	-	-	-	0.00	0.01	0.01	0.00	0.01	0.01
Total	8.00	8.00	8.00	8.00	8.00	5.00	5.00	5.00	5.00	5.00	5.00	5.00	5.00	5.00	10.00	10.00	10.00	10.00	10.00	10.00
XMg	0.33	0.34	0.31	0.35	0.34	-	-	-	-	-	-	-	-	-	0.39	0.38	0.37	0.37	0.36	0.38
XAn	-	-	-	-	-	1.00	1.00	1.00	1.00	1.00	0.99	1.00	0.99	0.98	-	-	-	-	-	-
XGrs	-	-	-	-	-	-	-	-	-	-	-	-	-	-	-	-	-	-	-	-
XAlm	-	-	-	-	-	-	-	-	-	-	-	-	-	-	-	-	-	-	-	-
XPy	-	-	-	-	-	-	-	-	-	-	-	-	-	-	-	-	-	-	-	-
XSps	-	-	-	-	-	-	-	-	-	-	-	-	-	-	-	-	-	-	-	-

Tabela S4: Dados de química mineral da amostra BD03 a partir de microanálises de sonda eletrônica.

Sample	BD03																			
Wt%	Grt Core	Grt Core	Grt Rim	Grt Rim	Grt Core	Grt Rim	Grt Rim	Grt	Grt	Grt Core	Grt Core	Grt Core	St	St	St	St	St	St	St	Bt
	1/1.	2/1.	3/1.	5/1.	13/1.	14/1.	23/1.	24/1.	25/1.	26/1.	27/1.	28/1.	8/1.	11/1.	19/1.	22/1.	33/1.	34/1.	38/1.	7/1.
SiO2	36.62	36.57	37.40	36.54	36.75	37.20	36.84	36.73	36.60	36.70	36.93	36.66	27.14	27.31	27.57	27.65	27.12	27.16	27.39	35.28
TiO2	0.04	0.07	0.06	0.08	0.05	0.06	0.03	0.09	0.08	0.02	0.06	0.07	0.83	0.56	0.63	0.67	0.82	0.81	0.52	1.41
Al2O3	20.76	20.90	20.95	21.02	20.68	21.16	20.84	21.15	20.83	20.78	21.01	20.85	53.21	54.09	53.59	53.66	53.14	53.12	54.38	18.58
FeO	29.01	29.28	33.02	32.56	28.97	31.69	33.56	30.89	29.86	29.38	28.72	29.44	13.42	12.55	13.28	13.37	13.66	13.74	12.87	19.61
MnO	8.78	8.91	3.93	4.88	8.45	5.41	3.41	6.31	7.69	8.64	8.70	8.17	0.18	0.24	0.20	0.19	0.26	0.18	0.26	0.11
MgO	1.92	1.84	2.64	2.44	1.78	2.32	2.72	2.12	2.02	1.84	1.85	1.89	1.39	1.36	1.87	1.73	1.67	1.72	1.61	9.75
CaO	2.66	2.83	2.68	2.65	2.98	2.69	2.20	3.00	2.75	2.94	2.82	2.93	0.00	0.00	0.00	0.04	0.00	0.00	0.00	0.00
Na2O	0.05	0.01	0.03	0.02	0.00	0.00	0.00	0.04	0.03	0.01	0.05	0.02	0.01	0.01	0.02	0.03	0.03	0.00	0.01	0.08
K2O	0.00	0.00	0.00	0.01	0.00	0.00	0.00	0.00	0.00	0.00	0.00	0.00	0.02	0.01	0.00	0.00	0.00	0.00	0.00	9.42
Cr2O3	0.02	0.01	0.03	0.06	0.00	0.00	0.01	0.04	0.00	0.00	0.05	0.02	0.08	0.03	0.10	0.06	0.11	0.08	0.12	0.13
ZnO	0.00	0.00	0.00	0.00	0.00	0.00	0.00	0.00	0.00	0.00	0.00	0.00	0.16	0.19	0.14	0.15	0.17	0.19	0.17	0.00
Total	99.87	100.41	100.75	100.25	99.65	100.53	99.60	100.37	99.86	100.30	100.20	100.04	96.43	96.34	97.39	97.55	97.00	97.02	97.33	94.38
Si	2.98	2.96	3.00	2.96	2.99	2.99	2.99	2.97	2.98	2.98	2.99	2.98	3.92	3.93	3.93	3.94	3.89	3.90	3.90	2.72
AlIV	0.02	0.04	0.00	0.04	0.01	0.01	0.01	0.03	0.02	0.02	0.01	0.02	0.08	0.07	0.07	0.06	0.11	0.10	0.10	1.28
AlVI	1.97	1.96	1.98	1.96	1.98	1.99	1.98	1.98	1.97	1.96	1.99	1.97	9.04	9.17	9.00	9.00	8.96	8.96	9.11	0.40
Cr	0.00	0.00	0.00	0.00	0.00	0.00	0.00	0.00	0.00	0.00	0.00	0.00	0.01	0.00	0.01	0.01	0.01	0.01	0.01	0.01
Fe3+	0.03	0.04	0.02	0.03	0.02	0.00	0.02	0.02	0.03	0.04	0.00	0.03	0.00	0.00	0.00	0.00	0.00	0.00	0.00	0.00
Ti	0.00	0.00	0.00	0.00	0.00	0.00	0.00	0.01	0.00	0.00	0.00	0.00	0.00	0.00	0.00	0.00	0.00	0.00	0.00	0.08
Fe2+	1.95	1.95	2.19	2.17	1.95	2.13	2.26	2.07	2.01	1.96	1.94	1.98	1.62	1.51	1.58	1.59	1.64	1.65	1.53	1.26
Mn	0.61	0.61	0.27	0.33	0.58	0.37	0.23	0.43	0.53	0.59	0.60	0.56	0.02	0.03	0.02	0.02	0.03	0.02	0.03	0.01
Mg	0.23	0.22	0.32	0.29	0.22	0.28	0.33	0.26	0.24	0.22	0.22	0.23	0.30	0.29	0.40	0.37	0.36	0.37	0.34	1.12
Ca	0.23	0.25	0.23	0.23	0.26	0.23	0.19	0.26	0.24	0.26	0.24	0.25	0.00	0.00	0.00	0.01	0.00	0.00	0.00	0.00
Na	0.01	0.00	0.00	0.00	0.00	0.00	0.00	0.01	0.01	0.00	0.01	0.00	0.00	0.00	0.00	0.01	0.01	0.00	0.00	0.01
K	0.00	0.00	0.00	0.00	0.00	0.00	0.00	0.00	0.00	0.00	0.00	0.00	0.00	0.00	0.00	0.00	0.00	0.00	0.00	0.93
Zn	0.00	0.00	0.00	0.00	0.00	0.00	0.00	0.00	0.00	0.00	0.00	0.00	0.02	0.02	0.01	0.02	0.02	0.02	0.02	0.00
Total	8.00	8.00	8.00	8.00	8.00	8.00	8.00	8.00	8.00	8.00	8.00	8.00	15.00	15.00	15.00	15.00	15.00	15.00	15.00	8.00
XMg	0.11	0.10	0.13	0.12	0.10	0.12	0.13	0.11	0.11	0.10	0.10	0.10	0.16	0.16	0.20	0.19	0.18	0.18	0.18	0.47
XAn	-	-	-	-	-	-	-	-	-	-	-	-	-	-	-	-	-	-	-	-
XGrs	0.08	0.08	0.08	0.08	0.09	0.08	0.06	0.09	0.08	0.08	0.08	0.08	-	-	-	-	-	-	-	-
XAlm	0.65	0.64	0.73	0.72	0.65	0.71	0.75	0.69	0.66	0.65	0.65	0.65	-	-	-	-	-	-	-	-
XPy	0.08	0.07	0.10	0.10	0.07	0.09	0.11	0.08	0.08	0.07	0.07	0.08	-	-	-	-	-	-	-	-
XSps	0.20	0.20	0.09	0.11	0.19	0.12	0.08	0.14	0.18	0.20	0.20	0.19	-	-	-	-	-	-	-	-

Tabela S4: Continuação...

Sample	BD03																			
Wt%	Bt	Bt	Bt	Bt	Bt	Ms	Ms	Ms	Ms	Ms	Pl	Pl	Pl	Pl	Pl	Chl	Chl	Chl	Ilm in Grt	Ilm in St
	17/1.	18/1.	30/1.	37/1.	40/1.	6/1.	15/1.	21/1.	32/1.	41/1.	12/1.	16/1.	20/1.	29/1.	39/1.	31/1.	36/1.	42/1.	4/1.	10/1.
SiO2	35.75	35.60	35.63	35.13	34.90	45.59	45.40	45.81	45.75	45.71	59.53	60.42	60.30	59.57	59.95	24.74	24.16	24.78	0.03	0.00
TiO2	0.75	1.19	1.63	1.47	1.37	0.39	0.31	0.43	0.45	0.40	0.00	0.00	0.00	0.00	0.03	0.13	0.08	0.10	52.57	52.85
Al2O3	19.20	19.91	19.34	20.08	19.73	37.33	36.91	36.96	37.13	36.63	24.95	24.63	24.88	24.98	24.63	23.29	23.30	22.56	0.04	0.03
FeO	18.23	18.03	17.42	19.22	18.54	0.81	0.80	0.75	0.73	0.74	0.12	0.03	0.25	0.08	0.08	23.48	24.70	23.73	44.70	45.55
MnO	0.09	0.10	0.09	0.13	0.09	0.03	0.01	0.00	0.04	0.00	0.01	0.00	0.00	0.01	0.00	0.17	0.16	0.12	0.97	0.85
MgO	10.39	10.01	10.20	8.62	9.99	0.53	0.49	0.58	0.56	0.52	0.00	0.00	0.00	0.00	0.00	15.02	14.36	15.23	0.53	0.30
CaO	0.00	0.00	0.00	0.00	0.00	0.00	0.00	0.00	0.01	0.00	7.01	7.06	6.75	6.86	6.95	0.02	0.06	0.02	0.07	0.00
Na2O	0.06	0.16	0.20	0.11	0.07	1.29	1.19	1.16	1.23	1.24	7.76	8.18	8.11	7.85	7.95	0.00	0.00	0.00	0.01	0.01
K2O	9.48	9.06	9.29	9.37	9.19	9.19	9.48	9.39	9.41	9.46	0.08	0.10	0.09	0.10	0.10	0.03	0.03	0.06	0.00	0.00
Cr2O3	0.00	0.09	0.04	0.07	0.09	0.03	0.10	0.17	0.18	0.15	0.00	0.03	0.00	0.00	0.00	0.03	0.03	0.04	0.02	0.03
ZnO	0.00	0.00	0.00	0.00	0.00	0.00	0.00	0.00	0.00	0.00	0.00	0.00	0.00	0.00	0.00	0.00	0.00	0.00	0.00	0.00
Total	93.94	94.12	93.84	94.20	93.97	95.18	94.68	95.25	95.48	94.84	99.47	100.46	100.37	99.45	99.68	86.92	86.88	86.65	98.94	99.61
Si	2.74	2.71	2.72	2.70	2.68	3.01	3.02	3.03	3.02	3.04	2.67	2.69	2.68	2.67	2.68	2.60	2.56	2.62	0.00	0.00
AlIV	1.26	1.29	1.28	1.30	1.32	0.99	0.98	0.97	0.98	0.96	1.32	1.29	1.30	1.32	1.30	1.40	1.44	1.38	0.00	0.00
AlVI	0.48	0.50	0.47	0.52	0.47	1.92	1.92	1.91	1.91	1.90	0.00	0.00	0.00	0.00	0.00	1.49	1.48	1.43		
Cr	0.00	0.01	0.00	0.00	0.01	0.00	0.01	0.01	0.01	0.01	0.00	0.00	0.00	0.00	0.00	0.00	0.00	0.00	0.00	0.00
Fe3+	0.00	0.00	0.00	0.00	0.00	0.00	0.00	0.00	0.00	0.00	0.00	0.00	0.01	0.00	0.00	0.00	0.00	0.00	0.00	0.00
Ti	0.04	0.07	0.10	0.09	0.08	0.02	0.02	0.02	0.02	0.02	0.00	0.00	0.00	0.00	0.00	0.01	0.01	0.01	1.00	1.01
Fe2+	1.17	1.15	1.11	1.23	1.19	0.04	0.04	0.04	0.04	0.04	0.00	0.00	0.01	0.00	0.00	2.08	2.20	2.11	0.95	0.96
Mn	0.01	0.01	0.01	0.01	0.01	0.00	0.00	0.00	0.00	0.00	0.00	0.00	0.00	0.00	0.00	0.02	0.01	0.01	0.02	0.02
Mg	1.19	1.14	1.16	0.99	1.14	0.05	0.05	0.06	0.06	0.05	0.00	0.00	0.00	0.00	0.00	2.37	2.28	2.41	0.02	0.01
Ca	0.00	0.00	0.00	0.00	0.00	0.00	0.00	0.00	0.00	0.00	0.34	0.34	0.32	0.33	0.33	0.00	0.01	0.00	0.00	0.00
Na	0.01	0.02	0.03	0.02	0.01	0.17	0.15	0.15	0.16	0.16	0.67	0.70	0.70	0.68	0.69	0.00	0.00	0.00	0.00	0.00
K	0.93	0.88	0.91	0.92	0.90	0.77	0.80	0.79	0.79	0.80	0.00	0.01	0.01	0.01	0.01	0.00	0.00	0.01	0.00	0.00
Zn	0.00	0.00	0.00	0.00	0.00	0.00	0.00	0.00	0.00	0.00	0.00	0.00	0.00	0.00	0.00	0.00	0.00	0.00	0.00	0.00
Total	8.00	8.00	8.00	8.00	8.00	7.00	7.00	7.00	7.00	7.00	5.00	5.00	5.00	5.00	5.00	10.00	10.00	10.00	2.00	2.00
XMg	0.50	0.50	0.51	0.44	0.49	0.54	0.52	0.58	0.58	0.55	-	-	-	-	-	0.53	0.51	0.53	0.02	0.01
XAn	-	-	-	-	-	-	-	-	-	-	0.33	0.32	0.31	0.32	0.32	-	-	-	-	-
XGrs	-	-	-	-	-	-	-	-	-	-	-	-	-	-	-	-	-	-	-	-
XAlm	-	-	-	-	-	-	-	-	-	-	-	-	-	-	-	-	-	-	-	-
XPy	-	-	-	-	-	-	-	-	-	-	-	-	-	-	-	-	-	-	-	-
XSps	-	-	-	-	-	-	-	-	-	-	-	-	-	-	-	-	-	-	-	-

Tabela S5: Concentração de elementos traços (ppm) obtidos por LA-ICP-MS em cristais de granada na lâmina MAB51B (*spot* = 40 µm).

	Y	Zr	Nb	La	Ce	Pr	Nd	Sm	Eu	Gd	Tb	Dy	Ho	Er	Tm	Yb	Lu	Hf	Ta	Pb	Th	U
Lim. det.	0.02	0.05	0.02	0.005	0.005	0.005	0.01	0.01	0.01	0.03	0.005	0.01	0.005	0.01	0.005	0.01	0.005	0.05	0.02	0.04	0.01	0.01
MAB51B_4	1849	2.7	0.03	0.025	0.084	0.025	0.31	2.23	1.10	29.9	17.7	238	70.6	241	37.0	232	24.5	0.08	< DL	0.11	0.13	0.07
MAB51B_5	1974	i	0.04	< DL	0.008	0.008	0.27	2.10	0.90	29.3	17.2	234	74.8	271	43.0	285	34.2	i	0.02	< DL	i	i
MAB51B_6	2148	i	0.03	< DL	0.007	0.008	0.28	2.35	0.81	30.7	18.1	244	77.3	295	47.3	319	38.6	i	0.02	< DL	< DL	0.09
MAB51B_7	1986	2.8	0.04	< DL	0.007	0.009	0.30	2.45	0.81	31.4	17.8	228	71.6	258	41.2	275	33.2	0.08	0.03	< DL	< DL	0.10
MAB51B_8	2049	3.1	0.04	0.008	0.038	0.014	0.32	2.42	0.83	31.1	17.6	233	72.7	261	42.5	284	33.8	0.08	0.04	< DL	0.13	0.12
MAB51B_9	2096	3.3	0.05	0.011	i	0.019	0.43	2.39	0.84	31.1	17.3	233	73.4	270	44.3	305	37.3	0.06	0.05	< DL	0.02	0.16
MAB51B_10	2133	3.5	0.07	< DL	0.010	0.010	0.33	2.53	0.89	33.6	18.7	245	75.6	271	43.2	299	35.2	0.07	0.04	< DL	< DL	0.14
MAB51B_11	2062	i	i	i	i	i	i	i	i	i	19.1	242	76.8	290	48.1	336	41.3	i	i	i	i	i
MAB51B_12	1993	4.7	0.06	i	i	i	0.79	2.35	0.80	32.1	17.6	234	72.3	263	43.0	293	35.0	0.11	0.05	i	i	0.21
MAB51B_13	1933	i	i	i	i	0.059	0.45	2.24	0.69	28.6	16.2	218	68.9	255	41.8	287	34.3	i	i	i	i	i
MAB51B_17	1376	i	0.05	< DL	0.017	0.014	0.36	2.80	1.00	32.3	15.5	177	49.4	168	26.3	174	21.4	i	i	< DL	i	i
MAB51B_18	2066	i	0.03	< DL	0.010	0.010	0.29	2.44	0.79	31.7	17.9	245	78.2	283	46.1	308	37.0	i	0.03	< DL	i	i
MAB51B_19	1676	i	0.11	i	0.205	0.040	0.38	2.22	1.06	27.9	17.2	226	65.8	220	32.9	204	21.1	i	0.02	0.42	i	i
MAB51B_20	1808	i	0.07	0.030	0.115	0.027	0.31	2.07	1.05	27.1	16.9	234	69.9	239	36.5	231	23.9	i	0.03	0.29	0.12	i
MAB51B_21	1916	2.8	0.06	0.028	0.086	0.023	0.25	1.62	0.98	22.0	15.0	231	80.0	306	51.4	349	39.0	i	< DL	0.27	0.08	0.05
MAB51B_22	1645	2.3	0.12	0.040	0.125	0.028	0.19	0.78	0.67	14.9	10.7	190	78.3	355	67.2	511	72.3	0.08	0.02	0.31	0.20	0.04
MAB51B_23	1697	1.8	< DL	< DL	< DL	< DL	0.15	1.39	0.99	18.5	12.9	203	69.7	256	40.0	253	28.5	0.05	0.02	< DL	< DL	0.04
MAB51B_24	1840	2.9	0.03	i	i	i	i	1.86	0.77	27.7	17.6	232	70.2	244	36.8	234	26.3	0.06	0.02	0.24	0.05	0.14
MAB51B_25	1575	2.6	< DL	< DL	0.003	< DL	0.21	2.07	0.93	30.6	18.6	222	56.9	163	21.6	118	11.5	0.05	0.02	< DL	< DL	0.02
MAB51B_26	1748	3.0	0.02	< DL	0.010	0.011	0.30	2.59	0.86	38.3	19.8	228	63.3	211	31.4	198	23.9	0.07	0.03	< DL	< DL	0.08
MAB51B_30	1529	3.5	0.06	< DL	0.015	0.015	0.44	3.52	1.09	45.7	21.0	214	54.2	169	24.1	153	18.2	0.08	0.05	< DL	0.01	0.15
MAB51B_31	1379	3.7	0.08	< DL	0.013	0.013	0.45	3.65	1.10	46.2	20.6	202	47.7	139	19.5	122	14.1	0.09	0.06	< DL	< DL	0.15
MAB51B_32	1230	4.5	0.08	0.262	2.007	0.270	1.61	3.83	1.18	43.8	19.0	183	41.9	123	17.2	106	12.1	0.10	0.05	0.89	0.18	0.74
MAB51B_33	1550	3.4	0.07	0.005	0.027	0.017	0.44	3.53	1.07	43.2	20.1	212	53.9	172	25.6	166	20.8	0.05	0.04	< DL	< DL	0.14
MAB51B_34	1548	3.6	0.06	< DL	0.011	0.013	0.38	3.20	1.10	45.1	20.8	216	54.4	168	24.5	156	19.0	0.07	0.05	< DL	< DL	0.14
MAB51B_35	1131	3.1	0.08	< DL	0.011	0.014	0.45	3.54	1.03	42.9	18.1	169	36.7	103	13.7	82	9.5	0.05	0.04	< DL	0.01	0.12
MAB51B_36	1666	2.6	0.03	< DL	0.011	0.012	0.33	2.99	0.88	42.7	20.9	229	59.0	185	26.6	165	19.2	0.07	0.03	< DL	< DL	0.07
MAB51B_37	1646	3.3	0.04	< DL	i	0.012	0.37	3.05	1.04	44.5	22.5	240	58.0	165	21.3	119	12.2	0.08	0.03	< DL	0.01	0.07
MAB51B_38	1564	3.3	0.03	< DL	0.012	0.009	0.27	2.69	1.01	36.7	20.7	231	57.7	168	21.9	123	12.0	0.09	0.03	< DL	< DL	0.05
MAB51B_39	1755	2.7	0.02	i	0.025	0.009	0.24	2.25	1.05	31.4	19.7	246	66.6	201	27.2	151	14.6	< DL	0.02	< DL	< DL	0.05
MAB51B_40	1985	1.8	i	< DL	0.012	< DL	0.14	1.57	1.07	21.7	15.9	243	80.5	279	41.1	246	24.5	< DL	< DL	< DL	< DL	0.02

Tabela S6: Concentração de elementos traços (ppm) obtidos por LA-ICP-MS em cristais de granada na lâmina MAB56A (*spot* = 40 µm).

	Y	Zr	Nb	La	Ce	Pr	Nd	Sm	Eu	Gd	Tb	Dy	Ho	Er	Tm	Yb	Lu	Hf	Ta	Pb	Th	U
Lim. det.	0.02	0.05	0.02	0.005	0.005	0.005	0.01	0.01	0.01	0.03	0.005	0.01	0.005	0.01	0.005	0.01	0.005	0.05	0.02	0.04	0.01	0.01
MAB56A_4	507	i	0.04	0.008	0.023	0.010	0.23	1.92	1.34	18.1	7.15	69.5	18.83	59.54	8.86	58.37	8.09	i	0.03	0.17	i	i
MAB56A_5	309	6.1	0.10	< DL	0.009	0.007	0.21	1.93	1.36	17.3	5.89	49.4	11.51	33.20	4.50	29.42	3.91	0.10	0.02	< DL	< DL	0.02
MAB56A_6	461	5.7	0.06	0.005	0.016	0.008	0.20	1.78	1.48	17.4	6.35	61.7	15.85	53.46	8.15	57.87	8.06	0.06	0.02	< DL	< DL	0.03
MAB56A_7	641	5.7	0.06	< DL	0.007	0.005	0.19	1.82	1.55	18.8	7.74	81.0	21.15	66.27	9.91	66.11	8.77	0.07	0.03	< DL	< DL	0.03
MAB56A_8	687	6.3	i	< DL	0.006	0.008	0.21	1.86	1.59	19.1	8.19	84.3	23.44	80.69	12.72	92.12	13.43	0.08	0.06	< DL	< DL	0.04
MAB56A_9	698	4.3	0.08	< DL	< DL	0.006	0.21	1.69	1.40	15.3	6.67	73.8	21.77	76.48	12.62	92.52	12.81	0.06	0.02	< DL	< DL	0.03
MAB56A_10	112	5.2	0.15	< DL	0.009	0.009	0.29	2.10	1.73	10.5	2.59	17.1	3.16	8.18	1.06	6.77	0.79	0.11	0.03	< DL	< DL	0.06
MAB56A_11	237	8.4	16.62	< DL	0.024	0.013	0.36	2.44	2.19	13.1	3.99	31.6	6.85	21.66	3.52	24.45	3.23	0.20	1.44	0.06	0.10	0.23
MAB56A_12	71	3.3	0.25	< DL	0.009	0.009	0.28	1.57	1.65	6.53	1.49	10.4	2.07	5.59	0.91	6.51	0.75	0.08	0.04	i	< DL	0.05
MAB56A_13	597	i	0.49	0.113	0.447	0.081	0.83	3.40	2.65	20.1	6.80	63.6	16.23	57.18	9.28	71.04	9.13	i	0.12	0.46	0.66	0.24
MAB56A_17	243	7.7	0.89	< DL	0.026	0.024	0.74	3.79	3.20	17.1	4.21	30.8	6.05	17.29	2.64	17.62	2.23	0.16	0.16	< DL	0.02	0.20
MAB56A_18	833	i	i	< DL	0.012	0.011	0.31	2.06	1.84	15.7	6.28	75.1	25.76	112.46	23.13	197.27	30.79	i	i	i	i	i
MAB56A_19	717	i	i	< DL	0.018	0.012	0.31	1.90	1.90	14.9	5.98	68.4	21.47	85.57	16.11	129.64	18.55	i	i	0.06	i	i
MAB56A_20	849	i	0.29	< DL	0.011	0.008	0.27	1.87	1.74	15.0	6.35	78.0	26.08	110.77	21.97	185.52	27.56	i	i	0.04	< DL	0.09
MAB56A_21	703	i	14.78	0.013	0.031	0.016	0.27	1.88	1.73	15.3	6.29	68.2	21.48	86.46	16.05	130.97	19.39	i	i	0.07	i	i
MAB56A_22	440	i	i	0.010	0.027	0.010	0.30	2.01	1.77	13.9	4.88	47.6	13.11	48.45	8.69	66.24	9.53	i	i	< DL	i	i
MAB56A_23	539	6.6	0.32	< DL	0.012	0.011	0.37	2.17	1.84	16.1	5.66	57.5	16.22	61.30	10.97	86.27	12.81	0.13	0.10	< DL	< DL	0.08
MAB56A_24	459	i	0.30	< DL	0.011	0.012	0.36	2.48	2.01	15.7	5.20	50.6	13.65	49.06	8.58	65.53	9.31	0.25	0.09	< DL	i	0.10
MAB56A_25	107	6.8	0.05	< DL	0.008	0.012	0.35	2.69	1.85	17.4	4.21	23.0	3.15	6.82	0.85	5.44	0.73	0.10	< DL	< DL	< DL	0.04
MAB56A_26	139	i	i	< DL	0.009	0.013	0.37	2.91	2.07	19.9	5.29	30.4	4.37	8.87	1.00	5.61	0.64	i	0.03	< DL	i	i
MAB56A_30	89	6.8	0.11	< DL	0.013	0.017	0.53	3.78	2.48	19.4	4.22	20.7	2.63	4.44	0.45	2.20	0.25	0.11	0.02	< DL	< DL	0.05
MAB56A_31	359	5.6	< DL	< DL	0.007	0.010	0.32	2.42	1.65	19.8	7.01	57.7	11.97	32.98	4.30	26.22	3.56	0.08	< DL	< DL	< DL	0.04
MAB56A_32	107	7.0	0.04	< DL	0.005	0.006	0.25	2.31	1.63	18.6	4.43	25.3	3.69	7.72	0.86	4.78	0.50	0.16	< DL	< DL	< DL	0.02
MAB56A_33	309	4.4	< DL	< DL	< DL	0.006	0.22	2.30	1.59	21.2	7.53	58.9	10.76	26.16	3.18	18.05	2.12	0.08	< DL	< DL	< DL	0.01
MAB56A_34	554	5.2	< DL	< DL	< DL	< DL	0.16	1.57	1.28	20.0	9.09	86.0	18.75	49.39	6.24	36.43	4.20	0.10	< DL	< DL	< DL	0.01
MAB56A_35	328	5.9	0.03	< DL	< DL	< DL	0.15	1.56	1.24	17.7	6.67	56.4	10.98	26.21	3.29	18.19	2.07	0.09	0.03	< DL	< DL	0.02
MAB56A_36	912	4.3	< DL	< DL	< DL	< DL	0.11	0.91	0.91	14.0	7.79	101.6	31.62	119.25	19.86	144.64	20.74	0.07	< DL	< DL	< DL	< DL
MAB56A_37	2787	3.1	0.04	< DL	< DL	< DL	0.07	0.59	0.48	10.6	8.72	185.1	97.48	564.14	132.34	1228.36	199.71	0.05	0.03	< DL	< DL	< DL
MAB56A_38	2328	3.7	0.08	< DL	< DL	< DL	0.07	0.74	0.72	13.4	10.12	183.7	80.20	383.42	78.27	624.68	94.78	0.06	0.03	< DL	< DL	< DL
MAB56A_39	1198	4.4	0.04	< DL	< DL	< DL	0.13	1.19	0.86	16.3	9.71	135.1	43.07	155.88	25.01	172.48	24.79	0.07	< DL	< DL	< DL	0.01
MAB56A_40	976	5.3	0.08	< DL	< DL	0.005	0.17	1.51	1.21	20.0	10.24	123.7	34.87	120.28	17.99	117.68	15.36	0.08	0.03	< DL	< DL	0.02
MAB56A_41	873	4.5	0.03	0.019	0.063	0.009	0.17	1.51	1.21	21.3	10.75	120.2	31.67	98.49	13.83	85.24	10.95	0.06	< DL	< DL	< DL	0.02
MAB56A_42	392	6.4	0.07	0.011	0.048	0.009	0.21	1.97	1.36	22.4	8.34	68.3	14.20	35.84	4.48	25.94	3.28	0.07	0.03	< DL	< DL	0.02
MAB56A_43	198	7.0	0.08	0.009	0.028	0.008	0.27	2.39	1.63	21.3	6.09	42.3	7.76	18.36	2.29	12.33	1.54	0.12	0.03	< DL	< DL	0.03

Tabela S7: Concentração de elementos traços (ppm) obtidos por LA-ICP-MS em cristais de granada na lâmina BD03 (*spot* = 40 μm).

	Ti	Y	La	Ce	Pr	Nd	Sm	Eu	Gd	Tb	Dy	Ho	Er	Tm	Yb	Lu	Hf	U
Lim. det.	5	0.2	0.005	0.005	0.005	0.05	0.1	0.05	0.1	0.05	0.1	0.05	0.1	0.05	0.1	0.04	0.03	0.005
BD03_5	216	677	< DL	< DL	< DL	0.186	1.73	0.543	17.5	7.51	83.8	24.36	86.0	13.4	96.1	14.12	0.12	0.020
BD03_6	i	447	0.037	0.085	0.017	0.287	1.73	0.585	16.2	6.17	59.8	15.75	52.2	7.75	55.3	8.29	i	i
BD03_7	403	420	< DL	0.009	0.009	0.257	1.78	0.689	16.1	5.92	57.4	15.34	51.3	7.90	56.4	8.89	0.12	0.036
BD03_8	389	320	< DL	0.017	0.009	0.248	1.79	0.800	16.1	5.28	47.5	11.43	35.1	5.03	35.0	5.19	i	i
BD03_9	335	221	0.064	0.187	0.037	0.422	2.27	0.924	14.9	4.48	34.6	7.67	23.1	3.41	23.4	3.50	0.11	0.058
BD03_10	635	446	< DL	0.023	0.010	0.272	2.10	0.851	16.5	5.91	57.7	15.80	54.1	8.44	60.7	9.07	0.11	0.062
BD03_11	417	384	0.022	0.068	0.020	0.290	1.62	0.785	13.8	4.89	48.8	13.04	46.7	7.46	57.6	8.88	0.10	0.068
BD03_12	398	299	< DL	0.010	0.006	0.296	1.64	0.924	14.1	4.61	40.6	10.13	32.6	4.81	33.7	5.00	0.12	0.047
BD03_13	496	239	< DL	0.013	0.013	0.374	2.50	1.227	15.7	4.45	35.3	7.27	19.8	2.69	17.4	2.12	0.21	0.090
BD03_14	861	78	0.096	0.314	0.059	0.568	2.28	1.099	11.9	2.79	15.3	2.18	4.47	0.49	2.9	0.42	i	i
BD03_17	611	220	0.094	0.288	0.048	0.482	1.92	0.933	12.4	3.74	30.7	7.27	24.1	3.92	28.4	4.35	i	i
BD03_18	511	415	i	i	i	i	i	i	15.1	5.42	50.4	13.76	48.8	8.23	59.9	9.52	i	i
BD03_19	523	450	0.921	0.967	0.139	0.759	1.99	0.911	15.2	5.43	54.2	14.79	53.0	8.91	63.9	9.79	0.18	0.133
BD03_20	i	452	i	i	i	i	i	i	21.4	6.34	58.2	15.37	53.2	8.62	62.7	9.55	i	i
BD03_21	11380	529	265	573	64.0	239.6	51.5	10.7	53.3	10.89	76.5	18.67	63.0	9.96	74.0	11.37	i	i
BD03_22	473	416	0.144	0.732	0.070	0.485	1.94	0.937	15.6	5.42	51.6	14.24	50.4	8.39	62.2	9.90	0.22	0.140
BD03_23	503	302	0.440	0.644	0.140	0.862	1.91	0.886	14.3	4.60	41.2	10.55	35.9	5.81	40.7	6.39	0.13	0.082
BD03_24	422	436	0.315	0.829	0.089	0.540	1.77	0.715	14.9	5.45	53.5	15.41	55.5	9.32	70.4	11.50	0.23	0.166
BD03_25	407	398	0.008	0.033	0.011	0.261	1.89	0.838	15.5	5.40	51.6	13.82	48.6	7.80	56.4	8.95	0.12	0.067
BD03_26	423	386	0.030	0.131	0.025	0.318	1.69	0.737	15.9	5.59	52.3	13.96	44.1	7.06	49.6	7.53	0.15	0.059
BD03_29	357	417	i	i	i	i	1.94	0.670	15.4	5.72	54.0	14.64	49.2	7.87	56.7	8.92	0.16	0.056
BD03_30	376	341	0.082	0.185	0.040	0.319	1.81	0.654	15.8	5.31	47.5	11.77	38.4	5.63	40.8	6.06	0.13	0.057
BD03_31	345	364	< DL	0.012	0.008	0.229	1.74	0.664	15.8	5.62	51.4	12.82	41.0	5.95	40.1	5.97	0.10	0.035
BD03_32	365	297	< DL	0.016	0.006	0.232	1.73	0.606	15.8	5.20	45.0	10.75	32.4	4.69	30.1	4.32	i	i
BD03_33	263	385	0.051	0.148	0.022	0.287	1.97	0.704	16.7	6.12	54.7	13.25	40.9	6.01	38.9	5.69	0.12	0.042
BD03_34	203	569	< DL	< DL	< DL	0.197	1.91	0.594	18.8	7.55	78.1	19.25	59.1	8.26	49.5	6.31	0.09	0.016

Tabela S8: Concentração de elementos terras raras (ppm) obtidos por LA-ICP-MS nos *mounts* de monazita das amostra MAB51B e MAB56A (*spot* = 16 μm).

		La	Ce	Pr	Nd	Sm	Eu	Gd	Tb	Dy	Ho	Er	Tm	Yb	Lu
Det. Lim.		1	2	0.6	2	2	0.5	2	0.2	0.5	0.2	0.5	0.1	0.2	0.05
mon_5		141479	259559	26973	90787	12611	110	5681	570	2334	324	667	64.8	312	34.4
mon_6		128785	253516	29376	107206	16223	102	8872	903	3885	491	929	73.6	277	24.7
mon_7		136588	259306	28398	100231	16116	137	8629	933	3818	476	799	63.3	245	20.5
mon_8		106824	234607	29092	114664	22945	40	14443	1721	7358	967	1823	157	658	59.4
mon_9		107428	240915	29821	117559	21311	107	10829	1115	4424	567	1058	90.7	382	35.2
mon_10		120538	245690	28882	102613	19265	21	12678	1500	6838	972	1981	163	638	60.4
mon_14		115435	249160	30190	122607	28929	52	17342	1806	7051	849	1554	144	620	59.4
mon_15	MAB51B	138489	267787	28854	97432	12702	53	6324	647	2758	368	650	46.2	155	12.7
mon_16		137403	270210	29387	107315	13811	44	6397	551	2035	243	377	24.0	74	6.24
mon_17		119370	241850	28500	103624	18631	72	11753	1469	6592	906	1797	156	647	60.5
mon_18		129765	243555	26717	97204	16869	30	10924	1290	6002	894	1844	154	636	59.1
mon_19		131913	254202	29082	106437	18398	109	10688	1157	4836	674	1287	109	457	44.5
mon_20		120596	232592	26554	95833	16936	121	10348	1218	5306	700	1279	112	454	43.2
mon_24		146649	259227	27489	96894	12859	57	6351	579	2233	281	487	36.5	127	11.5
mon_25		131388	261191	29019	101719	14222	71	7297	801	3667	566	1184	113	489	51.3
mon_26		136995	255783	28711	98247	14083	69	8633	999	4815	716	1479	135	570	56.5
mon_27		135649	260876	28965	97464	14309	97	6933	655	2567	353	707	68.4	356	45.3
mon_28		113505	223199	26093	101512	19602	2126	12711	1259	4446	476	598	28.7	64	3.84
mon_29		143627	246251	26671	96850	15734	2129	10823	1253	5465	770	1475	117	449	41.2
mon_30		127063	255325	29976	111284	16332	2339	7926	821	2787	258	308	15.8	41	2.56
mon_34		138780	247336	26267	99233	13858	1782	5518	604	2318	237	293	15.5	46	3.27
mon_35		124451	234706	26310	101659	18887	2341	13312	1528	6516	830	1322	84.1	241	15.7
mon_36		122073	229836	25935	101344	18931	2362	13207	1517	6232	787	1270	81.1	236	15.4
mon_37	MAB56A	118558	223553	25463	99576	19862	2457	15621	2006	9192	1185	2063	143	451	29.2
mon_38		na	na	na	na	na	na	na	na	na	na	na	na	na	na
mon_39		151162	249457	26252	92754	14826	2161	9972	1271	6063	863	1650	133	519	46.5
mon_40		126108	238927	27610	106668	19605	1804	11883	995	3015	286	351	17.2	40	2.37
mon_44		120333	228027	26617	103609	19221	1886	11791	1045	3354	336	428	21.1	52	2.96
mon_45		119856	229463	26676	100934	17617	2145	10167	910	2784	245	257	12.5	30	1.86
mon_46		118595	239054	29131	109421	21354	2711	11497	741	1287	67	60	2.8	8.5	0.66
mon_47		102099	208342	23150	91849	15672	1929	8253	674	1864	165	212	12.8	37	2.73
mon_48		129468	239727	27465	100052	15392	1606	8105	720	2301	220	276	15.2	43	2.96
mon_49		145617	252186	27059	98857	15032	1637	9254	932	4185	636	1279	110	446	42.1

Tabela S9: Partição dos elementos terras raras entre monazita e granada calculados para as amostras MAB51B (granada 1 e 2) e MAB56A (granada 3 e 4).

GRANADA 1	La	Ce	Pr	Nd	Sm	Eu	Gd	Tb	Dy	Ho	Er	Tm	Yb	Lu
mon_5 -Gtcore	-	-	455616.71	201302.2	5622.417	158.9532	198.7062	35.2232	10.70128	4.70964	2.611928	1.549715	1.086406	1.001828
mon_6 -Gtcore	-	-	496218.21	237707.9	7232.87	146.4646	310.3091	55.80044	17.81342	7.127679	3.638606	1.759923	0.964005	0.720967
mon_7 -Gtcore	-	-	479695.64	222242.5	7184.842	197.2189	301.8086	57.63041	17.50358	6.911229	3.128114	1.513847	0.852878	0.596964
mon_8 -Gtcore	-	-	491421.99	254245	10229.68	57.77253	505.1836	106.2968	33.73414	14.03468	7.135211	3.749402	2.292932	1.731539
mon_9-Gtcore	-	-	503728.96	260663.1	9501.2	153.9158	378.7812	68.84609	20.28446	8.231311	4.141161	2.168601	1.331334	1.02541
mon_10-Gtcore	-	-	487872.24	227522.5	8588.964	30.56539	443.4526	92.66775	31.34788	14.10424	7.754498	3.902656	2.2225	1.760685
mon_14-Gtcore	-	-	509971.9	271856.4	12897.67	75.06231	606.5745	111.561	32.32683	12.32235	6.084047	3.453328	2.160239	1.731274
mon_15-Gtcore	-	-	487392.05	216035.7	5663.041	76.49219	221.2086	39.93374	12.645	5.33563	2.544451	1.105821	0.53964	0.36936
mon_16-Gtcore	-	-	496406.63	237949.4	6157.257	64.01679	223.7499	34.00977	9.330435	3.522727	1.475992	0.573236	0.259084	0.181765
mon_17-Gtcore	-	-	481419.38	229765.6	8306.258	103.2664	411.0792	90.72435	30.2196	13.15041	7.033568	3.73962	2.252807	1.763334
mon_18-Gtcore	-	-	451298.68	215528.8	7520.699	43.85413	382.0748	79.70633	27.51584	12.98437	7.217742	3.692666	2.215026	1.723325
mon_19-Gtcore	-	-	491254.61	236002.8	8202.391	157.3265	373.8208	71.47903	22.17195	9.786057	5.036906	2.604235	1.59311	1.298323
mon_20-Gtcore	-	-	448539.62	212490.6	7550.505	174.1834	361.9495	75.21927	24.32539	10.16669	5.008114	2.676188	1.580031	1.258048
mon_24-Gtcore	-	-	464334.31	214841.9	5732.882	82.23796	222.1314	35.75439	10.23815	4.076919	1.906906	0.871701	0.441339	0.334119
mon_25-Gtcore	-	-	490180.44	225540.6	6340.55	101.9546	255.2358	49.45196	16.8106	8.216397	4.633182	2.697926	1.703382	1.495456
mon_26-Gtcore	-	-	484980.65	217841.9	6278.446	99.97376	301.9419	61.675	22.07446	10.39067	5.789511	3.236164	1.985679	1.64728
mon_27-Gtcore	-	-	489278.56	216106.5	6379.471	140.2991	242.4834	40.45426	11.76888	5.12723	2.7682	1.634929	1.241331	1.32111
mon_5-Gt1mant	12410397	-	1427116.9	211133.3	5272.191	131.4493	182.6691	33.05876	10.03423	4.421426	2.469888	1.462299	1.023443	0.921274
mon_6-Gt1mant	11296914	-	1554292	249316.9	6782.327	121.1217	285.2648	52.37154	16.70305	6.691489	3.440734	1.66065	0.908136	0.662996
mon_7-Gt1mant	11981371	-	1502538.7	233096.2	6737.291	163.0939	277.4505	54.08906	16.41253	6.488285	2.958003	1.428454	0.80345	0.548963
mon_8-Gt1mant	9370546	-	1539268.9	266661.6	9592.46	47.77609	464.4116	99.76495	31.63138	13.17581	6.747189	3.537906	2.160046	1.59231
mon_9-Gt1mant	9423497	-	1577817.7	273393.1	8909.361	127.2836	348.2108	64.61555	19.02006	7.727582	3.91596	2.046275	1.254177	0.942959
mon_10-Gt1mant	10573496	-	1528150.1	238634	8053.949	25.27663	407.6627	86.97339	29.39386	13.24111	7.332799	3.682516	2.093696	1.619113
mon_14-Gt1mant	10125850	-	1597372.3	285133.2	12094.26	62.0742	557.6194	104.7057	30.31178	11.56827	5.75319	3.258533	2.035043	1.592066
mon_15-Gt1mant	12148199	-	1526646	226586.3	5310.284	63.25667	203.3555	37.47984	11.85679	5.009107	2.406081	1.043444	0.508365	0.33966
mon_16-Gt1mant	12052907	-	1554882.2	249570.2	5773.715	52.9399	205.6916	31.91989	8.748837	3.307148	1.395725	0.540901	0.244069	0.16715
mon_17-Gt1mant	10471018	-	1507938	240986.7	7788.853	85.39813	377.9021	85.14941	28.33591	12.34565	6.651074	3.528676	2.122246	1.621549
mon_18-Gt1mant	11382919	-	1413591.6	226054.7	7052.227	36.266	351.2385	74.80843	25.80068	12.18977	6.825232	3.48437	2.086655	1.584757
mon_19-Gt1mant	11571272	-	1538744.6	247528.5	7691.456	130.1041	343.6507	67.08669	20.7899	9.187183	4.762993	2.457335	1.500782	1.193928
mon_20-Gt1mant	10578586	-	1404949.5	222868	7080.176	144.0443	332.7375	70.5971	22.80911	9.544525	4.735767	2.52523	1.48846	1.156892
mon_24-Gt1mant	12863951	-	1454422.8	225334.1	5375.775	68.00824	204.2037	33.55731	9.599972	3.827425	1.803206	0.82253	0.415762	0.307254
mon_25-Gt1mant	11525230	-	1535380	236555.4	5945.591	84.3133	234.6364	46.41318	15.76273	7.713581	4.381224	2.545742	1.604662	1.37521
mon_26-Gt1mant	12017139	-	1519092.8	228480.7	5887.356	82.6752	277.5729	57.88511	20.69849	9.754792	5.47467	3.053618	1.8706	1.514827
mon_27-Gt1mant	11899034	-	1532555.1	226660.5	5982.088	116.023	222.9132	37.96838	11.03528	4.813461	2.617662	1.542706	1.169389	1.214883
mon_5-Gt1Rim	3563691	2073153	956471.95	485493.6	16085.56	163.9205	381.5318	53.34552	12.29478	4.145157	1.881001	0.963991	0.609716	0.475615
mon_6-Gt1Rim	3243950	2024889	1041706.3	573295.6	20693.02	151.0417	595.8184	84.50974	20.46597	6.273378	2.620371	1.094749	0.541022	0.342277
mon_7-Gt1Rim	3440494	2071135	1007020.6	535996.6	20555.61	203.382	579.4969	87.28123	20.10999	6.082871	2.252736	0.941679	0.478655	0.283407
mon_8-Gt1Rim	2690787	1873857	1031637.7	613179.1	29266.79	59.57792	969.9933	160.9865	38.75739	12.35253	5.138478	2.332292	1.286846	0.822044
mon_9-Gt1Rim	2705992	1924244	1057473.6	628658	27182.64	158.7256	727.2904	104.2674	23.30495	7.244732	2.98229	1.348965	0.747175	0.486811
mon_10-Gt1Rim	3036218	1962378	1024185.7	548730.7	24572.76	31.52056	851.4647	140.3453	36.0158	12.41375	5.584463	2.427623	1.247318	0.835881
mon_14-Gt1Rim	2907675	1990099	1070579.3	655653.8	36899.85	77.40801	1164.672	168.9591	37.14052	10.84543	4.381475	2.148121	1.212376	0.821918
mon_15-Gt1Rim	3488400	2138876	1023177.6	521027.3	16201.79	78.88258	424.7384	60.47963	14.52793	4.696118	1.832406	0.687869	0.302858	0.175353
mon_16-Gt1Rim	3461036	2158230	1042101.9	573878	17615.72	66.01732	429.6178	51.50778	10.7198	3.100504	1.062947	0.356578	0.145404	0.086293
mon_17-Gt1Rim	3006791	1931707	1010639.3	554140.5	23763.95	106.4935	789.3052	137.402	34.71952	11.57424	5.065279	2.326207	1.264328	0.837139
mon_18-Gt1Rim	3268647	1945327	947407.16	519804.8	21516.49	45.22457	733.6144	120.7152	31.61314	11.42811	5.197914	2.296999	1.243124	0.818144
mon_19-Gt1Rim	3322733	2030370	1031286.3	569183.2	23466.79	162.243	717.766	108.255	25.47351	8.613131	3.627368	1.619948	0.89409	0.616375
mon_20-Gt1Rim	3037680	1857763	941615.09	512477.2	21601.76	179.6266	694.9722	113.9196	27.94761	8.948145	3.606633	1.664706	0.88675	0.597255
mon_24-Gt1Rim	3693931	2070503	974772.73	518148	16401.6	84.8079	426.5102	54.15001	11.76268	3.588272	1.373273	0.542236	0.24769	0.158622
mon_25-Gt1Rim	3309512	2086188	1029031.3	543950.9	18140.12	105.1407	490.0733	74.89497	19.31381	7.231606	3.336622	1.678228	0.955977	0.709964
mon_26-Gt1Rim	3450765	2042993	1018115.4	525383.5	17962.44	103.0979	579.7527	93.40675	25.36151	9.145273	4.169362	2.013035	1.114409	0.782042
mon_27-Gt1Rim	3416851	2083678	1027138	521198	18251.47	144.6834	465.5876	61.26796	13.52134	4.512697	1.993541	1.016997	0.696663	0.627193

GRANADA 2	La	Ce	Pr	Nd	Sm	Eu	Gd	Tb	Dy	Ho	Er	Tm	Yb	Lu
mon_5 Gt2core	-	19813643	2037198.6	204016.4	3455.091	100.0495	122.8858	27.69615	11.58221	6.79514	4.789597	3.332087	2.560667	2.439512
mon_6 Gt2core	-	19352371	2218740	240913	4444.747	92.18892	191.9043	43.87611	19.27983	10.28392	6.672257	3.784062	2.272167	1.755597
mon_7 -Gt2core	-	19794359	2144862.7	225239	4415.233	124.1351	186.6474	45.31502	18.94448	9.971627	5.736148	3.254966	2.010241	1.453642
mon_8 Gt2core	-	17908925	2197294.7	257673	6286.346	36.36364	312.4205	83.58162	36.51114	20.24946	13.08412	8.061697	5.404459	4.216401
mon_9-Gt2core	-	18390489	2252322.9	264177.6	5838.682	96.87887	234.2495	54.13396	21.95428	11.87626	7.593813	4.662772	3.137965	2.496935
mon_10-Gt2core	-	18754938	2181422.7	230590.2	5278.095	19.23871	274.2442	72.86503	33.92845	20.34981	14.21974	8.391213	5.238451	4.287373
mon_14-Gt2core	-	19019876	2280236.9	275521.9	7925.885	47.24631	375.1236	87.72087	34.98798	17.77888	11.15656	7.425099	5.0917	4.215756
mon_15-Gt2core	-	20441781	2179275.6	218948.5	3480.055	48.14631	136.802	31.40006	13.68594	7.698328	4.665862	2.377658	1.271936	0.899413
mon_16-Gt2core	-	20626752	2219582.5	241157.7	3783.761	40.29395	138.3735	26.74202	10.09852	5.082645	2.706585	1.232531	0.610664	0.442609
mon_17-Gt2core	-	18461808	2152570	232863.5	5104.366	64.99876	254.2235	71.33692	32.70729	18.97361	12.89774	8.040664	5.309885	4.293825
mon_18-Gt2core	-	18591981	2017891.4	218434.8	4621.624	27.60301	236.2864	62.67341	29.78095	18.73405	13.23546	7.939706	5.220835	4.1964
mon_19-Gt2core	-	19404758	2196546.3	239184.8	5040.538	99.02568	231.1818	56.20425	23.99715	14.11947	9.236377	5.599439	3.754973	3.161494
mon_20-Gt2core	-	17755112	2005554.8	215355.6	4639.94	109.6359	223.8403	59.14522	26.32786	14.66866	9.18358	5.754148	3.724145	3.063423
mon_24-Gt2core	-	19788322	2076177.6	217738.6	3522.974	51.76286	137.3726	28.11382	11.08096	5.882241	3.49677	1.87427	1.040241	0.813601
mon_25-Gt2core	-	19938220	2191743.3	228581.6	3896.399	64.17307	157.8454	38.88428	18.19445	11.85474	8.496052	5.800888	4.014884	3.641525
mon_26-Gt2core	-	19525397	2168493.5	220779.1	3858.234	62.92627	186.7298	48.4953	23.89164	14.99181	10.61646	6.958168	4.680262	4.011227
mon_27-Gt2core	-	19914235	2187710.8	219020.3	3920.316	88.30815	149.9589	31.80935	12.73769	7.397646	5.07616	3.515307	2.925826	3.216982
mon_5-Gt2mant	-	23596247	2249583.7	275949.3	4217.753	125.0335	133.0759	27.2984	10.19597	5.502035	3.605853	2.439183	1.88631	1.786524
mon_6-Gt2mant	-	23046914	2450051.6	325854.9	5425.862	115.21	207.8177	43.24601	16.97228	8.326909	5.023215	2.770041	1.673787	1.285674
mon_7-Gt2mant	-	23573283	2368472.2	304654.6	5389.833	155.1336	202.1248	44.66426	16.67707	8.074041	4.318464	2.382728	1.48084	1.064544
mon_8-Gt2mant	-	21327902	2426370.5	348524.3	7673.968	45.44423	338.3275	82.3813	32.14123	16.39602	9.850393	5.901393	3.981184	3.087791
mon_9-Gt2mant	-	21901400	2487135.5	357322.3	7127.489	121.0711	253.6743	53.35654	19.32663	9.616227	5.717009	3.413282	2.311575	1.828577
mon_10-Gt2mant	-	22335426	2408843.7	311892.5	6443.159	24.04293	296.9855	71.81862	29.86765	16.47727	10.70534	6.142608	3.858894	3.139766
mon_14-Gt2mant	-	22650943	2517959.7	372666.4	9675.412	59.04447	406.2301	86.46112	30.80036	14.39558	8.399228	5.435385	3.75079	3.087318
mon_15-Gt2mant	-	24344302	2406472.8	296146.2	4248.227	60.16923	148.146	30.94913	12.04791	6.233348	3.512698	1.740514	0.936969	0.658666
mon_16-Gt2mant	-	24564587	2450981.9	326186	4618.972	50.356	149.848	26.35798	8.889855	4.115425	2.037655	0.902248	0.449844	0.324135
mon_17-Gt2mant	-	21986336	2376983.1	314967.4	6231.082	81.23001	275.3046	70.31246	28.79264	15.36296	9.710072	5.885996	3.911516	3.144491
mon_18-Gt2mant	-	22141359	2228263.7	295451.4	5641.782	34.49592	255.88	61.77336	26.21655	15.16899	9.96433	5.812092	3.845917	3.073143
mon_19-Gt2mant	-	23109302	2425544	323517.5	6153.165	123.754	250.3522	55.3971	21.125	11.43256	6.953614	4.09895	2.766093	2.315252
mon_20-Gt2mant	-	21144725	2214641	291286.5	5664.141	137.0137	242.4019	58.29584	23.17676	11.87724	6.913867	4.212201	2.743384	2.243432
mon_24-Gt2mant	-	23566093	2292626.4	294509.7	4300.62	64.68889	148.764	27.71008	9.754709	4.762859	2.632546	1.372019	0.766291	0.595823
mon_25-Gt2mant	-	23744607	2420240.4	309175.7	4756.473	80.19812	170.9344	38.32586	16.01681	9.598804	6.39626	4.246416	2.957556	2.666793
mon_26-Gt2mant	-	23252973	2394566.7	298622.2	4709.884	78.63998	202.2141	47.79886	21.03211	12.13889	7.992611	5.093578	3.447705	2.937535
mon_27-Gt2mant	-	23716044	2415787.4	296243.2	4785.67	110.3601	162.394	31.35254	11.21315	5.989885	3.821592	2.573306	2.155304	2.355887
mon_5-Gt2Rim	-	22492090	-	639347.2	8027.423	102.5648	262.4023	35.97878	9.607193	4.032318	2.394197	1.578015	1.265526	1.405263
mon_6-Gt2Rim	-	21968462	-	754973.8	10326.75	94.50652	409.78	56.99742	15.99219	6.102605	3.335291	1.792062	1.122945	1.011299
mon_7-Gt2Rim	-	22470200	-	705854.7	10258.18	127.2558	398.5547	58.86665	15.71403	5.917283	2.867354	1.541492	0.993496	0.83736
mon_8-Gt2Rim	-	20329889	-	807496.4	14605.45	37.27781	667.1224	108.577	30.28519	12.01627	6.540418	3.817872	2.670978	2.428826
mon_9-Gt2Rim	-	20876551	-	827880.6	13565.37	99.31437	500.2011	70.32291	18.21059	7.047517	3.795953	2.208203	1.550837	1.438341
mon_10-Gt2Rim	-	21290268	-	722624.2	12262.92	19.72236	585.6032	94.65558	28.1429	12.07582	7.108082	3.973925	2.588934	2.469709
mon_14-Gt2Rim	-	21591020	-	863431.4	18414.69	48.43406	801.0145	113.9541	29.02176	10.5502	5.57688	3.516391	2.516407	2.428455
mon_15-Gt2Rim	-	23205141	-	686141.5	8085.423	49.3567	292.118	40.79036	11.35219	4.568281	2.332345	1.126015	0.628613	0.5181
mon_16-Gt2Rim	-	23415117	-	755740.8	8791.042	41.30692	295.4739	34.73932	8.3765	3.016103	1.352952	0.583704	0.301801	0.254962
mon_17-Gt2Rim	-	20957512	-	729748.4	11859.28	66.63281	542.8524	92.67049	27.12998	11.25917	6.447248	3.807911	2.624238	2.473426
mon_18-Gt2Rim	-	21105281	-	684531.7	10737.7	28.29694	504.5505	81.41612	24.70264	11.11701	6.616069	3.760099	2.580227	2.417305
mon_19-Gt2Rim	-	22027931	-	749558.1	11710.99	101.5152	493.6506	73.01233	19.90511	8.378665	4.617028	2.651792	1.855773	1.821155
mon_20-Gt2Rim	-	20155284	-	674882	10780.26	112.3921	477.974	76.83281	21.83839	8.70456	4.590637	2.725059	1.840537	1.764662
mon_24-Gt2Rim	-	22463346	-	682349.9	8185.14	53.06416	293.3366	36.52137	9.191412	3.490593	1.747946	0.88762	0.514105	0.468669
mon_25-Gt2Rim	-	22633508	-	716329.7	9052.74	65.78636	337.0527	50.51276	15.0919	7.034748	4.246959	2.747194	1.984226	2.097673
mon_26-Gt2Rim	-	22164879	-	691878.2	8964.07	64.50821	398.7306	62.99799	19.81759	8.896322	5.306896	3.295261	2.313067	2.310637
mon_27-Gt2Rim	-	22606281	-	686366.4	9108.31	90.52819	320.2125	41.32205	10.56564	4.389853	2.537442	1.664785	1.445994	1.853118

GRANADA 3	La	Ce	Pr	Nd	Sm	Eu	Gd	Tb	Dy	Ho	Er	Tm	Yb	Lu
mon_28-Grt3 Core	-	12196641	2211311.2	329583	10300.32	1119	855.989	210.5914	64.97682	22.15269	6.993318	1.783195	0.493605	0.206812
mon_29-Grt3 Core	-	13456328	2260221.9	314447.9	8268.103	1120.431	728.8344	209.4907	79.86941	35.85553	17.2348	7.27442	3.460913	2.218574
mon_30-Grt3 Core	-	13952206	2540342.8	361311.6	8582.339	1230.828	533.7086	137.3199	40.72576	12.02989	3.59748	0.979064	0.317382	0.138201
mon_34-Grt3 Core	-	13515623	2225987.7	322183.6	7282.358	938.0909	371.5764	101.0231	33.86686	11.0196	3.424416	0.961571	0.3556	0.176427
mon_35-Grt3 Core	-	12825446	2229641.8	330060.9	9924.746	1232.077	896.404	255.5002	95.22857	38.64801	15.45486	5.218103	1.85661	0.848812
mon_36-Grt3 Core	-	12559337	2197890.6	329039.2	9948.216	1243.115	889.345	253.7215	91.06678	36.65834	14.84197	5.034705	1.821267	0.827738
mon_37-Grt3 Core	-	12215990	2157859	323298.7	10436.99	1292.943	1051.95	335.4454	134.3204	55.19245	24.11062	8.881553	3.478724	1.573144
mon_39-Grt3 Core	-	13631517	2224757.3	301148.7	7790.608	1137.287	671.5256	212.5874	88.60348	40.21214	19.27757	8.275492	3.999677	2.509189
mon_40-Grt3 Core	-	13056134	2339814.3	346325.3	10302.14	949.378	800.1959	166.4168	44.05643	13.33997	4.105092	1.06766	0.309388	0.12791
mon_44-Grt3 Core	-	12460504	2255644.1	336392.5	10100.44	992.5502	794.0392	174.7112	49.01346	15.67049	4.998672	1.308617	0.401041	0.159765
mon_45-Grt3 Core	-	12538978	2260682.6	327707.7	9257.292	1129.033	684.6195	152.1237	40.68683	11.39306	3.00902	0.773658	0.233444	0.100466
mon_46-Grt3 Core	-	13063040	2468725.7	355264.5	11221.13	1426.593	774.2057	123.9328	18.81299	3.103273	0.704792	0.176627	0.065566	0.035678
mon_47-Grt3 Core	-	11384828	1961894.5	298211.7	8235.169	1015.019	555.7466	112.6908	27.2342	7.705466	2.482391	0.797359	0.282741	0.147023
mon_48-Grt3 Core	-	13099842	2327510	324844.2	8088.091	845.0766	545.7986	120.3983	33.63225	10.24262	3.222455	0.942385	0.334002	0.159765
mon_49-Grt3 Core	-	13780665	2293108.6	320964.7	7899.135	861.7943	623.1607	155.8939	61.1635	29.63882	14.94842	6.856837	3.437421	2.271992
mon_28-Grt3 Mant	-	19241252	2350763.3	272149	9045.455	1158.007	789.0401	222.4976	77.28774	29.32295	9.762124	2.618712	0.741752	0.299482
mon_29-Grt3 Mant	-	21228517	2402758.4	259651.3	7260.821	1159.487	671.8306	221.3347	95.00198	47.46105	24.05843	10.68285	5.200797	3.212689
mon_30-Grt3 Mant	-	22010808	2700544.6	298348.5	7536.775	1273.732	491.966	145.0835	48.44192	15.92366	5.0218	1.437806	0.476938	0.200128
mon_34-Grt3 Mant	-	21322061	2366365.3	266039	6395.167	970.7912	342.5145	106.7347	40.28349	14.58637	4.780217	1.412116	0.534369	0.255482
mon_35-Grt3 Mant	-	20233246	2370249.8	272543.6	8715.64	1275.025	826.2942	269.9454	113.2712	51.15738	21.57378	7.663048	2.789972	1.229153
mon_36-Grt3 Mant	-	19813437	2336496.3	271700	8736.25	1286.448	819.7873	268.0662	108.3209	48.52371	20.71823	7.393718	2.736862	1.198637
mon_37-Grt3 Mant	-	19271777	2293940.2	266959.8	9165.478	1338.012	969.675	354.4105	159.7696	73.05683	33.65653	13.04301	5.227563	2.27805
mon_39-Grt3 Mant	-	21504893	2365057.3	248669.7	6841.499	1176.931	619.004	224.6065	105.3909	53.22778	26.90998	12.15298	6.010411	3.633525
mon_40-Grt3 Mant	-	20597176	2487370.2	285973.7	9047.057	982.4718	737.6107	175.8256	52.40365	17.65777	5.730387	1.567912	0.464925	0.185225
mon_44-Grt3 Mant	-	19657520	2397891.9	277771.8	8869.933	1027.149	731.9356	184.5888	58.29986	20.74263	6.977755	1.92177	0.602653	0.231353
mon_45-Grt3 Mant	-	19781319	2403248.2	270600.5	8129.5	1168.39	631.0739	160.7244	48.39562	15.08071	4.200356	1.136156	0.350801	0.145483
mon_46-Grt3 Mant	-	20608072	2624411.1	293355.2	9854.088	1476.322	713.6533	130.9396	22.37742	4.107723	0.983835	0.259385	0.098528	0.051664
mon_47-Grt3 Mant	-	17960548	2085617.5	246244.5	7231.9	1050.401	512.2803	119.062	32.39417	10.19953	3.465223	1.170962	0.424882	0.212902
mon_48-Grt3 Mant	-	20666129	2474289.9	268236	7102.739	874.5346	503.1104	127.2053	40.00442	13.5579	4.498295	1.38394	0.501913	0.231353
mon_49-Grt3 Mant	-	21740187	2437719.1	265032.5	6936.804	891.835	574.4219	164.7077	72.75192	39.23215	20.86682	10.06961	5.165495	3.290043
mon_28-Grt3 Rim	-	34285488	2718070.1	317223.6	8099.793	1292.462	642.6409	179.6486	77.11349	39.73418	18.14488	6.680761	2.440538	1.07763
mon_29-Grt3 Rim	-	37826544	2778189.4	302656.1	6501.736	1294.114	547.1785	178.7096	94.78778	64.3123	44.71746	27.2537	17.11185	11.56027
mon_30-Grt3 Rim	-	39220487	3122504.7	347762.4	6748.839	1421.625	400.6862	117.143	48.3327	21.57743	9.334032	3.668076	1.569239	0.720123
mon_34-Grt3 Rim	-	37993227	2736109.8	310101.7	5726.582	1083.509	278.9641	86.17948	40.19267	19.76532	8.884999	3.602537	1.7582	0.919305
mon_35-Grt3 Rim	-	36053096	2740601.3	317683.6	7804.459	1423.067	672.9828	217.9588	113.0158	69.32103	40.09923	19.54968	9.179669	4.42288
mon_36-Grt3 Rim	-	35305048	2701573.9	316700.3	7822.915	1435.817	667.6832	216.4414	108.0767	65.75226	38.50901	18.86258	9.004923	4.313075
mon_37-Grt3 Rim	-	34339880	2652368.4	311175	8207.269	1493.368	789.7605	286.1574	159.4094	98.99597	62.55747	33.27484	17.19992	8.19714
mon_39-Grt3 Rim	-	38319011	2734597.5	289855.6	6126.251	1313.584	504.1534	181.3513	105.1532	72.12653	50.01764	31.00423	19.77567	13.07457
mon_40-Grt3 Rim	-	36701574	2876021.8	333338.1	8101.228	1096.546	600.7537	141.9647	52.2855	23.92724	10.65108	4	1.529714	0.666496
mon_44-Grt3 Rim	-	35027224	2772562.5	323777.8	7942.622	1146.411	596.1315	149.0403	58.16842	28.10739	12.96957	4.902748	1.982872	0.832482
mon_45-Grt3 Rim	-	35247819	2778755.7	315418.7	7279.598	1304.051	513.9838	129.7718	48.28651	20.43518	7.807211	2.89852	1.15422	0.523493
mon_46-Grt3 Rim	-	36720989	3034475.4	341942.1	8823.888	1647.737	581.2414	105.723	22.32696	5.566188	1.828656	0.661734	0.32418	0.185904
mon_47-Grt3 Rim	-	32003434	2411495.3	287028.7	6475.838	1172.363	417.2314	96.1328	32.32113	13.82092	6.440818	2.987315	1.397961	0.766088
mon_48-Grt3 Rim	-	36824439	2860897.7	312662.6	6360.18	976.0763	409.7628	102.7078	39.91423	18.37169	8.36099	3.530655	1.651411	0.832482
mon_49-Grt3 Rim	-	38738274	2818612.7	308928.5	6211.593	995.3855	467.8431	132.9879	72.5879	53.16169	38.78521	25.68922	16.9957	11.83861

GRANADA 4	La	Ce	Pr	Nd	Sm	Eu	Gd	Tb	Dy	Ho	Er	Tm	Yb	Lu
mon_28-Grt4 Core	-	-	-	1526490	33110.64	4429.375	1201.459	144.4193	24.01622	4.879136	1.060762	0.217072	0.052095	0.01921
mon_29-Grt4 Core	-	-	-	1456390	26578.04	4435.038	1022.986	143.6645	29.52071	7.897191	2.614212	0.885529	0.365262	0.206072
mon_30-Grt4 Core	-	-	-	1673443	27588.16	4872.027	749.109	94.17118	15.05274	2.649588	0.545674	0.119183	0.033496	0.012837
mon_34-Grt4 Core	-	-	-	1492219	23409.34	3713.277	521.5415	69.27961	12.5176	2.427071	0.519423	0.117054	0.03753	0.016387
mon_35-Grt4 Core	-	-	-	1528703	31903.36	4876.97	1258.185	175.2168	35.19764	8.512236	2.344228	0.63521	0.195945	0.078842
mon_36-Grt4 Core	-	-	-	1523971	31978.81	4920.663	1248.277	173.9971	33.65939	8.074011	2.251263	0.612884	0.192215	0.076884
mon_37-Grt4 Core	-	-	-	1497383	33549.98	5117.898	1476.509	230.0417	49.64646	12.15615	3.657152	1.081168	0.367141	0.146121
mon_39-Grt4 Core	-	-	-	1394794	25043.12	4501.761	942.5477	145.7882	32.74893	8.856735	2.924065	1.007391	0.422122	0.233065
mon_40-Grt4 Core	-	-	-	1604033	33116.51	3757.955	1123.148	114.1253	16.2838	2.938132	0.622669	0.129968	0.032653	0.011881
mon_44-Grt4 Core	-	-	-	1558029	32468.15	3928.845	1114.507	119.8134	18.11597	3.451431	0.75821	0.1593	0.042325	0.01484
mon_45-Grt4 Core	-	-	-	1517804	29757.82	4469.091	960.9263	104.3234	15.03835	2.509326	0.456415	0.094179	0.024637	0.009332
mon_46-Grt4 Core	-	-	-	1645436	36070.62	5646.932	1086.669	84.99062	6.953509	0.683497	0.106904	0.021501	0.00692	0.003314
mon_47-Grt4 Core	-	-	-	1381191	26472.17	4017.784	780.0412	77.28107	10.06609	1.697131	0.376535	0.097064	0.02984	0.013656
mon_48-Grt4 Core	-	-	-	1504542	25999.39	3345.095	766.0784	82.56672	12.43089	2.255941	0.488789	0.114718	0.03525	0.01484
mon_49-Grt4 Core	-	-	-	1486573	25391.98	3411.269	874.6632	106.9089	22.60677	6.527959	2.267409	0.834696	0.362782	0.211033
mon_28-Grt4 Mant	-	-	4814293.9	583399.8	13006.97	1760.017	637.1647	122.9821	35.93602	13.63975	4.975209	1.596847	0.54377	0.249763
mon_29-Grt4 Mant	-	-	4920778.3	556608.9	10440.74	1762.267	542.5158	122.3393	44.1725	22.0768	12.26124	6.514225	3.812651	2.679332
mon_30-Grt4 Mant	-	-	5530635.7	639563.1	10837.55	1935.905	397.2718	80.19265	22.52375	7.406992	2.559331	0.87675	0.349638	0.166903
mon_34-Grt4 Mant	-	-	4846246.2	570301.9	9195.97	1475.474	276.5869	58.99592	18.73037	6.784941	2.436209	0.861084	0.39174	0.213068
mon_35-Grt4 Mant	-	-	4854201.6	584245.7	12532.71	1937.869	667.2481	149.2081	52.66702	23.79618	10.99495	4.672798	2.0453	1.025095
mon_36-Grt4 Mant	-	-	4785075.5	582437.3	12562.35	1955.23	661.9936	148.1694	50.36531	22.57111	10.55892	4.508565	2.006365	0.999645
mon_37-Grt4 Mant	-	-	4697921.8	572275.8	13179.56	2033.602	783.0308	195.8949	74.28712	33.98285	17.15286	7.953408	3.832272	1.899858
mon_39-Grt4 Mant	-	-	4843567.6	533067.8	9837.775	1788.779	499.8574	124.1477	49.00296	24.75924	13.71451	7.410683	4.406171	3.030303
mon_40-Grt4 Mant	-	-	5094060.7	613035.6	13009.27	1493.227	595.6345	97.18484	24.36581	8.213625	2.920458	0.956087	0.340832	0.154474
mon_44-Grt4 Mant	-	-	4910811.8	595453.4	12754.58	1561.13	591.0517	102.0286	27.10734	9.648565	3.556172	1.171863	0.441799	0.192945
mon_45-Grt4 Mant	-	-	4921781.3	580080.4	11689.87	1775.798	509.604	88.83789	22.50222	7.014886	2.140687	0.692809	0.257169	0.12133
mon_46-Grt4 Mant	-	-	5374716.5	628859	14169.75	2243.814	576.2884	72.37482	10.40469	1.910733	0.501406	0.158169	0.07223	0.043087
mon_47-Grt4 Mant	-	-	4271283.1	527868.9	10399.16	1596.47	413.676	65.80966	15.06212	4.744375	1.766031	0.714033	0.311476	0.177557
mon_48-Grt4 Mant	-	-	5067272.7	575011.7	10213.43	1329.177	406.2711	70.31072	18.60062	6.306541	2.29253	0.843903	0.367947	0.192945
mon_49-Grt4 Mant	-	-	4992376.7	568144.4	9974.821	1355.471	463.8565	91.0396	33.82703	18.24908	10.63466	6.14028	3.786772	2.743845
mon_28-Grt4 Rim	12074972	7971376	3209529.2	381622.4	8201.464	1301.163	595.9417	206.7876	105.115	61.291	32.59358	12.56112	5.189855	2.49926
mon_29-Grt4 Rim	15279473	8794671	3280518.8	364097.5	6583.347	1302.826	507.4164	205.7068	129.2072	99.20337	80.32581	51.2422	36.3887	26.81078
mon_30-Grt4 Rim	13517365	9118763	3687090.5	418360.8	6833.553	1431.195	371.5693	134.8395	65.8833	33.28374	16.76669	6.896689	3.33702	1.670121
mon_34-Grt4 Rim	14763830	8833425	3230830.8	373054.6	5798.463	1090.803	258.6924	99.19839	54.78745	30.48852	15.96009	6.773463	3.738848	2.13207
mon_35-Grt4 Rim	13239456	8382345	3236134.4	382175.7	7902.423	1432.647	624.0788	250.8852	154.0542	106.9295	72.0301	36.75717	19.52075	10.25763
mon_36-Grt4 Rim	12986476	8208424	3190050.3	380992.8	7921.111	1445.482	619.1642	249.1387	147.3215	101.4246	69.1736	35.46528	19.14916	10.00296
mon_37-Grt4 Rim	12612557	7984022	3131947.9	374345.8	8310.289	1503.422	732.3705	329.3865	217.2942	152.7038	112.3718	62.5631	36.57598	19.01096
mon_39-Grt4 Rim	16081060	8909170	3229045.1	348698.5	6203.149	1322.427	467.5178	208.7476	143.3366	111.257	89.8465	58.29391	42.05338	30.32277
mon_40-Grt4 Rim	13415762	8533116	3396040.5	401008.2	8202.917	1103.928	557.0984	163.411	71.27144	36.90839	19.1325	7.52077	3.252968	1.545751
mon_44-Grt4 Rim	12801343	8143830	3273874.5	389507.1	8042.32	1154.128	552.8121	171.5555	79.29057	43.35637	23.29719	9.21811	4.216619	1.930708
mon_45-Grt4 Rim	12750596	8195118	3281187.5	379451.1	7370.974	1312.83	476.6338	149.376	65.82033	31.52179	14.02406	5.449775	2.454472	1.214095
mon_46-Grt4 Rim	12616463	8537630	3583144.4	411358.9	8934.648	1658.829	539.004	121.6943	30.43434	8.585989	3.284809	1.244187	0.689376	0.431152
mon_47-Grt4 Rim	10861643	7440798	2847522.1	345297.7	6557.124	1180.255	386.9122	110.6553	44.0576	21.31912	11.56962	5.616727	2.972794	1.776725
mon_48-Grt4 Rim	13773194	8561682	3378181.8	376135.4	6440.015	982.6472	379.9864	118.2236	54.40791	28.3388	15.01882	6.638311	3.51176	1.930708
mon_49-Grt4 Rim	15491139	9006649	3328251.1	371643.3	6289.563	1002.086	433.8461	153.0781	98.94606	82.00328	69.66974	48.30067	36.14171	27.45632

Artigo 3
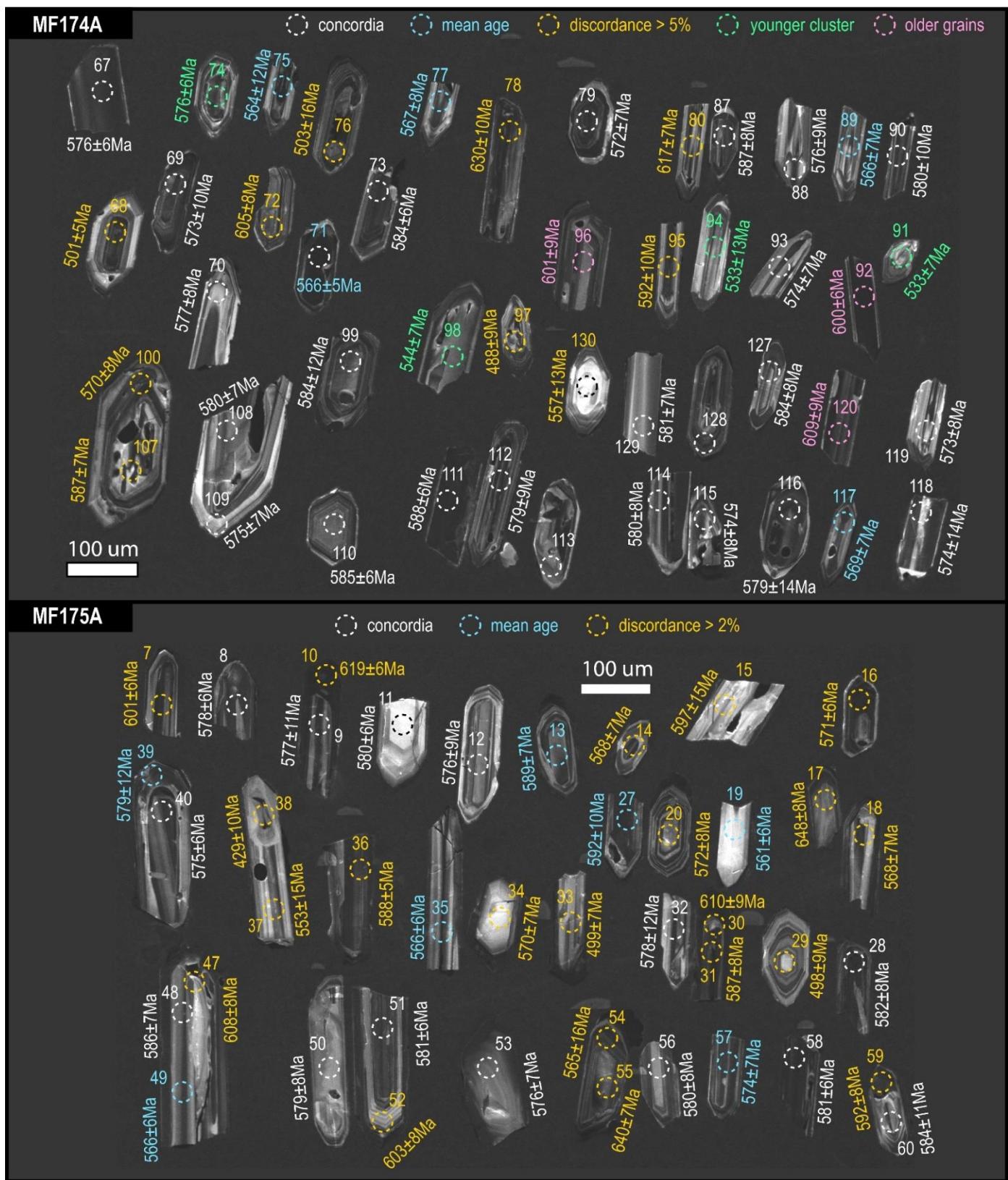
Figura S1. Imagens de catodoluminescência dos cristais de zircão estudados nas amostras MF-174A e MF-175A com idade $^{238}U-^{206}Pb$ indicada. As diferentes cores dos pontos analisados foram utilizadas para distinguir as análises nos diagramas concórdia das figuras 4b e 5b.
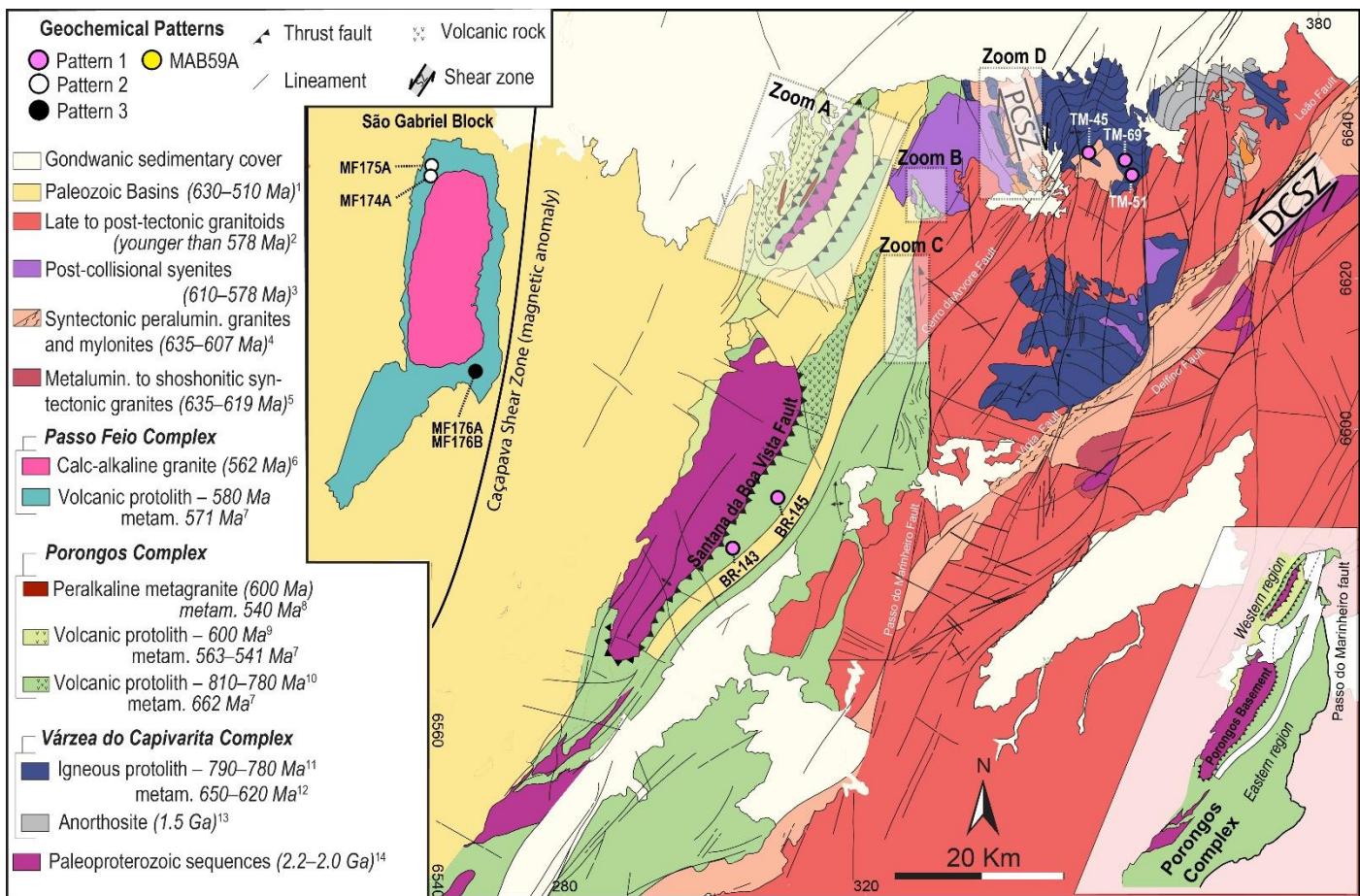
Figura S2. Mapa com a localização das amostras de geoquímica discutidas neste artigo. Nas próximas páginas, mapas de detalhes das áreas indicadas são apresentados: a) Região oeste do Complexo Porongos (modificado de Hofig et al., 2018); (b) e (c) Região leste do Complexo Porongos (modificado de Battisti et al., 2018) e; d) Complexo Várzea do Capivarita (modificado de Martil et al., 2011). A legenda dos mapas de detalhe segue as do mapa principal, exceto quando indicado.
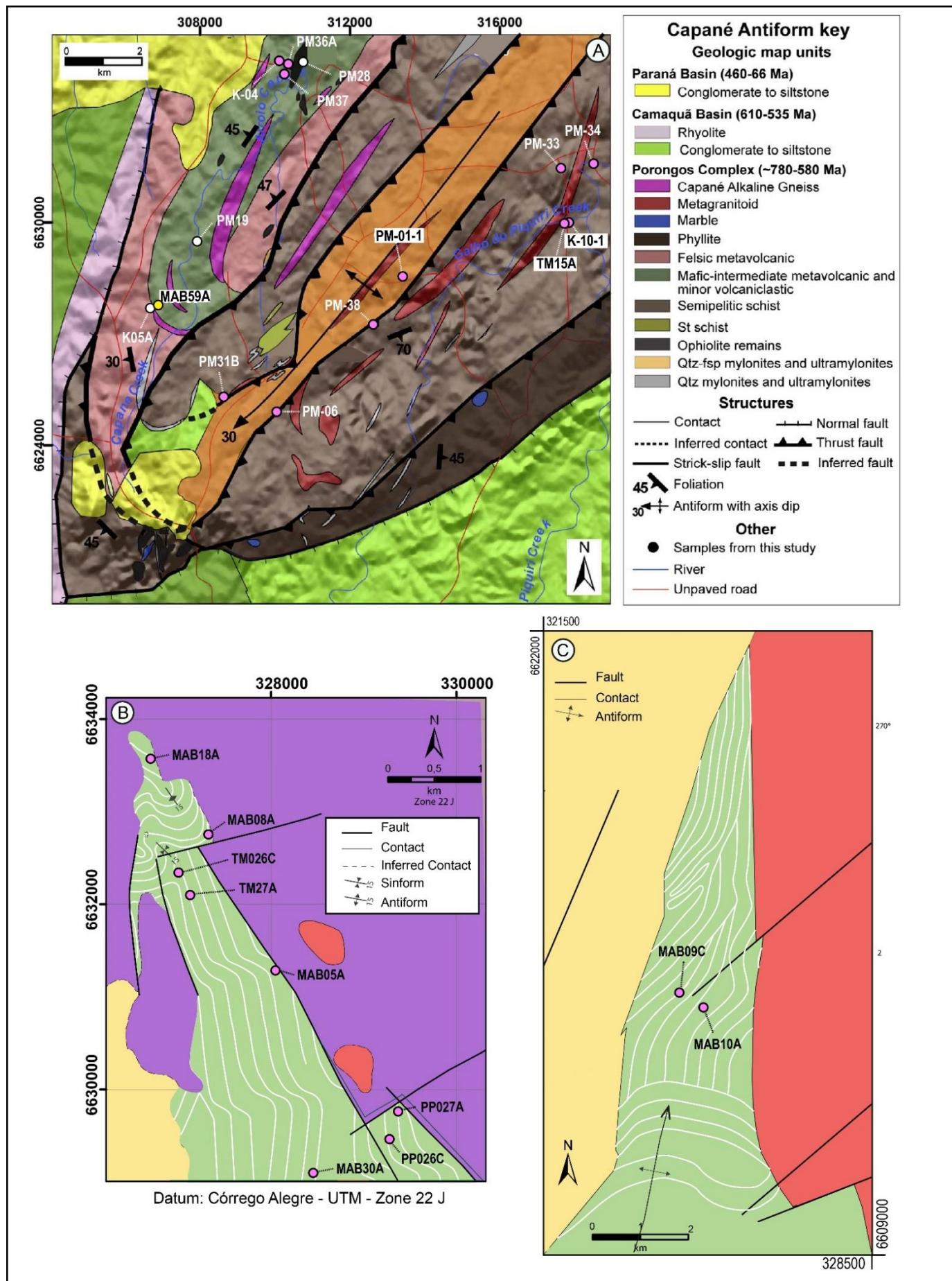
Figura S3. Localização das amostras discutidas no artigo: a) Região oeste do Complexo Porongos (Hofig et al., 2018, modificado); (b), (c) Região leste do Complexo Porongos (Battisti et al., 2018, modificado).
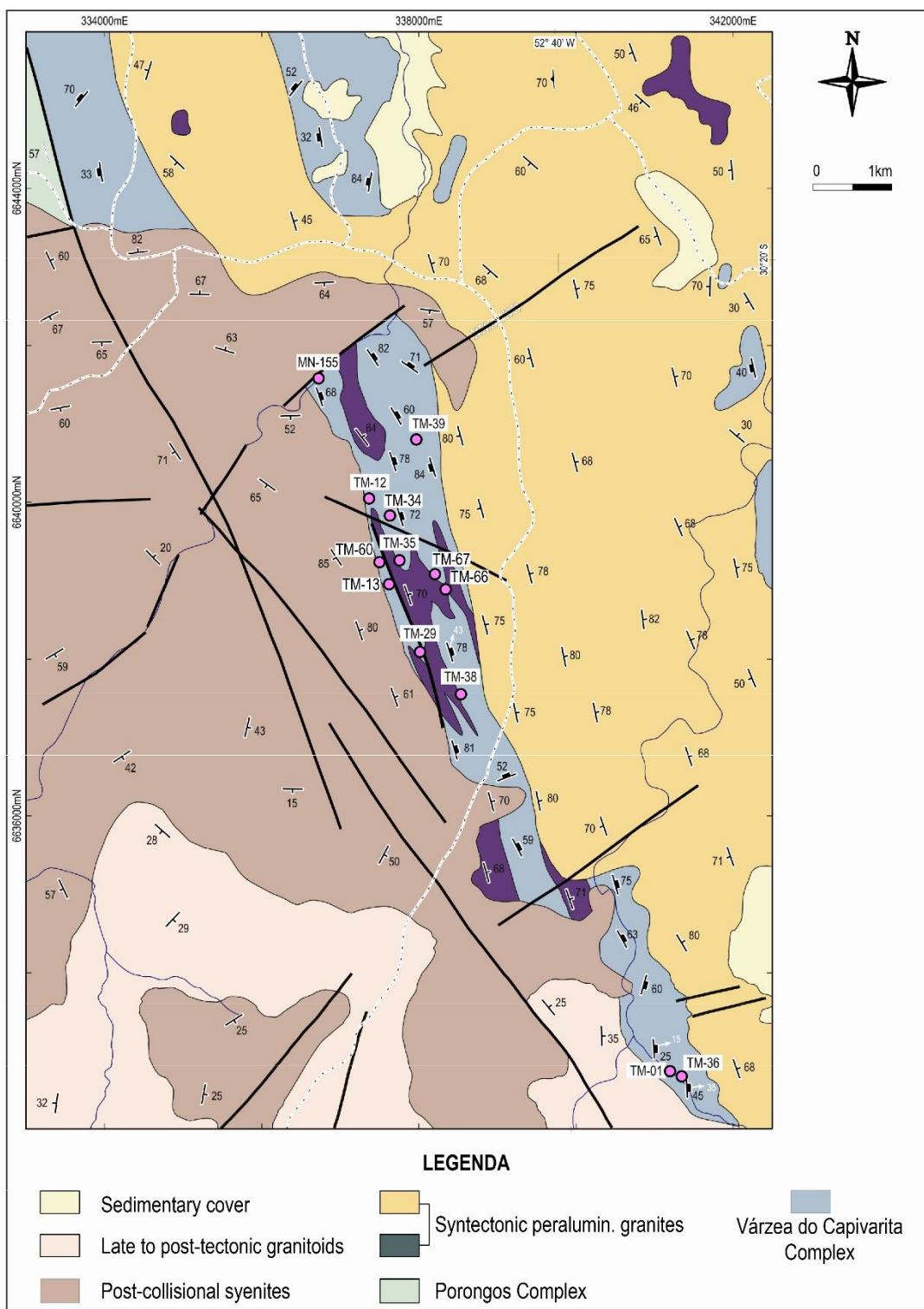
Figura S4. Localização das amostras discutidas no artigo: d) Complexo Várzea do Capivarita (modificado de Martil et al., 2011).

Tabela S1: Resumo dos dados LA-ICPMS U-Pb em zircão da amostra MF-174A.

Grain Spot	ppm Pb	ppm U	ppm Th	^{232}Th/^{238}U	^{206}Pb/^{238}U Age	±2σ	^{207}Pb/^{206}Pb Age	±2σ	% discordant	^{207}Pb*/^{206}Pb*	±2σ	^{207}Pb*/^{235}U	±2σ	^{206}Pb*/^{238}U	±2σ	err corr
Spot 67	700	764	399	1.92	576	6	559	31	0.0	0.0592	0.0008	0.7640	0.0110	0.0936	0.0011	0.2866
Spot 68	197	220	444	0.50	501	5	743	33	9.4	0.0646	0.0010	0.7270	0.0120	0.0809	0.0009	0.4604
Spot 69	235	259	398	0.65	573	10	572	51	0.5	0.0599	0.0014	0.7670	0.0190	0.0930	0.0018	0.4333
Spot 70	215	240	158	1.52	577	8	547	60	0.2	0.0593	0.0017	0.7700	0.0220	0.0937	0.0013	0.0892
Spot 71	1278	1306	1846	0.71	566	5	573	23	0.4	0.0594	0.0006	0.7498	0.0072	0.0918	0.0009	0.5695
Spot 72	888	876	674	1.30	605	8	788	27	6.5	0.0659	0.0009	0.8940	0.0130	0.0985	0.0014	0.4299
Spot 73	348	380	662	0.57	584	6	577	25	-0.1	0.0595	0.0007	0.7781	0.0094	0.0949	0.0010	0.5956
Spot 74	238	294	510	0.58	523	8	651	43	4.8	0.0620	0.0012	0.7190	0.0130	0.0846	0.0013	0.3663
Spot 75	2890	2870	1011	2.84	564	12	575	35	0.1	0.0595	0.0010	0.7460	0.0160	0.0915	0.0020	0.7442
Spot 76	3640	1505	1290	1.17	503	16	3150	120	63.9	0.2910	0.0180	3.5900	0.2800	0.0814	0.0028	0.8479
Spot 77	353	401	244	1.65	567	8	555	47	0.0	0.0595	0.0013	0.7480	0.0150	0.0920	0.0014	0.3111
Spot 78	1530	1105	788	1.40	630	10	1690	51	32.0	0.1069	0.0033	1.5130	0.0620	0.1027	0.0018	0.6129
Spot 79	257	277	397	0.70	572	7	569	47	0.4	0.0595	0.0013	0.7630	0.0150	0.0928	0.0011	0.2568
Spot 80	610	562	258	2.18	618	7	1411	51	25.1	0.0918	0.0025	1.2710	0.0380	0.1006	0.0012	0.1593
Spot 87	254	283	385	0.74	587	8	584	41	-0.6	0.0598	0.0011	0.7780	0.0150	0.0954	0.0013	0.4528
Spot 88	292	313	175	1.79	577	10	589	61	0.6	0.0605	0.0017	0.7740	0.0230	0.0936	0.0017	0.4315
Spot 89	288	323	160	2.02	566	7	617	48	2.4	0.0614	0.0014	0.7760	0.0170	0.0918	0.0013	0.2084
Spot 90	579	648	382	1.70	580	10	541	45	-0.8	0.0586	0.0012	0.7630	0.0140	0.0943	0.0017	0.4567
Spot 91	346	392	189	2.07	534	7	509	45	-0.6	0.0583	0.0012	0.6900	0.0150	0.0864	0.0012	0.4597
Spot 92	2331	2078	1007	2.06	600	6	651	27	1.7	0.0616	0.0008	0.8250	0.0110	0.0975	0.0011	0.4265
Spot 93	29	27	322	0.08	574	7	608	33	1.2	0.0605	0.0009	0.7750	0.0120	0.0932	0.0012	0.3043
Spot 94	331	358	267	1.34	533	13	576	58	1.7	0.0601	0.0017	0.7090	0.0200	0.0863	0.0022	0.5151
Spot 95	495	523	231	2.26	592	6	889	37	10.2	0.0694	0.0013	0.9190	0.0170	0.0962	0.0011	0.0528
Spot 96	73	77	124	0.62	601	9	533	58	-1.6	0.0596	0.0016	0.7990	0.0210	0.0978	0.0015	0.1868
Spot 97	434	820	282	2.90	498	9	1567	44	33.0	0.0991	0.0022	1.0870	0.0230	0.0804	0.0015	0.2800
Spot 98	302	342	267	1.28	545	7	579	39	1.5	0.0601	0.0011	0.7260	0.0130	0.0882	0.0011	0.2357
Spot 99	193	203	343	0.59	584	12	592	61	0.2	0.0605	0.0017	0.7820	0.0220	0.0949	0.0021	0.3869
Spot 100	460	494	663	0.75	571	8	825	40	8.5	0.0672	0.0013	0.8500	0.0150	0.0926	0.0014	0.2750
Spot 107	493	524	498	1.05	588	7	756	32	5.8	0.0648	0.0010	0.8520	0.0130	0.0955	0.0012	0.3455
Spot 108	92	104	211	0.49	580	8	562	41	-0.6	0.0597	0.0011	0.7680	0.0130	0.0942	0.0013	0.0190
Spot 109	279	306	404	0.76	575	7	568	32	0.1	0.0595	0.0009	0.7640	0.0110	0.0934	0.0011	0.3843
Spot 110	120	130	193	0.67	585	7	559	42	-0.5	0.0595	0.0012	0.7780	0.0150	0.0951	0.0011	0.3335
Spot 111	1321	1350	736	1.83	588	6	575	26	-0.3	0.0595	0.0007	0.7815	0.0086	0.0955	0.0009	0.4851
Spot 112	552	615	614	1.00	579	10	640	42	2.1	0.0615	0.0012	0.7930	0.0170	0.0940	0.0016	0.5395
Spot 114	338	355	312	1.14	580	8	578	39	0.3	0.0600	0.0011	0.7770	0.0140	0.0943	0.0014	0.4645
Spot 115	426	470	242	1.94	574	8	569	47	0.1	0.0598	0.0013	0.7660	0.0160	0.0931	0.0014	0.4333
Spot 116	323	350	619	0.57	579	14	633	57	1.0	0.0612	0.0017	0.7820	0.0230	0.0941	0.0024	0.5365
Spot 117	349	392	204	1.92	569	7	575	44	0.6	0.0598	0.0012	0.7600	0.0150	0.0923	0.0013	0.2860
Spot 118	222	224	246	0.91	574	14	615	58	1.5	0.0611	0.0016	0.7810	0.0250	0.0932	0.0023	0.6341
Spot 119	476	532	242	2.20	574	8	587	48	0.8	0.0603	0.0013	0.7700	0.0160	0.0931	0.0014	0.3392
Spot 120	790	811	645	1.26	609	9	683	38	2.5	0.0628	0.0011	0.8540	0.0160	0.0992	0.0015	0.2919
Spot 127	427	481	250	1.92	584	8	581	49	0.5	0.0603	0.0014	0.7860	0.0170	0.0948	0.0014	0.2970
Spot 129	161	177	130	1.36	581	7	539	46	-0.6	0.0591	0.0012	0.7700	0.0160	0.0944	0.0012	0.3674
Spot 130	41	37	68	0.55	557	13	1027	89	16.5	0.0766	0.0033	0.9430	0.0400	0.0904	0.0022	0.0156

Tabela S2: Resumo dos dados LA-ICPMS U-Pb em zircão da amostra MF-175A.

Grain Spot	ppm Pb	ppm U	ppm Th	$^{232}Th/^{238}U$	$^{206}Pb/^{238}U$ Age	±2σ	$^{207}Pb/^{206}Pb$ Age	±2σ	% discordant	$^{207}Pb^*/^{206}Pb^*$	±2σ	$^{207}Pb^*/^{235}U$	±2σ	$^{206}Pb^*/^{238}U$	±2σ	err corr
Spot 7	180	187	296	0.63	601	7	727	43	4.0	0.0642	0.0014	0.8570	0.0160	0.0977	0.0011	0.2276
Spot 8	287	334	333	1.00	578	6	549	35	-0.9	0.0590	0.0010	0.7600	0.0110	0.0938	0.0011	0.3728
Spot 9	869	912	950	0.96	577	11	590	36	0.4	0.0600	0.0010	0.7720	0.0160	0.0937	0.0019	0.7381
Spot 10	1356	1107	1475	0.75	619	7	960	22	11.2	0.0713	0.0008	0.9900	0.0110	0.1009	0.0011	0.6111
Spot 11	23	26	53	0.49	580	10	541	74	-0.7	0.0596	0.0020	0.7710	0.0260	0.0943	0.0017	0.2388
Spot 12	116	135	193	0.70	576	9	604	55	1.0	0.0609	0.0015	0.7780	0.0200	0.0935	0.0016	0.0327
Spot 13	126	149	204	0.73	589	7	575	41	-0.4	0.0597	0.0011	0.7850	0.0140	0.0957	0.0011	0.3474
Spot 14	186	196	303	0.65	568	7	825	33	8.8	0.0672	0.0011	0.8500	0.0140	0.0921	0.0011	0.5402
Spot 15	63	34	74	0.46	597	15	1918	77	37.8	0.1207	0.0048	1.5950	0.0640	0.0971	0.0026	0.0841
Spot 16	679	709	1065	0.67	571	6	866	24	9.9	0.0683	0.0008	0.8690	0.0120	0.0926	0.0011	0.6532
Spot 17	128	79	198	0.40	648	8	1162	65	17.3	0.0818	0.0026	1.1780	0.0310	0.1058	0.0014	0.0908
Spot 18	658	543	527	1.03	568	7	2189	89	46.1	0.1499	0.0064	1.9230	0.0920	0.0921	0.0012	0.5151
Spot 19	98	118	97	1.21	561	7	526	57	-0.4	0.0595	0.0017	0.7400	0.0180	0.0910	0.0011	0.0249
Spot 20	157	174	284	0.61	573	8	852	44	9.4	0.0682	0.0015	0.8690	0.0170	0.0929	0.0013	0.2007
Spot 27	629	718	528	1.36	592	10	593	40	-0.1	0.0602	0.0011	0.7910	0.0150	0.0961	0.0017	0.5155
Spot 28	565	669	551	1.22	582	8	577	54	0.2	0.0597	0.0015	0.7770	0.0170	0.0945	0.0013	0.1102
Spot 29	83	91	172	0.53	498	9	779	57	10.1	0.0662	0.0018	0.7300	0.0200	0.0804	0.0015	0.3592
Spot 30	2502	2204	2755	0.80	610	9	741	27	4.4	0.0643	0.0008	0.8760	0.0140	0.0992	0.0015	0.7135
Spot 31	783	672	573	1.17	587	8	1721	36	33.6	0.1068	0.0020	1.4040	0.0320	0.0954	0.0013	0.5515
Spot 32	297	348	383	0.91	578	12	592	56	0.2	0.0602	0.0015	0.7680	0.0200	0.0938	0.0021	0.4779
Spot 33	207	230	244	0.94	499	7	834	51	12.5	0.0683	0.0017	0.7580	0.0190	0.0804	0.0011	0.1972
Spot 34	67	73	163	0.44	570	8	841	58	10.1	0.0688	0.0020	0.8740	0.0230	0.0925	0.0013	0.0582
Spot 35	542	653	421	1.55	566	6	574	34	-0.1	0.0594	0.0009	0.7450	0.0120	0.0917	0.0010	0.4501
Spot 36	470	556	421	1.32	588	5	662	29	2.8	0.0621	0.0008	0.8165	0.0096	0.0956	0.0009	0.2562
Spot 37	126	128	179	0.72	553	15	1022	77	15.3	0.0738	0.0027	0.9100	0.0350	0.0897	0.0025	0.3576
Spot 38	256	74	236	0.31	429	10	2751	47	59.5	0.1971	0.0058	1.9280	0.0890	0.0689	0.0017	0.8341
Spot 39	537	646	502	1.29	579	12	605	56	1.0	0.0604	0.0015	0.7800	0.0180	0.0941	0.0021	0.3758
Spot 40	127	148	318	0.46	575	6	570	37	0.4	0.0596	0.0010	0.7650	0.0120	0.0933	0.0010	0.3989
Spot 47	565	294	510	0.58	608	8	2422	55	48.1	0.1635	0.0055	2.2250	0.0760	0.0990	0.0013	0.3078
Spot 48	203	236	416	0.57	586	7	558	36	-0.7	0.0592	0.0010	0.7760	0.0130	0.0952	0.0012	0.1476
Spot 49	305	359	339	1.06	566	6	565	33	0.7	0.0594	0.0009	0.7560	0.0120	0.0918	0.0010	0.3701
Spot 50	71	79	123	0.65	579	8	533	53	-1.1	0.0587	0.0014	0.7620	0.0170	0.0941	0.0013	0.2822
Spot 51	303	351	413	0.85	581	5	566	33	0.0	0.0594	0.0009	0.7730	0.0110	0.0943	0.0009	0.2904
Spot 52	108	74	110	0.67	603	8	1718	40	33.1	0.1062	0.0023	1.4390	0.0300	0.0980	0.0013	0.2376
Spot 53	65	75	254	0.30	576	7	589	41	0.6	0.0602	0.0011	0.7730	0.0140	0.0935	0.0011	0.3658
Spot 54	248	220	543	0.40	565	16	1071	51	16.2	0.0758	0.0019	0.9420	0.0260	0.0916	0.0026	0.6057
Spot 55	718	422	332	1.27	640	7	2783	46	52.7	0.1982	0.0056	2.8420	0.0890	0.1043	0.0012	0.7486
Spot 56	66	71	110	0.65	580	8	523	52	-1.0	0.0592	0.0014	0.7660	0.0170	0.0942	0.0013	0.1550
Spot 57	221	254	236	1.08	574	7	541	37	-0.6	0.0590	0.0010	0.7580	0.0130	0.0932	0.0011	0.0505
Spot 58	817	877	729	1.20	581	6	589	27	0.8	0.0600	0.0007	0.7820	0.0100	0.0943	0.0011	0.4412
Spot 59	485	518	411	1.26	592	a	753	37	5.9	0.0649	0.0012	0.8600	0.0140	0.0962	0.0014	0.0185
Spot 60	102	110	192	0.57	584	11	550	54	-0.3	0.0592	0.0015	0.7770	0.0220	0.0949	0.0019	0.5492

<u>Tabela S3</u>: Detalhes técnicos do equipamento utilizado para as análises U-PC por LA-ICPMS.

LA-ICP-MS U-(Th-)Pb data(reporting template according to *Horstwood et al. 2016*)	
Laboratory and Sample Preparation	
Laboratory name	Institute of Geology of the Czech Academy of Sciences, Prague, Czech Republic
Sample type/mineral	magmatic zircon
Sample preparation	Conventional mineral separation, 1 inch resin mount, 0.05 mm polish to finish
Imaging	CL, JEOL JXA-8530F Field Emission EPMA, Institute of Petrology and Structural Geology, Charles University in Prague
Laser ablation system	
Make, Model and type	Teledyne Cetac Analyte Excite laser
Ablation cell and volume	built-in 2- volume cell HelEx II, 100x100 mm
Laser wavelength (nm)	193 nm
Pulse width (ns)	< 4 ns
Fluence (J cm-2)	3.5 J cm-2
Repetition rate (Hz)	5 Hz
Ablation duration (s)	35 s
Spot diameter (mm)	25 mm
Sampling mode/pattern	Static spot ablation
Carrier gas	100% He + little addition N2 in the cell, Ar make-up gas combined using a Y-piece along the sample transport line to the torch. All gases and aerosole are mixed in the in-house glass signal homogenizer (design of *Tunheng and Hirata, 2004*) right before entering torch
Cell carrier gas flow (l min-1)	0.89 l min-1
N2 flow (ml min-1)	4.5 ml min-1
Ar make-up gas flow (l min-1)	0.66 l min-1
ICP-MS Instrument	
Make, Model and type	Thermo Scientific double-focusing magnetic sector field Element 2 HR-ICP-MS
Sample introduction	Dry ablation aerosol
RF power (W)	1200 W
Detection system	discrete dynode, dual mode secondary electron multiplier (SEM); analysis possible in 3 modes (cps-analog-both)
Masses measured (mode)	204 (cps), 206 (both), 207 (cps), 208 (cps), 232 (both), 235 (cps), 238 (both)
Integration time per peak/dwell times (ms)	204 (10 ms), 206 (15 ms), 207 (30 ms), 208 (10 ms), 232 (10 ms), 235 (20 ms), 238 (10 ms)
Total integration time per output data point (s)	~ 0.12 s (time resolution of the data)
Data Processing	
initial calculation	The accuracy of 238 mass measured in "both" mode is dependent on the correctly determined ACF (Analog Correction Factor). In order to correct for this variability, the data are pre-processed using a Python routine for decoding the Thermo Element ICPMS dat files (*Hartman et al., 2017*) and an in-house Excel macro. As a result, the intensities of 238 are left unchanged if measured in a counting mode and recalculated from 235U intensities (using the natural 138U/135U of 137.818) in all cases the 238U was acquired in analog mode, thus eliminating the non-linearity between pulse counting and analog detecting modes.
Gas blank	15 s on-peak zero subtracted
Calibration strategy	Plešovice used as primary reference material, 91500 and GJ1 used as secondaries/validation
Reference Material information, reference age	Plešovice (*Sláma et al. 2008*), 337 Ma (Concordia age); 91500 (*Wiedenbeck et al. 1995*), 1065 Ma (Concordia age); GJ1 (*Jackson et al. 2004*), 609 Ma (206Pb/207Pb age)
Data processing package used/Correction for LIEF	Iolite v3.5 software (*Paton et al. 2010*) with the VizualAge utility (*Petrus and Kamber, 2012*) used for data normalisation, uncertainty propagation and export blank intensities and instrumental bias interpolated using an automatic spline function; down-hole inter-element fractionation (LIEF) corrected using an exponential function LIEF correction assumes reference material and samples behave identically Isoplot v4_16 (*Ludwig, 2008*) used for pooled age uncertainty propagation, age calculation and plotting.
Common-Pb correction, composition and uncertainty	No common-Pb correction applied to the data
Uncertainty level and propagation	Ages are quoted at 2s absolute, propagation is by quadratic addition. Reproducibility and age uncertainty of reference material are propagated where appropriate following the recommendation of *Horstwood et al. (2016)*
Quality control/Validation	91500 – Concordia age = 1061 ± 8 Ma (2s, MSWD = 0.95, n = 14). GJ-1 – Wtd ave 206Pb/238U age = 604 ± 6 (2s, MSWD = 0.8, n =14). Systematic uncertainty for propagation is 2% (2s).
Other information	20 s wait time between ablations.
References:	Hartman, J., Franks, R., Gehrels, G., Hourigan, J., Wenig, P., 2017. Decoding dat files from a Thermo ElementTM ICP Mass Spectrometer. 15p. manual available online at https://github.com/jhh67/extractdat.git Horstwood, M.S.A., Košler, J., Gehrels, G., Jackson, S.E., McLean, N.M., Paton, C., Pearson, N.J., Sircombe, K., Sylvester, P., Vermeesch, P., Bowring, J.F., Condon, D.J. and Schoene, B. (2016), Community-Derived Standards for LA-ICP-MS U-(Th)Pb Geochronology – Uncertainty Propagation, Age Interpretation and Data Reporting. Geostand Geoanal Res, 40: 311-332. Jackson, S.E., Pearson, N.J., Griffin, W.L., Belousova, E.A., 2004. The application of laser ablation-inductively coupled plasma-mass spectrometry to to in situ U-Pb zircon geochronology. Chemical Geology 211, 47–69. Ludwig, K.R., 2008. User's manual for Isoplot 3.70: a geochronological toolkit for Microsoft Excel. Berkeley Geochronological Center, Special Publication 4, 1–76. Paton, C., Woodhead, J.D., Hellstrom, J.C., Hergt, J.M., Greig, A., Maas, R., 2010. Improved laser ablation u-pb zircon geochronology through robust downhole fractionation correction. Geochemistry Geophysics Geosystems, 11. Petrus, J.A., Kamber, B.S., 2012. VizualAge: A Novel Approach to Laser Ablation ICP-MS U-Pb Geochronology Data Reduction. Geostand. Geoanal. Res. 36, 247–270. Sláma, J., Kosler, J., Condon, D.J., Crowley, J.L., Gerdes, A., Hanchar, J.M., Horstwood, M.S.A., Morris, G.A., Nasdala, L., Norberg, N., Schaltegger, U., Schoene, B., Tubrett, M.N., Whitehouse, M.J., 2008. Plesovice zircon – a new natural reference material for U-Pb and Hf isotopic microanalysis. Chemical Geology 249, 1–35. Tunheng, A., Hirata, T., 2004. Development of signal smoothing device for precise elemental analysis using laser ablation-ICP-mass spectrometry. Journal of Analytical Atomic Spectrometry 19, 932. Wiedenbeck, M., Alle, P., Corfu, F., Griffin, W.L., Meier, M., Oberli, F., Vonquadt, A., Roddick, J.C., Speigel, W., 1995. 3 natural zircon standards for U-Th-Pb, Lu-Hf, trace-element and REE analyses. Geostandards Newsletter, 19, 1–23.

Tabela S4. Dados de geoquímica das amostras discutidas no artigo.

Complex	Passo Feio Complex				Porongos Complex – Eastern Region							
Sample name	MF-176A	MF-176B	MF-174A	MF-175A	MAB 05 A	MAB 09 C	MAB 10 A	MAB 18 A	MAB 30 A	PP 026 C	PP 027 A	TM 27 A
SiO2	55.03	55.12	68.36	72.54	68.05	67.00	68.11	67.78	69.38	69.71	69.58	69.18
TiO2	1.22	1.32	0.48	0.16	0.707	0.667	0.676	0.61	0.637	0.627	0.652	0.654
Al2O3	16.69	15.38	15.66	14.84	14.03	13.8	13.02	12.73	13.68	14.03	12.58	13.97
Fe2O3T	7.33	8.51	2.78	1.54	5.48	5.49	5.51	5.7	5	4.81	5.71	5.21
MnO	0.09	0.11	0.04	0.02	0.098	0.107	0.105	0.113	0.084	0.087	0.11	0.089
MgO	4.14	4.47	1.17	0.63	2.1	2.26	2.23	2.06	1.74	1.83	2.03	1.91
CaO	5.58	5.42	2.71	0.50	2.99	2.96	3.77	2.04	3.22	3.43	3.09	2.75
Na2O	6.16	6.14	4.46	6.75	2.59	2.57	1.6	2.44	2.06	2.03	2.26	2.46
K2O	1.29	1.20	2.80	1.39	3.07	2.88	2.53	3.19	2.87	2.41	2.73	2.49
P2O5	0.57	0.58	0.14	0.07	0.09	0.09	0.09	0.12	0.12	0.12	0.11	0.12
LOI	1.4	1.3	1.1	1.3	1.02	2.02	2.29	2.62	1.21	1.09	1.23	1.36
Total	99.64	99.68	99.85	99.92	100.2	99.86	99.94	99.41	99.99	100.2	100.1	100.2
Sc	16	17	4	2	16	18	18	16	15	15	20	17
Be					3	2	2	4	3	3	2	3
V	155	164	33	21	89	92	93	86	83	76	97	87
Ba	950	911	1735	1370	625	591	481	757	562	534	634	673
Sr	1194.4	743.4	633.8	407.5	149	109	150	532	175	164	129	151
Y	25.2	26.9	8.4	4.3	26	27	24	25	29	28	25	25
Zr	302.3	329.7	151.3	79.4	213	206	199	197	212	216	201	222
La	69.2	72.2	46.5	19.7	34	30.2	28	27.7	34.8	35	26.8	32.2
Ce	136.7	143.0	76.3	34.7	70.4	62.2	57	57.5	71.5	72.4	55.8	66.9
Pr	15.61	16.58	7.59	3.40	8	7.02	6.55	6.56	8.29	8.29	6.41	7.58
Nd	59.9	64.1	24.9	11.7	29.7	26.6	24.4	25.2	30.7	30.7	24.2	28.9
Sm	10.55	11.54	3.43	1.80	5.6	5.2	4.8	5.1	6	6.1	4.9	5.5
Eu	2.28	2.23	0.93	0.51	1.1	1.1	1.02	1.03	1.12	1.13	1.06	1.17
Gd	7.89	8.64	2.42	1.30	4.9	4.5	4.3	4.6	5.2	5.2	4.5	4.9
Tb	1.01	1.04	0.33	0.15	0.8	0.7	0.7	0.8	0.8	0.8	0.7	0.7
Dy	5.16	5.20	1.68	0.80	4.8	4.5	4.2	4.6	5.1	4.9	4.5	4.5
Ho	0.93	0.93	0.29	0.15	1	0.9	0.8	0.9	1	1	0.9	0.9
Er	2.60	2.62	0.81	0.33	2.8	2.7	2.5	2.6	2.9	2.9	2.7	2.7
Tm	0.32	0.33	0.12	0.06	0.42	0.4	0.38	0.4	0.43	0.42	0.42	0.39
Yb	2.11	2.24	0.71	0.41	2.7	2.8	2.6	2.7	3	2.9	2.8	2.8
Lu	0.33	0.32	0.11	0.05	0.44	0.42	0.41	0.42	0.47	0.45	0.43	0.45
Hf	7.7	8.3	3.9	2.2	5.5	5.2	5	5	5.1	5.5	5.1	5.5
Ta	0.9	1.0	0.8	0.7	0.9	0.7	0.7	0.7	0.8	0.8	0.7	0.7
W	-	-	-	-	< 1	2	< 1	< 1	< 1	< 1	< 1	< 1
Pb	-	-	-	-	16	14	14	43	19	18	15	18
Th	19.5	21.3	9.6	4.7	12.3	9.5	8.4	10.4	12.5	12.9	8.2	11.4
U	7.0	7.5	1.4	1.5	3.1	2.4	2.1	2.5	3	3.3	2.1	2.8
Co	28.1	28.4	6.8	5.1	12	12	13	12	11	11	13	12
Ni	35	49	<20	<20	20	< 20	20	< 20	20	20	< 20	20
Cu	35	49	<20	<20	20	10	20	20	30	20	20	10
Zn	29.6	10.6	1.7	4.9	70	70	70	100	60	60	80	70
Ga	19.6	17.6	13.7	11.7	16	16	14	15	16	16	15	16
Rb	46.3	41.1	39.1	15.2	136	103	91	135	130	120	109	101
Nb	16.5	18.5	17.7	10.3	10	8	8	9	9	9	9	9
Cs	0.9	0.8	0.7	<0.1	4.5	1.9	1.9	4	5.2	4.5	4.9	4.5
Cr					50	40	40	40	40	40	30	40
Geochemical Pattern*	2	2	3	3	1	1	1	1	1	1	1	1
Igneous age (Ma)	580 ± 2	580 ± 1	uncertain	uncertain	-	-	-	-	-	-	-	-
Reference		This paper						Battisti et al (2018)				

Complex	Porongos Complex – Eastern Region				TM-015A	Porongos Complex – Western Region						
Sample name	TM-026C	MAB-08A	BR-143/1	BR-145/1	TM-015A	PM-01-1	PM-06	PM-19	PM-28	PM-31B	PM-33	PM-34
SiO2	70.42	62.68	64.03	63.41	71.74	75.03	71.65	67.73	68.06	72.50	70.67	70.95
TiO2	0.43	0.93	0.82	0.78	0.44	0.198	0.461	0.569	0.512	0.428	0.31	0.399
Al2O3	13.62	14.32	16.34	14.51	13.99	12.88	13.27	15.27	13.84	13.07	14.28	14.14
Fe2O3T	4.13	6.76	6.42	6.1	3.36	1.01	3.61	3.97	4.53	3.21	2.64	2.79
MnO	0.06	0.1	0.14	0.1	0.07	0.008	0.046	0.078	0.059	0.024	0.046	0.049
MgO	1.25	3.13	2.09	2.52	0.73	0.4	0.58	1.32	2.26	1.28	0.49	0.56
CaO	2.18	3.27	0.89	3.61	1.44	0.06	1.66	1.9	1.93	0.14	1.07	0.89
Na2O	2.69	2.44	1.35	2.08	3.23	0.43	2.95	4.81	3.7	0.31	3.21	2.53
K2O	3.23	4.4	3.83	3.41	3.4	7.8	3.77	2.49	2.06	7.37	4.75	5.18
P2O5	0.06	0.26	0.12	0.2	0.1	0.06	0.17	0.17	0.07	0.12	0.11	0.1
LOI	1.7	1.4	0.01	0.02	1.3	1.67	1.15	1.45	1.81	1.83	1.23	1.38
Total	99.8	99.8	99.37	99.11	99.76	99.55	99.29	99.76	98.82	100.3	98.81	98.98
Sc	12	18	16.3	17.6	7	-	-	-	-	-	-	-
Be	3	<1			6							
V	45	125	92	88	39	13	22	57	59	19	31	33
Ba	728	661	560	832	528	2018	1022	1388	1450	1290	637	686
Sr	167.8	154.8	85	159	150.7	203	168	525	577	71	135	103
Y	26	30.7	27	27	40.3	23	31	14	9	30	42	48
Zr	147.4	303.9	104	85	319.2	177	231	217	136	338	254	295
La	33.5	40.2	43	42	50.7	64.1	33.4	48.1	17.1	49	25.8	62.2
Ce	64.4	87.8	89	89	103.2	129	77	88.4	37.5	105	58.9	123
Pr	7.47	9.8	-	-	11.98	12.8	7.43	8.99	3.82	11.3	6.7	14
Nd	27.8	39.6	38	40	43.1	40.7	26.2	30.2	13.6	39.4	24.9	53.8
Sm	5.29	7.92	7.6	8	8.3	6.8	5	5.2	2.4	6.9	5.7	11.1
Eu	0.97	1.46	1.2	1.2	1.13	1.21	0.94	1.41	0.75	1.08	0.8	1.38
Gd	4.64	6.54	-	-	7.55	5.6	4.6	4	1.9	5.7	5.5	10.5
Tb	0.69	1.02	1	1	1.11	0.9	0.9	0.6	0.3	0.9	1	1.7
Dy	4.88	5.74	-	-	7.11	4.6	5.6	3.1	1.6	5.4	6.5	9.1
Ho	0.99	1.17	-	-	1.25	0.8	1.2	0.5	0.3	1.1	1.3	1.7
Er	2.46	3.46	-	-	3.69	2.4	3.7	1.6	0.9	3.5	4.2	4.9
Tm	0.4	0.49	-	-	0.54	0.36	0.56	0.23	0.14	0.56	0.68	0.78
Yb	2.51	3.17	4	3	3.65	2.3	3.4	1.5	0.9	3.6	4.4	4.9
Lu	0.38	0.49	0.6	0.4	0.56	0.33	0.48	0.21	0.14	0.55	0.66	0.71
Hf	4.3	7.5	6	5.9	9.1	4.1	6.5	5.7	3.4	8.9	7.5	9
Ta	0.5	1.2	-	-	1.3	0.3	0.3	0.9	0.7	1.2	1.8	1.6
W	-	1.5	-	-	-	-	-	-	-	-	-	-
Pb	3.4	4.5	16	31	8.2	90	112	95	121	138	216	151
Th	10.8	19.9	16	21	23.6	19.9	9.8	9.1	5.8	21.1	16.5	20.1
U	2.5	5.9	4	5	5	1.7	0.6	0.8	0.5	3.2	5.1	4.5
Co	10.3	17.9	27	22	5.8	2	8	10	19	6	4	6
Ni	8.6	24	35	25	56.2	<20	70	30	120	<20	<20	60
Cu	15.7	47.1	26	23	10.6	<10	50	20	20	20	10	20
Zn	47	78	58	109	56	<30	40	50	60	50	70	60
Ga	14.4	16.8	12	-	18.9	-	-	-	-	-	-	-
Rb	116.1	221	-	-	179.5	167	91	60	66	195	217	226
Nb	7.7	7.5	15	16	17.3	7	7	14	11	17	15	19
Cs	3.6	7.7	-	-	13.8	1.4	0.7	1.2	2	2.7	10.4	9.7
Cr	50	-	42	48	40	<20	20	40	260	<20	<20	20
Geochemical Pattern*	1	1	1	1	1	1	1	2	2	1	1	1
Igneous age	788 ± 5	-		789 ± 7		uncertain	uncertain	uncertain	uncertain	uncertain	uncertain	uncertain
Reference	Battisti el al. (2018, 2020)		Sallmann et al (2005, 2011)		Martil et al (2017)	Gollmann et al (2008)						

| Complex | Porongos Complex – Western Region | | | | | | | Várzea do Capivarita Complex | | | | |
Sample name	PM-36A	PM-37	PM-38	K-04C	K-05A	K-10-1	MAB59A	TM 01 E	TM 12 E	TM-13E	TM 29B	TM 35 A
SiO2	65.83	60.59	69.42	56.49	63.07	72.43	52.40	68.28	69.38	65.93	69.55	65.48
TiO2	0.605	0.845	0.553	1.46	0.54	0.476	1.23	0.535	0.587	0.77	0.53	0.76
Al2O3	15.7	16.85	14.9	15.63	17.59	13.42	13.36	14.99	13.43	13.96	13.63	14.51
Fe2O3T	4.68	7.39	3.81	8.66	6.36	2.82	11.73	5.02	4.75	6.83	3.82	6.01
MnO	0.112	0.159	0.056	0.14	0.04	0.055	0.28	0.09	0.08	0.1	0.05	0.11
MgO	1.72	3.17	0.78	4	2.61	0.7	6.41	1.67	1.72	2.07	0.97	2.14
CaO	1.16	1.47	0.44	3.29	0.43	0.86	1.66	4.22	3.78	3.61	2.51	3.23
Na2O	2.8	1.98	2.73	2.57	4.44	2.99	3.37	3.04	2.32	1.97	2.89	2.56
K2O	4.11	3.48	4.34	3.2	2.61	3.72	0.19	1.52	2.3	3.63	3.63	3.41
P2O5	0.22	0.24	0.13	0.29	0.21	0.12	0.24	0.1	0.1	0.13	0.12	0.14
LOI	1.81	2.81	2.32	3.96	0.9	1.89	0.24	1.35	1.93	0.8	1.16	0.95
Total	98.75	99	99.48	98.7	100.4	99.48	98.31	100.8	100.4	99.77	98.85	99.31
Sc	-	-	-	-	-	-	29	16	16	18	12	18
Be	-	-	-	-	-	-	1	4	4	3	3	3
V	76	114	51	152	-	39	222	78	81	89	61	89
Ba	1032	997	609	662	-	540	102	427	516	846	1310	796
Sr	411	259	135	397.1	178	138	91	145	177	186.3	372	216
Y	32	31	33	32.1	23.7	42	19	22	18	13.4	14	22
Zr	204	209	236	186.8	123.9	302	99	201	211	257.2	229	211
La	50.9	50	41	37.5	30.5	59.3	20.6	26.2	28.3	39.7	52.7	33.9
Ce	102	100	94.1	78.4	59.4	104	40.8	53.7	56.5	65.3	103	69.9
Pr	11.2	11.4	10.5	9.23	6.89	13.6	4.83	6.65	6.96	7.44	12	8.5
Nd	40.9	42.5	38.3	34.9	26	47.9	20.1	21.8	23	27.7	38	27.6
Sm	7.7	8.1	7.8	7.1	4.5	9.7	4.2	4.5	4.4	4.16	6.2	5.5
Eu	1.33	1.69	1.11	1.68	1.33	1.3	1.35	1.03	1.02	1.35	1.32	1.45
Gd	6.5	6.9	6.6	6.3	3.7	9.2	3.8	3.8	3.6	3.17	4.3	4.4
Tb	1	1.1	1.1	1	0.5	1.4	0.6	0.7	0.6	0.4	0.6	0.7
Dy	5.7	5.9	6.5	5.6	2.4	7.2	3.5	3.9	3.2	2.41	3.1	4
Ho	1.1	1.1	1.2	1.1	0.4	1.3	0.7	0.7	0.7	0.42	0.5	0.8
Er	3.2	3.3	3.8	3.2	1.2	3.9	2	2.8	2	1.63	1.4	2.5
Tm	0.52	0.52	0.61	0.48	0.17	0.6	0.26	0.42	0.29	0.19	0.19	0.38
Yb	3.3	3.3	4	3.1	1.1	3.9	1.6	2.7	2	1.71	1.2	2.5
Lu	0.46	0.46	0.59	0.45	0.16	0.55	0.25	0.41	0.31	0.23	0.17	0.38
Hf	5.9	5.8	7.5	4.9	3.2	8.6	2.6	5.8	6.4	6.6	7.1	6.8
Ta	1.4	1.5	1.7	1.8	0.5	1.6	1.6	0.7	0.7	1	0.4	0.6
W	-	-	-	-	-	-	<1	-	-	-	-	-
Pb	188	166	205	-	-	189	6	14	13	7.3	24	28
Th	17.4	14.3	20.6	9.8	1.9	21.9	2.2	7.4	9.3	12.9	14.9	94
U	4.8	3.7	2.5	-	-	5.5	0.6	0.9	1.4	1.1	0.9	1.9
Co	14	27	9	24	18	7	49	10	7	13.7	5	12
Ni	30	100	<20	60	26	<20	220	< 20	< 20	<20	< 20	< 20
Cu	30	40	30	30	12	20	<10	10	10	74.6	30	20
Zn	80	100	110	69	66	80	90	90	60	76	60	110
Ga	-	-	-	-	-	-	14	17	17	17.1	18	20
Rb	166	136	216	101.9	92.6	205	6	114	102	135.2	114	140
Nb	18	20	21	18.9	6	19	29	8	9	15.6	8	13
Cs	7.4	7.5	7.1	7.2	-	-	0.6	13	4.1	5.1	2.1	9.9
Cr	60	160	40	95	43	30	560	40	40	-	< 20	50
Geochemical Pattern*	1	1	1	1	2	1	Individual	1	1	1	1	1
Igneous age	uncertain	uncertain	uncertain	uncertain	uncertain	uncertain	600 Ma	791 ± 30	-	-	-	-
Reference	Gollmann et al (2008)						This paper	Martil et al (2017)				

Complex						Várzea do Capivarita						
Sample name	TM 35 B	TM 36 G	TM 36 J	TM 38 A	TM 39 A	MN 155 G	TM 34 A	TM 60 A	TM 66 B	TM 38 C	TM 67 A	TM 51 A
SiO2	63.8	61.69	67.08	65.16	73.49	69.97	66.27	65.7	61.87	65.49	70.3	65.41
TiO2	0.781	0.816	0.64	0.707	0.388	0.541	0.76	0.73	0.82	0.72	0.54	0.62
Al2O3	14.13	16.42	15.62	14.76	12.13	13.35	14.03	14.10	16.41	14.31	13.47	14.97
Fe2O3T	6.65	7.26	5.24	6.32	3.21	4.02	5.63	5.86	6.36	6.23	4.19	6.24
MnO	0.12	0.10	0.08	0.11	0.06	0.06	0.09	0.10	0.11	0.12	0.05	0.12
MgO	2.57	2.07	1.47	2.14	0.95	1.46	2.13	2.29	2.18	2.51	1.39	2.65
CaO	3.63	5.17	4.67	4.4	2.43	2.67	2.94	3.82	3.90	3.53	4.16	4.36
Na2O	2.77	2.92	2.9	2.3	2.65	2.67	2.17	2.26	3.01	2.33	2.06	1.77
K2O	1.66	1.65	1.13	2.59	2.38	3.66	4.07	2.91	2.89	3.27	1.88	2.09
P2O5	0.1	0.15	0.12	0.11	0.09	0.11	0.14	0.12	0.14	0.12	0.10	0.09
LOI	2.5	0.95	1.31	0.98	2.28	1.37	1.5	1.9	2.1	1.1	1.6	1.5
Total	98.72	99.2	100.3	99.58	100.1	99.87	99.73	99.79	99.79	99.77	99.77	99.82
Sc	19	24	19	20	9	9	16	17	19	19	14	19
Be	5	5	3	3	3	9	4	3	5	3	<1	2
V	115	105	78	100	32	62	90	96	105	102	72	96
Ba	408	432	508	736	657	937	996	762	899	889	630	489
Sr	351	199	154	265	121	318	348.4	290.4	264.0	197.9	190.9	155.0
Y	17	22	28	10	27	12	18.4	15.9	19.9	15.8	13.0	23.5
Zr	209	329	191	198	206	188	349.2	244.5	261.0	208.4	182.2	165.9
La	28.3	22.3	27.7	22.7	29.8	43.4	36.4	36.7	37.5	31.5	29.5	25.5
Ce	58.3	44.2	57.5	44.2	60.8	74.9	75.3	77.1	83.8	67.6	59.9	55.0
Pr	7.25	5.78	7.27	5.24	7.47	8.13	8.07	8.20	8.85	7.64	6.63	6.11
Nd	24.3	19.9	24.5	17.1	25.1	23.3	30.9	31.2	33.5	28.5	25.1	23.5
Sm	4.8	4.1	5	3.1	4.9	3.8	5.22	4.84	5.82	5.33	4.49	4.41
Eu	1.14	1.09	1.07	1.24	0.81	0.99	1.34	1.20	1.15	1.38	1.09	0.96
Gd	3.8	3.7	4.5	2.3	4.3	2.5	4.25	3.67	4.71	4.07	3.50	3.99
Tb	0.6	0.6	0.9	0.4	0.8	0.4	0.62	0.52	0.69	0.64	0.50	0.67
Dy	3	3.6	4.9	2	4.4	2.3	3.25	2.88	3.71	3.27	2.76	4.01
Ho	0.6	0.7	1	0.4	0.9	0.4	0.64	0.57	0.71	0.59	0.48	0.85
Er	1.7	2.2	3	1.3	2.8	1.3	1.85	1.68	1.95	1.92	1.51	2.47
Tm	0.26	0.35	0.47	0.21	0.46	0.19	0.29	0.29	0.33	0.28	0.22	0.39
Yb	1.7	2.2	3	1.5	2.7	1.2	1.81	1.83	2.07	1.67	1.29	2.45
Lu	0.27	0.35	0.45	0.24	0.4	0.18	0.28	0.29	0.34	0.30	0.22	0.37
Hf	6.6	9.2	5.9	6	6.5	5.8	9.2	6.6	7.1	6.3	4.9	4.6
Ta	0.9	0.8	0.7	0.5	0.7	1.5	0.8	0.9	1.3	0.8	0.5	0.7
W	-											
Pb	23	12	14	16	15	30	8.2	8.2	9.0	10.5	7.1	6.4
Th	14.2	6.1	9.5	3.9	11.6	32.9	14.1	10.8	12.5	14.8	9.8	8.8
U	1.1	0.9	1.3	0.6	2.4	8.9	2.4	2.1	2.1	1.5	1.3	2.1
Co	14	10	7	11	4	6	13.8	14.3	14.8	17.9	12.1	15.8
Ni	< 20	< 20	< 20	< 20	< 20	< 20	18.1	18.3	13.5	19.9	11.1	15.9
Cu	40	40	10	10	< 10	20	24.7	22.1	18.0	19.0	67.7	25.8
Zn	110	120	80	70	70	70	65	62	84	45	31	64
Ga	21	22	20	18	16	20	16.2	16.0	18.1	17.0	15.8	14.7
Rb	92	137	107	106	117	230	178.4	124.8	188.1	136.9	94.0	167.7
Nb	15	11	9	9	8	19	14.4	15.1	14.3	11.3	7.8	9.0
Cs	6	27.8	19.2	4.9	6.6	14.6	7.0	8.2	11.3	5.4	5.0	14.3
Cr	90	30	20	40	< 20	30	5	5	4	62	41	5
Geochemical Pattern*	1	1	1	1	1	1	1	1	1	1	1	1
Igneous age	-	-	-	-	-	-	-	-	-	-	-	-
Reference						Martil el al (2017)						

Sample name	Várzea do Capivarita Complex						
	TM 45 B	TM 45 C	TM 45 E	TM 45 G	TM 45 H	TM 45 I	TM 69 A
SiO2	72.75	72.91	75.53	72.95	72.43	72.75	65.95
TiO2	0.33	0.33	0.12	0.31	0.34	0.3	0.62
Al2O3	14.02	13.7	13.07	13.88	13.71	14.01	14.43
Fe2O3T	2.68	2.93	1.86	2.68	2.88	2.63	6.2
MnO	0.05	0.06	0.06	0.06	0.06	0.05	0.11
MgO	1.00	1.08	0.27	0.95	1.06	0.93	3.1
CaO	3.24	2.78	1.59	3.09	2.93	2.94	4.41
Na2O	2.99	3.26	3.64	2.67	2.89	3.2	1.31
K2O	1.92	1.9	2.82	2.39	2.3	2.1	2.27
P2O5	0.07	0.08	0.05	0.06	0.08	0.06	0.09
LOI	0.8	0.8	0.9	0.8	1.2	0.9	1.3
Total	99.85	99.87	99.88	99.86	99.87	99.87	99.83
Sc	9	10	8	9	9	9	19
Be	2	3	4	2	6	2	3
V	35	41	9	36	42	36	101
Ba	709	400	625	610	492	553	457
Sr	145.0	135.7	169.1	131.5	117.4	131.2	136.5
Y	20.5	34	29.5	27.4	27.4	26.7	20.5
Zr	151.9	170.8	109.5	135.6	147.2	151.5	164.8
La	30.1	42.3	30	33	32.4	30.5	24.9
Ce	65.0	89.5	64.8	65.4	65.1	62.9	52.4
Pr	6.87	10.25	7.57	7.61	7.45	7.42	5.91
Nd	25.9	38.6	29.6	28.7	29.8	28.4	25.2
Sm	4.54	7.2	6.26	5.39	5.36	5.42	4.47
Eu	0.87	0.83	0.87	0.96	0.78	0.86	0.95
Gd	3.94	5.95	5.42	4.49	4.8	4.7	3.74
Tb	0.65	1.03	0.89	0.8	0.83	0.82	0.63
Dy	3.61	6.59	5.95	4.84	5.08	5.08	4.06
Ho	0.72	1.24	1.07	0.93	0.92	0.98	0.74
Er	2.19	3.91	3.97	3.08	3.12	2.9	2.38
Tm	0.34	0.59	0.56	0.46	0.45	0.46	0.38
Yb	2.08	3.46	3.3	2.84	2.73	2.97	2.35
Lu	0.31	0.54	0.55	0.43	0.44	0.49	0.4
Hf	4.1	5.3	4	4.5	4.9	4.9	4.4
Ta	0.7	1	0.6	0.8	1.1	0.7	0.7
W							
Pb	3.3	3.1	4.9	3	3.5	3.8	10.2
Th	11.5	19	11.9	12.7	12.8	12.4	8.7
U	2.6	3.8	2.2	2.6	3.1	3.3	1.8
Co	5.5	6.3	1.5	5.6	6.8	5.5	17
Ni	5.9	8	0.8	6.3	7.5	6.4	18.7
Cu	19.8	2.8	1.6	4.4	8.7	2.4	9.1
Zn	37	42	37	37	50	40	64
Ga	14.1	17.1	16.6	15.9	16.7	15.5	16.8
Rb	147.5	129.1	116.5	157.1	166.3	157.6	134.9
Nb	8.8	9.7	8.2	8.3	9.7	7.7	8.8
Cs	7.6	7.9	2.8	13.4	9.9	13.2	11.5
Cr	3	27	<13	21	27	21	68
Geochemical Pattern*	1	1	1	1	1	1	1
Igneous age	-	-	-	789 ± 7	-	-	-
Reference				Martil el al (2017)			

Tabela S5. Dados isotópicos de Rb-Sr e Sm-Nd originais das amostras discutidas nesse artigo.

Ref	Complex	Sample name	Sm (ppm)	Nd (ppm)	147Sm/144Nd	143Nd/144Nd	Error (ppm)	eNd	Age	eNd(t)	TDM (Ma)	143Nd/144Nd (t)	Rb (ppm)	Sr (ppm)	Rb/Sr	87Rb/86Sr	Error (SD abs)	87Sr/86Sr (present)	Error (SD Abs)	Age	87Sr/86Sr(t)
GROUP 1																					
This paper		MAB 05 A	6	30	0.1139	0.51172	5.86624E-06	-17.9	790	-9.5	2019	0.51113	136	149	0.91	2.6539		0.75479	0.000007	790	0.72485
This paper		MAB 09 C	5	28	0.1161	0.51171	5.53168E-06	-18.1	790	-9.9	2080	0.51111	103	109	0.94	2.7494		0.76148	0.000007	790	0.73046
Martil et al. 2017		TM-026C	7	42	0.1011	0.51171	0.000009	-18.2	790	-8.5	1796	0.51118	116	168	0.69	0.6919		0.74515	0.00001	790	0.72248
Saalmann et al. 2006		BR-143/1	7	34	0.1190	0.51189	15	-14.6	780	-6.9	1846		175	127	1.38	4.0371	0.002873	0.75583	0.000096	780	0.71090
Saalmann et al. 2006		BR-152/1	4	26	0.1052	0.51111	14	-29.7	780	-20.6	2710		184	106	1.73	1.6293	0.16293	0.74253	0.000224	780	0.72440
Saalmann et al. 2006		BR-152/2	3	22	0.0908	0.51099	14	-32.3	780	-21.7	2547		61	237	0.26	0.7270	0.072699	0.72337	0.0008	780	0.71530
This paper		TM-015A	9	44	0.1202	0.51192	0.000006	-13.9	790	-6.2	1822	0.51130	180	151	1.19	3.4608		0.74738	0.000007	790	0.70833
Gollmann et al. 2008	Porongos	PM-01-1	7	41	0.0960	0.51103		-31.2	770	-21.3	2593	0.51055									
Gollmann et al. 2008		PM-06	5	26	0.1096	0.51144		-23.2	770	-14.7	2330	0.51089									
Gollmann et al. 2008		PM-31B	7	39	0.1074	0.51132		-25.7	770	-16.9	2463	0.51078									
Gollmann et al. 2008		PM-33	6	25	0.1377	0.51218		-8.8	770	-3.0	1703	0.51149									
Gollmann et al. 2008		PM-34	11	54	0.1239	0.51215		-9.7	770	-2.5	1519	0.51152									
Gollmann et al. 2008		PM-36A	8	41	0.1112	0.51179		-16.5	770	-8.1	1847	0.51123									
Gollmann et al. 2008		PM-38	8	38	0.1216	0.51204		-11.6	770	-4.2	1643	0.51143									
Gollmann et al. 2008		K-10-1	10	48	0.1175	0.51203		-11.9	770	-4.1	1594	0.51144									
Gollmann et al. 2008		PM-37	8	43	0.1153	0.51192		-13.9	770	-5.9	1719	0.51134									
Gollmann et al. 2008		K-04C	7	35	0.1184	0.51223		-10.6	770	-4.6	1508	0.51163									
Martil et al. 2017	Várzea do Capivarita	TM 01 E	4	23	0.1158	0.51185	0.000007	-15.4	790	-7.2	1841	0.51110	111	136	0.81	0.8116		0.74287	0.000016	790	0.71628
Martil et al. 2017		TM 29B	7	43	0.1027	0.51170	0.000009	-18.4	790	-8.9	1834	0.51114	98	346	0.28	0.2832		0.73428	0.000009	790	0.72501
Martil et al. 2017		TM 35 A	5	23	0.1320	0.51190	0.000006	-14.2	790	-7.9	2120	0.51122	148	204	0.73	0.2832		0.74776	0.00001	790	0.72364
Martil et al. 2017		TM 35 B	5	28	0.1144	0.51170	0.000007	-18.4	790	-10.1	2052	0.51117	82	334	0.25	0.2471		0.73140	0.000013	790	0.72332
Martil et al. 2017		TM 36 G	5	22	0.1312	0.51180	0.00001	-16.4	790	-9.8	2287	0.51112	131	187	0.70	0.7028		0.74000	0.000014	790	0.71698
Martil et al. 2017		TM 45 B	5	27	0.1047	0.51166	0.000013	-19.1	790	-9.8	1920	0.51125	134	134	1.00	0.9998		0.75670	0.000011	790	0.72390
Martil et al. 2017		TM 45 C	7	35	0.1124	0.51176	0.000009	-17.1	790	-8.6	1916	0.51176	120	116	1.03	1.0289		0.75885	0.000016	790	0.72509
Martil et al. 2017		TM 45 G	6	29	0.1226	0.51179	0.000015	-16.6	790	-9.1	2087	0.51115	159	143	1.11	1.1095		0.75993	0.000007	790	0.72352
Martil et al. 2017		TM 45 H	6	33	0.1105	0.51171	0.000012	-18.1	790	-9.8	1956	0.51112	166	108	1.54	1.5380		0.76886	0.000012	790	0.71834
GROUP 2																					
This Paper	Passo Feio	MF-174A	2	13	0.0856	0.51172	8	-17.9	580	-9.8	1570	0.51139	39	634	0.06	0.1780	0.02 (%)	0.70498	0.001 (%)	580	0.70351
This Paper		MF-175A	4	27	0.0780	0.51165	15	-19.2	580	-10.4	1553	0.51136	15	408	0.04	0.1064	0.01 (%)	0.70501	0.0016 (%)	580	0.70413
Gollmann et al. 2008	Porongos	PM-19	5	30	0.0967	0.51154		-21.4	770	-11.6	1949	0.51105									
Gollmann et al. 2008		PM-28	2	14	0.1056	0.51164		-19.4	770	-10.4	1959	0.51111									
Gollmann et al. 2008		K-05A	5	26	0.1042	0.51120		-28.0	770	-18.9	2556	0.51068									
GROUP 3																					
This Paper	Passo Feio	MF-176B	12	65	0.1102	0.51220	0.000004	-8.5	580	-2.1	1235	0.51179	41	743	0.06	0.1600		0.70636	0.000006	580	0.70504
Bmvc																					
This Paper	Porongos	MAB59A	4	19	0.1250	0.51242	0.000006	-4.3	600	1.2	1079	0.51193	6	91	0.07	0.1908		0.70810	0.000005	600	0.70647

Dissolution precipitation creep as a process for the strain localisation in mafic rocks

Amicia Lee[1], Holger Stünitz[1, 2], Mathieu Soret[2], Matheus Ariel Battisti[3]

[1]Department of Geosciences, UiT – Arctic University of Norway, Norway
[2]Institut des Sciences de la Terre (ISTO), Université d´Orléans, France
[3]Instituto de Geociências, Universidade Federal do Rio Grande do Sul, Brazil

Abstract

The lower crust is, on average, mafic in composition and composed of minerals that remain mechanically strong up to high temperatures. Here we show that dissolution-precipitation creep (as a type of diffusion creep) plays a major role in deformation of gabbro bodies at upper amphibolite facies conditions. The Kågen gabbro, N. Norway, is comprised of undeformed gabbro lenses enclosed by mylonitised margins that deformed at 690 ± 25 °C and 1.0 to 1.1 GPa. The evolution of the microstructures and fabric of the low strain gabbro to high strain margins were investigated. Original clinopyroxene and plagioclase dissolved during mineral reactions and precipitated as new minerals phases: new plagioclase and clinopyroxene (different compositions relative to the magmatic parents) and additional amphibole and garnet. Microstructural and crystallographic preferred orientation (CPO) data indicate that dissolution-precipitation creep is the dominant deformation mechanism. Amphibole shows a strong CPO that is primarily controlled by orientated growth in the stretching direction. The progression of mineral reactions and weakening is directly connected to a fluid-assisted transformation process that facilitates diffusion creep deformation of strong minerals at far lower stresses and temperatures than required by dislocation creep. Initially strong lithologies can become weak, provided that reactions proceed during deformation.

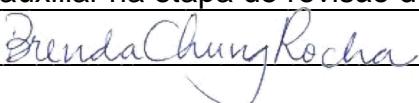| |
|---|
| **ANEXO I** |
| Título da Dissertação/Tese: |
| **"EVOLUÇÃO GEOLÓGICA (800–560 Ma) DO SETOR CENTRAL DO CINTURÃO DOM FELICIANO COM BASE NO ESTUDO PETROLÓGICO, GEOCRONOLÓGICO E DE PROVENIÊNCIA DOS COMPLEXOS PORONGOS, VÁRZEA DO CAPIVARITA E PASSO FEIO, RS"** |
| Área de Concentração: Geoquímica |
| Autor: **Matheus Ariel Battisti** |
| Orientadora: Profa. Dra. Maria de Fátima Bitencourt |
| Examinadora: Profa. Dra. Brenda Chung da Rocha |
| Data: 28/03/22 |
| Conceito: A |
| PARECER:
O presente trabalho teve como objetivo investigar a história evolutiva pré-colisional e colisional do domínio central do Cinturão Dom Feliciano, a partir da relação temporal e espacial dos Complexos Porongos, Várzea do Capivarita e Passo Feio utilizando uma abordagem detalhada com metodologias distintas. A história pré-colisional do Cinturão Dom Feliciano foi investigada a partir de geocronologia U-Pb utilizada para determinar a idade de cristalização magmática de litotipos do Complexo Varzea do Capivarita e Complexo Porongos, e proveniência de rocha metassedimentar do Complexo Varzea do Capivarita e isótopos de oxigênio. A história colisional foi investigada utilizando uma abordagem petrocronológica utilizando datação U-Pb SIMS em monazita, Lu-Hf rocha-total em granada aliada com o cálculo de pseudosseções para delimitar as condições P-T em rochas metassedimentares dos Complexos Porongos e Passo Feio. Dados de geoquímica de rocha-total, isótopos de Sr e Nd e geocronologia U-Pb LA-ICP-MS em zircão em litotipos do Complexo Passo Feio foram utilizados para elucidar questões relacionadas ao ambiente tectônico e estabelecer as possíveis relações entre os complexos Porongos, Varzea do Capivarita e Passo Feio. A presente tese é apresentada na forma de três artigos submetidos a revistas internacionais de grande prestígio na literatura internacional, todas com conceito A1. O trabalho está bem organizado, bem escrito e demonstra bastante maturidade do candidato com relação ao seu tema de pesquisa, e atesta que os objetivos centrais do trabalho foram alcançados com sucesso. Encaminho um pdf comentado da tese, com alguns comentários referentes à apresentação e tratamento dos dados, que podem influenciar na interpretação de parte dos dados petrológicos e geocronológicos, e que podem auxiliar na etapa de revisão dos artigos submetidos. |
| Assinatura: *Brenda Chung Rocha*   Data:28/03/22 |

Ciente do Orientador:

Ciente do Aluno:

ANEXO I
Título da Dissertação/Tese:
"EVOLUÇÃO GEOLÓGICA (800–560 Ma) DO SETOR CENTRAL DO CINTURÃO DOM FELICIANO COM BASE NO ESTUDO PETROLÓGICO, GEOCRONOLÓGICO E DE PROVENIÊNCIA DOS COMPLEXOS PORONGOS, VÁRZEA DO CAPIVARITA E PASSO FEIO, RS"
Área de Concentração: Geoquímica
Autor: **Matheus Ariel Battisti**
Orientadora: Profa. Dra. Maria de Fátima Bitencourt
Examinadora: Profa. Dra. Cristine Lenz
Data: 29/03/2022
Conceito: A

PARECER:

A tese de doutorado do aluno Matheus Ariel Battisti é constituída de 3 artigos submetidos em revistas internacionais, com resultados inéditos sobre rochas da região central e oeste do CDF. Os três artigos estão muito bem organizados, com descrições detalhadas e interpretações pertinentes.

Algumas questões ficaram em aberto e devem ser revisadas, tais como: empilhamento vertical do CVC sob o CP implicaria em idades um pouco mais antigas do CVC, considerando que ele também apresenta evidencias de magmatismo sin-sedimentação, considero mais adequado colocá-lo lado a lado durante o evento sedimentar. Revisar ao longo do texto a localização das unidades segundo a subdivisão do CDF (ex: CVC seria Domínio Central ou Leste?, no artigo 3 até o CPF acabou entrando no central). Rever a aplicabilidade do conceito de *Hinterland* e *Foreland*. Avaliar se o magmatismo tem características de magmatismo Adakitico, caso contrário indicar a fusão proveniente da cunha do manto astenosférico (Figuras dos modelos geológicos). Sugiro fundir o texto do Lu-Hf em granada+elementos traços com o texto sobre a monazita (Artigo 2) para viabilizar as *plates* com informações de ambos os temas. No mesmo artigo, colocar metodologia utilizada nas análises Lu-Hf em granada. No artigo 3, fazer um teste com amostras com menor % de sílica possível, para posterior comparação entre elas. Sugiro normalizar os dados do diagrama multielementar para manto primitivo, o que facilita a comparação quando se trabalha com ambientes tectônicos diferentes. No diagrama Harker, não vejo necessidade de relacionar a cor com a quantidade de SiO2, considerando que essa informação já consta no eixo x. Na figura 14 do terceiro artigo, sugiro substituir pré-orogênico por pré-colisional e adicionar a informação no texto de qual arco estaria relacionado ao *back arc* (*ca. 600-580 Ma magmatism*).

Por fim, gostaria de enfatizar que o trabalho adiciona novos e importantes dados para distintos eventos geológicos que ocorreram ao longo de paleobacias da região central e oeste do CDF e seus magmas associados. Esses dados serão essenciais para a evolução dos conhecimentos acerto da história geológica do

CDF no RS.

Assinatura: Cristine Lenz

Data:29/03/2022

Ciente do Orientador:

Ciente do Aluno:

ANEXO I	
Título da Dissertação/Tese:	
"EVOLUÇÃO GEOLÓGICA (800–560 Ma) DO SETOR CENTRAL DO CINTURÃO DOM FELICIANO COM BASE NO ESTUDO PETROLÓGICO, GEOCRONOLÓGICO E DE PROVENIÊNCIA DOS COMPLEXOS PORONGOS, VÁRZEA DO CAPIVARITA E PASSO FEIO, RS"	
Área de Concentração: Geoquímica	
Autor: **Matheus Ariel Battisti**	
Orientadora: Profa. Dra. Maria de Fátima Bitencourt	
Examinador: Prof. Dr. Sebástian Oriolo	
Data: 24/03/2022	
Conceito: A (EXCELENTE)	
PARECER: The thesis of Matheus Ariel Battisti is well-written and organized, and presents a novel and large database of analytical data focused on petrological, geochemical and petrochronological constraints on the Neoproterozoic evolution of the central Dom Feliciano Belt. The quality of the data and their analysis is thoroughful, particularly when integrating new data with those of the literature. As far as I'm concerned, the outcomes of the geochronological (U-Pb zircon) and coupled thermobarometric-petrochronological data (P-T-t) are particularly relevant, since they reveal the existence of multiple tectonometamorphic and magmatic events in the Dom Feliciano Belt. Based on all aforementioned aspects, I consider this work as highly outstading.	
Assinatura: Data: 24/03/2022	
Ciente do Orientador:	
Ciente do Aluno:	